Universitat de Girona

SERVICEABILITY BEHAVIOUR OF FIBRE REINFORCED POLYMER REINFORCED CONCRETE BEAMS

Cristina BARRIS PEÑA

Universitat de Girona

PhD Thesis

Serviceability behaviour of fibre reinforced polymer reinforced concrete beams

Cristina Barris Peña

2010

Universitat de Girona

PhD Thesis

Serviceability behaviour of fibre reinforced polymer reinforced concrete beams

Cristina Barris Peña

2010

Technology Doctorate Program

Thesis Supervisor

Dr. Lluís Torres Llinàs

A thesis submitted for the degree of Doctor of Philosophy by the University of Girona

To whom it might concern,

Dr. Lluís Torres Llinàs, Professor of the Department of Mechanical Engineering and Industrial Construction at the University of Girona,

CERTIFIES that the study entitled 'Serviceability behaviour of fibre reinforced polymer reinforced concrete beams' has been carried out under his supervision by Cristina Barris Peña to obtain the doctoral degree with the European mention.

Girona, October 2010.

Dr. Lluís Torres Llinàs

A la meva filla Sara,

Sigues lliure i camina cap a l'estel
que vulguis guanyar

Abstract

Corrosion of steel reinforcement in aggressive environments can cause considerable damage in reinforced concrete (RC) structures. Fibre reinforced polymer (FRP) bars have emerged as an alternative to steel for RC elements subjected to those environments, due to their non-corrosive properties. The mechanical properties of FRP bars can yield to large crack widths and deflections. As a result, the design of concrete elements reinforced with FRP materials is often governed by the serviceability limit states (SLS).

This study investigates the short-term serviceability behaviour of FRP RC beams through theoretical and experimental analysis. Twenty-six RC beams reinforced with glass-FRP (GFRP) and one steel RC beam are tested under four-point loading. The main variables considered in the study are the concrete grade, the reinforcement ratio and the effective depth to total height ratio. Deformations on the concrete and on the reinforcement and crack widths and spacings are measured and analysed.

The experimental results are discussed and compared to some of the most representative prediction models of deflections and cracking for steel and FRP RC. Results show that, in general, prediction models for crack widths and deflections provide adequate values up to the service load. Additionally, cracked section analysis (CSA) is used to analyse the flexural behaviour of the specimens until failure. CSA estimates the FRP RC ultimate load with accuracy. However, an increment of the experimental deflection is reported compared to that provided by CSA when the load increases beyond the service load level. This increment is mainly attributed in this work to shear induced deflection and it is experimentally calculated.

A discussion on the main aspects of the SLS of FRP RC is introduced. The influence of the different parameters affecting the stresses in materials, maximum crack width and the allowable deflection is studied and analysed. It is reported that at a cross-section level, for lightly reinforced members, the crack width limitation results more restrictive than the stresses in concrete; however, for sections with high reinforcement ratios, the predominant restriction is the concrete stress.

Because SLS result determining for the design of FRP RC elements, a methodology is presented for the design of FRP RC at the serviceability requirements. This procedure allows optimizing the overall depth of the element with respect to more generalised methodologies, since it takes account of the specific properties of materials and the loading conditions.

Resumen

La corrosión del acero como refuerzo estructural en ambientes agresivos puede provocar deterioros importantes en las estructuras de hormigón armado. El uso de materiales compuestos de matriz polimérica (FRP) emerge como alternativa al hormigón convencionalmente armado con acero debido a la mayor resistencia a la corrosión de dichos materiales. Sin embargo, las propiedades mecánicas de este tipo de barras ocasionan deformaciones y niveles de fisuración elevados en elementos de hormigón armados con FRP. En consecuencia, los estados límites de servicio suelen gobernar el diseño de dichos elementos.

El presente estudio investiga el comportamiento en servicio de vigas de hormigón armadas con barras de FRP mediante un análisis teórico y experimental. Se presentan los resultados experimentales de veintiséis vigas de hormigón armadas con barras de material compuesto de fibra de vidrio (GFRP) y una armada con acero, todas ellas ensayadas a flexión de cuatro puntos. Las principales variables consideradas son el tipo de hormigón, la cuantía geométrica de armadura y la relación entre el canto útil y el canto total de la viga. Las principales medidas experimentales del estudio incluyen flechas, giros, curvaturas y deformaciones en ambos materiales, hormigón y armadura.

Los resultados experimentales son analizados y comparados con algunos de los modelos de predicción más significativos de flechas y fisuración para hormigón armado con acero y con FRP. Los resultados muestran que, en general, los modelos de predicción para anchos de fisura y deformaciones siguen con bastante precisión el comportamiento experimental observado hasta cargas de servicio. Adicionalmente, se emplea el análisis seccional de sección fisurada (CSA) para analizar el comportamiento a flexión de los elementos ensayados hasta la carga de ruptura. CSA estima la carga última de los especímenes con precisión, aunque se registra un incremento de la flecha experimental respecto a la calculada mediante CSA para cargas superiores a las de servicio. Esta diferencia se atribuye a la influencia de las deformaciones por esfuerzo cortante y se calcula experimentalmente.

Se presentan los aspectos principales que influyen en los estados límites de servicio. Se detallan los parámetros que afectan a las tensiones de los materiales y al ancho máximo de fisura, mientras que se estudia y analiza la flecha máxima permitida. A nivel seccional, se concluye que para elementos débilmente armados la limitación de ancho máximo de fisura resulta más restrictiva que las tensiones en el hormigón, pero para secciones fuertemente armadas, el diseño es regido por la limitación de tensión en el hormigón.

Debido a que los estados límites de servicio resultan determinantes en el diseño de elementos de hormigón armados con FRP, se presenta una metodología para el diseño de dichos elementos bajo las condiciones de servicio. El procedimiento presentado permite optimizar las dimensiones de la sección respecto a metodologías más generales, ya que tiene en cuenta las propiedades específicas de los materiales y las condiciones de carga.

Acknowledgements/Agraïments

First of all, I would like to thank my supervisor, Dr. Lluís Torres, for his excellent guidance and encouragement throughout the duration of this work. I would also thank Dr. Kypros Pilakoutas and Dr. Maurizio Guadagnini for their good advices and support during my research stay at the University of Sheffield.

Gràcies a tots els companys de les àrees d'Enginyeria de la Construcció i Mecànica dels Medis Continus i Teoria d'Estructures, especialment a Xavier Cahís, Albert Turon, Jordi Renart, Enric Simon, Jordi Comas, Miquel Llorens i Antoni Blàzquez per donar-me suport durant la realització d'aquest treball. També Ángel Mateos, el meu primer professor d'estructures.

El treball experimental no hagués estat possible sense l'ajuda i assistència dels tècnics de laboratori, Sergi Ortiz, Jordi Vicens i més recentment Sergi Saus. Moltes gràcies a tots aquells que van dedicar gran part del seu temps a col·laborar en la realització dels assaigs, molt especialment a Albert Turon, Marta Baena, Cristina Miàs i Irene Vilanova.

Gràcies a tots els companys d'AMADE, pel dia a dia. Als companys del departament d'EMCI, en especial a Joan Andreu Mayugo, Norbert Blanco, MªLuisa Garcia-Romeu, Dani Trias i Inés Ferrer, per les llargues estones de discussió sobre la tesi i per ser molt més que companys. També a Josep Costa, pels valuosos comentaris sobre la redacció, i a Emili Gonzalez, per les estones intentant simulacions.

A special thank you for the colleagues at the University of Sheffield who really made me feel at home, very specially to Andreea, Angela, Kyriacos, Panos, Harris and Anca.

A Noe i la Neus, per les fantàstiques vivències des de la època universitària, a la MªLuisa, pels sempre bons consells personals i professionals, a l'Airu, per les llargues passejades amb cotxets del darrer any i a la Clara, per cuidar de la meva esquena quan ho he necessitat.

Al meu pare Salvador, a qui dec, entre moltes coses, la professió, i a la meva mare Montserrat, a qui dec la vocació entre moltes altres més. Als meus germans Salva, Natàlia i Ignasi, per la complicitat que sempre ens ha unit. A la meva família política, per haver-me fet sentir sempre com a casa.

Finalment, el meu més profund i sincer agraïment a en Norbert, qui ha estat darrera d'aquest treball des del primer fins l'últim dia. Gràcies per estar al meu costat, i per cuidar de la nostra petita Sara durant les llargues estones d'escriptura de la tesi.

Table of contents

Chapter 1
Introduction and objectives

1.1. Introduction

Corrosion of steel reinforcement in aggressive environments can cause considerable damage in reinforced concrete (RC) structures. The high costs of maintenance, repair or substitution associated to these pathologies have led designers and codes of practice to adopt stricter specifications to enhance the durability of steel RC in these environments.

In order to avoid such problems, the use of fibre reinforced polymer (FRP) bars for internal longitudinal flexural reinforcement has emerged as an alternative solution (fib 2007). FRPs are composite materials made of continuous fibres embedded in a polymeric matrix. These composites are typically classified according to the fibre type in: glass-FRP (GFRP), carbon-FRP (CFRP) and aramid-FRP (AFRP). Owing to their non corrosive nature, the use of FRP bars can reduce maintenance and rehabilitation costs, leading to economic and environmental benefits (Pilakoutas et al. 2007). Moreover, the magnetic neutrality of FRP bars can be exploited in applications where interferences with magnetic fields have to be avoided. Highway infrastructures, bridges (Figure 1-1a), marine environments, or chemical plants are examples of places where applications or demonstration projects have been successfully carried out (Nanni 2001, Hollaway 2010). Other specific properties can lead to new uses, as the use for diaphragm walls in temporary applications (Figure 1-1b), for which the high cuttability of FRPs is a major advantage (fib 2007, Pilakoutas et al. 2007).

(a)   (b)

Figure 1-1. Applications of FRP to RC elements: (a) The first concrete footbridge in Europe with only FRP reinforcement (EUROCRETE project) (b) Soft eye FRP reinforcement (fib 2007).

When FRP bars are used, different structural behaviour is expected due to their different mechanical and bond properties compared with those of steel rebars, in particular, their relatively low modulus of elasticity and their linear stress-strain behaviour until failure. The lower stiffness of FRP bars can yield to large strains being mobilized in the bars at low levels of external loads and lead to large crack widths and deflections. As a result, the design of concrete elements reinforced with FRP materials is often governed by the serviceability limit states (SLS) (Matthys and Taerwe 2000, Nanni 2003), especially in the case of GFRP, which normally has an elastic modulus of only 35-45 GPa. In addition, FRPs may exhibit significant creep rupture (or static fatigue) and fail under sustained loads at stresses lower than their tensile short-term strength (ACI Committee 440 2006, fib 2007).

FRP bars are yet not standardised, and have different mechanical and bond characteristics which depend on the type of fibre and the manufacturing process (Ceroni et al. 2006, Baena et al. 2009). Hence, new design models and guidelines are needed that can cope with the plurality of products in the market.

In the last two decades, a number of studies were carried out to investigate the flexural response of FRP RC beams. Most of them show a limited number of experimental results and comparisons that often arrive at proposals for modifications of existing design procedures.

In the case of serviceability, and specifically for deflections of FRP RC elements, several authors propose coefficients to modify Branson's equation used in steel design codes (ACI Committee 318 2005), whereas other researchers suggest a modified equivalent moment of inertia derived from the integration of curvatures along the beam. These different approaches have been adopted in the various design guideline proposals for FRP RC (ISIS Canada 2001, CAN/CSA 2002, ACI Committee 440 2006, fib 2007).

For the case of cracking behaviour of FRP RC elements, design equations and prediction models are generally based on similar formulation to that of steel RC, with coefficients that depend on the different characteristics of the rebars and their interaction with concrete. The

design formulation for crack width, however, is still under discussion even for steel RC (Beeby 2004, Beeby et al. 2005, fib 2010).

1.2. Research objectives

This study aims at investigating the serviceability behaviour of FRP RC beams, both experimentally and analytically, taking into account the contribution of the most important aspects of their flexural behaviour.

For this purpose, the following specific objectives are identified:

- To investigate, through literature, the serviceability behaviour of concrete beams reinforced with FRP bars, in terms of stresses in materials (concrete and reinforcement), cracking (crack spacing and crack width) and short- and long-term deformations.

- To test FRP RC beams in order to examine short-term deflection profiles and crack patterns, as well as other flexural parameters such as strains and rotations that can help to correctly understand the overall behaviour of these beams under the serviceability requirements.

- To compare the experimental results of deflections and crack widths and spacings to the available prediction models and to examine the goodness of fit of the different existing approaches.

- To study the SLS of FRP RC elements, in terms of cracking, stresses in materials and deformations, from an analytical point of view. To evaluate the service load level requirements at which the different SLS are fulfilled and to provide practical formulation for the design of FRP RC elements under the SLS.

The following secondary objectives are also identified:

- To investigate, through literature, the flexural modes of failure of FRP RC elements and to identify other aspects affecting deflections that take place before the failure of the element.

- To test the FRP RC beams used in the study until failure to examine failure modes and the flexural behaviour beyond the serviceability limits.

1.3. Outline of the thesis

In Chapter 2, a literature review on the main aspects of the flexural behaviour of steel and FRP RC elements is undertaken, enhancing those related to the SLS. A summary of the most representative prediction models on cracking and deflections is also presented.

Chapter 3 describes the experimental program carried out in this work. The design philosophy, main parameters and instrumentation are detailed. The characterisation of materials is further examined.

In Chapter 4 the experimental results are shown and comparisons between them are represented. Strains in the concrete and in the reinforcement are shown, as well as curvatures in the central zone and along the length of the beam. The cracking patterns are commented and the deflection behaviour is discussed. The failure load is provided. A measure of the bond behaviour and tension stiffening is also analysed. The influence of the main parameters taking place at the SLS is commented and discussed.

Chapter 5 presents analytical comparisons between the experimental data and some of the most representative prediction models for cracking and deflections of FRP RC elements. Cracked section analysis is introduced as an analytical tool to compare the experimental response at high load levels. Strains, curvatures and deflections are discussed. Finally, an evaluation of the experimental deflection until the failure load is presented.

Chapter 6 studies the serviceability requirements for FRP RC elements from an analytical point of view. A formulation to calculate the bending condition that fulfils the sectional SLS is presented and a methodology is proposed to calculate the dimensions of a FRP RC element that fulfils stresses in materials, crack width and deflection conditions.

In Chapter 7 the conclusions of the present work are drawn and future works to be developed are pointed out.

Chapter 2
Literature review

2.1. Introduction

Plain concrete is a material that works well under the action of compressive stresses but presents a brittle (or quasi-brittle) behaviour in tension. Reinforcing concrete with steel has been a traditional solution to the brittleness problem. Because of its physical and mechanical properties, steel gives to the reinforced concrete (RC) composite material the capability to work well in flexure, by an adequate bond transfer. Steel reinforcement, however, corrodes rapidly under aggressive conditions such as marine environments. Other materials, such as Fibre Reinforced Polymers (FRP), have emerged as an alternative to steel reinforcement when the exposure situation of the RC member requires durability under aggressive conditions. These materials present different mechanical properties from steel, which can affect the flexural behaviour of the RC element.

This chapter includes a review of the basic aspects of the flexural behaviour of FRP RC elements. The review starts describing the main mechanical properties of concrete and FRP bars as internal reinforcement of RC. Next, an overview of the flexural capacity of RC beams is considered. The flexural modes of failure are presented and briefly discussed, and the equations for the moment resistance are detailed. The shear capacity for FRP RC beams is also included. The cracking behaviour for both steel and FRP RC is detailed and the equations for the calculation of crack width and crack spacing are described. The deflection behaviour for RC elements is presented, and code provisions for evaluating the flexural deflection of steel and FRP RC are considered. An overview of the long-term and shear-induced deflections is also considered. Finally, the requirements for the serviceability limit states for FRP RC are presented and discussed.

2.2. Material properties

2.2.1. Concrete

Concrete is a brittle material that works satisfactorily under compressive stresses. Although under practical situations concrete rarely works in one direction only, an assumed uniaxial stress condition can be justified in many cases (Park and Paulay 1975). In this section, the uniaxial stress behaviour of concrete is described. First, the concrete behaviour under compression is shown and second the tensile behaviour is drawn.

Concrete in compression

The constitutive relationship of concrete under uniaxial compression is commonly derived from experimental tests on cylinders with a height to diameter ratio of 2. From this data, it is usually stated that the stress-strain behaviour of a concrete sample subjected to a uniaxial compressive stresses follows an approximate parabolic curve, as shown in Figure 2-1. The constitutive relationship under compression is normally considered linear up to stress values lower than 40% of the mean compressive strength f_{cm}, however, once this limit is attained, the stress-strain behaviour becomes clearly non-linear.
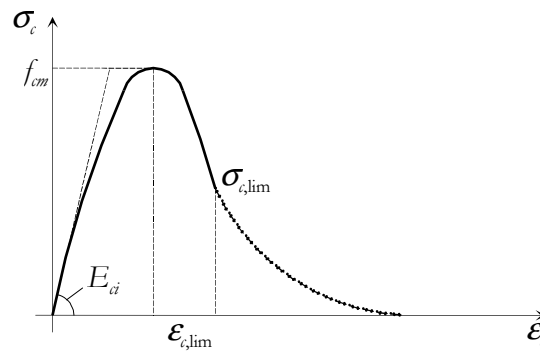
Figure 2-1. General stress-strain curve for uniaxial compression.

The stress-strain curve for concrete in compression has been studied extensively, and several approaches are found in the literature to model the curve depending on different factors, such as the sample dimensions, the rate of loading, the shape of the cross section, the possible confinement, etc. (Hognestad 1951, Hognestad et al. 1955, Rüsch 1960, Carreira and Chu 1985).

Among those proposals, Park and Paulay (1975) adopted Hognestad et al. (1955) approach:

$$\frac{\sigma_c}{f_{cm}} = \frac{2\varepsilon_c}{\varepsilon_{c0}} - \left(\frac{\varepsilon_c}{\varepsilon_{c0}}\right)^2 \text{ if } \varepsilon_c \leq \varepsilon_{c0} \tag{2-1}$$

$$\frac{\sigma_c}{f_{cm}} = 1 - 100(\varepsilon_c - \varepsilon_{c0}) \text{ if } \varepsilon_{c0} \leq \varepsilon_c \leq \varepsilon_{cu} \tag{2-2}$$

In Eqs. (2-1) and (2-2), σ_c is the concrete stress, f_{cm} is the concrete compressive strength, ε_c is the concrete strain, ε_{c0} is the concrete strain at the peak stress ($\sigma_c = f_{cm}$) and ε_{cu} is the ultimate compressive strain. According to Park and Paulay (1975), ε_{c0} equals to 0.2% and ε_{cu} equals to 0.38%.

Desayi and Krishnan (1964) proposed a simple model, which was developed to describe the stress-strain curve of normal strength concrete (NSC). This equation was adopted by many researchers due to its simplicity (MacGregor 1997; Choi et al. 2008):

$$\frac{\sigma_c}{f_{cm}} = \frac{2\left(\varepsilon_c / \varepsilon_{c0}\right)}{1 + \left(\varepsilon_c / \varepsilon_{c0}\right)^2} \tag{2-3}$$

Collins et al. (1993), who extended the early work by Thorenfeld et al. (1987), described the relationship between the compressive stress at any strain to the maximum stress:

$$\frac{\sigma_c}{f_{cm}} = \frac{\varepsilon_c}{\varepsilon_{c0}} \left(\frac{n}{n - 1 + \left(\varepsilon_c / \varepsilon_{c0}\right)^{nk}} \right) \tag{2-4}$$

$$\varepsilon_{c0} = \frac{f_{cm}}{E_c} \frac{n}{n-1} \tag{2-5}$$

$$n = 0.8 + f_{cm}/17 \tag{2-6}$$

$$k = 1 \text{ if } \varepsilon_c \leq \varepsilon_{c0}$$
$$k = 0.67 + f_{cm}/62 \text{ if } \varepsilon_c > \varepsilon_{c0} \tag{2-7}$$

Carreira and Chu (1985) defined a model based only on three parameters that could be experimentally determined from compression tests in which the strain rate would be controlled:

$$\frac{\sigma_c}{f_{cm}} = \frac{\beta\left(\varepsilon_c / \varepsilon_{c0}\right)}{\beta - 1 + \left(\varepsilon_c / \varepsilon_{c0}\right)^{\beta}} \tag{2-8}$$

This model has the limits of the perfectly elastic material when β tends to infinity and the perfectly plastic materials when β equals to the unity, providing a non-linear transition for these two extreme cases. The model was further extended by Loov (1991) to include the stress-strain behaviour of not only normal strength concrete but also high performance concrete.

Design codes for steel RC provide equations to assess the flexural behaviour of a section by using non-linear analysis. Model Code 90 (CEB-FIB 1990), for instance, follows the expression proposed by Sargin (1971), described as follows:

$$\frac{\sigma_c}{f_{cm}} = -\frac{\dfrac{E_{ci}}{E_{c0}}\dfrac{\varepsilon_c}{\varepsilon_{c0}} - \left(\dfrac{\varepsilon_c}{\varepsilon_{c0}}\right)^2}{1 + \left(\dfrac{E_{ci}}{E_{c0}} - 2\right)\dfrac{\varepsilon_c}{\varepsilon_{c0}}} \quad \text{for } |\varepsilon_c| < |\varepsilon_{c,\lim}| \tag{2-9}$$

where E_{ci} is the concrete modulus of elasticity, computed in Eq. (2-10) with $E_{c0} = 2.15 \cdot 10^4$ MPa and $f_{cm0} = 10$ MPa, ε_{c0} equals to -0.22% and E_{c1} is the secant modulus of elasticity from the origin to the peak compressive stress f_c, defined in Eq. (2-11).

$$E_{ci} = E_{c0}\left(f_{cm}/f_{cm0}\right)^{1/3} \tag{2-10}$$

$$E_{c1} = \frac{f_{cm}}{|\varepsilon_{c0}|} \tag{2-11}$$

Moreover, Eurocode 2 (CEN 2004) and the Spanish code for steel RC *Instrucción de Hormigón Estructural* EHE (CPH 2008), use a modified version of the same model that allows using concretes with characteristic strengths up to 90 MPa (Eqs. (2-12) to (2-15)):

$$\frac{\sigma_c}{f_{cm}} = \frac{kn - n^2}{1 + (k-2)n} \tag{2-12}$$

$$n = \frac{\varepsilon_c}{\varepsilon_{c0}} \tag{2-13}$$

$$\varepsilon_{c0}(\%) = 0.07 f_{cm}^{0.31} < 0.28\% \tag{2-14}$$

$$k = 1.1 E_{cm} \frac{\varepsilon_{c0}}{f_{cm}} \tag{2-15}$$

In Eq. (2-15) E_{cm} is the concrete modulus of elasticity, in MPa, defined as:

$$E_{cm} = 22000\left(f_{cm}/10\right)^{0.3} \tag{2-16}$$

Concrete in tension

Concrete under tensile stresses behaves linearly until the tensile strength f_{ct} is reached. For values of strain larger than that corresponding to the tensile strength, the stress decreases, with an increase of the measured strain.

The strain along a tensile RC element is not constant, since cracking is a discrete phenomenon that takes place at a certain location (Figure 2-2). In a cracked concrete element, a part of the concrete between two consecutive cracks contributes to the load-carrying capacity, thanks to the bond contribution between the concrete and the reinforcement. This phenomenon

produces an increment of the stiffness of the element and is extensively known as *tension stiffening*.

Figure 2-2 shows the stress and strain evolution of a RC element subjected to a pure tensile force. In the figure, ε_s refers to the strain in the steel reinforcement, ε_{s2} and σ_{s2} are the steel strain and stress in steel if no concrete exists, σ_c is the stress of the concrete and τ_b is the bond stress between the concrete and the steel, being ε_{sm} the mean strain of the element.
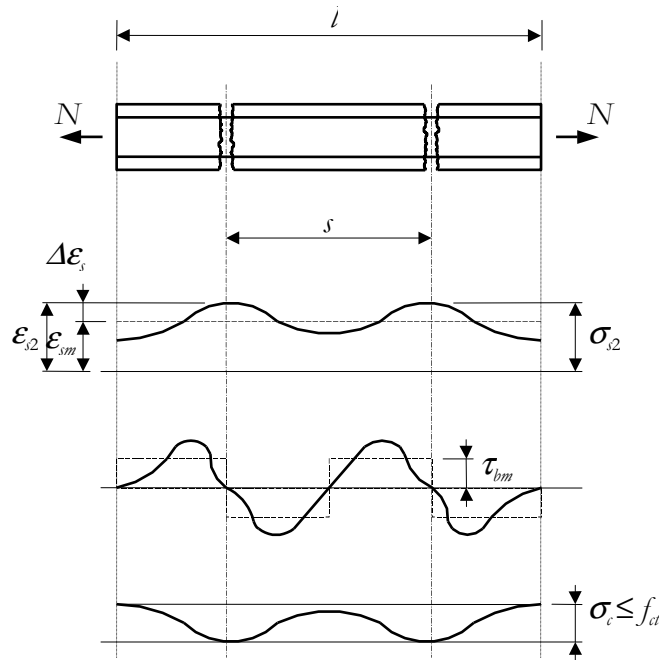
Figure 2-2. Cracking mechanism of a concrete member (CEB 1983).

The tension stiffening effect is of major importance when serviceability states are evaluated, especially when deflections are computed. Several models have been proposed in the literature with different degrees of complexity and can be classified, according to their background in:

1) Models based on the variation of the constitutive equations of steel (Gilbert and Warner 1978) or of concrete (Scanlon and Murray 1974, Lin and Scordelis 1975, Gilbert and Warner 1978, Bazant and Oh 1984, Torres et al. 2004).

2) Models based on the bond-slip behaviour between the concrete and the reinforcement (Floegl and Mang 1982, Gupta and Maestrini 1990, Russo and Romano 1992, Aiello and Ombres 2000a). According to these models, when a crack appears, slip occurs between the concrete and the reinforcement, and bond stresses appear following a previously defined bond-slip law, affecting the behaviour of both materials. Those methodologies present the highest degree of complexity of the models presented in this summary, and can be included in a finite element discrete cracking model.

3) Models based on an estimate of the equivalent stiffness in flexure. The most known model was developed by Branson (Branson 1968, Branson 1977), and it is based on an equivalent moment of inertia I_e calculated from the interpolation between the non-cracked moment of inertia (or the gross moment of inertia I_g) and the cracked moment of inertia I_{cr}.

4) Models based on the mean stress-strain behaviour of a cross-section (CEB 1983, CEB-FIP 1990, CEN 2004). Those models are based on assuming a mean strain between the cracked and uncracked states.

2.2.2. Fibre Reinforced Polymers

Composite materials can be defined as those materials resulting from the combination of two or more materials (known as components or constituents). The first manmade composite material was straw-reinforced clay for bricks and pottery, whilst modern composite materials use ceramic, metal or polymer binders reinforced with different fibres or particles. In the resulting composite material, the components conserve their initial identity without dissolving or mixing completely. Usually, the constituents can be physically distinguished and it is possible to identify the interface between components. Taking into account their structural properties, composite materials can be defined as those materials having a reinforcement component (fibres or particles) immersed in a resin matrix.

With the combination of different matrices (usually polymeric matrices or light metals) and different fibres (glass, carbon, organic and polymeric fibres, among others), it is possible to obtain composite materials with different mechanical properties specially designed for certain applications. Thus, the great number of possible combinations results in a great number of composites. Composites can be distinguished in function of their typology (such as long or short fibres, random or oriented, single or multiple plies) or in function of their components (thermoset or thermoplastic polymeric matrix, aluminium or titanium metal matrix, inorganic or organic fibres, among others). The type of composite materials used in the present work consists of continuous fibres embedded in a polymeric matrix and are referred to as fibre reinforced polymer (FRP).

Bars made of FRP are innovative materials in structural engineering. These composites have a wide range of physical and mechanical properties. FRPs can be designed choosing the type and quantity of fibres and matrix, and commercial products can be manufactured with different characteristics. In addition, FRP rebars with different outer surface treatments vary the performances, in terms of bar-concrete bond, that influence many behavioural aspects such as crack width, deflections and anchorage length.

Constituent materials of FRP bars

FRP bars are made of continuous fibres impregnated with polymeric resins. In fibrous polymeric composites, continuous fibres with high strength and high stiffness are embedded

in and bonded together by the low modulus polymeric matrix. The reinforcing fibres constitute the backbone of the material and they determine its strength and stiffness in the direction of the fibres. The matrix gives physical and environmental protection.

The most common fibre types used in the construction industry are carbon, glass and aramid (Wallenberger et al. 2001, Walsh 2001, Chang 2001). Carbon fibres are the stiffest, most durable and most expensive fibres. The stiffness of these fibres is similar to that of steel. Carbon is quite resistant to most environmental conditions and can withstand high sustained and fatigue loading conditions. Glass fibres have lower strengths and significantly lower stiffness but at reduced cost. At present, one of the concerns with glass fibres is durability. Unprotected glass fibres degrade in most environments, especially hot/wet or highly alkaline environments. Glass is also susceptible to a phenomenon known as creep rupture, which results in the eventual failure of the material under sustained loads higher than a fraction of the instantaneous ultimate load. Finally, aramid fibres have mechanical characteristics between those of glass and carbon, but with improved durability and excellent impact resistance. At present, these fibres are the least common in the construction industry.

The polymeric matrix (sometimes referred to as the resin) protects the fibres from damage, ensures that the fibres remain aligned and allows load to be distributed among many of the individual fibres in the composite. Resins used in FRP composites are generally classified as either thermosetting or thermoplastic resins. Generally, the construction industry utilizes thermosetting resins, such as epoxy and vinyl ester. These resins start as a low viscosity, flowable material that cures to a final solid form, and most of them are sensitive to heat and ultra-violet light exposure.

Mechanical properties of FRP bars

FRP materials are anisotropic and are characterized by high tensile strength with no yielding only in the direction of the reinforcing fibres. FRP bars present linear stress-strain behaviour under tension up to failure. Compared to ductile steel, FRPs generally have higher tensile capacity, limited strain range and lower modulus of elasticity. Table 2-1 and Figure 2-3 summarize the typical mechanical tensile properties of FRP bars compared to those of steel reinforcement.

Table 2-1 Typical tensile properties of steel and FRP rebars (ACI Committee 440 2006).

	Steel	CFRP	GFRP	AFRP
Nominal yield stress (MPa)	276-517	N/A	N/A	N/A
Tensile strength (MPa)	483-690	600-3690	483-1600	1720-2540
Elastic Modulus (GPa)	200	120-580	35-51	41-125
Yield strain (%)	0.14-0.25	N/A	N/A	N/A
Rupture strain (%)	6.0-12.0	0.5-1.7	1.2-3.1	1.9-4.4
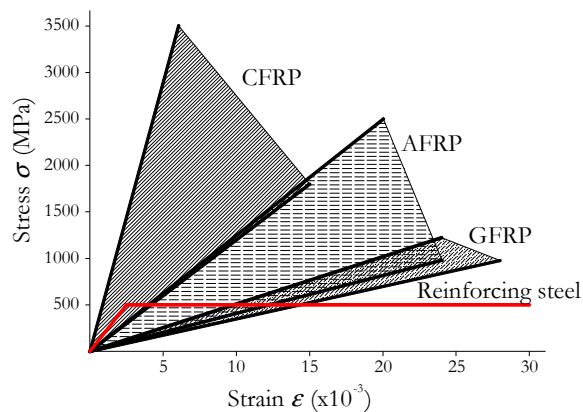
Figure 2-3. Stress-strain curves of FRP and steel materials (Pilakoutas 2000).

The anisotropic behaviour of FRP bars affects the shear strength and dowel action, as well as their bond performance (Nanni 2003). At present, however, no standard test methods are yet available to characterise the FRP compressive and shear behaviour.

FRP bars present different surface conditions such as sand coated, ribbed, indented or braided (Baena et al. 2009). In addition, shapes different from round reinforcement can be used, such as deformed-square (Howell and Higgins 2007) or dog-bone shapes (Ferreira et al. 2001).

FRP bars offer several advantages in comparison to steel reinforcement. In addition to the high tensile strength, FRPs are corrosion resistant, which makes them ideal in situations where steel reinforcement suffers from corrosion, such as marine RC structures. Moreover, FRP offer electromagnetic permeability, which is essential in specialized applications where steel causes electromagnetic interferences, for example in MRI rooms in hospitals and the mobile telecommunications industry. FRP reinforcement, particularly GFRP, presents high cuttability, making it the ideal material to temporary RC structures such as diaphragm walls, which have to be partially destroyed by tunnel boring machines. Finally, FRP are lighter than steel, facilitating transportation and speeds construction (ACI Committee 440 2006, fib 2007, Pilakoutas et al. 2007).

The unique mechanical properties of FRPs, however, have a significant effect on the structural performance of concrete elements reinforced with these materials. In particular, the modulus of elasticity is relatively low when compared with steel, especially for GFRP. This can yield to large strains being mobilized in the bars at low levels of external loads and lead to larger crack widths and deflections. As a result, serviceability requirements often govern the design of FRP RC elements (Matthys and Taerwe 2000, Nanni 2003). In addition, FRPs exhibit creep rupture (or static fatigue) which means that they can fail under sustained loads at stresses lower than their tensile short-term strength (ACI Committee 440 2006, fib 2007). Finally, the wide range of commercially available products can differ substantially in terms of fibre/matrix make-up, geometry, and surface characteristics, making it difficult for code writers to implement simple design rules that can model adequately the mechanical performance of composite bars in concrete. Despite several design guidelines, codes and recommendations have recently been

published for FRP RC elements (JSCE 1997, IStructE 1999, ISIS Canada 2001, CAN/CSA 2002, ACI Committee 440 2006, CNT-DT-203 2006), the lack of agreed standards for design and manufacturing is still perceived as a barrier to the extensive use of FRPs in construction.

2.3. Flexural capacity of FRP RC beams

The flexural capacity of any RC beam can be defined as the maximum capacity of a beam of absorbing an external load. When the flexural capacity of a beam is reached, in at least one section of the beam, one or both of its materials have reached their maximum strain or strength. To assess the flexural capacity of a beam, some assumptions need to be made (Park and Paulay 1975):

- Plain sections remain plain under bending forces

- Reinforcement stress-strain relationship is known

- Tensile strength of concrete is negligible

- Concrete stress-strain in compression is known

Considering these hypothesis, it is possible to evaluate the flexural capacity of a beam by a Cracked Section Analysis (CSA, Figure 2-4), without considering the type of reinforcement that is used, as long as the bond behaviour is adequate between the concrete and the reinforcement.
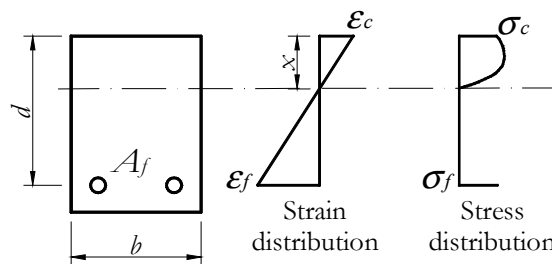
Figure 2-4. Strains and stresses in CSA.

2.3.1. Modes of failure of FRP RC elements

In concrete elements working under flexural stresses and reinforced with only tensile reinforcement, two main modes of failure can be defined, depending on which material achieves its maximum capacity first. When concrete arrives at its maximum strain (usually considered between 0.3% (ACI Committee 440 2006) and 0.35% (ISIS Canada 2001, CEN 2004), the section fails in a quasi-brittle manner by compression of the concrete block. This failure is usually referred to as *concrete crushing*, and it is independent of the material that is used as reinforcement. On the contrary, when the reinforcement achieves its tensile strength prior to concrete arrives at its maximum compressive strain, the section fails by rupture of the

reinforcement. This failure can be brittle or ductile, depending on the mechanical characteristics of the reinforcement. For instance, if steel is used as internal reinforcement, when steel reaches its yielding strength, it starts to yield, and eventually fails when the ultimate strain is reached, giving a ductile failure. But in the case of FRPs, which present a linear stress-strain relationship until failure, when they reach their maximum strength, the failure of the section is sudden and catastrophic, giving a brittle failure as a result. A third mode of failure, usually called as the balanced mode of failure consists of the simultaneous rupture of the FRP and crushing of the concrete.

When designing RC with steel, ductile failure is desirable, therefore, beams are usually designed to fail after the reinforcement has exceeded its yielding strength. Nevertheless, when FRPs are used as internal reinforcement, it is not possible to achieve a pure ductile failure, thus, concrete crushing, which is slightly less brittle that the failure of the reinforcement, is preferred by most designers and codes of practice (ISIS Canada 2001, Nanni 2003, ACI Committee 440 2006).

Different approaches to calculate the failure mode and the ultimate load capacity of FRP RC elements are proposed in the literature. In some design codes (JSCE 1997, ACI Committee 440 2006), to compensate for the lack of ductility, the suggested safety margins against failure are higher than those used in traditional steel RC design. Moreover, approaches based on safety considerations have emerged (Pilakoutas et al. 2002), and the concept of ductility is modified to reflect deformabilities of FRP RC (Newhook et al. 2002).

In general, the design of FRP RC members for flexure is analogous to the design of steel RC members (ACI Committee 440 2006, fib 2007), based on assumptions similar to those made for steel reinforcement, and taking into account the uniaxial stress-strain relationship of the FRP material. A reinforcement ratio ρ_f, defined in Eq. (2-17), shall be compared to the balanced reinforcement ratio ρ_{fb} to control the failure mode. Reinforcement ratios higher than ρ_{fb} lead to a concrete crushing, whereas ρ_f lower than the balanced value cause the rupture of the FRP rebars. The balanced reinforcement ratio is influenced by the mechanical properties of FRP and concrete, and it is calculated from expressions derived by considering internal force equilibrium. ACI 440.1R-06 (ACI Committee 440 2006) proposes to calculate ρ_{fb} as follows:

$$\rho_f = \frac{A_f}{bd} \tag{2-17}$$

$$\rho_{fb} = 0.85\beta_1 \frac{f_c'}{f_{fu}} \frac{E_f \varepsilon_{cu}}{E_f \varepsilon_{cu} + f_{fu}} \tag{2-18}$$

In Eq. (2-17), A_f is the area of FRP reinforcement, b is the width of the section and d is the effective depth. In Eq. (2-18), β_1 is the ratio of depth of equivalent rectangular stress block to depth of the neutral axis, f_c' is the specified concrete compressive strength, f_{fu} is the rebar

tensile strength, E_f is the modulus of elasticity of the FRP rebar, and ε_{cu} is the maximum concrete strain (0.3% for ACI provisions).

Similarly, Pilakoutas et al. (2002) proposed Eq. (2-19), derived from Eurocode 2 for FRP RC beams, which accounts for the variability of concrete properties.

$$\rho_{fb} = \frac{0.81(f_{ck} + 8)\varepsilon_{cu}}{f_{fk}\left(\dfrac{f_{fk}}{E_f} + \varepsilon_{cu}\right)} \tag{2-19}$$

In Eq. (2-19), f_{ck} and f_{fk} are the characteristic concrete cylinder compressive strength and tensile strength of the FRP reinforcement, respectively.

2.3.2. Moment resistance of an FRP RC element

The flexural capacity of a cross section can be evaluated by assuming that the constitutive relationship of concrete in compression is known, the stress-strain curve of the FRP is linear up to failure, and there is perfect bond between concrete and the FRP reinforcement (Figure 2-4). When the amount of longitudinal reinforcement ρ_f is higher than ρ_{fb}, flexural failure is expected to occur due to concrete crushing.

The ultimate moment resistance of an FRP RC section that fails by concrete crushing can be calculated assuming different equivalent stress-strain distributions of concrete under compression until failure. Eurocode 2 (CEN 2004), for instance, defines a parabola-rectangular and a bilinear diagram for the design of cross-sections. Additionally, it suggests a rectangular stress block that is based on the parabola-rectangular diagram. In Figure 2-5 the equivalent rectangular stress blocks defined by ACI 440.1R-06 and Eurocode 2 are shown.
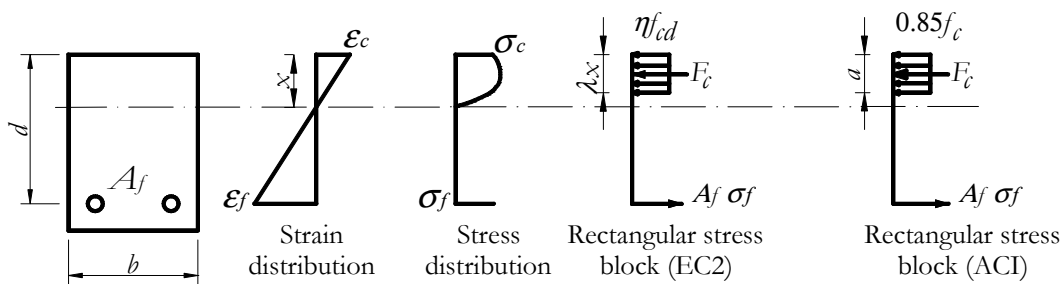
Figure 2-5. Rectangular stress block from Eurocode 2 and ACI provisions.

Following Eurocode 2 provisions, the moment resistance can be calculated using the rectangular stress block with Eq. (2-20). This formulation is the one adopted in fib (2007) for the design of FRP RC elements.

$$M_u = \eta f_{cd} b d^2 (\lambda\xi)\left(1 - \frac{\lambda\xi}{2}\right) \tag{2-20}$$

$$\lambda = 0.8 \text{ for } f_{ck} \leq 50\text{MPa}$$

$$\lambda = 0.8 - \left(\frac{f_{ck} - 50}{400} \right) \text{ for } 50 < f_{ck} \leq 90\text{MPa} \tag{2-21}$$

$$\eta = 1 \text{ for } f_{ck} \leq 50\text{MPa}$$

$$\eta = 1.0 - \left(\frac{f_{ck} - 50}{200} \right) \text{ for } 50 < f_{ck} \leq 90\text{MPa} \tag{2-22}$$

$$\xi = \frac{x}{d} = \frac{\varepsilon_{cu}}{\varepsilon_f + \varepsilon_{cu}} \tag{2-23}$$

In Eqs. (2-20) to (2-23), the λ factor defines the effective height of the compression zone, the η factor defines the effective strength and ξ is the dimensionless ratio x/d. The design value of the concrete compressive strength f_{cd} is defined as:

$$f_{cd} = \frac{\alpha_{cc} f_{ck}}{\gamma_c} \tag{2-24}$$

being α_{cc} a nationally determined parameter with a recommended value of 1 and γ_c the partial factor for concrete. The reinforcement strain ε_f when concrete reaches its maximum compressive strain ε_{cu} is found from equilibrium of forces of the rectangular stress block:

$$\varepsilon_f = \frac{-\varepsilon_{cu} + \sqrt{\varepsilon_{cu}^2 + \dfrac{4\eta\alpha_{cc} f_{ck} \lambda \varepsilon_{cu}}{\gamma_c \rho_f E_f}}}{2} \tag{2-25}$$

ACI 318.R-05 and ACI 440.1R-06 (ACI Committee 318 2005, ACI Committee 440 2006) simplify the shape of the constitutive relationship to an equivalent rectangular stress block with an average stress of 0.85 the compressive strength and equivalent depth of $a = \beta_1 x$, being x the distance of the neutral axis depth from the top of the section and β_1 a parameter depending on the concrete strength (equal to 0.85 for concrete with compressive strength lower than 27.58 MPa and reduced at a rate of 0.05 per each 6.89 MPa of strength in excess of 27.58 MPa, but not taken less than 0.65). ACI codes propose the moment resistance to be calculated on the basis of the ACI equivalent stress block of concrete in compression, and based on the equilibrium of forces and strain compatibility, the following formulation is obtained:

$$M_u = \rho_f f_f \left(1 - 0.59 \frac{\rho_f f_f}{f_c'} \right) bd^2 \tag{2-26}$$

$$f_f = \left(\sqrt{\frac{(E_f \varepsilon_{cu})^2}{4} + \frac{0.85\beta_1 f_c'}{\rho_f} E_f \varepsilon_{cu}} - 0.5 E_f \varepsilon_{cu} \right) \leq f_{fu} \tag{2-27}$$

If the amount of reinforcement in an FRP RC section results lower than ρ_{fb}, FRP rupture is the expected failure type and an iterative procedure is needed to find the flexural moment at which the stress in the FRP attains its tensile strength.

With regards to the available experimental results on FRP RC elements, Benmokrane et al. (1996), Masmoudi et al. (1998) and Thériault and Benmokrane (1998) reported that the ultimate moment was 15% underestimated by ACI formulae when the section failed by concrete compression, but it was 5% overestimated in the case that the section failed by FRP tension. This difference was attributed to the variability of the compressive strength of concrete and tensile strength of the FRP reinforcing bars. Rafi et al. (2008) found out that ACI formulation underestimated the moment capacity of their four tested FRP beams to about 33%, probably because the actual strain in concrete exceeded the maximum concrete strain of 0.3% as a result of the confinement provided especially by the stirrups. Matthys and Taerwe (2000) compared the experimental moment capacity of eight slabs reinforced FRP grids to theoretical predictions using Model Code 90 formulation for concrete stress-strain parabola-rectangular curve, reporting that when the slabs failed by concrete crushing, the experimental values resulted 25% higher than the predictions. This difference was attributed to a higher ultimate compressive strain of the concrete. Pecce (Pecce et al. 1998, Pecce et al. 2000) compared the experimental ultimate load of two FRP RC beams to the predicted theoretical load considering three different models of concrete in compression: the Eurocode 2 parabola-rectangle, the stress block with a depth of $0.8x_{pl}$ being x_{pl} the neutral axis at failure and Mander et al. (1988) constitutive relationship. Pecce reported the equivalence of the three models of concrete behaviour and perfect agreement of the numerical results with the experimental ones. Ashour (2006) presented a simplified method based on cracked section analysis to predict the flexural capacity of GFRP RC beams, reporting good agreements with his experimental database.

2.4. Shear capacity of FRP RC beams

The shear resistance of RC elements is generally determined by the contribution of the uncracked compression zone, aggregate interlock, dowel action and, when provided, shear reinforcement. When FRPs are used as internal reinforcement, due to the lower modulus of elasticity of the FRPs, wider cracks and higher deflections are expected, leading to lower contribution of the uncracked compression zone in shear and less shear-load carrying by aggregate interlock and dowel action (Guadagnini 2002).

Failure of RC elements due to shear is always preceded by the formation of cracks inclined to the main axis of the element. In addition to the typical shear modes of failure that can occur in a conventionally steel RC element, most commonly diagonal tension failure and shear compression failure, FRP RC elements can also fail in shear due to fracture of the shear reinforcement (fib 2007).

Several approaches for predicting the ultimate shear load capacity that modify the actual proposals for steel RC are found in the literature (Guadagnini et al. 2006, Sherwood et al. 2008, Nehdi et al. 2008, or Hoult et al. 2008, among others). Design codes for FRP RC have adopted some of these empirical approaches. In particular, ACI Committee 440 (2006) proposes the model developed by Tureyen and Frosch (Tureyen and Frosch 2002, Tureyen and Frosch 2003) to calculate the concrete shear contribution. The Japanese code JSCE (1997) proposes to calculate the shear capacity of the concrete following the same format as that provided for steel RC, including a modifying term E_f/E_s to account for the different stiffness of the reinforcement. The FRP shear capacity is computed according to the classical formulations for steel RC in which the yield stress is substituted by the modulus of elasticity of the FRP shear reinforcement and its strain design value. Similarly, the British Standard IStructE (1999) suggests modifying the existing formulation to compute the shear capacity of the concrete by a factor $E_f/200$, whilst the shear strength of the shear reinforcement could be evaluated using formulation derived from the truss analogy theory, as far as the maximum strain developed in the stirrup is controlled.

2.5. Cracking behaviour of RC beams

Cracking in flexural RC members is a discrete phenomenon produced when the tensile stress in concrete exceeds the tensile strength at a singular point, creating the appearing of a crack, which can be originated by different causes, such as flexure, tension, shear, torsion, excessive bond or the effects of concentrated loads (CEB 1983). The occurrence of cracking in concrete subjected to bending forces is unavoidable due to the presence of tensile stresses and the low tensile strength of concrete.

2.5.1. Available formulation for the calculation of crack width and crack spacing

Several semi theoretical and empirical methods exist to determine the average and maximum crack spacing and the average and characteristic crack width of a tension or flexural RC element.

For the calculation of the average crack spacing, most of the available approaches can be expressed following the general form defined by Borosnyói (2002) as a linear function of the concrete cover c, the reinforcing bar spacing s, the bar diameter ϕ and the relationship between ϕ and the effective reinforcement ratio ρ_{eff} (CEB-FIB 1990, CEN 1992, CEN 2004, CHP 2008, CEB 1983, Broms 1965, Broms and Lutz 1965, Farra and Jaccoud 1992, Ferry 1966):

$$s_{rm} = A_1 + A_2 c + A_3 s + A_4 \phi + A_5 \frac{\phi}{\rho_{eff}} \qquad (2\text{-}28)$$

Other approaches adopt more complex expressions for the crack spacing calculation to better adjust their experimental data (Leonhardt 1977, Oh and Kang 1987, Bernardi 1999). The

dependence of crack spacing on some of these parameters, however, is still under discussion even for steel RC (Beeby 2004, Beeby et al. 2005, fib 2010).

For the calculation of the average and characteristic crack width (crack width corresponding to 95% fractile that could be expected in a flexural member), Borosnyói (Borosnyói 2002, Borosnyói 2005) classified the different approaches found in the literature in five categories according to their underlying principles:

5) From average crack width, where crack spacing and average strain of the reinforcement can be determined either by theoretical or empirical relationships (Broms 1965, Broms and Lutz 1965, Ferry 1966, CEB 1983, Rizkalla and Hwang 1984, CEN 1992).

6) As the product of the characteristic (maximum) crack spacing and average strain of the reinforcement, where crack spacing and average strain of the reinforcement can be determined either by theoretical or empirical relationships (CEB-FIB 1990, CEN 2004).

7) By empirical relationships based on large number of experimental data, with or without explicit expression of crack spacing and average strain of the reinforcement (Gergely and Lutz 1968, Rao and Dilger 1992, Toutanji and Saafi 2000, ACI Committee 224 2001, Salib and Abdel-Sayed 2004).

8) By analytical approaches, with or without explicit expression of crack spacing and average strain of the reinforcement (Bazant and Oh 1984, Nawy 1985, Oh and Kang 1987, Yang and Chen 1988, Farra and Jaccoud 1992, Bernardi et al. 1999, Scholz 1991).

9) By mixed models.

2.5.2. Code provisions for control of cracking of RC members

Design codes usually provide a formulation to calculate the design crack width w_k that can appear in a concrete member. This value should not be greater than a maximum allowable crack width w_{max} (Eq. (2-29)), which value mainly depends on the exposure class of the element, being more restrictive for exposed than for protected environments.

$$w_k \leq w_{max} \tag{2-29}$$

Several design codes (CEN 1992, CNR-DT-203 2006, CPH 2008) calculate the characteristic crack width w_k from its average value w, following the relationship:

$$w_k = \beta \cdot w \tag{2-30}$$

$$w = s_{rm} \varepsilon_m \tag{2-31}$$

where s_{rm} is the average crack spacing, ε_m is the average strain and β is a factor relating the average crack width to the characteristic value, being 1.7 for load induced cracking and 1.3 for restrained cracking in sections with a minimum dimension depth, breadth or thickness of 300 mm or less.

According to Eurocode 2 (CEN 1992), the average crack spacing s_{rm} is dependent on the area of reinforcement, the bond characteristics, the concrete tensile strength and the cover c from the reinforcement to the concrete surface. When the member is subjected to bending, an effective reinforcement ratio ρ_{eff} and a different strain distribution shall be considered. Therefore, the resulting formula is:

$$s_{rm} = 2c + 0.25 k_1 k_2 \phi / \rho_{eff} \tag{2-32}$$

where k_1 is a coefficient taking account of the bond properties of the interaction concrete-reinforcement (0.8 for high bond bars and 1.6 for smooth bars), k_2 is a coefficient depending on the form of stress distribution (0.5 for bending and 1.0 for pure tension), and ϕ is the diameter of the bar. Eurocode 2 (CEN 1992) assumes a typical concrete cover of 25 mm, giving as a result:

$$s_{rm} = 50 + 0.25 k_1 k_2 \phi / \rho_{eff} \tag{2-33}$$

The effective reinforcement ratio ρ_{eff} is defined as the area of reinforcement A_f divided by the effective concrete area in tension $A_{c,eff}$:

$$\rho_{eff} = \frac{A_f}{A_{c,eff}} = \frac{A_f}{b \cdot h_{eff}} \tag{2-34}$$

According to Eurocode 2 (CEN 1992), the effective height h_{eff} is 2.5(h-d), being h the total height and d the effective depth of the beam.

EHE (CPH 2008), in turn, proposes a formulation that takes into consideration the bar spacing s and assumes high bond between the concrete and the reinforcement:

$$s_{rm} = 2c + 0.2s + 0.4 k_1 \phi / \rho_{eff} \tag{2-35}$$

In Eq. (2-35) k_1 is a coefficient that accounts for the strain distribution in the tensile zone of the section, being 0.125 for pure flexure and 0.25 for pure tension. The effective height h_{eff} is here considered as the minimum value between ($c + \phi/2 + 7.5\phi$) and $h/2$.

The average strain in the reinforcement according to Eurocode 2 (CEN 1992) is directly obtained from an interpolation between the strain in the reinforcement at a cracked and an uncracked section:

$$\varepsilon_{sm} = \frac{\sigma_s}{E_s}\left(1 - \beta_1\beta_2\left(\frac{\sigma_{sr}}{\sigma_s}\right)^2\right)$$ (2-36)

where β_1 is a bond coefficient (1.0 for high bond and 0.5 for plain bars), β_2 is a coefficient which takes account of the duration of the loading or of repeated loading (1.0 for short-term loading and 0.5 for sustained load or for many cycles of repeated loading), and σ_{sr} is the stress in the tension reinforcement calculated on the basis of a cracked section under the loading conditions causing first cracking.

To calculate the mean strain in the reinforcement, EHE (CPH 2008) follows Eurocode 2 (CEN 1992) formulation, but does not account for the different bond characteristics between the rebar and the concrete, assuming high bond. Furthermore, EHE considers that the minimum mean strain should be higher than 40% the strain at the reinforcement at a cracked section:

$$\varepsilon_{sm} = \frac{\sigma_s}{E_s}\left(1 - k_2\left(\frac{\sigma_{sr}}{\sigma_s}\right)^2\right) \geq 0.4\frac{\sigma_s}{E_s}$$ (2-37)

In Eq. (2-37), k_2 refers to the duration of the load, being 0.5 for long-term loads and 1.0 for instantaneous loading.

The Italian code for FRP RC (CNR-DT-203 2006) adopts Eurocode 2 (CEN 1992) formulation with bond coefficients of $k_1 = 1.6$ in Eq. (2-33) and $\beta_1 = 0.5$ in Eq. (2-36), corresponding to low bond characteristics between the FRP reinforcement and the concrete.

Other design codes calculate the characteristic crack width as the product of the maximum crack spacing and the average strain of the reinforcement (Eq. (2-38)). This is the case of Eurocode 2 (CEN 2004) and Model Code 90 (CEB-FIB 1990).

$$w_k = s_{r,\max}\left(\varepsilon_{sm} - \varepsilon_{cm}\right)$$ (2-38)

Eurocode 2 (CEN 2004) proposes the calculation of a maximum crack spacing $s_{r,\max}$ assuming that a reasonable estimate of the maximum crack spacing is 1.7 times the average value:

$$s_{r,\max} = 3.4c + 0.425k_1k_2\phi / \rho_{eff}$$ (2-39)

The effective height h_{eff} is here considered as the lesser of 2,5(h-d), (h-x)/3, or h/2.

Model Code 90, in turn, proposes calculating the maximum crack spacing when cracking is stabilised as:

$$l_{s,\max} = \frac{\phi}{3.6\rho_{eff}}$$ (2-40)

where $l_{s,\max}$ is the length of the rebar where the relative slip between steel and concrete is produced and ϕ is the rebar diameter. The effective height of the reinforcement h_{eff} is the lesser between $2,5(h-d)$ and $(h-x)/3$.

According to Eurocode 2 (CEN 2004), the average strain ε_m is computed as the strain in the reinforcement taking into account the tension stiffening effect ε_{sm} minus the average concrete strain at the surface ε_{cm}, as follows:

$$\varepsilon_{sm} - \varepsilon_{cm} = \frac{\sigma_s}{E_s} - \frac{k_t f_{ct,eff}\left(1+\alpha_e\rho_{eff}\right)}{E_s\rho_{eff}} \geq 0.6\frac{\sigma_s}{E_s}$$ (2-41)

where σ_s is the stress in the tension reinforcement calculated assuming a cracked section, α_e is the modular ratio (E_s/E_c), k_t is an empirical factor depending on the duration of the load (0.6 for short-term loads and 0.4 for long-term loads).

The same expression is adopted in Model Code 90 (CEB-FIB 1990), with the only difference that k_t is represented as β and it is defined as a factor to assess the average strain within $l_{s,\max}$ (being 0.6 for short-term and instantaneous loading and 0.38 for long term and repeated loading at the stabilised cracking phase). Moreover, Model Code 90 does not place any minimum value of ε_{sm}-ε_{cm}, as follows:

$$\varepsilon_{sm} - \varepsilon_{cm} = \frac{\sigma_s}{E_s} - \beta\frac{f_{ctm}(t)}{\rho_{eff}E_s}\left(1+\alpha_e\rho_{s,eff}\right)$$ (2-42)

where $f_{ctm}(t)$ is the mean value of the tensile strength at the time t when the crack forms Additionally, Model Code 90 allows computing the strain due to shrinkage, which shall be subtracted to ε_{sm}-ε_{cm}.

Other code provisions involve empirical relationships based on large number of experimental data. This is the case of ACI 318-95 (ACI Committee 318 1995), who adopts Gergely and Lutz (1968) equation to calculate the maximum crack width in beams and thick one-way slabs. The simplified equation for the calculation of the most probable crack width at the tensile face of the beam is:

$$w = 2.2\beta\varepsilon_s\sqrt[3]{d_c A}$$ (2-43)

in which ε_s is the strain in the steel reinforcement at the cracked section, d_c is the concrete cover measured from the centroid of tension reinforcement to the extreme tension surface (Figure 2-6), A is the effective tension area of concrete surrounding the flexural tension reinforcement and having the same centroid as that reinforcement, divided by the number of rebars, and β is the ratio of distance between neutral axis and tension face to distance between neutral axis and reinforcing steel, with a usual value of 1.2:

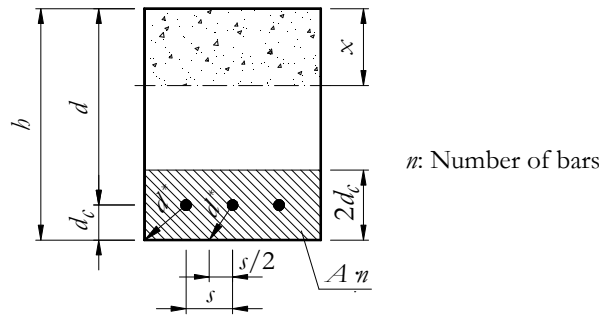$$\beta = \frac{h-x}{d-x} \tag{2-44}$$

Figure 2-6. Parameters for the calculation of the crack width.

Eq. (2-43) was adopted in ACI 440.1R-01 and ACI 440.1R-03 (ACI Committee 440 2001 and ACI Committee 440 2003, respectively) for FRP RC, where a coefficient k_b was included to account for the different bond properties of FRPs with concrete:

$$w = 2.2\beta\varepsilon_f k_b \sqrt[3]{d_c A} \tag{2-45}$$

Gao et al. (1998) adjusted the bond coefficient k_b to their experimental data, obtaining $k_b =$ 0.71 to 1.83, and ACI proposed $k_b = 1.20$ for deformed FRP bars until more data became available.

ACI 318R-05 (ACI Committee 318 2005), however believed that it could be misleading to pretend to effectively calculate crack widths, given the inherent variability in cracking. Moreover, they did not make any distinction between interior and exterior exposures and require that for crack control, the spacing of reinforcement closest to a surface in tension shall not exceed that given by:

$$s = 380\left(\frac{280}{\sigma_s}\right) - 2.5c_c \leq 300\left(\frac{280}{\sigma_s}\right) \tag{2-46}$$

where σ_s is the calculated stress in reinforcement at service load (permitted to be considered 2/3 of f_y) and c_c is the clear cover from the nearest surface in tension to the flexural tension reinforcement.

ACI 440.1R-06 (ACI Committee 440 2006) imposes calculating the maximum probable crack width following Frosch (1999), which is based on a physical model rather than being empirically derived. This design equation considers the maximum distance from the centre of the bar to the concrete surface ($d*$ in Figure 2-6) rather than d_c and includes the same fundamental parameters as those considered to affect crack opening in steel RC, but introduces the bond coefficient k_b to accounts for the different bond behaviour of FRP bars with surrounding concrete:

$$w = 2\frac{\sigma_f}{E_f}\beta k_b \sqrt[3]{d_c^2 + \left(\frac{s}{2}\right)^2}$$
(2-47)

In Eq. (2-47), σ_f is the reinforcement stress, s is the bar spacing, and β and d_c are defined in Figure 2-6. For FRP bars having bond behaviour similar to uncoated steel bars, the bond coefficient shall be assumed equal to 1.0. Inferior bond behaviour implies k_b larger than 1.0 and vice versa. ACI 440.1R-06 reached the consensus that, for the case where k_b is not known from experimental data, a conservative value of 1.4 should be assumed, and further analysis is needed before a value of k_b is proposed. Nevertheless, from an analysis of crack width data performed by ACI Committee 440, average k_b values ranged from 0.60 to 1.72, with a mean of 1.10 (Bakis et al. 2006).

The Canadian code CAN/CSA-S806 (CAN/CSA 2002) introduces a parameter z for cracking control, based on Gergely and Lutz (1968) equation:

$$z = k_b \frac{E_s}{E_f}\sigma_f \sqrt[3]{d_c A}$$
(2-48)

This z parameter should not exceed 45 kN/mm for interior exposure and 38 kN/mm for exterior exposure. The value of k_b shall be determined experimentally, but in the absence of test data, it may be taken as 1.2 for deformed rods.

Based on Gergely and Lutz (1968) equation, ISIS Canada calculates the crack width at the tensile face of the beam as follows:

$$w = 11\frac{E_s}{E_f}\sigma_f k_b \beta \sqrt[3]{d_c A} \cdot 10^{-6}$$
(2-49)

where k_b is the bond dependent coefficient that shall be previously determined. If the k_b coefficient is not known, the value of 1.2 may be used for calculations. This expression results equal to Eq. (2-45) suggested by ACI 440.1R-01 and ACI 440.1R-03. To control the crack width, ISIS Canada (2001) limits the tensile strain at the reinforcement to 2000 $\mu\varepsilon$ (Newhook et al. 2002).

Finally, the Japanese code JSCE (1997) proposes Eq. (2-50) to calculate the crack width, to be less than the allowable crack width:

$$w = k\left(4c + 0.5(s - \phi)\right)\frac{\sigma_f}{E_f} \tag{2-50}$$

in which k is a coefficient expressing the effects of bond characteristics and multiple placement of reinforcing materials (generally between 1.0 and 1.3) and ϕ is the reinforcing bar diameter (mm).

2.5.3. Experimental investigations on flexural cracking of FRP RC members

In the experimental field, Benmokrane et al. (1996) and Masmoudi et al. (1998) reported that cracking general patterns and spacings in FRP RC beams were similar to those in conventionally steel RC beams at low loads.

Matthys and Taerwe (2000) reported that CEB-FIB (1990) and CEN (1992) gave better predictions of the crack width for their experimental data than ACI 318-95 and JSCE (1997).

Pecce et al. (2000) concluded that CEN (1992) gave values of crack width better fitted to their experimental results than ACI 440.1R-03 (ACI 440 Committee 440 2003) approach. CEN (1992) also provided a correct estimate of the crack spacing

Toutanji and Deng (2003) concluded that ACI 440.1R-01 (ACI 440 Committee 440 2001) predicted crack width satisfactorily if FRP bars were placed in one layer. Moreover, Toutanji and Saafi (2000) proposed a modification to the Gergely-Lutz equation, where the bond coefficient was adjusted to the reinforcement ratio, and Saikia et al. (2007) proposed a modification to Toutanji and Saafi (2000) equation adjusted to their experimental data.

El-Salakawy and Benmokrane (2004) reported that ACI 440.1R-01 approach with a k_b coefficient of 1 gave good correlation to test results on slabs, yet conservative, and that all specimens gave a z factor lower than 38 kN/mm.

Ospina and Bakis (Ospina and Bakis 2006, Ospina and Bakis 2007) proposed a new formulation for bar spacing based on Frosch (1999) approach adapted to the particular case of FRP reinforcement:

$$s = 1.2\left(\frac{w}{\varepsilon_f k_b}\right) - 2.5c_c \le 0.95\left(\frac{w}{\varepsilon_f k_b}\right) \tag{2-51}$$

where w is the maximum allowable crack width, ε_f is the strain in the reinforcement at the cracked section and k_b is the bond coefficient.

More recently, El-Gamal et al. (2009) concluded that the experimental crack widths of their tested slabs fitted well with the values predicted by ACI 440.1R-06 using a bond coefficient k_b value of 1.4.

2.6. Deflections of RC beams

Deflection due to flexural stresses can be evaluated from purely geometrical considerations by the basic relationship between curvature (κ) and deflection (y), as shown the following:

$$\kappa = \frac{d^2 y}{dx^2} \tag{2-52}$$

This equation is valid for a concrete beam reinforced with any material, as long as rotations along the beam are small, which is usually the case of RC elements at service loads. Since the evolution of curvatures along the beam is known, the differential equation (2-52) can be simply solved by using curvature-area methods (Gere and Timoshenko 1972).

The difficulty in RC elements arises from the discrete behaviour of concrete cracking, leading to non linear distributions of bond stresses between cracks, and thus the curvature at a section can not be established easily. Moreover, these bond stresses between concrete and the reinforcement cause tension-stiffening effects that should be taken into account. Codes of practice usually state simplifications in equations to provide calculation of curvatures taking into account the cracking behaviour, bond and tension-stiffening effects.

In the case of FRP RC elements, wider and deeper cracks compared to those of steel RC structures are expected. The characteristics of such cracks have significant interaction with the stresses and displacements induced in the concrete and the reinforcing bars crossing the crack (dowel action of bars), as well as on the contribution of the stirrups at crack location (Al-Sunna 2006).

2.6.1. Code provisions for instantaneous deflections of steel RC members

A common and accepted methodology to estimate deflections is the Branson equation (Branson 1968, Branson 1977). The deflection may be calculated using usual elastic theory equations for elastic uncracked elements. The flexural stiffness EI of the member is considered, being E the modulus of elasticity of the concrete and I the moment of inertia of the equivalent section. Until the maximum tensile stress in the element does not reach the tensile strength of the concrete, it shall be considered that the section remains uncracked, thus I is the gross moment of inertia about the centroidal axis I_g. When the bending moment is great enough for the tensile stress to exceed the tensile strength of concrete, cracks will form and the moment of inertia is suddenly reduced at the cracked section. Between cracks, tension is transferred from the reinforcement to concrete by bond stresses (the *tension stiffening* phenomenon), thus an equivalent moment of inertia I_e is proposed as:

$$I_e = \left(\frac{M_{cr}}{M_a}\right)^3 I_g + \left[1 - \left(\frac{M_{cr}}{M_a}\right)^3\right] I_{cr} \leq I_g \tag{2-53}$$

where M_a is the maximum moment in the member at the stage at which the deflection is being computed and M_{cr} is the moment at first cracking. This methodology was adopted by the ACI 318R-05 (ACI Committee 318 2005) to calculate short-term deflections.

In contrast, Model Code 90 (CEB-FIB 1990) suggests calculating flexural deflexions from curvatures, by applying appropriate procedures, such as the principle of virtual work or double integration. The mean curvature at any section of an element may be given by the relationship (2-54),

$$\kappa = \frac{1}{r} = \frac{\varepsilon_{sm} - \varepsilon_{cm}}{d} \tag{2-54}$$

where ε_{sm} is the mean steel strain assessed on the basis of tension stiffening effect, ε_{cm} is the mean concrete strain and d is the effective depth. The mean curvature evolution with moment for a steel RC section is represented in Figure 2-7.
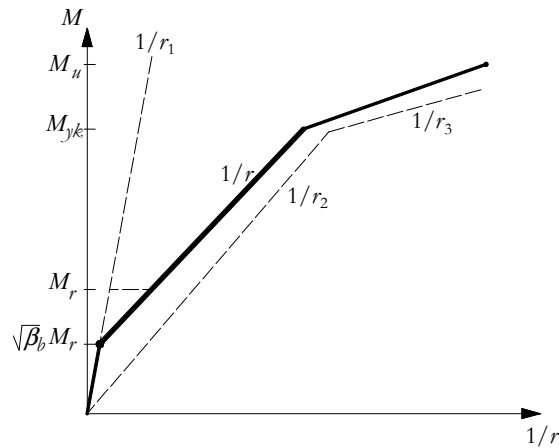

Figure 2-7. Mean curvature for simple bending (CEB-FIB 1990).

Eurocode 2 (CEN 1992, CEN 2004), in turn, proposes an interpolation of a deformation parameter α, which can be either curvature or a deflection, between its uncracked (α_I) and fully cracked (α_{II}) states:

$$\alpha = \zeta \alpha_{II} + (1 - \zeta)\alpha_I \tag{2-55}$$

where ζ is a distribution coefficient allowing for the tension stiffening at a section, given by:

$$\zeta = 1 - \beta \left(\frac{\sigma_{sr}}{\sigma_s} \right)^2 \tag{2-56}$$

in which β is equal to $\beta_1\beta_2$ according to Eurocode 2 (CEN 1992), being β_1 equal to 1.0 for high bond and 0.5 for plain bars, and β_2 equal to 1.0 for short-term loading and 0.5 for sustained loads. In Eurocode 2 (CEN 2004), β is equal to β_2, since high bond is assumed between the steel bar and the concrete. In Eq. (2-56), σ_s is the stress in the tension reinforcement calculated on the basis of a cracked section and σ_{sr} is the reinforcement stress under the loading conditions causing first cracking, calculated on the basis of a cracked section. The ratio σ_{sr}/σ_s may be replaced by M_{cr}/M_a for flexure, where M_{cr} is the cracking moment and M_a is the applied moment.

Finally, EHE (CPH 2008) proposes Branson's equation (Branson 1977) to easily calculate the instantaneous deflection at a certain load step.

2.6.2. Prediction models for instantaneous flexural deflections of FRP RC members

In the last two decades, a number of researchers have proposed adjustments to adapt Branson equation to experimental results on deflections of FRP RC elements. In general, it was reported that Branson equation overestimated the effective moment of inertia developed in Eq. (2-53), consequently underestimating deflections (Faza and GangaRao 1992, Benmokrane et al. 1996, Brown and Barholomew 1996, Masmoudi et al. 1998, Pecce et al. 2000, Razaqpur et al. 2000, Toutanji and Saafi 2000). The main reason for this difference in deflections was attributed to the fact that Branson equation was calibrated for moderately reinforced concrete beams having an I_g/I_{cr} ratio less than 3 (Bischoff 2005), whereas most of the cases of FRP RC elements have I_g/I_{cr} ratios between 5 and 25 (Bischoff et al. 2009) and reinforcement ratios higher than those of steel RC. Moreover, the bond behaviour between the FRP bar and the concrete is different than that of steel and consequently, the tension stiffening effect should be re-evaluated.

Most attempts at computing deflection in FRP RC flexural members have involved modifications to Branson's original expression that soften the member response. Among them, Benmokrane et al. (1996) adds two reduction factors to Eq. (2-53) and adjusts them to their experimental data as follows:

$$I_e = \alpha I_{cr} + \left(\frac{I_g}{\beta} - \alpha I_{cr} \right) \left(\frac{M_{cr}}{M_a} \right)^3 \tag{2-57}$$

For their data, α equals to 0.84 and β equals to 7. These factors were attributed to the nature of the FRP reinforcement, which exhibited larger deflection than the steel reinforcement, resulting in greater reduction of the compressed concrete section when the applied moment reached the cracking moment.

Other authors modified the power of the (M_{cr}/M_a) ratio in Branson equation to achieve the same softened response. Toutanji and Saafi (2000) adjusted this power factor to account for the modulus of elasticity of the rebar and the reinforcement ratio of their experimental results (three sets of GFRP RC beams with I_g/I_{cr} ratios of 13 to 23):

$$I_e = \left(\frac{M_{cr}}{M_a}\right)^m I_g + \left(1 - \left(\frac{M_{cr}}{M_a}\right)^m\right) I_{cr} \leq I_g \tag{2-58}$$

$$m = 6 - \frac{10 E_f}{E_s} \rho_f \ \text{if} \ \frac{E_f}{E_s} \rho_f < 0.3$$

$$m = 3 \ \text{if} \ \frac{E_f}{E_s} \rho_f \geq 0.3 \tag{2-59}$$

Brown and Bartholomew (1996), in turn, used a value of 5 for m to adjust their experimental values of two GFRP RC beams with I_g/I_{cr} ratios close to 11, whilst Alsayed et al. (2000) proposed m equal to 5.5 according to their experimental data.

ACI 440.1R-01 (ACI Committee 440 2001) adopted the modification of Branson equation proposed by Gao et al. (1998):

$$I_e = \left(\frac{M_{cr}}{M_a}\right)^3 \beta_d I_g + \left(1 - \left(\frac{M_{cr}}{M_a}\right)^3\right) I_{cr} \leq I_g \tag{2-60}$$

in which β_d was the correction factor. This factor was initially set equal to 0.6, based on Masmoudi et al. (1998) and Thériault and Benmokrane (1998) studies. ACI 440.1R-01 and ACI 440.1R-03 (ACI Committee 440 2001 and ACI Committee 2003, respectively) recommend calculating β_d as follows:

$$\beta_d = \alpha_b \left(\frac{E_f}{E_s} + 1\right) \tag{2-61}$$

where α_d is a bond-dependent coefficient. According to test results on simply supported beams, the value of α_d for a given GFRP bar was found to be 0.5 (Gao et al. 1998). Later on, ACI 440.1R-03 calibrated the α_d coefficient depending on the amount of longitudinal reinforcement, based on 48 experimental tests on GFRP RC beams, giving:

$$\alpha_b = 0.064 \left(\frac{\rho_f}{\rho_{fb}}\right) + 0.13, \tag{2-62}$$

where ρ_f is the actual reinforcement ratio and ρ_{fb} is the balanced reinforcement ratio, defined in Eqs. (2-17) and (2-18) respectively. ACI 440-1R-06 (ACI Committee 440 2006), adapts the

β_d coefficient based on a more extended experimental database that included both GFRP and CFRP RC elements:

$$\beta_d = \frac{1}{5}\left(\frac{\rho_f}{\rho_{fb}}\right) \tag{2-63}$$

The coefficient β_d was calibrated for GFRP an CFRP RC elements with a E_f/f_{fu} ratio close to 60 (Bischoff et al. 2009), which was the typical value for most commercially available GFRP and CFRP bars at that time, and depends on the balanced reinforcement ratio. Hence, according to this formulation, the deflection of a FRP RC element would depend on the tensile strength of the FRP bar, which results meaningless.

More recently, Rafi and Nadjai (2009) adjusted Branson equation to an extensive experimental database, by introducing a γ factor that reduces the portion of the cracked moment of inertia:

$$I_e = \left(\frac{M_{cr}}{M_a}\right)^3 \beta_d I_g + \left(1-\left(\frac{M_{cr}}{M_a}\right)^3\right)\frac{I_{cr}}{\gamma} \leq I_g \tag{2-64}$$

$$\gamma = 0.86\left(1+\frac{E_f}{400}\right) \tag{2-65}$$

According to this approach, β_d is calculated by Eq. (2-63).

ISIS Canada (2001) recommends Ghali et al. (2001) relationship for the effective moment of inertia I_e, derived from curvature methods, as an alternative to Eq. (2-60):

$$I_e = \frac{I_g I_{cr}}{I_{cr} + \left(1 - 0.5(M_{cr}/M_a)^2\right)\left(I_g - I_{cr}\right)} \tag{2-66}$$

CAN/CSA-S806 (CAN/CSA 2002), adopts Razaqpur et al. (2000) methodology, which assumes that tension stiffening is insignificant in cracked regions on an FRP beam, using $E_c I_g$ when $M_a < M_{cr}$ and $E_c I_{cr}$ when $M_a > M_{cr}$ to integrate the curvature M/EI along the beam span. This leads to simple expressions for beam deflection. Eq. (2-67) shows the expression to calculate the maximum deflection δ_{max} for a four-point bending configuration, with two loads P at a distance a from the supports, being L_g the distance that the beam is uncracked:

$$\delta_{max} = \frac{PL^3}{24E_c I_{cr}}\left[3\left(\frac{a}{L}\right) - 4\left(\frac{a}{L}\right)^3 - 8\left(1-\frac{I_{cr}}{I_g}\right)\left(\frac{L_g}{L}\right)^3\right] \tag{2-67}$$

This formulation was used by Saikia et al. (2007), finding good agreement with their experimental data.

CNR-DT-203 (2006) adopts Eurocode 2 (CEN 1992) formulation (Eq. (2-55)), α being the flexural deflection δ, with a bond coefficient β_1 equal to 0.5, corresponding to the minimum bond between the FRP bar and the concrete.

Other approaches involving integration of curvature M/EI along the length of the beam have been proposed for FRP RC beams. This is used in lieu of assuming a constant average value of I_e over the entire length of the beam. However, the accuracy of these approaches depends on the values assumed for the post cracking curvature. Among these approaches, Faza and GangaRao (1992) developed a model for a modified moment of inertia, based on the assumption that the concrete section between the point loads is fully cracked, while the end sections are assumed to be partially cracked (Figure 2-8). Furthermore, Faza and GangaRao (1992) used FRP reinforcing bars with different coatings and found out that the deflection behaviour was highly dependent on the type of coating (being the deflection response improved when sand coated rebars were used instead of the ones with a smooth surface).
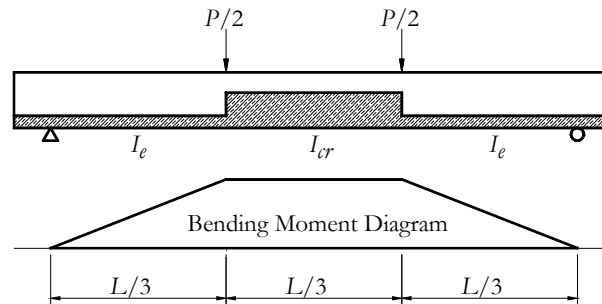
Figure 2-8. Distribution of moments of inertia depending on the bending moment diagram, after Faza and GangaRao (1992).

An expression for this partially cracked moment of inertia I_m was developed for several load cases. For the case of two concentrated point loads applied at the third points of the beam, the maximum deflection is calculated as follows:

$$\Delta_{max} = \frac{23PL^3}{648 E_c I_m} \qquad (2\text{-}68)$$

where I_m is the modified equivalent moment of inertia:

$$I_m = \frac{23 I_{cr} I_e}{8 I_{cr} + 15 I_e} \qquad (2\text{-}69)$$

Based on Favre and Charif method for deflection calculations (Favre and Charif 1994), Abdalla (2002) proposed the calculation of the equivalent moment of inertia, as follows:

$$I_e = \frac{I_g I_{cr}}{I_{cr} \xi + 1.15 I_g (1 - \xi)} \qquad (2\text{-}70)$$

$$\xi = \frac{0.5M_{cr}}{M_a} \tag{2-71}$$

Eq. (2-70) includes a reduction factor of 1/0.85 to account for the reduction in tension stiffening in the fully cracked FRP concrete section.

Hall and Ghali (2000) defined a mean moment of inertia I_m from the mean curvature defined as:

$$\kappa_m = \frac{M}{E_c I_m} \tag{2-72}$$

Rearranging terms between Eq. (2-55) with α being curvature (κ) and Eq. (2-72), I_m equals to:

$$I_m = \frac{I_g I_{cr}}{(1-\zeta)I_{cr} + \zeta I_g} \tag{2-73}$$

where ζ is defined in Eq. (2-56).

Bischoff (Bischoff 2005, Bischoff 2007a, Bischoff 2007b, Bischoff and Scanlon 2007) proposed an equation derived from integration of curvatures along the beam taking account of the tension-stiffening effect:

$$I_e = \frac{I_{cr}}{1 - \left(1 - \frac{I_{cr}}{I_g}\right)\left(\frac{M_{cr}}{M_a}\right)^2} \tag{2-74}$$

Almusallam (2006) developed an iterative numerical solution procedure based on the incremental deformation technique. The solution starts by assuming a value for the strain at the concrete extreme compression fibre and a location for the neutral axis. Then, iterations follow by changing the neutral axis depth until the equilibrium of forces is satisfied for the assumed extreme compression strain. This solution does not yield to analytical expressions easy to apply in analysis and design; however, provides good predictions of the flexural deflection of steel and GFRP RC beams.

Aiello and Ombres (2000b) proposed a theoretical procedure for the calculation of deflections derived from a cracking analysis based on slip and bond stresses. This methodology was experimentally compared to flexural tests on AFRP RC beams. Although the block model gave satisfactory predictions that were in agreement with the experimental results, the procedure appeared to be onerous from a computational point of view and its use for design practice was difficult.

Vogel and Švecová (Vogel and Švecová 2008, Vogel and Švecová 2009) presented a procedure to calculate deflections taking into account the effects of tension stiffening that incorporated

material properties of the reinforcement as well as the effects of concrete non-linearity in compression.

Mota et al. (2006) presented a critical review of deflection formulae for FRP RC members, finding that the accuracy of the deflection equations varies at different load ratios and highly depends on the accuracy to calculate the cracking moment. Furthermore, it concluded that there is a critical need for reliability analysis of FRP code equations.

2.6.3. Long-term flexural deflection of FRP RC

For FRP RC elements, the relative curvature increment associated with creep and shrinkage is lower than that for conventional steel RC elements, due to the smaller compressed area of concrete. As a consequence, lower time-dependent deflections are expected in FRP RC beams. Several studies have reported experimental work and analytical proposals on this topic (Arockiasamy et al. 2000, Hall and Ghali 2000, Al-Salloum and Almusallam 2007, Miàs et al. 2010).

ACI 440.1R-06 (ACI Committee 440 2006), based on tests carried out by Brown (Brown and Bartholomew 1996, Brown 1997), proposes multiplying the factor used for steel RC elements by 0.6, although the code recognizes that further work is necessary to validate this coefficient. In turn, CAN/CSA-S806 (2002) proposes a more conservative approach, adopting the same coefficients as for steel, defined in CAN/CSA-A23.3 (1994).

Recent studies propose simplified methodologies for the evaluation of the time-dependent deflections of FRP RC elements based on factors that take into account the modular ratio of materials n (equal to E_f/E_c) and the reinforcement ratio ρ (Miàs et al. 2010).

2.6.4. Shear-induced deflection of FRP RC

In general, for short, deep rectangular steel RC beams, the deformations caused by shear forces may become insignificant (Park and Paulay 1975). However, when FRPs are used as internal reinforcement, the contribution of the shear cracks at high levels of loading can result significant in the contribution of the total deflection of the element, especially after diagonal cracking has taken place.

Several researchers have computed the shear deflection through experimental tests, both for steel RC elements (Ueda et al. 2002 through using a laser speckle method, or Debernardi and Taliano 2006), and for FRP RC elements (Guadagnini 2002 or Imjai 2007).

To compute the shear deformation, CEB Design Manual on Cracking and Deformations (CEB 1983) proposes calculating the shear strain γ for steel RC at a cracked state (state II) as an interpolation between states I (uncracked section, Eq. (2-75)) and II_0 (fully cracked section, Eq. (2-76) for the case of stirrups perpendicular to the beam axis).

$$\gamma_1 = \frac{V}{G_c A_w} \approx \frac{3V}{E_c b_w d} \tag{2-75}$$

$$\gamma_2 = \frac{V}{0.9 b_w d} \cdot \left(\frac{1}{\rho_w E_s} + \frac{4}{E_c} \right) \tag{2-76}$$

In Eq. (2-75) and (2-76), V is the shear force acting at the section, G_c is the shear modulus of concrete, A_w is the web area of the beam, E_c and E_s are the elastic modulus of concrete and steel respectively, b_w is the web thickness of the beam, d is the effective depth and the shear reinforcement ratio ρ_w is:

$$\rho_w = \frac{A_w}{b_w s} \tag{2-77}$$

being s the spacing of the shear reinforcement. The mean shear deformation γ_m is computed in the transition stage between states I and II_0 is computed as:

$$\gamma_m = (1 - \varsigma)\gamma_1 + \varsigma\gamma_2 \tag{2-78}$$

$$\varsigma = 0 \ \text{ for } V < V_r$$

$$\varsigma = 1 - \left(\frac{4V_r - V}{3V_r} \right)^2 \text{ for } V_r < V < 4\,V_r \tag{2-79}$$

$$\varsigma = 1 \ \text{ for } V > 4\,V_r$$

where V_r is the shear cracking force:

$$V_r = \tau_r k (1 + 50\rho) b_w d \tag{2-80}$$

In Eq. (2-80), τ_r is the shear strength of concrete and k is 1600-d (d in mm).

Other theoretical approaches for the calculation of shear deflections are found in the literature for steel RC. Ueda et al. (2002) propose a model based on calculating an additional flexural deformation due to shear cracking plus a shear deformation, which was calculated before and after shear cracking is attained. Debernardi and Taliano (2006) presented a model based on the application of the constitutive laws of the modified compressive field theory.

2.7. Verification of the serviceability limit states of FRP RC elements

Serviceability limit states (SLS) are applied to RC structures to ensure their functionality and structural integrity under service conditions. For FRP RC structures, the specific mechanical characteristics of the FRP rebars (especially their lower modulus of elasticity but also their

different bond behaviour) are expected to result in SLS-governed design (Matthys and Taerwe 2000, ISIS Canada 2001, Nanni 2003, fib 2007).

The SLS to be considered are generally the stresses in materials, deflections (short and long-term) and crack width and spacing. The SLS of vibrations is not included in this study.

2.7.1. Control of stresses in materials

Stresses in concrete

Design codes usually limit the compressive stress that can be developed in concrete under service conditions to avoid problems arising from the occurrence of longitudinal cracks, micro-cracks and high levels of creep.

Although specific limits on concrete compression stresses under service conditions are not prescribed explicitly in all of the existing design provisions, the concrete stresses are generally assumed to be within the linear range. ACI440.1R-06 (ACI Committee 440 2006), for instance, adopted this latter approach. A limiting value of $0.45f'_c$, however, is explicitly recommended in ACI.440.2R-08 (ACI Committee 440 2008) for RC elements strengthened with FRPs.

Furthermore, Eurocode 2 (CEN 2004) limits the maximum stress in concrete under the quasi-permanent combination of loads to $0.45f_{ck}$ to assume linear creep and a maximum of $0.60f_{ck}$ under the characteristic combination of loads to avoid the appearance of longitudinal cracks, which could greatly affect durability. Model Code 90 (CEB-FIB 1990), in turn, maintains the limitation of $0.60f_{ck}$ to avoid longitudinal cracking, but limits the compressive stress in concrete to $0.40f_{ck}$ under the quasi-permanent combination to correctly use the lineal model for the assessment of creep. EHE (CPH 2008) only limits the compressive stress in concrete to $0.60f_{ck}$ under the most unfavourable combination of loads.

Stresses in the FRP reinforcement

The stress in the FRP reinforcement should be limited to avoid creep rupture or stress corrosion, which consists in the creep of the material under a constant load after a certain "endurance" time (fib 2007). Stress corrosion related problems are only significant, however, when using glass fibre reinforced composites.

Existing design recommendations (JSCE 1997, IStructE 1999, ISIS Canada 2001, CAN/CSA 2002, ACI Committee 440 2006) have already provided different stress limits for the different types of FRP reinforcement (Table 2-2). These factors take into account the influence of environmental conditions as well as the effect of sustained permanent loads, which are considered jointly or separately, and generally lead to severe reductions in the value of allowable stress when compared to the bar strength (taking values from 0.20 to 0.55 times the ultimate tensile strength of the bar, f_{fu}).

Table 2-2. Reduction factors used in existing guidelines

Factor	ACI 440.1R-06	CAN/CSA-S806	JSCE	IStructE	CNR-DT-203
Reduction for environmental deterioration	C_E GFRP: 0.7-0.8 AFRP: 0.8-0.9 CFRP: 0.9-1.0	Φ_{FRP} GFRP: 0.5 AFRP: 0.6 CFRP: 0.75	$1/\gamma_{fm}$ GFRP: 0.77 AFRP: 0.87 CFRP: 0.87	$1/\gamma_m$ "material factor"	η_a GFRP: 0.7-0.8 AFRP: 0.8-0.9 CFRP: 0.9-1.0
Stress limit for permanent load	GFRP: 0.2 AFRP: 0.3 CFRP: 0.55	Pre/Post tension: GFRP: 0.25-0.3 AFRP: 0.35-0.4 CFRP: 0.65-0.7	$0.8 \times$ "creep failure strength" $\leq$ 0.7	Stress limits not specified	η_l GFRP: 0.3 AFRP: 0.5 CFRP: 0.9

Other less conservative approaches can be considered if specific data on the durability properties of the reinforcement are available (fib 2007, Huang and Aboutaha 2010). fib Bulletin 40 (fib 2007), for instance, presents a procedure based on durability specifications that allows determining appropriate margins of safety depending on environmental and stress conditions, generic FRP type, and required design life. Following this methodology, the FRP design strength f_{fd} can be obtained from the characteristic short term strength f_{fk0}, divided by a material factor γ_f, and by an environmental strength reduction factor $\eta_{env,t}$:

$$f_{fd} = \frac{f_{fk0}}{\eta_{env,t}\gamma_f}$$ (2-81)

The value of $\eta_{env,t}$ can be obtained from:

$$\eta_{env,t} = \frac{f_{fk1000h}}{f_{fk0}\left(\dfrac{100-R_{10}}{100}\right)^n}$$ (2-82)

in which $f_{fk1000h}$ is the residual strength at 1000 hours, and R_{10} is the standard reduction in strength per logarithmic decade, both values obtained from specific durability tests. The coefficient n accounts for the moisture and temperature conditions, the service life (years), and the rebar diameter.

2.7.2. Control of cracking

Design codes for steel or FRP RC limit the maximum crack width for several reasons. Among the most common ones, the general appearance of the structure is important to be maintained in a way that does not alarm the society and the clients for whom the structure is destined to. Another particular reason is found in certain type of structures, in which the possibility of

leakage of water or other liquids or gases through cracks has to be considered. Finally, an important structural reason for controlling cracking is the protection against corrosion of steel reinforcement.

For the case of steel RC, Eurocode 2 (CEN 1992, CEN 2004) and Model Code 90 (CEB-FIB 1990) limit the maximum crack width (w_{max}) of non-presstressed members to about 0.3 mm under the quasi-permanent combination of loads for situations where corrosion may take place. However, for exposure classes with no risk of corrosion or attack, this limit is relaxed to 0.4 mm to guarantee acceptable appearance. EHE (CPH 2008) maintains these two limits but drops w_{max} until 0.1-0.2 mm for situations exposed to very high corrosive environments. ACI 318-95 (ACI Committee 318 1995), instead of limiting the maximum crack width, limits the bar spacing closest to the tension face of the beam (Eq. (2-46)), while CAN/CSA-A23.3 distinguishes between exterior and interior exposures, limiting the maximum crack width to 0.3 mm and 0.4 mm respectively.

For corrosion resistant FRP reinforcement, when the primary reason for crack width limitation is the corrosion of reinforcement, this limitation can be relaxed. ACI 440.1R-06 (ACI Committee 440 2006), for example, increases the allowable crack width limits to 0.5 and 0.7 mm for interior and exterior exposures respectively, while JSCE (1997) and CNR-DT-203 (2006) recommend maximum crack width of 0.5 mm in both cases. ISIS Canada (2001) limits the maximum strain in FRP to 2000 $\mu\varepsilon$ for crack width control. Likewise, CAN/CSA-S806 defines the quantity z (Eq. (2-48)) not to exceed 45 kN/mm for interior exposure and 38 kN/mm for exterior exposure.

2.7.3. Control of deflections

Verification of deflections

The deformation of a member or structure shall not be such that it adversely affects its proper functioning or appearance (CEN 2004). Deformations should not exceed those that can be accommodated by other connected elements such as partitions, glazing, cladding, services or finishes. Design codes propose different limitations for the relative sag of the element to the supports.

In the case of Eurocode 2 and Model Code 90 for steel RC, the sag of the element is limited to $L/250$ under the quasi-permanent combination of loads. In addition, Eurocode 2 limits the deflection after construction of non-structural elements, which is the sum of the long-term deflection due to all sustained loads and the immediate deflection due to any additional variable load, to $L/500$.

Conversely, ACI 318R-05, does not limit the total deflection and only limits the deflection after construction of non-structural elements to $L/240$ (for roofs or floors supporting elements not likely to be damaged by deflections) and $L/480$ (for roofs or floors supporting elements likely to be damaged by deflections).

In the case of FRP RC structures, CAN/CSA-S806 and ACI 440.1R-06 adopt ACI 318R-05 criterion, whereas CNR-DT-203 does not suggest any limitation.

Dimensioning for deflection control: Span-to-depth ratios

The limit state of deformation can be checked either by direct calculation of deflections or by limiting the span-to-depth ratio (L/d) to a certain value. Eurocode 2 (CEN 2004) provides Eqs. (2-83) and (2-84) to calculate the minimum L/d ratio not to calculate deflections for steel RC:

$$L/d = K\left(11 + 1.5\sqrt{f_{ck}}\,\frac{\rho_0}{\rho} + 3.2\sqrt{f_{ck}}\left(\frac{\rho_0}{\rho} - 1\right)^{3/2} \right) \text{ if } \rho \le \rho_0 \qquad (2\text{-}83)$$

$$L/d = K\left(11 + 1.5\sqrt{f_{ck}}\,\frac{\rho_0}{\rho - \rho'} + \frac{1}{12}\sqrt{f_{ck}}\left(\frac{\rho'}{\rho}\right)^{1/2} \right) \text{ if } \rho > \rho_0 \qquad (2\text{-}84)$$

where K is the factor that accounts for the different structural systems (being 1 for simply supported elements, 1.3 for end span of a continuous beam, 1.5 for interior span of a beam, 1.2 for a slab supported on columns without beams and 0.4 for cantilever beams), ρ_0 is the reference reinforcement ratio (equal to $\sqrt{f_{ck}}\,10^{-3}$), ρ is the required tension reinforcement ratio at midspan (at support for cantilevers) and ρ' is the required compression reinforcement. Eqs. (2-83) and (2-84) have been derived from the assumption that the stress in the steel reinforcement at a cracked section at the midspan (or at the support in the case of a cantilever) is 310 MPa, which is considered an appropriate design flexural level for the SLS. This procedure is adopted by EHE (CPH 2008).

Model Code 90 proposes Eq. (2-85) for RC flexural elements without axial force:

$$L/d \le \lambda = \lambda_0 k_T k_L \left(\frac{400}{f_{yk}}\right) \qquad (2\text{-}85)$$

where λ_0 adopts different values depending on the reinforcing level (highly or lightly stressed) and on the boundary conditions ($\lambda_0 = 18$ for a simply supported beam with $\rho = 1.5\%$), k_T is a coefficient that accounts for the shape of the beam ($k_T = 1$ for rectangular sections), $k_L = 7/L \le 1$ (L in m), and f_{yk} is the yield stress of the reinforcing steel (in MPa). In the case of Eurocode 2, EHE and Model Code 90, Eqs. (2-83), (2-84) and (2-85) were calculated to limit the midspan total deflection to $L/250$.

In the case of FRP RC elements, Ospina et al. (2001) proposed a maximum span-to-total depth ratio L/h, corresponding to the limiting curvature associated with a target deflection-to-span ratio:

$$\frac{L}{h} = \frac{48\,d/h}{5K_1}\left(\frac{1-k}{\varepsilon_f}\right)\left(\frac{\delta}{L}\right)_{max}$$ (2-86)

where K_1 is a parameter that accounts for the boundary conditions ($K_1 = 1$ for a simply-supported beams, 0.8 for one end continuous, 0.6 for both ends continuous and 2.4 for cantilevered spans), ε_f is the reinforcement tensile strain under the service load, $(\delta/L)_{max}$ is the limiting service load deflection-span ratio (in that case, $1/250$) and k is a dimensionless parameter defined as:

$$k = \sqrt{2n\rho + (n\rho)^2} - n\rho$$ (2-87)

being n the modular ratio. This procedure assumes no tensile contribution of concrete between cracks and can be applied to any type of reinforcement.

Later on, Ospina and Gross (2005) modified Eq. (2-86) to account for the tension stiffening effect by using the moment-curvature model of the Model Code 90:

$$\frac{L}{h} = \frac{48\,d/h}{5K_1}\left[\frac{1}{\left[(1-\zeta)\dfrac{15\,d/h}{57000}+\zeta\,\dfrac{\varepsilon_f}{1-k}\right]}\right]\left(\frac{\delta}{L}\right)_{max}$$ (2-88)

where the parameter ζ is defined in Eq. (2-56). This last procedure was adopted by ACI 440.1R-06 to recommend the maximum span-to-depth ratios.

Based on the study of Ghali et al. (2001), ISIS Canada (2001) proposes another equation for the span-to-total depth ratio for FRP RC $(L/h)_f$, based on the L/h ratio for steel RC defined in CAN/CSA-A23.3-94, $(L/h)_s$:

$$\left(\frac{L}{h}\right)_f = \left(\frac{L}{h}\right)_s\left(\frac{\varepsilon_s}{\varepsilon_f}\right)^{\alpha_d}$$ (2-89)

In Eq. (2-89), α_d is a dimensionless coefficient ($\alpha_d = 0.50$ for a rectangular section). This equation was developed and verified by parametric studies (Hall and Ghali 2000).

Hegger and Kurth (2009) proposed span-to-total depth ratios for FRP RC slabs based on a simplified methodology to compute deflections described in Zilch and Donaubauer (2006).

Table 2-3 summarizes the typical standard values for the span-to-depth ratios of different codes of practice, both for steel and FRP RC elements.

Table 2-3. Span-to-depth ratios for steel and FRP RC members

Structural system		Eurocode 2 (CEN 2004), EHE (CPH 2008)		ACI 318R-05, CAN/CSA-A23.3-94	ACI 440.1R-06
		$\rho = 0.5\%$	$\rho = 1.5\%$		
Simply supported	Beam	$L/d = 20$	$L/d = 14$	$L/h = 16$	$L/h = 10$
	One-way slab			$L/h = 20$	$L/h = 13$
One end continuous	Beam	$L/d = 26$	$L/d = 18$	$L/h = 18.5$	$L/h = 12$
	One-way slab			$L/h = 24$	$L/h = 17$
Both ends continuous	beam	$L/d = 30$	$L/d = 20$	$L/h = 21$	$L/h = 16$
	One-way slab			$L/h = 28$	$L/h = 22$
Cantilever	beam	$L/d = 8$	$L/d = 6$	$L/h = 8$	$L/h = 4$
	One-way slab			$L/h = 10$	$L/h = 5.5$

2.8. General remarks

The unique mechanical properties of FRP bars have a significant effect on the structural performance of RC elements. In particular, these bars present linear stress-strain behaviour under tension until rupture, higher tensile capacity and generally lower modulus of elasticity compared to that of steel, and limited strain range. In addition, those bars present different surface conditions such as sand coated, ribbed, indented or braided. All these characteristics have a direct effect on the flexural behaviour of FRP RC, generally leading to higher deflections and crack widths than for the case of steel RC. Thus, serviceability criteria may govern the design of FRP RC and needs to be reassessed.

Despite several design guidelines, codes and recommendations have recently been published, the lack of agreed standards for design is still perceived as a barrier to the extensive use of FRPs in construction.

Chapter 3
Experimental program

3.1. Introduction

This chapter presents the details of the experimental program carried out in this work. The main aim of the experimental program was to obtain the most reliable data on strains, deflections and cracks at the serviceability stages of loading. The beams were tested until failure to additionally evaluate the failure load and the flexural behaviour at the ultimate limit state.

The beam specifications, the design philosophy, the preparation of the tests, the test setup and the procedure are detailed next. Moreover, the general instrumentation is described, and a summary of the properties of the materials is shown.

3.2. Test details

3.2.1. Beam specifications

The focus of this study was to investigate the serviceability behaviour of GFRP RC beams. Hence, deflections, cracking and stress levels were intended to be registered for the different types of RC beam specimens. More specifically, different concrete grades f_c, the reinforcement ratios ρ and the effective-to-overall depth ratios d/h were used to investigate their effects on tension stiffening, cracking and deflections.

The concrete properties were expected to directly affect the stiffness of the beam, not only before cracking, but also once cracking had taken place and until rupture. The compressive

strength of the concrete was a design parameter, while the tensile strength would define the cracking load. The reinforcement ratio was considered a parameter of main importance due to its influence on the stiffness of the cracked beam. Moreover, ρ was expected to have an influence on the tension stiffening effect and cracking. Finally, the effective-to-overall depth ratio was considered a parameter directly related to crack spacing and, consequently, to crack width. Furthermore, the effective-to-overall depth ratio was expected to affect the relationship between the cracked and uncracked moments of inertia (I_{cr}/I_g) and consequently, the post-cracking flexural behaviour (Torres et al. 2003; Torres et al. 2004), involving the deflection behaviour in the serviceability range.

A total amount of twenty-six GFRP RC beams was designed with an adequate amount of longitudinal and shear reinforcement to fail by crushing of concrete in the central zone. Additionally, one steel RC beam with similar stiffness to one type of the GFRP RC elements was tested for comparison purposes. The total length of each beam was 2050 mm, with a rectangular cross-section of b mm wide (variable) and 190 mm deep. The specimens were tested under four-point bending, with 1800 mm total span, and 600 mm shear span, the distance between loads being 600 mm. The shear span was reinforced with an amount of steel stirrups enough to avoid shear failure (ϕ8mm@70mm). In the pure bending zone no stirrups were provided so as to not influence crack development in the constant moment zone. Two 6 mm steel rebars were used as top reinforcement to hold stirrups in the shear span zone. The beam tests layout is detailed in Figure 3-1.
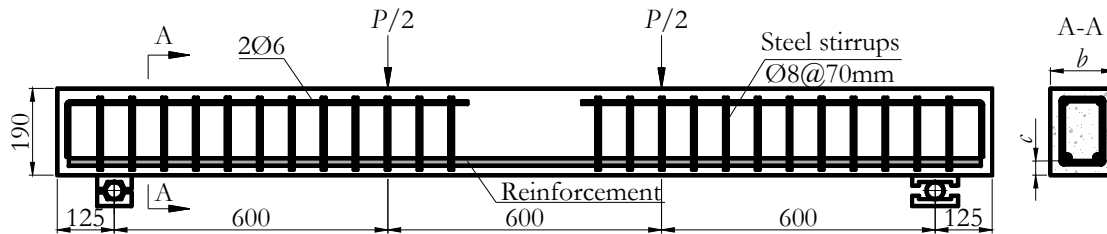
Figure 3-1. Geometric and reinforcement details (dimensions in mm).

Three different amounts of longitudinal reinforcement (2ϕ12, 2ϕ16 and 3ϕ16), two different effective depth to total depth ratios (0.75 and 0.86) and two different concrete grades (30 and 50 MPa) were used. The width of the beams was changed so as to maintain a reinforcement ratio of 0.99%, 1.77% and 2.66%, respectively. The steel RC beam was designed to behave with the same cracked stiffness as the GFRP RC element reinforced with 3ϕ16.

The beam types were identified as C*x-yyy*-D*z*. The first term of the identification corresponded to a beam series. Beams series C1 stands for a target concrete strength of 30 MPa, whilst for beam series C2 and C3 the target concrete strength was of 50 MPa.

The second parameter that identified the beam specimen was the reinforcement ratio ρ. Three different amounts of reinforcement were used: 2 rebars of 12 mm diameter (Cx-212), 2 rebars of 16 mm diameter (Cx-216), and 3 rebars of 16 mm diameter (Cx-316).

Finally, the effective depth to the overall depth ratio d/h was studied by changing the concrete clear cover c to the main flexural bar. Thus, beams Cx-yyy-D1 had a concrete cover of 20 mm, and beams Cx-yyy-D2 had a concrete cover of 40 mm. This d/h parameter slightly varied between beams with different diameters, since d was h minus a fixed concrete cover c and one rebar radius $\phi/2$. As a result, the width b of the beam was changed accordingly to maintain the reinforcement ratio in beams with different depth ratios. The minimum lateral concrete cover of the bars was 20 mm. The use of such covers was made to avoid splitting bond failure. The geometric characteristics of the different sections are summarized in Table 3-1 and Figure 3-2.

Table 3-1. Geometric characteristics of the sections of the tested beams.

Beam Designation	b (mm)	c (mm)	d/h	Main Rebar	Reinforcement ratio, ρ (%)	Target Compressive Strength, f_c (MPa)
C1-212-D1	140	20	0.86	2ϕ12	0.99	30
C1-216-D1	140	20	0.85	2ϕ16	1.77	30
C1-316-D1	140	20	0.85	3ϕ16	2.66	30
C1-212-D2	160	40	0.75	2ϕ12	0.99	30
C1-216-D2	160	40	0.74	2ϕ16	1.77	30
C1-316-D2	160	40	0.74	3ϕ16	2.66	30
C2-212-D1	140	20	0.86	2ϕ12	0.99	50
C2-216-D1	140	20	0.85	2ϕ16	1.77	50
C2-316-D1	140	20	0.85	3ϕ16	2.66	50
C2-212-D2	160	40	0.75	2ϕ12	0.99	50
C2-216-D2	160	40	0.74	2ϕ16	1.77	50
C2-316-D2	160	40	0.74	3ϕ16	2.66	50
C3-316-D1	140	20	0.85	3ϕ16	2.66	50
C3-212-D1-S	140	20	0.86	2ϕ12 (*)	0.99	50

(*) Steel reinforcing bars were used in this beam

Two specimens were tested for each beam type, except for the steel RC beam, where only one specimen was tested. Specimen Cx-yyy-Dz-A was prepared uncracked whilst specimen Cx-yyy-Dz-B had a notch in the midspan section to ensure the initiation of a crack at this specific position and to facilitate precise measurements of strain in that region. In some cases, specimen type -A was also pre-cracked to acquire complementary data. The pre-crack was created by placing a 1 mm wide steel rectangular sheet into the moulds prior to casting. The height of the steel sheet was 5 mm in the first two tested series (C1 and C2). This notch

ensured the propagation of a flexural crack assuming a variability of the concrete tensile strength f_{ct} of 10%. For the third experimental series (C3), this height was decided to be of 10 mm (corresponding to a variability of 20% f_{ct}), since it was observed that, in some cases, other flexural cracks in the central zone started to open before the midspan crack, even thought the crack eventually propagated at midspan.

Appendix A shows all details for each beam specimen.
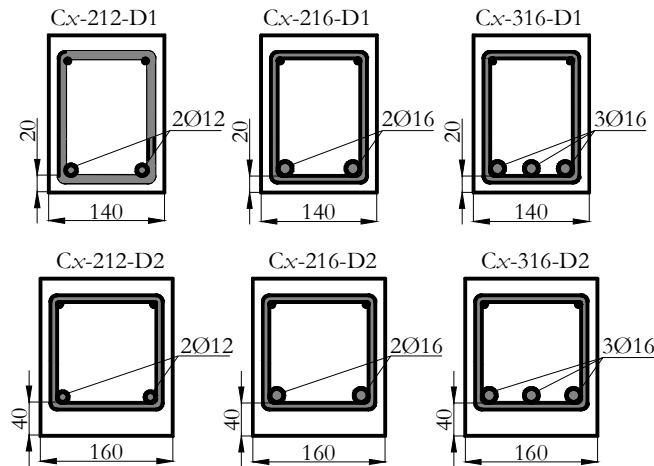
Figure 3-2. Geometric characteristics of sections (all dimensions in mm).

3.2.2. Beam design philosophy

Regarding the flexural failure modes of FRP RC elements, concrete crushing is generally preferred since it leads to a less brittle and catastrophic failure than the rupture of the FRP reinforcement (ISIS Canada 2001, ACI Committee 440 2006). In this study, following this design criterion, all GFRP RC beams were designed to fail by concrete crushing. The failure was expected to occur when concrete achieved its maximum compressive strain ε_{cu} at the weakest section of the beam. Hence, ε_{cu} would be a decisive parameter to correctly predict the ultimate load.

ACI 440.1R-06 states that this failure mode is attained when the reinforcement ratio ρ_f (Eq. (2-17)) is greater than the balanced reinforcement ratio ρ_{fb} (Eq. (2-18)). In this work, the variability of the concrete properties have been taken into consideration and the minimum reinforcement ratio proposed by Pilakoutas et al. (2002) has been also considered (Eq. (2-19)).

One steel RC beam was designed in C3 beam series. The predicted mode of failure was yielding of the reinforcement followed by crushing of concrete.

Table 3-2 summarizes the different proposed reinforcement ratios for the GFRP RC beams and compares them with Eqs. (2-18) and (2-19). To calculate these ratios, the experimental values of the mechanical properties of materials were taken into account.

Table 3-2 Balanced and actual reinforcement ratio for the tested GFRP RC beam specimens.

Beam Designation	Reinforcement ratio, ρ_f (%)	Balanced Reinforcement ratio, ρ_{fb}, Eq. (2-18) (%)	Balanced Reinforcement ratio, ρ_{fb}, Eq. (2-19) (%)
C1-212-D1	0.99	0.21	0.25
C1-216-D1	1.78	0.36	0.42
C1-316-D1	2.68	0.35	0.41
C1-212-D2	0.99	0.21	0.25
C1-216-D2	1.78	0.35	0.41
C1-316-D2	2.67	0.35	0.41
C2-212-D1	0.99	0.30	0.46
C2-216-D1	1.78	0.49	0.72
C2-316-D1	2.68	0.48	0.71
C2-212-D2	0.99	0.24	0.31
C2-216-D2	1.78	0.50	0.79
C2-316-D2	2.67	0.50	0.77
C3-316-D1	2.68	0.48	0.69

Since all beams had a higher reinforcement ratio than the balanced ratios, concrete crushing was expected for all beams.

3.2.3. Test preparations

The tests were prepared and carried out in three series, being the first one that of C2 beams (12 specimens), the second one of C1 beams (12 specimens) and the last one of C3 beams (3 specimens). For each beam series, plywood moulds were prepared to accommodate the reinforcement cages. To act as a crack inducer, a thin steel sheet was introduced in the mid-length of the bottom mould surface. The reinforcement cages were carefully put inside the moulds. Plastic spacers were used to allocate the reinforcement cage at the correct bottom and side distance from the moulds. Prior to casting, the clear cover to the main rebar was checked in three different positions of the length of the cage by means of go-no go gauges. In Figure 3-3, the go-no go gauge control can be observed, as well as the crack inducer introduced for beams C*x-yyy*-D*z*-B.
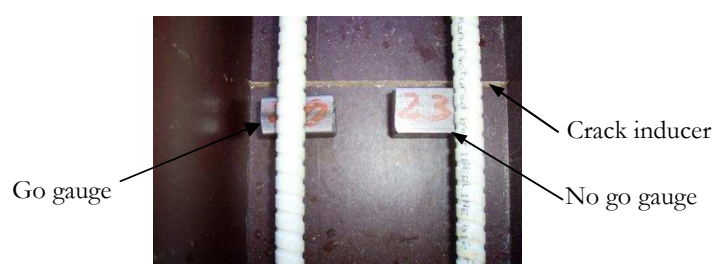
Figure 3-3. Go-no go gauges and crack inducer in a mould with FRP bars.

Figure 3-4 shows the appearance of the mould with the reinforcement cage inside ready for casting. The left hand side reinforcing cage is simply placed inside the mould, whilst the reinforcing cage on the right has the plastic spacers and is correctly placed.
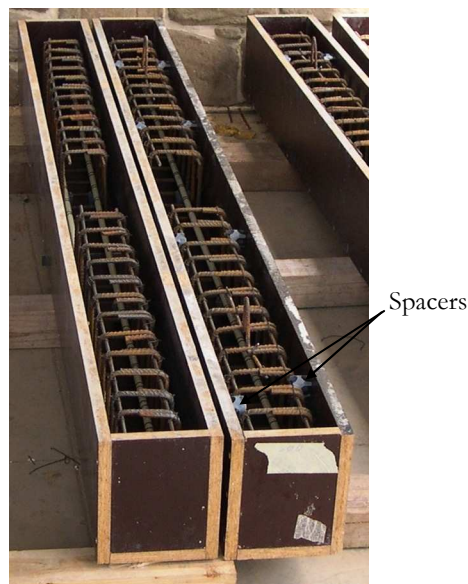
Figure 3-4. Reinforcement cages in moulds prior to casting.

Each of the beam series was cast on the same day, together with several cylinders to determine the concrete mechanical properties. Just after casting, the concrete was vibrated by traditional methods and the top concrete surface was levelled. Due attention was paid not to move the cage or damage the internal instrumentation. All elements (beams and cylinders) were covered with a plastic sheet and were watered the first days to maintain the humidity during curing.

Beams and cylinders were demoulded one week after casting and were kept in the same environmental conditions until testing, which was between 28 and 41 days after casting.

3.2.4. Instrumentation

The instrumentation of the beam specimens was designed to register the maximum quantity and most reliable data of local strains, deflections, crack spacings and crack widths. To register deflections, linear variable differential transducers (LVDTs) and strain based transducers were used. Two inclinometers were placed at the central zone, and Demec points were glued on the concrete surface to measure average strains. Additionally, on the concrete surface and on the rebar surface of some beams, strain gauges were located to register strain profiles.

The specimens were tested in three different beam series. The first beam series to be cast and tested was the C2 series. In C1 series, some improvements, deduced from the analysis on the previous series, were introduced in the instrumentation. Similarly, the C3 beam series, which was the last to be cast and tested, had the most extensive and complete instrumentation.

Appendix A shows the complete instrumentation details for all beam specimens.

Deflections at different locations of the beam

In order to measure the deflection of the tested beams, a minimum of three vertical transducers (linear variable differential transformers LVDTs and strain gauge based transducers) were used: one at each support and one at the midspan section.

The transducers on the supports were Vishay HLS10B type, with a displacement range of 11.2 mm. In some of the initial tested beam specimens, two transducers were used in the same support to control the non-rotation or torsion of the beam. The transducer at midspan was a Vishay HS100B type, with a displacement range of 102.0 mm.

All transducers were attached to vertical metallic elements and fixed in vertical position during the test. In the C2 beam series, the needle of the midspan transducer was positioned on an aluminium angle glued to the side of the test element (Figure 3-5), whilst in the case of the C1 and C3 series the needle was placed on a thin sheet glued to the bottom surface of the beam.
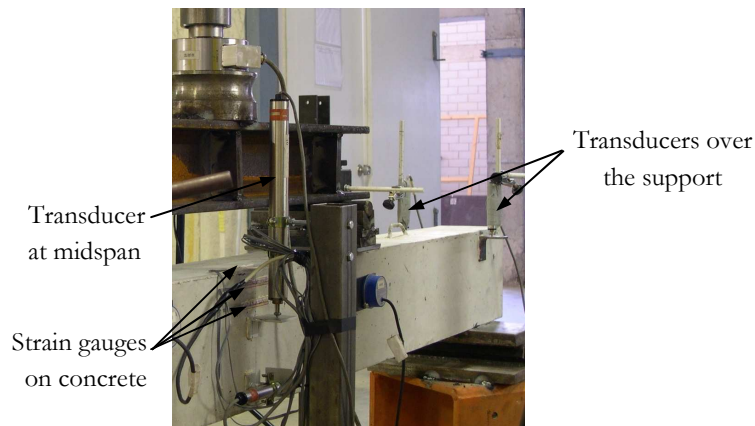
Figure 3-5. Arrangement of vertical transducers used during the C2 tests.

For the C1 beam series, two more vertical transducers were added at the shear span, at 450 mm from the supports. These transducers were Solartron LVDT type with a measurement range from ±2.5 mm to 75 mm. Since no torsion was detected in the C2 beam series, only one transducer was placed over each support for the susbsequent C1 and C3 series (Figure 3-6).

Figure 3-6. Arrangement of the vertical transducers used for the C1 and C3 tests.

Rotations and mean curvatures in the central zone

Two inclinometers were placed on both sides of the pure bending zone, each one located at 225 mm from the midspan section, and at a height of 50 mm from the top surface of the beam specimen. This configuration allowed sectional rotations to be measured and the average curvature of the pure bending zone to be calculated. The inclinometers used had a measurement range of ±10º, a sensitivity of 9.6 mV/degree and an offset voltage of 2.49 V. Both inclinometers were glued to steel sheets that were carefully placed on the correct position of the beam (Figure 3-7).
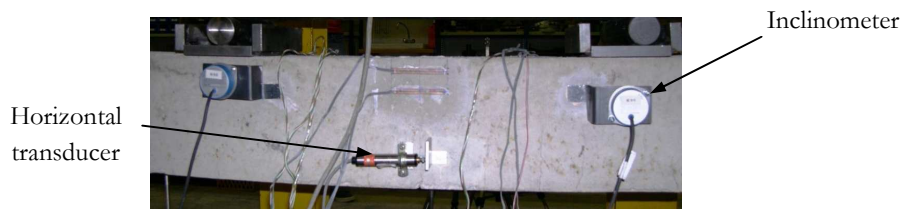
Figure 3-7. Instrumentation with inclinometers of the central section of the beams.

As a complement to the electronically registered data of the inclinometers, a dial mechanical extensometer with a capacity to measure strains of 1.07×10^{-5} was used in the midspan zone to manually measure horizontal top and bottom strains in the front face of the beam specimens (Figure 3-8).
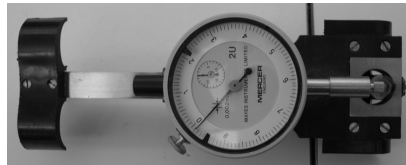
Figure 3-8. Demec mechanical strain gauge extensometer.

For this purpose, Demec points were bonded to the concrete surface every 150 mm along the central 450 mm of the beam with HBM Z70 single component adhesive made of cyanocrylate. The Demec points were located in two horizontal rows, one at the height of the upper steel rebars and the other at the height of the reinforcement GFRP rebars, as shown in Figure 3-9.
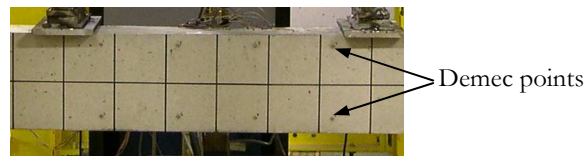
Figure 3-9. Demec points for mechanical extensometer (C2 beam series).

This configuration gave good results in terms of mean curvature in the central zone for the C2 beam series. Hence, for the C1 beam series, it was decided to implement the Demec points not only in the central 450 mm but rather along the whole length of the beam, so as to register

values of curvatures at every 150 mm. Moreover, for this beam series, the two horizontal rows of Demec points were 150 mm apart so as to measure vertical strains (Figure 3-10a).

| (a) | (b) |

Figure 3-10. (a) Demec points for mechanical extensometer in C1 beam series (b) Detail of additional diagonal Demec points in C3 beam series.

In the C3 series, this instrumentation was extended to measure, besides horizontal and vertical strains, diagonal strains along the length of the beam. This measurement was achieved by placing additional Demec points at each of the diagonals with a gauge length of 200 mm (Figure 3-10b). A digital mechanical extensometer with a capacity to measure strains of $4 \cdot 10^{-6}$ was used for this purpose.

Concrete strains on the midspan section surface

As mentioned in the previous section, the -B beam specimens and some of the -A specimens were cast with a pre-crack in the midspan section. These specimens were additionally instrumented with three concrete strain gauges bonded on the surface of the midspan section. These strain gauges were evenly distributed along the height of the theoretical concrete compressive block (one on the top surface, one 20 mm from the top and one 48 mm from the top) to quantify the evolution of the concrete strain with load.

The concrete strain gauges used in the experimental program were type PL-60-11 from *TML*, with the following characteristics: wire-type, three-wired, with a resistance of 120 Ω, a gauge factor of 2.12 ± 1%, a gauge length of 60 mm and a gauge width of 1 mm with a maximum strain of 2%. The strain gauges were bonded to the previously treated surface of the beam with HBM X-60 two components adhesive. Figure 3-5 shows the arrangement of the concrete strain gauges in the midspan section.

GFRP strains along the beam length

Some of the -B beam specimens reinforced with diameter of 16 mm bars were instrumented with strain gauges bonded on the surface of one of their GFRP rebars. The main aim of this instrumentation was to register rebar strains at different locations, in order to study the influence of cracks on the rebar strain and to obtain bond profiles.

Four of the gauges were evenly distributed over the shear span length, one being over the support, one under the point load and two more between these locations. In the central zone of the beam, six to eight gauges were located on the reinforcement at a spacing of 22 mm

starting from the midspan section (Figure 3-11), to allow the study of strain profiles between the induced crack at the location of the notch and one natural contiguous crack on one side of the beam specimen. As the crack spacing was expected to depend on the clear cover thickness, it was decided to locate six gauges when the concrete cover was 20 mm (thus covering a distance of 132 mm) and eight gauges in those cases when the concrete cover was 40 mm (distance of 176 mm). In both cases this distance was higher than four times the clear cover, which was considered the upper bound value for the maximum expected crack spacing. In order to minimise the effect on the rebar-concrete bond, the midspan gauges were placed helicoidally around the rebar, leaving free the bottom surface, so as not to damage the strain gauges with the stirrups and do not affect the bond on this location of the bar.

Figure 3-11. Helicoidal arrangement of strain gauges on GFRP bar.

In the C3 beam series, more strain gauges were placed in the central zone, so as to cover the apparition of a crack and two adjacent cracks (distance of 220 mm). Moreover, the strain gauges were placed at the height of the centroid of the bar, leaving the top and bottom faces free.

The FRP strain gauges used in the experimental program were type 6/350LY41 from *HBM*, with the following characteristics: wire-type, three-wired, with a resistance of 350 ± 0.3 Ω, a gauge factor of 2.04 ± 1%, a gauge length of 6 mm and a gauge width of 2.7 mm with a maximum strain of 5%. The strain gauges were bonded to the GFRP surface with HBM Z70 single component adhesive made of cyanocrylate. Prior to bonding the strain gauge, the surface of the bar was treated and the minimum height of rib was mechanised at each location (Figure 3-11). A HBM SG250 transparent silicon rubber was applied as a protective coating to isolate the gauges from the alkaline environment of concrete.

Crack width

To measure crack widths, an optical micrometer with an accuracy of 0.05 mm was used for all beam specimens. Additionally, a horizontal transducer was used at the midspan section of those beam specimens with a pre-crack at the height of the reinforcement to measure the width of the anticipated midspan crack (Figure 3-7).

Slip between rebar and concrete at the end face of the beam

For the C2 series, in those beams with internal strain gauges on the GFRP rebar, an horizontal transducer was placed at the end face of the beam specimen between the instrumented rebar and the concrete surface, to control the slip between concrete and rebar at this position (Figure 3-12).
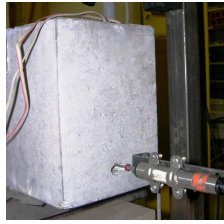
Figure 3-12. Horizontal transducer at the end face of the C2 beam series.

In all cases, it was observed that the slip was negligible. Consequently, this transducer was not further instrumented in the subsequent series C1 and C3.

3.2.5. Test setup and procedure

All beam specimens were tested under a static four-point loads test to study their flexural behaviour and to compare the experimental results with the analytical predictions. A servo-controlled hydraulic jack with a capacity of 300 kN was used to apply the load to the test beam through a spreader steel beam (HEB-160). The load was applied in displacement control mode at a displacement rate of 0.6-0.8 mm/min, and all data were collected by a data acquisition system. The test was stopped every 10-20 kN to register the evolution of cracks and the strains along the beam. The test set-up is shown in Figure 3-13.
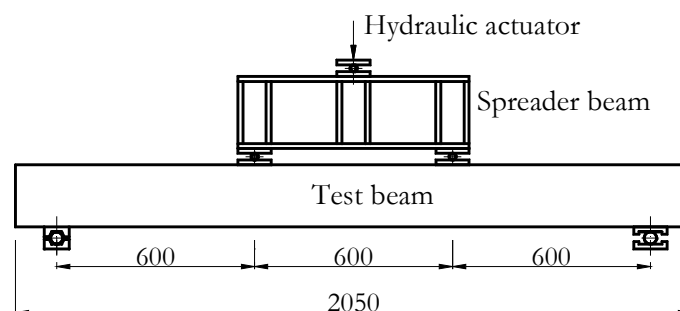
Figure 3-13. Scheme of the test set-up (dimensions in mm).

A grid was drawn on the front face of the beam to make easy the positioning and identification of cracks during and after the test. The grid dimensions for C1 and C2 beams series were 100 x 95 mm between supports and 125 x 95 mm from the supports to the end of the beam. In the case of C3 series, the grid dimensions between supports were changed to 150 x 95 mm to match up with the distance between Demec points.

Prior to placing the beam into the testing frame, auxiliar steel angles and sheets were glued to the concrete surface in their adequate position with HBM X-60 two component adhesive. Then, the test beam was carefully placed over the supports and all the instrumentation was positioned and connected to the data acquisition system.

The test started with a small pre-load cycle of about 5 kN (corresponding to a midspan deflection of the beam of about 0.3 mm) to settle the beam and to maintain positioning before

the beginning of the test. The data were monitored in real-time and were downloaded digitally to a PC. Every second, a minimum of two data were recorded. At some steps of load, the crack width was registered by using the optical micrometer and the strains were measured along the Demec points by using the mechanical extensometer. For safety reasons, this data was collected up to a load of approximately 75-80% the predicted ultimate load.

Once the test was finished, the crack pattern was studied and additional photographs were taken. Finally, the beam was removed from the testing frame and the concrete cover was checked at different locations. In the case of beam specimens with gauges on the rebar, the surrounding concrete was taken out and the exact position of the midspan gauge was registered.

3.3. Materials

The mechanical properties of concrete and GFRP rebars were experimentally determined, using standardised methods. These tests and a discussion of the results are presented in this section.

3.3.1. Concrete

Two different concrete grades were used, one for each initial beam series C1 (30 MPa) and C2 (50 MPa). Subsequently, a third beam series was planned with the same target concrete compressive strength of C2 series (50 MPa), although the concrete mix was different from the one used in C2 beams. The different admixtures used for the concrete types are detailed in Table 3-3.

Table 3-3. Concrete mixes for the different series of beams.

Admixture	Concrete C1	Concrete C2	Concrete C3
Cement type	CEM II/AV 42.5R	CEM I 52.5	CEM II/AV 42.5R
Cement content (kg/m^3)	310	385	450
Water content (kg/m^3)	180	162	160
w/c ratio	0.58	0.42	0.36
Fine aggregate (sand) content (kg/m^3)	880	842	815
Maximum coarse aggregate size (mm)	12	10	12
Coarse aggregate (gravel) content (kg/m^3)	875	940	875
Additives	*	**	***

* Sikament 290 0.8% in weight of cement and Sikament 500 1.0% in weight of cement.

** Super plasticizer Glenium ACE 325 3.46 kg/m^3.

*** Sika 290 0.6% in weight of cement and Sika 5920 1.0% in weight of cement.

Concrete C2 was mixed in situ, using cement type CEM I-52.5, 10 mm maximum aggregate size, and a water/cement ratio of 0.42. Beam specimens were cast in pairs. In an attempt to produce concrete batches as similar as possible, a rigorous quality control was enforced on the production of concrete. Initially, twelve cylinders were kept from different pairs of beams and were later tested: six in compression, four in tension, and two to determine the modulus of elasticity. After a first analysis of the results, high variability was found in them. This fact motivated to take additional control samples (with a diameter-to-height ratio of 1:2) directly from each tested beam for additional comparisons before removing the specimens from the laboratory. From these samples, a more reliable compressive strength and modulus of elasticity for each couple of beams were determined.

Concrete C1 was obtained from a local ready-mix factory. All beams were cast from the same batch; therefore the properties of concrete were uniform for all beam specimens. The admixture was made of cement type CEM II/A-V-42.5R, 12 mm maximum aggregate size and a water/cement ratio of 0.58. A total of 8 cylinders were extracted from this series, from which the compressive stress-strain curve, the modulus of elasticity and the tensile strength were determined.

Concrete C3 was also obtained from a local ready-mix factory. Although the target concrete strength was the same than for C2 series, the concrete mix was slightly modified by the ready-mix factory as shown in Table 3-3. In this case, a total of 9 cylinders were kept and the same parameters than in the previous series were found.

In all series, the cylindrical specimens (150x300 mm) and control samples were kept in the same exposure conditions of temperature and humidity until testing. From these cylinders, the compressive strength f_c, compressive modulus of elasticity E_c and tensile strength f_{ct} were tested. All tests on concrete were carried out at the age of 28 to 41 days. These properties were compared with the theoretical provisions of ACI, Model Code 90 and Eurocode 2. A discussion of the results is presented next.

Compressive strength f_c

The compressive strength was determined from cylindrical specimens, except for the case of C2-*yyy*-Dz beams, where control samples from the tested beams were used instead. The tests were carried out at the laboratory of structures of the University of Girona and at an external laboratory (*Centre d'Estudis de la Construcció i Anàlisi de Materials*, CECAM) for comparison purposes. The equipment used to perform these tests was a universal SERVOSIS MUE-60 model with a capacity of 600 kN and a SERVOSIS MES-250 model with a capacity of 2500 kN, respectively.

The compressive strength was determined according to UNE 83.304/84 Standard, testing the specimens at the same temperature and humidity conditions than the beam specimens. Model Code 90 (CEB-FIB 1990) formulation was used to adapt the concrete strength at the corresponding age of the beam:

$$f_c(t) = \beta_{cc}(t) \cdot f_c \qquad\qquad (3\text{-}1)$$

$$\beta_{cc}(t) = e^{s\left(1-\sqrt{28/t}\right)} \qquad\qquad (3\text{-}2)$$

In Eq. (3-1), $\beta_{cc}(t)$ is a conversion coefficient and f_c is the concrete compressive strength at the age of 28 days. In Eq. (3-2), s is a coefficient that takes account of the type of cement hardening (0.25 for normal cement hardening) and t is the time (in days).

In Table 3-4, a summary of the compressive strength $f_c(t)$ deduced from the cylindrical specimens and control samples is detailed. Moreover, the 28-days f_c is calculated and the corresponding compressive strength at the age that the beams were tested is reported. The results are shown for each couple of beams tested, except for the case of C3 beam specimens, where the compressive strength refers to the three tested beams.

Table 3-4. Experimental values of the compressive strength f_c.

Beam Designation	$f_c(t)$ from cylinders		28-days f_c (MPa)	Corresponding $f_c(t)$ on beams	
	Age (days)	Mean (MPa)		Age (days)	Mean (MPa)
C1-212-D1	31	32.1	31.7	31	32.1
C1-216-D1	31	32.1	31.7	35	32.5
C1-316-D1	31	32.1	31.7	34	32.4
C1-212-D2	31	32.1	31.7	30	32.0
C1-216-D2	31	32.1	31.7	28	31.7
C1-316-D2	31	32.1	31.7	29	31.8
C2-212-D1	29	60.1	59.8	28	59.8
C2-216-D1	36	56.5	54.8	35	56.3
C2-316-D1	34	55.6	54.3	32	55.2
C2-212-D2	34	39.7	38.8	33	39.6
C2-216-D2	30	62.0	61.4	29	61.7
C2-316-D2	36	60.5	58.7	34	60.1
C3-yyy-D1	30	54.5	53.9	28	53.9

Modulus of elasticity E_c

The modulus of elasticity of concrete E_c is one of the main parameters affecting the flexural behaviour of RC beams since it is directly related to the stiffness. With the purpose of accurately determining E_c, several tests were carried out in the laboratory of structures of the University of Girona. The equipment used to perform these tests was a universal SERVOSIS (MUE-60) testing machine with a capacity of 600 kN.

Each of the tested specimens was instrumented with three strain gauges located at 120°. The test was carried out following ASTM C 469/87 Standard. The procedure consists of performing three cycles of compressive loading up to a value of 40% of the compressive strength. The modulus of elasticity is evaluated as the mean value of the last two cycles of loading, using the following expression,

$$E_c = \frac{\sigma_2 - \sigma_1}{\varepsilon_2 - \varepsilon_1} \tag{3-3}$$

where ε_1 has a value of 50×10^{-6}, ε_2 is the corresponding strain to 40% of the concrete strength, and σ_1 and σ_2 are the corresponding stresses to the previous strains. When the age of the beam specimen did not coincide with the age of the control sample or cylinder, Model Code 90 formulation was used to transform the concrete modulus of elasticity to that corresponding to the age of the beam specimen:

$$E_c(t) = \sqrt{\beta_{cc}(t)} \cdot E_c \tag{3-4}$$

In Eq.(3-4), $\beta_{cc}(t)$ is the conversion coefficient defined in Eq.(3-2) and E_c is the concrete modulus of elasticity at the age of 28 days. Table 3-5 summarizes the resulting values of E_c for the cylinder samples and the corresponding E_c for concrete of beam specimens.

Table 3-5. Experimental values of the modulus of elasticity E_c.

Beam Designation	$E_c(t)$ from cylinders		28-days E_c (MPa)	Corresponding $E_c(t)$ on beams	
	Age (days)	Mean (MPa)		Age (days)	Mean (MPa)
C1-212-D1	35	25845	25506	31	25665
C1-216-D1	35	25845	25506	35	25845
C1-316-D1	35	25845	25506	34	25803
C1-212-D2	35	25845	25506	30	25615
C1-216-D2	35	25845	25506	28	25506
C1-316-D2	35	25845	25506	29	25562
C2-212-D1	28	27053	26939	28	26939
C2-216-D1	35	26566	26176	35	26524
C2-316-D1	32	25093	24726	32	24926
C2-212-D2	33	23124	22897	33	23163
C2-216-D2	29	27262	27202	29	27318
C2-316-D2	34	26910	28370	34	26910
C3-yyy-D1	30	28491	28370	28	28370

Since it was of main interest to model the concrete elastic behaviour with the maximum accuracy, the experimental values of E_c were compared with theoretical values derived from f_c

provided by different codes of practice. ACI 318R-05 (ACI Committee 318 1995), Model Code 90 (CEB-FIB 1990) and Eurocode 2 (CEN 2004) were used for this purpose.

ACI 318R-05 defines E_c as the slope of the line drawn from a zero stress point to a compressive stress of $0.45f_c$ for normal weight concrete. E_c can be calculated following Eq. (3-5), where f_c' is the specified compressive strength.

$$E_c = 4750\sqrt{f_c'} \tag{3-5}$$

Model Code 90 gives expression (3-6) to estimate the initial modulus of elasticity for normal weight concrete E_{ci} at the age of 28 days,

$$E_{ci} = E_{c0}\left(f_c / f_{cm0}\right)^{1/3} \tag{3-6}$$

where f_c is the actual value of the concrete strength at the age of 28 days, f_{cm0} is 10 MPa and E_{c0} is $2.15 \cdot 10^4$ MPa. The secant modulus of elasticity E_c is taken as 85% of E_{ci}.

Eurocode 2 provides Eq. (3-7) to calculate the secant modulus of elasticity E_c, considered the slope of the line drawn from zero stress to $0.4f_c$ for concretes with quartzite aggregates. When limestone aggregates are used, its value can be reduced by 10%.

$$E_c = 22000\left(f_c / 10\right)^{0.3} \tag{3-7}$$

Table 3-6 shows the theoretical values of E_c at the age of 28 days according to ACI 318R-05, Model Code 90 and Eurocode 2. For comparison purposes, for each approach examined, a variable δ is defined as the value of E_c calculated according to the approach divided by the experimental value of E_c.

Table 3-6. Theoretical values of E_c (MPa) deduced from the experimental values of f_c.

Beam designation	ACI 318R-05		Model Code 90		Eurocode 2	
	E_c	δ	E_c	δ	E_c	δ
C1-*yyy*-D*z*	26744	1.05	26846	1.05	27989	1.10
C2-212-D1	36732	1.36	33171	1.23	33859	1.26
C2-216-D1	35163	1.34	32219	1.23	32984	1.26
C2-316-D1	35002	1.42	32121	1.30	32893	1.33
C2-212-D2	29588	1.29	28717	1.25	29738	1.30
C2-216-D2	37220	1.37	33464	1.23	34128	1.25
C2-316-D2	36393	1.28	32966	1.16	33671	1.19
C3-*yyy*-D1	34873	1.23	32042	1.13	32820	1.16

As observed in Table 3-6, the modulus of elasticity obtained from the experimental tests results always lower than the theoretically predicted from the compressive strength. ACI 318 provides, in general, the highest values for E_c, with a mean value of δ equal to 1.29, whereas Model Code 90 and Eurocode 2 provide similar moduli between them, being $\bar{\delta}$ equal to 1.20 and 1.23 respectively.

Compressive stress-strain curve

Some of the cylindrical specimens that were tested in compression were previously instrumented with strain gauges. This configuration allowed registering the ascending branch of the stress-strain curve, as well as the concrete strain corresponding to the compressive strength. Table 3-7 summarizes the obtained values of ε_{c1}.

Table 3-7. Experimental strain corresponding to the compressive strength ε_{c1}.

Beam designation	ε_{c1}
C1-*yyy*-Dz	2450
C2-212-D1	2920
C2-216-D1	2900
C2-316-D1	2850
C2-212-D2	2640
C2-216-D2	2950
C2-316-D2	2940
C3-*yyy*-D1	2820

As it can be seen in Figure 3-14, in this test it was not possible to register the descending branch of the stress-strain curve because the set-up did not allow registering this data.
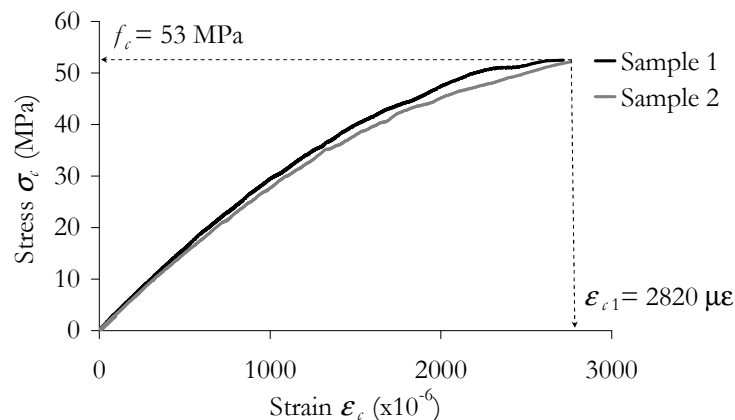
Figure 3-14. Experimental stress-strain curve for concrete C3.

Tensile strength f_{ct}

The tensile strength is the concrete mechanical property that presents the largest scatter of values. It is influenced by the superficial shape and structure of aggregates and can be substantially reduced by environmental effects (CEB-FIB 1990, Scanlon and Bischoff 2008). Different definitions for the tensile strength can be distinguished: the axial tensile strength (the tensile strength of a specimen subjected to an axial stress), the flexural tensile strength (that of a specimen subjected to a flexural stress) or the splitting tensile strength (derived from the well known Brazilian test).

In this work, the concrete tensile strength was determined by splitting tensile tests on cylindrical specimens. The tests were carried out at an external laboratory (CECAM), and the equipment used was a SERVOSIS MES-250 model with a capacity of 2500 kN. The splitting tensile strength $f_{ct,sp}$ was tested according to UNE 83306/85 Standard, at the same temperature and humidity conditions than the beam specimens were tested. Its value was transformed to the tensile strength f_{ct} following Model Code 90 formulation:

$$f_{ct} = 0.9 f_{ct,sp} \tag{3-8}$$

When the age of the tested beam did not coincide with the age of the cylindrical specimen, Model Code 90 formulation was used to transform f_{ct} to that of the age corresponding to the beam tests (Eqs. (3-1) and (3-9)).

$$f_{ct} = f_{ctk0,m} \left(f_{ck} / f_{ck0} \right)^{2/3} \tag{3-9}$$

In Eq. (3-9), f_{ck0} is 10 MPa and $f_{ctk0,m}$ is 1.40 MPa.

Table 3-8 summarizes the experimental values for the tensile strength, showing the splitting tensile strength of cylinders, the 28-days tensile strength f_{ct} ant the transformed value of f_{ct} corresponding to the age of the beam specimens.

Table 3-8. Concrete tensile strength f_{ct} from cylindrical samples.

Beam Designation	$f_{ct,sp}$ from cylinders		28-days f_{ct} (MPa)	Corresponding f_{ct} on beams	
	Age (days)	Mean (MPa)		Age (days)	Mean (MPa)
C1-212-D1	31	2.8	3.1	31	3.1
C1-216-D1	31	2.8	3.1	35	3.1
C1-316-D1	31	2.8	3.1	34	3.1
C1-212-D2	31	2.8	3.1	30	3.1
C1-216-D2	31	2.8	3.1	28	3.1
C1-316-D2	31	2.8	3.1	29	3.1
C2-212-D1	29	3.9	4.0	28	3.1
C2-216-D1	29	3.9	4.0	35	4.0
C2-316-D1	29	3.9	4.0	32	4.0
C2-212-D2	41	3.2	3.3	33	3.3
C2-216-D2	41	3.2	3.3	29	3.3
C2-316-D2	41	3.2	3.3	34	3.3
C3-yyy-D1	29	4.1	4.1	28	4.1

The tensile strength was also calculated according to theoretical proposals from ACI 318R-95, Model Code 90 and Eurocode 2, based on the experimental values of the compressive strength. ACI 318R-95 defines the modulus of rupture of concrete f_r for normal weight concrete that can be considered as a flexural tensile strength:

$$f_r = 0.62\sqrt{f_c} \tag{3-10}$$

Model Code 90 differentiates between the tensile strength f_{ct} (Eq. (3-9)) and the flexural tensile strength $f_{ct,fl}$. The flexural tensile strength depends on the height of the beam h_b and can be derived from f_{ct} as follows:

$$f_{ct,fl} = \frac{f_{ct}}{\left(\dfrac{1,5 \cdot (h_b/100)^{0,7}}{1 + 1,5 \cdot (h_b/100)^{0,7}} \right)} \tag{3-11}$$

Eurocode 2 also provides formulation to calculate the tensile strength f_{ct} (Eq. (3-12)) and the flexural tensile strength $f_{ct,fl}$ (Eq. (3-13)).

$$f_{ct} = 0.3 f_{ck}^{2/3} \text{ if } f_c \leq 50 \text{ MPa}$$
$$f_{ct} = 2.12 \ln(1 + (f_c/10)) \text{ if } f_c > 50 \text{ MPa} \tag{3-12}$$

$$f_{ct,fl} = \max\{(1.6 - h/1000)f_{ct}; f_{ct}\} \tag{3-13}$$

In Eq. (3-13), h is the total member depth in mm. Eq. (3-12) gives the same tensile strength f_{ct} than Model Code 90 for concretes with $f_c \leq 50$ MPa, but gives slightly lower values for concretes with $f_c > 50$ MPa.

Table 3-9 summarizes the different values for the tensile strength f_{ct} calculated from the compressive strength according to Eurocode 2 and Model Code 90 and the theoretical concrete flexural tensile strength $f_{ct,fl}$ following Eurocode 2 and Model Code 90, and the modulus of rupture f_r according to ACI provisions. The δ value, defined as the ratio between the theoretical value of f_{ct} and the 28-days f_{ct} described in Table 3-8, is also shown for comparison purposes.

Table 3-9. Theoretical values of f_{ct} (MPa) and $f_{ct,fl}$ (MPa) calculated from the experimental f_c.

Beam Designation	Eurocode 2				Model Code 90				ACI 318R-05	
	f_{ct}	δ	$f_{ct,fl}$	δ	f_{ct}	δ	$f_{ct,fl}$	δ	f_r	δ
C1-*yyy*-D*z*	3.0	0.97	4.2	1.35	3.0	0.97	4.3	1.39	3.5	1.13
C2-212-D1	4.1	1.03	5.8	1.45	4.6	1.15	6.6	1.65	4.8	1.20
C2-216-D1	4.0	1.00	5.6	1.40	4.4	1.10	6.2	1.55	4.6	1.15
C2-316-D1	4.0	1.00	5.6	1.40	4.3	1.08	6.2	1.55	4.6	1.15
C2-212-D2	3.4	1.03	4.9	1.48	3.5	1.06	4.9	1.48	3.9	1.18
C2-216-D2	4.2	1.27	5.9	1.79	4.7	1.42	6.7	2.03	4.9	1.48
C2-316-D2	4.1	1.24	5.8	1.76	4.6	1.39	6.5	1.97	4.8	1.45
C3-*yyy*-D1	3.9	0.95	5.5	1.34	4.3	1.05	6.1	1.49	4.6	1.12

Results show that the $f_{ct,fl}$ is always higher than f_{ct}, as it was expected. Moreover, in general there is a good fit between the theoretical values of f_{ct} and the experimental results from the cylindrical samples 28-days f_{ct} (Table 3-8).

The values obtained from the experimental cylinders and theoretical approaches were compared to the tensile strength that can be deduced from the experimental load-deflection curves of the tests on beams. A typical load-deflection curve with the determination of the cracking load P_{cr} is depicted in Figure 3-15 and the corresponding experimental values of f_{ct}, calculated following Eq. (3-14) are summarized in Table 3-10.

$$M_{cr,\exp} = \frac{P_{cr}L}{6} = \frac{f_{ct,\exp}}{W} \tag{3-14}$$

In Eq. (3-14), $M_{cr,\exp}$ is the experimental cracking moment, L is the total length of the beam, W is the section modulus of the uncracked section, which in a simplified way can be assessed as the modulus of the concrete gross section:

$$W \approx W_g = \frac{1}{6}bh^2 \tag{3-15}$$

where b and h are the width and height of the section.
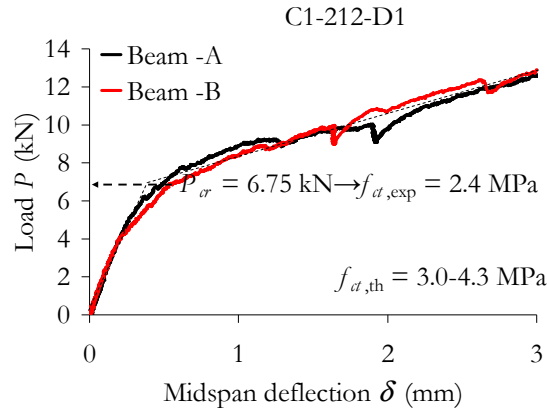
Figure 3-15. Experimental tensile strength obtained from beam tests.

Table 3-10. Experimental concrete tensile strength $f_{ct,exp}$ (MPa) from beam tests.

Beam designation	$f_{ct,exp}$ (MPa)
C1-212-D1	2.4
C1-216-D1	2.6
C1-316-D1	3.2
C1-212-D2	2.3
C1-216-D2	1.9
C1-316-D2	2.3
C2-212-D1	3.5
C2-216-D1	3.3
C2-316-D1	3.8
C2-212-D2	3.0
C2-216-D2	3.3
C2-316-D2	3.6
C3-yyy-D1	4.0

The experimental tensile strength $f_{ct,exp}$ deduced from load-deflection curves was found to be about 17% lower than the values obtained from cylinder samples or code predictions (Table 3-8) and about 19% to 25% lower than the predicted by Eurocode 2 and Model Code 90 respectively (Table 3-9). Scanlon and Bischoff (2008) attributed this decrease of the cracking moment to the tensile stresses that develop in the concrete from restraint to shrinkage, and the recent ACI 440 ballot suggests using 80% of the cracking moment for calculations (Bischoff et al. 2009). In this study, the experimental value of the tensile strength $f_{ct,exp}$ deduced from load-deflection curves was used for the analytical comparisons.

3.3.2. GFRP reinforcement

As a flexural reinforcement, ribbed GFRP ComBAR rebars with 75% of glass content in volume (Schöck Bauteile GmbH 2006) were used. These bars present a relatively high modulus of elasticity (60 GPa, corresponding to the nominal internal diameter) compared to other commonly used GFRP bars (35-45 GPa). For the experimental program, two nominal diameters were used (12 and 16 mm). The used rebars are manufactured by a pultrusion process, in which boron-free ECR glass fibres are drawn through a tool in a continual process and are impregnated with liquid synthetic VEU (vinyl ester-urethane) resin. The bar is then processed to obtain a ribbed surface (Figure 3-16).
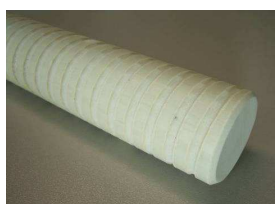
Figure 3-16. ComBAR GFRP rebar.

The mechanical properties of the bars were tested following ACI 440.3R-04 (ACI Committee 440 2004) for characterisation. Five specimens were tested for each diameter. The results are shown in Table 3-11.

Table 3-11. Mechanical properties of GFRP rebars.

Diameter (mm)		12	16
Rupture Tensile Strength, f_{fu} (MPa)	Average (MPa)	1321 (1000)	1015 (1000)
	St. Deviation (MPa)	17	81
Modulus of Elasticity, E_f (MPa)	Average (MPa)	63437 (60000)	64634 (60000)
	St. Deviation (MPa)	957	822
Ultimate strain, ε_{fu}		- (1.8%)	- (1.8%)

Values provided by manufacturer in brackets

The elastic modulus of the GFRP bars was determined using an external axial extensometer over a length of 100 mm. This extensometer was removed prior to bar failure to avoid damage, so the strain at failure was not measured. The resulting typical tensile stress-strain curves were linear up to failure, as shown in Figure 3-17.
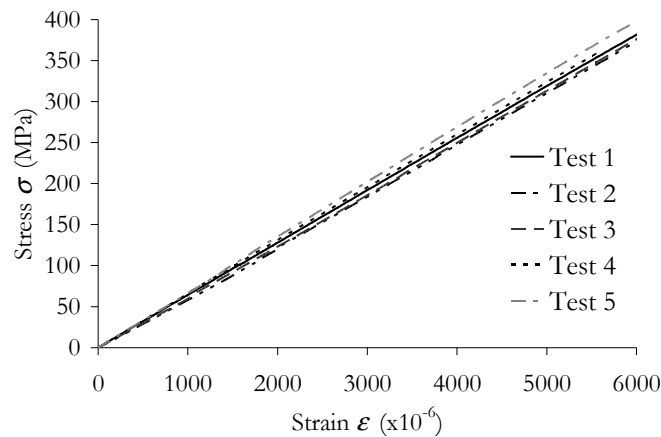
Figure 3-17. Experimental stress-strain curve for diameter 16 mm GFRP bars.

As previously explained, some of the beam specimens were instrumented with strain gauges bonded on the surface of the GFRP rebar. Prior to bonding the strain gauge, the surface of the bar was mechanised to obtain a flat and regular base. Although only the rib of the bar was locally removed, additional tensile tests were carried out in some diameter 16 mm bars to check that this mechanization had no effect on the effective area and modulus of elasticity of the bars.

This additional tensile test was performed in two phases. First, the axial extensometer was placed at the same position of the strain gauge, the specimen was loaded up to 50% the ultimate strength and it was checked that the stress-strain curve at the strain gauge and at the axial extensometer were the same (Figure 3-18a). Then, the specimen was unloaded and a second cycle of testing was performed with the axial extensometer out of the area of the mechanisation of the bar. In both cycles, it was observed that the stress-strain curve of the bar was not affected by the local mechanization of a rib (Figure 3-18b).

3.3.3. Steel rebars and stirrups

Steel was used in stirrups and in the upper reinforcement. Steel stirrups were placed in the shear span to avoid shear failure and the upper reinforcement had the only purpose of holding the shear links.

The nominal properties of steel were a tensile strength of 500 MPa and a modulus of elasticity of 200 GPa.
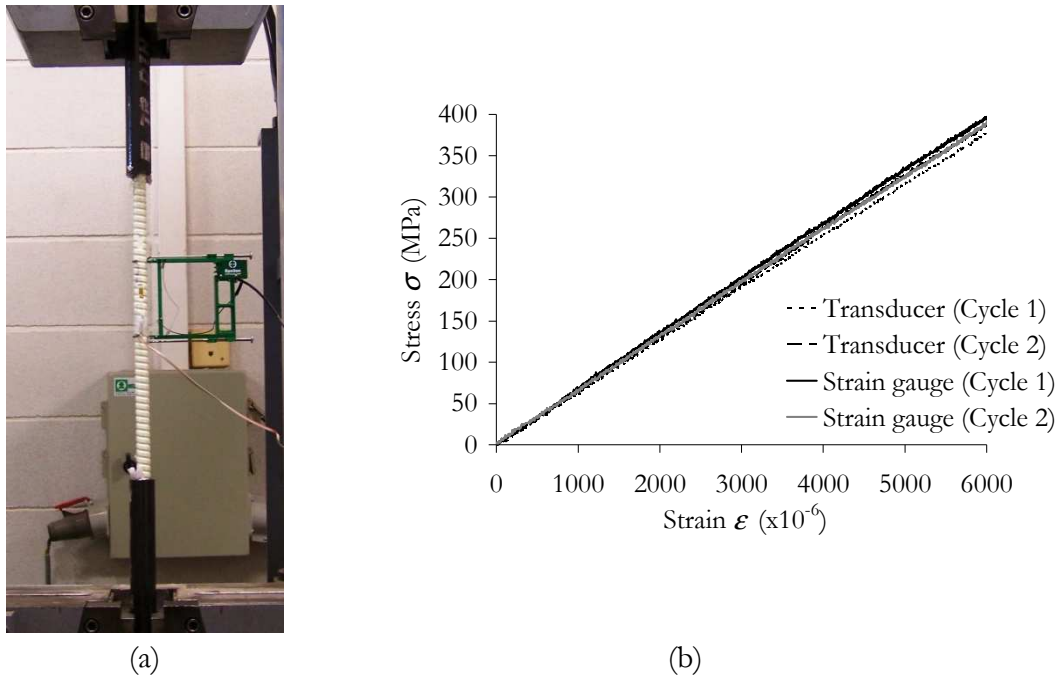
Figure 3-18. Additional tests with axial extensometer and strain gauge in a mechanised bar. (a) General view of the tests, (b) Stress-strain resultant curves.

3.4. General remarks

This chapter presents the details of the experimental program carried out in this work. Twenty-six GFRP and one steel RC beams were designed and tested under a four-point bending configuration to study the serviceability behaviour of GFRP RC beams. The main parameters of the experimental program were the concrete grade, the reinforcement ratio and the effective depth to overall height ratio. The beams were designed to fail by concrete crushing and were tested until failure to additionally evaluate the failure load and the flexural behaviour at the ultimate limit state.

The instrumentation of the beams was designed to register local strains, deflections, crack spacings and crack widths. Deflections were registered by linear variable differential transducers and strain based transducers. Rotations were measured with two inclinometers in the central zone. Some of the beams were additionally instrumented with strain gauges on the concrete surface at midspan and the GFRP rebars were instrumented with strain gauges bonded on the surface of the bar. A mechanical extensometer was used to measure horizontal and vertical average strains at every 150 mm along the length of the beam specimens. Besides, vertical strains were measured with a digital extensometer with a gauge length of 200 mm.

Three different concrete mixes were used, each of them corresponding to a series of tests. The concrete compressive strength, modulus of elasticity, tensile strength and compressive stress-strain curves were characterised for the three series and compared to the theoretical values

calculated by ACI 318, Eurocode 2 and Model Code 90. The experimental modulus of elasticity and tensile strength were found to be lower than the theoretically predicted.

The tensile strength and modulus of elasticity of the GFRP bars used for the tests were also experimentally determined and compared to the manufacturer specifications, obtaining experimental values equal or higher than the ones provided by the manufacturer.

Chapter 4
Discussion of the experimental results

4.1. Introduction

In this chapter, the most relevant experimental results are summarized and discussed. The detailed experimental results for each tested beam can be found in Appendix B.

First, the results at the midspan section are analysed, in terms of strain distribution along the depth of the midspan section and the evolution of neutral axis depth with load. The load at which the serviceability limit state (SLS) of stresses in materials is attained is shown for each beam tested.

Then, the central zone, under pure bending stresses, is analysed. The moment-curvature relationship obtained with the different instrumentation devices is represented and discussed.

Next, the overall beam behaviour is examined. The curvature evolution with load along the length of the beam is analysed and the profile of strains on the FRP reinforcement is studied at different significant load stages. The experimental mode of failure and the ultimate load of the beam specimens are also analysed.

The deflection and cracking behaviour are depicted afterwards. The deflection at the midspan section and the shear span section are shown and the corresponding results coming from the different instrumentation systems are compared. The cracking pattern is commented and crack spacing and crack width are examined. The loads at which the SLS of cracking and deflection are reached are also included.

Finally, an analysis on tension stiffening and bond behaviour is conducted.

4.2. Results at the midspan section

Using the data provided by the three strain gauges on the concrete surface of the midspan section (Figure 4-1), an analysis of strains along the depth of the section is carried out and the experimental neutral axis is deduced.
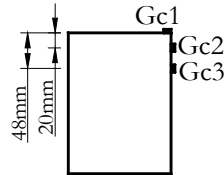
Figure 4-1. Position of strain gauges on concrete at midspan section.

4.2.1. Concrete strain distribution along the depth of the midspan section

A typical representation of the experimental load-concrete compressive strain relation is shown in Figure 4-2 for the local strain gauges at midspan.
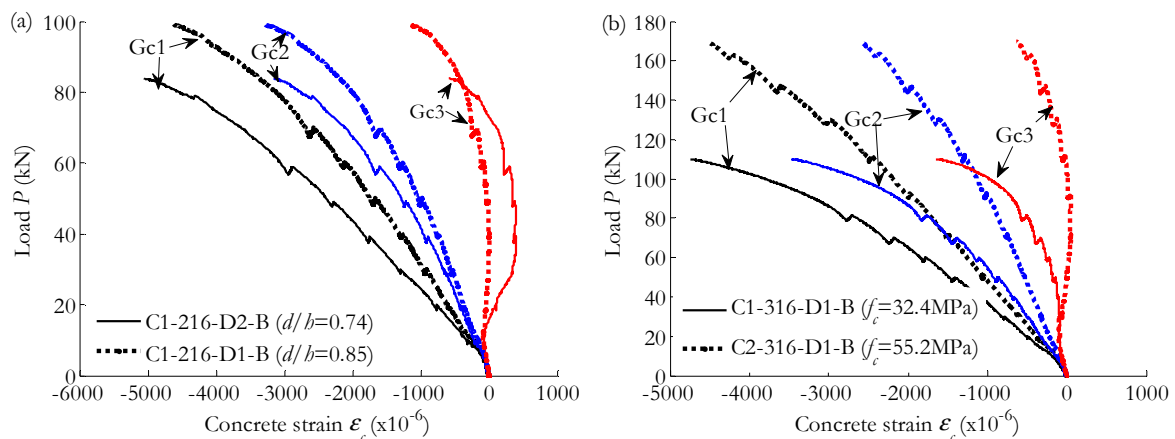
Figure 4-2. Typical evolution of concrete strain at midspan. (a) Comparison for different d/h ratios, (b) comparison for different concrete grades.

A relatively small first linear branch, corresponding to the uncracked condition of the section is evident. In this first step of the test, the three experimental curves of the strain gauges indicate similar behaviour with low values of strain, in agreement with the high stiffness of the uncracked section. When cracking occurs, the differences between them increase rapidly. As expected, the maximum concrete strain in compression is reached by the strain gauge at the top surface, whilst the gauge located 48 mm from the top can be either in compression or in tension, depending on the position of the experimental neutral axis.

Comparing Figure 4-2a and Figure 4-2b, it is observed that the higher the reinforcement ratio is, the less compressive strain is measured at the strain gauge Gc1 for the same load level. Furthermore, as depicted in Figure 4-2a, as d/h increases, lower values of concrete strain are

observed at the top of the beam (Gc1). Finally, a higher concrete grade eventually results in smaller strains for the same level of loading (Figure 4-2b).

The concrete strain at the extreme compressive fibre behaves non-linearly with load until failure, especially in those beams with lower concrete compressive strengths (beams type C1).

The maximum compressive strain ε_{cu} was observed to range between 0.4% and 0.55%. These values result higher than the usual ones established by the American codes of practice (ACI Committee 318 2005, ACI Committee 440 2006) or the European standards (CEB-FIB 1990, CEN 2004, CPH 2008), which consider ε_{cu} to be between 0.3% and 0.35% for the given concrete grades. Matthys and Taerwe (2000) obtained similar values for concrete slabs reinforced with FRP grids and suggested considering ε_{cu} equal to 0.55% although further research was recommended to confirm this value. According to Park and Paulay (1975), studies on unconfined specimens subjected to flexural stresses (Rüsch 1955, Hognestad et al. 1955) confirmed that 0.3% is a reasonably conservative value and that at this strain, the compressed concrete in a flexural member will not normally show any visible compressive cracking or spalling, probably because of the presence of the less strained material closer to the neutral axis. Additionally, Rüsch (1960) stated that the ultimate concrete strain of a flexural element also depends on other factors such as the shape of the section, the position of the neutral axis or the strain rate. Hence, several factors could contribute to justify the relatively high values of the maximum compressive strain attained by the concrete.

Two typical evolutions of the strain profile along the depth of the section for different load levels are represented in Figure 4-3.
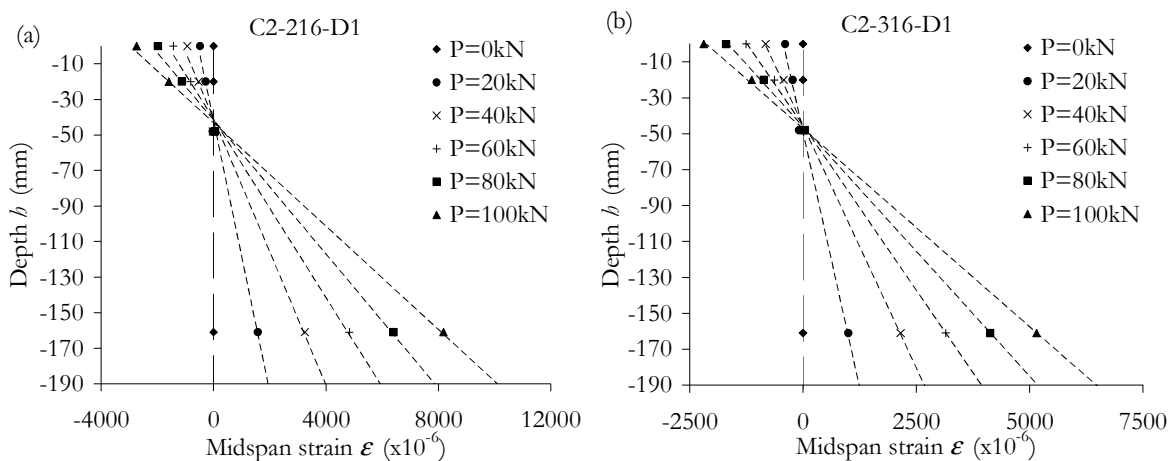
Figure 4-3. Typical strain evolution along the midspan depth.

A linear relation between the three strain values is observed, thus the Bernoulli hypothesis can be confirmed, both before and after cracking. In Figure 4-3, the strain on the GFRP reinforcement is also included for comparison purposes. It is observed a good fit between the strain at the reinforcement and the linear trend of strains deduced from gauges on concrete.

4.2.2. Neutral axis depth at the midspan section

The experimental position of the neutral axis is deduced by linear interpolation of the data provided by the three concrete strain gauges at each load level. Taking into account that the cracking load for the beams depicted in Figure 4-4 ranged between 6.8 and 9.1 kN, it is observed that the neutral axis depth before cracking is located at approximately the mid-height of the section and decreases just after cracking. Afterwards, its value remains constant or decreases slightly, and for high loads it increases until the maximum load is achieved showing that concrete is arriving to its plastic stage.
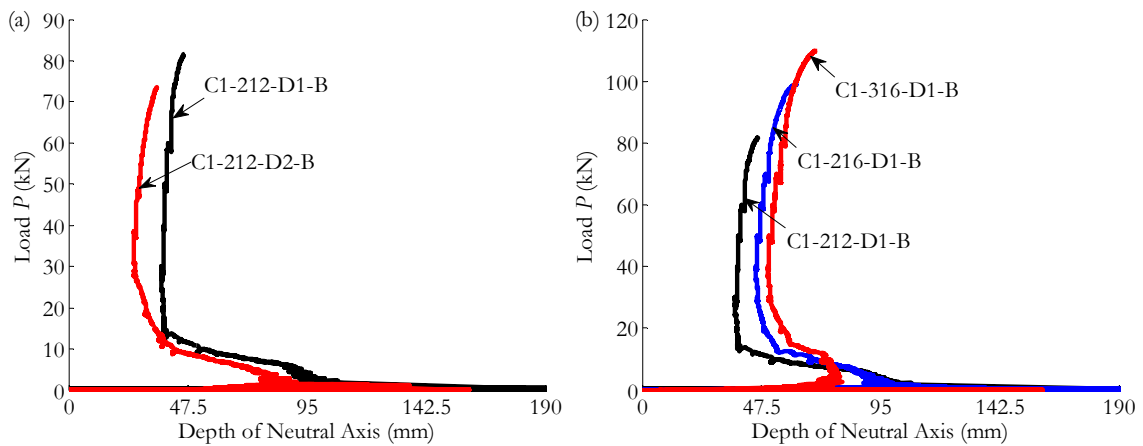
Figure 4-4. Experimental neutral axis depth for the C1 beam series. (a) Comparison for different d/h ratios, (b) comparison for different reinforcement ratios.

The neutral axis depth x increases with the reinforcement ratio, since equilibrium of forces requires a larger compression block for the greater forces arising from larger areas of reinforcement. For the same reinforcement ratio, specimens having higher effective depth to total height ratios (D1 beams) present higher neutral axis depths (compared to D2 beams), since a larger effective depth allows to a more effective force distribution in the section. These observations are in agreement with the usual formulation to calculate the neutral axis position in the serviceability conditions in the absence of compression reinforcement:

$$x = d \cdot n\rho \cdot \left(-1 + \sqrt{1 + \frac{2}{n\rho}} \right)$$

(4-1)

being n the modular ratio (E_f / E_c).

4.2.3. Experimental service load for the SLS of stresses in materials

By examining the data from strain gauges, additional information about the stresses in materials in the serviceability range can be obtained. As explained in § 2.7.1. , the compressive stress in the concrete is usually limited at the service load in order to avoid longitudinal cracks, micro-cracks or high levels of creep, where they could result in unacceptable effects on the

function of the structure (CEN 2004). According to Eurocode 2, to avoid longitudinal cracks, the compressive stress in concrete is limited to $0.60f_{ck}$ under the characteristic combination of loads, whereas to consider linear creep, this stress is limited to $0.45f_{ck}$ under the quasi-permanent loading condition. In Table 4-1 and Table 4-2, the experimental load at which the concrete reaches these limits is registered, taking into account the experimental compressive strength f_c (Table 3-4), the experimental modulus of elasticity E_c (Table 3-5) and the experimental ultimate load P_u (Table 4-3). The corresponding tensile stress in the reinforcement is also shown for those cases where strain gauges were bonded on the reinforcement.

Table 4-1. Experimental values for the service load and FRP stress for $\sigma_c = 0.60f_c$.

Beam Designation	Service load for $\sigma_c = 0.60f_c$			Corresponding tensile stress σ_f	
	ε_c ($\times 10^{-6}$)	Load P (kN)	% of P_u	ε_f ($\times 10^{-6}$)	% of f_{fu}
C1-212-D1-B	750	20.1	24.6%	--	--
C1-216-D1-B	754	24.6	24.8%	--	--
C1-316-D1-B	753	28.7	26.1%	--	--
C1-212-D2-B	750	17.1	23.3%	--	--
C1-216-D2-A	746	19.2	23.8%	1750	11.1%
C1-216-D2-B	746	19.2	23.4%	1750	11.1%
C1-316-D2-B	746	24.9	26.2%	--	--
C2-212-D1-B	1332	32.7	27.6%	--	--
C2-216-D1-B	1274	53.5	37.3%	4350	27.7%
C2-316-D1-B	1329	63.7	37.5%	3340	21.3%
C2-212-D2-B	1026	21	24.7%	--	--
C2-216-D2-B	1355	45.5	33.7%	4000	25.5%
C2-316-D2-B	1340	51.5	32.8%	2850	18.2%
C3-316-D1-A	1140	49.3	32.7%	--	--
C3-316-D1-B	1140	50.4	33.6%	2450	15.6%
C3-212-D1-S	1140	53.9	85.7%	--	--

Results in Table 4-1 and Table 4-2 show that at a load of about 29% of the ultimate load, the concrete stress reaches the indicated limit to avoid longitudinal cracking ($\sigma_c = 0.60f_c$) whilst at a load of about 22% of the ultimate, concrete stress is working at a rate of 45% of f_c. These percentages are extremely low compared to those of the conventional steel RC beam (86% and 65% respectively), which corroborates the assumption that for this type of beams, high stresses are developed in the concrete at already early stages of loading.

For the ranges of loading corresponding to $\sigma_c = 0.60f_c$, the tensile rebar stress varies between 11% (for C1-216-D2-A and C1-216-D2-B) and 28% (for C2-216-D1-B) of its nominal tensile strength f_{fu}. This range of values results below that at which creep rupture of the reinforcement may become a concern according to fib methodology (fib 2007). However, ACI 440.1R-06

would limit the stress of the GFRP bar to $0.20\,f_{fu}$, in which case, beams C2-216-D1-B, C2-316-D1-B and C2-216-D2-B would reach this limit before the concrete stress reaches $\sigma_c = 0.60f_c$. For the case where $\sigma_c = 0.45f_c$, σ_f varies from 8% to 21% f_{fu}.

Table 4-2. Experimental values for the service load and FRP stress for $\sigma_c = 0.45f_c$

Beam Designation	Service load for $\sigma_c = 0.45f_c$			Corresponding tensile stress σ_f	
	ε_c ($\times10^{-6}$)	Load P (kN)	% of P_u	ε_f ($\times10^{-6}$)	% of f_{fu}
C1-212-D1-B	563	14.2	17.3%	--	--
C1-216-D1-B	566	18.8	18.9%	--	--
C1-316-D1-B	565	21.9	19.9%	--	--
C1-212-D2-B	562	13.2	18.0%	--	--
C1-216-D2-A	559	15.2	18.9%	1320	8.4%
C1-216-D2-B	559	15.2	18.5%	1260	8.0%
C1-316-D2-B	560	18.9	19.8%	--	--
C2-212-D1-B	999	25.3	21.3%	--	--
C2-216-D1-B	955	41.0	28.6%	3320	21.1%
C2-316-D1-B	997	47.9	28.2%	2490	15.9%
C2-212-D2-B	769	17.2	20.2%	--	--
C2-216-D2-B	1016	32.4	24.0%	2740	17.5%
C2-316-D2-B	1005	38.5	24.5%	2110	13.4%
C3-316-D1-A	855	38.4	25.5%	--	--
C3-316-D1-B	855	38.9	25.9%	1690	10.8%
C3-212-D1-S	855	41.0	65.2%	--	--

4.3. Moment – Curvature results at the pure bending zone

The mean curvature of the central 450 mm is derived from different experimental measurements. First, by considering a constant value of the curvature, the mean curvature deduced from the inclinometer data in this region, κ_{mean}, can be calculated as follows,

$$\kappa_{mean} = \frac{\theta_2 - \theta_1}{L_1}$$

(4-2)

where L_1 is the distance between inclinometers, and θ_2-θ_1 is the difference between the measured angles by the inclinometers (Figure 4-5). Second, another measure of the mean curvature κ_{mean} is calculated by using the data from mechanical extensometer at each load step. This curvature is calculated dividing the difference between strains at the top and bottom (ε_{top}-ε_{bot}) of the beam by the corresponding distance L_2 (Figure 4-5).
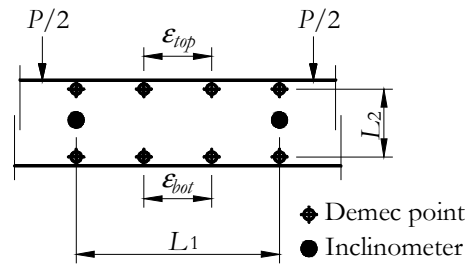
Figure 4-5. Scheme of the instrumentation to measure the mean curvature at the central zone.

Similarly, a local curvature at the midspan section can be calculated from the three strain gauges bonded on the concrete (κ_{local}) considering a linear strain distribution (Figure 4-6, Eq. (4-3)).
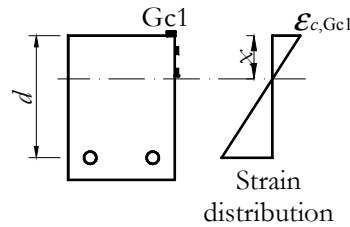
Figure 4-6. Scheme of the instrumentation and strain distribution to measure the local curvature from strain gauges at the midspan section.

$$\kappa_{local} = \frac{\varepsilon_{c,Gc1}}{x} \qquad (4\text{-}3)$$

Figure 4-7 shows a typical representation of the experimental mean and local moment - curvature relationship of the central zone.
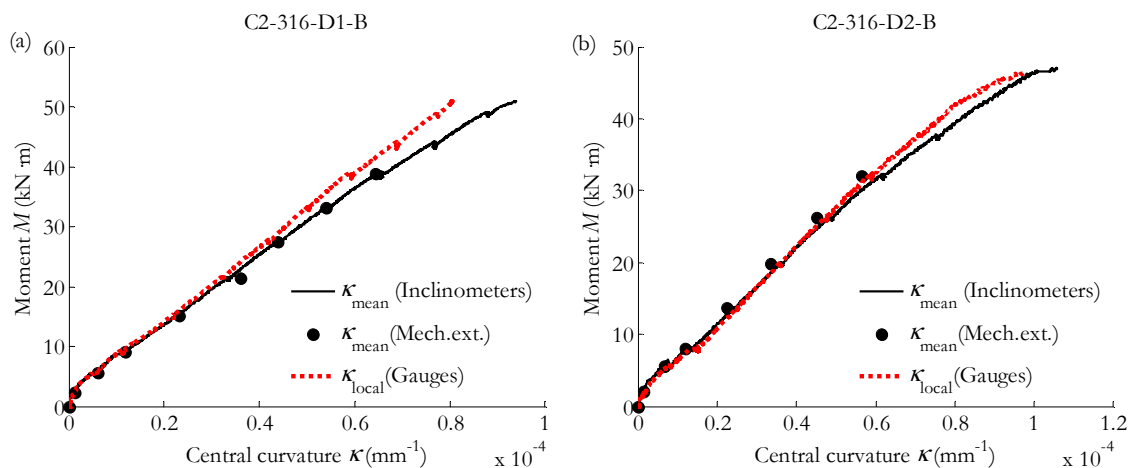
Figure 4-7. Typical experimental Moment - Curvature curve at the central zone.

Before the cracking moment is achieved, a steep linear branch is observed, corresponding to the uncracked condition of the beam. Shortly after the cracking load is attained, the curvature increases rapidly with load and finally arrives to a stabilised phase until failure. Results show that both average curvature measurements are in good agreement with each other. Moreover, it is generally observed that the local curvature at the midspan section generally fits well with the mean curvature along the central 450 mm.

After Figure 4-7 and similarly to the experimentally observed concrete strain evolution along the test, higher reinforcement ratios and d/h ratios lead to stiffer responses. The same tendency is observed for the concrete grade: the higher the concrete strength, the stiffer the beam response and the lower the experimental curvature in the central zone of the tested beam.

4.4. Overall beam behaviour

In this section, the whole beam behaviour is analysed in terms of serviceability and ultimate limit states. First, the curvature evolution along the length of the beam is studied. Second, the FRP rebar strain profile along the length of the beam is detailed. Finally, the experimental modes of failure and the ultimate load are examined.

4.4.1. Curvature evolution with load over the length of the beam

The distribution of the curvature over the length of the beam is deduced from the strains registered by the mechanical extensometer at every load step and it is reported in Figure 4-8 in dotted black lines. For comparison purposes, the evolution of the curvature taking into account the central curvature from inclinometers is also depicted in dashed red lines at the same load steps.
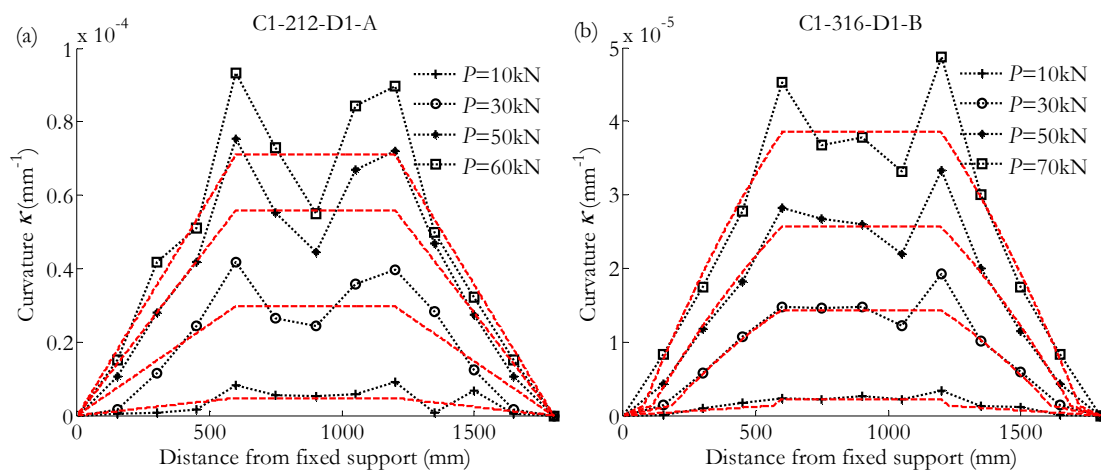
Figure 4-8. Typical evolution of curvature along the beam at different load steps (from inclinometers in dashed lines and from mechanical extensometer in dotted lines).

Since inclinometers only provide the mean curvature in the central zone, the evolution of the curvature at the shear spans is estimated assuming a linear evolution from curvature equal to zero at the supports until the cracking curvature at the point where the moment equals the experimental cracking moment. Then, another linear curve is considered from the cracking curvature until the first point corresponding to the central curvature.

Punctual increments of curvature with respect to the mean curvature obtained with the inclinometers are generally observed along the central zone of the beam. Those increments coincide with the appearing of two or three cracks along the gauge length of the mechanical extensometer (150 mm), in comparison with the appearing of one single crack in the adjacent 150 mm. In 8 of the 14 GFRP RC beams analysed, these "peaks" in the curvature appear in the proximity of the load application points (Figure 4-8), and can be attributed to the influence of the punctual loads and shear forces around the load points. Nonetheless, the randomly behaviour of the concrete tensile strength also has an influence on this phenomenon.

4.4.2. FRP strain profile along the beam

The strain gauges bonded on the GFRP surface give a general idea of the strain profile at the height of the bar at discrete locations along the beam. In Figure 4-9, a typical representation of the rebar strain profile along half the length of the beam is shown at the serviceability load stages, together with the cracking pattern until these loading conditions. The figure also indicates at which load each of the cracks appear.

Results in Figure 4-9 show that before cracking takes place, the reinforcement strain is approximately constant (curve for $P = 5$ kN). When the first crack develops at 8 kN, a noticeable increase in rebar strain is captured at the gauges near this crack. At the load step of 10 kN, two more cracks appear and the rebar strain gauges near these cracks also show a large increment in the recorded strain.

The same procedure is expected at every appearance of a new crack. However, and due to the number and position of strain gauges placed along the beam, this behaviour was not able to be registered for cracks out of this central zone.

In all cases, over the support (i. e. at a distance of 0 mm), the rebar strain is negligible.

C1-216-D2-B
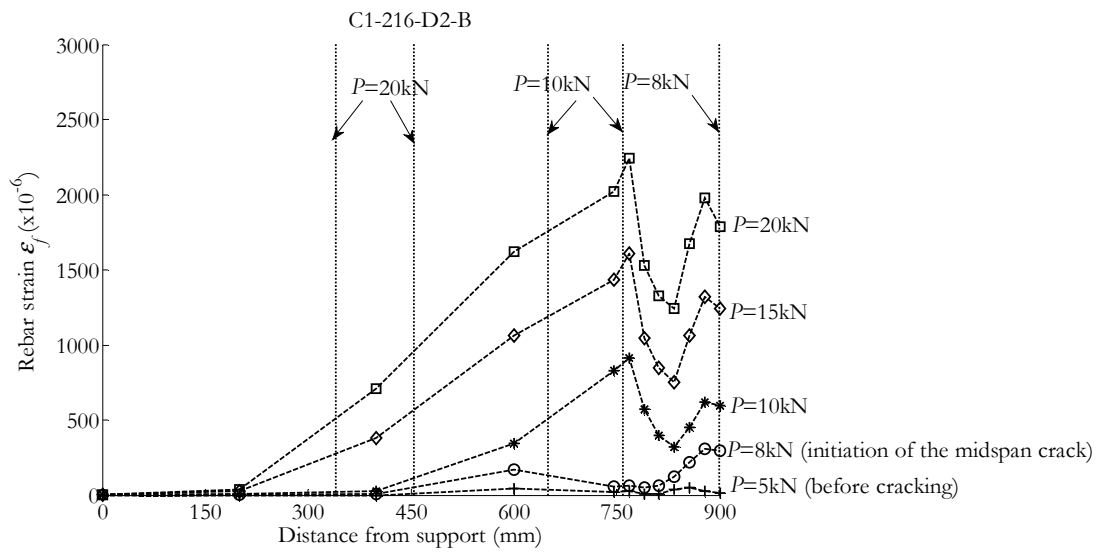
Figure 4-9. Evolution of the rebar strain along the beam under serviceability conditions.

In Figure 4-10, the strain profile for the same beam is shown, this time being for the whole range of load values until rupture. In Figure 4-10, only the principal appearing cracks until rupture are shown.

C1-216-D2-B
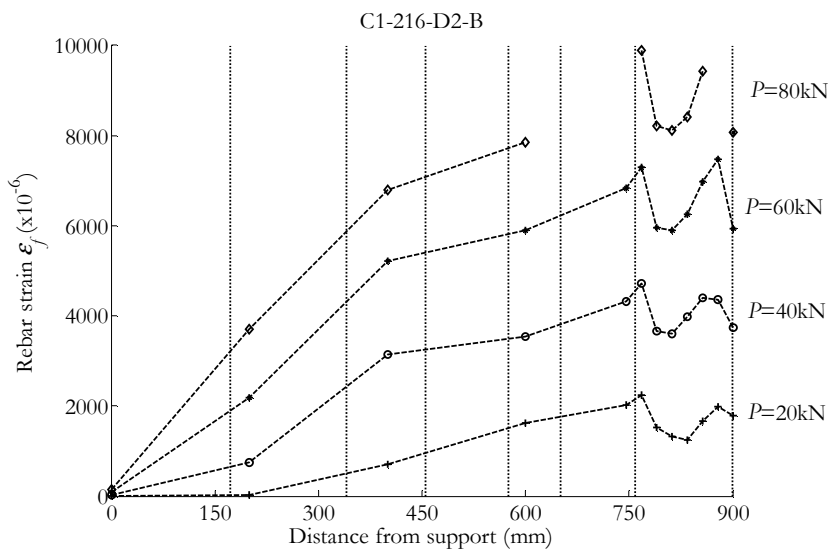
Figure 4-10. Evolution of the rebar strain along the beam until rupture.

It is observed that the rebar strain profile between cracks in the central zone is maintained and proportional to the load since $P = 10$ kN. At the shear span, the gradual apparition of cracks along the test determinates the proportionality of strains.

4.4.3. Modes of failure and ultimate load

As previously explained, all GFRP RC beams were designed to fail by crushing of concrete. During the tests, this mode of failure was clearly obtained for all of the GFRP RC beam specimens. The steel RC beam failed by yielding of the bars followed by concrete crushing.

The concrete crushing took place in the central zone at the top of the beam. The beam failure was observed to start at the top of a principal crack, opened relatively wider and faster than the surrounding cracks. A concrete block popped upwards and this initial crack spread to both sides of the section. At this load stage, the beam failed and the load suddenly dropped. Figure 4-11 shows the typical concrete crushing failure obtained.
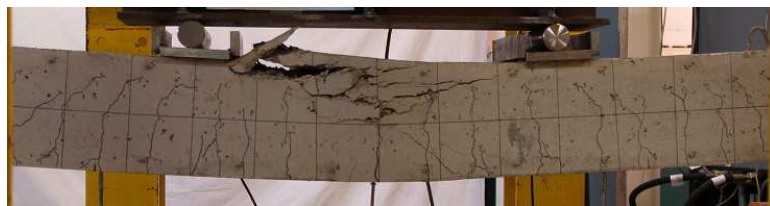
Figure 4-11. Typical concrete crushing failure (Beam C1-212-D1-A).

The concrete crushing failure is brittle. However, due to the plasticity of concrete in compression at its last state, it can be observed a small sign of ductility when it cracks. The concrete failure was more fragile for C2 beams, meaning that the higher concrete strength gave a smaller amount of plasticity in the concrete. Table 4-3 summarizes the experimental load capacities (P_u) for all 27 tested beams.

Table 4-3. Experimental load capacity (P_u) of the tested beams

Beam Designation	Load Capacity Beam -A (kN)	Load Capacity Beam -B (kN)
C1-212-D1	79.9	81.7
C1-216-D1	98.8	99.2
C1-316-D1	104.8	109.9
C1-212-D2	72.1	73.5
C1-216-D2	80.7	84.0
C1-316-D2	92.4	95.2
C2-212-D1	127.4	118.6
C2-216-D1	150.2	143.4
C2-316-D1	164.6	169.8
C2-212-D2	92.3	85.1
C2-216-D2	140.5	134.9
C2-316-D2	144.0	157.2
C3-316-D1	150.6	150.3
C3-212-D1-S	62.9	

As observed, there is a good repeatability in the experimental load capacity between beams -A and -B. The load capacity of the experimental beams increases with the reinforcement ratio, the *d/h* ratio and the concrete strength.

4.5. Results on deflection behaviour

The deflection behaviour is studied in the following. First, the load-midspan deflection deduced from different instrumentation is compared and discussed. Next, an approximate value of the experimental load corresponding to a deflection limitation similar to those suggested by codes of practice is shown. Finally, the load-shear span deflection is examined.

4.5.1. Load - midspan deflection

In this section, three different representations of the evolution of the experimental midspan deflection with load are shown. First, the total midspan deflection is registered with a vertical LVDT placed at the midspan position.

Second, the experimental deflection is calculated from the double integration of the distribution of curvatures deduced from the mechanical extensometer data. This measure of the deflection only takes into consideration the deflection coming from curvatures along the beam.

Finally, a calculation of the deflection by using the data of inclinometers in the central zone is undertaken. The curvature profile considered in § 4.4.1. is double integrated to obtain a measure of the deflections from the inclinometers' data. This methodology only uses the experimental moment - curvature derived from rotation of the central zone, hence, only the flexural effects in the central zone are taken into account.
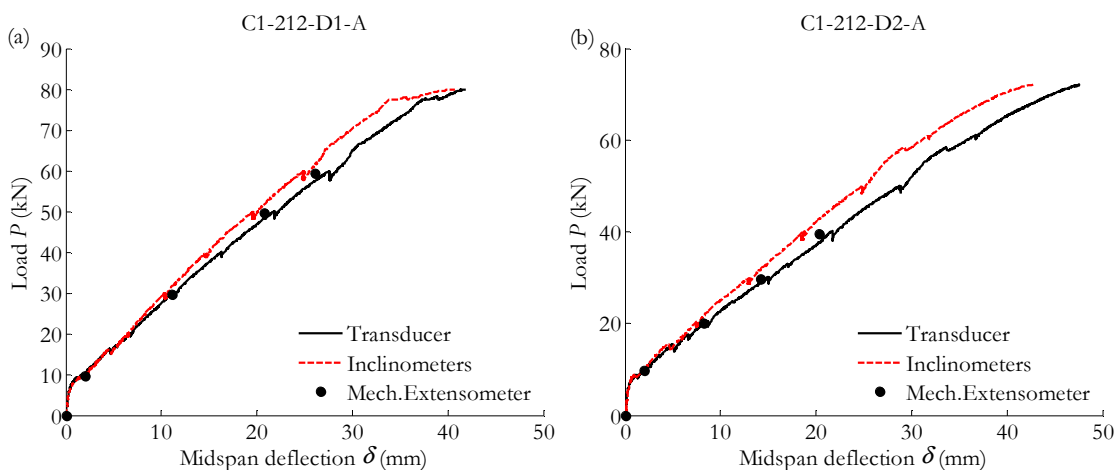
Figure 4-12. Typical experimental Load - Midspan deflection curves for C1 and C2 series.
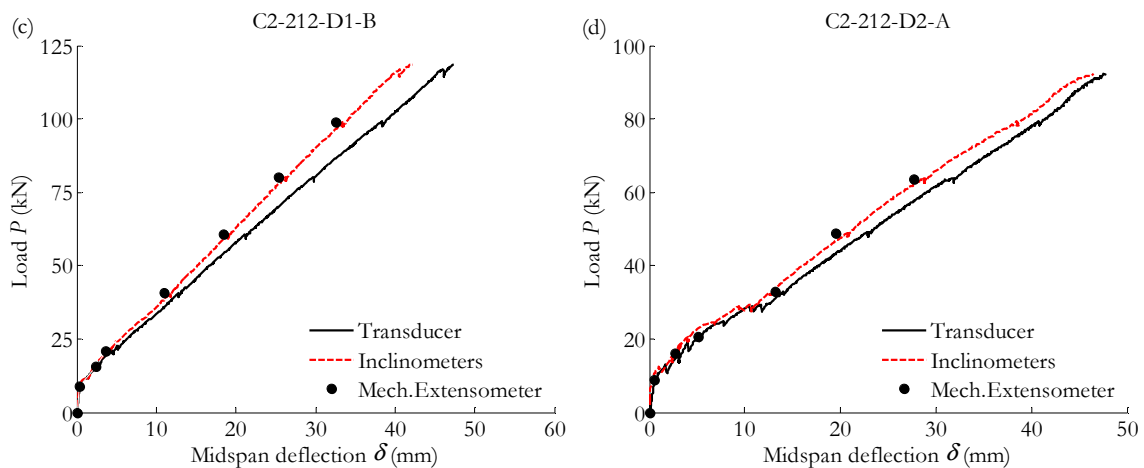
Figure 4-12. Typical experimental Load - Midspan deflection curves for C1 and C2 series (continuation).

Comparing the experimental curves (Figure 4-12), it is observed that at low load levels, the three measurements are in good agreement, proving that only flexural deflection is taking place. As the load increases, the three curves separate, being the deflection registered by the transducer the highest for the same load. These differences are mostly attributed to other effects than flexural that are taking place at these stages of loading. In most cases, the experimental deflection obtained from the mechanical extensometer is marginally higher than that calculated from inclinometers' data (Figure 4-12a and Figure 4-12b), as it is expected since it takes into consideration the deflection due to the increment of curvatures under the load points positions.

For the case of C2 beams, only the central 450 mm were instrumented with Demec points. No substantial differences were observed in the central moment-curvature relationship, between the data from inclinometers and from mechanical extensometer (see § 4.3.). Hence, it is evident that the deflection profiles from both data will be very similar, as observed in Figure 4-12c and Figure 4-12d.

Larger deformations are obtained for lower reinforcement ratios, and vice versa. Moreover, for the same reinforcement ratio, lower effective depths also cause larger deflections. The pre-crack created in beams -B was observed to have no influence on the deflection response.

4.5.2. Experimental service load for the SLS of deflections

According to codes of practice, the deformation of a member shall not be such that it adversely affects its proper functioning or appearance (CEN 2004). In Eurocode 2, the sag of the element is limited to $L/250$ and the deflection after construction of adjacent parts is limited to $L/500$, both under the quasi-permanent combination of loads. Table 4-4 summarizes the experimental load at which the instantaneous midspan total deflection of the beam reaches $L/250$.

Table 4-4. Experimental load at which the instantaneous deflection δ equals to $L/250$.

Beam Designation	Load P (kN)		% of P_u	
	Beam -A	Beam -B	Beam –A	Beam -B
C1-212-D1	21.2	20.6	26.5%	25.2%
C1-216-D1	29.6	30.3	30.0%	30.6%
C1-316-D1	39.5	39.4	37.7%	35.9%
C1-212-D2	18.2	19.7	25.2%	26.8%
C1-216-D2	23.7	25.5	29.4%	30.4%
C1-316-D2	30.0	31.8	32.5%	33.4%
C2-212-D1	25.4	27.3	19.9%	23.0%
C2-216-D1	34.6	33.2	23.0%	23.2%
C2-316-D1	46.6	45.8	28.3%	27.0%
C2-212-D2	24.1	23.4	26.1%	27.5%
C2-216-D2	30.0	29.2	21-4%	21.7%
C2-316-D2	35.6	36.1	24.7%	23.0%
C3-316-D1	48.3	46.5	32.1%	30.9%
C3-212-D1	42.5		67.6%	

The instantaneous deflection of the beams reaches $L/250$ at an average load ratio of 27% of the ultimate load. This mean value is similar to the one obtained for the control of stresses (22-29% of P_u). It is therefore observed that the percentage of service load for GFRP RC is again much lower than for the steel RC beam (in this study, 67.6% P_u), showing the importance of the SLS when designing GFRP RC elements.

4.5.3. Load - shear span deflection

In C1 and C3 series, additional vertical LVDTs were placed on the tested beams to better monitor the deflection profile. These transducers were placed at 450 mm from the supports (transducers "Shear span section 1" and "Shear span section 2" in Figure 4-13). Similarly to in the previous section, this data is compared to the experimental shear span deflection deduced from the mechanical extensometer data and their values are represented in Figure 4-14.
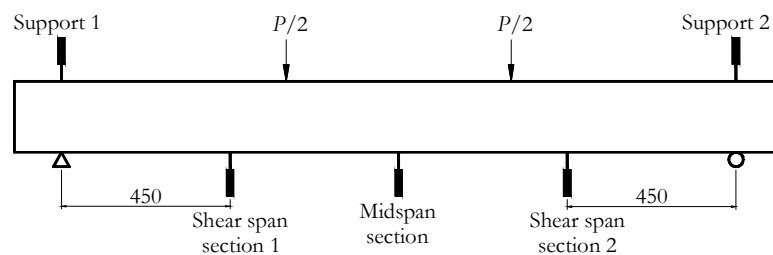
Figure 4-13. Position of the vertical transducers along the length of the beam.
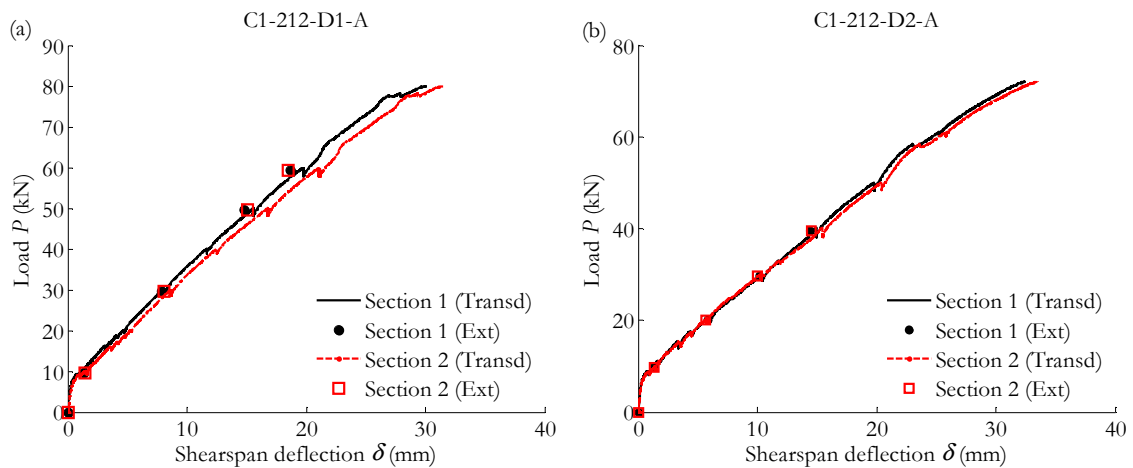
Figure 4-14. Typical experimental Load – Shear span deflection curves.

The vertical transducers at the shear spans registered deflections very similar to those calculated with the mechanical extensometer data along the duration of the test. Only in few cases, at the last stages of loading, the deflection from the mechanical extensometer was slightly smaller than that registered by the vertical transducer (Figure 4-14a). This provided evidence that other effects than flexural were taking place.

4.6. Results on cracking behaviour

When dealing with cracking, two different stages are usually distinguished: the crack formation phase and the stabilised cracking phase (CEB-FIB 1990). In the crack formation phase, cracks form at random positions according to the locally weak sections. At the cracked section, strain compatibility between concrete and reinforcement is no longer maintained as the concrete stress drops to zero and the total force is carried by the reinforcement. Due to bond transfer between materials, at a certain distance from the crack, concrete progressively acquires tensile stresses until the strain compatibility is again recovered. From this minimum distance, a new crack could appear as the load increases. The better the bond properties between concrete and reinforcement, the shorter the length for re-establishing strain compatibility.

Once cracking has been stabilised, no more new cracks appear and the ones that have been formed become wider with the increase of loading. Therefore, at the stabilised cracking phase, crack spacing remains constant whilst crack width continues to grow.

4.6.1. Cracking patterns

The cracking patterns were documented along the whole length of the beams at the different load steps. Figure 4-15 shows a typical crack pattern. It is observed that during the crack formation phase, cracks form at random positions and are mostly vertical, starting at the central zone. As the load increases, additional inclined cracks appear due to the effect of shear forces on the principal tensile stresses, and those that were vertical at the shear span also start

to incline due tot the combined flexural-shear effects in the zones with larger bending moment (in the case depicted in Figure 4-15, inclined cracks are considered to appear at a load of 29.6 kN). Finally, no more cracks appear and the existing ones widen.

For the case of C2 beam series, crack pattern was slightly different and some splitting cracks appeared at the height of the reinforcement, at loads of approximately 50% of the ultimate load. This phenomenon made more complicated to measure the crack width and spacing objectively, and it was mainly attributed to the concrete type, which was manufactured in-situ, and may have led to a creation of microcracks during casting that produced a scattered cracking phenomenon. For this reason, the data related to the C2 beam series was discarded in the analysis of the crack width and crack spacing. Nevertheless, the crack patterns of those beams are shown in Appendix B.

4.6.2. Crack spacing

The experimental average and maximum crack spacing were measured in the central zone at the height of the reinforcement, at different load steps. In Table 4-5, the maximum, average and minimum crack spacing are shown. These values correspond to the load level at which cracking was stabilised, which is included at the last column of the table.

Table 4-5. Experimental maximum, average and minimum crack spacing and the load level at which cracking stabilises

Beam Designation	$s_{r,\max}$ (mm)		$s_{r,\mean}$ (mm)		$s_{r,\min}$ (mm)		% of P_u	
	Beam -A	Beam -B	Beam -A	Beam -B	Beam -A	Beam -B	Beam -A	Beam -B
C1-212-D1	145	143	99	94	70	53	24.9	24.1
C1-216-D1	95	90	61	80	33	75	29.8	19.7
C1-316-D1	75	74	58	56	39	29	38.1	35.9
C1-212-D2	108	130	79	127	29	124	41.1	25.8
C1-216-D2	181	152	127	150	71	148	22.2	11.4
C1-316-D2	137	156	102	114	65	88	31.2	20.2
C3-316-D1	136	102	86	90	39	78	13.3	13.3
C3-212-D1	122		102		93		31.8	

The crack spacing ranged between 29 mm and 181 mm for the different tested beams. The loading level at which crack spacing was stabilised ranged between 11.4% and 41.1% of the ultimate load P_u, with a mean value of 25.1% P_u and a standard deviation of 9.3% P_u.

Load = 9.6 kN
Av. Crack width = 0.02 mm

Load = 19.7 kN
Av. Crack width = 0.05 mm

Load = 29.6 kN
Av. Crack width = 0.25 mm

Load = 39.4 kN
Av. Crack width = 0.42 mm

Load = 49.3 kN
Av. Crack width = 0.60 mm

Load = 59.4 kN
Av. Crack width = 0.70 mm

Failure
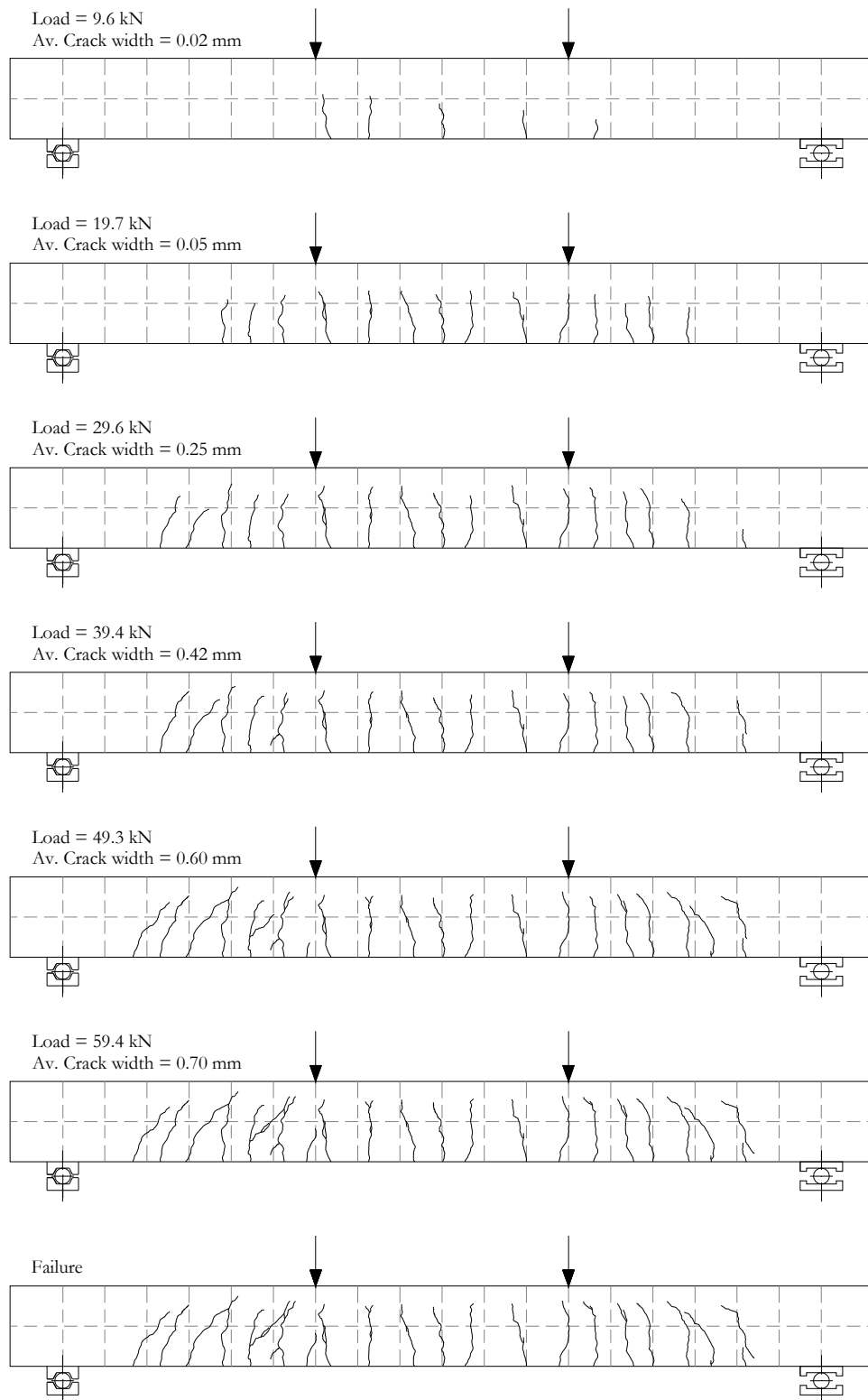
Figure 4-15. Crack pattern for beam C1-212-D2-B.

Based on strain compatibility, a minimum crack spacing $s_{r,\min}$ can be defined following Eq. (4-4), as the closest point to an existing crack at which another crack can form.

$$s_{r,\min} = \frac{f_{ctm}\phi}{4\tau_{bm}\rho_{eff}}$$

(4-4)

In Eq. (4-4), f_{ctm} is the mean tensile strength of concrete, ϕ is the nominal diameter of the reinforcement, τ_{bm} is the average bond stress along the disturbed zone and ρ_{eff} is the effective reinforcement ratio. Crack spacings are expected to vary between $s_{r,\min}$ and $s_{r,\max} = 2s_{r,\min}$. Values for the mean crack spacing $s_{r,\mathrm{mean}}$ for steel RC are proposed in the literature, varying from 1.33 to 1.54 times the minimum value, whilst maximum crack spacing can be expressed as $s_{r,\max} = 2s_{r,\min}$ (Borosnyói 2002):

$$\frac{s_{r,\min}}{s_{r,\mathrm{mean}}} = 0.67 \text{ to } 0.77$$

(4-5)

$$\frac{s_{r,\max}}{s_{r,\mathrm{mean}}} = 1.33 \text{ to } 1.54$$

(4-6)

Figure 4-16 compares the ratios minimum to average and maximum to average crack spacing. As observed, the mean values of these two ratios agree well with the predicted in Eqs. (4-5) and (4-6) and the minimum one is around twice the maximum value.
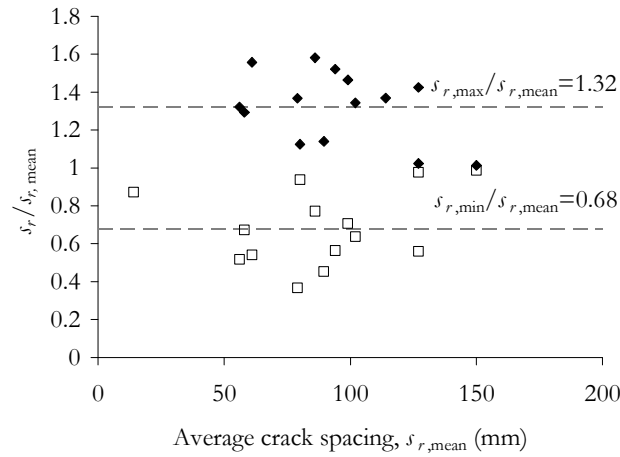
Figure 4-16. Ratios of minimum and maximum vs. average crack spacing.

4.6.3. Crack width

The experimental crack width at the flexural zone was measured by an optical micrometer at every load step. The flexural cracks appearing under the load points were observed to either widen more than the rest of the cracks in the central zone or appear at a lower spacing. This effect was attributed to a probably increase of curvature and strains at these zones. Consequently, the cracks under the load points were discarded for the study of the average

and maximum crack width. Additionally, in those beams that had a pre-crack at the midspan section, a horizontal transducer registered the width of this local midspan crack along the duration of the test.

Figure 4-17 shows two typical evolutions of the average crack width in the flexural zone measured with the optical micrometer w_{mean} compared to the midspan crack width registered with the horizontal transducer w_{local}. In Figure 4-18, two typical evolutions of the maximum crack width are depicted.
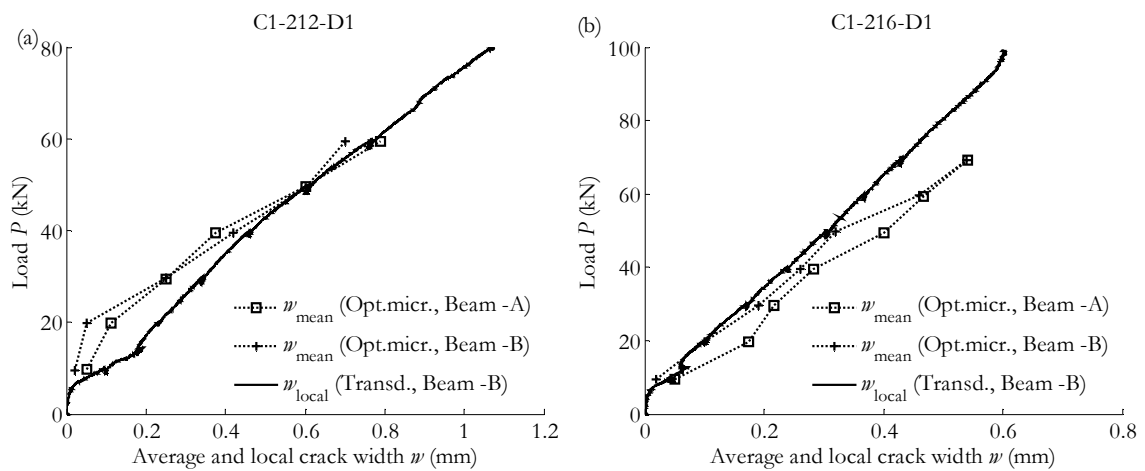
Figure 4-17. Typical experimental average and local crack width evolution with load.
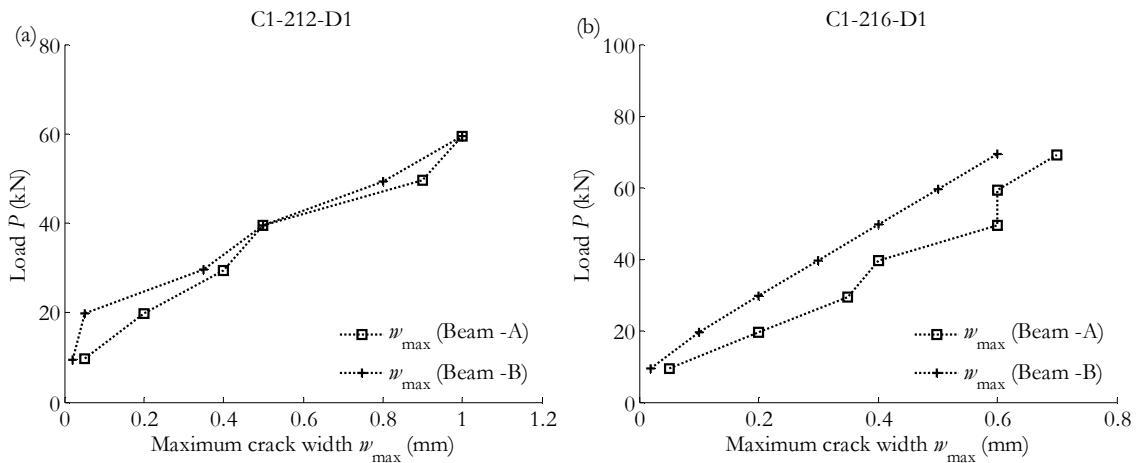
Figure 4-18. Typical experimental maximum crack width evolution with load.

Even though the crack width is usually a scattered parameter, a fairly good repeatability is observed in some of the pairs of beams -A and -B. In some cases, it is observed that at the first stages of cracking and before cracking is stabilised, the average crack width is slightly lower than the midspan crack width (Figure 4-17a), which proves that the midspan crack, which has been pre-cracked prior to start testing, develops earlier than the adjacent cracks. However, at high loads, the average trend matches up fairly well with the local crack, showing

that once the cracking is stabilised, there are no evident differences between the midspan cracks.

Several authors and standards propose in their formulae a coefficient to calculate the characteristic crack width from the average crack width value (Broms 1965a, Broms and Lutz 1965b, Ferry 1966, Rizkalla and Hwang 1984, CEN 1992). For example, Eurocode 2 (CEN 1992) proposes a β coefficient of 1.3 to 1.7. Taking into account that the characteristic crack width corresponds to the 95% fractile of the crack width that could be expected in a flexural element, in this study the maximum registered crack width is taken instead, and it is compared to the mean value at every load step for each tested beam. In Figure 4-19 an example for two beam tests is shown.
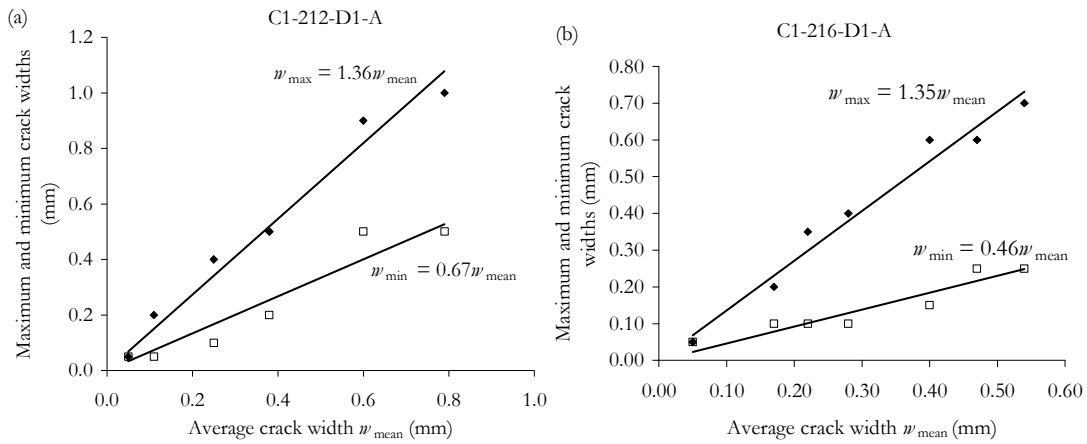
Figure 4-19. Maximum and minimum crack width versus average crack width.

The average ratio w_{max}/w_{mean} and w_{min}/w_{mean} is represented as a function of the effective reinforcement ratio ρ_{eff} in Figure 4-20. The average ratio w_{max}/w_{mean} for the tested beams is found to be 1.32, which fits well with the proposed by Eurocode 2 (1992), and w_{min}/w_{mean} is 0.59 for the tested specimens.
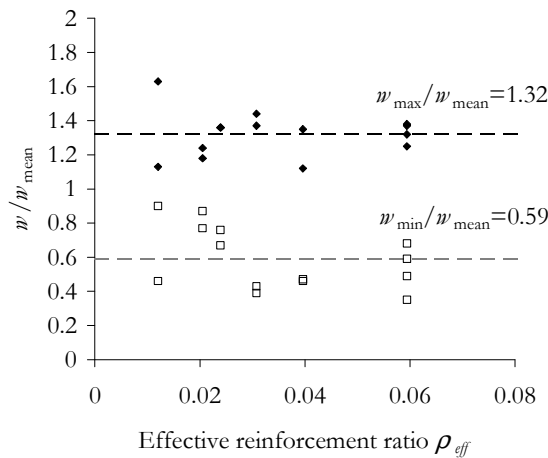
Figure 4-20. Ratio of maximum and minimum vs. average crack width as a function of ρ_{eff}.

4.6.4. Experimental load for the SLS of cracking

Following ACI 440.1R-06 and CAN/CSA-S806, the crack width for the FRP RC experimental beams is generally limited to 0.5 to 0.7 mm. Table 4-6 summarizes the resulting load at which the maximum crack width arrives to 0.5-0.7 mm for each beam tested.

Table 4-6. Experimental load at which the maximum crack width w_{max} equals to 0.5-0.7 mm.

Beam Designation	Load P (kN)		% of P_u	
	Beam -A	Beam -B	Beam -A	Beam -B
C1-212-D1	39.5	39.5	49.4%	48.3%
C1-216-D1	69.1	69.3	70.0%	69.9%
C1-316-D1	79.3	80.7	75.6%	73.4%
C1-212-D2	29.6	28.4	41.1%	38.6%
C1-216-D2	28.6	29.5	35.4%	35.2%
C1-316-D2	48.7	39.7	52.7%	41.7%
C3-316-D1	90.0	90.0	59.8%	59.9%
C3-212-D1	50.0		79.5%	

The maximum crack width reaches the value of 0.5-0.7 mm at a load of about 54% the ultimate load. This mean value results higher than the previously obtained in the study of the SLS for stresses in materials (22-29% of P_u) and in the control of deflections (27% of P_u). For the case of the steel RC beam, the ratio of ultimate load is 79.5%, higher than the mean value of the GFRP RC beams.

4.7. Data analysis on tension stiffening

In this section, a measure of tension stiffening is drawn by evaluating the experimental rebar strain profile. The beam C3-316-D1-B, which was especially instrumented for this purpose with enough strain gauges at the central zone to monitor the formation and development of three adjacent cracks, is analysed herein.

In Figure 4-21, the rebar strain at the midspan crack is compared to the average strain at the rebar between two adjacent cracks. The strain at the midspan crack was obtained directly from the strain profile, while the average rebar strain between the cracks was evaluated by numerical integration. This experimental approach has the advantage that tension stiffening is evaluated in the structural test itself, and not in a different test setup, as typically happens in a tension test. However, it presents several limitations that shall be taken into consideration. Firstly, the strain gauges could not be placed at smaller spacing within the measurement zone in order to minimize the disruption to bond; hence, the strain was only registered at local positions. Secondly, only three cracks were examined, which was the minimum possible to have measurements on both sides of a crack. Moreover, the cracks and their location, as well as the

strain and slip in the reinforcement may not be symmetric around the crack, because of the inherent variability of concrete. Similar comments and methodology are found in Al-Sunna (2006).
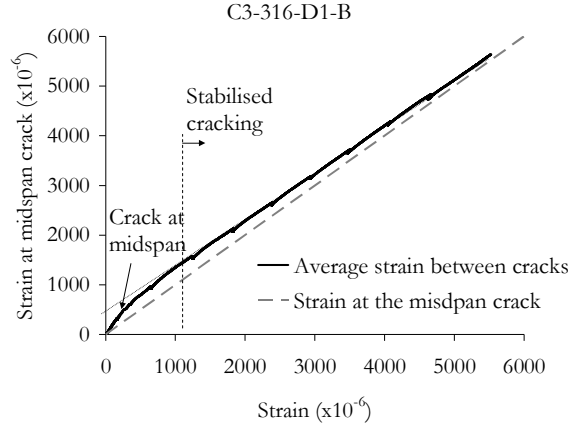
Figure 4-21. Crack strain vs. average strain relationship.

At the crack, the tensile force is entirely carried by the reinforcement, while between cracks the tensile force is carried both by the concrete and the rebar through bond. Hence, the average strain in the rebar is expected to be less than the strain at a crack, as it is observed in Figure 4-21. Moreover, results show that once the cracking phase has stabilized, an essentially linear relationship between the average strain and the crack strain is shown. The line representing the average strain tends to join the strain at the crack, which proves that at high loads, tension stiffening tends to be almost negligible.

The effect of tension stiffening can be also drawn as an effective modulus of elasticity of the reinforcement (E_{eff}) defined as the ratio of the stress at a crack (σ_{cr}) to the average strain between cracks (ε_{ave}) (Al-Sunna 2006). This effective modulus of elasticity can be related to the actual modulus (E), defined as the ratio of stress to strain (ε_{cr}) at the crack:

$$\frac{E_{eff}}{E} = \frac{\varepsilon_{cr}}{\varepsilon_{ave}} \tag{4-7}$$

The ratio defined in Eq. (4-7) gives a rational measure of tension stiffening after cracks have formed, and it is represented in Figure 4-22a. Results show that E_{eff}/E reduces tending to a value of 1.0 as the average strain increases in the stabilized cracking phase, which means that tension stiffening is effectively reducing.

Finally, a modelisation of the tension stiffening effect can be drawn by modifying the stress-strain curve of the FRP reinforcement, as shown in Figure 4-22b, similarly to what proposed by Gilbert and Warner (1978) for steel RC.
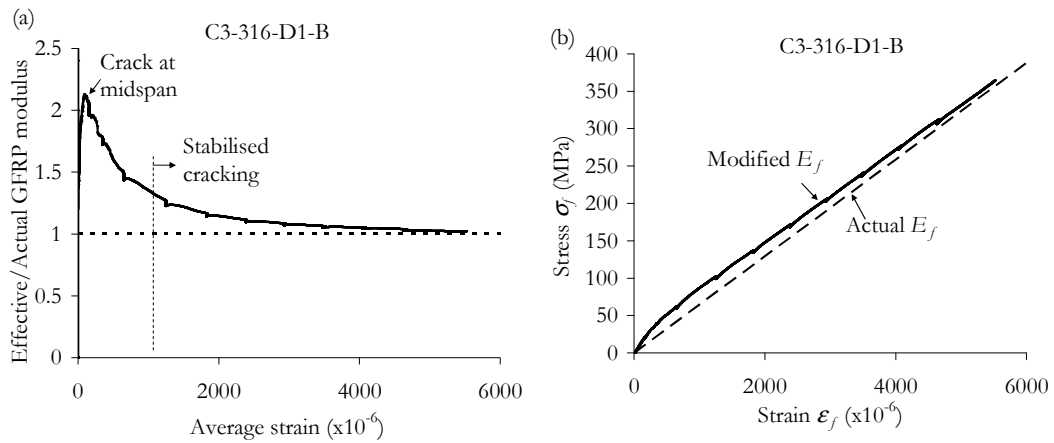
Figure 4-22. Effective modulus of elasticity (left) and modified stress-strain curve for the reinforcement taking into account the tension stiffening effect (right).

4.8. Data analysis on bond behaviour

By using the rebar strain data, a measure of an average bond between the rebar strain gauges is shown for the beam C3-316-D1-B. Considering the force equilibrium of a rebar segment as shown in Figure 4-23, the average bond stress τ on the surface of the rebar can be expressed as in Eq. (4-8).
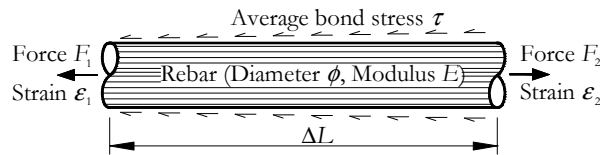
Figure 4-23. Equilibrium of a segment of the reinforcement.

$$\tau = \frac{E\phi(\varepsilon_2 - \varepsilon_1)}{4\Delta L} \qquad (4-8)$$

In Figure 4-24a, the average bond profile of the beam along the central zone is shown at different load levels in the service range. It is observed that at a load of 5 kN, where the beam is uncracked, the bond stress profile is fairly constant and almost negligible. At 10 kN, the midspan crack is registered (at 900 mm from the support), jointly with a crack appearing at 713 mm from the support. The corresponding bond stresses at 10 kN increase on either sides of the cracks until they reach a maximum value at about 30 mm from the crack, but then reduce with increasing distance. This bond stress profile simply increases at 15 kN, where no more cracks develop. At 20 kN, a new crack appears at 95 mm from the midspan location. The stress profile and the no-slip point change so as to adequate to the new bond requirement. Thereafter, and since no more cracks appear, the bond stress profile maintains

the same shape, only with increases on the stress values. At $P = 80$kN (Figure 4-24b), which is about 53% of the ultimate load, the maximum bond stress attains values of 4 MPa.
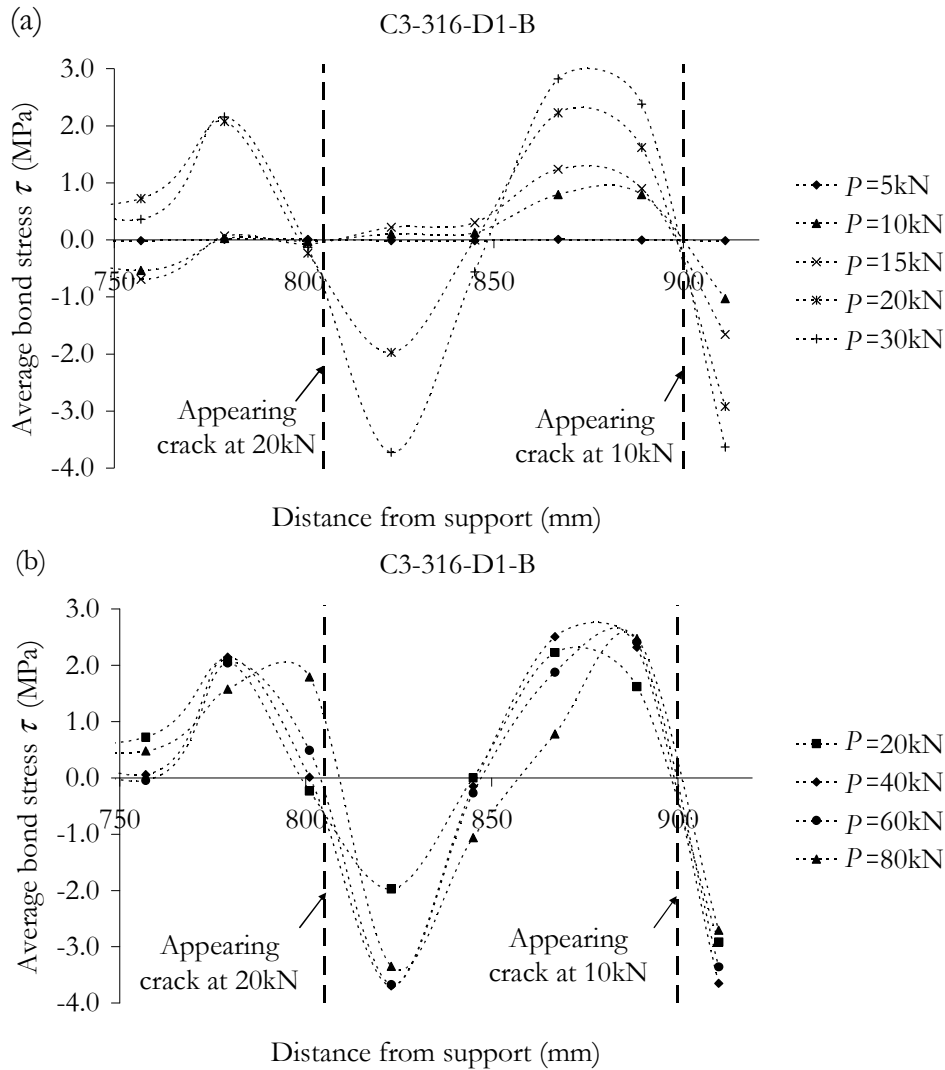
Figure 4-24. Experimental average bond stress, (a) until service load, (b) beyond service load.

For the correct interpretation of this profile, it shall be taken into consideration that each of the points depicted in the figure represents the average value of bond stress between the rebar and the concrete along 22 mm. Moreover, the bond conditions around the cracks are observed to be unsymmetrical. To obtain a better bond profile, closer strain data would be needed. However, it was believed that additional strain gauges bonded on the surface of the rebar would significantly affect the bond. Since it was not the purpose of this study to investigate bond-strain or bond-slip models, it is considered that the average bond stress was adequately captured with the actual data.

4.9. Experimental governing parameters for the SLS

Based on the findings of the previous sections, the governing parameters for the SLS are those limitations that are attained at the lowest value of load. The studied SLS are:

- Stresses on materials limitation: the concrete compressive stress is limited to 45% the compressive strength f_c. The service load is the load at which the maximum concrete compressive strain (read by the strain gauge located at the top of the midspan section) measures:

$$\varepsilon_c = 0.45 \frac{f_c}{E_c} \qquad (4\text{-}9)$$

This data is only available for those tested beams where strain gauges were glued on the concrete surface.

- Crack width limitation: the maximum crack width is limited to 0.5 - 0.7 mm. The service load is the load at which the maximum value of crack width (measured at the central zone at the height of the reinforcement) equals to:

$$w_{max} = 0.5 \div 0.7 \text{ mm} \qquad (4\text{-}10)$$

- Deflection limitation: the deflection is limited $L/250$. The service load is the load at which the instantaneous experimental midspan deflection (read by the vertical transducer) is:

$$\delta_{midspan} = \frac{L}{250} \qquad (4\text{-}11)$$

The obtained service load P_s for each SLS is related to the ultimate load P_u and to the cracking load P_{cr} for comparison purposes, and it is represented in Figure 4-25 (service load to the ultimate load, P_s/P_u) and in Figure 4-26 (service load to the cracking load, P_s/P_{cr}). Table 4-7 and Table 4-8 summarize these results.

It is observed that for none of the tested specimens the SLS of cracking results the most restrictive limitation. On the contrary, the determinant criterion is either the concrete stress limitation or the deflection limitation, being for the steel RC beam, the concrete stress limitation.

The limitation of stress in concrete keeps fairly constant at a mean load ratio of 21.95% the ultimate load or 2.87 times the cracking load, with only a standard deviation of the mean value of 3.82% when referring to P_u and 0.83 when comparing with P_{cr}. On the other hand, the maximum crack width limitation presents the most scattered results, probably owing to the

high variability of the experimental maximum crack width parameter. The standard deviation of the mean value in the case of maximum crack width rises up to 15.67% and 2.47 for P/P_u and P/P_{cr} respectively. The deflection limitation gives values of P/P_u and P/P_{cr} fairly similar to that obtained for the stresses in materials limitation.
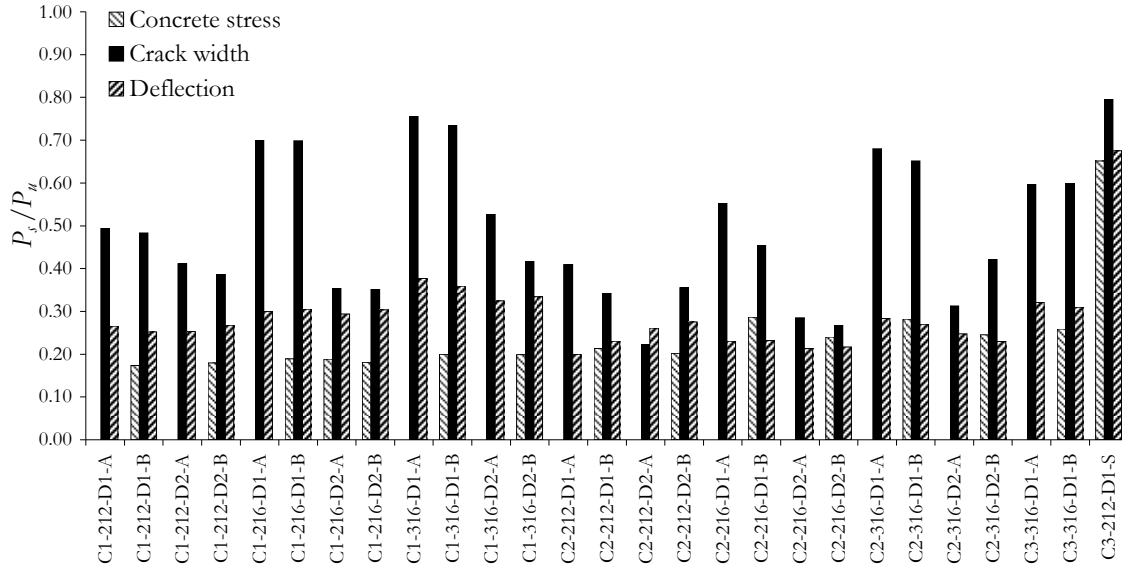
Figure 4-25. Experimental service load related to the ultimate load P_s/P_u.
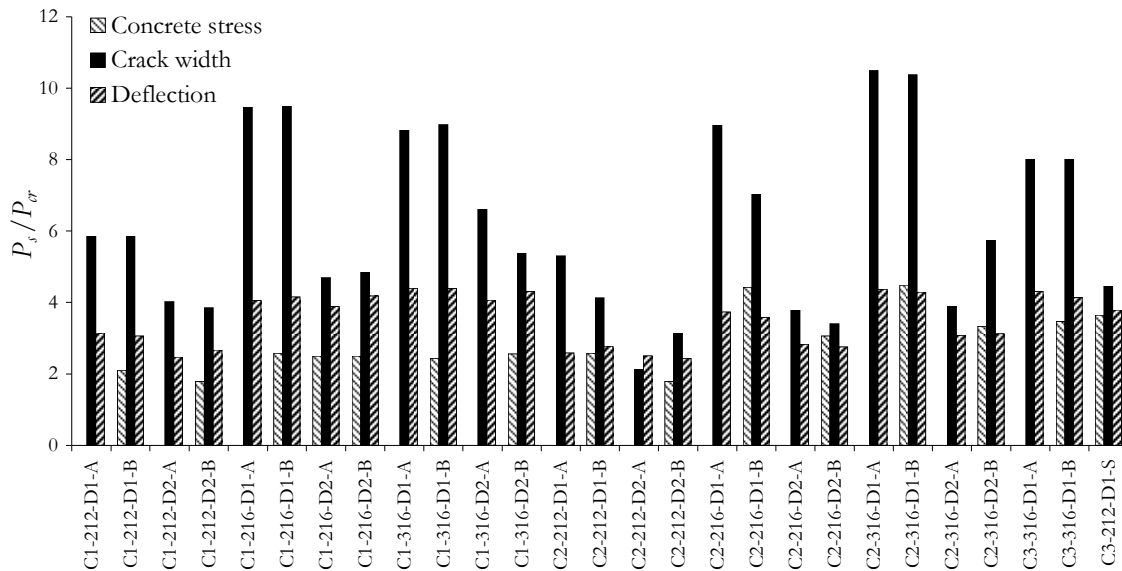
Figure 4-26. Experimental service load related to the cracking load P_s/P_{cr}.

Table 4-7. Experimental values for the service load related to the ultimate load P_s/P_u.

Beam Designation	$\sigma_c = 0.45 f_c$		$w_{max} = 0.5\text{-}0.7$ mm		$\delta = L/250$	
	Beam -A	Beam -B	Beam -A	Beam -B	Beam -A	Beam -B
C1-212-D1	-- (*)	17.4%	49.4%	48.3%	26.5%	25.2%
C1-216-D1	-- (*)	19.0%	70.0%	69.9%	30.0%	30.6%
C1-316-D1	-- (*)	19.9%	75.6%	73.4%	37.7%	35.9%
C1-212-D2	-- (*)	18.0%	41.1%	38.6%	25.2%	26.8%
C1-216-D2	18.8%	18.1%	35.4%	35.2%	29.4%	30.4%
C1-316-D2	-- (*)	19.9%	52.7%	41.7%	32.5%	33.4%
C2-212-D1	-- (*)	21.3%	40.9%	34.2%	19.9%	23.0%
C2-216-D1	-- (*)	28.6%	55.3%	45.4%	23.0%	23.2%
C2-316-D1	-- (*)	29.2%	68.0%	65.2%	28.3%	27.0%
C2-212-D2	-- (*)	20.2%	22.2%	35.5%	26.1%	27.5%
C2-216-D2	-- (*)	24.0%	28.5%	26.7%	21.4%	21.7%
C2-316-D2	-- (*)	24.5%	31.3%	42.1%	24.7%	23.0%
C3-316-D1	25.5%	25.9%	59.8%	59.9%	32.1%	30.9%
C3-212-D1	65.2%		79.5%		67.6%	

(*): No data available for this beam

Table 4-8. Experimental values for the service load related to the cracking load P_s/P_{cr}.

Beam Designation	$\sigma_c = 0.45 f_c$		$w_{max} = 0.5\text{-}0.7$ mm		$\delta = L/250$	
	Beam -A	Beam -B	Beam -A	Beam -B	Beam -A	Beam –B
C1-212-D1	-- (*)	2.11	5.86	5.85	3.15	3.06
C1-216-D1	-- (*)	2.58	9.47	9.50	4.05	4.15
C1-316-D1	-- (*)	2.44	8.82	8.98	4.40	4.39
C1-212-D2	-- (*)	1.79	4.01	3.85	2.47	2.67
C1-216-D2	2.49	2.49	4.69	4.84	3.89	4.18
C1-316-D2	-- (*)	2.56	6.60	5.37	4.06	4.31
C2-212-D1	-- (*)	2.57	5.30	4.13	2.58	2.78
C2-216-D1	-- (*)	4.42	8.97	7.02	3.73	3.58
C2-316-D1	-- (*)	4.49	10.49	10.37	4.37	4.29
C2-212-D2	-- (*)	1.79	2.13	3.14	2.50	2.43
C2-216-D2	-- (*)	3.06	3.78	3.40	2.83	2.76
C2-316-D2	-- (*)	3.33	3.90	5.73	3.08	3.13
C3-316-D1	3.42	3.46	8.01	8.01	4.30	4.14
C3-212-D1	3.65		4.45		3.78	

(*): No data available for this beam

Finally, it shall be taken into consideration that the SLS of stresses in materials limiting the concrete strain to $0.45f_{ck}$ and the crack width limitation refer to the quasi-permanent loading condition. Hence, the maximum load would be increased depending on the quasi-permanent to total load relationship.

Moreover, the deflection limitation usually refers to the long-term deflection rather than the instantaneous one. In this study, since experimental values for the long-term deflection were not available, the instantaneous deflection has been considered instead, and consequently the maximum load causing deflections to reach these limiting values would be lower than that presented in the figures. Hence, the design under the SLS would probably be determined by the deflection limitation for these beams.

4.10. Concluding remarks

This chapter presents the results of the experimental program on twenty-six GFRP RC beams and one steel RC beam. The main conclusions draw from these results are summarized in the following.

4.10.1. Results at the midspan section and the pure bending zone

The use of strain gauges on concrete at the midspan section allowed to adequately monitoring the concrete strain evolution and the concrete strain distribution along the depth of the midspan section. The Bernoulli hypothesis was validated, and the evolution of the neutral axis depth with load was derived and examined.

The concrete tested showed a relatively high ultimate compressive strain (varying from 0.4% to 0.55%), compared to the values typically considered in standards (0.3% to 0.35%). This behaviour had been previously reported by other authors (Rüsch 1960, Matthys and Taerwe 2000).

The inclinometers placed at the central zone of the beam and the data from mechanical extensometer at this area allowed calculating the average moment-curvature relationship along the test. Moreover, the local curvature at the midspan section was deduced from the strain gauges on concrete and compared to the average, obtaining similar results from the three data.

High reinforcement ratios, concrete grades and d/h ratios led to higher depths of neutral axis and, consequently, smaller strains at the top concrete fibre and smaller curvatures.

4.10.2. Overall beam behaviour

The curvature evolution along the length of the beam at different load steps was represented using the strain data deduced from the mechanical extensometer. This representation showed that punctual increments of curvature were registered along the central zone of the beam. Those increments, which coincided with the appearing of two or three cracks along the gauge

length of the mechanical extensometer, were observed to appear in the proximity of the load points in 8 of the 14 beams analysed. The appearing of these "peaks" was attributed to the influence of the punctual loads and shear forces around the load points. However, the randomly behaviour of the concrete tensile strength also had an influence on this phenomenon.

The strain gauges on the FRP bar allowed representing its strain evolution at precise locations of the beam. An increase of the bar strain was recorded when a crack was created near its position.

The mode of failure obtained for all the twenty-six GFRP RC beams was concrete crushing, and good repeatability was observed in the load capacity between specimens -A and -B. Moreover, the load capacity increased with the reinforcement ratio, the d/h ratio and the concrete strength.

4.10.3. Results on deflection

The midspan deflection was directly acquired by a LVDT vertical transducer. Furthermore, it was compared to the experimental deflection obtained by integration of curvatures along the length of the beam, deduced from the data of the mechanical extensometer and from the inclinometers. Results showed that for relatively low loads the three experimental data fitted each other. Nonetheless, as the load increased, the deflection from the LVDT became higher than the calculated from curvatures. This difference was attributed to the fact that at high loads, deflection is not only a result of flexural curvatures, and the influence of shear cracks shall be accounted for in the calculation of deflections.

The experimental shear span deflection at 450 mm from the supports was also registered and computed. Similar results to the midspan deflection were found, even though the differences between the deflection registered by the LVDT and the deflection computed from curvatures were less accentuated.

A stiffer response was obtained as the reinforcement ratio, the concrete grade and the d/h ratio increased.

4.10.4. Results on cracking

The crack patterns were examined for the beam series C1 and C3. Two different cracking stages were observed: first, a crack formation phase where cracks were appearing as the load increased and second a stabilised cracking phase, in which no more cracks appeared and the ones that had been formed became wider with the increase of the load. The beam series C2 was discarded in the analysis of cracking because of a high dispersion in the results on both crack spacing and crack width.

The load level at which cracking stabilised was about 25.1% of P_u. The ratio maximum to mean crack spacing was 1.32 and the ratio minimum to mean values was 0.68. Both ratios agree well with typical values found in the literature.

The experimental crack width at the flexural zone was registered by an optical micrometer. In those cases were a midspan pre-crack was made prior to testing, the crack width was registered with a horizontal transducer.

The average crack width is generally in good agreement with the local midspan crack width. The maximum values are affected by a large scatter, as it was expected.

The ratios maximum to average and minimum to average crack width were calculated for each tested beam, resulting an average value of 1.32 and 0.59 respectively. These mean values result highly close to the ratios obtained for the crack spacing.

4.10.5. Results on bond and tension stiffening behaviour

A measure of tension stiffening was performed by evaluating the strain profile at the rebar. The strain at a crack was compared with the average strain between cracks B, obtaining that the average strain between cracks was lower than the strain at the midspan crack due to the tensile load carrying capacity thanks to bond transfer between the concrete and the rebar. Once cracking was stabilized, an essentially linear relationship between the average strain and the crack strain was reported. The line representing the average strain tended to join the strain at the crack, which proved that at high loads, tension stiffening diminished.

The average bond behaviour was also examined by studying the rebar strain data. It was observed that before cracking takes place, the bond stresses were almost negligible. As the first crack appeared, the bond stresses increased on both sides of the crack. This bond stress profile and the no-slip point were modified at every crack appearing, so as to adequate the new bond requirements.

4.10.6. Experimental values for the service load

The load at which the experimental instantaneous serviceability limits states were reached has been calculated. For this computation, the concrete has been considered to behave linearly until a compressive stress of 45% the concrete strength, the maximum crack width has been restricted to 0.5-0.7 mm and the instantaneous deflection has been limited to $L/250$.

Results indicate that the most restrictive SLS of the GFRP RC beams were the stresses on concrete (approximately 29% of P_u) and the midspan deflection (27% of P_u), with the maximum crack width being the less limiting condition (54% of P_u). Similarly what obtained for the GFRP RC beams, the governing SLS for the steel RC beam was the stress on concrete limitation (65.2% of P_u), followed by the deflection limitation (67.6% of P_u), whilst the crack width was found to be the less restrictive condition (79.5% of P_u).

For the correct interpretation of these comparisons, it shall be taken into account that the deflection limitation usually refers to the long-term deflection rather than the instantaneous one. In this study, since experimental values for the long-term deflection were not available, the instantaneous deflection has been considered instead and consequently, the maximum load causing long-term deflections to reach these limiting values would be lower than that presented in this study.

Chapter 5
Data analysis and comparisons
with prediction models

5.1. Introduction

In this chapter, the experimental data is analysed and compared to analytical tools. First, the crack spacing and the crack width are compared to some of the most significant prediction models, both for steel and FRP RC. The data is compared at different load rates within the serviceability range. For the crack spacing, the influence of the concrete cover, the bar spacing and the effective reinforcement ratio is evaluated. Furthermore, bond coefficients are adjusted to the experimental data. A measure of the characteristic crack spacing is also provided. The crack width is examined in terms of the maximum and average width at the central zone of the beam and adjusted bond coefficients to the experimental results are provided. The experimental instantaneous deflection is compared to prediction models and a discussion about the results is presented. This section provides a statistical analysis for each parameter examined.

Second, the cracked section analysis is presented. A suitable stress-strain curve for the concrete is selected for this purpose. The results in terms of strains, curvatures and deflections are compared with the experimental data and discussed. A measure of the ultimate load is also provided.

Finally, an analysis on the short-term deflection up to failure is given. The possible reasons for the differences obtained when computing deflections are analysed and the shear crack induced deflection is experimentally evaluated.

5.2. Prediction models for crack spacing and crack width

5.2.1. Crack spacing

Crack spacing is a parameter directly related to the crack width, being of major importance to correctly evaluate the crack spacing value to predict with reasonable precision adequate values of crack widths. In the present study, the experimental data from the tests reported in Chapter 4 is used to evaluate the parameters that take part on the usual formulation of crack spacing. Bond coefficients are adjusted to the experimental data. For this purpose, the Eurocode 2 formulation (both the 1992 and 2004 editions), Model Code 90 and EHE prediction models are considered.

Influence of the different parameters on the experimental crack spacing

In general, the available formulation to calculate crack spacing generally states that crack spacing is dependent on the concrete cover c, the bar spacing s, the bond properties of the reinforcement, the distribution of strains, and the ϕ/ρ_{eff} relationship (CEN 1992, Borosnyói 2002, CEN 2004, Borosnyói 2005, CPH 2008), being ϕ the bar diameter and ρ_{eff} the effective reinforcement ratio taking account of the effective area of concrete in tension surrounding the reinforcement $A_{c,eff}$.

In Figure 5-1, the effects of c, s, and ϕ/ρ_{eff} are represented and studied. In those cases where a minimum relationship between the examined parameter and the average crack spacing is observed, the least squares method is used to determine the best-fit linear regression and its equation is represented in the figure.
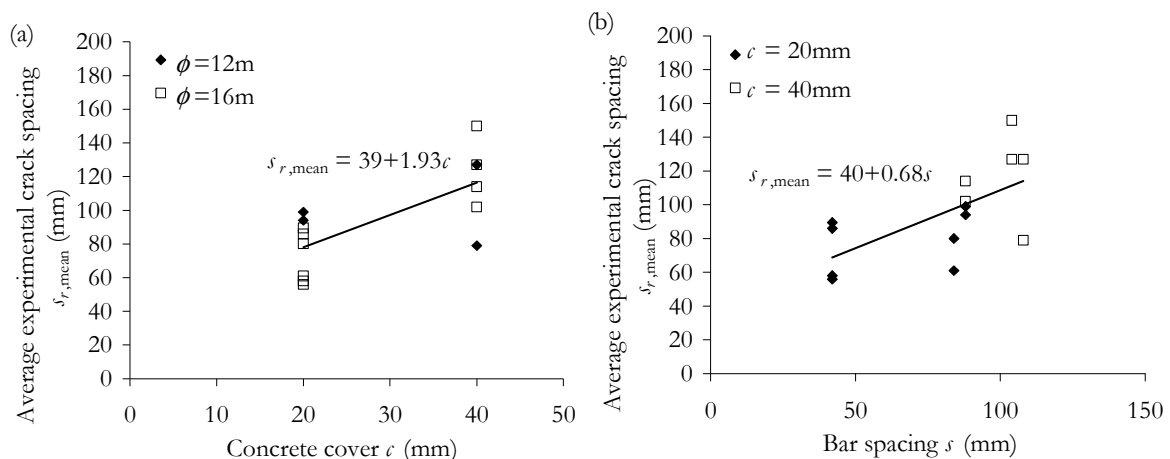
Figure 5-1. Average experimental crack spacing versus (a) d/h ratio (b) bar spacing.
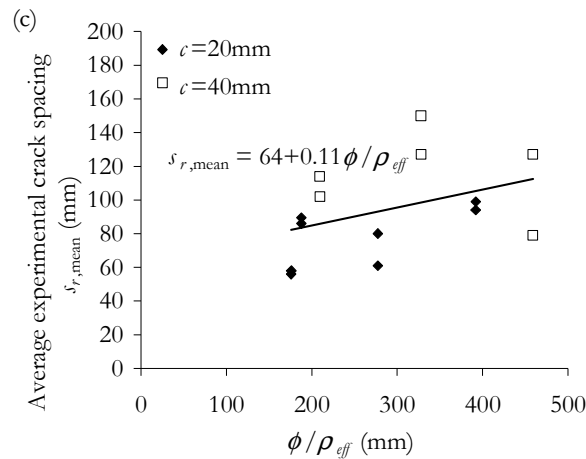
Figure 5-1. Average experimental crack spacing versus (c) ϕ/ρ_{eff} ratio (continuation).

Results in Figure 5-1a show that the crack spacing increases with the concrete cover at a ratio of approximately $1.93c$. This factor results very close to $2c$, suggested in Eurocode 2 (CEN 2004). Furthermore, it is observed in Figure 5-1b and Figure 5-1c that, even though crack spacing is a highly randomized parameter, it increases with the bar spacing and with the ϕ/ρ_{eff} ratio.

Code provisions for the experimental data

The experimental, maximum and average, experimental crack spacings are next compared to the theoretical models presented in Eurocode 2 (for both last editions 1992 and 2004), Model Code 90 and the EHE. The formulation presented in these approaches is summarized in Table 5-1. The experimental crack spacing corresponds to that at the load level at which cracking was considered to be stabilised. In the case of Eurocode 2 approaches, a high quality bond coefficient (k_1) between the rebar and the concrete has been considered.

Table 5-1. Formulation for crack spacing considered in the study

Parameter	Approach	Expression
Average crack spacing	Eurocode 2 (CEN 1992)	$s_{rm} = 50 + 0.25 k_1 k_2 \phi / \rho_{eff}$
	EHE (CPH 2008)	$s_{rm} = 2c + 0.2s + 0.4 k_1 \phi / \rho_{eff}$
Maximum crack spacing	Model Code 90 (CEB-FIP 1990)	$l_{s,max} = \dfrac{\phi}{3.6 \rho_{eff}}$
	Eurocode 2 (CEN 2004)	$s_{r,max} = 3.4c + 0.425 k_1 k_2 \phi / \rho_{eff}$

Notation:

ϕ: rebar diameter; ρ_{eff}: effective reinforcement ratio; c: cover; k_1: 0.8 for high bond bars or 1.6 for smooth bars; k_2: 0.5 for bending or 1 for pure tension.

Figure 5-2a compares the experimental versus theoretical maximum crack spacing and Figure 5-2b compares the average values. Eurocode 2 (CEN 2004) tends to overestimate $s_{r,\max}$. EHE formulation, which takes into account the bar spacing, provides the best fitted values to $s_{r,\mathrm{mean}}$, whilst Eurocode 2 (CEN 1992) slightly overestimates the experimental response.
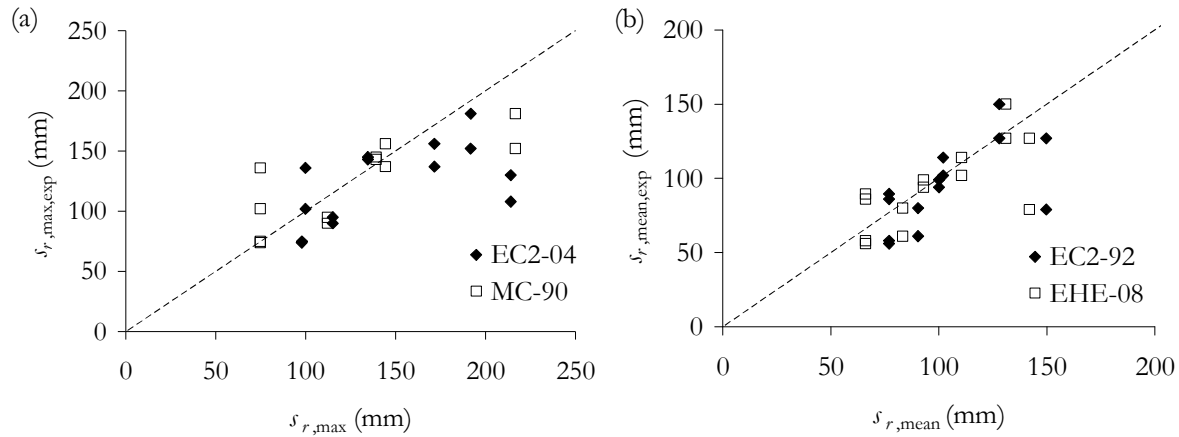
Figure 5-2. Experimental vs. theoretical (a) maximum and (b) average crack spacing.

One of the differences between the standards evaluated lies in the equation to calculate the effective height of the area of concrete surrounding the tensile reinforcement $h_{c,eff}$. This is function of the diameter of the bar ϕ and the concrete cover c, but also depends on the neutral axis depth x and it is related to the total height h (Table 5-2).

Table 5-2. Effective height of the area of concrete surrounding the tensile reinforcement $h_{c,eff}$ for a beam specimen following the different codes.

Approach	Expression
Eurocode 2 (CEN 1992)	$h_{c,eff} = 2.5(h-d)$
EHE (CPH 2008)	$h_{c,eff} = \min\{(c+\phi/2+7.5\phi), h/2\}$
Model Code 90 (CEB-FIP 1990)	$h_{c,eff} = \min\{2.5(h-d),(h-x)/3\}$
Eurocode 2 (CEN 2004)	$h_{c,eff} = \min\{2.5(h-d),(h-x)/3, h/2\}$

Notation:
h: height; d: effective depth; ϕ: bar diameter; c: cover; x: neutral axis depth.

For the studied experimental configurations, Eurocode 2 (CEN 2004) and Model Code 90 approaches, which take into account the position of the neutral axis depth x, give the minimum values of $h_{c,eff}$ ($0.25h$ - $0.29h$). In turn, EHE provides $h_{c,eff} = 0.50h$ and Eurocode 2 (1992) gives $h_{c,eff} = 0.36h$ - $0.64h$. The ratio between the maximum and minimum values of $h_{c,eff}$ according to the different approaches ranges between 1.7 and 2.5. Since the position of the neutral axis depth for FRP RC elements diminishes considerably with respect to that for steel RC elements, it seems relevant to reassess the influence of x on $h_{c,eff}$. Hence, more research would be needed, although an accurate study of $h_{c,eff}$ is beyond the scope of this work.

On the other hand, Eurocode 2 formulation provides a bond coefficient, k_1. In this work, the method of least squares is subsequently applied to recalibrate its value, taking into account the experimental data. This methodology is applied to the Eurocode 2 formulation, for both versions 1992 (for the mean value) and 2004 (for the maximum value). For comparison purposes, the bond coefficient is additionally adjusted using Eurocode 2 (CEN 2004) formulation compared to the mean crack spacing. In that case, the equation presented in Table 5-1 for the maximum crack spacing is divided by 1.7 to obtain the mean crack spacing, resulting:

$$s_{rm} = 2c + 0.25k_1k_2\phi / \rho_{eff} \tag{5-1}$$

The main difference between this equation and the one of Eurocode 2 (CEN 1992) is that in Eq. (5-1), the actual concrete cover is taken into account, whereas in Eurocode 2 (CEN 1992), a nominal value of 25 mm is assumed for the concrete cover.

According to the least squares methodology, the sum of the squared residuals (Res_i), defined as the difference between the experimental and the theoretical crack spacing, is derived and equalled to zero to obtain the optimum value of k_1, as shown:

$$\frac{d\left(\sum_i \left(Res_i\right)^2\right)}{d\left(k_1\right)} = 0 \tag{5-2}$$

Developing Eq. (5-2), an expression to calculate the adjusted value of k_1 is found and its value is shown in Table 5-3 for the different approaches.

Table 5-3. Bond coefficient for the maximum and average experimental crack spacing

Approach	Expression	Adjusted bond coefficient
Eurocode 2 (CEN 1992)	$s_{rm} = 50 + 0.25k_1k_2\phi / \rho_{eff}$	$k_1 = 0.64$
Eurocode 2 (CEN 2004)	$s_{r,max} = 3.4c + 0.425k_1k_2\phi / \rho_{eff}$	$k_1 = 0.37$
Eurocode 2 (CEN 2004)	$s_{rm} = 2c + 0.25k_1k_2\phi / \rho_{eff}$	$k_1 = 0.95$

Taking into consideration that the reference value of k_1 is 0.80 for high bond bars (CEN 1992, CEN 2004), the resultant values of k_1 indicate that bond between the rebar and concrete used in the experimental program was at least similar to that of steel bars.

In Table 5-3, the original values of $h_{c,eff}$ have been used for the calculation of ρ_{eff} for each approach. If in Eurocode 2 (CEN 1992) formulation, instead of using $h_{c,eff} = 2.5(h-d)$, the corresponding value of ρ_{eff} from Eurocode 2 (CEN 2004) is used (Table 5-2), k_1 equals to 1.19 instead of 0.64, which shows the importance of ρ_{eff} in the formulation for the crack spacing.

The difference observed between $k_1(s_{\text{mean,EC2-04}}) = 0.95$ and $k_1(s_{\text{max,EC2-04}}) = 0.37$ reasserts the idea that experimental values of s_{max} are lower than 1.7 times s_{mean}, as it was previously observed in § 4.6. (Figure 4-16).

The comparison between $k_1(s_{\text{mean,EC2-04}}) = 0.95$ and $k_1(s_{\text{mean,EC2-92}}) = 1.19$ (calculated with ρ_{eff} from EC2-04) shows the importance of considering the concrete cover in the formulation..

For each approach examined, a variable δ, its mean value and standard deviation are defined as:

$$\delta_i = \frac{\text{code}_i}{\text{exp}_i} \tag{5-3}$$

$$\overline{\delta} = \frac{1}{m}\sum_{i=1}^{m}\delta_i \tag{5-4}$$

$$\sigma_\delta = \sqrt{\frac{1}{m-1}\sum_{i=1}^{m}\left(\delta_i - \overline{\delta}\right)^2} \tag{5-5}$$

These statistical parameters are calculated taking into account the bond coefficient of 0.80 for Eurocode 2 approaches and the adjusted bond coefficients are reported in Table 5-4 and Table 5-5.

Table 5-4. Statistical study for code provisions of maximum crack spacing.

	s_{max}(EC2-04)		s_{max}(MC-90)
	$k_1 = 0.80$	$k_1 = 0.37$	
$\overline{\delta}$	1.21	0.99	1.21
σ_δ	0.31	0.25	0.55

Table 5-5. Statistical study for code provisions of average crack spacing.

	s_{mean}(EC2-92)		s_{mean}(EC2-04)		s_{mean}(EHE-08)
	$k_1 = 0.80$	$k_1 = 0.64$	$k_1 = 0.80$	$k_1 = 0.95$	
$\overline{\delta}$	1.14	1.01	0.93	0.99	1.05
σ_δ	0.29	0.26	0.23	0.25	0.25

The maximum crack spacing is about 21% overestimated by both Eurocode 2 (CEN 2004) and Model Code 90. In general, when using the adjusted bond coefficients, the statistical values show better fitted results than when the bond coefficient is taken as 0.80, as it was expected. It is noteworthy the good fit between the experimental results and the EHE predictions for the case of the average crack spacing.

Finally, it is worth pointing out that these conclusions are exclusively drawn from the experimental data of this study. Similar experimental results on concrete beams reinforced

with different types of FRP bars would allow expanding the database and would enable to determine the values of the bond coefficient associated to specific FRP products.

Characteristic crack spacing

Codes of practice define a safety factor to multiply the mean crack width so as to obtain the characteristic crack width, which is defined as the 95% percentile of crack widths that could be expected in a flexural member (CEB-FIB 1990, CEN 1992). This coefficient is derived from assuming a log-normal distribution of crack widths measured on a member subjected to constant strain (CEB 1983). In the case of Model Code 90 and Eurocode 2, this coefficient varies from 1.3 for restrained cracking elements to 1.7 for load induced cracking and restrained cracking in sections with a minimum dimension in excess of 800 mm.

In this section, the theoretical mean crack spacing calculated with Eurocode 2 (CEN 2004) formulation ($s_{mean,EC2-04}$) considering the adjusted bond coefficient is assumed to have a log-normal distribution. In order to check the reliability of this assumption, in Figure 5-3 the experimental curve of cumulative frequency compared to the theoretical log-normal distribution with the same mean and standard deviation as the experimental database is shown.
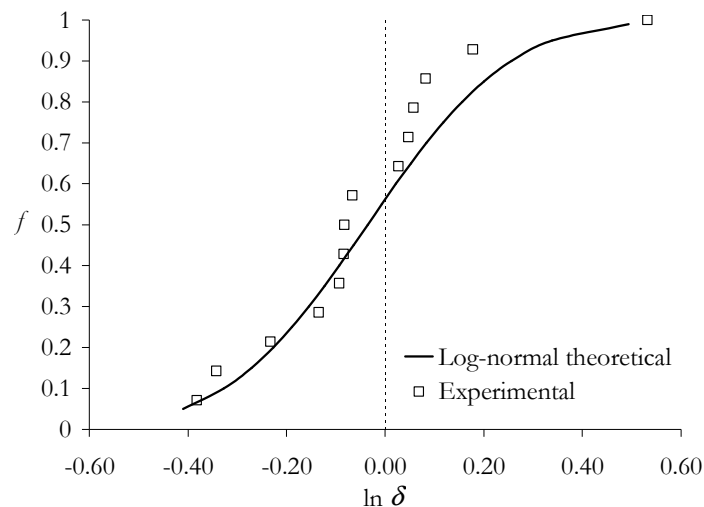
Figure 5-3. Experimental vs. theoretical curve of cumulative frequency of variable ln δ.

Given the difficulty in defining the reliability of this assumption based only on the qualitative comparison between the experimental and the theoretical curves, some statistical tests reported in Mood et al. (1974) or Shapiro and Wilk (1965) rejected the hypothesis of a Gaussian distribution of variable δ, but referring to the variable ln δ, none of the tests rejected the hypothesis of Gaussian distribution (Ceroni and Pecce 2009).

On the assumption that variable δ has a log-normal distribution, the theoretical 95% percentile of this distribution is estimated as $\delta_{95\%} = 1.40$. Assuming that the related value of probability is the same, the corresponding characteristic value of variable δ is $\delta_k = \delta_{95\%} = 1.40$.

Finally, the characteristic value of the crack spacing can be defined applying the same reduction factor existing between the characteristic ($\delta_k = 1.40$) and the mean ($\bar{\delta} = 0.97$) values of variable δ:

$$s_{rm,k} = s_{rm} \cdot \frac{\delta_k}{\bar{\delta}} = s_{rm} \cdot \frac{1.40}{0.97} = 1.45 s_{rm} \qquad (5\text{-}6)$$

Values for the maximum crack spacing $s_{r,\max}$ for steel RC are proposed in the literature, varying from 1.3 to 1.5 times the mean value (Borosnyói 2002). The value of 1.45 found in Eq. (5-6) for the characteristic crack spacing fits with the theoretically predicted range of value for steel RC, and fairly coincides with the experimental relation between the maximum and average crack widths represented in § 4.6. ($s_{\max}/s_{\mean}$ = 1.32). What is more, this value results lower than 1.7, which is the value assumed in Eurocode 2 (CEN 2004) to calculate the maximum crack spacing from the mean values.

5.2.2. Crack width

Prediction models for crack width

In this section, the experimental crack widths, both maximum and average, are compared to Eurocode 2 (CEN 1992, CEN 2004), ACI 440.1R-06, Model Code 90, ISIS Canada (2001), JSCE (1997) and EHE (CPH 2008) approaches. In Table 5-6 the formulation for the considered code provisions is summarized. The evolution of the crack width, both theoretical and experimental, is shown up to a load level of 35% the ultimate load, which can be considered a rough estimate of the range of the service load.

According to Eurocode 2, Model Code 90 and EHE, crack width is derived from the difference of strains in the reinforcement and in concrete (associated to the tension stiffening effect), and from crack spacing. In the case of Eurocode 2, crack spacing is influenced by bond behaviour between concrete and rebar, and a coefficient has been adjusted in the previous section. Model Code 90 and EHE do not provide any bond coefficient, assuming by default high bond behaviour between the steel rebar and the concrete.

In this study, Eurocode 2, Model Code 90 and EHE approaches are compared to the experimental average crack width in Figure 5-4. For Eurocode 2 (CEN 1992) and EHE equations, the β coefficient has been considered equal to 1. In all the analytical approaches, the experimental average crack spacing is used instead of the theoretically predicted, so as not to influence its variability in the results of crack width. EHE approach is not depicted in Figure 5-4 because for the same crack spacing, it would have given the same trend than Eurocode 2 (CEN 1992) approach with $\beta_1 = 1.0$.

Table 5-6. Formulation for crack width considered in the study.

Approach	Expression
Eurocode 2 (1992)	$$w_k = \beta s_{rm} \varepsilon_{sm}$$ $$\varepsilon_{sm} = \frac{\sigma_s}{E_s}\left(1 - \beta_1 \beta_2 \left(\frac{M_{cr}}{M_a}\right)^2\right)$$
EHE (2008)	$$w_k = \beta s_{rm} \varepsilon_{sm}$$ $$\varepsilon_{sm} = \frac{\sigma_s}{E_s}\left(1 - k_2 \left(\frac{M_{cr}}{M_a}\right)^2\right) \geq 0.4\frac{\sigma_s}{E_s}$$
Eurocode 2 (2004)	$$w_k = s_{rm}\left(\varepsilon_{sm} - \varepsilon_{cm}\right)$$ $$\varepsilon_{sm} - \varepsilon_{cm} = \frac{\sigma_s}{E_s} - \frac{k_t f_{ctm}\left(1 + \alpha_e \rho_{p,eff}\right)}{E_s \rho_{p,eff}} \geq 0.6\frac{\sigma_s}{E_s}$$
Model Code 90	$$w_k = l_{s,\max}\left(\varepsilon_{sm} - \varepsilon_{cm} - \varepsilon_{cs}\right)$$ $$\varepsilon_{sm} - \varepsilon_{cm} = \varepsilon_{s2} - \beta\frac{f_{ctm}(t)}{\rho_{s,eff}E_s}\left(1 + \alpha_e \rho_{s,eff}\right)$$
ACI 440.1R-06	$$w = 2\frac{\sigma_f}{E_f}\beta k_b \sqrt[3]{d_c^2 + \left(\frac{s}{2}\right)^2}$$
ISIS Canada (2001)	$$w = 11\frac{E_s}{E_f}\sigma_f k_b \beta\sqrt[3]{d_c A}\cdot 10^{-6}$$
JSCE (1997)	$$w = k\left(4c + 0.5(s - \phi)\right)\frac{\sigma_f}{E_f}$$

Notation:

β (EC2, EHE): Coefficient that relates the average crack width to the design; β_1: 1.0 for high-bond or 0.5 for plain rebars; β_2, k_2: 1.0 for short-term loading or 0.5 for sustained; M_{cr}: cracking moment; M_a: applied moment; σ_f, σ_s: stress at the reinforcement (subscript s for steel, f for FRP); E_f, E_s: modulus of elasticity of the reinforcement; k_t: 0.6 for short-term loading or 0.4 for sustained; f_{ctm}: mean value of the tensile strength; α_e: E_f/E_c; β (ACI, ISIS Canada): $(x\text{-}h)/(x\text{-}d)$; k_b (ACI, ISIS Canada), k(JSCE): 1.0 for bars with bond similar to that of steel ; s: bar spacing; d_c: concrete cover measured from the centroid of tension reinforcement; A: effective tension area of concrete surrounding the flexural tension reinforcement and having the same centroid as that reinforcement, divided by the number of rebars; c: concrete cover; ϕ: bar diameter.
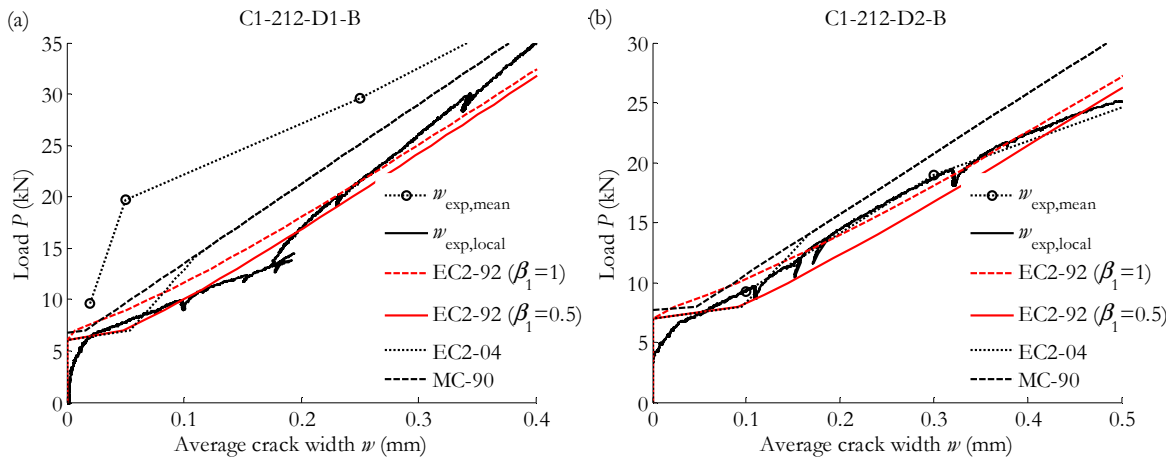
Figure 5-4. Typical cases of average crack width, theoretical vs. experimental.

The results in Figure 5-4 show that the midspan crack ($w_{exp,local}$ in the figure) generally follows the theoretical predictions, both considering low or high bond behaviour ($\beta_1 = 0.5$ or 1 respectively). Higher variability was found in the experimental mean crack width ($w_{exp,mean}$ in the figure) making difficult to arrive to a more solid conclusion in that case.

On the other hand, ACI 440.1R-06, ISIS Canada and JSCE give the same equation for the calculation of the maximum probable crack width for steel and FRP, with different bond quality coefficients (k_b for ACI 440.1R-06 and ISIS Canada and k for JSCE). In the present study, the maximum experimental crack width is compared to these approaches in Figure 5-5. As discussed in the previous section, high bond seems to exist between the concrete and the rebar, thus the bond coefficients considered in the analytical approaches are those corresponding to a this bond condition: k_b(ACI440.1R-06) = 1.0, k_b(ISIS Canada) = 1.0 and k(JSCE) = 1.0.
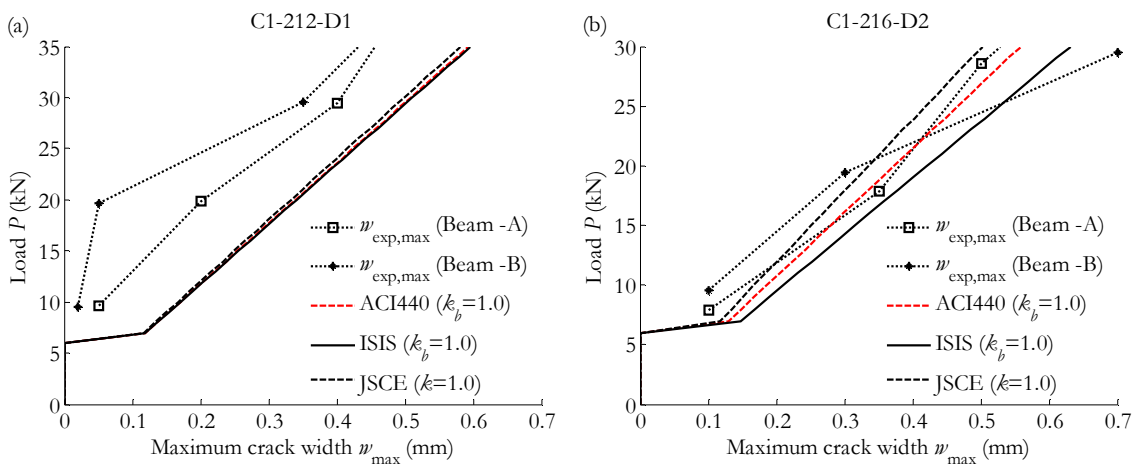
Figure 5-5. Typical cases of maximum crack width, theoretical vs. experimental.

Results depicted in Figure 5-5 show that the maximum crack width predicted with a bond coefficient of 1 gives an adequate upperbound value of the maximum experimental crack width.

Analysis of the experimental versus theoretical models

The ratio theoretical vs. experimental maximum crack width is calculated at three different load levels that may cover the service loading conditions: at a moment ratio (M_a/M_{cr}) of 1.5, 3 and 4.5. The outcome is depicted in Figure 5-6, and the mean value and the standard deviation of w_{th}/w_{exp} for the three moment ratios is shown in Table 5-7.
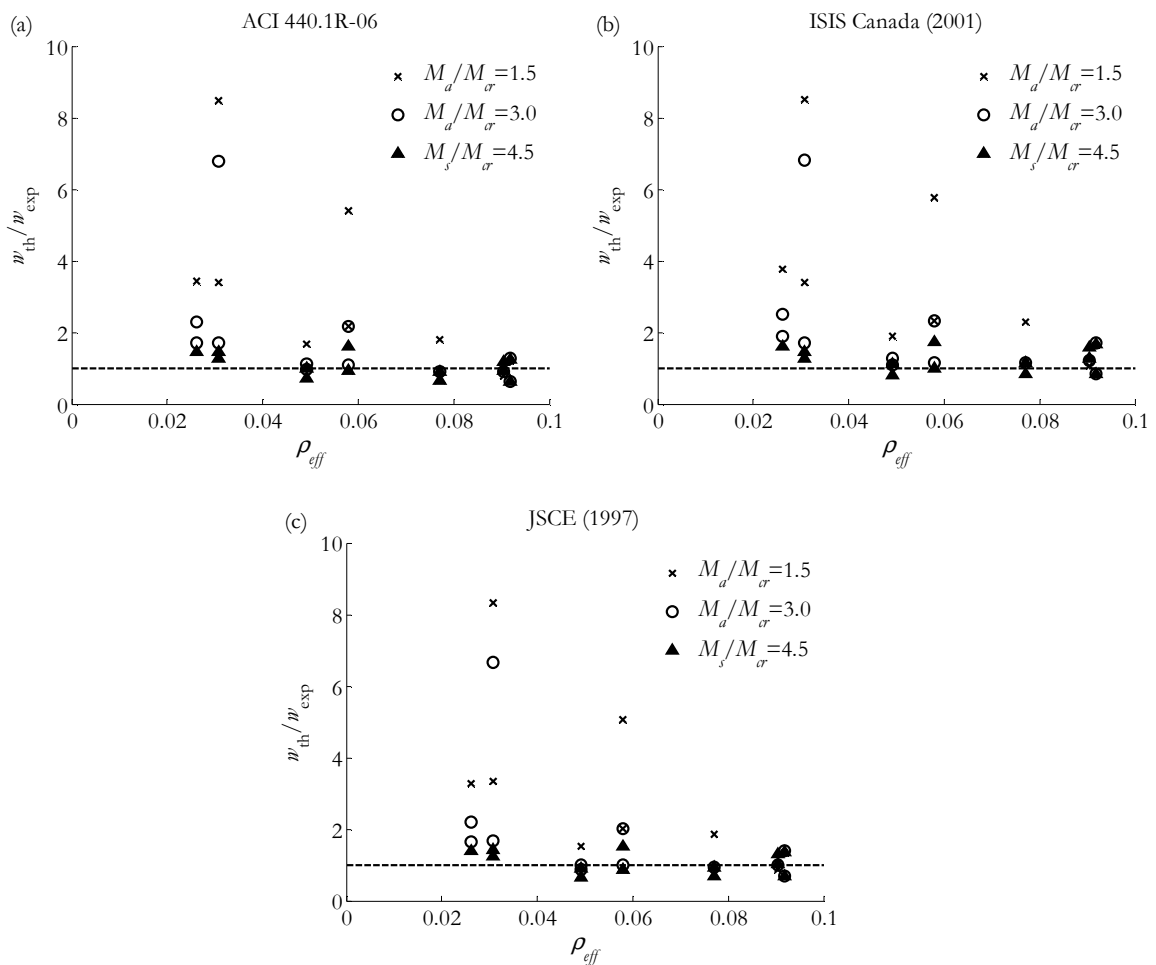
Figure 5-6. Maximum crack width ratio w_{th}/w_{exp} depending on ρ_{eff} for different approaches.

Figure 5-6 shows that there is generally a better agreement between the experimental and theoretical approaches as the effective reinforcement ratio increases. Furthermore, in Table 5-7 it is shown that the higher the moment ratio, the lower the scatter of results. All the analytical approaches tend to overestimate the crack width at M_a/M_{cr} = 1.5, whilst at M_a/M_{cr} = 4.5 they fit relatively well the experimental data (w_{th}/w_{exp} tends to 1 at M_a/M_{cr} = 4.5).

Table 5-7. Statistical parameters for the maximum crack width provisions.

Approach	$M_a/M_{cr} = 1.5$		$M_a/M_{cr} = 3.0$		$M_a/M_{cr} = 4.5$	
	$\overline{\delta}$	σ_δ	$\overline{\delta}$	σ_δ	$\overline{\delta}$	σ_δ
ACI 440.1R-06	2.60	2.15	1.67	1.56	1.11	0.33
ISIS Canada (2001)	2.87	2.11	1.86	1.51	1.29	0.33
JSCE (1997)	2.54	2.06	1.64	1.51	1.10	0.31

The bond coefficient provided by ACI 440.1R-06, ISIS Canada and JSCE is adjusted to the experimental data and shown in Table 5-8. This coefficient has been adjusted following the least squares methodology for the available data between 0.1 mm and 0.7 mm of maximum experimental crack width, taking into account the accuracy of the instrumentation used for measuring crack widths.

Table 5-8. Bond coefficient to the maximum experimental crack width.

Approach	Adjusted bond coefficient
ACI 440.1R-06	$k_b = 0.84\text{-}1.10$
ISIS Canada (2001)	$k_b = 0.68\text{-}0.89$
JSCE (1997)	$k = 0.82\text{-}1.07$

Results in Table 5-8 show bond coefficients that tend to 1 (recommended value for steel RC), proving that the adherence between the concrete and the GFRP rebar used in the experimental program was similar to that of steel RC.

5.3. Prediction models for deflections

Most of the prediction models to calculate the flexural deflection of a FRP RC element can be classified in those derived from Branson equation (Benmokrane et al. 1996, Toutanji and Saafi 2000, Yost et al. 2003), and those where deflection is calculated as an interpolation between a cracked and an uncracked state of a deformation parameter (curvature or deflection) (Faza and GangaRao 1992, CEN 2004, Bischoff 2005). Some of the existing design guidelines for FRP RC have adopted these approaches in their methodology to calculate deflections (ISIS Canada 2001, ACI Committee 440 2006).

In this section, the experimental load-midspan deflection is compared to ACI 440.1R-03, ACI 440.1R-06, Benmokrane et al. (1996), Yost et al. (2003), Toutanji and Saafi (2000), Eurocode 2 (CEN 1992, CEN 2004), Bischoff (2005), ISIS Canada (2001), CAN/CSA-S806 (2002) and Faza and GangaRao (1992) equations. The formulation for the considered analytical approaches is summarized in Table 5-9. The evolution of the deflection, both theoretical and experimental, is shown up to a load level of 35% the ultimate load. The experimental cracking

load has been considered independently of the approach used for the deflection calculation. Hence, the possible influence of the environmental factors has been inherently incorporated.

Table 5-9. Formulation for deflections considered in the study.

Approach	Expression
ACI 440.1R-03	$I_e = \left(\dfrac{M_{cr}}{M_a}\right)^3 \beta_d I_g + \left(1 - \left(\dfrac{M_{cr}}{M_a}\right)^3\right) I_{cr} \leq I_g$; $\beta_d = \alpha_b \left(\dfrac{E_f}{E_s} + 1\right)$; $\alpha_b = 0.5$
ACI 440.1R-06	$I_e = \left(\dfrac{M_{cr}}{M_a}\right)^3 \beta_d I_g + \left(1 - \left(\dfrac{M_{cr}}{M_a}\right)^3\right) I_{cr} \leq I_g$; $\beta_d = \dfrac{1}{5}\left(\dfrac{\rho}{\rho_{fb}}\right)$
Benmokrane et al. (1996)	$I_e = \alpha I_{cr} + \left(\dfrac{I_g}{\beta} - \alpha I_{cr}\right)\left(\dfrac{M_{cr}}{M_a}\right)^3$; $\alpha = 0.84$; $\beta = 7$
Yost et al. (2003)	$I_e = \left(\dfrac{M_{cr}}{M_a}\right)^3 \beta_d I_g + \left(1 - \left(\dfrac{M_{cr}}{M_a}\right)^3\right) I_{cr} \leq I_g$; $\beta_d = \alpha_b \left(\dfrac{E_f}{E_s} + 1\right)$; $\alpha_b = 0.064\left(\dfrac{\rho}{\rho_{fb}}\right) + 0.13$
Toutanji and Saafi (2000)	$I_e = \left(\dfrac{M_{cr}}{M_a}\right)^m I_g + \left(1 - \left(\dfrac{M_{cr}}{M_a}\right)^m\right) I_{cr} \leq I_g$; $m = 6 - 10\left(E_f / E_s\right)\rho$ if $\left(E_f / E_s\right)\rho < 0.3$ $m = 3$ if $\left(E_f / E_s\right)\rho \geq 0.3$
Eurocode 2 (CEN 1992)	$\delta = \zeta\delta_{II} + (1-\zeta)\delta_I$; $\zeta = 1 - \beta_1\beta_2\left(\dfrac{\sigma_{sr}}{\sigma_s}\right)^2$
Eurocode 2 (CEN 2004)	$\delta = \zeta\delta_{II} + (1-\zeta)\delta_I$; $\zeta = 1 - \beta\left(\dfrac{\sigma_{sr}}{\sigma_s}\right)^2$

Table 5-9. Formulation for deflections considered in the study (continuation).

Approach	Expression
Bischoff (2005)	$I_e = \dfrac{I_{cr}}{1 - \eta \left(\dfrac{M_{cr}}{M_{max}} \right)^2} \leq I_g \, ; \, \eta = 1 - \dfrac{I_{cr}}{I_g}$
ISIS Canada (2001)	$I_e = \dfrac{I_g I_{cr}}{I_{cr} + \left(1 - 0.5 \left(\dfrac{M_{cr}}{M_a} \right)^2 \right) \left(I_g - I_{cr} \right)}$
CAN/CSA-S806 (2002)	$\delta_{max} = \dfrac{PL^3}{24 E_c I_{cr}} \left[3 \left(\dfrac{a}{L} \right) - 4 \left(\dfrac{a}{L} \right)^3 - 8 \left(1 - \dfrac{I_{cr}}{I_g} \right) \left(\dfrac{L_g}{L} \right)^3 \right]$
Faza and GangaRao (1992)	$\delta_{max} = \dfrac{23 P L^3}{648 E_c I_m} \, ; \, I_m = \dfrac{23 I_{cr} I_e}{8 I_{cr} + 15 I_e}$

Notation:

I_e: effective moment of inertia; I_{cr}: cracked moment of inertia; I_g: gross moment of inertia; M_{cr}: cracking moment; M_a: applied moment; M_{max}: maximum applied moment; E_f, E_s: modulus of elasticity of the reinforcement (subscript s for steel, f for FRP); ρ: reinforcement ratio; ρ_{fb}: balanced reinforcement ratio; δ: deflection; δ_I: uncracked-state deflection; δ_{II}: cracked-state deflection; β_1: 1.0 for high-bond or 0.5 for plain rebars; β_2, β (EC2): 1.0 for short-term loading or 0.5 for sustained; P: applied load; L: beam length; L_g: distance of the uncracked beam; a: length of the shear span E_c: concrete modulus of elasticity.

5.3.1. Models based on Branson equation

Among those approaches that modify Branson equation to adapt it to the flexural behaviour of FRP RC elements, ACI 440.1R-03 reduces the gross moment of inertia I_g with a factor β_d that is function of the rebar modulus of elasticity and of a bond factor α_b, which is taken as 0.5 pending further research.

Yost et al. (2003) adjusts the bond factor α_b defined in ACI 440.1R-03 to a large number of experimental data: 48 GFRP RC beams with normal and high concrete strengths (from 36 to 80 MPa) and reinforcement ratios from $1.20\rho_{fb}$ to $4.32\rho_{fb}$. The resulting bond factor α_b is dependent on the ρ/ρ_{fb} ratio.

ACI 440.1R-06 relates the factor β_d to the relationship between ρ and the ρ_{fb}. From a theoretical point of view, it does not seem to be adequate that the equivalent stiffness of the element for the calculation of deflections at service depends on a factor such as the balanced reinforcement ratio, which is function of the rebar and concrete strengths.

In Figure 5-7, a typical experimental versus theoretical load-midspan deflection response for beams reinforced with different reinforcement ratios is shown for the prediction models for FRP RC elements derived from Branson equation.
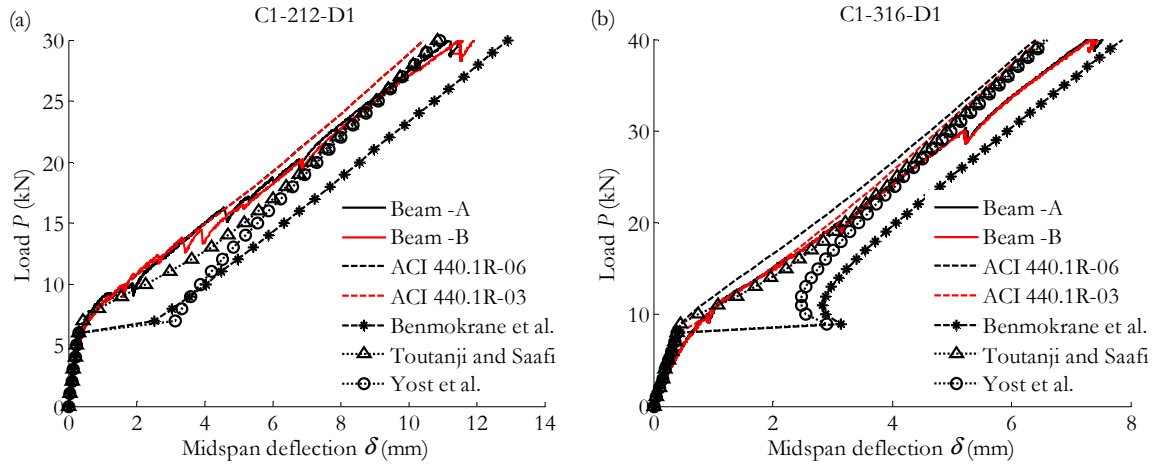
Figure 5-7. Experimental vs. theoretical midspan deflection. Code provisions derived from Branson equation. Comparison for beam with (a) $\rho = 0.99\%$, (b) $\rho = 2.66\%$.

These three analytical approaches reduce I_g once the section has attained the cracking load, and the interpolation between moments of inertia is consequently made between I_{cr} and $\beta_d I_g$. It is therefore expected that in any case between I_{cr} results lower than $\beta_d I_g$. In Table 5-10 the values for the coefficient β_d are compared to the ratio I_{cr}/I_g.

Table 5-10. Coefficient β_d according to different approaches compared to I_{cr}/I_g.

Beam Designation	β_d (ACI 440.1R-03)	β_d (ACI 440.1R-06)	β_d (Yost et al. 2003)	I_{cr}/I_g
C1-212-D1	0.6586	0.6609	0.1083	0.1390
C1-216-D1	0.6616	0.7228	0.1168	0.2211
C1-316-D1	0.6616	1.0000	0.1544	0.3055
C1-212-D2	0.6586	0.6607	0.1083	0.0938
C1-216-D2	0.6616	0.7352	0.1180	0.1500
C1-316-D2	0.6616	1.0000	0.1558	0.2065
C2-212-D1	0.6586	0.4460	0.0865	0.1333
C2-216-D1	0.6616	0.5227	0.0961	0.2165
C2-316-D1	0.6616	0.7997	0.1247	0.3137
C2-212-D2	0.6586	0.5724	0.0993	0.1022
C2-216-D2	0.6616	0.4766	0.0913	0.1419
C2-316-D2	0.6616	0.7339	0.1179	0.1915
C3-316-D1	0.6616	0.8077	0.1255	0.2837

It is observed that, while in ACI 440.1R-03 and ACI 440.1R-06 approaches β_d always results higher than I_{cr}/I_g, in Yost approach, β_d is generally lower than I_{cr}/I_g. Furthermore, as ρ increases, the ratio between I_{cr}/I_g and β_d increases as well. This result may be a consequence of the different values of ρ considered in this study compared to the values of ρ at which β_d was adjusted (ρ = 3.32-7.64ρ_{fb} in this work compared to ρ = 1.20- 4.32ρ_{fb} in Yost et al. 2003). As a consequence, Yost et al. (2003) formulation results especially inadequate for highly reinforced beams, as shown in Figure 5-7b.

Benmokrane et al. (1996) approach, which is also based on a modification of Branson equation, proposes that after the cracking load is attained, I_{cr} shall be reduced to $0.84I_{cr}$ and I_g shall be reduced to $I_g/7$. According to Benmokrane et al. (1996), the reduction of I_{cr} and I_g is attributed to the nature of the FRP reinforcement that exhibited larger deformation than the steel reinforcement, resulting in greater reduction of the compressed concrete section when the applied moment reached the cracking moment. Reducing the value of I_{cr}, however, implies obtaining more deformation than that calculated considering that the element is fully cracked. Therefore, it implicitly adds a percentage of deflection that may be justified because the materials lose their linearity or because other effects than flexural took place in their experiments.

In addition, if I_g/β results lower than αI_{cr}, the resultant response presents a horizontal shift just after the cracking load is attained, the deflection going beyond that corresponding to αI_{cr}, since the effective modulus of elasticity approximates to I_g/β. In Table 5-11 the reduced moments of inertia for the beams tested according to Benmokrane et al. (1996) approach are given.

Table 5-11. Reduced moments of inertia following Benmokrane et al. (1996) approach.

Beam Designation	αI_{cr} ($\times 10^{-6}$ mm^{-4})	I_g/β ($\times 10^{-6}$ mm^{-4})
C1-212-D1	9.34	11.43
C1-216-D1	14.87	11.43
C1-316-D1	20.53	11.43
C1-212-D2	7.21	13.07
C1-216-D2	11.53	13.07
C1-316-D2	15.87	13.07
C2-212-D1	8.96	11.43
C2-216-D1	14.56	11.43
C2-316-D1	21.09	11.43
C2-212-D2	7.85	13.07
C2-216-D2	10.90	13.07
C2-316-D2	15.25	13.07
C3-316-D1	19.07	11.43

It is observed that for the tested configurations, I_g/β is lower than αI_{cr} for high reinforcement ratios. For example, in Figure 5-7, where the deflection of two different tested beams is reproduced, it is observed that for $\rho = 0.99\%$ (Figure 5-7a), $\alpha I_{cr} < I_g/\beta$ and consequently the deflection after cracking is lower than the corresponding to αI_{cr}; however, for $\rho = 2.66\%$ (Figure 5-7b), $\alpha I_{cr} > I_g/\beta$ and the deflection after cracking undergoes values even lower than αI_{cr}, which in any case could be accepted.

Toutanji and Saafi (2000) approach modifies the power factor m of Branson equation depending on the reinforcement ratio, varying from 3 to 6. For the tested beams, m ranges from 5.91 to 5.97. This approach results to fit correctly the experimental deflection response.

5.3.2. Models based on interpolation of curvatures or deflections

In Figure 5-8, the approaches for the calculation of deflections based on interpolation of curvatures or deflections are compared to the experimental results.
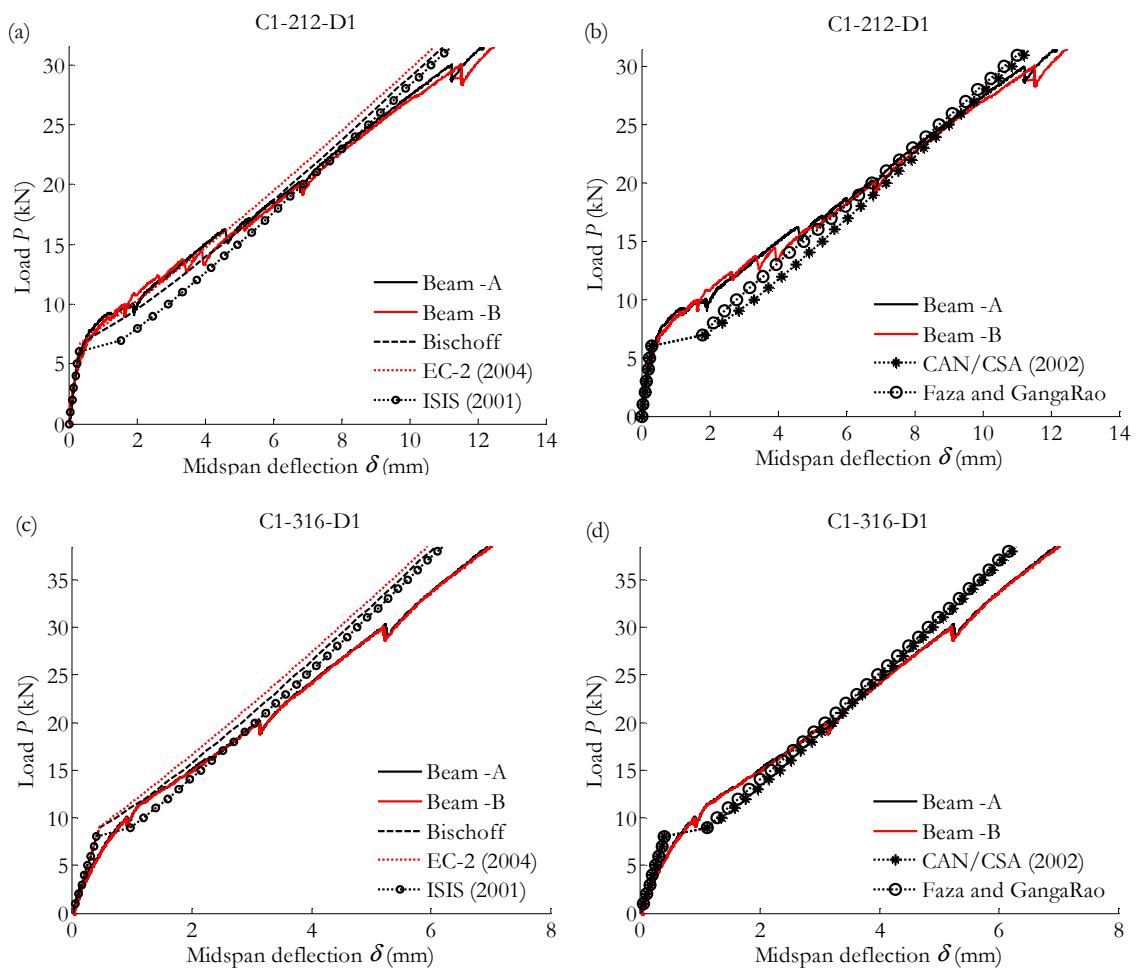
Figure 5-8. Experimental vs. theoretical midspan deflection. Code provisions and authors' approaches derived from integration of curvatures. Comparison for beam with (a) and (b) $\rho = 0.99\%$, (c) and (d) $\rho = 2.66\%$.

Results show that these approaches compare relatively well with the experimental data in the range of the serviceability loads. However, a tendency to underestimate deflections when the load increases is observed, similarly to the behaviour observed in Figure 5-7.

Eurocode 2 (CEN 2004) formulation evaluates deformations by interpolating between a cracked and an uncracked state. The deformations can be curvatures that are numerically integrated to obtain deflections or directly deflections. In this study, deflections are obtained by integration of curvatures along the member. In Figure 5-8, the resultant provisions taking into account a bond coefficient β_2 of 1, corresponding to a high bond factor, are shown. As it is observed, Eurocode 2 generally provides an adequate prediction of the deflection response up to the service load.

Bischoff (2005) uses a tension stiffening approach that allows deriving an effective moment of inertia for the member. The resultant deflection of the member is coincident with the one of Eurocode 2 from interpolation of deflections. Bischoff equation does not make any difference for the different bond behaviour of the reinforcement since it is considered to be adequate. As it is observed, Bischoff approach gives a theoretical curve that fits well with the experimental response.

ISIS Canada (2001) suggests a similar approach to Bischoff (2005) and Eurocode 2. The equation was originally intended for beams subjected to sustained or cyclic loading and includes a factor $\gamma = 0.5$ that shifts horizontally the deflection response just after the cracking load is attained. This factor may work for sustained or cyclic loading, but for instantaneous loads it is observed in Figure 5-8 that does not fit with the experimental data.

CAN/CSA-S806 (2002) formulation neglects the contribution of tension-stiffening in cracked regions on an FRP RC beam. This assumption leads to an overestimation of the experimental instantaneous deflection at the first stages of loading, where the experimental tension-stiffening effect was significant, as shown in § 4.7.

Faza and GangaRao (1992) equation is based on the assumption that in a four-point bending test, the RC sections between the point loads is fully cracked, while the shear span RC sections are partially cracked with a moment of inertia equal to I_e from Branson equation (Figure 2-8). This approach results in an overestimation of the deflection at load levels close to the cracking load, similarly to what is observed in CAN/CSA-S806 approach.

5.3.3. Analysis of the experimental versus theoretical models

In this section, a measure of the relative fitting between the experimental and the theoretical deflections is presented. The ratio theoretical vs. experimental deflection (δ_{th}/δ_{exp}) is depicted depending on the $n\rho$ parameter for the different studied theoretical approaches in Figure 5-9. The outcome is depicted for a moment ratio M_a/M_{cr} of 1.5, 3 and 4.5. This last value is considered a reasonable upper bound limit of the serviceability conditions.

Results show that at the moment ratio of M_a/M_{cr} =1.5 some approaches clearly overestimate the experimental deflection. This behaviour is especially observed for Benmokrane et al. (1996), CAN/CSA-S806 (2002), Faza and GangaRao (1992), ISIS Canada (2001) and Yost et al. (2003) prediction models. As the M_a/M_{cr} ratio approaches to 3 and 4.5, the ratio δ_{th}/δ_{exp} gets closer to the unity for all the studies, showing a better fit to the experimental data at these stages of loading.
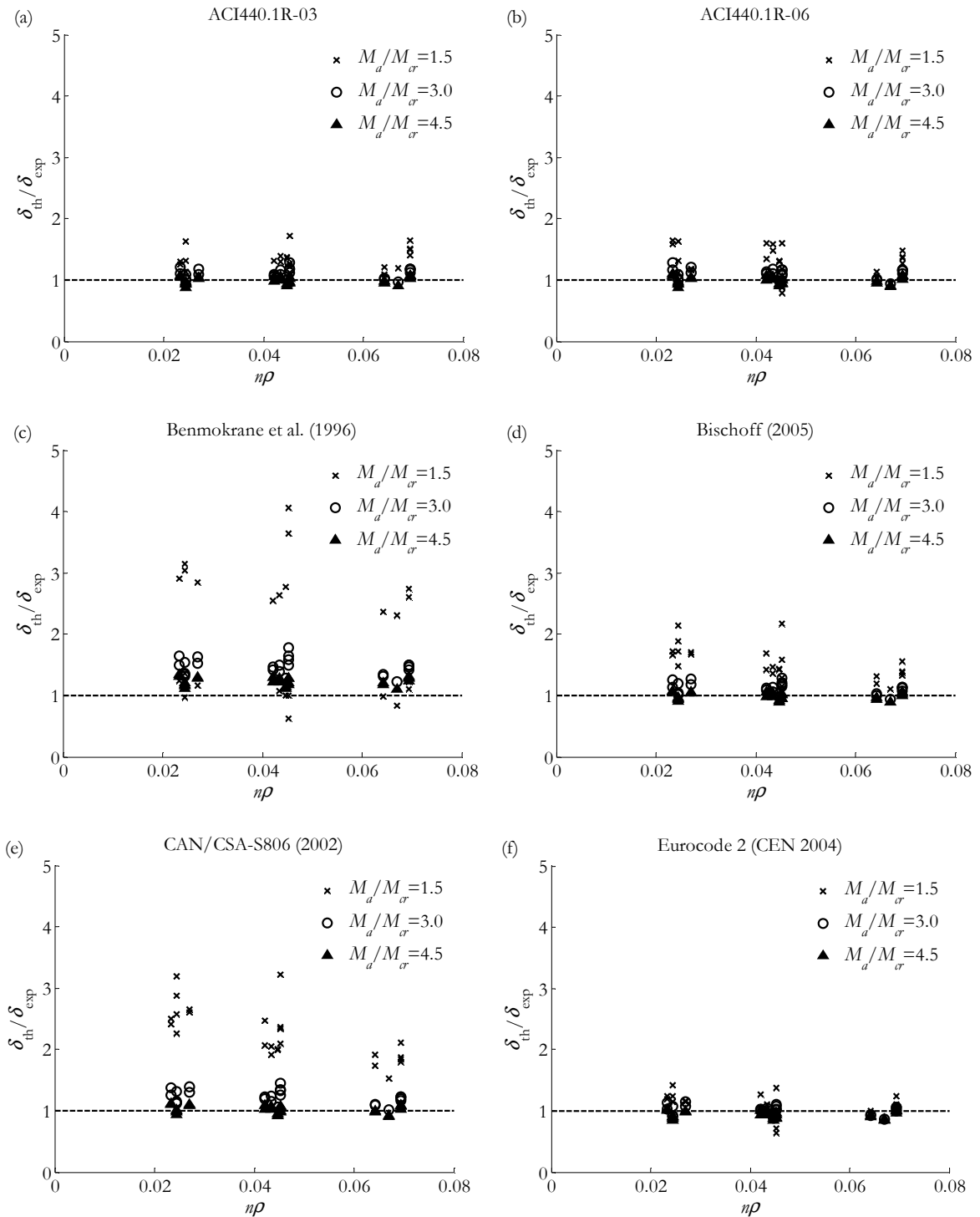
Figure 5-9. Ratio δ_{th}/δ_{exp} depending on $n\rho$ for different approaches.
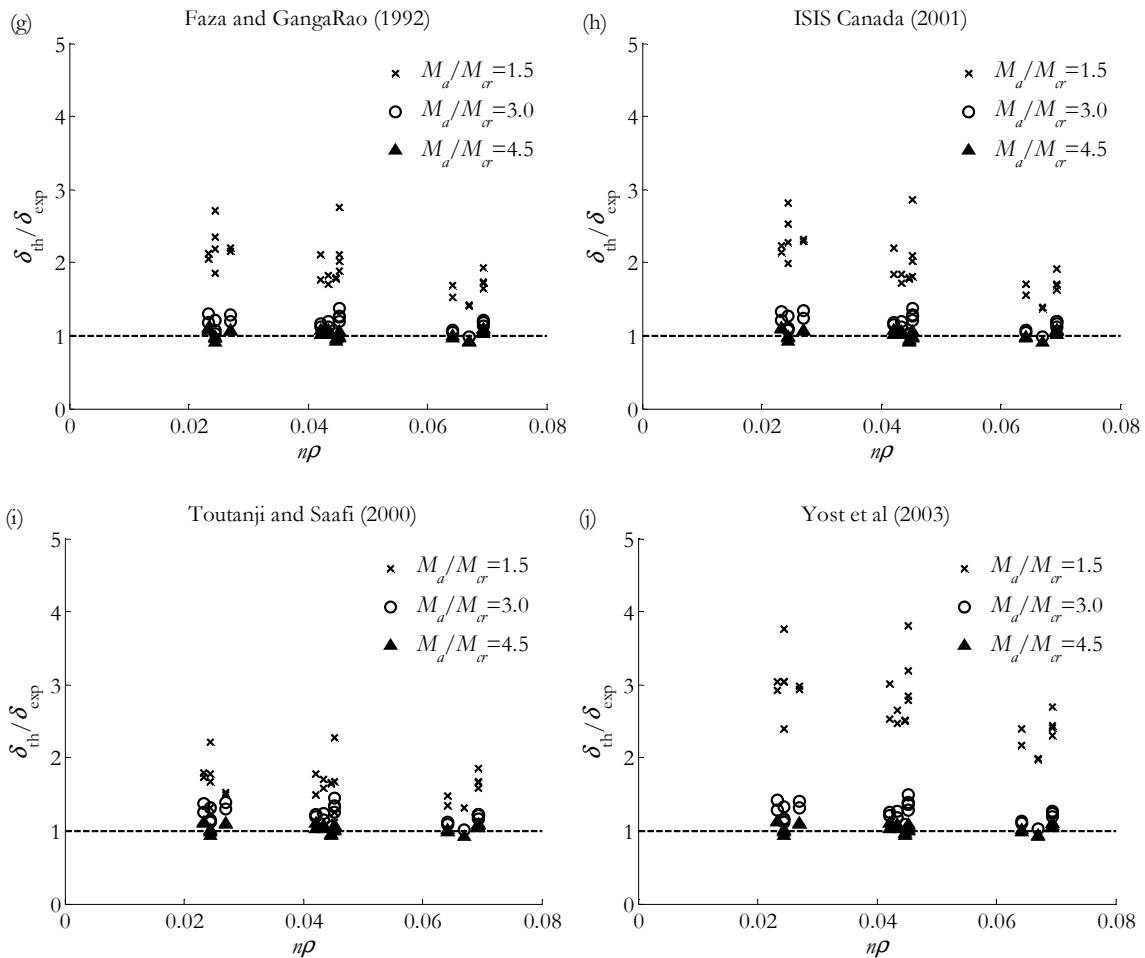
Figure 5-9. Ratio δ_{th}/δ_{exp} depending on $n\rho$ for different approaches (continuation).

In Table 5-12, the mean value and the standard deviation of the ratio δ_{th}/δ_{exp} for the three moment ratios are shown. As observed, the most scattered results, with $\sigma_\delta = 0.17\text{-}1.03$, are obtained for $M_a/M_{cr} = 1.5$.

At $M_a/M_{cr} = 1.5$, Benmokrane et al. (1996), CAN/CSA-S806 (2002), Faza and GangaRao (1992), ISIS Canada (2001) and Yost et al. (2003) prediction models propose a theoretical deflection that is about twice or more the experimentally obtained. On the contrary, Eurocode 2, which is a design code though for steel RC, presents the best estimate to the experimental deflection, together with ACI 440.1R-06 and ACI 440.1R-03. None of the studied approaches underestimates the experimental deflection.

At $M_a/M_{cr} = 3.0$, all of the approaches get closer to the experimental data. Evidence of that statement is that all the mean values and standard deviations of the ratio δ_{th}/δ_{exp} are closer to 1.0 and 0.0 respectively. Benmokrane et al. (1996), however, provides a theoretical deflection that is 45% higher than the experimental.

Finally, at $M_a/M_{cr} = 4.5$, the approaches converge even more to the experimental data, except Eurocode 2, who slightly underestimates deflections at this loading ratio.

Table 5-12. Statistical parameters for deflection provisions.

Approach	$M_a/M_{cr} = 1.5$		$M_a/M_{cr} = 3.0$		$M_a/M_{cr} = 4.5$	
	$\overline{\delta}$	σ_δ	$\overline{\delta}$	σ_δ	$\overline{\delta}$	σ_δ
ACI 440.1R-03	1.29	0.20	1.09	0.09	1.00	0.06
ACI 440.1R-06	1.27	0.26	1.09	0.09	1.00	0.07
Benmokrane et al. (1996)	1.98	1.03	1.45	0.14	1.23	0.07
Bischoff (2005)	1.51	0.28	1.10	0.10	0.99	0.06
CAN/CSA-S806 (2002)	2.23	0.45	1.20	0.12	1.03	0.06
Eurocode 2 (2004)	1.14	0.33	1.03	0.15	0.96	0.12
Faza and GangaRao (1992)	1.94	0.34	1.15	0.10	1.01	0.06
ISIS Canada (2001)	1.98	0.39	1.16	0.11	1.01	0.06
Toutanji and Saafi (2000)	1.62	0.26	1.21	0.18	1.03	0.06
Yost et al. (2003)	2.72	0.46	1.23	0.13	1.03	0.06

5.4. Cracked Section Analysis

Cracked Section Analysis (CSA) is an analytical tool that is used in the present work to theoretically assess the flexural behaviour of GFRP RC sections at high loads, when the linear behaviour of materials cannot be assumed. This methodology is expected to give an upper-bound theoretical value for flexural strains, rotations, curvatures and deflections.

In CSA (Figure 2-4) it is assumed that the RC section is completely cracked, and the contribution of tensioned concrete is insignificant. CSA assumes Bernoulli hypothesis, i.e., plain sections before bending remain plain after bending, considering a linear distribution of strains along the depth of the beam, and perfect bond between concrete and the reinforcement.

The stress-strain curve adopted for the calculations in CSA is composed in this study by a parabolic ascending branch taken from Eurocode 2 (CEN 2004) and a linear descending branch up to the ultimate compressive strain (Park and Paulay 1975), with a corresponding final stress 20% the compressive strength. The ascending branch is defined by Eqs. (5-7) to (5-9), corresponding to the constitutive relationship for non-linear structural analysis of short term uniaxial loading of Eurocode 2 (CEN 2004), which is represented in Figure 5-10.

$$\frac{\sigma_c}{f_c} = \frac{k\eta - \eta^2}{1 + (k-2)\eta} \tag{5-7}$$

$$\eta = \frac{\varepsilon_c}{\varepsilon_{c1}} \tag{5-8}$$

$$k = 1.05 E_c \frac{|\varepsilon_{c1}|}{f_c} \tag{5-9}$$

The parameter f_c is the mean value of concrete compressive strength, ε_c is the concrete strain, ε_{c1} is the strain at peak stress. The values of E_o, f_c and ε_{c1} are experimentally derived from the cylinders and test samples taken from the beams (Table 3-4, Table 3-5 and Table 3-7 respectively). The value of ε_{cu} is derived directly from the flexural tests.
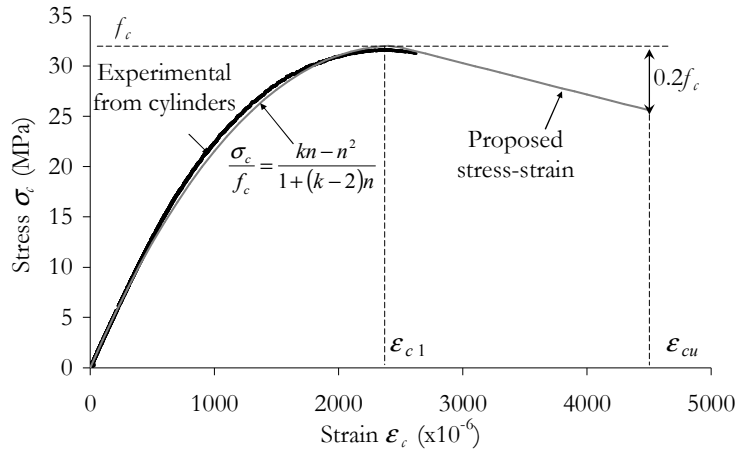
Figure 5-10. Concrete stress-strain relationship adopted for CSA compared to the experimental and stress-strain curve of concrete C1

The ascending branch of the constitutive equation is compared to the experimental stress-strain curve obtained from the tests samples and cylinders in Figure 5-10, giving a good fit between the experimental and theoretical values. Nevertheless, it is not possible to compare the theoretical and experimental descending branches due to the difficulty of acquiring this particular experimental data in the tests carried out.

Once the concrete compressive stress-strain curve is defined, the moment-curvature relation for a particular section is simply derived from equilibrium and compatibility (Figure 5-11, Eqs. (5-10) to (5-15)). A linear elastic behaviour up to failure is considered for the GFRP bar.
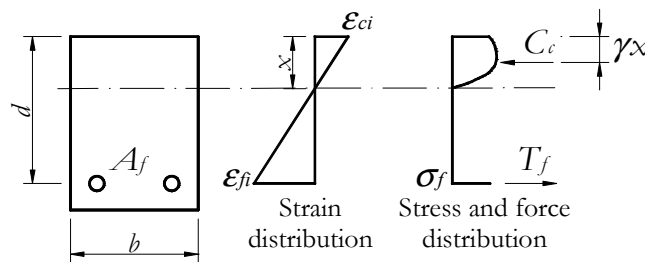
Figure 5-11. Strains and stresses in a RC cracked section

$$\alpha = \frac{\int_0^{\varepsilon_{ci}} \sigma_c d\varepsilon_c}{f_c \varepsilon_{ci}} \tag{5-10}$$

$$\gamma = 1 - \frac{\int_0^{\varepsilon_{ci}} \varepsilon_c \sigma_c d\varepsilon_c}{\varepsilon_{ci} \int_0^{\varepsilon_{ci}} \sigma_c d\varepsilon_c} \tag{5-11}$$

$$C_c = \alpha f_{cm} x b \ = \ T_f \ = \ A_f E_f \varepsilon_{fi} \tag{5-12}$$

$$\varepsilon_{fi} = \varepsilon_{ci} \frac{d-x}{x} \tag{5-13}$$

$$M = C_c \left(d - \gamma x \right) \tag{5-14}$$

$$\kappa = \frac{\varepsilon_{ci}}{x} \tag{5-15}$$

When the cracked and uncracked conditions of a section are combined in a concrete block under pure flexure, a sectional analysis can be made by considering a certain interpolation between both conditions. For example, in Figure 5-12, the sectional analysis using Eurocode 2 (CEN 2004) interpolation is used to represent the moment - curvature relationship until failure. This analysis allows comparing the flexural behaviour of the experimental tests for loads up to rupture, as far as only flexural effects are compared.
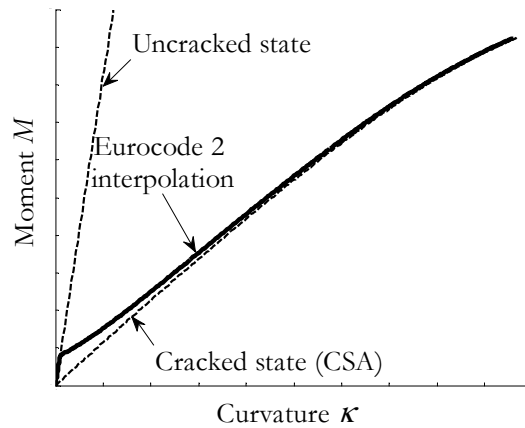
Figure 5-12. Moment-curvature relationship applying sectional analysis using CEN (2004) interpolation

5.4.1. Concrete strain at the midspan cracked section

Herein, CSA is used to compare the experimental evolution of the concrete strain at the top of the beam at the midspan cracked section (given by strain gauge Gc1) with the theoretical provisions (Figure 5-13).
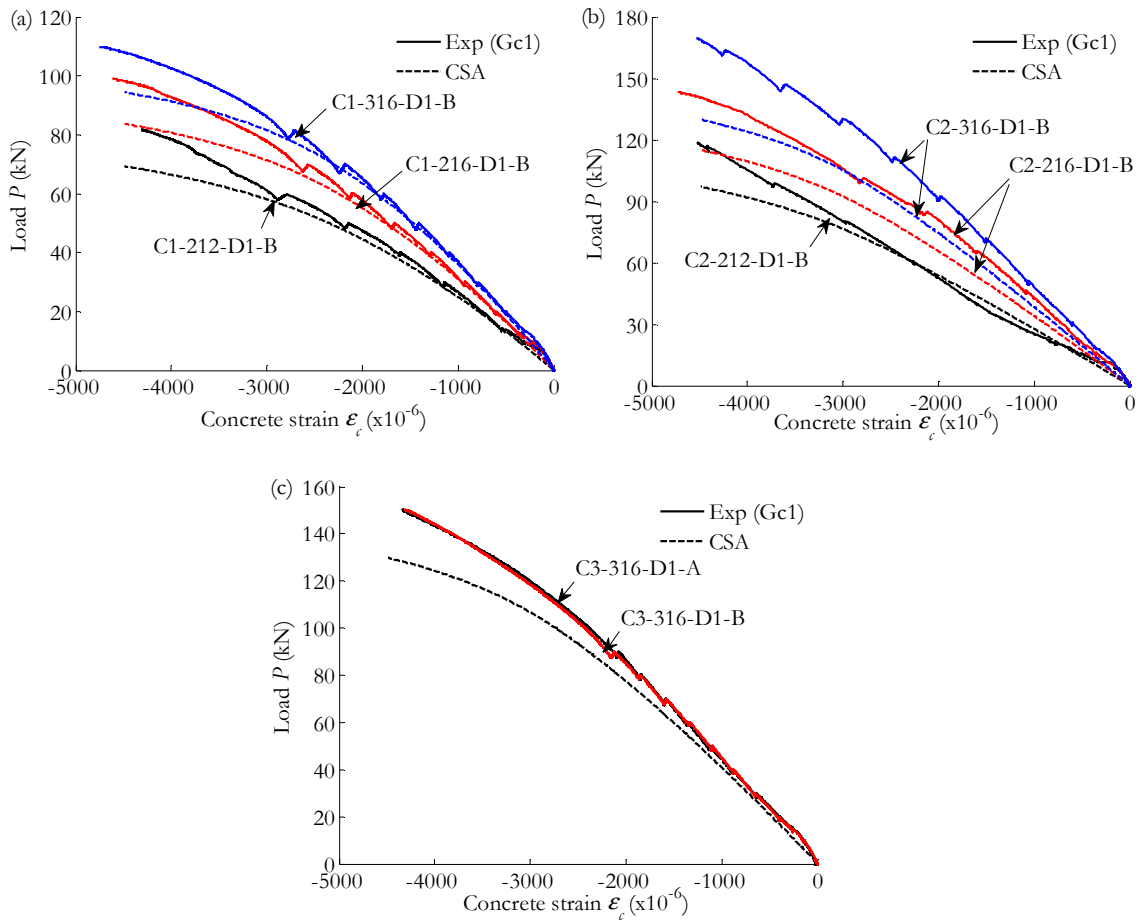
Figure 5-13. Concrete strain evolution at the top of the midspan section for beams with d/h = 0.85. Experimental vs. cracked section analysis (CSA). (a) C1 series, (b) C2 series, (c) C3 series.

It should be pointed out that sectional stresses are a very local phenomena, difficult to capture experimentally. Figure 5-13 shows that the strain predicted by CSA generally results higher than that experimentally registered. One of the factors that may have lead to this result is the influence of the strain gauge length (60 mm) over the local result of a cracked section. An average concrete strain evolution between cracks is subsequently obtained instead of that of a cracked section. Moreover, the concrete has been considered to be homogeneous for the CSA prediction. This hypothesis, which is usually assumed on a global member scale, may not be applicable when a local section is evaluated, where heterogeneity of concrete is expected. In some experiments, the differences between experimental and theoretical data were more evident than in others (C2-216-D1-B and C2-316-D1-B in Figure 5-13b). In these cases, it was experimentally observed that the midspan crack either was not clearly a primary crack or did not propagate from the beginning of cracking. Moreover, splitting appeared once the load was approximately 50% of the ultimate load. Hence, the unusual opening of this midspan crack would have affected the local strains in the section.

5.4.2. Moment-curvature relationship at the central zone

In this section, CSA is used to compare the experimental moment-curvature relationship at the central 450 mm with the theoretical prediction of a cracked section. Figure 5-14 represents this comparison for a typical case of a C1, a C2 and a C3 beam series. In this case, the experimental moment-curvature relationship is deduced from the inclinometers (see § 4.3.). It is observed that CSA generally predicts with accuracy the experimental cracked curvature of the beam.

Since the distance between inclinometers was relatively small (450 mm) and few cracks appeared in between (usually between 3 and 6), the location of appearing cracks inside or outside this region was found to be of major importance and explains the differences found between beam specimens C2-216-D1-A and C2-216-D1-B in Figure 5-14b or between C3-316-D1-A and C3-316-D1-B in Figure 5-14c.
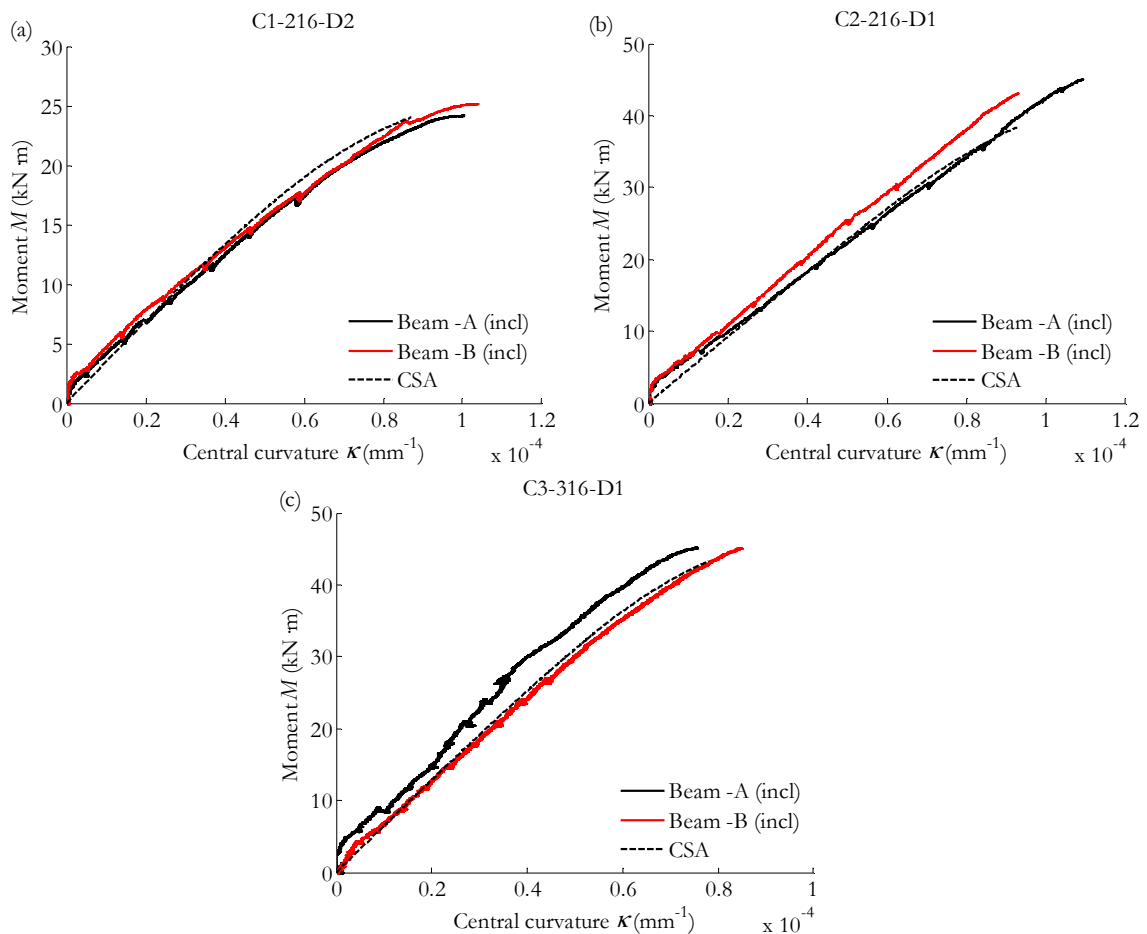
Figure 5-14. Typical moment-curvature relationship. Experimental versus cracked section analysis (CSA). (a) C1 series, (b) C2 series, (c) C3 series.

5.4.3. Reinforcement strain at a cracked section and along the length of the beam

Similarly to the analysis on concrete strains, in the following the strain in the reinforcement is next compared with CSA predictions. The experimental mean strain between cracks is shown and compared to the experimental strain at a crack and the theoretical strain deduced from CSA in Figure 5-15. From experimental results, it is observed that the strain at the crack results higher than the mean strain at the reinforcement since the appearance of the crack, as it was expected due to tension stiffening effects. Moreover, the strain at the crack remains slightly higher than the reinforcement strain predicted by CSA. This phenomenon can be attributed to several factors, being the main one the length of the strain gauge (6 mm), which may have contributed to register a mean value of the rebar strain instead of the punctual one at the crack.
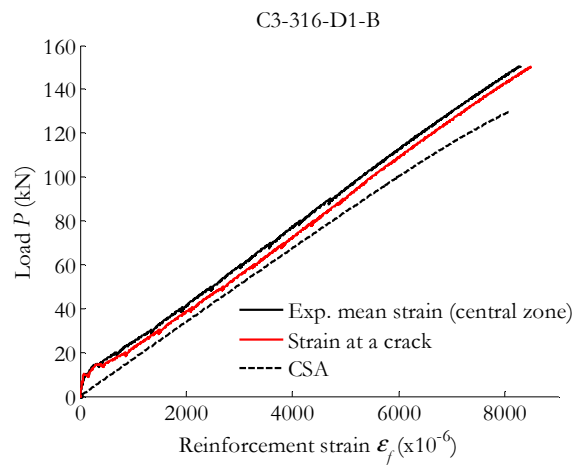
Figure 5-15. Mean reinforcement strain at the central zone compared to the strain at a crack and CSA.

The strain in the reinforcement under the hypothesis of a cracked section is calculated along the length of the beam by using CSA, and it is compared with the experimental strains in the FRP bar. Moreover, a theoretical sectional analysis interpolating the uncracked and the cracked state (using Eurocode 2 formulation) is also represented in Figure 5-16. This comparison provides a general idea of the evolution of the reinforcement strain not only in the central section but also along the shear span.

After Figure 5-16, it is observed that the rebar strain along the shear span is generally lower than CSA predictions for $P = 10$ kN and $P = 20$ kN. However, at higher loads, as cracks at the shear span start to widen and to incline towards the centre of the beam, the readings of the strain gauges at the shear span result higher than that predicted by CSA. Non homogeneous behaviour of the concrete may have had an influence on the strain distribution, leading to locally higher curvatures than expected. Moreover, the influence of the shear crack openings at these stages of loading may not be underestimated as will be further discussed in this chapter.
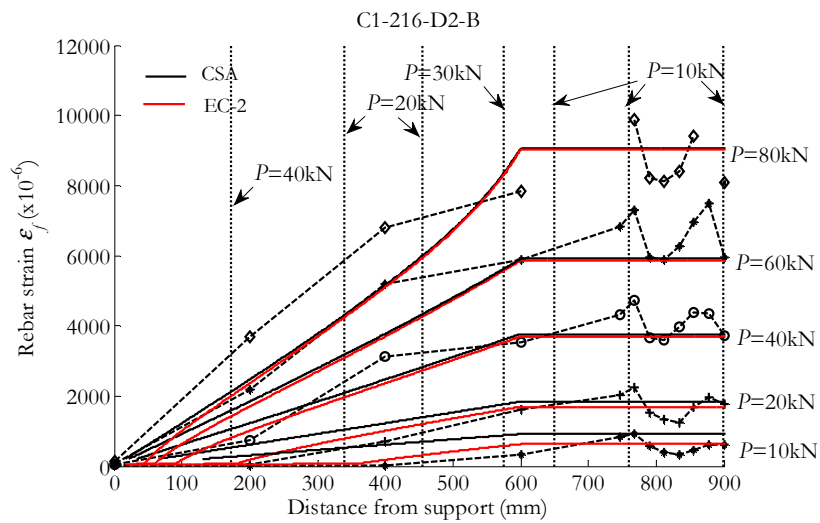
Figure 5-16. Typical rebar strain evolution along the length of the beam. Experimental vs. CSA and section analysis with EC-2 interpolation.

5.4.4. Curvature evolution along the length of the beam

A similar comparison dealing with curvature is show in the following. The experimental curvature shown in § 4.4.1. is compared with CSA in Figure 5-17. Moreover, a sectional analysis with Eurocode 2 interpolation between the cracked and the uncracked state is also represented for comparison purposes.
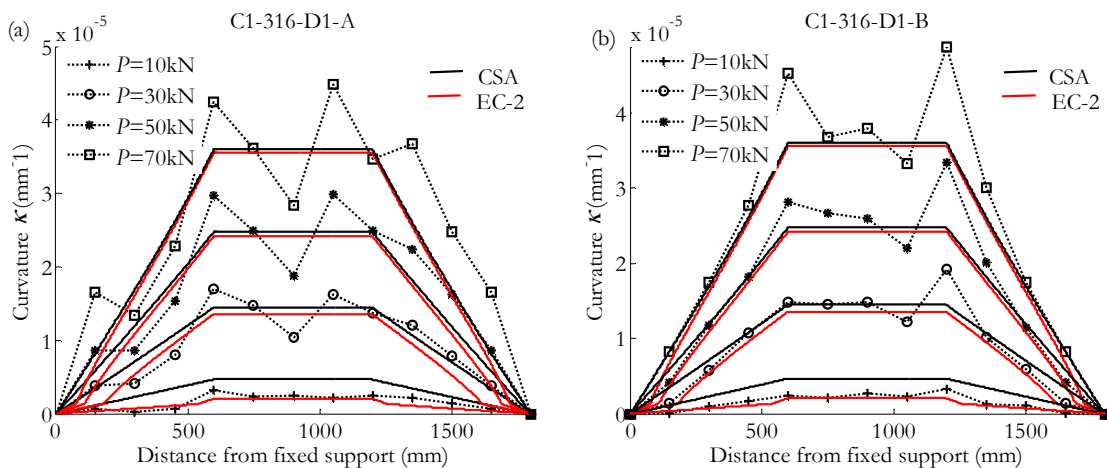
Figure 5-17. Curvature evolution along the length of the beam. Experimental vs. CSA and section analysis with EC-2 interpolation.

At a load of 10 kN, it is observed for both cases represented in Figure 5-17 that CSA slightly overpredicts the experimental curvature along the length of the beam. Nevertheless, the sectional analysis fits well with the experimental results, showing that at this load level, cracking is about to start or has just started and that Eurocode 2 formulation gives a good interpolation between the cracked and the uncracked states.

At the load points, situated at a distance of 600 and 1200 mm from the supports, an increment of the experimental curvature is registered. This increment is attributed to the influence of the punctual loads that may lead to an accumulation of cracks in these zones.

In some cases, another increment of curvature is also registered in the shear span area, as it is shown in Figure 5-17 for the case of the right hand side of beam C1-316-D1-A. This increment in the curvature might be attributed to a substantial shear crack opening, as will be further commented in this chapter.

5.4.5. Deflection response up to failure

Results in § 5.3. show that the experimental deflection is generally accurately estimated by the current prediction models up to the service load conditions (Figure 5-7 and Figure 5-8). However, these approaches are generally not intended to predict deflections beyond the serviceability conditions since their formulation takes as a reference the linear constitutive relationship of materials. This hypothesis is broken when concrete works in the upper part of its stress-strain curve.

In this section, the experimental deflection at the midspan section and at the shear span sections situated at 450 mm from the supports are compared to that obtained by CSA (see Figure 4-13 for the location of the shear span sections). The theoretical deflections are calculated by double integrating the flexural curvature along the length of the beam.

In Figure 5-18 typical results for the midspan deflection, both theoretical and experimental, for the three beam series are represented.
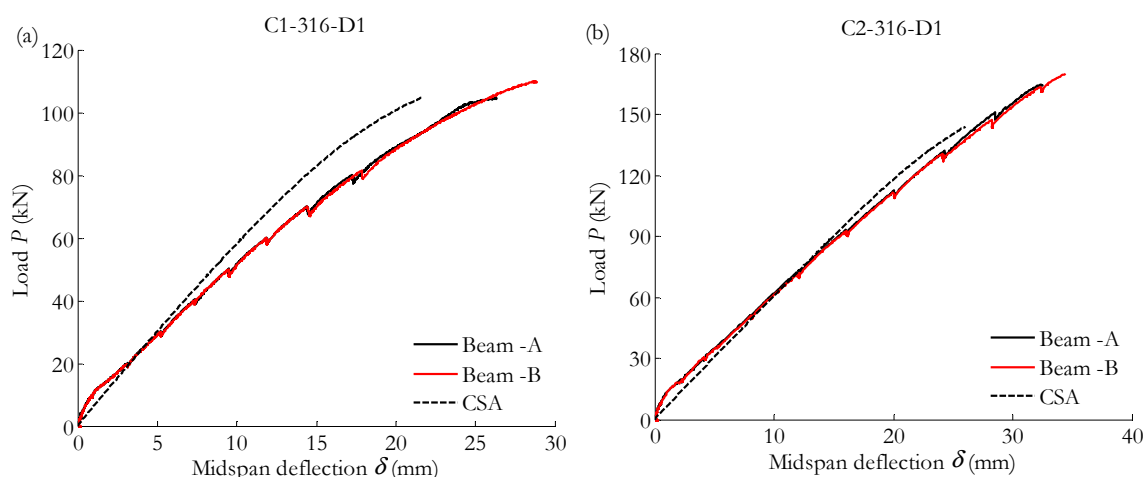
Figure 5-18. Experimental load-midspan deflection compared to CSA until failure. (a) C1-316-D1 beams, (b) C2-316-D1 beams.
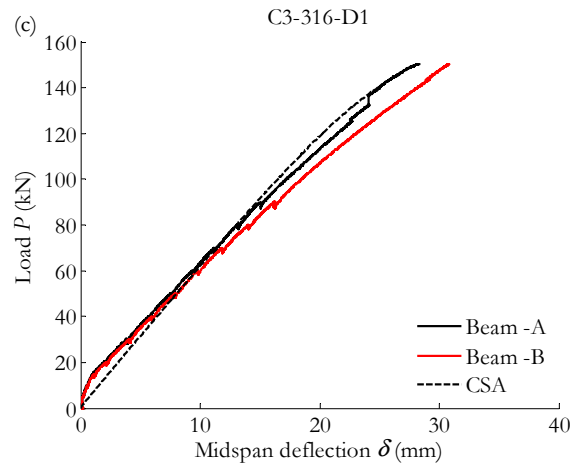
Figure 5-18. Experimental load-midspan deflection compared to CSA until failure. (c) C3-316-D1 beams (continuation).

Results show that CSA underestimates the total experimental deflection for all the beams tested, meaning that other effects than the non-linearity of materials are taking place.

The same phenomenon is observed for the deflection calculation at the shear span, as typically shown in Figure 5-19. The experimental curves cross the CSA curve, giving more deflection than the theoretically predicted.
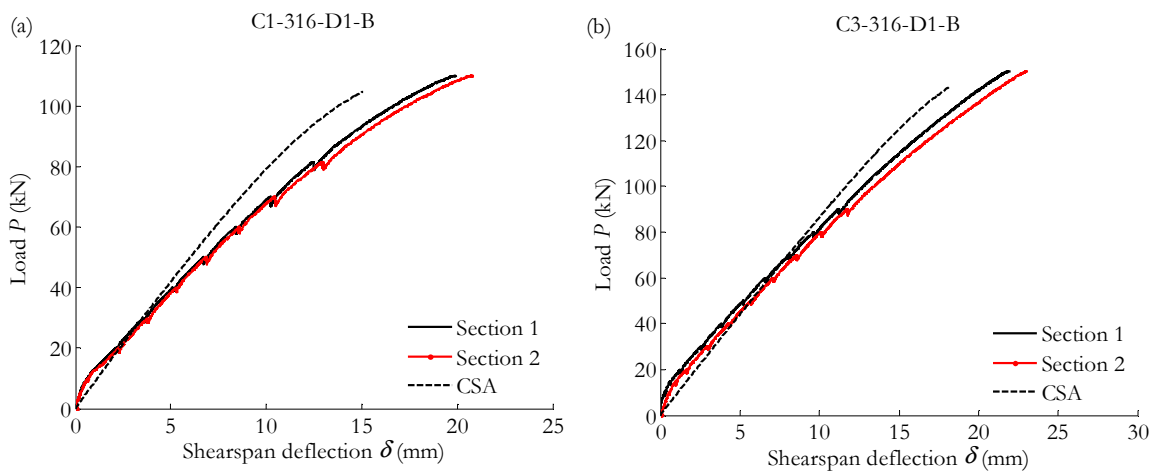
Figure 5-19. Experimental load-shear span deflection compared to CSA, (a) C1-316-D1-B beam, (b) C3-316-D1-B beam.

5.4.6. Ultimate load

In this section, the theoretical and experimental ultimate loads of the tested beams are compared. The theoretical load capacity of the beams is calculated by using the concrete stress blocks specified in ACI 440.1R-06 and Eurocode 2 provisions, and considering the

corresponding values for the ultimate concrete strain of 0.30% and 0.35% respectively. Both approaches are based on internal equilibrium of forces and strain compatibility, but their resulting compressive stress-strain blocks slightly differ in their equivalent factors (Figure 2-5). The theoretical load capacity calculated by CSA, considering the concrete constitutive relationship indicated in Figure 5-10 and taking into account the experimental value of ε_{cu} is also included. The results of this comparison are shown in Figure 5-20 and in Table 5-13.
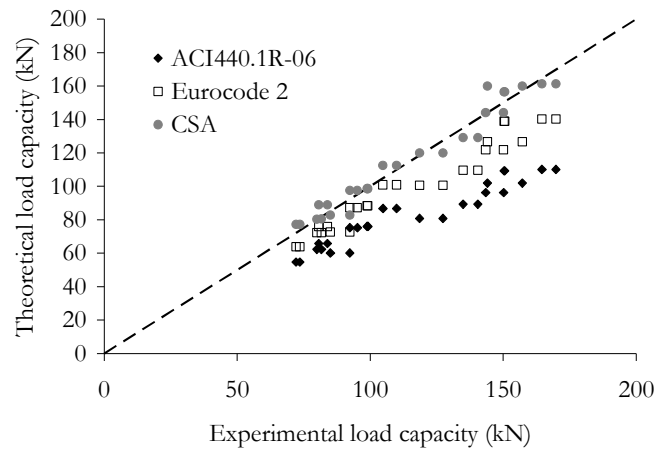
Figure 5-20. Experimental vs. theoretical ultimate load.

Table 5-13. Load capacity of experimental beams compared to code provisions and CSA.

Beam	Load capacity P_u (kN)				
Designation	Beam -A	Beam -B	ACI 440.1R-06	Eurocode 2	CSA
C1-212-D1	79.9	81.7	62.3	72.3	80.3
C1-216-D1	98.8	99.2	76.1	88.5	98.6
C1-316-D1	104.8	109.9	86.8	100.9	112.5
C1-212-D2	72.1	73.5	54.7	63.8	77.2
C1-216-D2	80.7	84.0	65.8	75.9	89.0
C1-316-D2	92.4	95.2	75.3	87.3	97.6
C2-212-D1	127.4	118.6	80.8	100.7	120.0
C2-216-D1	150.2	143.4	96.2	121.9	144.1
C2-316-D1	164.6	169.8	110.1	140.3	161.4
C2-212-D2	92.3	85.1	60.2	72.7	82.8
C2-216-D2	140.5	134.9	89.3	109.6	129.1
C2-316-D2	144.0	157.2	102.0	126.7	160.0
C3-316-D1	150.6	150.3	109.2	139.0	156.6

All beams withstand a higher load than the one theoretically predicted by ACI and Eurocode 2 approaches. A statistical analysis for the ratio between the theoretical and experimental load capacity is shown in Table 5-14.

Table 5-14. Statistical parameters for the load capacity provisions.

	$\overline{\delta}$	σ_δ
ACI 440.1R-06	0.72	0.06
Eurocode 2	0.87	0.05
CSA	1.01	0.05

The mean ratio between the theoretical and experimental values is 0.87 in the case of Eurocode 2 analysis and 0.72 for the ACI provisions. The ACI comparison gives an experimental to theoretical ultimate ratio slightly higher than the one reported in Masmoudi et al. (1998) and Pecce et al. (2000), whereas for the tested beams Eurocode 2 estimates the ultimate load more accurately. One possible reason for the difference between both theoretical approaches and the experimental values can be found in the value of the theoretical maximum compressive concrete strain that was considered. In all the tests carried out, this value was about 0.42-0.47%, which results 22-34% higher than the one suggested by the theoretical procedures. Hence, this maximum theoretical compressive strain in concrete may lead to be too conservative in view of the experimental results.

CSA, which takes into account the experimental ultimate compressive strain of the concrete, gives the most accurate theoretical predictions of the experimental load capacity of the beams, being the mean ratio between the experimental and the theoretical ultimate loads of 1.01.

In order to study the influence of the experimental ultimate concrete strain $\varepsilon_{cu,\exp}$ on the prediction of the load capacity, the same formulation (ACI and Eurocode 2) was used to re-calculate the ultimate load taking into account the $\varepsilon_{cu,\exp}$. The results are summarized in Figure 5-21 and Table 5-15.
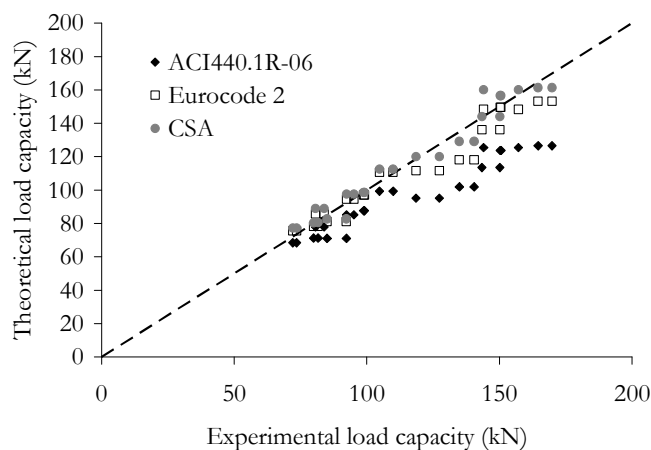
Figure 5-21. Experimental vs. theoretical ultimate load considering $\varepsilon_{cu,\exp}$.

Table 5-15. Statistical parameters for load capacity provisions considering $\varepsilon_{cu,\exp}$.

	$\overline{\delta}$	σ_{δ}
ACI 440.1R-06	0.85	0.07
Eurocode 2	0.97	0.06

As it is observed, both approaches estimate well to the experimental results. The mean ratio of the theoretical to experimental load capacity is 0.85 for ACI provisions and 0.97 for Eurocode 2. The mean percentage and absolute deviation also present an improvement in their values. Moreover, Eurocode 2 gives the closest predictions of the experimental data.

5.5. Analysis of the experimental short-term deflection

Results show that the experimental short-term deflection is underestimated by code predictions and cracked section analysis beyond the service loading conditions. This section presents an analysis of the two of the probably main factors that shall have induced higher deformations in the tested beams according to other experimental studies (Bischoff and Johnson 2008, Al-Sunna 2006, Imjai 2007a). Firstly, the possible influence of shrinkage on the deflection response is studied and secondly a computation of the shear induced effects on the total deformation is carried out.

5.5.1. Evaluation of shrinkage on the deflection response

Shrinkage before loading a RC element can cause larger short-term deformations than expected (Gilbert 1988, Bischoff and Johnson 2008). Shrinkage that takes place before a beam is loaded is locked into the member response, having the effect of reducing the cracking moment, which is caused by tensile stresses that develop in the concrete from restraint to shrinkage by the reinforcement (Bischoff and Johnson 2008, Figure 5-22). Additionally, shrinkage causes a shift in the bare bar response of the cracked transformed section. These two phenomena (lower cracking moment and shift in the cracked member response) work together to increase the immediate short-term deflection of a member loaded in flexure.

In this study, an estimate of the possible increment of curvature caused by shrinkage effects is calculated. This increment is calculated as the difference between the initial warping curvature κ_0 and the offset $\kappa_{0,cr}$ in the bare bar response (see Figure 5-22).

Nonetheless, the reduction of the cracking moment is not considered in this study, since it is implicitly taken into account by using the experimental value of the cracking moment.
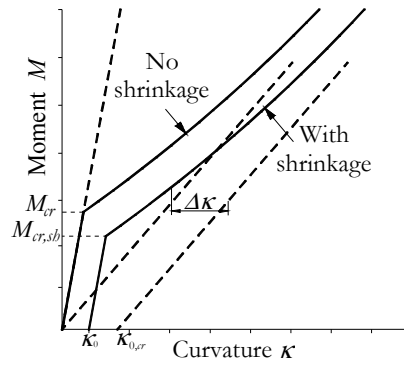
Figure 5-22. Idealised response for the moment-curvature relationship with and without shrinkage, after Bischoff and Johnson (2008).

The time-dependent values of the creep coefficient φ and the shrinkage strain ε_{cs} have been calculated according to Model Code 90 formulation, as follows:

$$\varphi = \varphi_0 \cdot \beta_c \left(t - t_0 \right) \tag{5-16}$$

$$\varepsilon_{cs} \left(t, t_s \right) = \varepsilon_{cs0} \cdot \beta_s \left(t - t_s \right) \tag{5-17}$$

In Eqs. (5-16) and (5-17), φ_0 and ε_{cs0} are the notational creep and shrinkage coefficients respectively, and $\beta_c(t\text{-}t_0)$ and $\beta_s(t\text{-}t_0)$ are the coefficients to describe the development of creep and shrinkage with time after loading. These coefficients depend on the geometry of the element, as well as on the concrete grade, the age at loading and the age at testing. According to the data recorded during casting, curing and until testing, the minimum relative humidity of the ambient environment is assumed to be 50%.

The initial warping curvature κ_0 in the uncracked member as well as the offset $\kappa_{0,cr}$ in the bare bar response are calculated according to the expressions developed by Bischoff and Johnson (2008) as follows:

$$\kappa_0 = \frac{M_{sh,unc}}{\overline{E}_c I_g} \tag{5-18}$$

$$\kappa_{0,cr} = \frac{M_{sh,cr}}{\overline{E}_c \overline{I}_{cr}} \tag{5-19}$$

where $M_{sh,unc}$ represents a fictious shrinkage restraint moment to account for shrinkage and it is defined in Eq. (5-20), $M_{sh,cr}$ is defined in Eq. (5-21), $\overline{E}_c$ is the age-adjusted elastic modulus of the concrete (Eq. (5-22)) and $\overline{I}_{cr}$ is the long-term moment of inertia of the cracked transformed section (Eq. (5-23)).

$$M_{sh,unc} = E_f \rho \varepsilon_{sh} \left[1 - \overline{k_{unc}} \cdot (h/d) \right] bd^2 \qquad (5\text{-}20)$$

$$M_{sh,cr} = E_f \rho \varepsilon_{sh} \left(1 - \overline{k_{cr}} \right) bd^2 \qquad (5\text{-}21)$$

$$\overline{E_c} = \frac{E_c}{1 + \chi \varphi} \qquad (5\text{-}22)$$

$$\overline{I_{cr}} = \frac{bd^3}{3} \overline{k_{cr}}^3 + A_f d^2 \left(1 - \overline{k_{cr}} \right)^2 \qquad (5\text{-}23)$$

In Eqs. (5-20) and (5-21), $\overline{k_{unc}}$ (Eq. (5-24)) and $\overline{k_{cr}}$ (Eq. (5-25)) represent the normalised neutral axis depth of the uncracked and the cracked sections respectively. They depend on the age-adjusted modular ratio, which is defined in Eq. (5-26).

$$\overline{k_{unc}} = \left(\frac{\left(\overline{n} - 1 \right) A_f d + bh^2/2}{\left(\overline{n} - 1 \right) A_f + bh} \right) \Big/ h \qquad (5\text{-}24)$$

$$\overline{k_{cr}} = \sqrt{\left(\overline{n} \rho \right)^2 + 2 \overline{n} \rho} - \overline{n} \rho \qquad (5\text{-}25)$$

$$\overline{n} = n \left(1 + \chi \varphi \right) \qquad (5\text{-}26)$$

In Eqs. (5-22) and (5-26), χ is the age adjusted coefficient, taken 0.85 in this study, being A_f the area of tensile reinforcement, ρ the reinforcement ratio, b the width of the section and h and d the height and effective depth of the section respectively.

The resultant additional curvature due to shrinkage effects, computed as $\kappa_{0,cr}$-κ_0, is summarized in Table 5-16 for each tested beam. For comparison purposes, this additional curvature is depicted in Figure 5-23 together with CSA predictions and the experimental results.

It is observed that the possible influence of shrinkage on the results is almost insignificant in these cases and cannot justify by itself the difference between the theoretical and experimental deflections. A maximum contribution in the curvature due to shrinkage of 1×10^{-6} mm^{-1} is found, which is not remarkable compared to the curvatures at ultimate (between 80 and 140 $\times 10^{-6}$ mm^{-1}) or at service (between 20 and 30 $\times 10^{-6}$ mm^{-1}). This represents an additional deflection of about 3-5% at service and around 1% at ultimate.

Table 5-16. Creep coefficient, shrinkage strain and additional curvature due to shrinkage in the experimental tests according to Bischoff and Johnson (2008).

Beam Designation	Creep coefficient, φ	Shrinkage strain, ε_{cs} ($\times 10^{-6}$)	Additional curvature, $\kappa_{0,cr}$-κ_0 ($\times 10^{-6}$ mm^{-1})
C1-212-D1	1.41	161	0.927
C1-216-D1	1.49	176	0.944
C1-316-D1	1.47	173	0.821
C1-212-D2	1.36	146	1.036
C1-216-D2	1.32	137	0.966
C1-316-D2	1.34	142	0.957
C2-212-D1	0.98	102	0.612
C2-216-D1	1.13	130	0.746
C2-316-D1	1.10	123	0.658
C2-212-D2	1.29	145	1.032
C2-216-D2	0.96	95	0.684
C2-316-D2	1.06	111	0.784
C3-316-D1	1.03	111	0.599
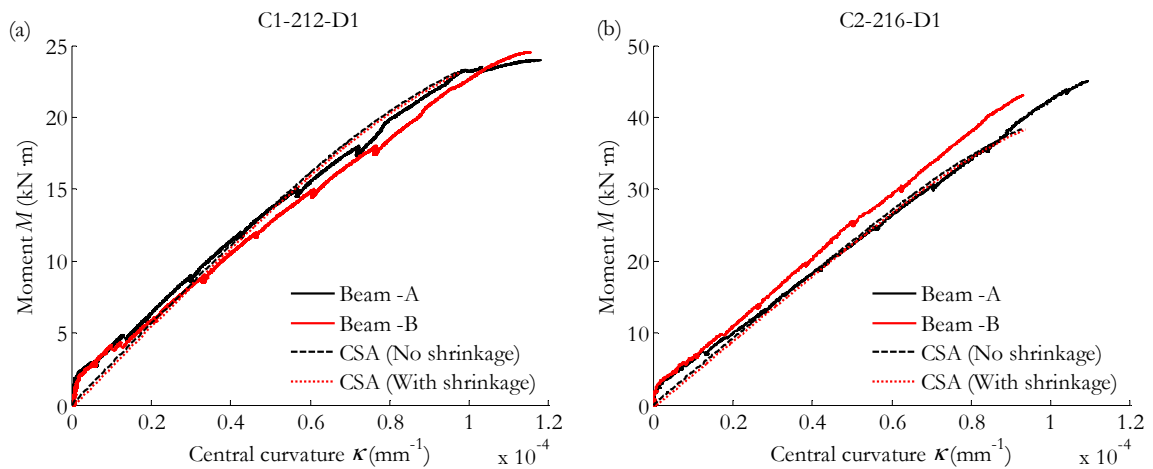
Figure 5-23. Shrinkage effect on the contribution to the total curvature.

5.5.2. Evaluation of the additional shear induced deformation

The experimental deflection captured by the vertical transducers starts to differ from the calculated from experimental curvatures at approximately 40% of the ultimate load. This load ratio matches up fairly well with the one at which diagonal cracking appears at the shear spans of the beams tested (around 45% of the ultimate load). Moreover, this is roughly the load ratio at which cracked section analysis underestimates the experimental midspan deflection (40-45% of the ultimate load). In Figure 5-24, the experimental deflection is compared to CSA and the load at which diagonal cracking appears is shown for the three series of beams.
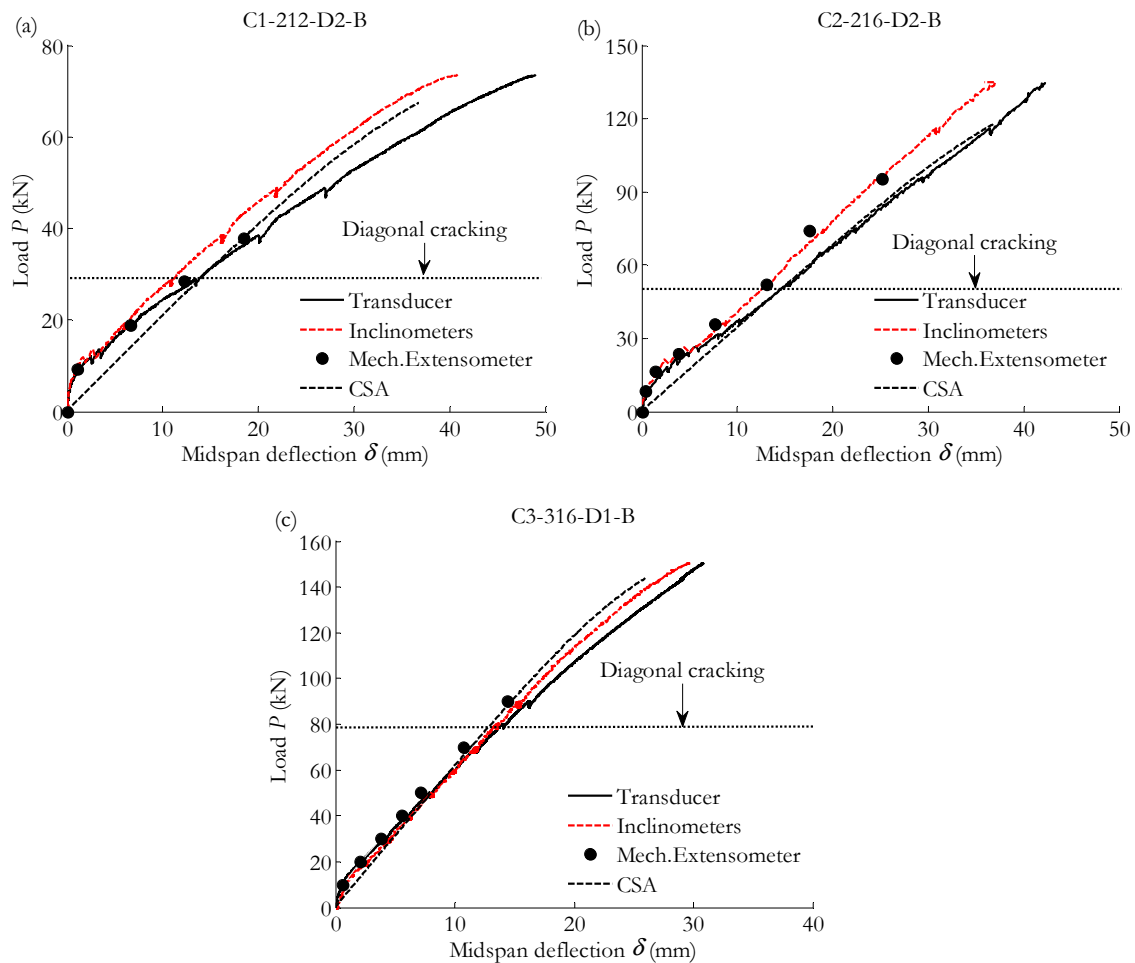
Figure 5-24. Typical experimental load-midspan deflection compared to CSA (a) C1 beam series (b) C2 beam series (c) C3 beam series

Furthermore, the rebar strain profiles within the shear span show an increment of the experimental strain with respect to the flexural requirements at high load (see § 5.4.3.) and similar increments of curvature are detected in the shear span zone (see § 5.4.4.).

From these observations, it seems likely that shear induced effects may be contributing to the total deflection of the beam for loads beyond 40-45% of the ultimate load. Previous works dealing with deflections of FRP RC beams already showed that the shear induced effects cannot be ignored for the computation of deflections at ultimate for FRP RC beams (Al-Sunna 2006, Imjai 2007a, Imjai et al. 2007b). This "shear induced deformation" arises as a consequence of deeper and wider cracks that appear in the shear span of the FRP RC element and cause a loss of the stiffness of the concrete blocks between inclined cracks. Local rotations are subsequently higher, leading to an increase of deflections (Al-Sunna 2006).

The experimental C3 test series was designed and carried out with the main aim of attempting a computation of the total versus the additional shear deflection. For this purpose, additional Demec points were placed in the diagonals of the basic frame previously established to

compute the flexural deflection (see Figure 3-10b). Two different approaches were used to compute the total vs. shear induced experimental deflection. These are described below.

Firstly, the virtual work methodology was used to check the measurements with the mechanical extensometer. The total midspan deflection of the beam was calculated by the unit-load method and compared to the experimental value directly obtained from the vertical transducer. According to the unit-load method, the deflection of a truss system at a particular point can be calculated by applying a virtual force at that point, with a unity value (Figure 5-25).
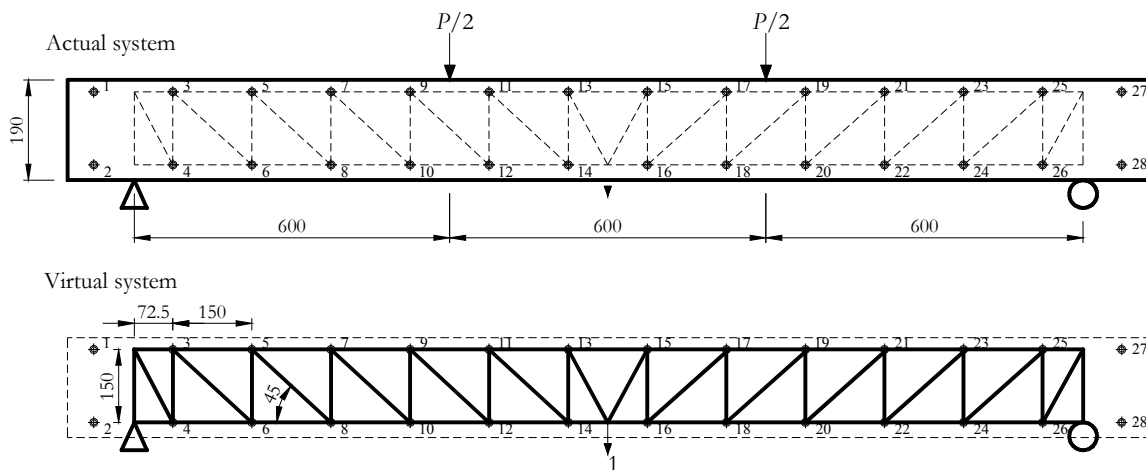
Figure 5-25. Unit-load method applied to the tested beams.

The actual deflection at that point is the sum of the product $(F_i \cdot \delta_s)$, where F_i are the resultant fictious forces at each element of the truss, and δ_s are the actual elongations of the elements in the tested truss.

$$(1)\delta_{mid} = \sum F_i(\delta_e) \tag{5-27}$$

This method was used to evaluate the total deflection of the tested beams. For comparison purposes, three different trusses were checked (Figure 5-26).

In Figure 5-27 the results of the unit-load method (namely Truss 1, Truss 2 and Truss 3) are represented and compared to the experimental midspan deflection. The total experimental deflection registered by the vertical transducer and the flexural deflection calculated from double integration of curvatures from the mechanical extensometer are depicted for comparison purposes.
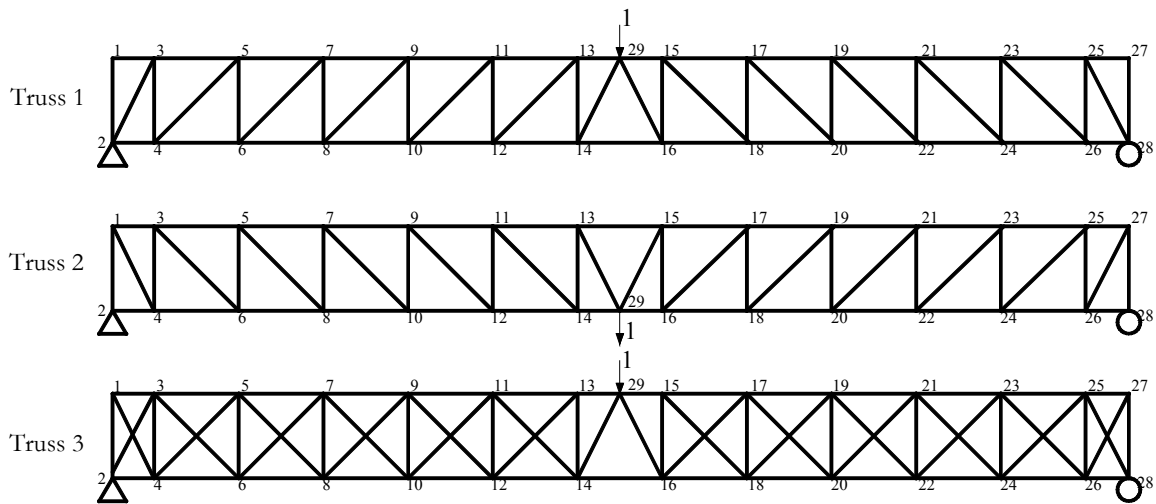
Figure 5-26. Tested geometries for the unit-load method.
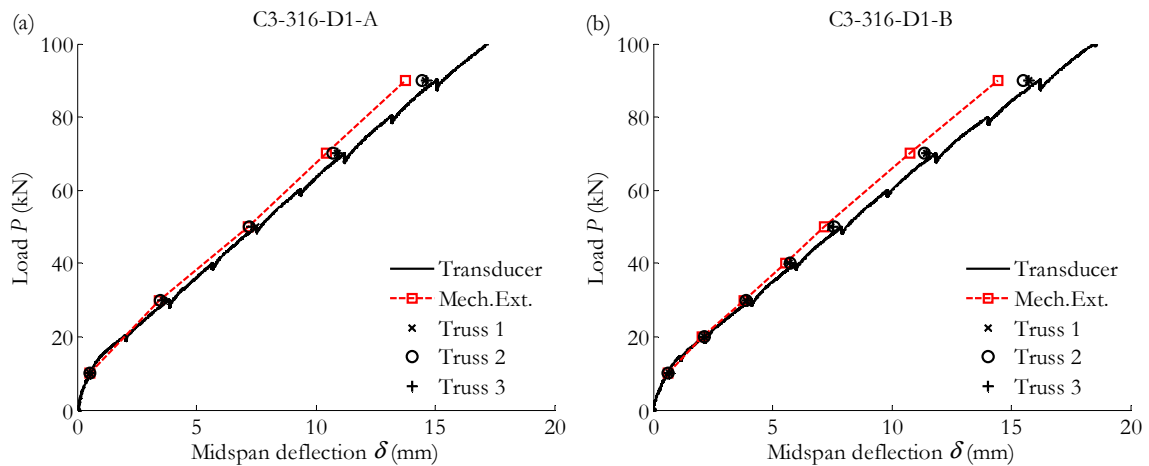
Figure 5-27. Midspan deflection: unit-load method compared to experimental results.

It is observed that this methodology computes fairly well the total experimental deflection, and it effectively captures the additional deflection produced by shear induced effects or the additional rotation at the load points.

Even though this methodology does not allow separating the flexural from the shear deflection by itself, the contribution of the additional shear deformation can be calculated as the difference between the total deformation computed by the unit-load method and the experimental flexural deformation obtained from double integration of curvatures of the mechanical extensometer data. The additional shear deformation is 0.8-1.2 mm at a load of 90 kN, representing about 5.5-7.5% of the total deflection at the midspan.

On the other hand, following the methodology developed in Debernardi and Taliano (2006) for steel RC beams with thin web, a second calculation of the shear deflection is shown in the following. A reference system is assumed with the origin in each C vertex of the truss, the y axis coincides with the CD direction and the z axis is orthogonal to y. In this system, the total

deformation of the A, B, C and D points is represented as A", B", C" and D". This deformation is considered as being made up of a curvature and a mean shear strain. The flexural deformation is represented as A', B', C' and D' points. Figure 5-28 and Figure 5-29 show the geometrical details of this configuration.
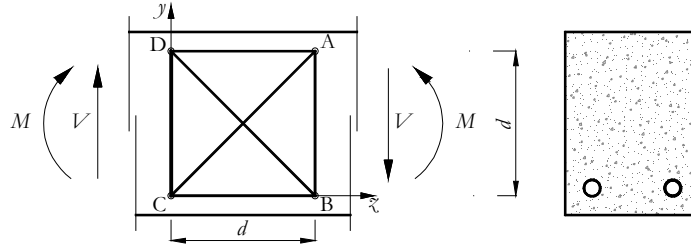
Figure 5-28. Scheme of the measuring lattice at the initial non-deformed state.
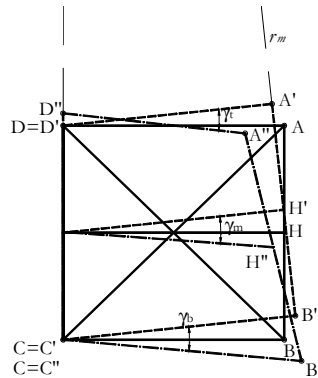
Figure 5-29. Deformed configuration of the measuring lattice subjected to bending and shear, after Debernardi and Taliano (2006).

The mean curvature κ_m, defined as the difference between the mean strain of the tension chord and the mean strain of the compression chord, divided by the distance between chords, can be expressed as:

$$\kappa_m = \frac{1}{r_m} = \left(\frac{B''C'' - BC}{d} - \frac{A''D'' - AD}{d} \right) \frac{1}{d} \qquad (5\text{-}28)$$

being d the original distance between points. The distances BC and AD are the initial lengths between Demec points for each square ABCD and the distances B"C" and A"D" are the final lengths between Demec points at the given load step. All these measures are directly obtained from the data of the mechanical extensometer.

The shear strain γ owing to the shear forces can be obtained by subtracting the displacement attributed to curvature from the total displacement, and is computed as the mean value between the top and bottom shear strains as follows:

$$\gamma_m = \frac{\gamma_b + \gamma_t}{2} = \frac{1}{2}\left(\frac{y_{B'} - y_{B''}}{d} + \frac{(y_{A'} - y_{A''}) - (y_{D'} - y_{D''})}{d}\right) \tag{5-29}$$

The distances $y_{B''}$ and $y_{A''}$ are calculated applying the law of cosines on the triangles B"C"D" and A"C"D" respectively (Eq. (5-30) and (5-31)). The distance $y_{D''}$ is directly the total elongation of the chord CD, i.e. C"D".

$$y_{B''} = \frac{(C''B'')^2 - (D''B'')^2 + (C''D'')^2}{2(C''D'')} \tag{5-30}$$

$$y_{A''} = \frac{(C''A'')^2 - (D''A'')^2 + (C''D'')^2}{2(C''D'')} \tag{5-31}$$

If the initial distance between points is d for all cases (CD, CB, AD and AB), the vertical point ordinates of the points A' and B' owing only to the effect of the curvature are:

$$y_{B'} = \frac{d^2}{2r_m} \tag{5-32}$$

$$y_{A'} = y_A + \frac{d^2}{2r_m} \tag{5-33}$$

Hence, the location of the point D' is d and Eq. (5-29) reduces to:

$$\gamma_m = \frac{d}{2r_m} + \frac{y_{D''} - y_{A''} - y_{B''}}{2d} \tag{5-34}$$

In this work, this methodology is used to calculate the shear deflection along the beam separately from the flexural deflection. The flexural deflection is computed by integrating the mean curvature κ_m along the length of the beam obtained in Eq. (5-28). The additional shear deflection is computed by multiplying the shear strain γ_m obtained in Eq. (5-29) by the distance d at every square *ABCD*. The total deflection of the beam is computed as the flexural plus the shear deformations.

In Figure 5-30, the resultant flexural (δ_{flex}) and total (δ_{tot}) deflections are depicted and compared to the experimental deflection registered by the transducers δ_{tot}(transd). The additional shear deformation is depicted as $\Delta\delta_{shear}$.
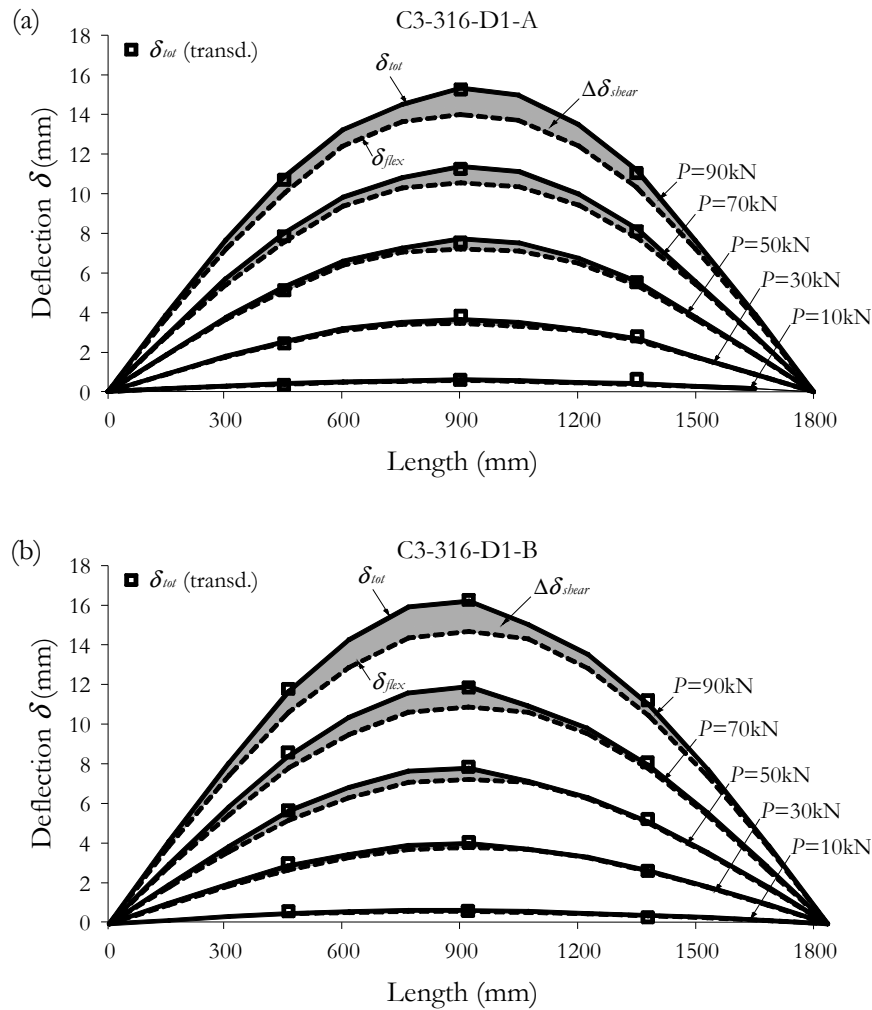
Figure 5-30. Total deflection vs. flexural and additional shear deflection, compared to experimental total deflection from vertical transducers.

From the results obtained, it can be concluded that the total deflection, computed as the sum of the flexural plus the shear deflections, fits with the experimental data obtained from vertical transducers placed not only in the midspan section but also at the shear spans, at 450 mm from the supports. Hence, the suspected shear induced effect on the evaluation of deflections is corroborated. The higher the load level, the higher the effects of the shear deflections on the total deformation.

At the last Demec points measurement ($P = 90$ kN, approximately 60% of P_u), the additional shear deformation was about 9.0-9.5% of the total deflection at the midspan, and about 7.5-8.0% at the shear spans. At $P = 50$ kN (33% of P_u, which could be considered a reasonable upper bound for the service load), the contribution of the shear deflection at the midspan was about 6.0-7.0% of the total deformation. These results justify the differences observed in the tests between the predicted flexural deformation and the experimentally obtained.

5.6. Concluding remarks

This chapter presents a comparison of the experimental results with some of the most widely accepted formulation on cracking and deflections for FRP and steel RC elements. Besides, the cracked section analysis is used to compare the experimental flexural results until the failure of the beam. Strains, curvatures and deflections are evaluated. Finally, an analysis on the deflection is carried out. Herein, a summary of the most important conclusions is drawn.

5.6.1. Code comparisons for cracking and instantaneous deflection

The experimental crack spacing is found to increase with the concrete cover, the bar spacing and the ϕ/ρ_{eff} ratio.

The maximum crack spacing is 21% overestimated by Eurocode 2 and Model code 90 formulation, whilst the mean crack spacing is adequately predicted by EHE and slightly overestimated by Eurocode 2. Significant differences are found in the evaluation of the effective height of the concrete area surrounding the tensile rebar.

The characteristic value of the crack spacing is calculated assuming a log-normal distribution of this parameter, obtaining a value of 1.45 times the mean crack spacing.

The experimental average and maximum crack widths are generally well predicted by codes of practice when the experimental crack spacing is considered in their formulation, up to a loading condition of 35% the ultimate load.

Bond coefficients are adjusted to fit the experimental crack spacing and maximum crack width to the corresponding formulae, obtaining similar resultant values to those suggested for steel RC.

The experimental midspan deflection is accurately predicted by Eurocode 2, ACI 440.1R-06, ACI 440.1R-03, Bischoff (2005) and Toutanji and Saafi (2000) models until the service load. Other approaches that suggest a large increase in deflections after the cracking load and rapidly approach the cracked response result in overestimating the experimental response at the first stages of loading.

5.6.2. Cracked section analysis

Cracked section analysis generally predicts with accuracy the curvature and strains at the central sections. However, CSA underestimates the rebar strain and the curvature at the shear span and under the load points at high load levels. Furthermore, CSA underestimates the midspan and the shear span total deflection also for high load levels. Nevertheless, CSA provides adequate predictions of the ultimate load.

5.6.3. Short-term deflection up to failure

The total deflection of the tested beams results higher than that predicted by CSA beyond the serviceability requirements. Shrinkage was found to not affect significantly the deformational behaviour of the beam. A maximum contribution of 1×10^{-6} mm^{-1} in the curvature was found, which was not remarkable compared to the curvatures either at ultimate (between 80 and 140 $\times 10^{-6}$ mm^{-1}) or at service (between 20 and 30 $\times 10^{-6}$ mm^{-1}), representing an additional deflection of 3-5% at service and around 1% at ultimate.

The difference between deflections is mainly attributed in this work to shear induced deformations produced along the shear span and under the load points. Following the methodology developed by Debernardi and Taliano (2006), a measure of the experimental contribution of the shear deflection is obtained. At 60% of the ultimate load, the contribution of the shear deformation to the deflection at midspan results 9.0-9.5% of the total deflection.

Chapter 6
Serviceability limit states of
FRP RC beams

6.1. Introduction

Due to the mechanical properties of FRP materials, the Serviceability Limit States (SLS) may govern the design of FRP RC elements (fib 2007; ISIS Canada 2001; Matthys and Taerwe 2000; Nanni 2003). At a cross-section level, two requirements limit the SLS: stresses in materials and cracking (CEN 2004). Stresses in concrete are limited to avoid longitudinal cracking, micro-cracks and high levels of creep. The stress in the FRP reinforcement should also be limited to avoid creep rupture or stress corrosion, which consists in the creep of the material under a constant load after a certain time (fib 2007). In general, cracking is controlled to ensure adequate structural performance as well as sufficient durability of the structure.

The SLS for steel RC elements are usually evaluated at about 60 to 65% of the nominal moment capacity (Bischoff 2005). Several published studies on SLS for FRP RC elements relate the load at which the SLS shall be evaluated to the ultimate load: Alsayed (Alsayed et al 1998; Alsayed et al. 2000) and Rafi et al. (2008) assume the service load to be about 35% of the ultimate load, whereas Bischoff (2005) states that the level of service load drops to about 25% of the nominal beam capacity for over-reinforced GFRP beams. Other investigations and codes of practice limit the tensile strain at the reinforcement to control crack width to a fix value (Ghali et al. 2001; Newhook et al. 2002; ISIS Canada 2001). Pecce et al. (2001), in turn, evaluates the serviceability load as the minimum between the loads corresponding to each of the SLS (namely, deflection, crack width and maximum stress in concrete) and the theoretical

ultimate load reduced by factor of 1.5, finding that in 80% of the cases, the serviceability load corresponds to the criterion of the concrete limiting stresses.

This chapter starts presenting a formulation to calculate the bending condition at which crack width and stresses in materials requirements are fulfilled. The presented equations are based on principles of equilibrium and strain compatibility, plane sections remaining plane after bending and linear elastic behaviour of materials. The formulation of CNR-DT-203 (2006) and CEN (1992) is considered for the crack width calculation. Comparisons between both limitations are presented in terms of the service moment related to the cracking moment and the corresponding tensile stress at the reinforcement.

Then, the deflection limitation is studied and the slenderness limits are redefined at the load level found in the previous analysis, that is, the bending situation that accomplishes both the maximum crack width and the stresses in materials limitations.

Finally, a methodology is proposed for the design under the serviceability conditions of FRP RC. This methodology allows optimizing the overall depth of the element with respect to more generalised methodologies, since it takes account of the specific characteristics of the RC element. The present study is developed for FRP RC cracked rectangular sections without compressive reinforcement.

6.2. Discussion on the serviceability limitations and proposed formulation

Nowadays there is no evidence for establishing the limits for the SLS of FRP RC elements different to those already considered in design codes for steel RC elements, such as Eurocode 2 (CEN 1992; CEN 2004), Model Code 90 (CEB-FIP 1990), ACI318R-05, or CAN/CSA-S806. Nevertheless, the different properties of FRP and steel reinforcements might justify different limits in the case of the short and long-term behaviour (fib 2007).

In this section, a discussion of the serviceability limitations for the case of FRP RC beams is made and a formulation to control the serviceability requirements is suggested.

6.2.1. Stresses in materials

When FRPs are used as internal reinforcement, the strength to stiffness ratio is an order of magnitude greater than that of concrete and, hence, the neutral axis depth for the balanced section is very close to the compressive end (fib 2007). As a result, higher compressive strains than in a steel RC section are expected to develop in the concrete for the same beam depth. Consequently, the maximum concrete strain/stress at service load should be considered carefully as to avoid any undesirable effects due to the occurrence of longitudinal cracks, micro-cracks, inelastic deformations and creep. Moreover, the stress at the FRP reinforcement shall be limited so as to avoid creep rupture and stress corrosion.

Stresses in concrete

Although specific limits on concrete compression stresses under service conditions are not prescribed explicitly in all of the existing design provisions, the concrete stresses are generally assumed to be within the linear range. While ACI440.1R-06 (ACI Committee 440 2006) adopts this latter approach, a limiting value of $0.45f_c'$ is explicitly recommended in ACI.440.2R-08 (ACI Committee 440 2008) for concrete elements strengthened with FRPs.

Eurocode 2 (CEN 2004), in turn, imposes a maximum stress in concrete under a characteristic combination of load of $0.60f_{ck}$ to avoid the appearance of longitudinal cracks, which could affect durability. A more restrictive limit of $0.45f_{ck}$ is recommended when considering quasi-permanent load conditions to enable the use of a simplified linear model for creep. The most restrictive limitation between them depends on the permanent-to-variable ratio of loading and on the use of the structure. For a typical permanent-to-total load ratio of 60-75%, the stress limitation under the quasipermanent combination of loads results more restrictive than that for the characteristic combination.

Consequently, in this study, the limitation of the concrete stress to $0.45f_{ck}$ and its effects are analysed. As a result, the service moment M_s (referred to the quasi-permanent load combination) at a cross-section related to the cracking moment M_{cr} that fulfils this condition is presented. The study is developed for FRP RC cracked rectangular sections.

Assuming an elastic behaviour and that the Bernoulli hypothesis is satisfied, the curvature of a cracked section κ_{cr} is:

$$\kappa_{cr} = \frac{\varepsilon_c}{x} \tag{6-1}$$

where ε_c is the maximum concrete strain at the cracked section and x is the distance from the top surface to the neutral axis under the fully cracked condition (Figure 6-1).
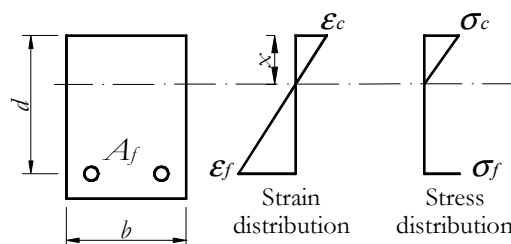
Figure 6-1. Strain and stress distribution at a cracked section at the serviceability conditions

When σ_c arrives to $0.45f_{ck}$, Eq. (6-1) can be rewritten as:

$$\kappa_{cr} = 0.45 \frac{f_{ck}}{E_c} \frac{1/d}{x/d} \tag{6-2}$$

where x/d is a dimensionless parameter that, in the absence of compression reinforcement, only depends on the modular ratio $n = E_f / E_c$ and the reinforcement ratio ρ:

$$x/d = n\rho \cdot \left(-1 + \sqrt{1 + \frac{2}{n\rho}} \right) \tag{6-3}$$

Alternatively, the curvature of a cracked cross-section defined in Eq. (6-1) can be written as the flexural moment divided by the stiffness of the cracked section as:

$$\kappa_{cr} = \frac{M}{E_c I_{cr}} \tag{6-4}$$

in which M is the applied moment, E_c is the concrete modulus of elasticity, and I_{cr} is the moment of inertia of the cracked section, calculated by:

$$I_{cr} = d^2 \cdot \left(\frac{1}{3} bd(x/d)^3 + nA_f \cdot (1 - x/d)^2 \right) \tag{6-5}$$

The dimensionless relationship between the applied moment M and the cracking moment M_{cr} is then rewritten as:

$$\frac{M}{M_{cr}} = \kappa_{cr} \frac{E_c}{f_{ct}} \frac{I_{cr}}{W} \tag{6-6}$$

being f_{ct} the concrete tensile strength and W the section modulus of the uncracked section, this in a simplified way can be assessed as the modulus of the concrete gross section:

$$W \approx W_g = \frac{1}{6} bh^2 \tag{6-7}$$

Therefore, the ratio I_{cr}/W can be simplified to:

$$\frac{I_{cr}}{W} = d \cdot (d/h)^2 \cdot \left(2(x/d)^3 + 6n\rho \cdot (1 - x/d)^2 \right) \tag{6-8}$$

Substituting Eqs. (6-2) and (6-8) into Eq. (6-6), the dimensionless service moment ratio M_s/M_{cr} is:

$$\frac{M_s}{M_{cr}} = \frac{0.45 f_{ck}}{f_{ct}} \cdot \frac{A}{(x/d)} \tag{6-9}$$

where A is a dimensionless parameter defined as:

$$A = (d/h)^2 \left(2(x/d)^3 + 6n\rho \cdot (1 - x/d)^2 \right) \tag{6-10}$$

It is concluded that the dimensionless service moment ratio M_s/M_{cr} is only governed by the concrete compressive and tensile strengths, $n\rho$ (modular ratio times reinforcement ratio) and the effective depth to overall height ratio d/h.

Figure 6-2 depicts M_s/M_{cr} depending on the reinforcement ratio ρ, for different concrete mechanical properties (f_{ck}, E_c), rebar modulus of elasticity E_f and d/h ratios. Figure 6-2a represents a typical case where d/h is 0.8 and Figure 6-2b a case where f_{ck} is 45 MPa and E_f is 80 GPa. In this study, the tensile strength f_{ct} and the modulus of elasticity E_c are calculated according to CEN (2004) formulation for a given concrete compressive strength f_{ck}. It is shown in Figure 6-2 that M_s/M_{cr} increases with ρ, f_c, E_f and d/h and, for the selected reinforcement ratios, its values range between 1 and 4.
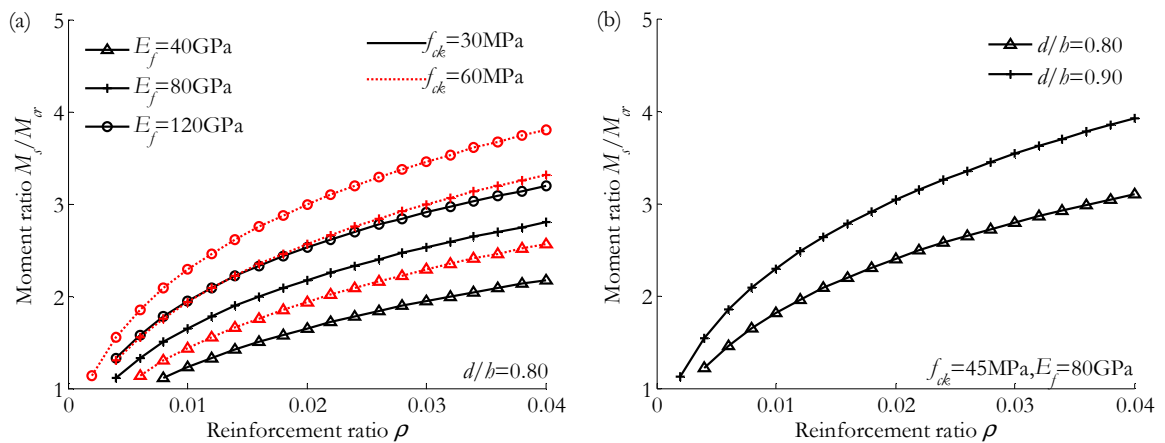
Figure 6-2. M_s/M_{cr} that accomplish $\sigma_c \leq 0.45 f_{ck}$.

Figure 6-2 shows somehow restrictive results of the flexural moment that accomplishes the maximum compressive stress in concrete. For the studied parameters, this service moment would range between 1.2 and 3.8 times the cracking moment. For example, after Figure 6-2b, for $\rho = 0.02$, $f_{ck} = 45$ MPa, $E_f = 80$ GPa and $d/h = 0.80$, the maximum flexural moment that accomplishes this condition is of 2.4 times the cracking moment. For the correct interpretation of this value, two assumptions shall be taken into account. First, this limitation corresponds to the quasi-permanent loading condition, which is only part of the characteristic service load. If only a portion of the service load is sustained, then the full service load corresponding to limiting the concrete stress to $0.45f_{ck}$ would be higher. Second, the concrete stress is usually limited to assume linear creep and to avoid longitudinal cracks that may lead to a reduction in durability. For concrete sections reinforced with FRPs, where durability may not be a concern, this limitation could be relaxed depending on the requirements of the structure and the accuracy on the estimation of creep effects.

On the other hand, the tensile strain developed in the reinforcement at the cracked section ε_f is also a useful parameter of design when considering the SLS (Newhooh et al. 2002). This parameter can be easily calculated considering the hypothesis that the concrete stress may be less than $0.45 f_{ck}$ and fully cracked section:

$$\varepsilon_f = \frac{0.45 f_{ck}}{E_c} \cdot \frac{1 - x/d}{x/d} \qquad (6\text{-}11)$$

Figure 6-3 represents the maximum value of ε_f that fulfils the condition $\sigma_c \leq 0.45 f_{ck}$ depending on ρ, for different concrete mechanical characteristics (f_{ck}, E_c) and rebar modulus of elasticity E_f.
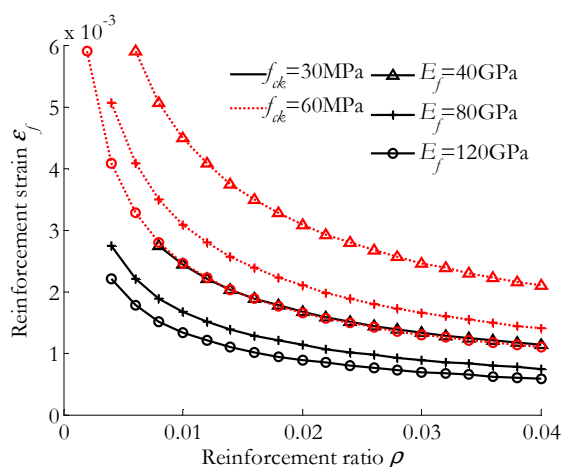
Figure 6-3. ε_f that accomplish $\sigma_c \leq 0.45 f_{ck}$.

It is observed that ε_f decreases with ρ, f_{ck}, and E_f. For low values of ρ, the allowable value of ε_f increases up to 3000-6000 $\mu\varepsilon$ and it descends to 600-3000 $\mu\varepsilon$ as ρ increases.

Stresses in the FRP reinforcement

The stress in the FRP reinforcement should be limited to avoid creep rupture or stress corrosion. Stress corrosion related problems are only significant, however, when using glass fibre reinforced composites. Different strength reduction factors are proposed in existing design documents to determine the appropriate limits depending on the different types of FRP reinforcement (see Table 2-2). On the other hand, FRP bars present high variability in their mechanical properties (modulus of elasticity and tensile strength). This variability makes difficult to establish a general limitation of stresses in FRP reinforcements.

ACI 440.1R-06, for example, proposes a stress limit of 0.20 the tensile strength of the reinforcement for the quasi-permanent loading condition. For the case of the GFRP bars used in the experimental program, with a modulus of elasticity of 60 GPa and a nominal tensile strength f_{fu} of 1000 MPa, the maximum allowable tensile strain for the permanent load in the reinforcement according to ACI 440.1R-06 would be 3333 $\mu\varepsilon$. Figure 6-4 shows this

requirement compared to the maximum compressive stress in concrete limitation. As shown, the limitation of stresses in FRP is more restrictive than the compressive stresses in concrete for a combination of low reinforcement ratios and high concrete strengths. For the rest of cases, the maximum compressive stress in concrete limitation results more restrictive than the stresses in FRP.
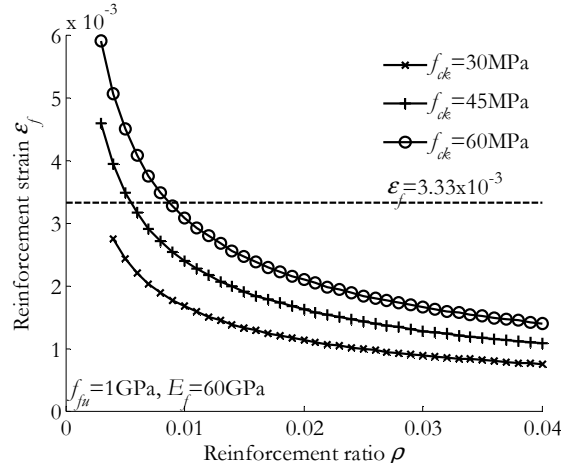
Figure 6-4. ε_f for tensile stress limitation of FRP compared with compressive stress limitation of concrete.

The stress limitation provided by ACI 440.1R-06 is compared to fib procedure (fib 2007), which results less restrictive, in the following. The tested bars present, according to the manufacturer, a characteristic short-term strength f_{fk0} of 1100 MPa, and a residual strength at 1000 hours f_{fk1000} of 1000 MPa. The standard reduction in strength per logarithmic decade is R_{10} of 18%, giving an environmental strength reduction factor $\eta_{env,t}$ of:

$$\eta_{env,t} = \frac{f_{fk1000h}}{f_{fk0}\left(\dfrac{100-R_{10}}{100}\right)^n} = \frac{1000 \text{ MPa}}{1100 \text{ MPa}\left(\dfrac{100-18}{1000}\right)^n} \tag{6-12}$$

where n varies from 2 to 4, for environments with a mean annual temperature varying from 10 to 30ºC, for a service life of 100 years and considering different moisture conditions. The resultant values of $\eta_{env,t}$ range between 1.35 and 2.01. Taking into account a material factor γ_f of 1.25, the resulting tensile strength is calculated as follows:

$$f_{fd} = \frac{f_{fk0}}{\eta_{env,t}\gamma_f} = \frac{1000 \text{ MPa}}{\eta_{env,t}1.25} \tag{6-13}$$

giving as a result a design tensile strength of 398-593 MPa. This gives a maximum tensile strain in the reinforcement of 6633-9883 $\mu\varepsilon$. In Figure 6-4, this limitation would be out-of-scale and the stresses in concrete would result more restrictive for all the considered cases.

As it is observed, significant differences are found in design codes to limit the stress in the FRP reinforcement in order to avoid creep rupture or stress corrosion. Hence, further studies would be needed to arrive to a more generalised conclusion, since this limitation highly depends on the FRP rebar properties (which are improving continuously owing to the rapid advances in manufacturing technology), the environmental conditions and the loading period. For these reasons, this limitation is excluded from this study.

6.2.2. Maximum crack width

In general, cracking in RC elements is controlled to ensure adequate structural performance as well as sufficient durability of the structure (CEN 2004). When FRPs are used as internal reinforcement, greater crack widths are likely to occur; nevertheless, as superior durability is expected from FRP RC elements, crack width limits could be relaxed in those cases where aesthetic appearance is not of primary concern.

On the basis of the above considerations, all the aspects of design that have a direct effect on the overall cracking behaviour of FRP RC elements, such as the minimum reinforcement area, maximum bar diameter or bar spacing, should be re-assessed to account for the mechanical and physical properties of FRPs, which are responsible of their unique bond behaviour.

Usually, crack width is limited by establishing an upper bound value such as 0.5 mm for interior exposures and 0.7 mm for exterior exposures (ACI 440.1R-06). Other approaches, however, limit the value of the tensile stress at the reinforcement to control the crack width. In the design of steel RC, the value of steel stress f_s at service loads is typically taken as 60% f_y (being f_y the reinforcement yielding strength) in crack control calculations, and the corresponding steel strain for this stress is 1200 $\mu\epsilon$. When GFRP are used as internal reinforcement an upper limit on bar strain equal to 2000 $\mu\epsilon$ is used to limit crack widths (ISIS Canada 2001; Newhook et al. 2002).

In this section, a formulation to calculate the maximum dimensionless service moment M_s/M_{cr} considering a crack width limitation of 0.5 mm (ACI Committee 440 2006) is developed. The value of the tensile reinforcement strain at a cracked section corresponding to M_s/M_{cr} is also provided.

First, the maximum crack width at the service moment is evaluated following the formulation of Eurocode 2 (CEN 1992) and CNR-DT-203 (2006):

$$w_k = \beta \cdot s_{rm} \cdot \varepsilon_{fm} \tag{6-14}$$

where w_k is the design crack width, s_{rm} is the average final crack spacing, ε_{fm} is the mean strain allowing under the relevant combination of loads for the effects of tension stiffening, shrinkage, etc, and β is a coefficient relating the average crack width to the design value. In this study, the value of β is taken as 1.7, corresponding to a case of a load induced cracking or

restrained cracking in sections with a minimum dimension in excess of 800 mm. The mean crack width w is therefore defined as the design crack width divided by the coefficient β:

$$w = w_k / \beta \tag{6-15}$$

The mean strain at the reinforcement ε_{fm} may be calculated from the relation:

$$\varepsilon_{fm} = \varepsilon_f \left(1 - \beta_1 \beta_2 \left(\frac{M_{cr}}{M_a} \right)^2 \right) \tag{6-16}$$

where ε_f is the strain in the tension reinforcement calculated on the basis of a cracked section, β_1 is 1.0 for high bond and 0.5 for plain bars, β_2 is 1.0 for single, short-term loading and 0.5 for sustained loads, M_{cr} is the cracking moment and M_a is the applied moment. In this study, the applied moment is the service moment M_s.

The average final crack spacing for members subjected dominantly to flexure or tension can be calculated from the equation:

$$s_{rm} = 50 + 0.25 \cdot k_1 \cdot k_2 \frac{\phi}{\rho_{eff}} \tag{6-17}$$

where ϕ is the bar size in mm, k_1 a bond coefficient, being 0.8 for high bond bars and 1.6 for plain bars, k_2 is 0.5 for bending and 1.0 for pure tension and ρ_{eff} is the effective reinforcement ratio, defined in Eq. (6-18), where A_f is the area of the reinforcement contained within the effective tension area, $A_{c,eff}$. In this study, the effective height of concrete surrounding the reinforcement has been considered equal to 2.5 times the distance from the tension face of the section to the centroid of the reinforcement.

$$\rho_{eff} = \frac{A_f}{A_{c,eff}} = \frac{A_f}{b \cdot 2.5(h-d)} = \frac{\rho}{2.5\left((d/h)^{-1} - 1\right)} \tag{6-18}$$

Considering $k_2 = 0.5$ (CNR-DT-203 2006), the average crack spacing s_{rm} can be written as:

$$s_{rm} = 50 + 0.3125 \cdot k_1 \frac{\phi}{\rho} \left((d/h)^{-1} - 1\right) \tag{6-19}$$

Figure 6-5 depicts s_{rm} depending on the ρ for different cases of ϕ, d/h and bond characteristics. The crack spacing increases with ϕ, and decreases with the ρ and d/h. The crack spacing decreases as the bond behaviour increases.
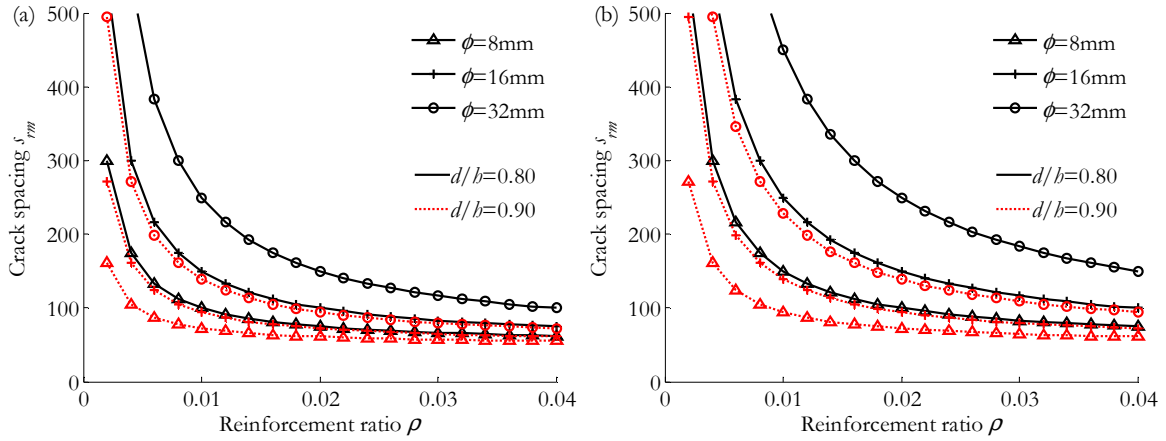
Figure 6-5. Crack spacing s_{rm} versus ρ for different ϕ, and d/h ratios. Assumptions: $w_k = 0.5$ mm long-term loading, $f_{ck} = 45$ MPa, $E_f = 80$ GPa, (a) high bond, (b) low bond.

The strain at the tension reinforcement ε_f calculated on the basis of a cracked section is derived from Eqs. (6-14) and (6-16):

$$\varepsilon_f \left(1 - \beta_1 \beta_2 \left(\frac{M_{cr}}{M_s} \right)^2 \right) = \frac{w}{s_{rm}} \tag{6-20}$$

The service moment M_s is derived from the curvature of the cracked section:

$$\kappa_{cr} = \frac{M_s}{E_c I_{cr}} = \frac{\varepsilon_f}{d - x} \tag{6-21}$$

Rearranging terms in Eq. (6-21), M_s is calculated by Eq. (6-22) and this moment related to the cracking moment M_{cr} is calculated by Eq.(6-23), which derives to Eq.(6-24):

$$M_s = \varepsilon_f \frac{1/d}{1 - x/d} E_c I_{cr} \tag{6-22}$$

$$\frac{M_s}{M_{cr}} = \kappa_{cr} \frac{E_c}{f_{ct}} \frac{I_{cr}}{W_g} \tag{6-23}$$

$$\frac{M_s}{M_{cr}} = \varepsilon_f \frac{E_c}{f_{ct}} \cdot \frac{A}{(1 - x/d)} \tag{6-24}$$

where A is the dimensionless parameter defined in Eq.(6-10). From Eqs. (6-20) and (6-24), the dimensionless moment ratio M_s/M_{cr} is:

$$\frac{M_s}{M_{cr}} = \frac{w/s_{rm} + \sqrt{(w/s_{rm})^2 + 4\beta_1 \beta_2 (f_{ct}/E_c)^2 \left(\frac{1 - x/d}{A} \right)^2}}{2 f_{ct} (1 - x/d)/(E_c \cdot A)} \tag{6-25}$$

The tensile strain at the reinforcement at a cracked section is also related to the same parameters, and by substituting Eq. (6-20) into Eq. (6-24), ε_f is calculated as:

$$\varepsilon_f = \frac{w/s_{rm} + \sqrt{(w/s_{rm})^2 + 4\beta_1\beta_2(f_{ct}/E_c)^2\left(\frac{1-x/d}{A}\right)^2}}{2} \tag{6-26}$$

Eqs. (6-25) and (6-26) allow calculating M_s/M_{cr} once the maximum permitted crack width w_k is set, depending on d/h, ρ, E_f, ϕ, the bond properties between the rebar and the concrete, the duration of the load, and the concrete mechanical properties E_c and f_{ct}.

The influence of these parameters on M_s/M_{cr} and its corresponding tensile strain at the reinforcement ε_f is represented in Figure 6-6 and Figure 6-7 respectively, for a maximum crack width w_k of 0.5 mm, assuming high bond properties and long-term loading.
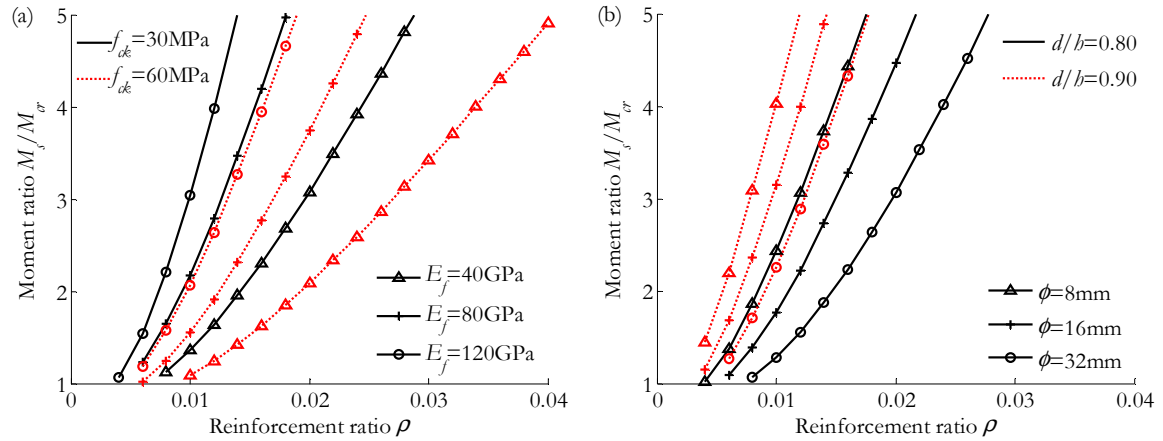
Figure 6-6. M_s/M_{cr} versus ρ for different f_{ck}, d/h, ϕ and E_f values. Assumptions: w_k = 0.5 mm, high bond, long-term loading, (a) ϕ = 16 mm, d/h = 0.80, (b) f_{ck} = 45 MPa, E_f = 80 GPa.
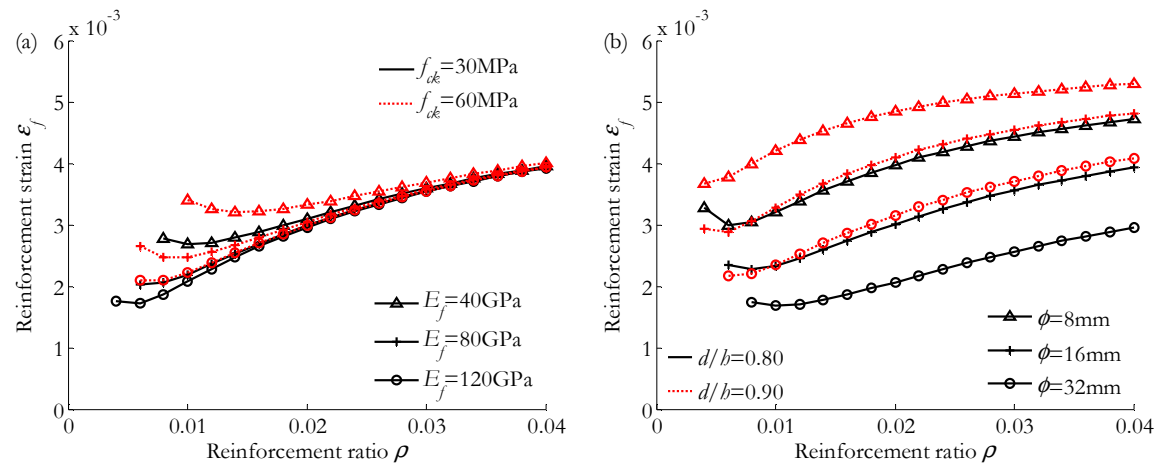
Figure 6-7. ε_f versus ρ for different f_{ck}, d/h, ϕ and E_f values. Assumptions: w_k = 0.5 mm, high bond and long-term loading, (a) ϕ = 16 mm, d/h = 0.80, (b) f_{ck} = 45 MPa, E_f = 80 GPa.

Results in Figure 6-6 show that M_s/M_{cr} clearly increases with the studied parameters ρ, E_f, ϕ, f_{ck} and d/h. The service moment ratio that accomplishes the crack width limitation ranges between 1 for low reinforcement ratios and 22 for the highest considered values (although this value is out-of-scale in Figure 6-6).

According to Figure 6-7, the reinforcement tensile strain ε_f is observed not to be a monotonic function of ρ. For high values of ρ, ε_f increases with d/h and f_{ck} whilst decreases with ϕ, and E_f is of less importance as ρ increases. This trend may be justified by the influence of the crack spacing parameter, which is independent of the moment ratio and shows an exponential decay relationship with the reinforcement ratio (Figure 6-5). For high reinforcement ratios, s_{rm} is relatively small, allowing higher values of ε_f. Moreover, a lower rebar diameter implies higher allowable values of rebar strains to accomplish the maximum target value of w_k. For the considered parameters, ε_f ranges between 1700 and 5300 $\mu\varepsilon$.

In the depicted case of f_{ck} = 45 MPa, E_f = 80 GPa, high bond condition and long-term loading, ε_f can be generally higher than 2000 $\mu\varepsilon$ to obtain maximum values of crack width of 0.5 mm. Only for the combination of ϕ = 32 mm and d/h = 0.80, ε_f shall be lower than 2000 $\mu\varepsilon$ to attain $w_k \leq$ 0.5 mm. Hence, in most cases where high bond is provided, limiting the tensile strain to 2000 $\mu\varepsilon$ to control the crack width (ISIS Canada 2001, Newhook et al. 2002) can lead to an oversizing of the cross-section.

The impact of the bond coefficient in the curves is depicted in Figure 6-8. As expected, better bond allows higher M_s/M_{cr} ratios and higher values of ε_f. For the case of low bond between the concrete and the rebar, the maximum value of ε_f can result lower than 2000 $\mu\varepsilon$ if $E_f \geq$ 80 GPa and ρ < 0.02, where the maximum value of ε_f ranges between 1200 and 2100 $\mu\varepsilon$.
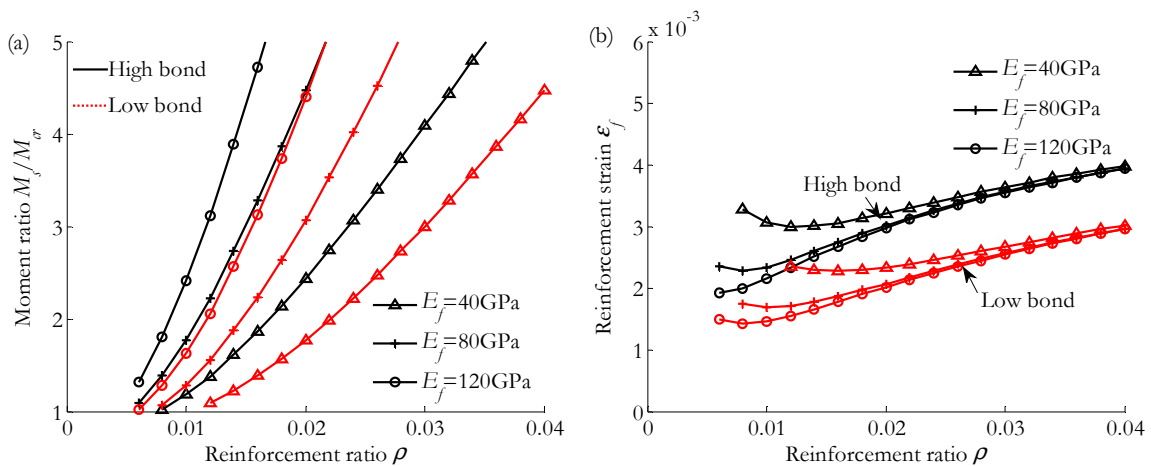
Figure 6-8. M_s/M_{cr} ratio and ε_f for different bond characteristics. Assumptions: w_k = 0.5 mm, long-term loading, f_{ck} = 45 MPa, ϕ = 16 mm, d/h = 0.80.

6.2.3. Serviceability requirements at a cross-section level: comparison between stresses in concrete and maximum crack width limitations

The allowable service moment that accomplishes the serviceability conditions at a cross-section level is found from comparison between the limitation of stresses in materials and from the maximum crack width limitation. The minimum value between these two limitations corresponds to the loading condition that fulfils both serviceability requirements. At the same time, this minimum moment gives the flexural condition that allows calculating the maximum tensile strain at the reinforcement. Both requirements refer to the quasi-permanent loading condition.

Maximum service moment related to the cracking moment

From comparison between Figure 6-2 (M_s/M_{cr} for the stresses in materials limitation) and Figure 6-6 (M_s/M_{cr} for the maximum crack width limitation), a value for the maximum M_s/M_{cr} ratio that fulfils both serviceability requirements can be obtained, assuming the minimum between them, and it is depicted in Figure 6-9.
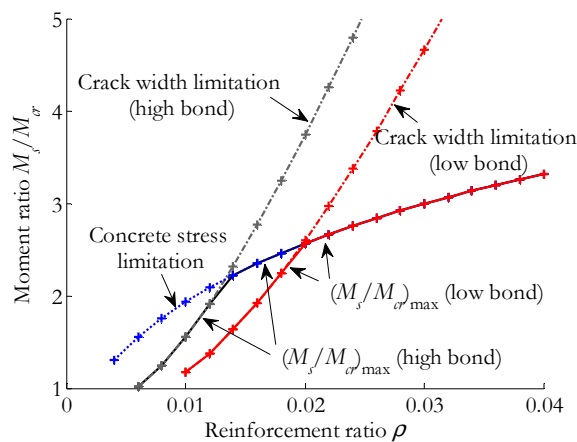
Figure 6-9. Maximum M_s/M_{cr} that accomplishes stresses in materials and maximum crack width limitations. Assumptions: $\sigma_c = 0.45f_{ck}$, $w_k = 0.5$ mm, $\phi = 16$ mm, $d/h = 0.80$, $f_{ck} = 60$ MPa, $E_f = 80$ GPa.

According to Figure 6-9, concrete stress limitation governs the design of FRP RC sections with high reinforcement ratios, whilst for lightly reinforced sections, the design would be governed by the crack width limitation. Furthermore, low bond between the concrete and the rebar results in a shift to the right hand side of the graph of the maximum M_s/M_{cr} ratio from crack width limitation, indicating that if low bond is reported, higher reinforcement ratios are needed for the same mechanical and loading characteristics.

In Figure 6-10 the resultant curves of the maximum M_s/M_{cr} ratio for the range of values considered in this study are shown.
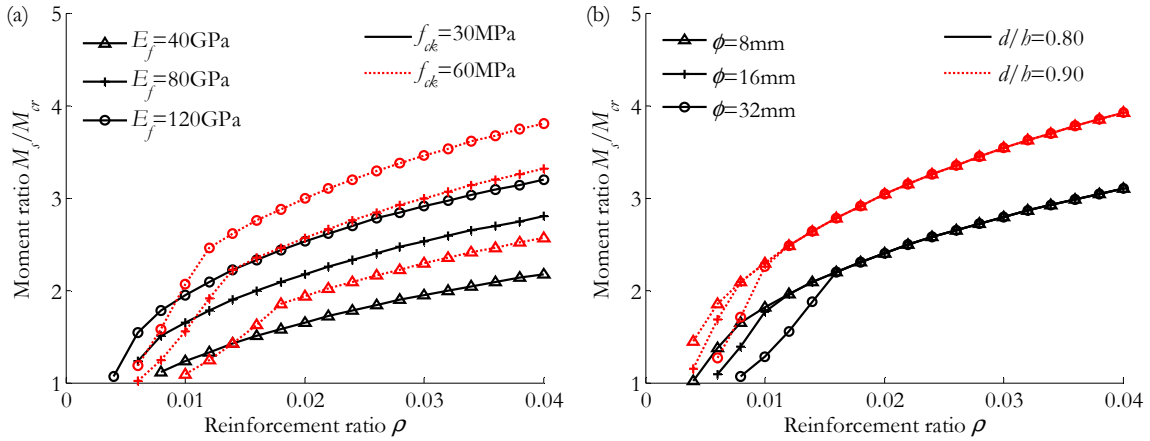
Figure 6-10. Maximum M_s/M_{cr} that accomplishes stresses in materials and maximum crack width limitations. Assumptions: $\sigma_c = 0.45f_c$, $w_k = 0.5$ mm and high bond, (a) $\phi = 16$ mm, $d/h = 0.80$, (b) $f_{ck} = 45$ MPa, $E_f = 80$ GPa.

Maximum service moment related to the ultimate moment

Assuming a typical concrete crushing failure of the section, the service moment related to the ultimate moment M_s/M_u can be found from the M_s/M_{cr} relationship. The service moment related to the ultimate or cracking moment can be defined by the relationship between the reduced flexural moments:

$$\frac{M_s}{M_u} = \frac{\mu_s}{\mu_u} \tag{6-27}$$

$$\frac{M_s}{M_{cr}} = \frac{\mu_s}{\mu_{cr}} \tag{6-28}$$

in which μ_s, μ_{cr} and μ_u are the reduced service, cracking and ultimate moment, respectively. From Eq. (6-27) and (6-32) the ratio service moment to ultimate moment is deduced:

$$\frac{M_s}{M_u} = \frac{M_s}{M_{cr}} \cdot \frac{\mu_{cr}}{\mu_u} \tag{6-29}$$

The reduced cracking moment μ_{cr} is calculated as:

$$\mu_{cr} = \frac{M_{cr}}{f_{cd}bd^2} = \frac{f_{ct}}{6f_{cd}(d/h)^2} \tag{6-30}$$

The reduced ultimate moment μ_u is deduced from equilibrium of forces between the reinforcement and the equivalent stress block of concrete in Figure 6-1. By computing the flexural moment and the axial force in the section, the following equations are deduced:

$$\mu_u = \eta \cdot \lambda \cdot \xi \cdot (1 - 0.5\lambda \cdot \xi) \tag{6-31}$$

$$\rho \frac{E_f}{f_{cd}} = \frac{\eta \cdot \lambda \cdot \xi^2}{\varepsilon_c (1 - \xi)} \tag{6-32}$$

where η is the dimensionless concrete stress σ_c/f_{cd}, ξ is the dimensionless neutral axis depth x/d under ultimate conditions, and λ is the proportional parameter of the concrete stress block.

At failure, and assuming a concrete crushing mode, the parabola-rectangle stress-strain relationship of Eurocode 2 for concrete and an ultimate concrete strain ε_{cu} of 0.35%, Eqs. (6-31) and (6-32) can be rewritten as:

$$\mu_u = 0.8095\xi \cdot (1 - 0.416\xi) \tag{6-33}$$

$$\rho \frac{E_f}{f_{cd}} = \frac{0.8095}{0.0035} \cdot \frac{\xi^2}{1 - \xi} \tag{6-34}$$

and the dimensionless neutral axis depth x/d at ultimate conditions ξ can be calculated as:

$$\xi = \frac{-1 + \sqrt{1 + 924.14 \dfrac{f_{cd}}{\rho E_f}}}{462.57 \dfrac{f_{cd}}{\rho E_f}} \tag{6-35}$$

Figure 6-11 represents the maximum service to ultimate moment ratio M_s/M_u.
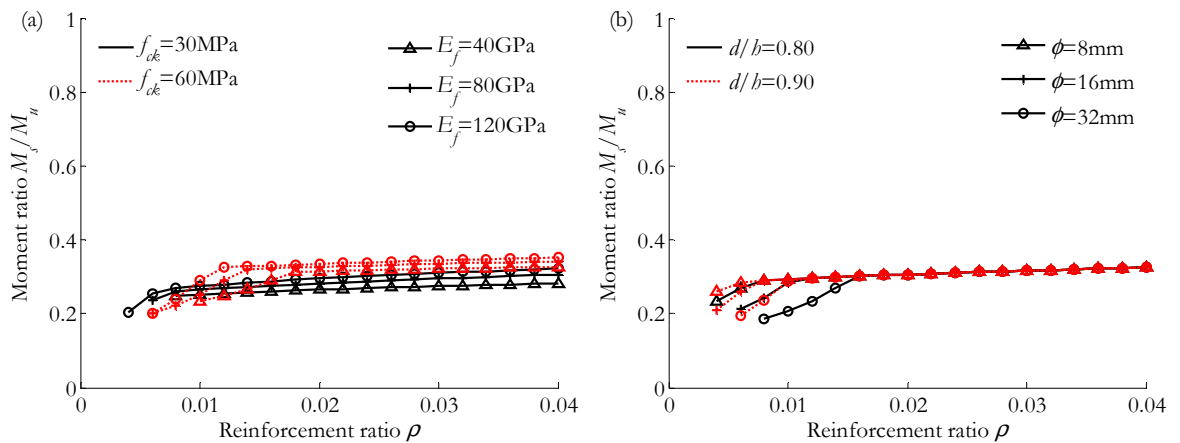
Figure 6-11. Maximum M_s/M_u that accomplishes stresses in materials and maximum crack width limitations. Assumptions: $\sigma_c = 0.45f_{ck}$, $w_k = 0.5$ mm and high bond, (a) $\phi = 16$ mm, $d/h = 0.80$, (b) $f_{ck} = 45$ MPa, $E_f = 80$ GPa.

For the studied range of values, the flexural moment that accomplishes both serviceability limitations varies from 20% to 38% M_u. Bischoff 2005, Ospina and Gross 2005 and Hegger and Kurth 2009 suggested a reference value for the service moment of FRP RC of $0.35M_u$; this value lies within the minimum and maximum of the interval obtained in the present study.

Maximum tensile strain at the reinforcement

Similarly, the maximum tensile strain at the reinforcement can be determined from comparison between Figure 6-3 (ε_f for the stresses in materials limitation) and Figure 6-7 (ε_f for the maximum crack width limitation), obtaining results similar to those indicated in Figure 6-12.
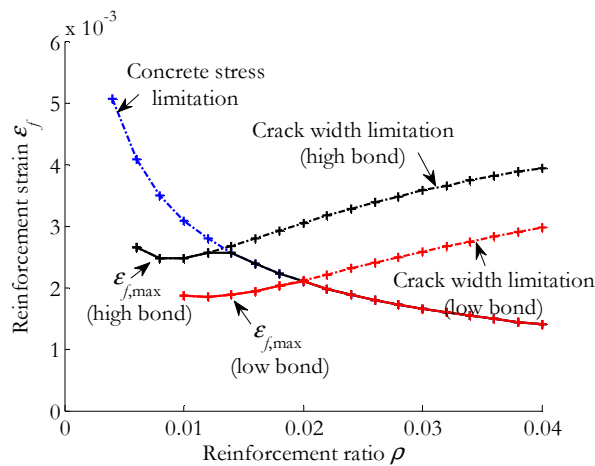
Figure 6-12. Maximum ε_f that accomplishes stresses in materials and maximum crack width limitations. Assumptions: $\sigma_c = 0.45 f_{ck}$, $w_k = 0.5$ mm, $\phi = 16$ mm, $d/h = 0.80$, $f_{ck} = 60$ MPa, $E_f = 80$ GPa.

For low reinforcement ratios, the crack width limitation allows lower values of ε_f than the concrete stress limitation, whilst for sections highly reinforced, the restrictive condition results the concrete stress.

In Figure 6-13 the resultant curves of the maximum values ε_f for the range of parameters considered.
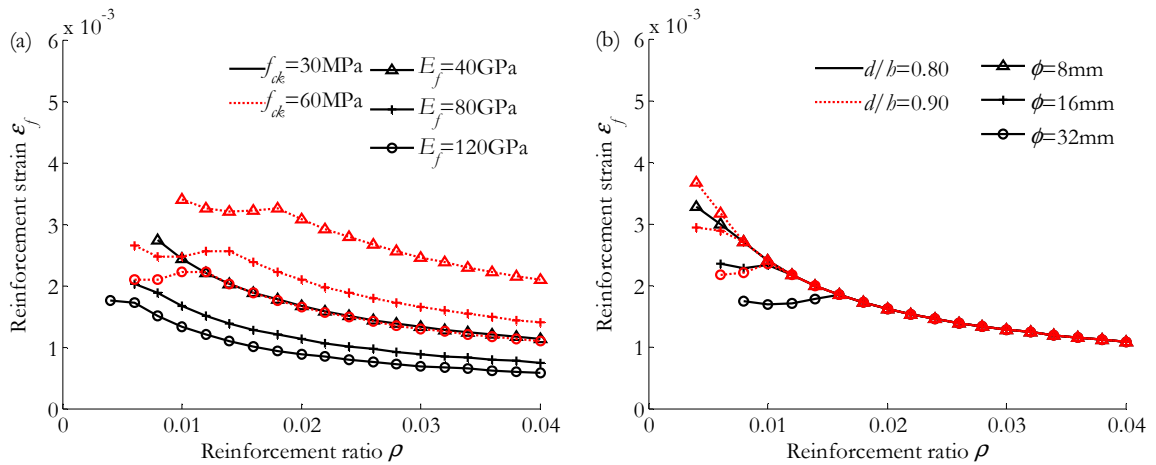
Figure 6-13. Maximum ε_f that accomplishes stresses in materials and maximum crack width limitations. Assumptions: $\sigma_c = 0.45f_{ck}$, $w_k = 0.5$ mm and high bond, (a) $\phi = 16$ mm, $d/h = 0.80$, (b) $f_{ck} = 45$ MPa, $E_f = 80$ GPa.

Maximum service moment related to the cracking moment for a steel RC section

For comparison purposes, the serviceability requirements for a steel RC section are analysed following the same presented methodology and are represented in Figure 6-14. The formulation is slightly changed to account for the usual compressive reinforcement ratio ρ' that steel RC sections present, and Eq. (6-3) is substituted by:

$$x/d = n\rho\left(1+\frac{\rho'}{\rho}\right)\cdot\left(-1+\sqrt{1+\frac{2\left(1+\frac{\rho'}{\rho}\left((d/h)^{-1}-1\right)\right)}{n\rho\left(1+\frac{\rho'}{\rho}\right)^2}}\right) \tag{6-36}$$

The results are evaluated up to a maximum reinforcement ratio of 0.02 to adequate them to the usual values of ρ for steel RC, and the target maximum crack width is lowered to 0.4 mm according to the normal design values. In addition, high bond is assumed between the concrete and the rebar and a concrete grade of 30 MPa is evaluated.

Results in Figure 6-14 show that for the same reinforcement ratio, the allowable service moment for a steel RC section to accomplish these two serviceability requirements is higher than the one obtained for a FRP RC, as expected due to the higher modulus of elasticity of steel compared to FRPs. Furthermore, the compressive reinforcement ratio eventually leads to higher service moments. Finally, similarly to in a FRP RC section, for high reinforcement ratios, the predominant limitation is the concrete stress rather than the maximum crack width.
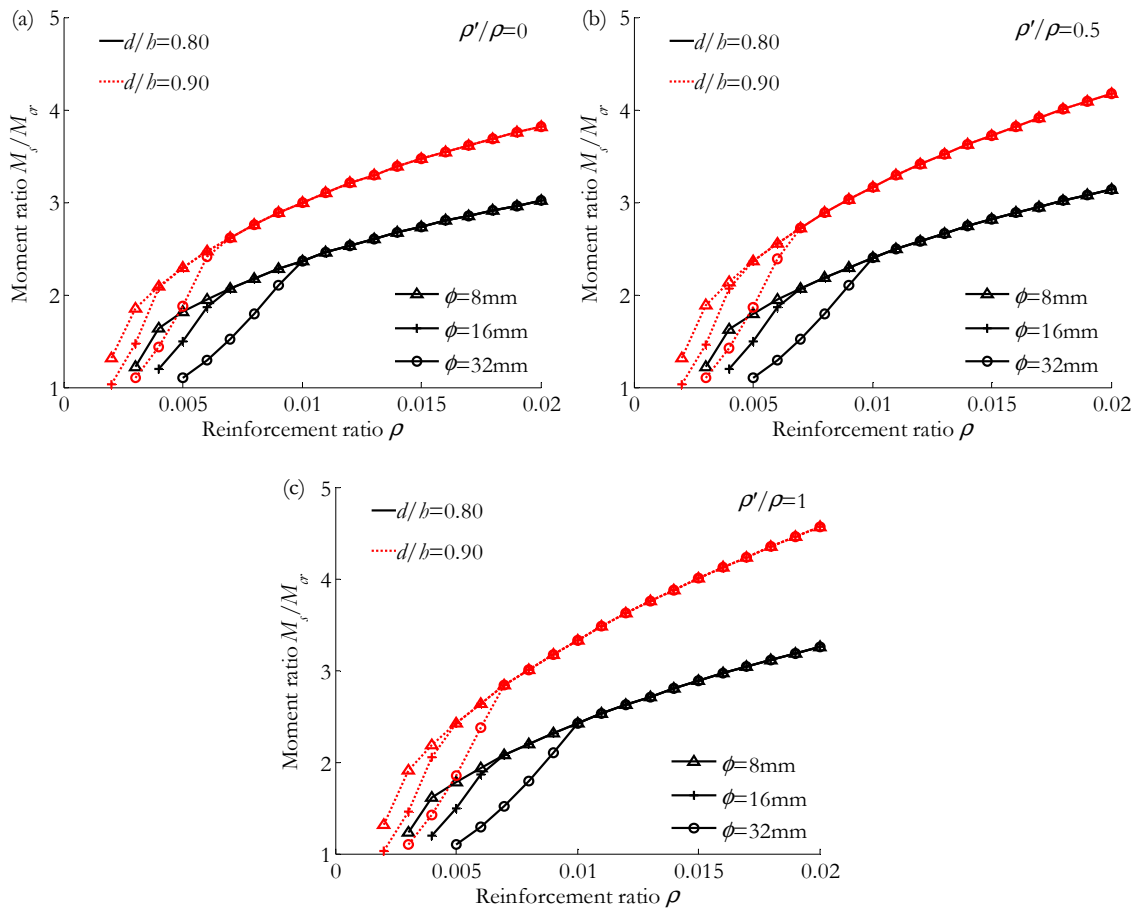
Figure 6-14. Maximum M_s/M_{cr} that accomplishes stresses in materials and maximum crack width limitations for a steel RC section. Assumptions: $\sigma_c = 0.45f_{ck}$, $w_k = 0.4$ mm, high bond, $f_{ck} = 30$ MPa, $E_s = 200$ GPa.

6.2.4. Deflection limitation and slenderness limits

The deformation of a RC member or structure is usually limited so as not to be such that it adversely affects its proper functioning or appearance. Appropriate limiting values of deflection taking into account the nature of the structure, of the finishes, partitions and fixings and upon the function of the structure should be established. Eurocode 2, for example, limits the sag of a beam, slab or cantilever subjected to quasi-permanent loads to span/250 not to impair the appearance and general utility of the structure.

The low stiffness of FRP reinforcement always results in the larger deflections of FRP RC elements in comparison to equivalent concrete elements reinforced with conventional steel reinforcement. As a result, required amounts of flexural reinforcement and initial element sizing, in terms of recommended span to depth ratios, have to be re-examined in the light of the above considerations.

Codes of practice usually propose a slenderness limitation to avoid calculation of deflections. In this section, a general formulation to calculate the slenderness limitation for FRP RC elements is suggested. This formulation is based on the instantaneous deflection proposed in Eurocode 2. For the sake of simplicity, a simplified procedure based on a multiplicative coefficient for FRP RC taken from ACI 440 is used for the calculation of long-term deflections. As a result, an L/d ratio is proposed for simply-supported beams at a service moment ratio.

Instantaneous deflection

The flexural deflection of a RC beam can be computed, according to Eurocode 2 (CEN 1992), from interpolation of deflections as:

$$\delta = \delta_2 \zeta + \delta_1 (1 - \zeta) \tag{6-37}$$

$$\zeta = 1 - \beta_1 \beta_2 \left(\frac{\sigma_{fr}}{\sigma_f} \right)^2 \tag{6-38}$$

where δ_1 is the deflection under the uncracked condition, δ_2 is the deflection under the fully cracked condition and ζ is a distribution coefficient defined in Eq. (6-38), being β_1 and β_2 the factors described in Eq. (6-16) and the ratio σ_{fr}/σ_f is equivalent to M_{cr}/M_a for flexure. Rearranging terms, Eq. (6-37) leads to the following expression:

$$\delta = \delta_1 \beta_1 \beta_2 \left(\frac{M_{cr}}{M_a} \right)^2 + \delta_2 \left(1 - \beta_1 \beta_2 \left(\frac{M_{cr}}{M_a} \right)^2 \right) \tag{6-39}$$

The generalized elastic equation for midspan deflection can be expressed depending on the curvature of the midspan section κ_i and the overall length as follows:

$$\delta_i = K_1 K_2 \kappa_i L^2 \tag{6-40}$$

where K_1 is the coefficient related to the loading condition, being 5/48 for uniform load or 23/216 for four-point loading with loads applied at $L/3$ and K_2 is the beam deflection coefficient depending on the boundary and loading conditions:

$$K_2 = 1.2 - 0.2 \frac{M_0}{M_m} \tag{6-41}$$

where M_0 is the total static moment and M_m refers to the moment at midspan. For uniform loading, $K_2 = 1$ for simply supported spans, $K_2 = 0.8$ for fixed-hinged beams and $K_2 = 1.6$ for fixed-fixed beams.

The uncracked and cracked curvatures of the midspan section can be calculated by Eq. (6-42) and (6-4), respectively.

$$\kappa_1 = \frac{M_s}{E_c I_g} = \frac{M_s}{M_{cr}} \frac{f_{ct}}{E_c} \frac{2}{h} \tag{6-42}$$

Substituting Eqs. (6-42) and (6-4) into Eqs. (6-39) and (6-40), and rearranging terms, the following expression is obtained:

$$\frac{\delta}{L} = \frac{L}{h} K_1 K_2 \left(2\frac{f_{ct}}{E_c}\beta_1\beta_2\left(\frac{M_{cr}}{M_s}\right) + \frac{\varepsilon_f}{d/h\left(1-x/d\right)}\left(1-\beta_1\beta_2\left(\frac{M_{cr}}{M_s}\right)^2\right)\right) \tag{6-43}$$

If the ratio δ/L is limited to $1/250$, the following expression is found for the L/d ratio:

$$\frac{L}{d} \leq \frac{1}{250K_1K_2}\left(d/h\right)^{-1}\left(2\frac{f_{ct}}{E_c}\beta_1\beta_2\left(\frac{M_s}{M_{cr}}\right)^{-1} + \frac{\varepsilon_f}{d/h\left(1-x/d\right)}\left(1-\beta_1\beta_2\left(\frac{M_s}{M_{cr}}\right)^{-2}\right)\right)^{-1} \tag{6-44}$$

The resulting L/d ratio depends on d/h, ρ, E_f, the bond properties between the rebar and the concrete, the duration of the load, the concrete mechanical properties E_c and f_{ct} and the dimensionless service moment related to the cracking moment M_s/M_{cr}, and its corresponding tensile strain ε_f at a cracked section.

Long-term deflection

The long-term deflection can be computed following different procedures with different degrees of complexity. One of the most simple and wide-spread procedures, adopted by ACI 318R-05 and EHE (2008) for the calculation of deflections for steel RC elements, consists of applying multiplicative coefficients to the instantaneous deflection. For the case of FRP RC, ACI 440.1R-06 proposes a reduction coefficient of 0.6, to be applied on the multiplicative coefficient used for steel RC elements.

In this study, FRP RC elements are supposed to support non structural elements not likely to be damaged by large deflections. For this case ACI 318R-05 limits the deflection to $L/240$, whilst Eurocode 2 states that other limits than $L/500$ may be considered, depending on the sensitivity of adjacent parts. In the following, for simplicity and comparative reasons, the long-term deflection δ_{LT} after construction of adjacent parts under the quasi-permanent loading condition is limited to $L/250$. However, the present formulation allows changing this limit if different cases are to be considered.

$$\delta_{LT} = (\delta_i)_Q + \lambda\left[(\delta_i)_G + \psi(\delta_i)_Q\right] = (\delta_i)_Q + \lambda(\delta_i)_{QP} \tag{6-45}$$

In Eq. (6-45), $(\delta)_Q$ is the instantaneous deflection of the variable loads, $(\delta)_G$ is the instantaneous deflection of the permanent loads, $(\delta)_{QP}$ is the instantaneous deflection of the quasi-permanent loads, ψ is the coefficient for the quasi-permanent value of the variable action (adopted 0.2 in this study) and λ is the factor to take into account the long-term deflection, defined in Eq. (6-46) for FRP RC elements following ACI 440.1R-06 recommendations:

$$\lambda = 0.6\xi \qquad (6\text{-}46)$$

where ξ is the multiplicative coefficient that takes into account creep and shrinkage. According to ACI318, $\xi = 2$ for a duration of load higher than 5 years.

The instantaneous deflection due to the variable loads is defined as a portion of the quasi-permanent deflection $(\delta_i)_{QP}$ as:

$$(\delta_i)_Q = r_{QP} \cdot (\delta_i)_{QP} \qquad (6\text{-}47)$$

$$r_{QP} = \frac{q_Q}{q_{QP}} = \frac{q_Q}{q_G + \psi q_Q} \qquad (6\text{-}48)$$

being q_Q is the variable load, q_G is the permanent load and q_{QP} is the quasi-permanent load. Hence, the relationship between the instantaneous and the long-term deflections can be defined as:

$$\delta_{LT} = (\delta_i)_{QP}\left(r_{QP} + \lambda\right) \qquad (6\text{-}49)$$

Considering δ_{LT}/L equal to 1/250, the following relationship is obtained for the instantaneous deflection:

$$\frac{(\delta_i)_{QP}}{L} = \frac{1}{250\left(r_{QP} + \lambda\right)} = \frac{1}{K_3} \qquad (6\text{-}52)$$

where K_3 is the coefficient that considers the deflection limitation (for the case of Eq. (6-52), δ_{LT}/L equals to 1/250) and the relationship between the instantaneous and the long-term deflection .

Consequently, the L/d ratio that limits the long-term deflection to $L/250$ is derived from Eqs. (6-43) and (6-52):

$$\frac{L}{d} \le \frac{1}{K_1 K_2 K_3}(d/h)^{-1}\left(2\frac{f_{ct}}{E_c}\beta_1\beta_2\left(\frac{M_s}{M_{cr}}\right)^{-1} + \frac{\varepsilon_f}{d/h(1-x/d)}\left(1-\beta_1\beta_2\left(\frac{M_s}{M_{cr}}\right)^{-2}\right)\right)^{-1} \quad (6\text{-}53)$$

$$K_3 = 250(r_{QP} + \lambda) \quad (6\text{-}54)$$

If other limits different from limiting the long-term deflection to $L/250$ want to be considered, K_3 should be changed accordingly.

Slenderness limitation at a service moment ratio

Expression (6-53) needs to be evaluated at a certain service moment ratio M_s/M_{cr}. The service moment M_s, calculated under the quasi-permanent loading condition, can be typically computed as a ratio of the ultimate moment M_u, depending on the percentage of moment derived from the permanent and variable loads:

$$M_u = \gamma_G M_G + \gamma_Q M_Q \quad (6\text{-}55)$$

$$M_s = M_G + \psi M_Q \quad (6\text{-}56)$$

where M_G is the flexural moment at a cross-section obtained from the permanent loads, M_Q is the obtained moment from the variable loads and γ_G and γ_Q are the partial factors for the permanent and variable loads respectively. Typical values for γ_G and γ_Q are 1.35 and 1.5 (CEN 2004). From Eqs. (6-55) and (6-56), M_s/M_u can be calculated as:

$$M_s/M_u = \frac{r + \psi(1-r)}{\gamma_G r + \gamma_Q(1-r)} \quad (6\text{-}57)$$

$$r = \frac{q_Q}{q_G + q_Q} \quad (6\text{-}58)$$

For a typical case where $r = 0.6$ and $\psi = 0.2$, the service moment is $M_s = 0.48M_u$ and the resultant L/d for a simply supported beam subjected to a uniform load ($K_1 = 5/48$, $K_2 = 1$) is depicted in Figure 6-15.

For the range of parameters considered in this study, the L/d ratio would arrive up to 15 for highly reinforced beams with low concrete strengths and high rebar modulus of elasticity. The L/d ratio only depends on ρ, f_{ck} and E_f. The influence of d/h, the bond coefficient β_1 and the time-loading coefficient β_2 result insignificant on the L/d response.
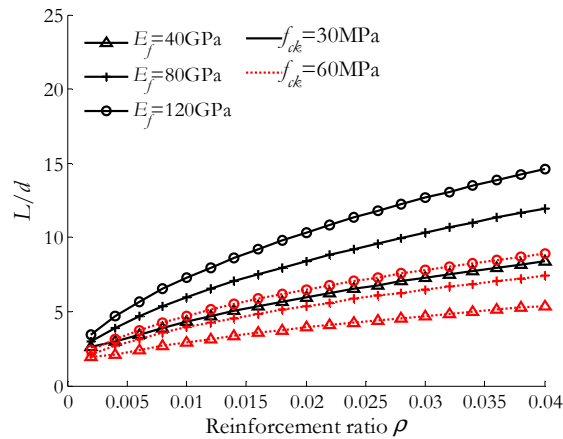
Figure 6-15. L/d at the service moment calculated as a ratio of the ultimate moment. Assumptions: $\delta_{LT} = L/250$, $K_1 = 5/48$, $K_2 = 1$, $r = 0.6$, $\psi = 0.2$, $d/h = 0.80$.

Results show that the allowable L/d ratio increases as ρ increases, which is the opposite behaviour of what is typically reported for steel RC (CEN 2004, Narayanan and Goodchild 2006, Vollum 2009, Corres et al. 2003) for a given M_s/M_u. The different design criterion for FRP RC (concrete failure instead of yielding of the steel reinforcement) and the low modulus of elasticity of the FRP rebars may explain this phenomenon. Moreover, the higher E_f, the higher allowable L/d ratio, whilst low values of f_{ck} allow higher L/d ratios.

Expression (6-53) can be applied to the conditions established in Ospina and Gross (2005) to calculate the instantaneous deflection and to compare the resultant slenderness limitations, in terms of L/h ratios. The results are depicted in Figure 6-16, and are compared to those proposed by Ospina and Gross (2005), taking into account the tension stiffening effect (Eq. (2-88)) and without considering the tension stiffening (Eq. (2-86)).
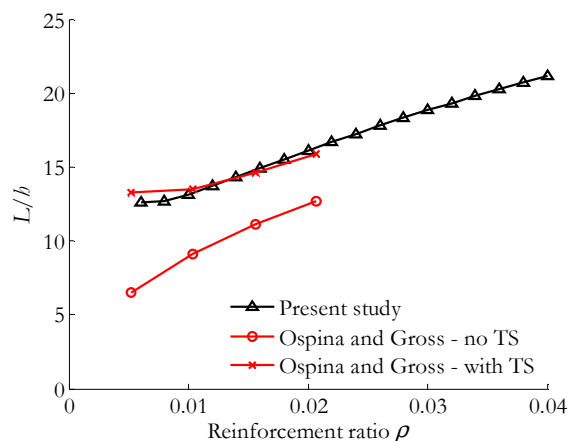
Figure 6-16. L/h ratios obtained by the present study compared with the proposed by Ospina and Gross (2005). Assumptions: $f_{ck} = 34.47$ MPa, $E_c = 27793$ MPa, $E_f = 41369$ MPa, $d/h = 0.90$, $M_s/M_u = 0.30$, $\delta_{inst} = L/240$, $K_1 = 5/48$, $K_2 = 1$, $\beta_1 = 1$, $\beta_2 = 1$.

From results in Figure 6-16, it is observed that the formulation presented in this work, based on Eurocode 2 model for calculating deflections, fits adequately the slenderness limitation proposed by Ospina and Gross (2005) taking into account the tension stiffening effect.

6.3. Methodology for the design of FRP RC elements under serviceability conditions

The present section proposes a methodology for the design of FRP RC elements under the SLS. This procedure gives as a result the optimal dimensions of a cross-section that accomplishes simultaneously the SLS. The considered SLS are the stress limitation, the crack width limitation and the deflection requirements. The methodology is valid for rectangular cracked sections designed for a concrete crushing failure that do not have compression reinforcement. First, the moment ratio at which deflections shall be evaluated is exposed and second the design methodology is shown.

6.3.1. Moment ratio to evaluate deflections

Equation (6-53), which provides the L/d condition that fulfils the deflection limitation, is associated to a loading situation (M_s/M_{cr} or M_s/M_u). Depending on the adopted moment ratio at which to evaluate the deflection, different L/d values will be obtained. The moment ratio is usually considered as a percentage of the ultimate moment. For example, Ospina and Gross (2005) consider a moment ratio M_s/M_u of 0.30 and Figure 6-16 shows the resultant L/h ratios for a given situation. However, that moment ratio can be taken as the moment ratio at which the stresses and/or the crack width limitations are fulfilled at a cross-section level. For instance, in Figure 6-17 the L/d ratio at the maximum M_s/M_{cr} ratio to fulfil the limitation of stresses is depicted for a simply-supported FRP RC beam. The beam is supposed to be subjected to uniform loading with $r = 0.6$ and $\psi = 0.2$.
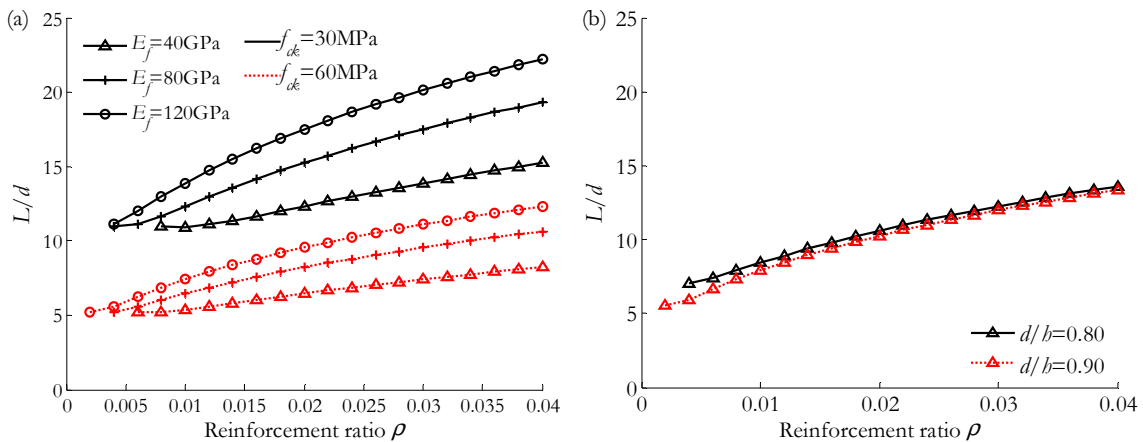
Figure 6-17. L/d ratio versus ρ for different f_{ck}, d/h, ϕ and E_f values. Assumptions: $\delta_{LT}/L = 1/250$, $\sigma_c = 0.45 f_{ck}$, high bond and long-term loading (a) $d/h = 0.80$, (b) $f_{ck} = 45$ MPa, $E_f = 80$ GPa.

For these conditions, it is observed that the L/d ratio increases with ρ and E_f, whilst it decreases with f_{ck}, and does not depend on ϕ while d/h seems of minor importance.

If the L/d ratio wants to be evaluated at the maximum M_s/M_{cr} ratio to fulfil the maximum crack width requirement, Figure 6-18 would be obtained instead. In this case, the beam is subjected to uniform loading with $r = 0.6$, and $\psi = 0.2$. The L/d ratio increases with ϕ, decreases with ρ and d/h, whilst f_{ck} and E_f are parameters of minor importance.
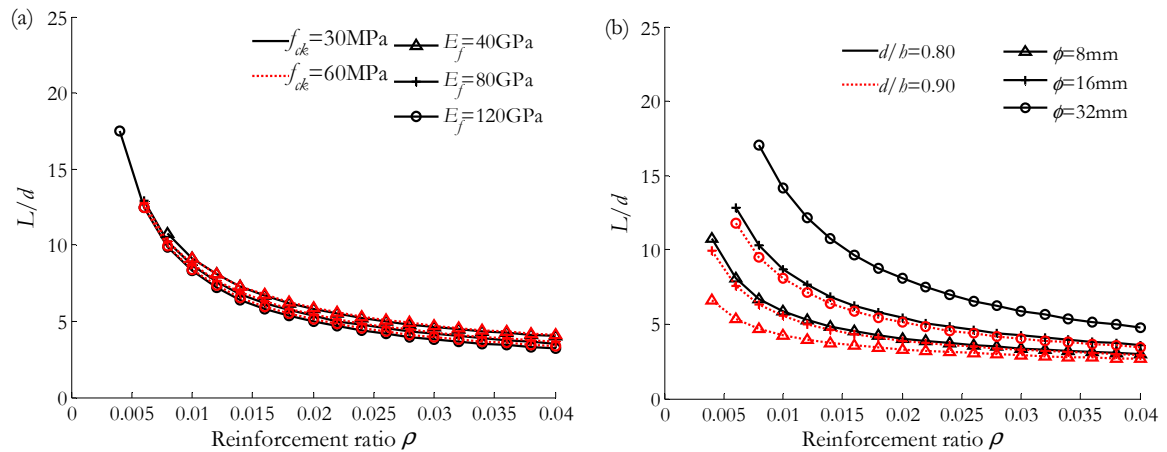
Figure 6-18. L/d ratio versus ρ for different f_{ck}, d/h , ϕ and E_f values. Assumptions: $\delta_{LT}/L = 1/250$, $w_k = 0.5$ mm, high bond and long-term loading, (a) $d/h = 0.80$, $\phi = 16$ mm, (b) $f_{ck} = 45$ MPa, $E_f = 80$ GPa.

Using Figure 6-17 and Figure 6-18 for the design of FRP RC elements implies that the section is designed to work under the maximum M_s/M_{cr} ratio to accomplish the serviceability conditions of cracking and stresses at a sectional level. Nevertheless, the section can work at a lower flexural moment than the maximum allowed. Hence, this moment ratio shall be considered a reference maximum value, and an iterative procedure is needed to find which M_s/M_{cr} ratio gives the optimal value of the dimensions of the element.

6.3.2. Proposed design methodology

The methodology aims at finding the optimal sectional height of a FRP RC element subjected to a particular loading situation and it is summarized in the flowchart of Figure 6-19. It starts calculating the maximum service moment that fulfils the SLS at a cross-section level, and finds the optimal height of the element using an iterative procedure.

The methodology is applicable to FRP RC rectangular cross-sections without compression reinforcement designed to fail by concrete crushing. The different mechanical and bond properties of the reinforcement are taken into consideration.

The problem is first defined by the input data, which are:

-   the geometric characteristics of the FRP RC element: length L, width b, and effective depth to overall height ratio d/h,

-   the loading conditions: permanent load q_G, variable load q_Q, coefficient of use of the element ψ, type of loading K_1, boundary conditions K_2 and duration of loading β_2,

-   the concrete mechanical properties: compressive strength f_{ck}, modulus of elasticity E_c and tensile strength f_{ct},

-   the FRP mechanical properties: modulus of elasticity E_f, bar diameter ϕ and reinforcement ratio ρ,

-   the bond characteristics: β_1 and k_1,

-   and the serviceability limitations (in this study: $\sigma_c \leq 0.45 f_{ck}$, $w_k \leq 0.5$ mm, $\delta_{LT} \leq L/250$).

Through Eqs. (6-59) and (6-60), the maximum ratio $(M_s/M_{cr})_{\max}$ is then defined as the maximum value of M_s/M_{cr} that accomplishes the stresses in materials and the crack width requirements at a cross section level.

$$\frac{M_s}{M_{cr}} = \frac{0.45 f_{ck}}{f_{ct}} \cdot \frac{A}{(x/d)}$$ (6-59)

$$\frac{M_s}{M_{cr}} = \frac{w/s_{rm} + \sqrt{(w/s_{rm})^2 + 4\beta_1\beta_2 (f_{ct}/E_c)^2 \left(\dfrac{1-x/d}{A}\right)^2}}{2 f_{ct} (1-x/d)/(E_c \cdot A)}$$ (6-60)

Eq. (6-59), previously described in Eq. (6-9), defines the maximum ratio M_s/M_{cr} to limit the stresses in concrete, while Eq. (6-60), described in Eq. (6-25), defines the maximum ratio M_s/M_{cr} to limit the maximum crack width. $(M_s/M_{cr})_{\max}$ is the minimum value between the obtained by Eqs. (6-59) and (6-60). If only the maximum crack width wants to be limited, $(M_s/M_{cr})_{\max}$ is directly obtained from Eq. (6-60).

For the given loading situation, and having calculated the service moment at the section M_s, the total height of the beam h_1^1 is calculated from the value of $(M_s/M_{cr})_i$, which for the first iteration is $(M_s/M_{cr})_{\max}$:

$$h_1^i = \left(\frac{6M_s}{bf_{ct}} \left((M_s/M_{cr})_i \right)^{-1} \right)^{0.5}$$ (6-61)

h_1^1 corresponds to the total height of the beam that fulfils the sectional serviceability requirements (cracking and stresses). However, h_1^1 does not ensure the fulfilment of the deflection limitation.

In a parallel way, and using Eq. (6-62), previously described in Eq. (6-53), the L/d ratio corresponding to the considered $(M_s/M_{cr})_i$ ratio is calculated and h_2^1 is obtained from Eq. (6-63):

$$\frac{L}{d} \leq \frac{1}{K_1 K_2 K_3}\left(d/h\right)^{-1}\left(2\frac{f_{ct}}{E_c}\beta_1\beta_2\left(\frac{M_s}{M_{cr}}\right)^{-1} + \frac{\varepsilon_f}{d/h\left(1-x/d\right)}\left(1-\beta_1\beta_2\left(\frac{M_s}{M_{cr}}\right)^{-2}\right)\right)^{-1} \tag{6-62}$$

$$h_2^i = \frac{1}{\left(L/d\right)^i}\frac{L}{d/h} \tag{6-63}$$

In the first iteration, the value of h_2^1 results always equal or higher than h_1^1 because it includes a new restriction that is the deflection limitation. For the case where the difference between h_2^1 and h_1^1 is lower than a previously defined tolerance (*Tol*), the optimal value of the total height can be taken as h_2^1 and the most restrictive limitation is the one governed by Eqs. (6-59) and (6-60).

On the contrary, if the difference between h_2^1 and h_1^1 is higher than the tolerance, initial $(M_s/M_{cr})_{max}$ should be reduced with a decrement $\Delta(M_s/M_{cr})$, since the stresses and cracking will be anyhow accomplished for a M_s/M_{cr} ratio lower than $(M_s/M_{cr})_{max}$. Then, h_1^i and h_2^i are recalculated again.

This procedure finishes when $\left|h_2^i - h_1^i\right| < Tol$ and the optimal height of the cross section is $h_{opt} = h_2^i$. If $h_2^i - h_1^i < 0$, the M_s/M_{cr} ratio shall be increased in the next step to arrive to the optimal solution.

The presented methodology, summarized in a flowchart in Figure 6-19, allows calculating the dimensions of FRP RC sections that fulfil the SLS in a more adjusted way than the ones obtained by other procedures, since it takes into consideration the actual service moment of the element and allows considering the different mechanical properties of materials, as well as the loading and geometric characteristics of the element.

As the element is further loaded, the resulting value of h increases. Consequently, for elements highly loaded, this methodology provides more restrictive values of h than those obtained by the slenderness limitations given in codes of practice. However, for elements that are not overly loaded, the value of h can result lower than the obtained by codes of practice.
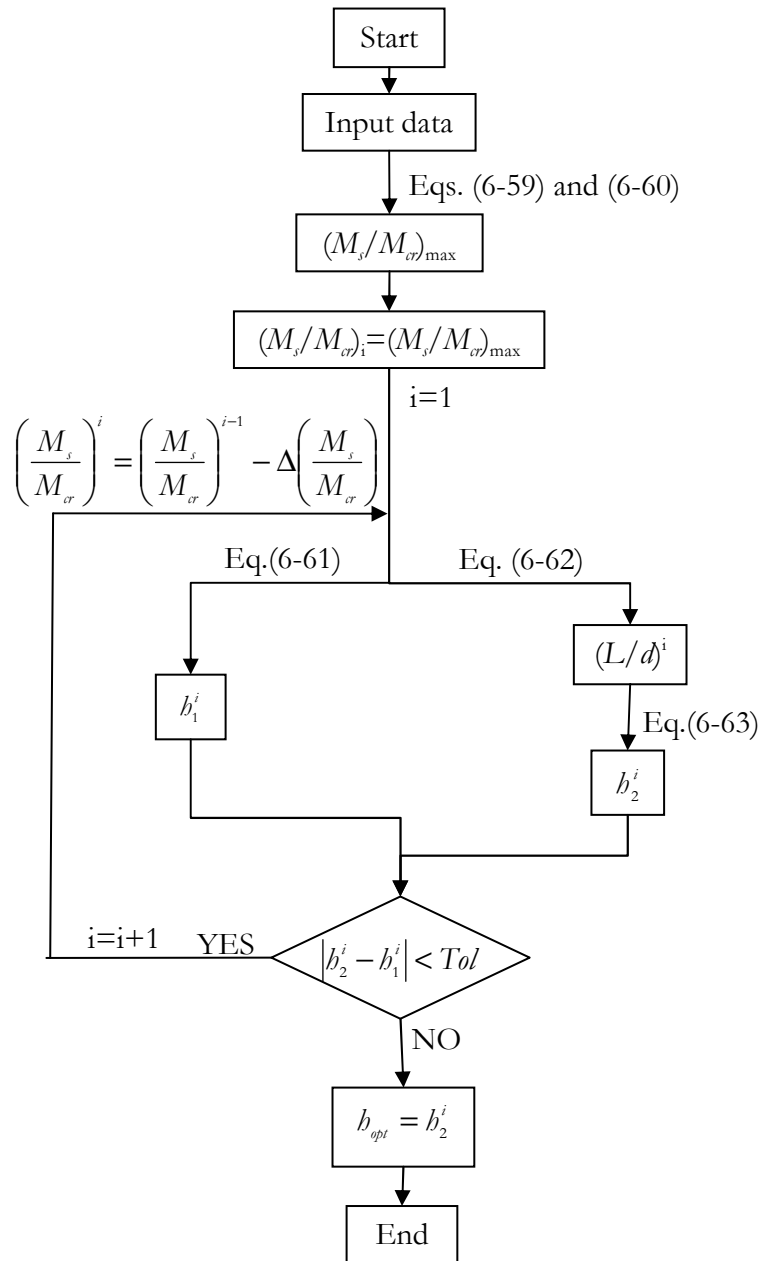
Figure 6-19. Design flowchart for the dimensioning of the overall depth of a FRP RC element.

Higher values of E_f, d/h and ρ result in lower values of h, as expected. The concrete grade has only relevant influence on the stress limitation, leading to lower sectional dimensions as the concrete strength increases. Finally, the effect of bond coefficients results secondary when it is compared to the previous ones. This finding corresponds to that, when evaluating the SLS as a whole, the SLS of cracking generally results the less restrictive one. The SLS of stresses in concrete does not consider the bond properties. The β_2 bond coefficient included in the SLS of deflections has only influence at loads close to the cracking load. As a result, at the service load, the effect of bond coefficients is usually insignificant.

6.3.3. Example: FRP RC beam subjected to uniform loading

The objective of this example is to illustrate the procedure previously presented. The overall depth of an FRP RC beam subjected to a uniform permanent load of 15 kN/m (including self-weight) and a uniform variable load of 10 kN/m, over a span of 3000 mm (Figure 6-20) wants to be determined.

The concrete characteristic compressive strength is 45 MPa, and GFRP bars with 16 mm of diameter and a modulus of elasticity of 60 GPa are used as internal reinforcement. The effective depth to overall depth ratio is 0.80, and the section is 300 mm wide with a reinforcement ratio of 2%. High bond is considered between concrete and reinforcement.
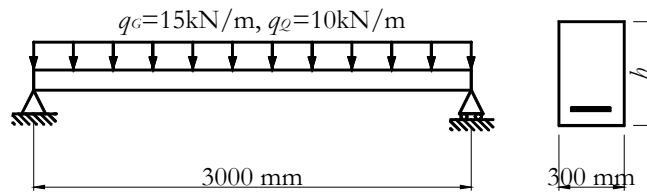
Figure 6-20. Scheme of the example: simply supported beam under uniform loading.

The coefficient for the quasi-permanent value of the variable action is considered $\psi = 0.2$. The characteristic crack width is limited to 0.5 mm, the active long-term deflection is limited to $L/250$ and the concrete compressive stress to $0.45f_{ck}$. In a first stage, the optimal depth of the section will be calculated to accomplish the crack width limitation and the deflection limitation. The stresses in concrete limitation is subsequently taken into consideration and the optimal depth is re-calculated accordingly.

<u>Solution:</u>

The beam is subjected to a service load, under the quasi-permanent condition of loading, of:

$$q_s = q_G + \psi q_Q = 17 \text{ kN/m} \tag{6-64}$$

The associated bending moment is:

$$M_s = \frac{q_s L^2}{8} = 19.13 \text{kNm} \tag{6-65}$$

The mechanical properties of concrete E_c and f_{ct} are calculated following Eurocode 2 (CEN 2004) formulation.

First, the overall height of the beam that fulfils the maximum crack width and the deflection limitations is calculated. A tolerance *Tol* of 5 mm between h_1^i and h_2^i will be used. Following Eq. (6-60) the moment ratio to accomplish the maximum crack width is $M_s/M_{cr} = 3.45$. This

value leads to $b_1^1 = 171$ mm. On the other hand, and by using Eq. (6-62) with $M_s/M_{cr} = 3.45$, $L/d = 8.25$, giving $b_2^1 = 441$ mm.

Since $\left|b_2^i - b_1^i\right| > 5\,\text{mm}$, the moment ratio M_s/M_{cr} is consequently reduced and the process is again repeated. In Table 6-1 several iterations are shown until the optimal depth of the section is obtained.

Table 6-1. Iterative procedure to find the optimal depth for the given example.

Iteration	M_s/M_{cr}	L/d	b_1^i	b_2^i
1	3.45	8.25	170	455
2	2.5	11.78	201	318
3	2	15.35	225	244
4	1.9	16.37	230	229

In iteration 4, it is observed that $\left|b_2^4 - b_1^4\right| < 5\,\text{mm}$, which indicates that the optimal value of the total height of the beam shall be $b_{opt} = b_1^4 = 230$ mm, being $(M_s/M_{cr})_{opt} = 1.9$ and $(L/d)_{opt} = 16.37$. This situation will accomplish the maximum crack width and the long-term deflection limitations.

In the following, the overall height of the beam that fulfils the three SLS (maximum crack width, deflection and stresses in concrete limitations) is calculated. If the maximum compressive stress in the concrete limitation is also taken into consideration, the initial $(M_s/M_{cr})_{max}$ is calculated as the minimum between the obtained by Eqs. (6-9) and (6-25). The resulting value is $(M_s/M_{cr})_{max} = 2.14$, giving $L/d = 14.14$, and obtaining $b_1^1 = 217$ mm and $b_2^1 = 265$ mm.

Since $\left|b_2^i - b_1^i\right| > 5\,\text{mm}$, the moment ratio M_s/M_{cr} is consequently reduced and the process is again repeated. Table 6-1 can be used from iteration 3, and the resulting optimal depth is again 230 mm.

This result is compared to the resultant heights obtained by ACI 440.1R-06 and other limitations present in the literature in Table 6-2. ACI 440.1R-06, which limits the deflection under service load δ_{serv} to $L/240$, proposes to calculate the height of a simply supported beam as $L/10$, whilst Ospina and Gross (2005), who also limit the deflection under the service load δ_{serv} to $L/240$, give Eq. (2-88) to calculate L/h.

Finally, if the formulation of the present study is used and the service moment M_s is limited to $0.30M_u$, as suggested by several authors (Alsayed et al. 2000, Ospina and Gross 2005 or Rafi et al. 2008 among others), for the deflection limitation $\delta_{LT} < L/250$, the resultant slenderness limitation would have been $L/d = 10.20$, giving as a result $h = 367$ mm. Hence, in this case, considering $M_s/M_u = 0.30$ leads to an oversizing of the section.

Table 6-2. Resulting depth following the present study compared to other approaches.

Approach	Serviceability limitation	Slenderness limitation	Resultant overall depth
ACI 440.1R-06	$\delta_{serv} \leq L/240$	$L/h = 10$	$h = 300$ mm
Ospina and Gross (2005), Eq. (2-88)	$\delta_{serv} \leq L/240$	$L/h = 12.45$	$h = 241$ mm
Present study	$M_s/M_u = 0.30$ and $\delta_{LT} \leq L/250$	$L/d = 10.20$ $(L/h = 8.16)$	$h = 367$ mm
Present study	$\sigma_c \leq 0.45 f_{ck}$, $w_k \leq 0.5$ mm, and $\delta_{LT} \leq L/250$	$L/d = 16.37$ $(L/h = 13.10)$	$h = 230$ mm

For the example presented, all the slenderness limitations from other approaches provide values for the total depth of the section that result higher than the one obtained from the present methodology.

The comparison between the value of h obtained by the present study with values provided by other slenderness limitations allows affirming that the present methodology gives more accurate values of h, because it uses the actual service moment derived from the actual loading condition and takes into account the mechanical properties of materials. Moreover, the formulation of the present methodology simultaneously satisfies the three SLS presented, whilst the serviceability limitations for the other approaches presented in Table 6-2 only limit the SLS of deflection.

The presented formulation allows easily changing the limits pre-established if needed. For example, if the deflection after construction of non-structural elements δ_{LT} had been limited to $L/500$ as stated in Eurocode 2 (i.e., considering that deflections could damage adjacent parts of the structure), the present methodology would have given $L/d = 14.12$ and $h = 279$ mm.

Moreover, this methodology takes into account the level of loading of the element. Following the same example, if the beam had been subjected to double the initial loading ($q_G = 30$ kN/m and $q_Q = 20$ kN/m), the present methodology would have given $h_{opt} = 295$ mm, instead of 230 mm, whilst other formulations or slenderness limitations do not account for the level of loading.

6.4. Concluding remarks

The design of concrete structures reinforced with FRP materials is likely to be controlled by the various criteria imposed at SLS. This chapter presents a discussion about the limits of the different SLS, starting from the requirements at a cross-section level to end up with the deflection limitation. Based on Eurocode 2 formulation, a methodology to fulfil the

serviceability requirements for the design of the overall depth of a FRP RC element is presented.

The study on stresses in materials shows that limiting the compressive stress in the concrete to $0.45f_{ck}$ under the quasi-permanent combination of loads gives somehow restrictive values of the maximum service moment to be attained at the section. However, this limitation shall be evaluated for every situation, since it refers mainly to assuming linear creep and to avoiding longitudinal cracks that may lead to a reduction in the durability.

The limitation of the tensile stress in the FRP reinforcement, which refers to avoiding the creep rupture, highly depends on the rebar properties (which are improving continuously owing to the rapid advances in manufacturing technology), the environmental conditions and the loading period. Although further studies would be needed to arrive to a more generalised conclusion, for the range of values studied in this work, limiting the stress in the FRP bar generally leads to less restrictive situations than limiting the concrete stress.

Limiting the maximum crack width to a characteristic value of 0.5 mm leads to service moments generally higher than those obtained for the SLS of concrete stress, with values up to 22 times the cracking moment for the highest considered values of parameters. Only in few cases with low reinforcement ratios, the crack width criterion may be governing the SLS at a cross-section level. The maximum allowable tensile strain is compared to the values established in the literature (ISIS Canada 2001, Newhook et al. 2002), finding that in most cases limiting ε_f to 2000 $\mu\varepsilon$, as stated by Newhook et al. (2002) or ISIS Canada (2001), can result too restrictive for the control of the maximum crack width, especially in those cases where high bond is reported or for reinforcement ratios higher than 2%.

Comparing the two serviceability limitations at a cross-section level (namely stresses in concrete and maximum crack width), it is concluded that for lightly RC sections, the crack width limitation results more restrictive than the stresses in concrete, however, for sections with higher amounts of reinforcement, the predominant restriction is the concrete compressive stress. Moreover, the service moment that fulfils the serviceability requirements at a cross-section level ranges between 0.20 and 0.38 times the ultimate moment for sections dimensioned to fail in concrete crushing. This range of values results in good agreement with the ones stated by Bischoff (2005), Ospina and Gross (2005) and Hegger and Kurth (2009).

A formulation to calculate the L/d ratio that fulfils the deflection limitation for an FRP RC element is provided. This equation allows considering the different properties of materials as well as the geometric and loading conditions of the element.

The obtained L/d ratio is assessed at a service moment defined as a portion of the ultimate moment, using the partial factors defined in Eurocode 2 (CEN 2004). Results show that the L/d ratio only depends on ρ, f_{ck} and E_f. Moreover, the L/d ratio increases with ρ, which is the opposite behaviour of what is typically reported for steel RC (Corres et al. 2003CEN 2004, Narayanan and Goodchild 2006, Vollum 2009).

The L/d ratio presented in this work also allows reproducing adequately the slenderness limitation proposed by Ospina and Gross (2005) taking into account the tension stiffening effect.

An iterative methodology to calculate the height of a FRP RC beam that can simultaneously satisfy all of the considered SLS is presented. This procedure allows optimizing the overall depth of the element with respect to more generalised methodologies, since it accounts for the specific characteristics of the RC element, such as the mechanical properties of materials and the geometric and loading conditions of the element.

This methodology provides higher values of h as the applied load increases, as expected. Hence, elements under light loading levels generally will have values of h lower than the obtained by the usual slenderness limitations given in codes of practice. On the contrary, elements submitted to high levels of loads generally will have more restrictive values of h than those obtained by codes of practice.

Moreover, high values of E_f, d/h and ρ result in lower values of h, whilst f_{ck} has only relevant influence on the limitation of the compressive stress, leading to lower values of h as the f_{ck} increases. The effect of bond factors results secondary, since it affects to the maximum crack width limitation, which is not usually restrictive.

Chapter 7
Final remarks

7.1. Conclusions

Fibre Reinforced Polymer bars have emerged as an alternative to steel reinforcement for concrete elements subjected to aggressive environments due to the non-corrosive properties of these composite materials. FRPs, however, present different mechanical properties than that of steel, such as linear stress-strain behaviour under tension until rupture, higher tensile capacity, generally lower modulus of elasticity and limited strain range. In addition, those bars present different surface conditions such as sand coated, ribbed, indented or braided. All these characteristics have a direct effect on the flexural behaviour of FRP RC under flexural stresses, generally leading to higher deflections and crack widths than that of steel RC. Thus, serviceability criteria may govern the design of FRP RC and needs to be reassessed.

In the present work, the short-term serviceability behaviour of FRP RC beams has been investigated through theoretical analysis and experiments. Previously, an overview on flexural and, more specifically, serviceability behaviour of FRP RC elements has been carried out. The most relevant experimental and analytical studies on deflections and cracking of FRP RC elements have been presented and discussed. Different prediction models for the evaluation of deflections and crack width have been analysed and compared. Most of these approaches propose coefficients that adjust a limited number of experimental data to existing design equations for steel RC

An experimental program has been planned and carried out to check the validity of the actual formulation to predict deflections and crack widths for FRP RC beams. Twenty-six GFRP RC beams and one steel RC beam have been tested under four-point loading. The main variables considered in the study are the concrete grade, the reinforcement ratio and the effective depth to total height ratio. The material properties have been obtained from parallel experimental tests and contrasted with the experimental data on the beam specimens. Deflections,

rotations, strains on the concrete and on the reinforcement and crack widths have been measured.

The experimental results have been compared and discussed between them. Furthermore, they have been compared to some of the most representative prediction models of deflections and cracking for steel and FRP RC elements. Additionally, cracked section analysis (CSA), which assumes a cracked section and takes into account the non-linearities of materials, has been used to analyse the flexural behaviour of the specimens until failure. An evaluation of the factors that can contribute to the flexural behaviour beyond the service load has also been introduced.

Finally, an analytical discussion on the three main aspects of the SLS of FRP RC, namely the stresses in materials, the maximum crack width and the allowable deflection, has been introduced. The influence of the different principal parameters that affect the SLS has been evaluated. The different mechanical characteristics of FRP, with modulus of elasticity between 40 and 120 GPa, bar diameters between 8 and 32 mm and reinforcement ratios between 0.5% and 2%, have been included. Furthermore, concrete grades between 30 and 60 MPa, d/h ratios between 0.8 and 0.9 and different bond characteristics have been taken into account.

Because SLS result determining for the design of FRP RC elements, an iterative methodology for the design of rectangular FRP RC beams has been developed. The elements designed according to the proposed methodology could simultaneously satisfy all of the considered SLS. The methodology has been summarised in a flow chart that could be used by practicing engineers.

The most relevant conclusions of the present work can be summarized as follows:

7.1.1. General remarks of the flexural behaviour of FRP RC beams

- All the GFRP RC beam specimens behaved linearly until cracking and, due to lack of plasticity in the reinforcement, almost linearly between cracking and failure, with a greatly reduced slope.

- As expected, the parameters chosen in the experimental program (concrete grade, reinforcement ratio and effective depth to height ratio) have an influence in the effective stiffness of the beam specimens, and therefore in their flexural behaviour. Higher values of ρ, f_c and d/h eventually led to higher depths of neutral axis, smaller strains at the top concrete fibre and smaller curvatures and deflections.

7.1.2. Concrete strain at the midspan section

- Evaluating the strain values at the midspan section at different load stages showed that Bernoulli hypothesis was valid for both cracked and uncracked sections.

- The concrete strain at the extreme compressive fibre behaved non-linearly with load until failure. This behaviour was more accentuated for those beams with lower concrete compressive strengths.

- The ultimate compressive strain of concrete under the flexural tests resulted relatively high (0.4% to 0.55%) compared to the typically considered in design standards (0.3% to 0.35%). This behaviour had been previously reported by other authors (Rüsch 1960, Matthys and Taerwe 2000).

- CSA generally predicted with accuracy the concrete strain at the top of the beam at the midspan cracked section.

7.1.3. Rebar strains, bond and tension stiffening

- The experimental rebar strain profile at the central zone subjected to pure flexure effectively reproduced the appearing of cracks with load.

- Whilst CSA predicted well the rebar strain at service load levels, the experimental rebar strain profile at the shear span reproduced higher strains than those predicted by CSA at high load levels. This high value of strains, greater than that predicted theoretically, was mainly attributed in this work to the openings of shear cracks. Shear cracks may have led to higher strains and curvatures, and consequently, to an increment of the deflection at high load levels.

- A measure of the bond and tension stiffening was derived by evaluating the experimental strain profile along the rebar. The average strain between cracks was lower than the strain at the crack due to the bond transfer between the concrete and the rebar.

7.1.4. Curvature at the central zone and along the length of the beam

- The experimental moment-curvature curves at the central zone deduced from different instrumentation devices compared well between beam specimens.

- CSA provided a good measure of the mean curvature at the central zone at high load levels and until the failure of the beam.

- Punctual increments of curvature were registered along the central zone of the beam. Those increments, which coincided with the appearing of two or three cracks along the gauge length of the mechanical extensometer, were observed to appear in the proximity of the load points in 8 of the 14 beams analysed. The appearing of these "peaks" was attributed to the influence of the punctual loads and shear forces around the load points. However, the randomly behaviour of the concrete tensile strength also had an influence on this phenomenon.

- Furthermore, in some cases, at high load levels the curvature at the shear spans resulted higher than that predicted by CSA. This increment in curvatures was mainly attributed in this work to shear crack openings.

7.1.5. Cracking behaviour

- The experimental crack spacing was found to increase with the concrete cover, the bar spacing and the ϕ/ρ_{eff} ratio.

- The maximum crack spacing was 21% overestimated by Eurocode 2 and Model Code 90 formulation. The mean crack spacing, however, was adequately predicted by EHE and slightly overestimated by Eurocode 2 approach.

- Significant differences were found in the evaluation of the effective height of the concrete area surrounding the tensile bar and more research is needed in this field to arrive to a more solid conclusion on the influence of the different parameters affecting crack spacing.

- The average crack width was generally well predicted by Eurocode 2 and Model Code approaches provided that the experimental crack spacing was taken into consideration in their formulation.

- Bond coefficients were adjusted to fit the experimental crack spacing and maximum crack width to the corresponding formulae, obtaining similar resultant values to those suggested for steel RC.

7.1.6. Deflections

- Up to the serviceability range of loading, the flexural deflection (calculated from strains from the mechanical extensometer's data) matched up with the total deflection (registered by a vertical transducer). However, for higher values of load, the total deflection became higher than the flexural deflection. This behaviour was observed not only at the midspan section, but also at the shear span sections located 450 mm from the supports.

- At the service load level, all of the theoretical approaches compared reasonably well with the experimental data.

- At load levels close to the cracking load, the load-deflection responses predicted by Benmokrane et al. (1996), Yost et al. (2003), Faza and GangaRao (1992), CAN/CSA-S806 (2002) and ISIS Canada (2001) formulations are characterized by a large increase in deflections, and rapidly approach the behaviour of a fully cracked element. This sudden loss in stiffness, however, was not observed during any of the experimental tests, and can be attributed to the tension stiffening effect.

- At loads beyond the service load, all of the theoretical approaches underestimated the experimental deflection.

- CSA, which generally predicted with accuracy strains and curvature at the central sections, underestimated the total deflection at high load levels, not only at the midspan section but also at the shear span sections located 450 mm from the supports.

- An evaluation of some of the factors that could contribute to obtain experimentally higher deflections than expected was undertaken, giving as a main result that:

    - In these experiments, shrinkage could not significantly affect the deformational behaviour of the beam. A maximum contribution of 1×10^{-6} mm^{-1} in the curvature was found, which was not remarkable compared to the curvatures at ultimate (between 80 and 140 $\times10^{-6}$ mm^{-1}) or at service (between 20 and 30 $\times10^{-6}$ mm^{-1}) representing an additional deflection of 3-5% at service and around 1% at ultimate.

    - Shear induced effects may had produced an additional shear deflection. This additional deflection was experimentally computed according to the unit-load and to Debernardi and Taliano (2006) methodologies. An additional shear deformation of 9-9.5% the total deflection was found at a load level of 60% the ultimate load.

7.1.7. Failure mode and ultimate load

- The mode of failure obtained for all the twenty-six GFRP RC beams was concrete crushing, in correspondence with their design.

- The load capacity increased with the reinforcement ratio, the d/h ratio and the concrete strength.

- CSA predicted with accuracy the ultimate load, provided that the stress-strain concrete curve took into consideration the experimental values of concrete.

7.1.8. Serviceability limitations for FRP RC elements

- The compressive stress in concrete is generally limited to assuming linear creep and to avoiding longitudinal cracks and its consideration shall be evaluated in each case. Limiting this stress to $0.45f_{ck}$ gives somehow restrictive values for the maximum service moment to be attained at a section under the quasi-permanent loading condition. For the studied parameters, this service moment would range between 1.2 and 3.8 times the cracking moment. The corresponding tensile strain at the reinforcement would be about 3000-6000 $\mu\varepsilon$ for low values of ρ and about 600-3000 $\mu\varepsilon$ as ρ increases.

- The tensile stress in the reinforcement is limited to avoid creep rupture or stress corrosion. This limitation highly depends on the rebar properties (which are improving continuously owing to the rapid advances in manufacturing technology), the environmental conditions and the loading period. Despite further studies would be needed to arrive to a more generalised conclusion, limiting the stress in the FRP bar generally leads to less restrictive situations than limiting the concrete stress.

- The maximum crack width is limited in design codes for aesthetic reasons as well as to ensure adequate structural performance and sufficient durability to the structure. The allowable tensile strain in the reinforcement for this limitation can be generally higher than 2000 $\mu\varepsilon$, contrarily to what is recommended Newhook et al. 2002 or ISIS Canada 2001, especially if high bond is reported or the reinforcement ratio is higher than 2%.

- Comparing the two serviceability limitations at a cross-section level (namely stresses in concrete and maximum crack width), it was observed that for lightly RC sections, the crack width limitation results more restrictive than the stresses in concrete, however, for sections with higher amounts of reinforcement, the predominant restriction is the concrete compressive stress.

- Moreover, the service moment that fulfils the serviceability requirements at a cross-section level ranges between 0.20 and 0.38 times the ultimate moment for sections dimensioned to fail in concrete crushing. This range of values results in good agreement with the ones stated by Bischoff (2005), Ospina and Gross (2005) and Hegger and Kurth (2009).

- A formulation to calculate the L/d ratio that fulfils the deflection limitation for an FRP RC element is provided. The obtained L/d ratio is assessed at a service moment defined as a portion of the ultimate moment, using the partial factors defined in Eurocode 2 (CEN 2004), resulting that the L/d ratio only depends on ρ, f_{ck} and E_f. The L/d ratio increases with ρ, which is the opposite behaviour of what is typically reported for steel RC (Corres et al. 2003, CEN 2004, Narayanan and Goodchild 2006, Vollum 2009).

- The L/d ratio presented in this work also fits adequately the slenderness limitation proposed by Ospina and Gross (2005) taking into account the tension stiffening effect.

- An iterative methodology to calculate the height of a FRP RC beam that can simultaneously satisfy all of the considered SLS is presented. This procedure allows optimizing the overall depth of the element with respect to more generalised methodologies, since it accounts for the specific characteristics of the RC element, such as the mechanical properties of materials and the geometric and loading conditions of the element.

- This methodology provides higher values of h as the applied load increases, as expected. Hence, elements under light loading levels generally will have values of h lower than the obtained by the usual slenderness limitations given in codes of practice. On the contrary, elements submitted to high levels of loads generally will have more restrictive values of h than those obtained by codes of practice.

- According to this methodology, high values of E_f, d/h and ρ result in lower values of h, whilst f_{ck} has only relevant influence on the limitation of the compressive stress, leading to lower values of h as the f_{ck} increases. The effect of bond factors results secondary, since it affects to the maximum crack width limitation, which is not usually restrictive.

7.2. Recommendations for future works

Based on the findings of this study, the following suggestions for future investigations are drawn:

- A detailed study on the crack width for FRP RC elements should be carried out, both analytically and experimentally. The main parameters involving crack width and spacing shall be taken into account: concrete cover, bar spacing and diameter and bond characteristics, including the rebar surface, the concrete strength and the modulus of elasticity of both concrete and FRP.

- Since SLS are likely to govern the design of FRP RC elements, a specific study on the long-term deflections of FRP RC elements, both analytical and experimental, should be performed to check the current expressions and to suggest modifications.

- A numerical model using discrete cracking, supported by experiments, can assist in determining the influence of the deeper cracks and higher deformations on the cross-section and overall behaviour of FRP RC elements.

- A specific study on the contribution of the shear induced deformations on the total deflection should be carried out. The main parameters affecting shear deformations shall be taken into consideration, being the most significant the element geometry and loading, the materials characteristics and the flexural and shear reinforcement ratio.

- Specific studies on the limitation of the stresses in the FRP reinforcement or of the allowable crack width based on durability or creep rupture concepts are recommended to assess the current limitations in FRP RC design codes.

Chapter 8
References

Abdalla, H. A. (2002). "Evaluation of deflection in concrete members reinforced with fibre reinforced polymer (FRP) bars." Composite Structures, 56(1), 63-71.

ACI Committee 224. (2001). "ACI 224R-01. Control of cracking in concrete structures." American Concrete Institute (ACI), Farmington Hills, Mich., USA, 46pp.

ACI Committee 318. (2005). "ACI 318R-05. Building code requirements for structural concrete (ACI 318-05) and commentary (ACI 318R-05)." American Concrete Institute (ACI), Farmington Hills, Mich., USA, 430pp.

ACI Committee 318. (1995). "ACI 318-95. Building code requirements for structural concrete (ACI 318-95) and commentary (ACI 318R-95)." American Concrete Institute (ACI), Farmington Hills, Mich., USA.

ACI Committee 440. (2008). "ACI 440.2R-08. Guide for the design and construction of externally bonded FRP systems for strengthening concrete structures." American Concrete Institute (ACI), Farmington Hills, Mich., USA, 41pp.

ACI Committee 440. (2006). "ACI 440.1R-06. Guide for the design and construction of concrete reinforced with FRP bars." American Concrete Institute (ACI), Farmington Hills, Mich., USA, 45pp.

ACI Committee 440. (2004). "ACI 440.3R-04. Guide Test Methods for Fiber-Reinforced Polymers (FRPs) for Reinforcing or Strengthening Concrete Structures." American Concrete Institute (ACI), Farmington Hills, Mich., USA, 40pp.

ACI Committee 440. (2003). "ACI 440.1R-03. Guide for the design and construction of concrete reinforced with FRP bars." American Concrete Institute (ACI), Farmington Hills, Mich., USA, 42pp.

ACI Committee 440. (2001). "ACI 440.1R-01. Guide for the design and construction of concrete reinforced with FRP bars." American Concrete Institute (ACI), Farmington Hills, Mich., USA, 41pp.

Aiello, M. A., and Ombres, L. (2000a). "Cracking analysis of FRP-reinforced concrete flexural members 1." Mechanics of Composite Materials, 36(5), 389-394.

Aiello, M. A., and Ombres, L. (2000b). "Load-deflection analysis of FRP reinforced concrete flexural members." Journal of Composites for Construction, 4(4), 164-170.

Almusallam, T. H. (2006). "Load-deflection behavior of RC beams strengthened with GFRP sheets subjected to different environmental conditions." Cement and Concrete Composites, 28(10), 879-889.

Al-Salloum, Y. A., and Almusallam, T. H. (2007). "Creep effect on the behavior of concrete beams reinforced with GFRP bars subjected to different environments." Construction and Building Materials, 21(7), 1510-1519.

Alsayed, S. H. (1998). "Flexural behaviour of concrete beams reinforced with GFRP bars." Cement and Concrete Composites, 20(1), 1-11.

Alsayed, S. H., Al-Salloum, Y. A., and Almusallam, T. H. (2000). "Performance of glass fiber reinforced plastic bars as a reinforcing material for concrete structures." Composites Part B: Engineering, 31(6-7), 555-567.

Al-Sunna, R. A. S. (2006). "Deflection behaviour of FRP reinforced concrete flexural members." PhD thesis, The University of Sheffield, Dept. of Civil and Structural Engineering, Sheffield, UK.

Arockiasamy, M., Chidambaram, S., Amer, A., and Shahawy, M. (2000). "Time-dependent deformations of concrete beams reinforced with CFRP bars." Composites Part B: Engineering, 31(6-7), 577-592.

Ashour, A. F. (2006). "Flexural and shear capacities of concrete beams reinforced with GFRP bars." Construction and Building Materials, 20(10), 1005-1015.

Baena, M., Torres, L., Turon, A., and Barris, C. (2009). "Experimental study of bond behaviour between concrete and FRP bars using a pull-out test." Composites Part B: Engineering, 40(8), 784-797.

Bakis, C. E., Ospina, C. E., Bradberry, T. E., Benmokrane, B., Gross, S. P., Newhook, J. P., and Thiagarahan, G. (2006). "Evaluation of crack widths in concrete flexural members reinforced with FRP bars." Proceedings of the 3rd International Conference on FRP Composites in Civil Engineering, Miami, Florida, USA, December 13-15, 2006, 307-310.

Bazant, Z. P., and Oh, B. H. (1984). "Deformation of progressively cracking reinforced concrete beams." Journal of the American Concrete Institute, 81(3), 268-278.

Beeby, A. W. (2004). "The influence of the parameter φ/ϱ_{eff} on crack widths." Structural Concrete, 5(2), 71-83.

Beeby, A. W., Ålander, C., Cairns, J., Eligehausen, R., Mayer, U., Lettow, S., Ferretti, D., Iori, I., Gambarova, P., Bamonte, P., Giuriani, E., Plizzari, G., Pantazopoulou, S., and Tastani, S. (2005). "The influence of the parameter φ/ϱ_{eff} on crack widths." Structural Concrete, 6(4), 155-165.

Benmokrane, B., Chaallal, O., and Masmoudi, R. (1996). "Flexural response of concrete beams reinforced with FRP reinforcing bars." ACI Structural Journal, 93(1), 46-55.

Bernardi, S., Mesureur, B., and Rivillon, P. (1999). "Study of high-strength concretes reinforced with high-strength reinforcement: Study of bonding laws and cracking in static system." ACI Materials Journal, 96(4), 491-499.

Bischoff, P. H. (2007a). "Deflection calculation of FRP reinforced concrete beams based on modifications to the existing branson equation." Journal of Composites for Construction, 11(1), 4-14.

Bischoff, P. H. (2007b). "Rational model for calculating deflection of reinforced concrete beams and slabs." Canadian Journal of Civil Engineering, 34(8), 992-1002.

Bischoff, P. H. (2005). "Reevaluation of deflection prediction for concrete beams reinforced with steel and fiber reinforced polymer bars." Journal of Structural Engineering, 131(5), 752-762.

Bischoff, P. H., Gross, S., and Ospina, C. E. (2009). "The story behind proposed changes to ACI 440 deflection requirements for FRP-reinforced concrete." American Concrete Institute, ACI Special Publication, 264 SP 53-76.

Bischoff, P. H., and Johnson, R. D. (2008). "Effect of shrinkage on short-term deflections of reinforced concrete beams and slabs." ACI Structural Journal, 105(4), 516-518.

Bischoff, P. H., and Scanlon, A. (2007). "Effective moment of inertia for calculating deflections of concrete members containing steel reinforcement and fiber-reinforced polymer reinforcement." ACI Structural Journal, 104(1), 68-75.

Borosnyói, A. (2005). "Models for flexural cracking in concrete: The state of the art." Structural Concrete, 6(2), 53-62.

Borosnyói, A. (2002). "Serviceability of CFRP prestressed concrete beams." PhD thesis, Budapest University of Technology and Economics. Faculty of Civil Engineering, Budapest, Hungary.

Branson, D. E. (1977). "Deformation of concrete structures." McGraw-Hill, New York.

Branson, D. E. (1968). "Design procedures for computing deflection." Journal of the American Concrete Institute, 65(9), 730-742.

Broms, B. B. (1965). "Crack width and crack spacing in reinforced concrete members." Journal of the American Concrete Institute, 1237-1256.

Broms, B. B., and Lutz, L. A. (1965). "Effects of arrangement of reinforcement on crack width and spacing of reinforced concrete members." Journal of the American Concrete Institute, 1395-1409.

Brown, V. L. (1997). "Sustained load deflections in GFRP-reinforced concrete beams." Proceedings of the 3rd International Symposium on Non-Metallic (FRP) Reinforced for Concrete Structures, Sapporo, Japan, October 14-16, 1997, 2495-502.

Brown, V. L., and Bartholomew, C. L. (1996). "Long-term deflections of GFRP-reinforced concrete beams." Fiber Composites in Infrastructure: Proceedings of the 1st International Conference on Composites in Infrastructure, H. Saadatmanesh and M.R. Ehsani, eds., Tucson, AZ, 389-400.

CAN/CSA. (2002). "CAN/CSA-S806. Design and construction of building components with fibre-reinforced polymers." Canadian Standards Association, Ontario, Canada, 177pp.

CAN/CSA. (1994). "CAN/CSA-A23.3. Design of concrete structures for buildings." Canadian Standards Association, Ontario, Canada, 220pp.

Carreira, D. J., and Chu, K. H. (1985). "Stress-Strain Relationship for Plain Concrete in Compression." Journal of the American Concrete Institute, 82(6), 797-804.

CEB. (1983). "Cracking and deformations." Comité Euro-International Du Béton. Design Manual.

CEB-FIP. (1990). "Model code 1990, Design code." Comité Euro-International Du Béton, Thomas Telford Services Ltd, London.

CEN. (2004). "Eurocode 2: Design of concrete structures - Part 1.1: General rules and rules for buildings (EN 1992-1-1:2004)." Comité Europeen De Normalisation, Brussels, 225 pp.

CEN. (1992). "Eurocode 2: Design of concrete structures - Part 1.1: General rules and rules for buildings (EN 1992-1-1:1992)." Comité Europeen De Normalisation, Brussels, 195 pp.

Ceroni, F., Cosenza, E., Gaetano, M., and Pecce, M. (2006). "Durability issues of FRP rebars in reinforced concrete members." Cement and Concrete Composites, 28(10), 857-868.

Ceroni, F., and Pecce, M. (2009). "Design provisions for crack spacing and width in RC elements externally bonded with FRP." Composites Part B: Engineering, 40(1), 17-28.

Chang, K. K. (2001). "Aramid Fibers." ASM Handbook, ASM International, Material Park, Ohio, 21 41-45.

Choi, K. K., Urgessa, G., Taha, M. M. R., and Maji, A. K. (2008). "Quasi-balanced failure approach for evaluating moment capacity of FRP underreinforced concrete beams." Journal of Composites for Construction, 12(3), 236-245.

CNR-DT 203. (2006). "Guide for the Design and Construction of Concrete Structures Reinforced with Fiber-Reinforced Polymer Bars." Advisory Committee on Technical Recommendations for Construction, 39pp.

Collins, M. P., Mitchell, D., and MacGregor, J. G. (1993). "Structural design considerations for high-strength concrete." Concrete International, 15(5), 27-34.

Corres, H., Pérez, A., López, J., and Edtbauer, J. (2003). "Serviceability limit states. Deflections. Supporting document." Grupo De Hormigón Estructural, ETSICCP-UPM, 28pp.

CPH. (2008). "Instrucción de Hormigón Estructural EHE-08." Comisión Permanente Del Hormigón. Ministerio De Fomento, Madrid (Spain), 722pp.

Debernardi, P. G., and Taliano, M. (2006). "Shear deformation in reinforced concrete beams with thin web." Magazine of Concrete Research, 58(3), 157-171.

Desayi, P., and Krishnan, S. (1964). "Equation for the stress-strain curve of concrete." Journal of the American Concrete Institute, 61(3), 345-350.

El-Gamal, S., Benmokrane, B., and El-Salakawy, E. (2009). "Cracking and deflection behavior of one-way parking garage slabs reinforced with CFRP bars." American Concrete Institute, ACI Special Publication, 264 SP 33-51.

El-Salakawy, E., and Benmokrane, B. (2004). "Serviceability of concrete bridge deck slabs reinforced with fiber-reinforced polymer composite bars." ACI Structural Journal, 101(5), 727-736.

Farra, B., and Jaccoud, J. P. (1992). "Bond behaviour, tension stiffening and crack prediction of high strength concrete." Proceedings of the International Conference of Bond in Concrete, Riga, Latvia, October 15-17, 1992.

Favre, R., and Charif, H. (1994). "Basic model and simplified calculations of deformations according to the CEB-FIP model code 1990." ACI Structural Journal, 91(2), 169-177.

Faza, S. S., and GangaRao, H. V. S. (1992). "Pre- and post-cracking deflection behaviour of concrete beams reinforced with fibre-reinforced plastic rebars." Proceedings of The First International Conference on the Use of Advanced Composite Materials in Bridges and

Structures, K.W. Neale and P. Labossière, Editors; Canadian Society for Civil Engineering, 1992, 151-160.

Ferreira, A. J. M., Camanho, P. P., Marques, A. T., and Fernandes, A. A. (2001). "Modelling of concrete beams reinforced with FRP re-bars." Composite Structures, 53(1), 107-116.

Ferry, J. (1966). "Cracking and Deformability of Reinforced Concrete Beams." IABSE Publication, 26 75-95.

fib. (2010). "Model code 2010. First complete draft." Féderation International Du Béton, Fib Bulletin 56, 288pp.

fib. (2007). "FRP reinforcement in RC structures." Féderation International Du Béton, Fib Task Group 9.3, Fib Bulletin 40, Lausanne, Switzerland, September 2007, 147pp.

Floegl, H., and Mang, H. A. (1982). "Tension stiffening concept based on bond slip." Journal of the Structural Division, 108(12), 2681-2701.

Frosch, R. J. (1999). "Another look at cracking and crack control in reinforced concrete." ACI Structural Journal, 96(3), 437-442.

Gao, D., Benmokrane, B., and Masmoudi, R. (1998). "A calculating method of flexural properties of FRP-Reinforced concrete beam: Part 1: Crack width and deflection." Technical Report, Department of Civil Engineering, University of Sherbrooke, Sherbrooke, Quebec, Canada, 24 pp.

Gere, J. M., and Timoshenko, S. (1972). "Timoshenko. Strength of Materials".

Gergely, P., and Lutz, L. A. (1968). "Maximum crack width in reinforced concrete flexural members." Causes, Mechanism, and Control of Cracking in Concrete, SP-20. American Concrete Institute, Farmington Hills, Mich., 87-117.

Ghali, A., Hall, T., and Bobey, W. (2001). "Minimum thickness of concrete members reinforced with fibre reinforced polymer bars." Canadian Journal of Civil Engineering, 28(4), 583-592.

Gilbert, R. I. (1988). "Time effects in concrete structures." Elsevier Science Publishers B.V., Amsterdam, the Netherlands, 321pp.

Gilbert, R. I., and Warner, R. F. (1978). "Tension stiffening in reinforced concrete slabs." Journal of the Structural Division ASCE, 104(12), 1885-1900.

Guadagnini, M. (2002). "Shear behaviour and design of FRP RC beams." PhD thesis, The University of Sheffield, Dept. of Civil and Structural Engineering, Sheffield, UK.

Guadagnini, M., Pilakoutas, K., and Waldron, P. (2006). "Shear resistance of FRP RC beams: Experimental study." Journal of Composites for Construction, 10(6), 464-473.

Gupta, A. K., and Maestrini, S. R. (1990). "Tension-stiffness model for reinforced concrete bars." Journal of Structural Engineering New York, N.Y., 116(3), 769-790.

Hall, T., and Ghali, A. (2000). "Long-term deflection prediction of concrete members reinforced with glass fibre reinforced polymer bars." Canadian Journal of Civil Engineering, 27(5), 890-898.

Hegger, J., and Kurth, M. (2009). "Indirect deflection control of concrete slabs reinforced with Fiber-Reinforced Polymers (FRP) based on calculated deflections." Proceedings of the 9th International Symposium on Fibre-Reinforced Polymer Reinforcement for Concrete Structures, Sydney, Australia, July 11-13th 2009, 4pp.

Hognestad, E. (1951). "A Study of Combined Bending and Axial Load in Reinforced Concrete Members." University of Illinois Engineering Experimental Station, Bulletion Series N°. 399 128pp.

Hognestad, E., Hanson, N. W., and McHenry, D. (1955). "Concrete stress distribution in ultimate strength design." Journal of the American Concrete Institute, 52(6), 455-479.

Hollaway, L. C. (2010). "A review of the present and future utilisation of FRP composites in the civil infrastructure with reference to their important in-service properties." Construction and Building Materials, In Press, Corrected Proof.

Hoult, N. A., Sherwood, E. G., Bentz, E. C., and Collins, M. P. (2008). "Does the use of FRP reinforcement change the one-way shear behavior of reinforced concrete slabs?" Journal of Composites for Construction, 12(2), 125-133.

Howell, D. A., and Higgins, C. (2007). "Bond and development of deformed square reinforcing bars." ACI Structural Journal, 104(3), 333-343.

Huang, J., and Aboutaha, R. (2010). "Environmental reduction factors for GFRP bars used as concrete reinforcement: New scientific approach." Journal of Composites for Construction, 14(5), 479-486.

Imjai, T. (2007). "Design and analysis of curved FRP composites as shear reinforcement for concrete structures." PhD thesis, The University of Sheffield, Dept. of Civil and Structural Engineering, Sheffield, UK.

Imjai, T., Guadagnini, M., and Pilakoutas, K. (2007). "Shear crack induced deformation of FRP RC beams." Proceedings of the 8th International Symposium on Fibre-Reinforced Polymer Reinforcement for Concrete Structures, Patras, Greece, July 16-18, 2007.

ISIS Canada. (2001). "Reinforcing concrete structures with fibre reinforced polymers - Design manual No. 3." ISIS Canada Corporation. University of Manitoba, Manitoba, Canada, 158pp.

IStructE. (1999). "Interim guidance on the design of reinforced concrete structures using fibre composite reinforcement." Institution of Structural Engineers (IStructE), SETO Ltd., London, .

JSCE. (1997). "Recommendation for design and construction of concrete structures using continuous fiber reinforcing materials." Japan Society of Civil Engineering (JSCE), Tokyo, Japan, 23 325pp.

Leonhardt, F. (1977). "Crack control in concrete structures." IABSE Publication, (S-4/77),.

Lin, C. S., and Scordelis, A. C. (1975). "Non linear analysis of RC shells of general form." Journal of the Structural Division ASCE, 101(3), 523-538.

Loov, R. E. (1991). "A general stress-strain curve for concrete: implications for high strength concrete columns." Annual Conference of the Canadian Society for Civil Engineering, 302-311.

MacGregor, J. G. (1997). "Reinforced concrete: mechanics and design." Prentice Hall, Upper Saddle River, New Jersey, USA, 1042pp.

Mander, J. B., Priestley, M. J. N., and Park, R. (1988). "Theoretical stress-strain model for confined concrete." Journal of Structural Engineering New York, N.Y., 114(8), 1804-1826.

Masmoudi, R., Thériault, M., and Benmokrane, B. (1998). "Flexural behavior of concrete beams reinforced with deformed fiber reinforced plastic reinforcing rods." ACI Structural Journal, 95(6), 665-676.

Matthys, S., and Taerwe, L. (2000). "Concrete slabs reinforced with FRP grids. I: One-way bending." Journal of Composites for Construction, 4(3), 145-153.

Miàs, C., Torres, L., Turon, A., Baena, M., and Barris, C. (2010). "A simplified method to obtain time-dependent curvatures and deflections of concrete members reinforced with FRP bars." Composite Structures, 92(8), 1833-1838.

Mood, A. M., Graybill, F. A., and Boes, D. C. (1974). "Introduction to the theory of statistics." McGraw-Hill, New York, USA, .

Mota, C., Alminar, S., and Svecova, D. (2006). "Critical review of deflection formulas for FRP-RC members." Journal of Composites for Construction, 10(3), 183-194.

Nanni, A. (2003). "North American design guidelines for concrete reinforcement and strengthening using FRP: Principles, applications and unresolved issues." Construction and Building Materials, 17(6-7), 439-446.

Nanni, A. (2001). "Relevant field applications of FRP composites in concrete structures." Composites in Construction, Porto, Portugal, October 10-12, 2001, J. Figueiras, L. Juvandes and R. Furia Eds., 661-670.

Narayanan, R. S., and Goodchild, C. H. (2006). "Concise Eurocode 2 for the design of in-situ concrete framed buildings to BS EN 1992-1:1:2004 and its UK National Annex :2005." The Concrete Centre and British Cement Association, .

Nawy, E. G. (1985). "Flexural cracking behaviour of pretensioned and post-tensioned beams: the state of the art." Journal of the American Concrete Institute, 82(6), 890-900.

Nehdi, M., Omeman, Z., and El-Chabib, H. (2008). "Optimal efficiency factor in strut-and-tie model for FRP-reinforced concrete short beams with (1.5 < a/d < 2.5)." Materials and Structures/Materiaux Et Constructions, 41(10), 1713-1727.

Newhook, J., Ghali, A., and Tadros, G. (2002). "Concrete flexural members reinforced with fiber reinforced polymer: Design for cracking and deformability." Canadian Journal of Civil Engineering, 29(1), 125-134.

Oh, B. H., and Kang, Y. J. (1987). "New formulas for maximum crack width and crack spacing in reinforced concrete flexural members." ACI Structural Journal, 84(2), 103-112.

Ospina, C. E., Alexander, S., and Cheng, J. J. (2001). "Behaviour of concrete slabs with fibre-reinforced polymer reinforcement." Structural Engineering Report N0.242, Department of Civil and Environmental Engineering, University of Alberta, Alberta, Canada 355pp.

Ospina, C. E., and Bakis, C. E. (2007). "Indirect flexural crack control of concrete beams and one-way slabs reinforced with FRP bars." Proceedings of the 8th International Symposium on Fibre-Reinforced Polymer Reinforcement for Concrete Structures.

Ospina, C. E., and Bakis, C. E. (2006). "Indirect crack control procedure for FRP-reinforced concrete beams and one-way slabs." Proceedings of the 3rd International Conference on FRP Composites in Civil Engineering, 535-538.

Ospina, C. E., and Gross, S. P. (2005). "Rationale for the ACI 440.1R-06 indirect deflection control design provisions." Proceedings of the 7th International Symposium on Fibre-Reinforced Polymer Reinforcement for Concrete Structures, 651-667.

Park, R., and Paulay, T. (1975). "Reinforced concrete structures". John Wiley and Sons, 769pp.

Pecce, M., Manfredi, G., and Cosenza, E. (2001). "A probabilistic assessment of deflections in FRP RC beams." Proceedings of the 5th International Symposium on Fibre-Reinforced Polymer Reinforcement for Concrete Structures, 2 887-896.

Pecce, M., Manfredi, G., and Cosenza, E. (2000). "Experimental response and code models of GFRP RC beams in bending." Journal of Composites for Construction, 4(4), 182-190.

Pecce, M., Manfredi, G., and Cosenza, E. (1998). "Experimental behaviour of concrete beams reinforced with glass FRP bars." Proceeding of the 8th European Conference on Composite Materials, 227-234.

Pilakoutas, K. (2000). "Composites in concrete construction." Failure Analysis of Industrial Composite Materials, E. E. Gdoutos, K. Pilakoutas, and C. A. Rodopoulos Eds., McGraw-Hill, London, 449-497.

Pilakoutas, K., Guadagnini, M., Neocleous, K., and Taerwe, L. (2007). "Design guidelines for FRP reinforced concrete structures." Proceedings of the Advanced Composites in Construction, University of Bath, Bath, UK.

Pilakoutas, K., Neocleous, K., and Guadagnini, M. (2002). "Design philosophy issues of fiber reinforced polymer reinforced concrete structures." Journal of Composites for Construction, 6(3), 154-161.

Rafi, M. M., and Nadjai, A. (2009). "Evaluation of ACI 440 deflection model for fiber-reinforced polymer reinforced concrete beams and suggested modification." ACI Structural Journal, 106(6), 762-771.

Rafi, M. M., Nadjai, A., Ali, F., and Talamona, D. (2008). "Aspects of behaviour of CFRP reinforced concrete beams in bending." Construction and Building Materials, 22(3), 277-285.

Rao, S. V. K. M., and Dilger, W. H. (1992). "Control of flexural crack width in cracked prestressed concrete members." ACI Structural Journal, 89(2), 127-138.

Razaqpur, A. G., Švecová, D., and Cheung, M. S. (2000). "Rational method for calculating deflection of fiber-reinforced polymer reinforced beams." ACI Structural Journal, 97(1), 175-184.

Rizkalla, S. H., and Hwang, L. S. (1984). "Crack prediction for members in uniaxial tension." Journal of the American Concrete Institute, 81(6), 572-579.

Rüsch, H. (1960). "Researches toward a general flexural theory for structural concrete." Journal of the American Concrete Institute, 57(1), 1-28.

Rüsch, H. (1955). "Versuche zur festigkeit der biegeduckzone." Bulletin nº 120, Deutscher Ausschuss Für Stahlbeton, 94pp.

Russo, G., and Romano, F. (1992). "Cracking response of RC members subjected to uniaxial tension." Journal of Structural Engineering New York, N.Y., 118(5), 1172-1190.

Saikia, B., Kumar, P., Thomas, J., Rao, K. S. N., and Ramaswamy, A. (2007). "Strength and serviceability performance of beams reinforced with GFRP bars in flexure." Construction and Building Materials, 21(8), 1709-1719.

Salib, S. R., and Abdel-Sayed, G. (2004). "Prediction of crack width for fiber-reinforced polymer-reinforced concrete beams." ACI Structural Journal, 101(4), 532-536.

Sargin, M. (1971). "Stress-strain relationship for concrete and the analysis of reinforced concrete sections." Dept. of Civil Eng. Univ. of Waterloo, Ontario, Canada, .

Scanlon, A., and Bischoff, P. H. (2008). "Shrinkage restraint and loading history effects on deflections of flexural members." ACI Structural Journal, 105(4), 498-506.

Scanlon, A., and Murray, D. W. (1974). "Time-dependent reinforced concrete slab deflections." Journal of the Structural Division ASCE, 100(9), 1911-1924.

Schöck Bauteile GmbH. (2006). http://www.schoeck-combar.com .

Scholz, H. (1991). "Simple deflection and cracking rules for partially prestressed members." ACI Structural Journal, 88(2), 199-203.

Shapiro, S. S., and Wilk, M. B. (1965). "An analysis of variance test for normality (complete samples)." Biometrika, 52 591-611.

Sherwood, E. G., Bentz, E. C., and Collins, M. P. (2008). "Prediction of the shear strength of FRP-reinforced slabs using the 2004 CSA A23.3 design code." Proceedings, Annual Conference - Canadian Society for Civil Engineering, 4 2505-2514.

Thériault, M., and Benmokrane, B. (1998). "Effects of FRP reinforcement ratio and concrete strength on flexural behavior of concrete beams." Journal of Composites for Construction, 2(1), 7-15.

Thorenfeldt, E., Tomaszewicz, A., and Jensen, J. J. (1987). "Mechanical properties of high-strength concrete and application in design." Proceedings of the Symposium Utilization of High Strength Concrete, 149-159.

Torres, L., López-Almansa, F., and Bozzo, L. M. (2004). "Tension-stiffening model for cracked flexural concrete members." Journal of Structural Engineering, 130(8), 1242-1251.

Torres, L., López-Almansa, F., Cahís, X., and Bozzo, L. M. (2003). "A numerical model for sequential construction, repairing and strengthening of 2-D concrete frames." Engineering Structures, 25(3), 323-336.

Toutanji, H., and Deng, Y. (2003). "Deflection and crack-width prediction of concrete beams reinforced with glass FRP rods." Construction and Building Materials, 17(1), 69-74.

Toutanji, H. A., and Saafi, M. (2000). "Flexural behavior of concrete beams reinforced with glass fiber-reinforced polymer (GFRP) bars." ACI Structural Journal, 97(5), 712-719.

Tureyen, A. K., and Frosch, R. J. (2003). "Concrete Shear Strength: Another Perspective." ACI Structural Journal, 100(5), 609-615.

Tureyen, A. K., and Frosch, R. J. (2002). "Shear tests of FRP-reinforced concrete beams without stirrups." ACI Structural Journal, 99(4), 427-434.

Ueda, T., Sato, Y., Ito, T., and Nishizono, K. (2002). "Shear deformation of reinforced concrete beam." Journal of Materials, Concrete Structures and Pavements, JSCE, 56(711), 205-215.

Vogel, H., and Švecová, D. (2009). "Effective moment of inertia expression for concrete beams reinforced with Fiber-Reinforced Polymer (FRP)." American Concrete Institute, ACI Special Publication, 264 SP 77-93.

Vogel, H., and Švecová, D. (2008). "New approach for estimating the deflection of beams reinforced with FRP reinforcement." Journal of Composites for Construction, 12(6), 579-587.

Vollum, R. L. (2009). "Comparison of deflection calculations and span-to-depth ratios in BS 8110 and Eurocode 2." Magazine of Concrete Research, 61(6), 465-476.

Wallenberger, F. T., Watson, J. C., and Hong, L. (2001). "Glass Fibers." ASM Handbook, ASM International, Material Park, Ohio, 21 27-34.

Walsh, P. J. (2001). "Carbon Fibers." ASM Handbook, ASM International, Material Park, Ohio, 21 35-40.

Yang, S., and Chen, J. (1988). "Bond slip and crack width calculations of tension members." ACI Structural Journal, 85(4), 414-422.

Yost, J. R., Gross, S. P., and Dinehart, D. W. (2003). "Effective Moment of Inertia for Glass Fiber-Reinforced Polymer-Reinforced Concrete Beams." ACI Structural Journal, 100(6), 732-739.

Zilch, K., and Donaubauer, U. (2006). "Numerical examination of the deformation of one-way and two-way spanning reinforced concrete slabs using the formulation of realistic rigidities and storage conditions and in view of time-dependent deformations." Deutscher Ausschuss Für Stahlbeton, Heft 533, 3-130.

Experimental details and instrumentation

A.1. Experimental details
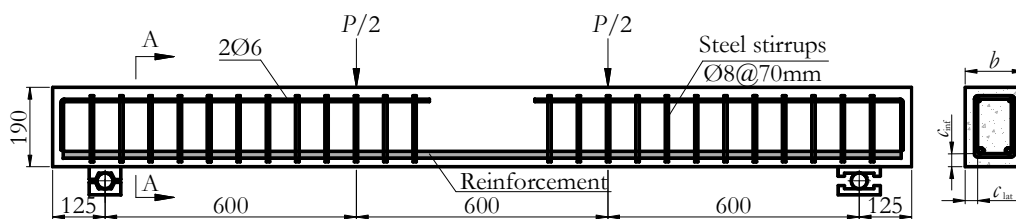
Figure A-1. Geometric layout and reinforcement.

Table A-1. Geometric details of the sections of the tested beams.
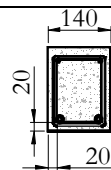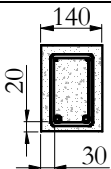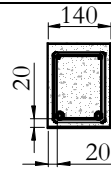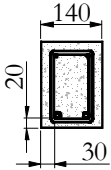
Beam Designation	b (mm)	c_{inf} (mm)	c_{lat} (mm)	Reinforcement	A-A
C1-212-D1-A	140	20	20	2ϕ12	
C1-212-D1-B	140	20	30	2ϕ12	
C1-216-D1-A	140	20	20	2ϕ16	
C1-216-D1-B	140	20	30	2ϕ16	

Table A-2. Geometric details of the sections of the tested beams (continuation).
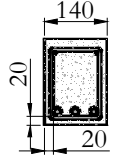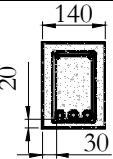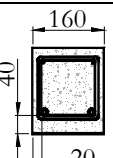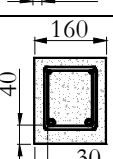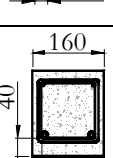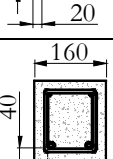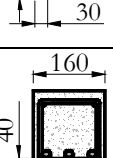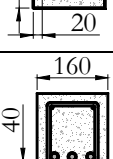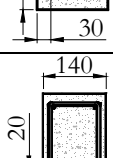
Beam Designation	b (mm)	c_{inf} (mm)	c_{lat} (mm)	Reinforcement	A-A
C1-316-D1-A	140	20	20	3ϕ16	
C1-316-D1-B	140	20	30	3ϕ16	
C1-212-D2-A	160	40	20	2ϕ12	
C1-212-D2-B	160	40	30	2ϕ12	
C1-216-D2-A	160	40	20	2ϕ16	
C1-216-D2-B	160	40	30	2ϕ16	
C1-316-D2-A	160	40	20	3ϕ16	
C1-316-D2-B	160	40	30	3ϕ16	
C2-212-D1-A	140	20	20	2ϕ12	

Table A-3. Geometric details of the sections of the tested beams (continuation).
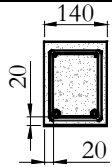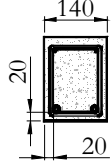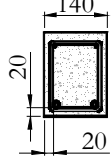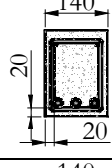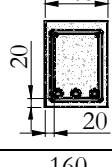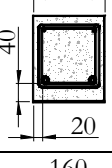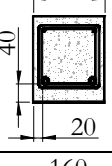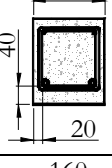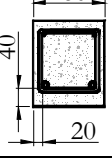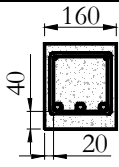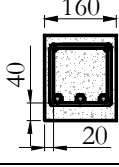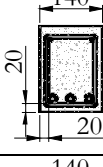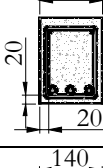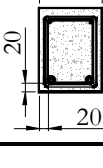
Beam Designation	b (mm)	c_{inf} (mm)	c_{lat} (mm)	Reinforcement	A-A
C2-212-D1-B	140	20	20	2ϕ12	
C2-216-D1-A	140	20	20	2ϕ16	
C2-216-D1-B	140	20	20	2ϕ16	
C2-316-D1-A	140	20	20	3ϕ16	
C2-316-D1-B	140	20	20	3ϕ16	
C2-212-D2-A	160	40	20	2ϕ12	
C2-212-D2-B	160	40	20	2ϕ12	
C2-216-D2-A	160	40	20	2ϕ16	
C2-216-D2-B	160	40	20	2ϕ16	

Table A-4. Geometric details of the sections of the tested beams (continuation).

Beam Designation	b (mm)	c_{inf} (mm)	c_{lat} (mm)	Reinforcement	A-A
C2-316-D2-A	160	40	20	3ϕ16	
C2-316-D2-B	160	40	20	3ϕ16	
C3-316-D1-A	140	20	20	3ϕ16	
C3-316-D1-B	140	20	20	3ϕ16	
C3-212-D1-S	140	20	20	2ϕ12 *	

A.2.   Instrumentation details
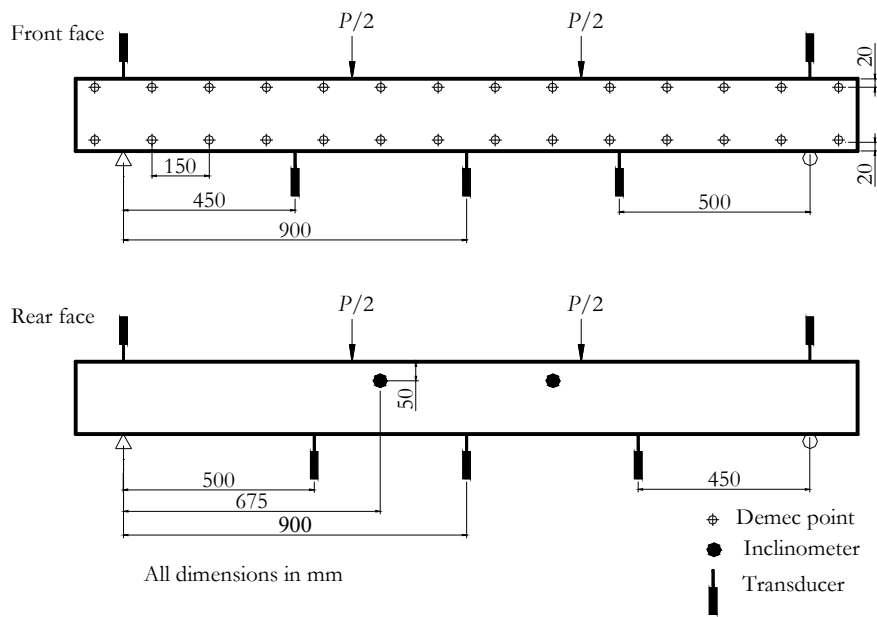
Figure A-2. Instrumentation details for beam C1-212-D1-A.
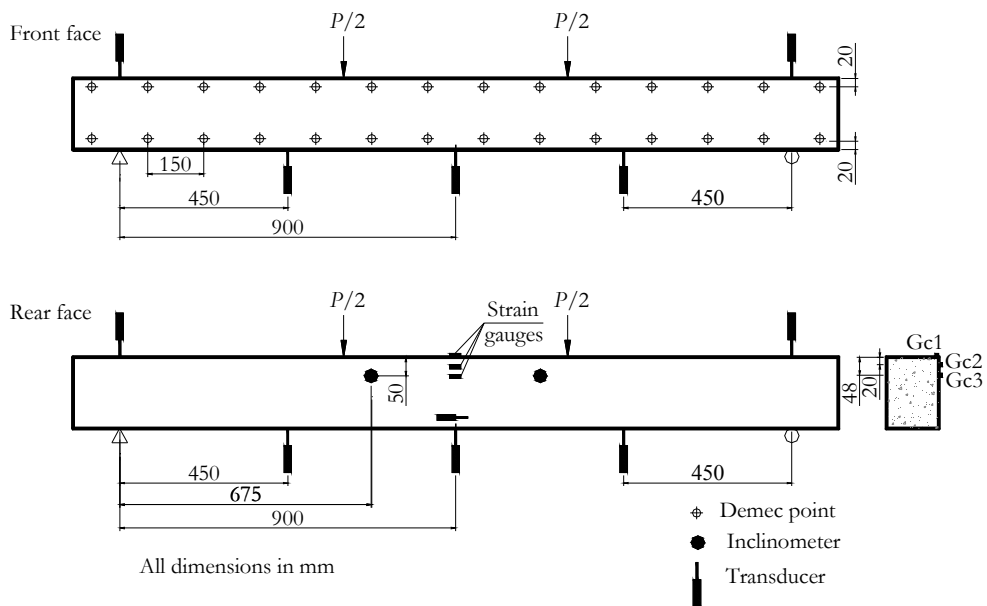
Figure A-3. Instrumentation details for beam C1-212-D1-B.
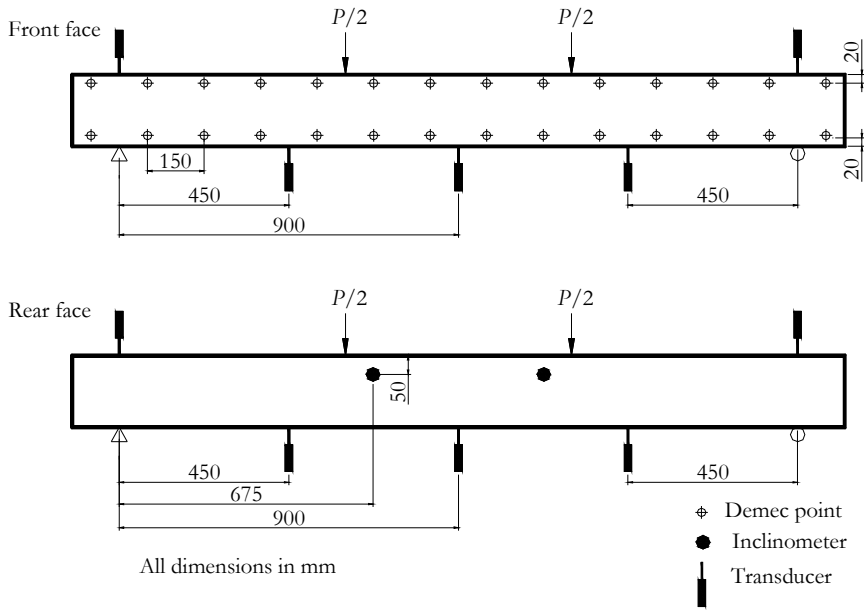
Figure A-4. Instrumentation details for beam C1-212-D2-A.
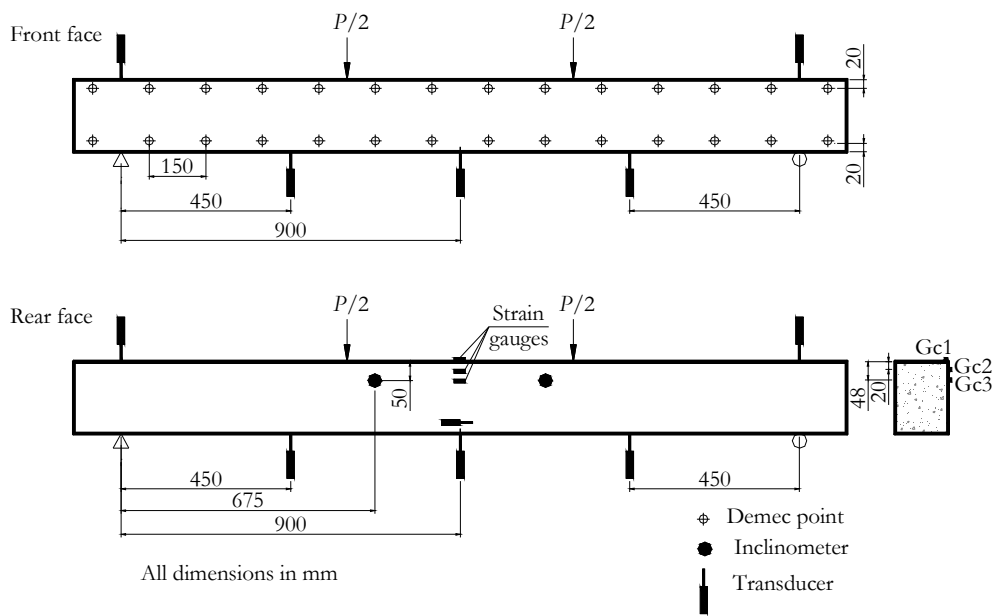
Figure A-5. Instrumentation details for beam C1-212-D2-B.
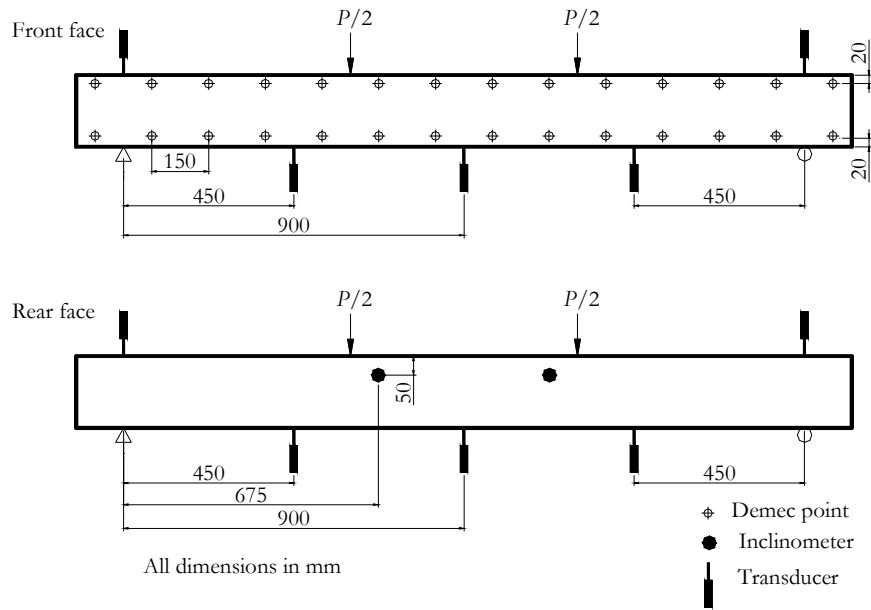
Figure A-6. Instrumentation details for beam C1-216-D1-A.
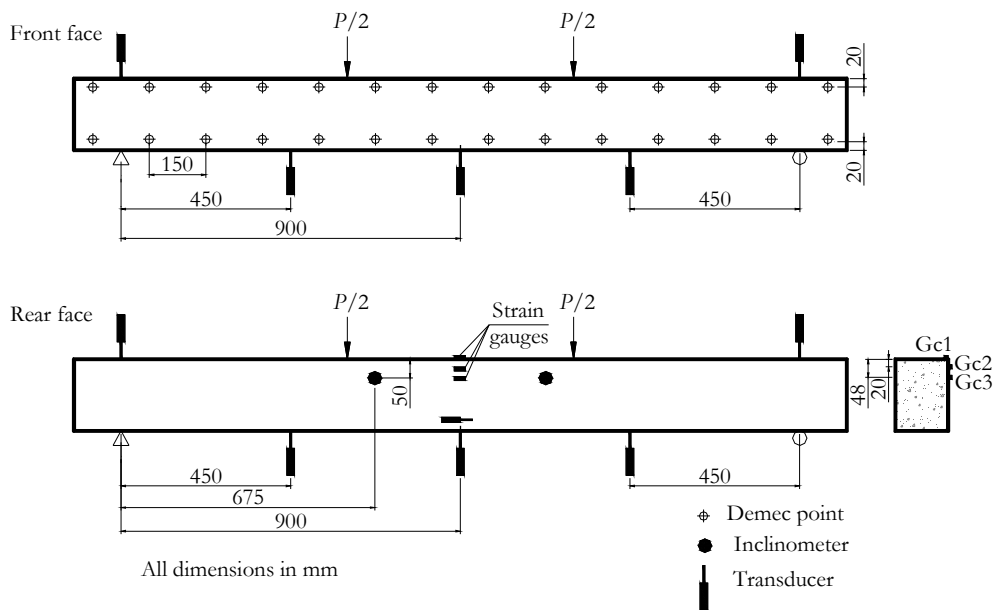
Figure A-7. Instrumentation details for beam C1-216-D1-B.
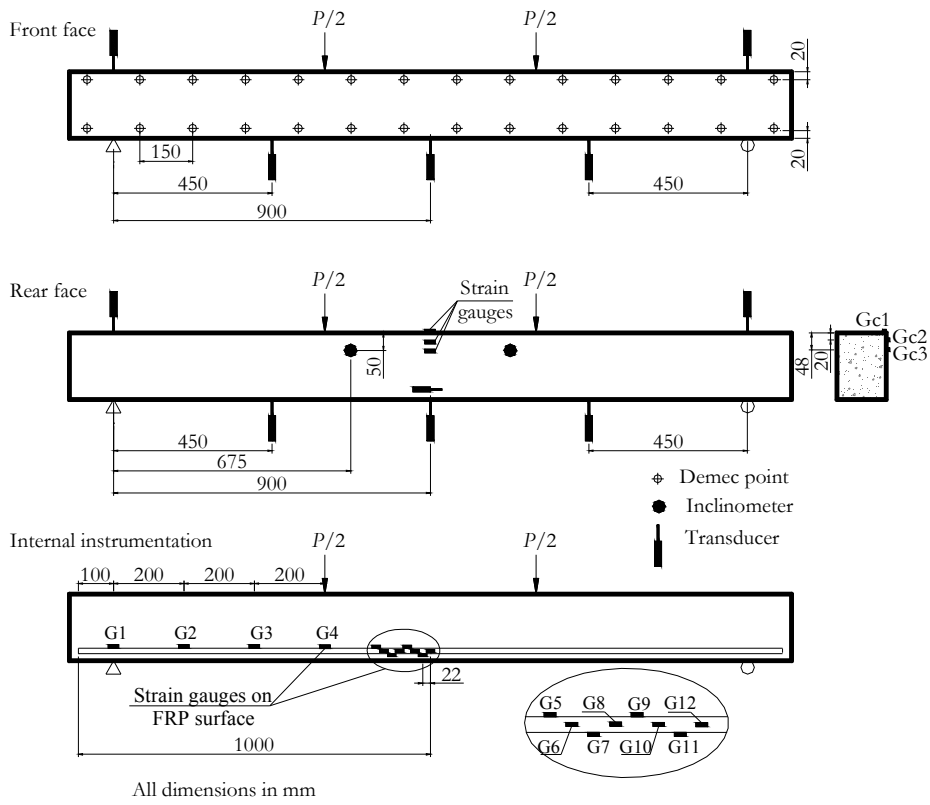
Figure A-8. Instrumentation details for beam C1-216-D2-A.
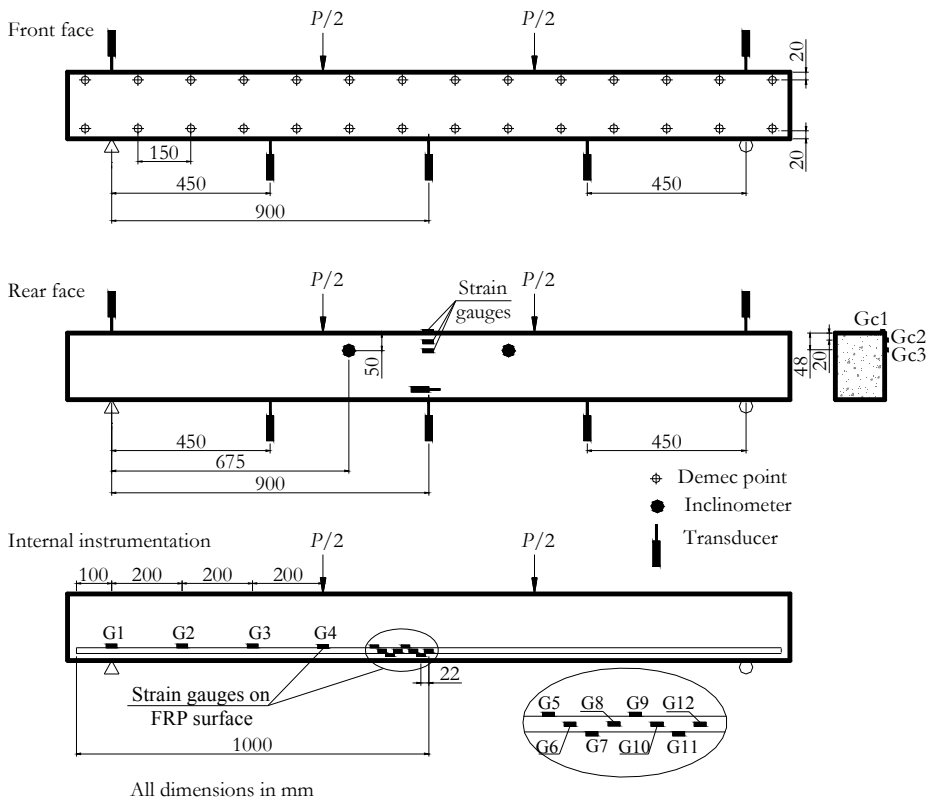
Figure A-9. Instrumentation details for beam C1-216-D2-B.
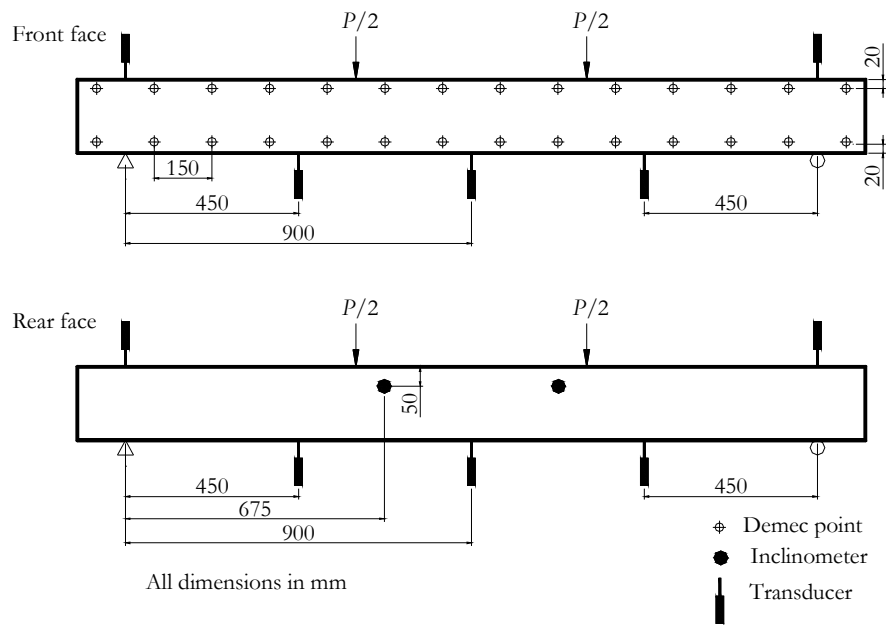
Figure A-10. Instrumentation details for beam C1-316-D1-A.
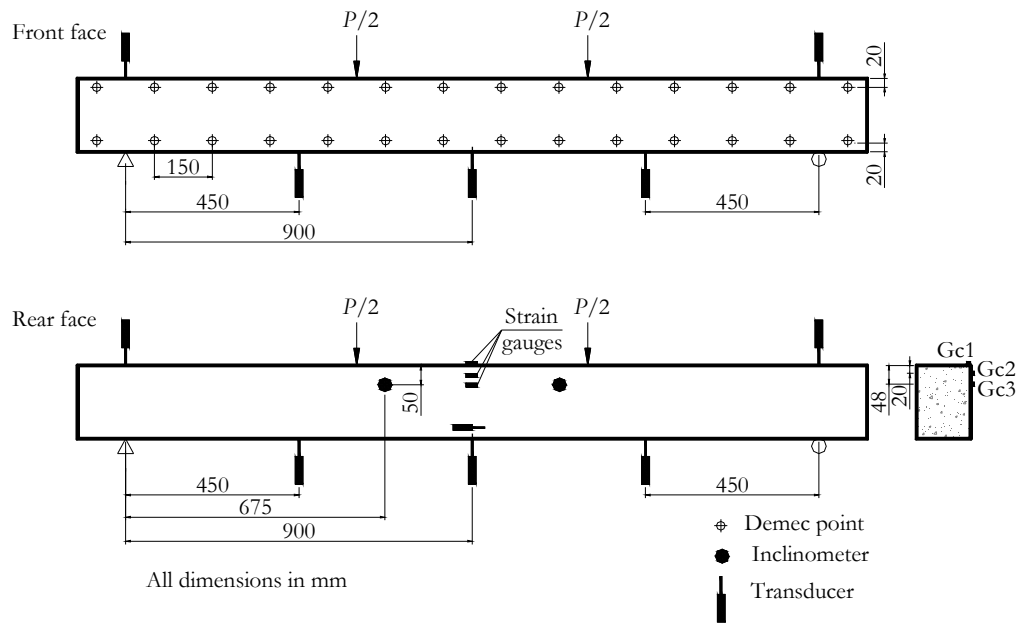
Figure A-11. Instrumentation details for beam C1-316-D1-B.
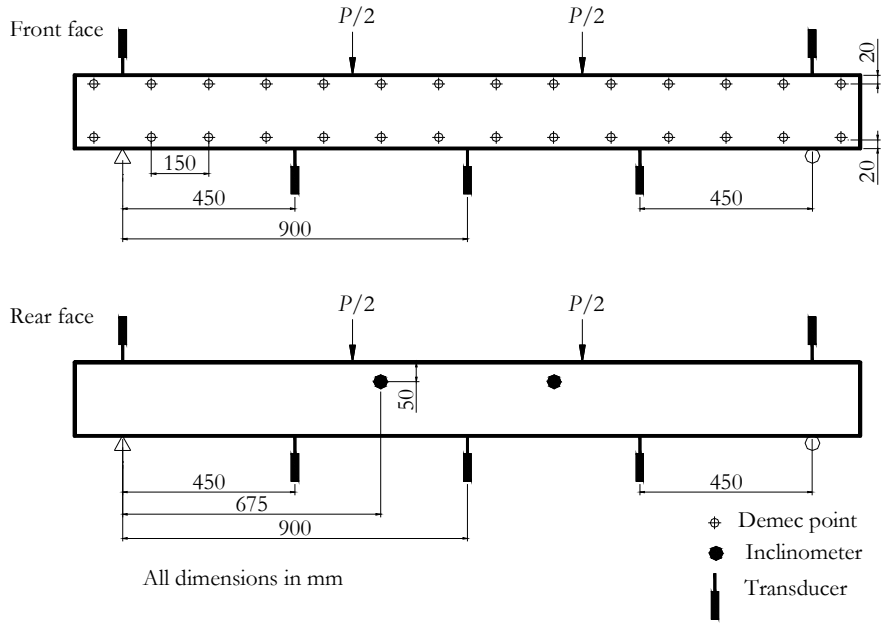
Figure A-12. Instrumentation details for beam C1-316-D2-A.
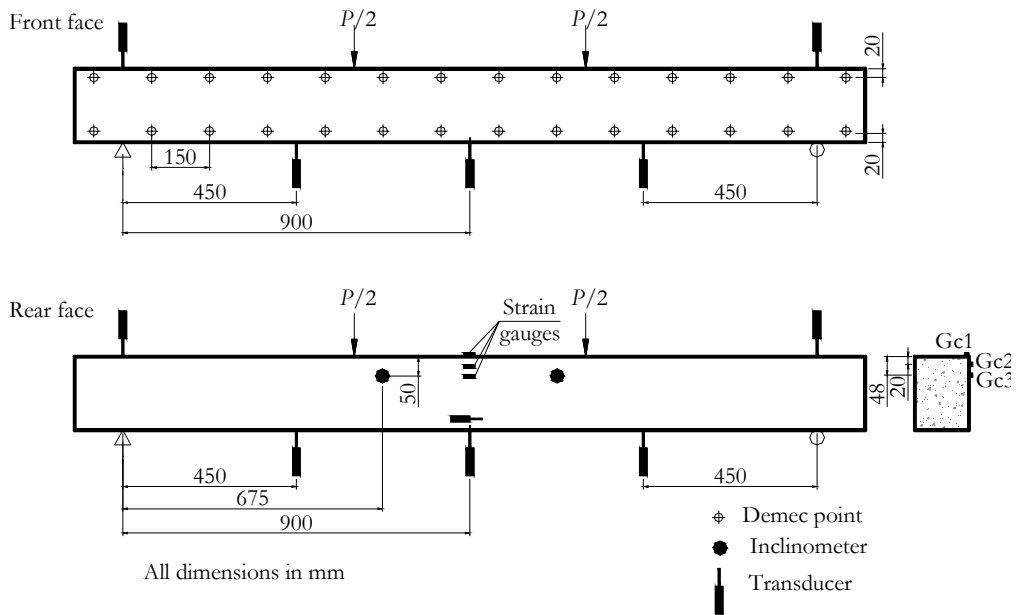
Figure A-13. Instrumentation details for beam C1-316-D2-B.
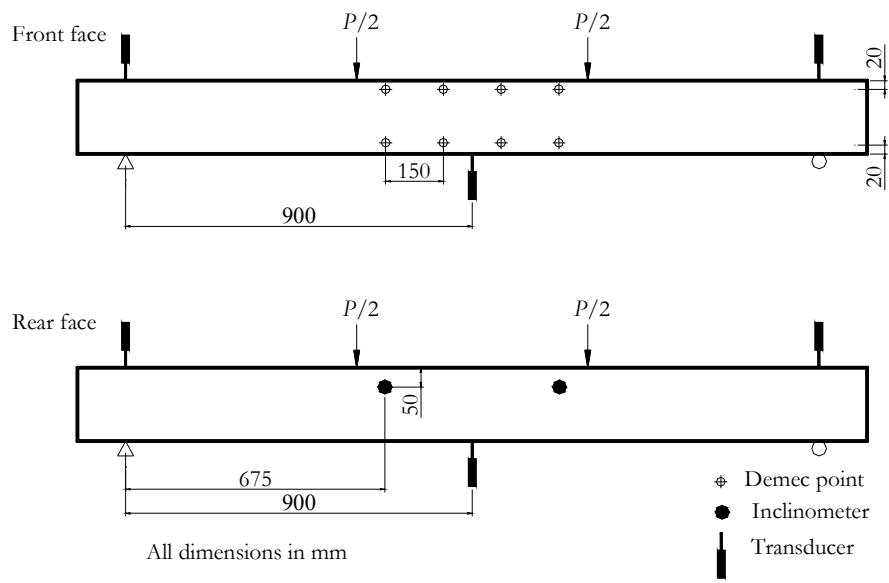
Figure A-14. Instrumentation details for beam C2-212-D1-A.
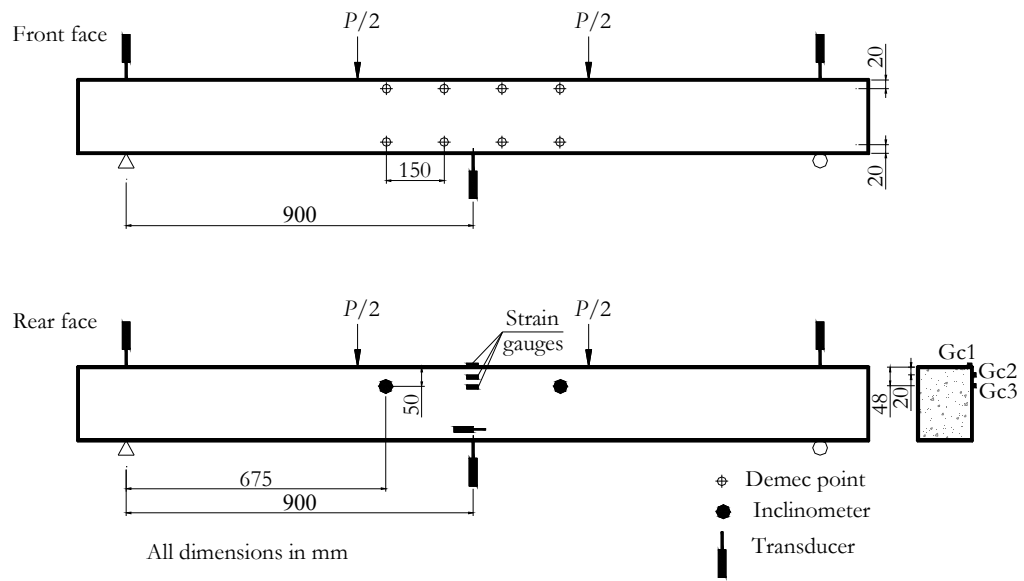
Figure A-15. Instrumentation details for beam C2-212-D1-B.
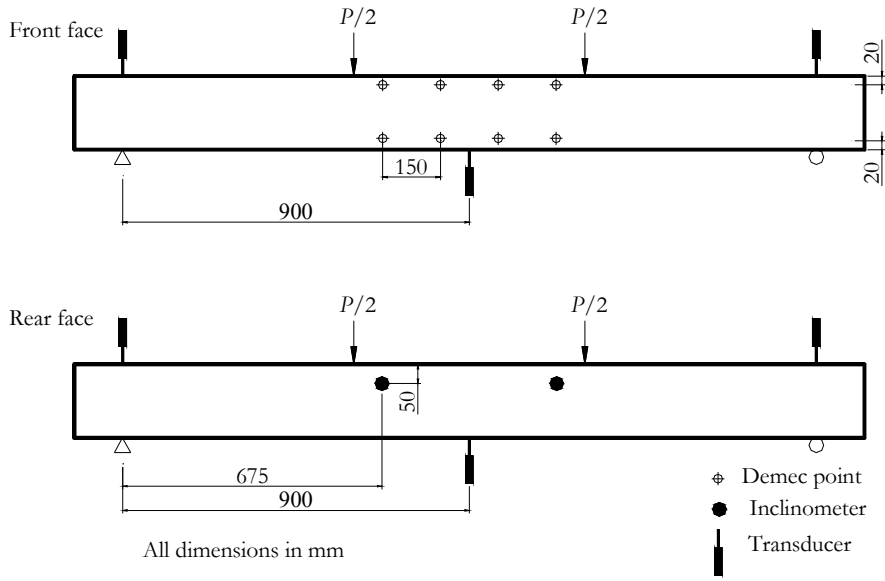
Figure A-16. Instrumentation details for beam C2-212-D2-A.
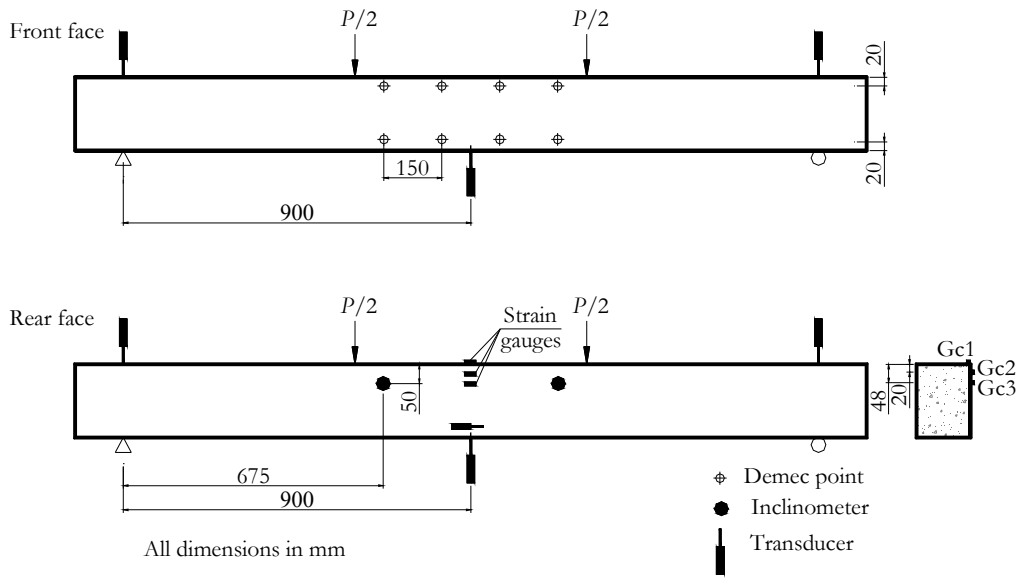
Figure A-17. Instrumentation details for beam C2-212-D2-B.
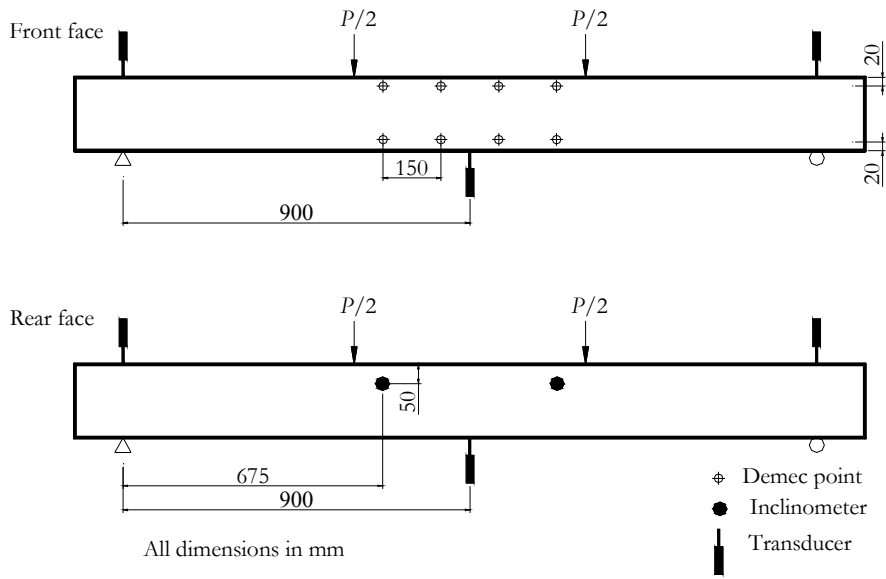
Figure A-18. Instrumentation details for beam C2-216-D1-A.
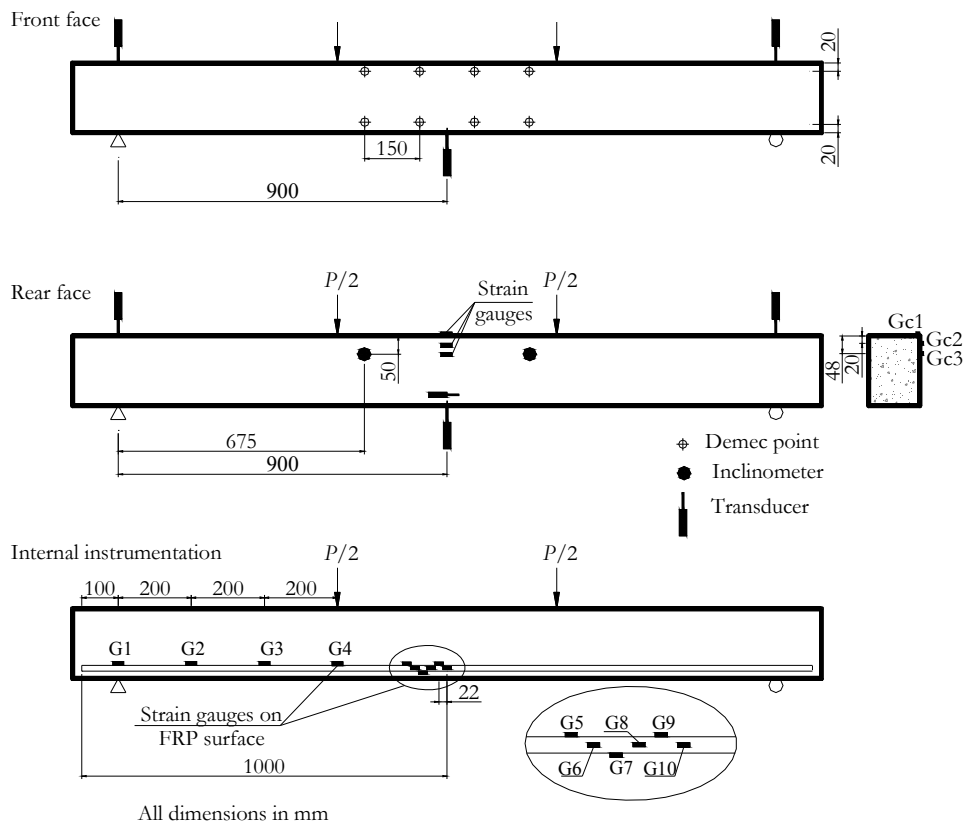
Figure A-19. Instrumentation details for beam C2-216-D1-B.
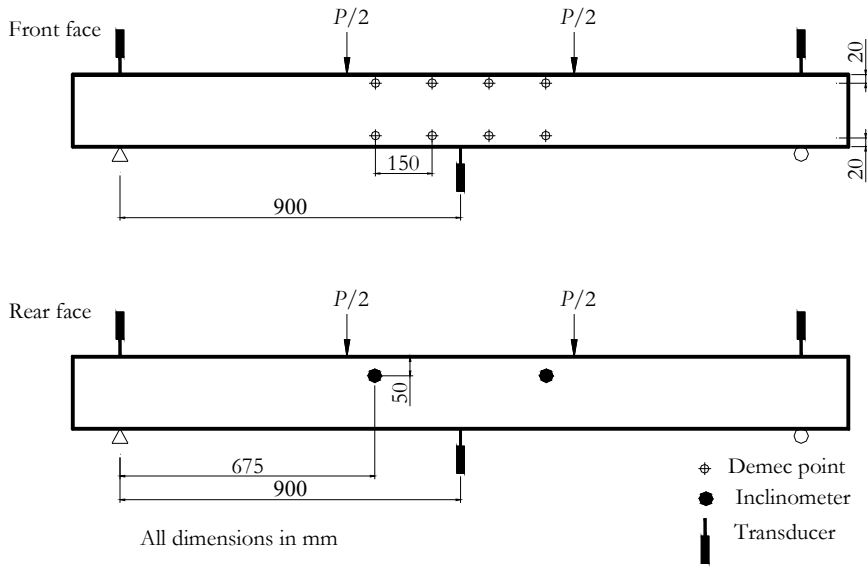
Figure A-20. Instrumentation details for beam C2-216-D2-A.
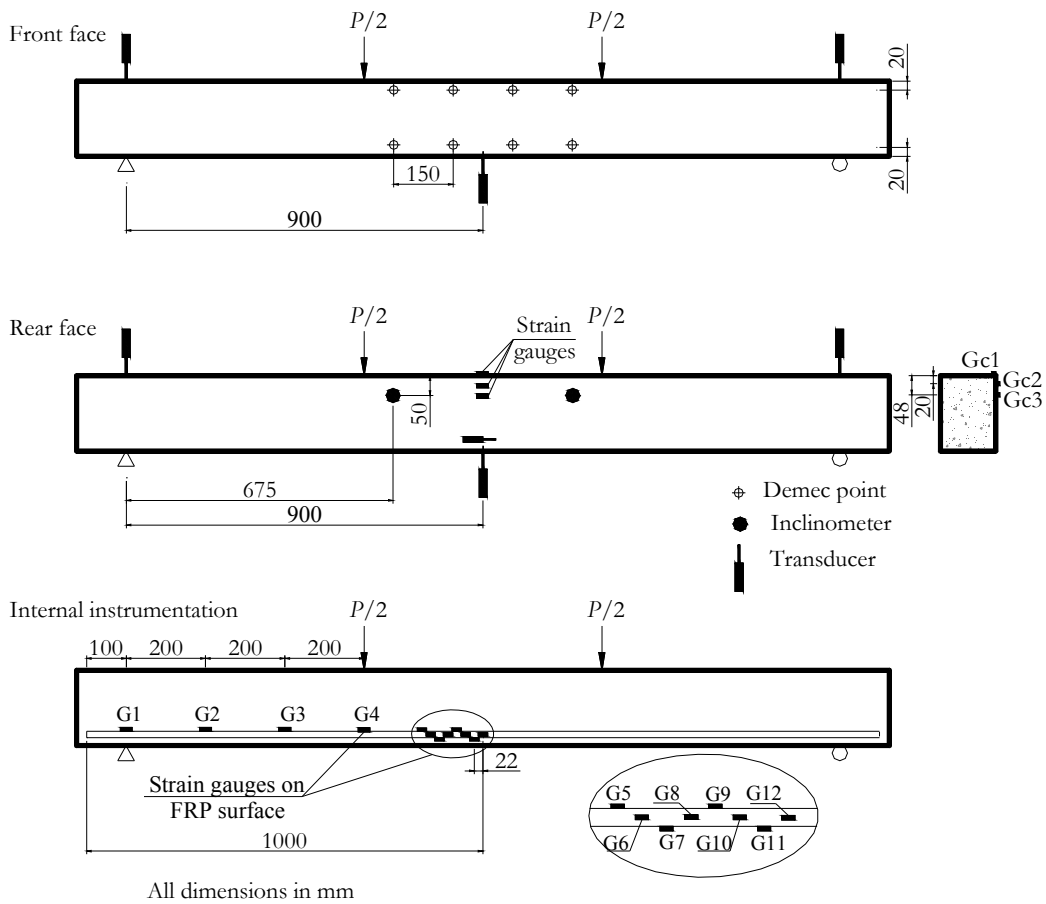
Figure A-21. Instrumentation details for beam C2-216-D2-B.
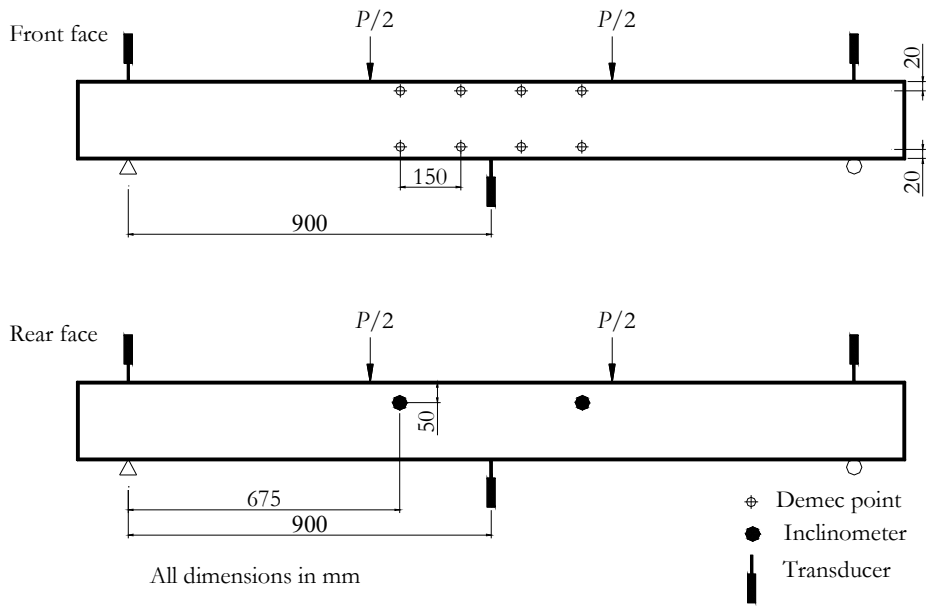
Figure A-22. Instrumentation details for beam C2-316-D1-A.
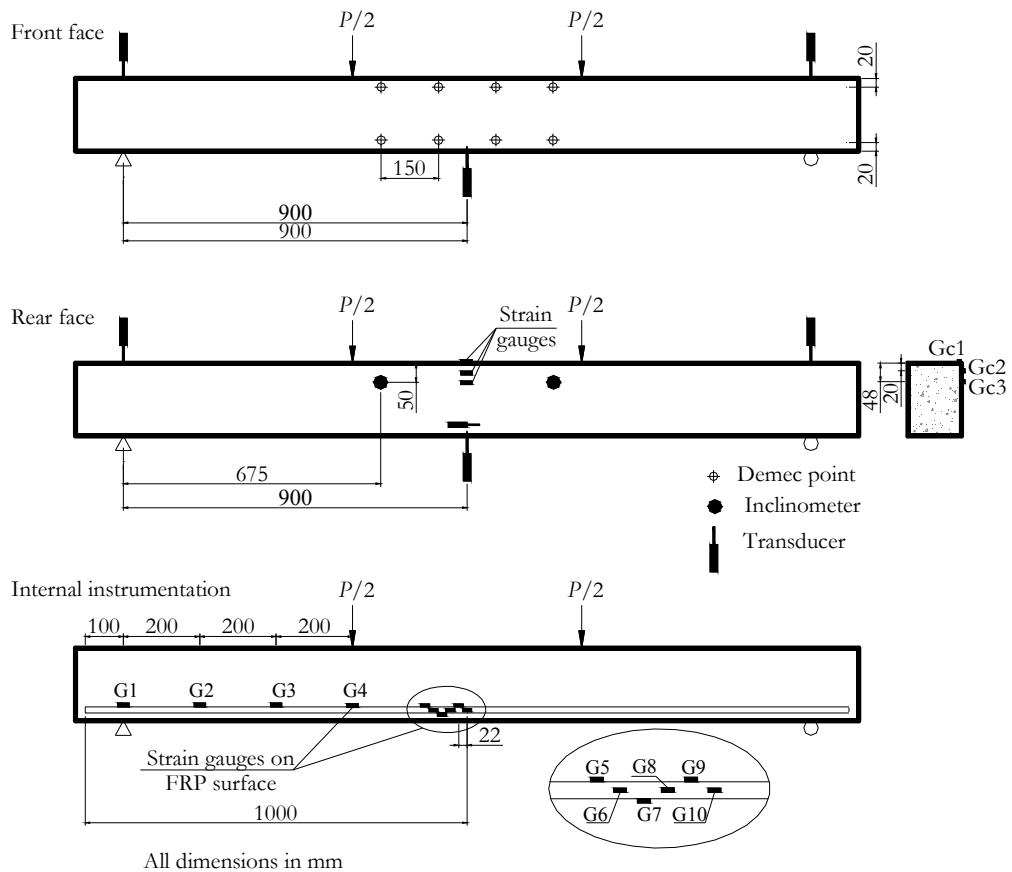
Figure A-23. Instrumentation details for beam C2-316-D1-B.
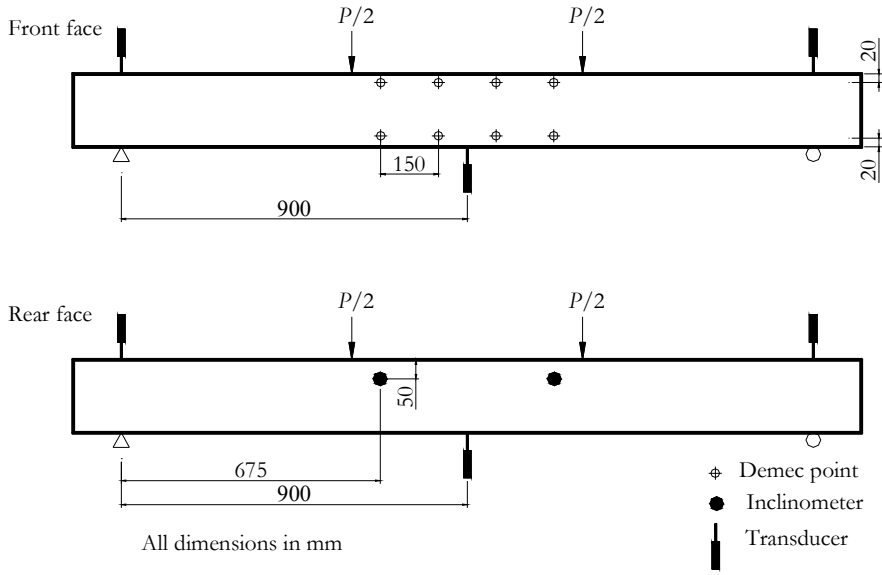
Figure A-24. Instrumentation details for beam C2-316-D2-A.
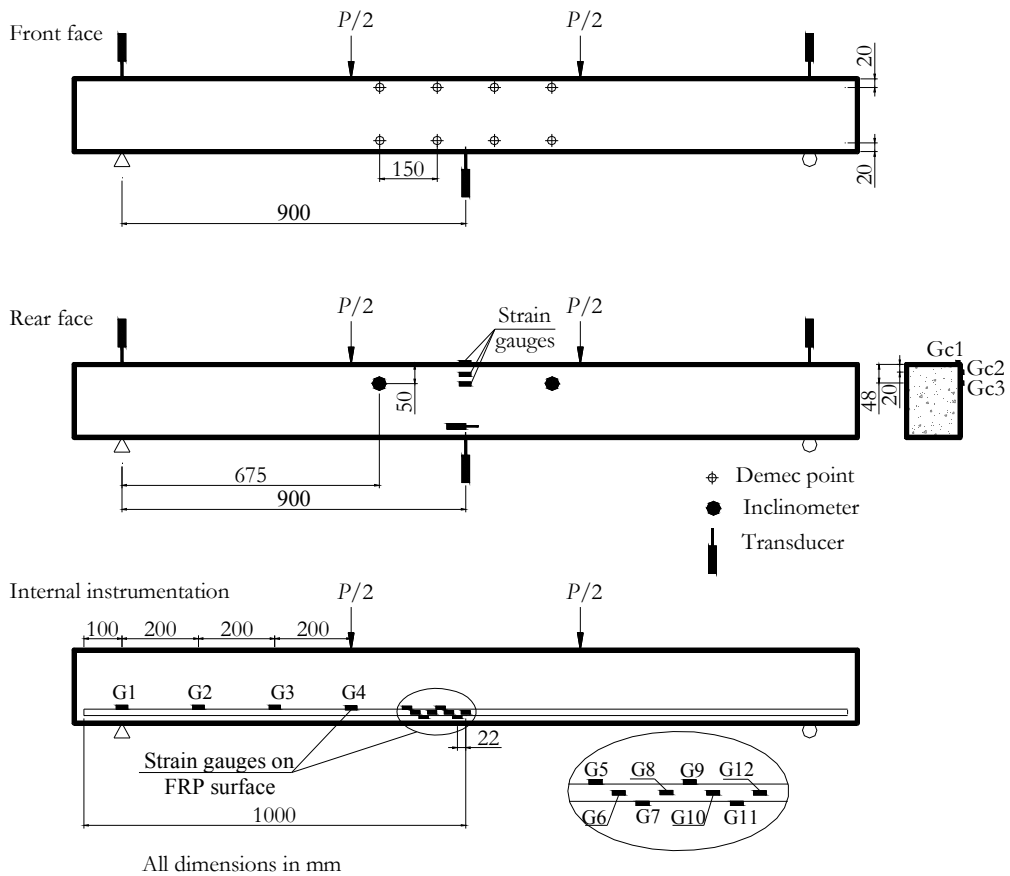
Figure A-25. Instrumentation details for beam C2-316-D2-B.
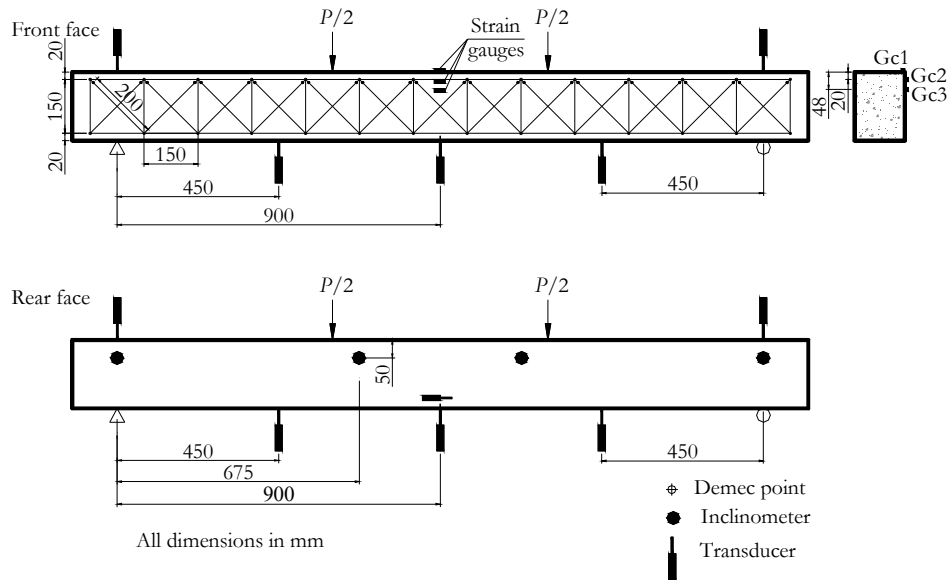
Figure A-26. Instrumentation details for beam C3-316-D1-A.
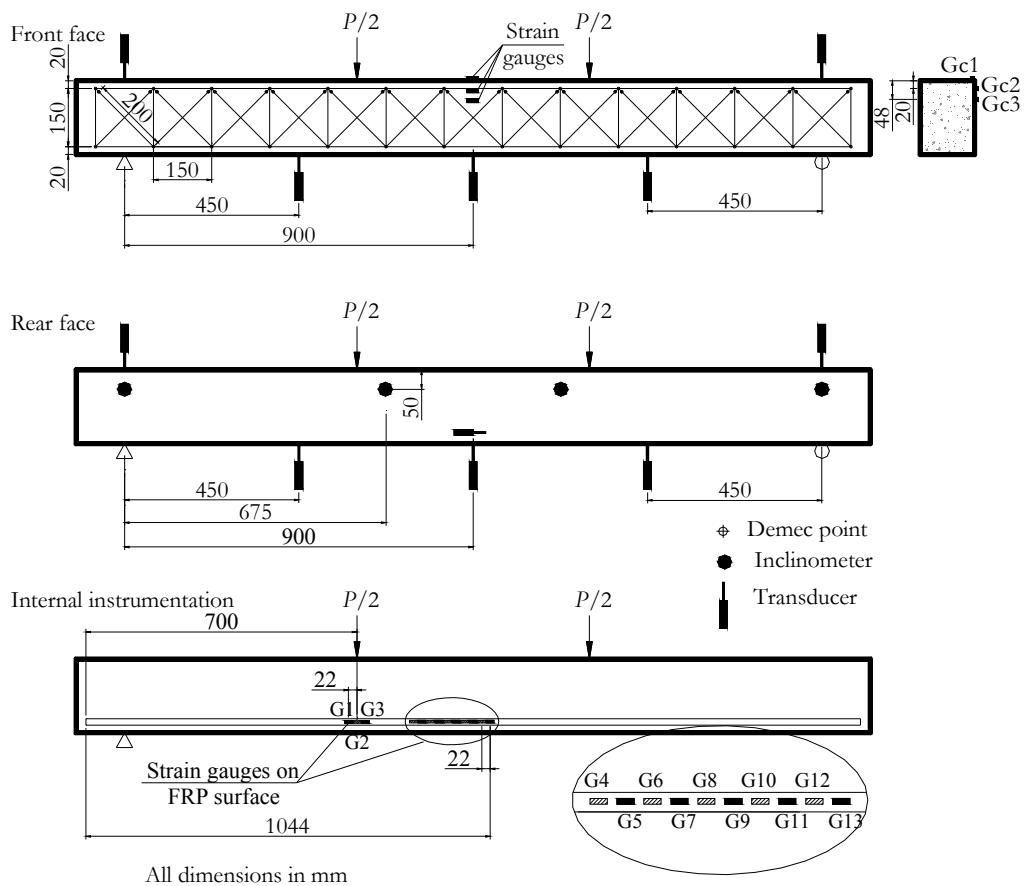
Figure A-27. Instrumentation details for beam C3-316-D1-B.
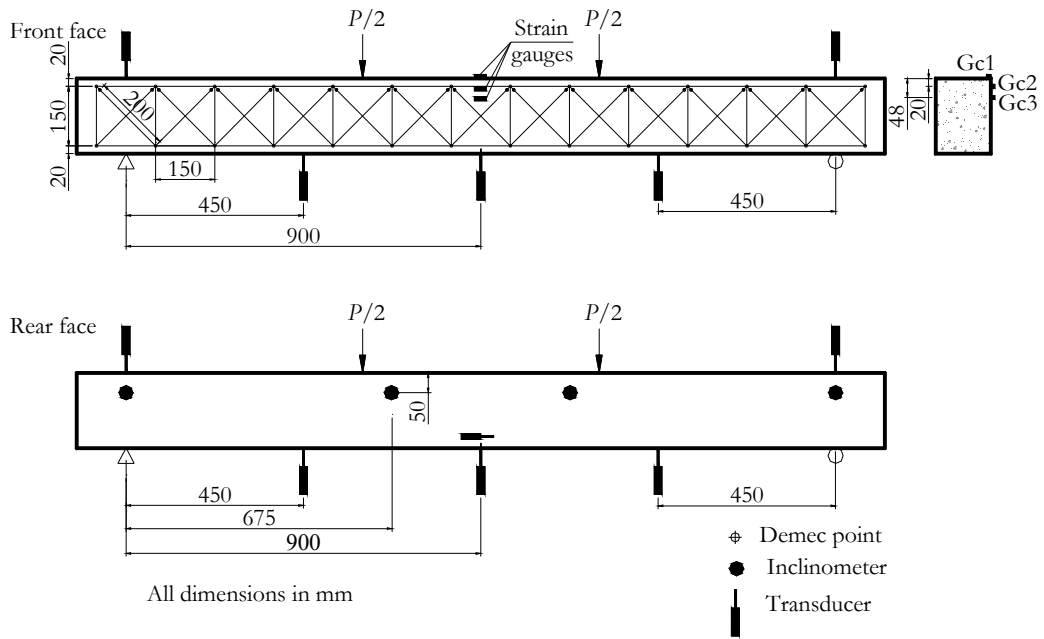
Figure A-28. Instrumentation details for beam C3-212-D1-S.

B.1. Results for the C1-212-D1 series

B.1.1. General data

	C1-212-D1-A	C1-212-D1-B
Cracking load (kN)	6.7	6.8
Load at reaching stabilised cracking phase (kN)	19.9	19.7
Average crack spacing at stabilised cracking phase (mm)	99	94
Maximum crack spacing at stabilised cracking phase (mm)	145	143
Minimum crack spacing at stabilised cracking phase (mm)	70	53
Load at which $\sigma_c = 0.45 f_c$ (kN)	--	14.2
Load at which w_{max}=0.5-0.7mm (kN)	39.5	39.5
Load at which $\delta = L/250$ (kN)	21.2	20.6
Ultimate load (kN)	79.9	81.7
Ultimate midspan deflection (mm)	41.9	41.7
Ultimate concrete strain (x10^{-6})	--	4310

B.1.2. Failure mode
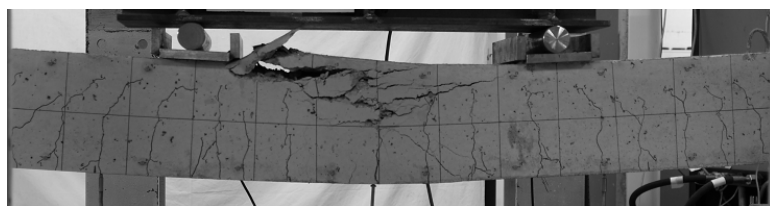
Figure B-1. Crushing of concrete for C1-212-D1-A.
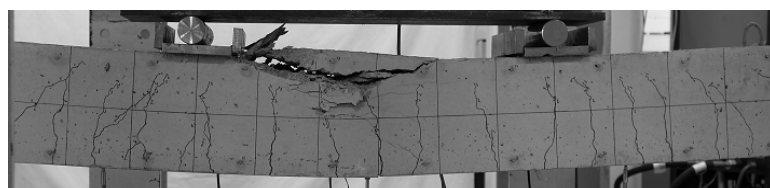
Figure B-2. Crushing of concrete for C1-212-D1-B.

B.1.3. Results at the midspan section
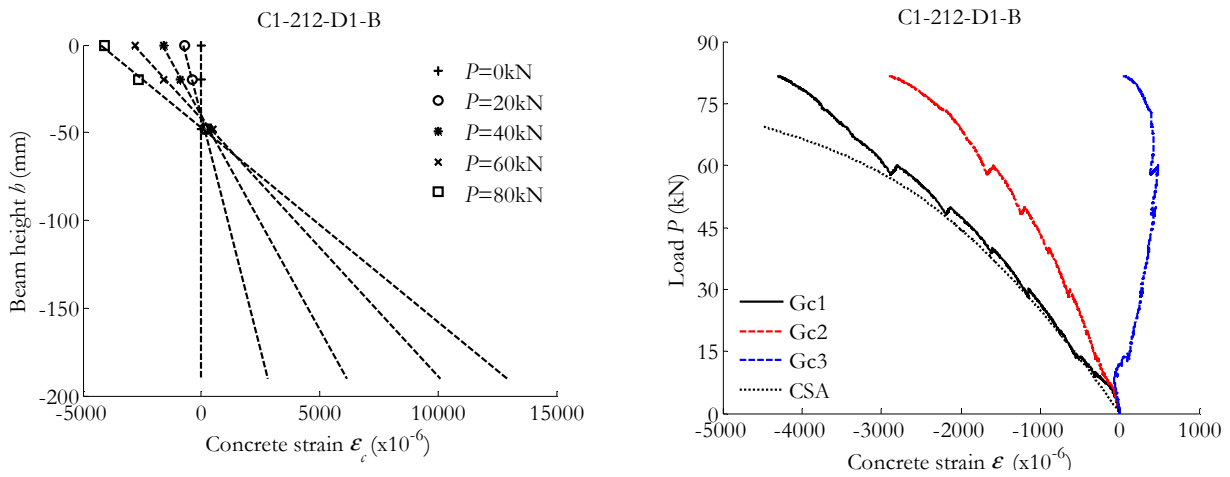
Figure B-3. Concrete strain in the midspan section: Along the height of the beam (left) /
Versus the load applied and compared to CSA predictions (right).
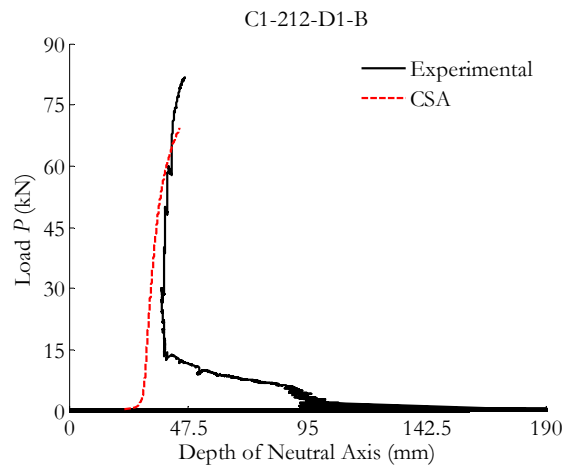
Figure B-4. Neutral axis depth compared to CSA predictions.
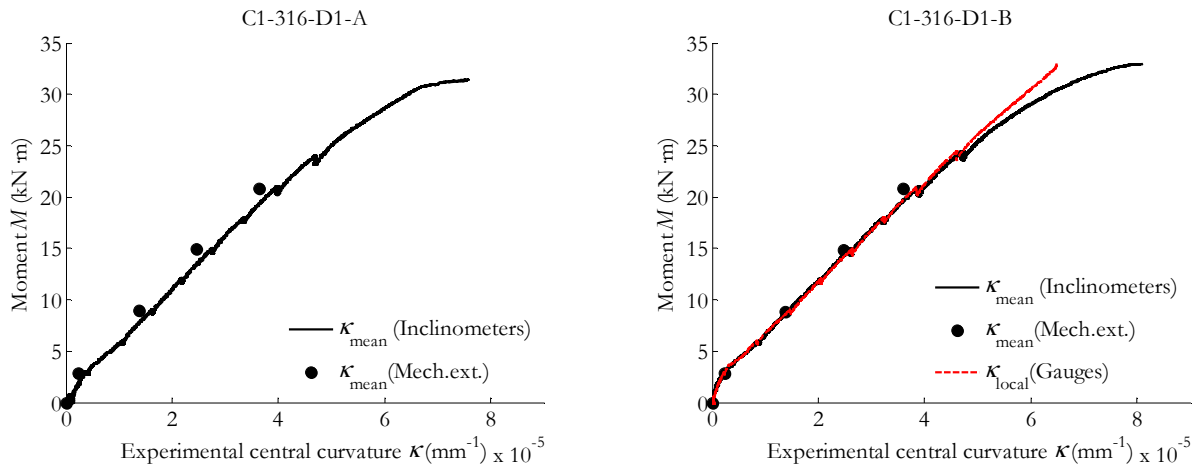
B.1.4. Results at the pure bending zone
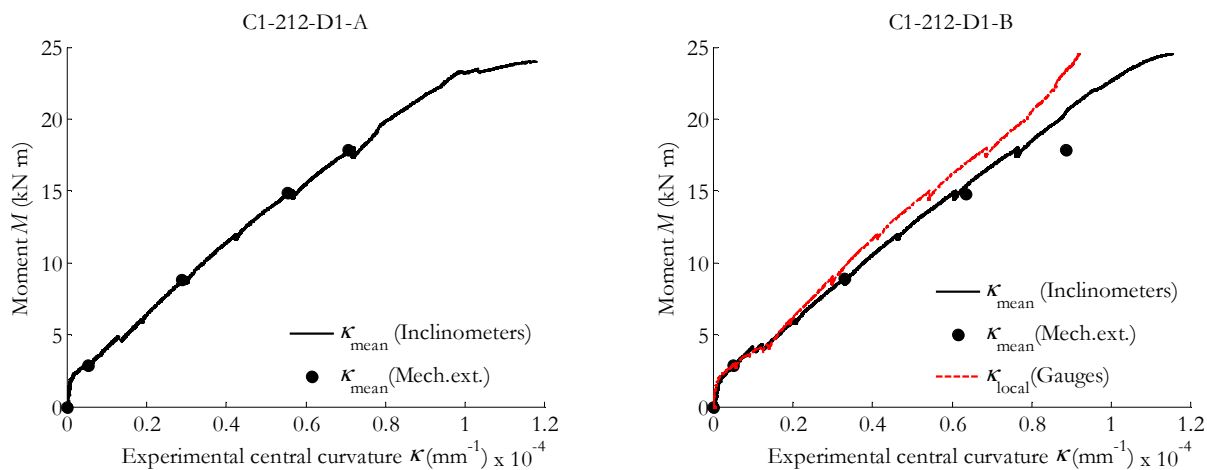
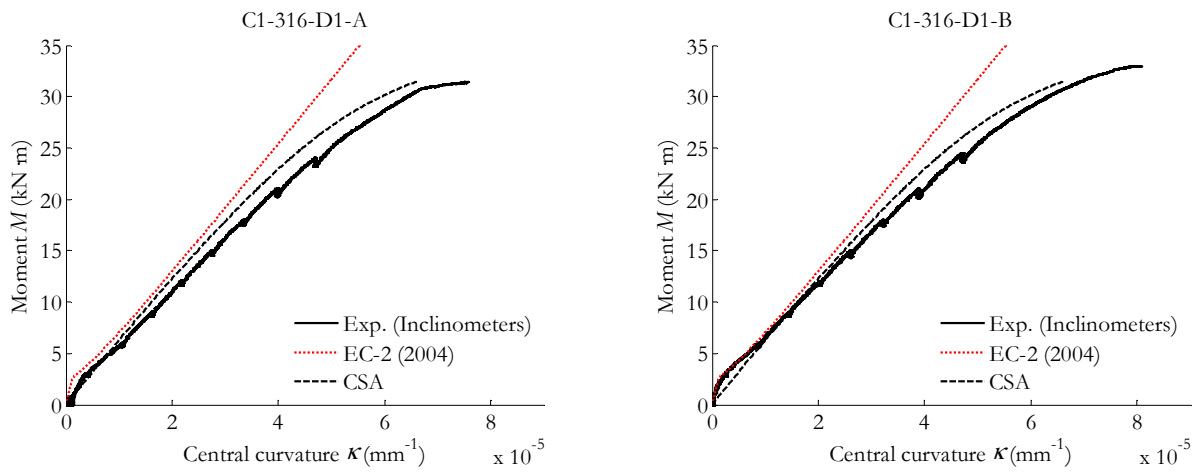Figure B-5. Experimental moment-curvature from inclinometers, mechanical extensometer and strain gauges on concrete.
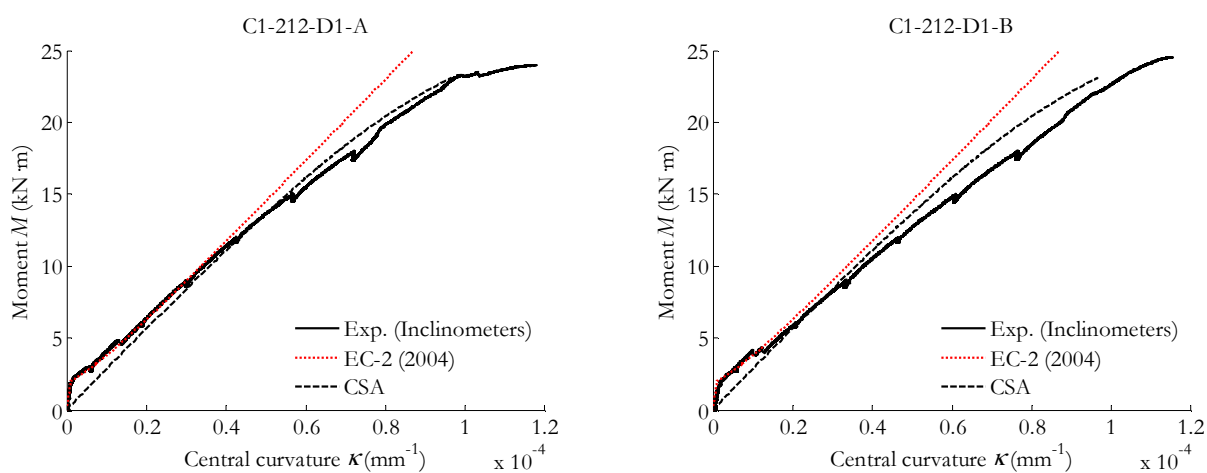
Figure B-6. Experimental moment-curvature from compared to Eurocode 2 (2004) and CSA predictions.

B.1.5. Results of the overall beam behaviour
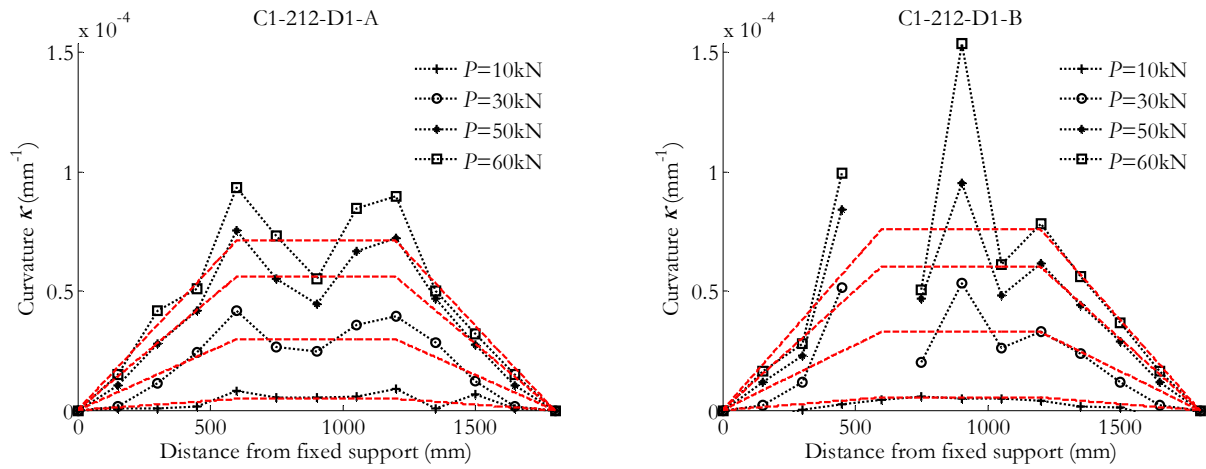
Figure B-7. Curvature along the length of the beam deduced form mechanical extensometer's data (dotted lines) compared to inclinometers' data (dashed lines).
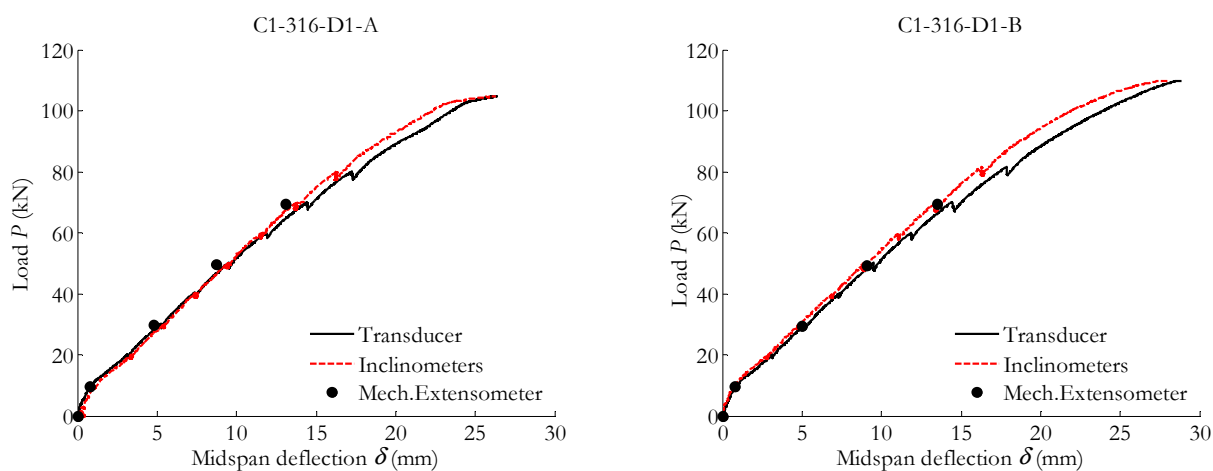
B.1.6. Results on deflection
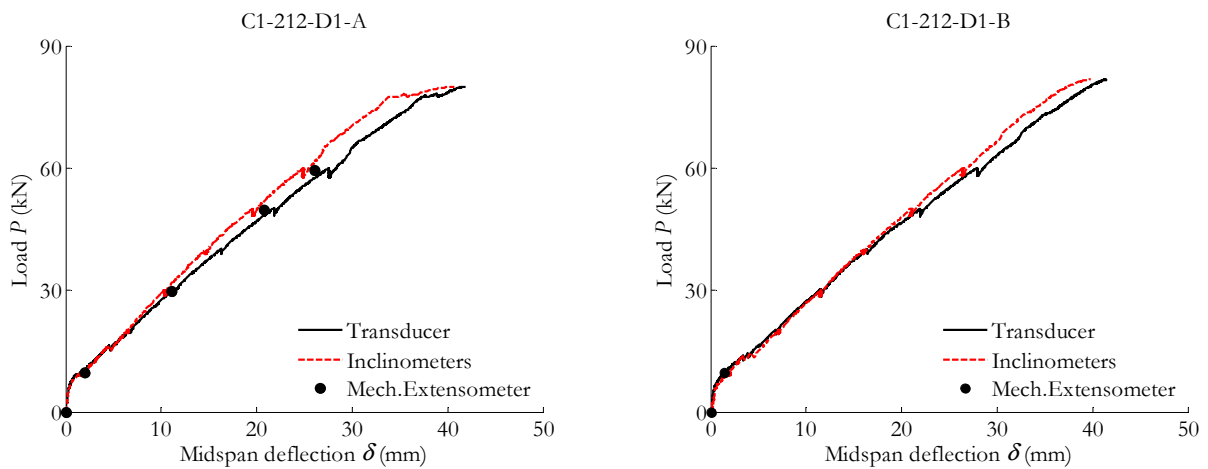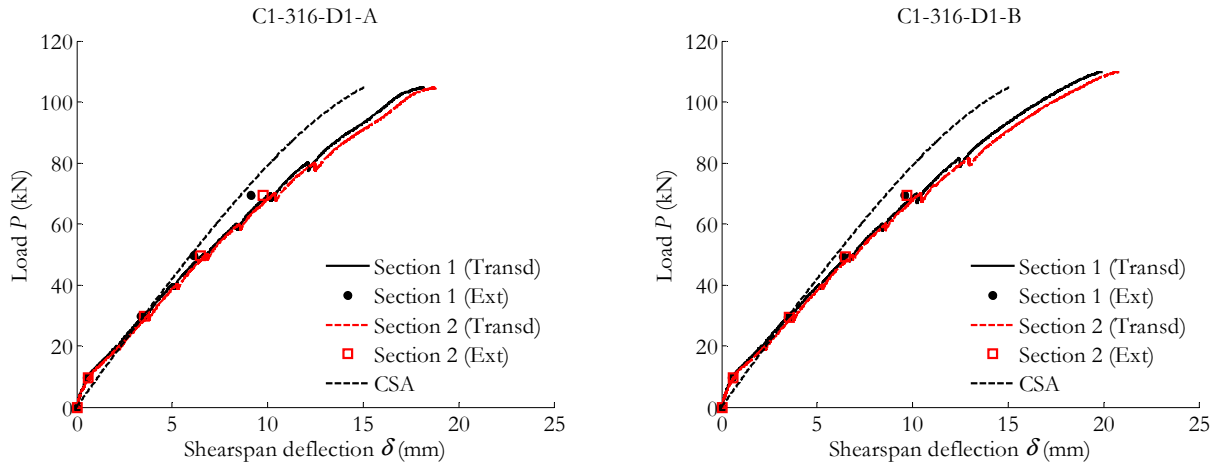

Figure B-8. Experimental midspan deflection.
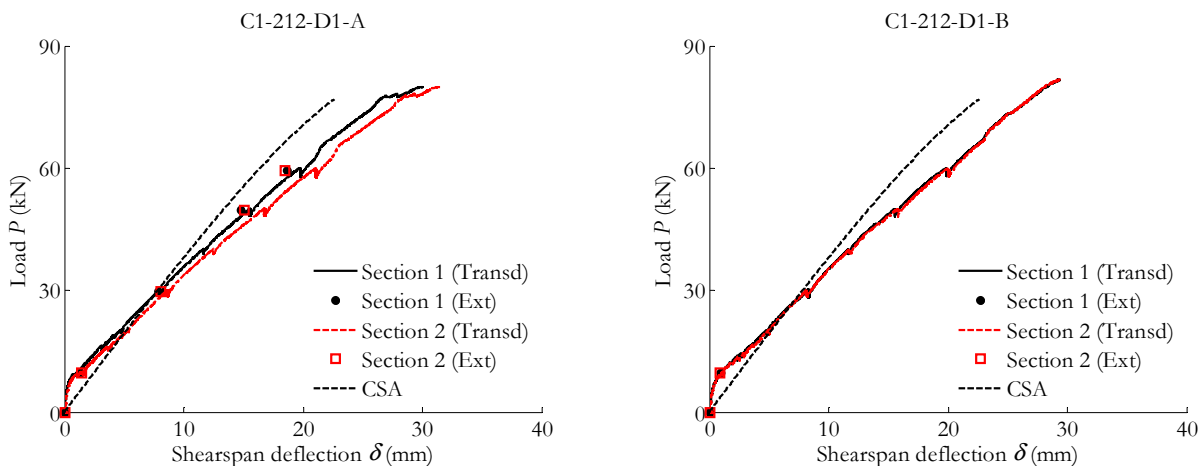
Figure B-9. Experimental shearspan deflection compared to cracked section analysis.
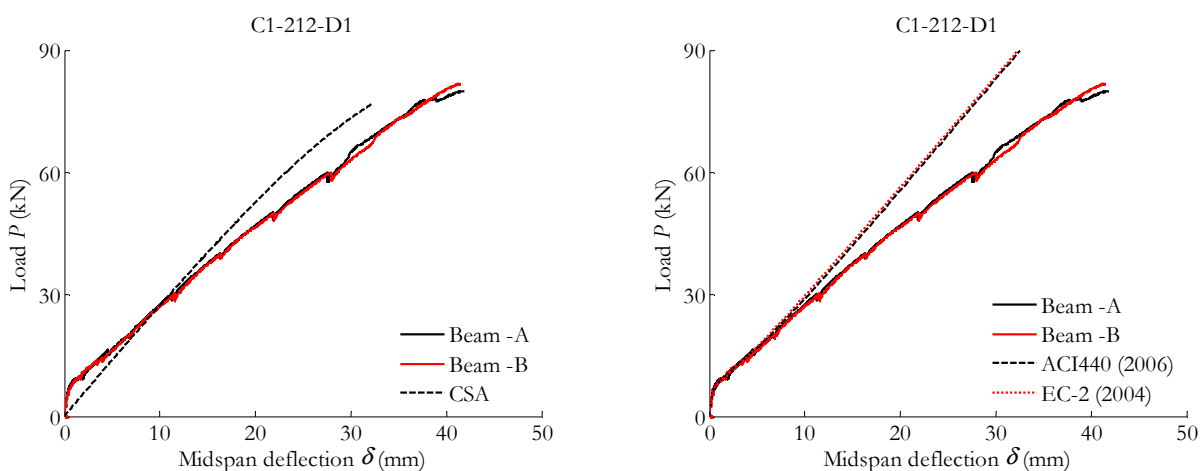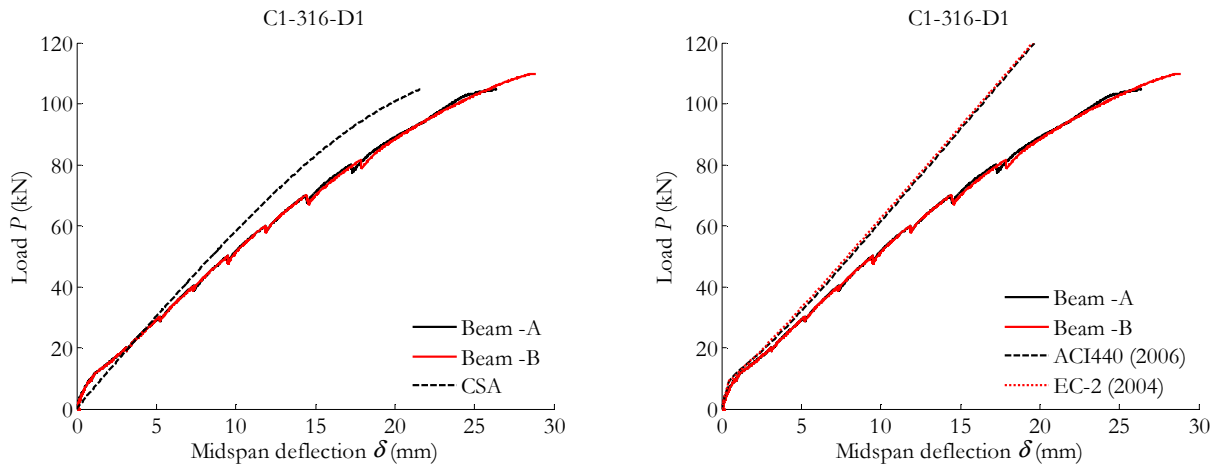

Figure B-10. Experimental midspan deflection (ultimate load) compared to cracked section analysis (left) / design codes (right).
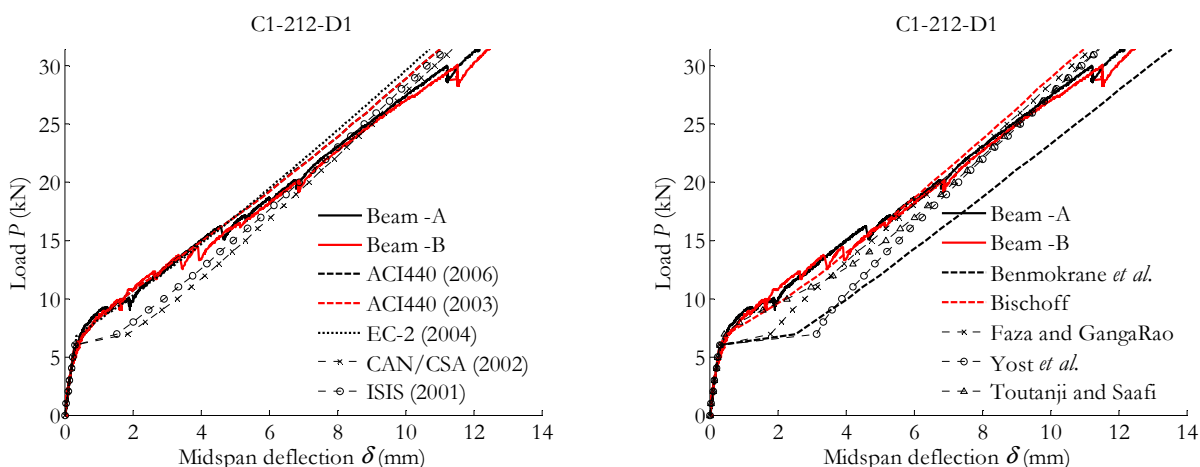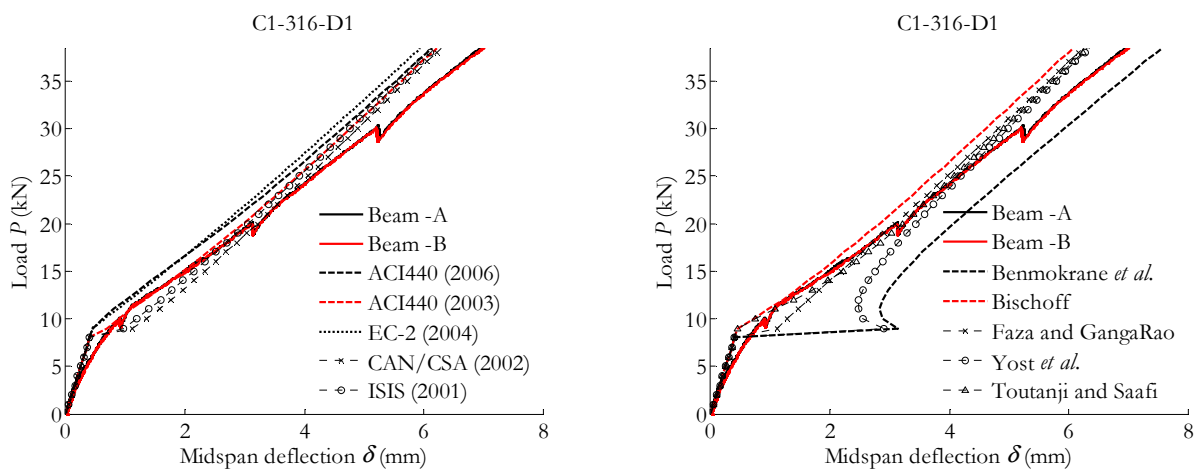

Figure B-11. Experimental vs theoretical midspan deflection (service load).
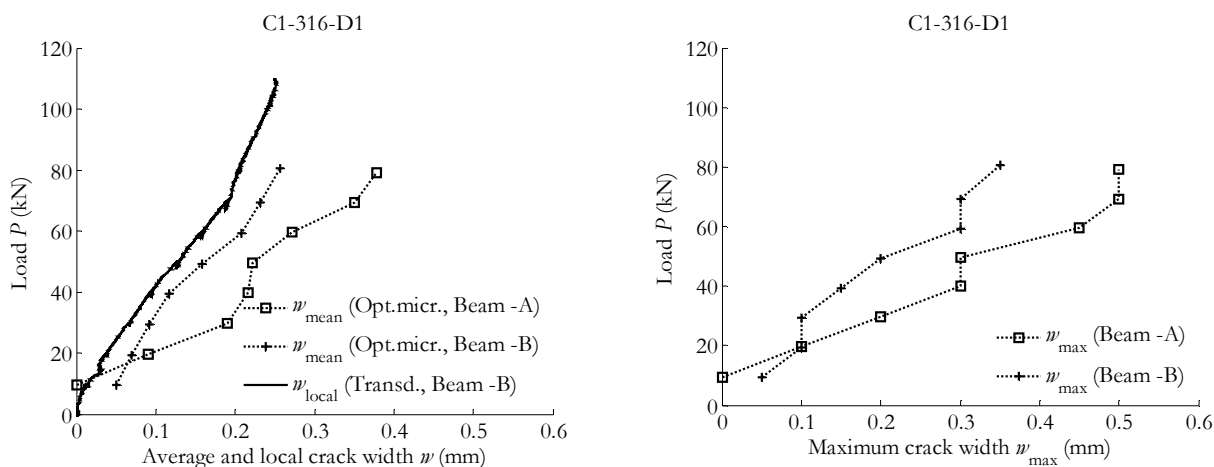
B.1.7. Results on cracking
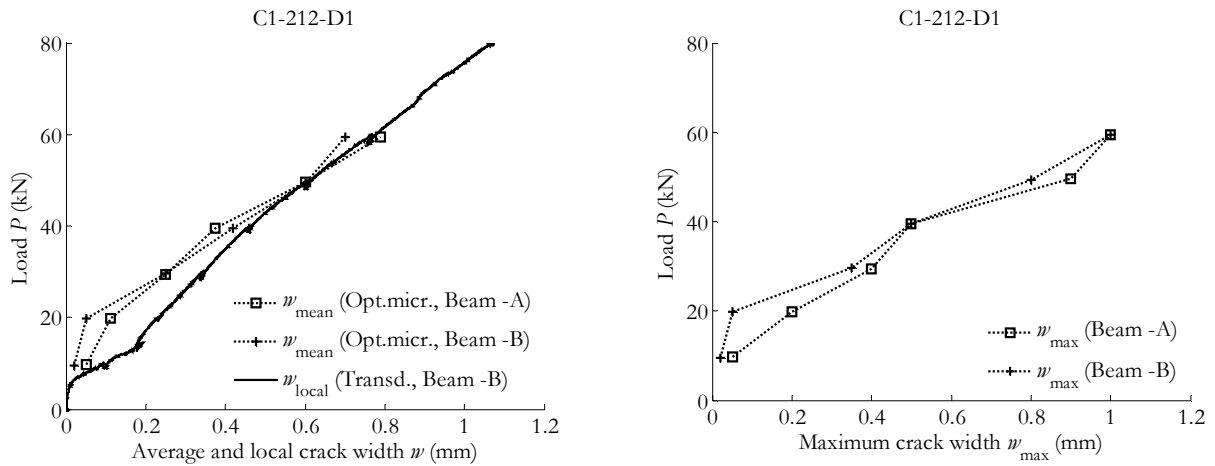
Figure B-12. Experimental crack width: average (left) and maximum (right).
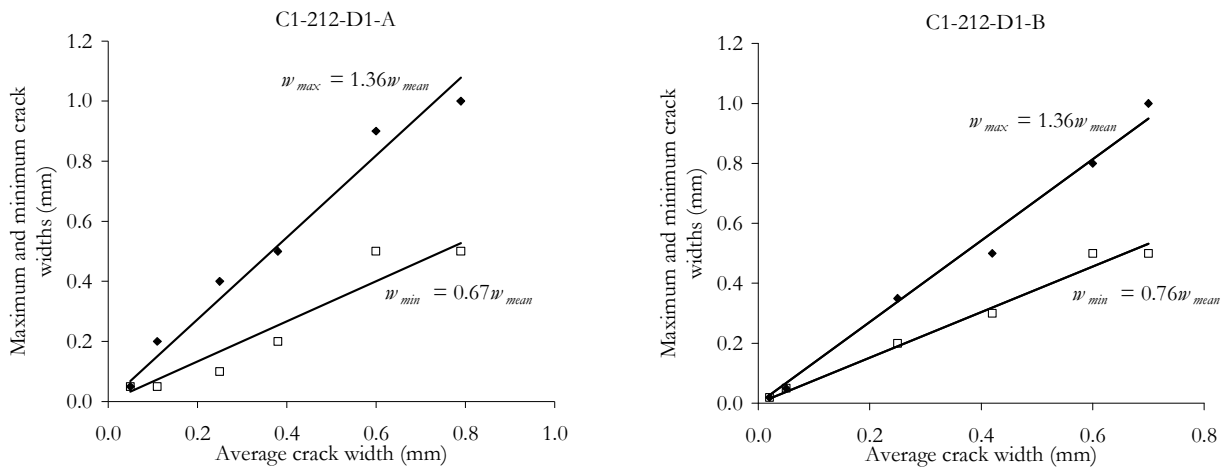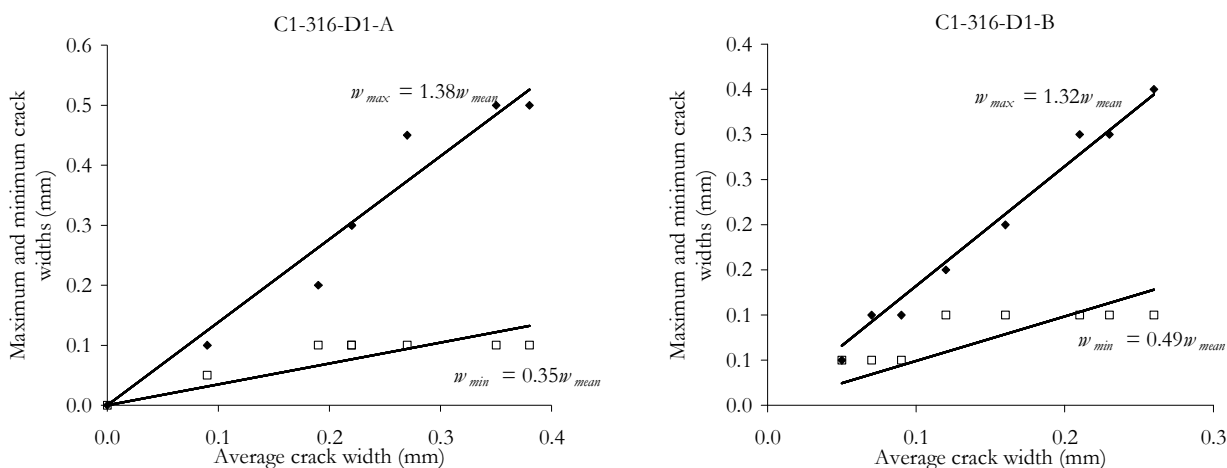

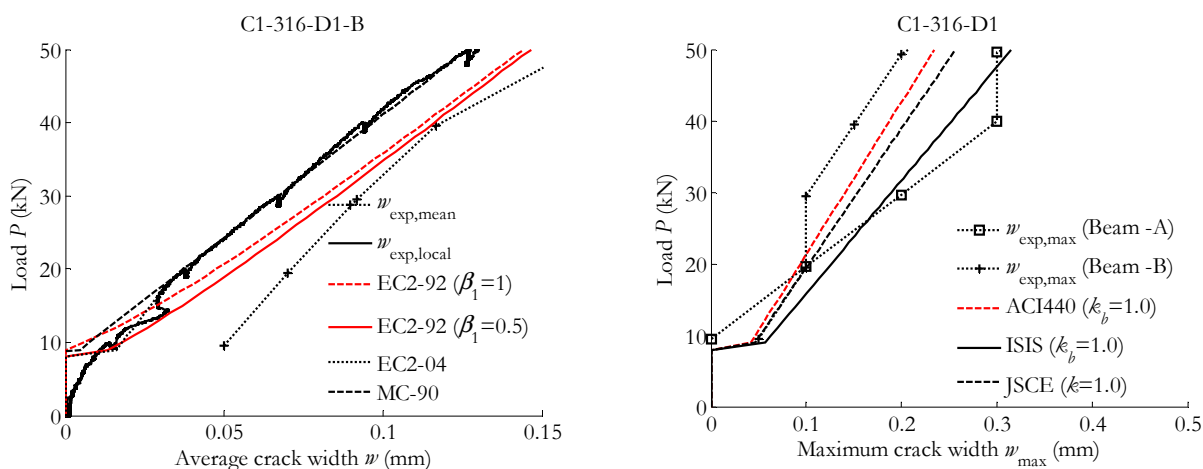Figure B-13. Experimental crack width: maximum and minimum vs. average.
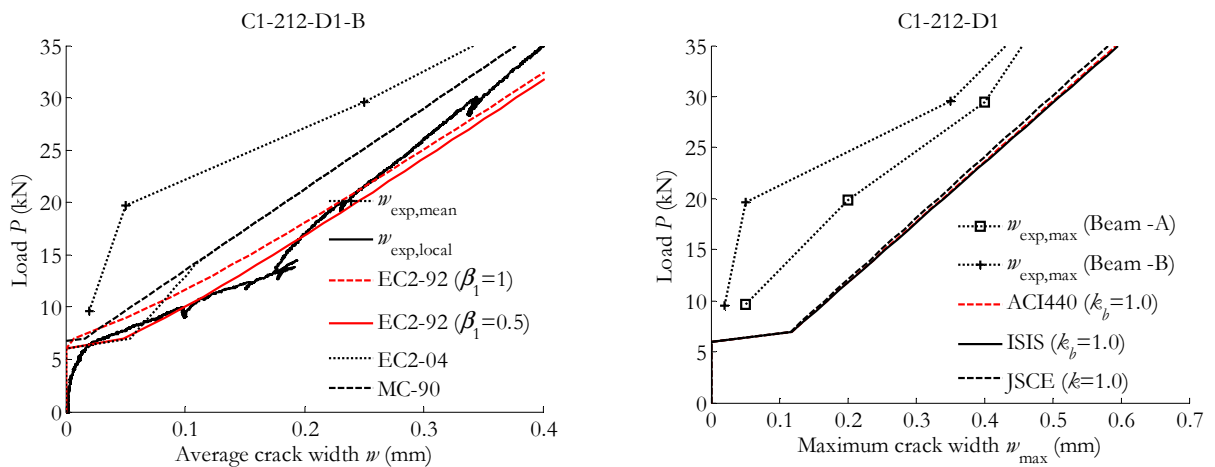
Figure B-14. Experimental vs theoretical crack width, (left) average (rigth) maximum.

Load = 9.6 kN
Av. Crack width = 0.05 mm

Load = 19.9 kN
Av. Crack width = 0.11mm

Load = 29.5 kN
Av. Crack width = 0.25 mm

Load = 39.5 kN
Av. Crack width = 0.38 mm

Load = 49.5 kN
Av. Crack width =0.60mm

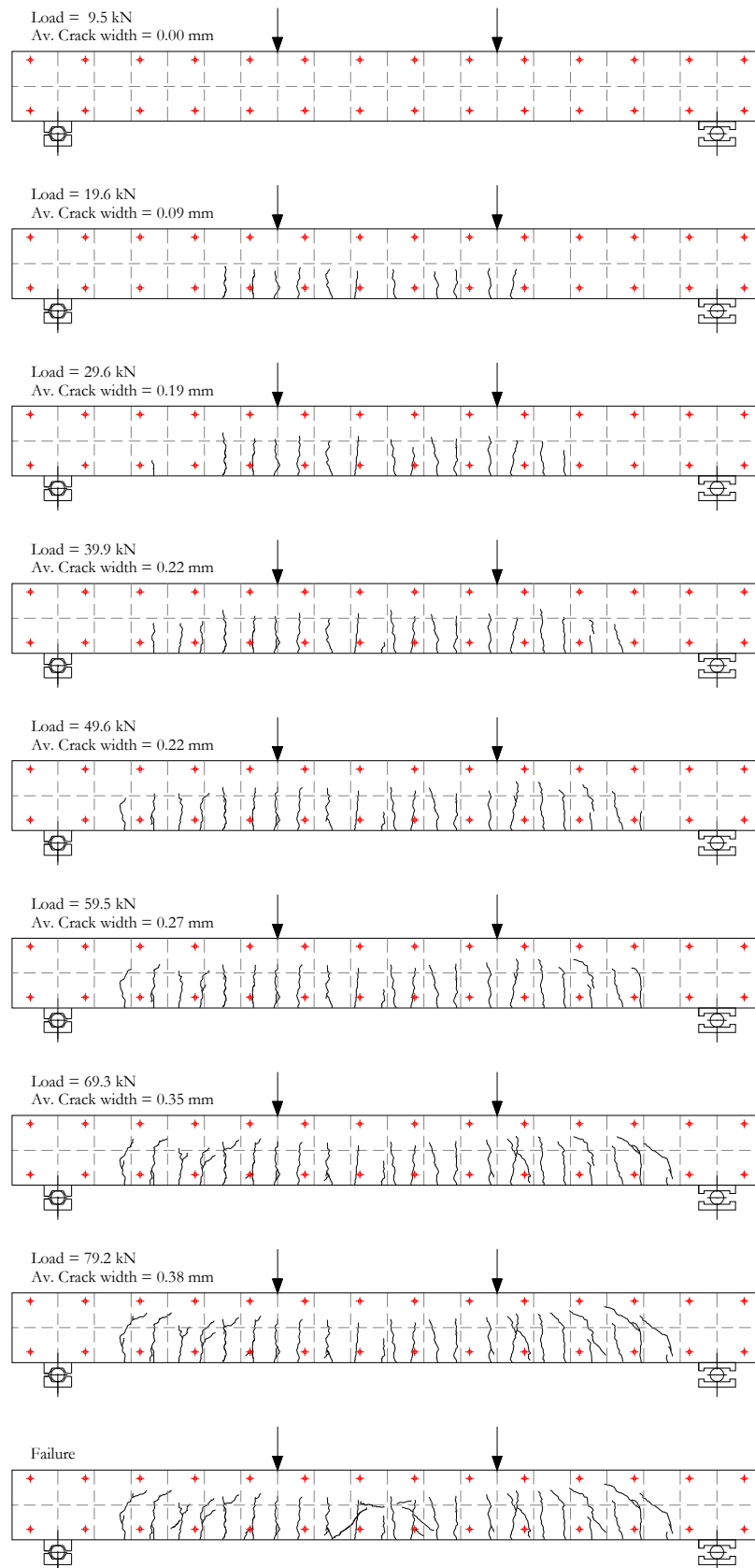Load = 59.4 kN
Av. Crack width =0.79mm

Failure
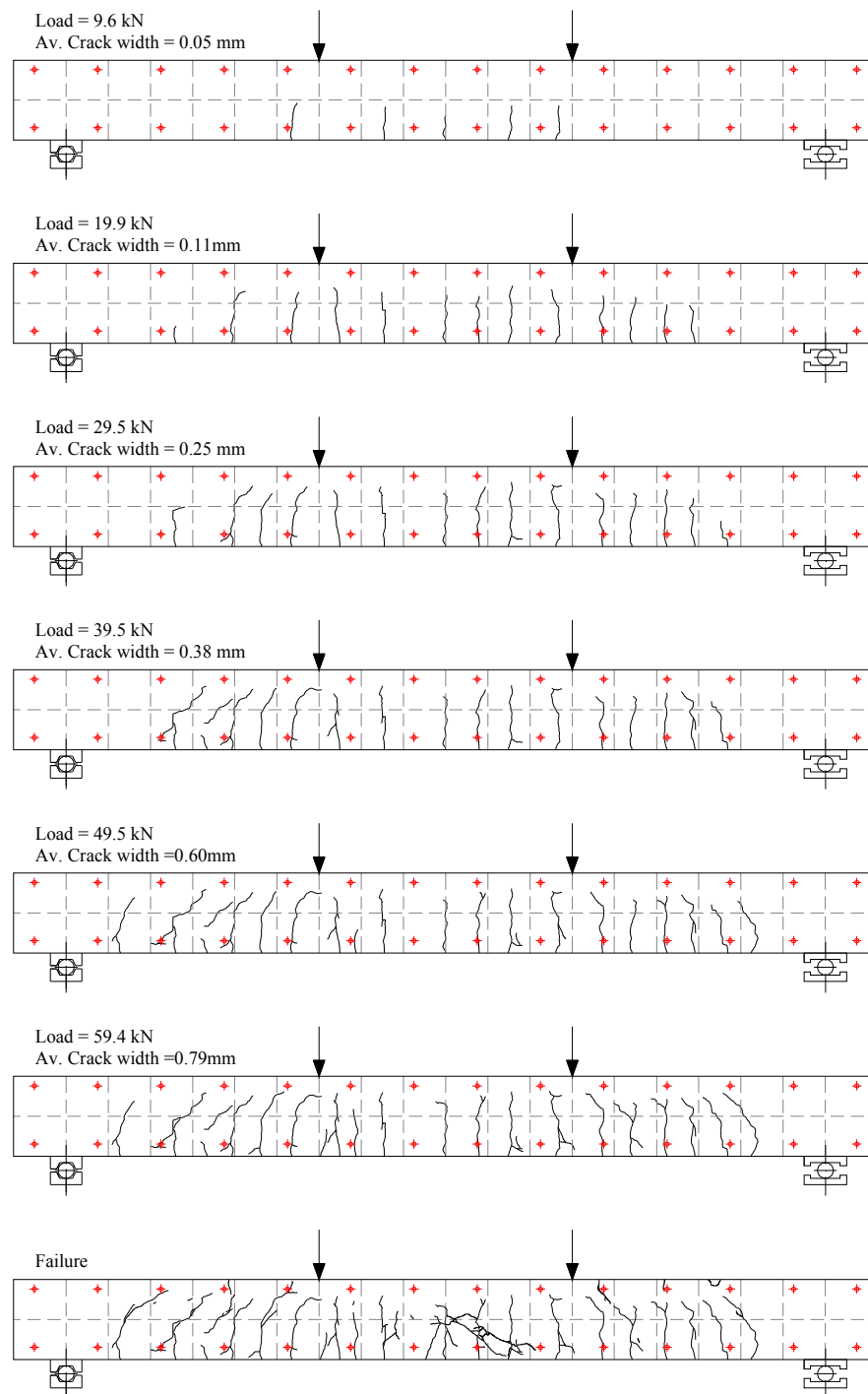
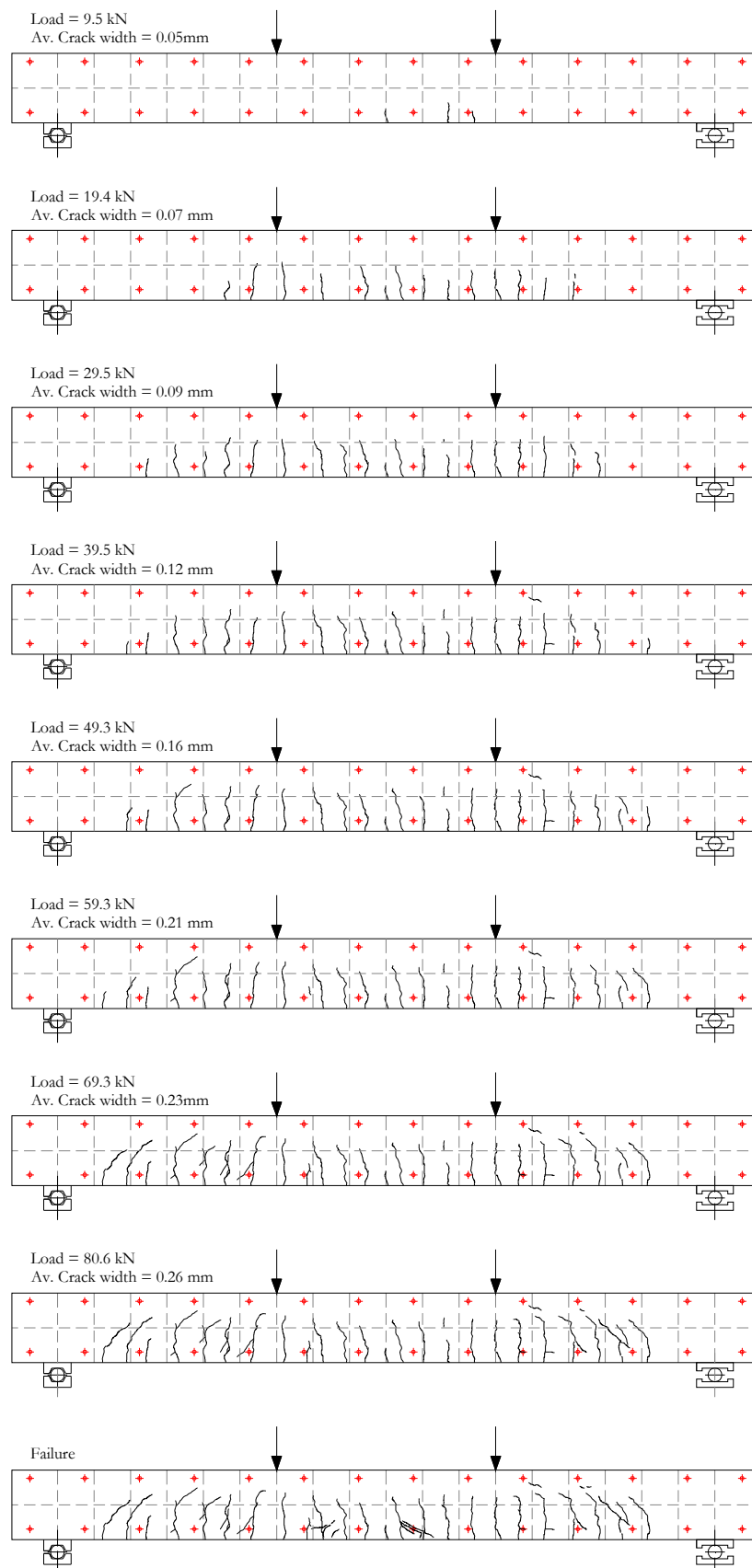Figure B-15. Crack pattern (C1-212-D1-A).
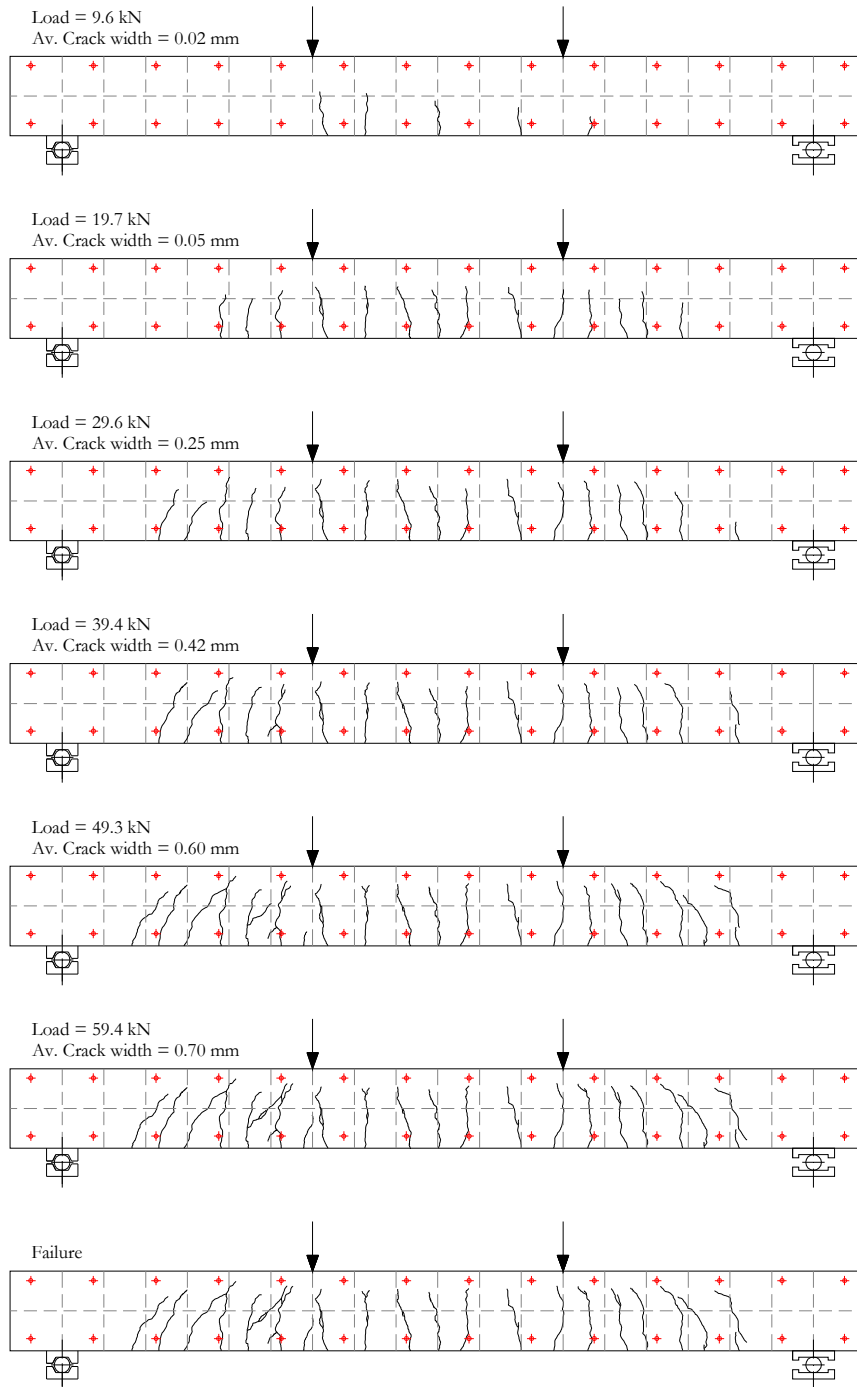
Figure B-16. Crack pattern (C1-212-D1-B).

B.2.   Results for the C1-212-D2 series

B.2.1.   General data

	C1-212-D2-A	C1-212-D2-B
Cracking load (kN)	6.6	8.0
Load at reaching stabilised cracking phase (kN)	29.6	18.9
Average crack spacing at stabilised cracking phase (mm)	79	127
Maximum crack spacing at stabilised cracking phase (mm)	108	130
Minimum crack spacing at stabilised cracking phase (mm)	29	124
Load at which $\sigma_c = 0.45 f_c$ (kN)	--	13.2
Load at which w_{max}=0.5-0.7mm (kN)	29.6	28.4
Load at which $\delta=L/250$ (kN)	18.2	19.7
Ultimate load (kN)	72.1	73.5
Ultimate midspan deflection (mm)	47.6	49.0
Ultimate concrete strain (x10^{-6})	--	5578

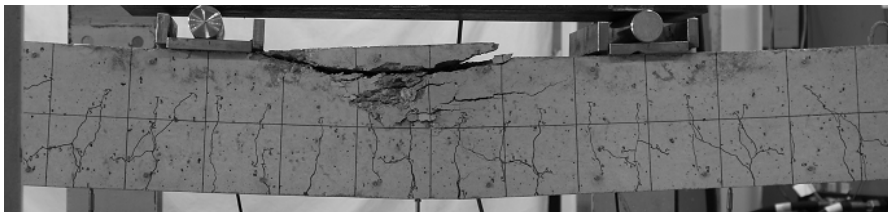### B.2.2.   Failure mode
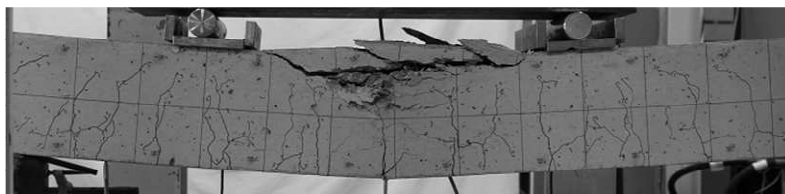
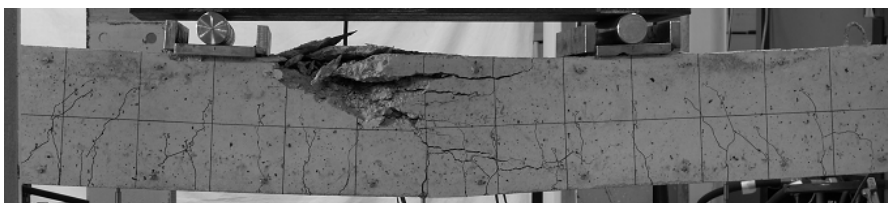Figure B-17. Crushing of concrete for C1-212-D2-A.
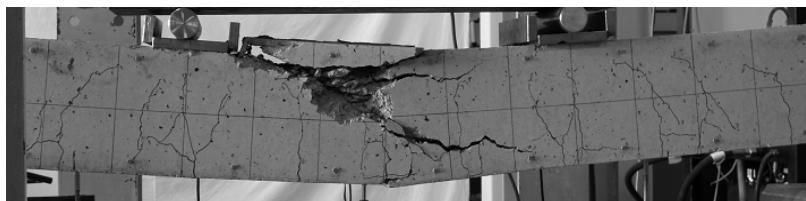
Figure B-18. Crushing of concrete for C1-212-D2-B.

B.2.3. Results at the midspan section
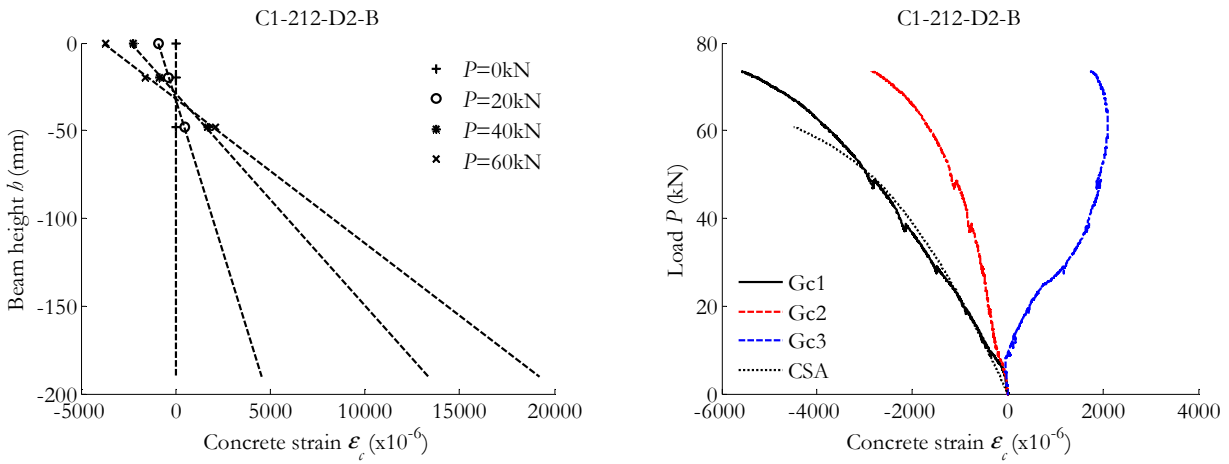
Figure B-19. Concrete strain in the midspan section: Along the height of the beam (left) /
Versus the load applied and compared to CSA predictions (right).
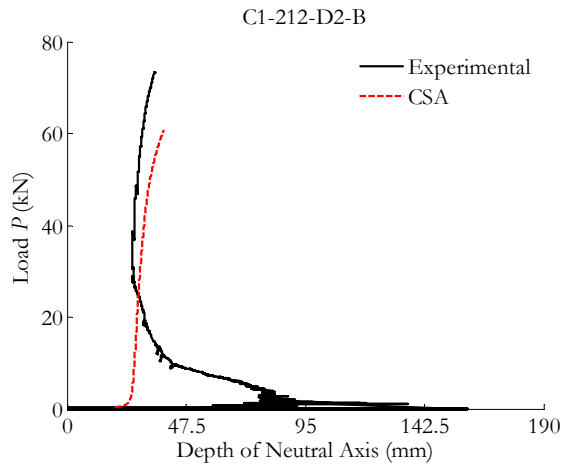
Figure B-20. Neutral axis depth compared to CSA predictions.

B.2.4. Results at the pure bending zone
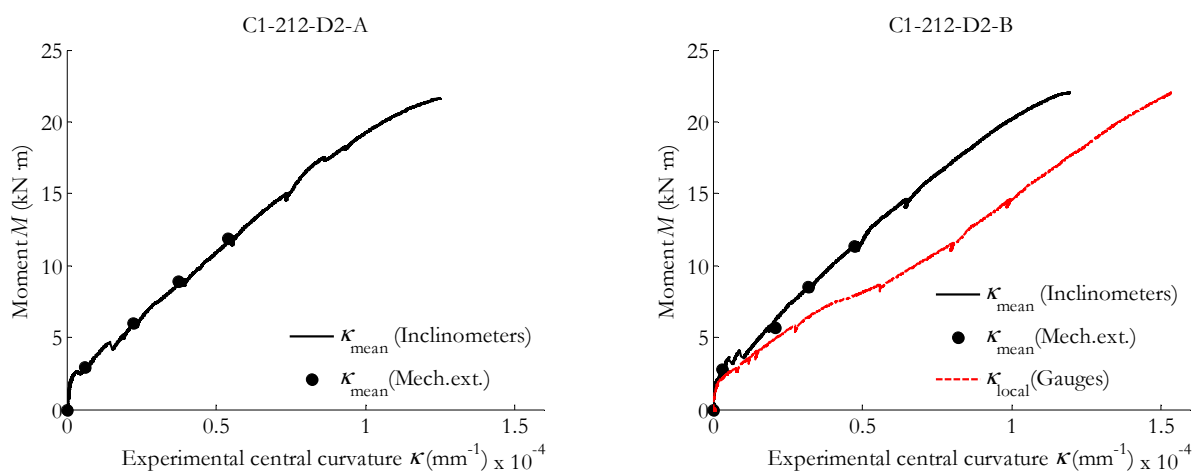
Figure B-21. Experimental moment-curvature from inclinometers, mechanical extensometer and strain gauges on concrete.
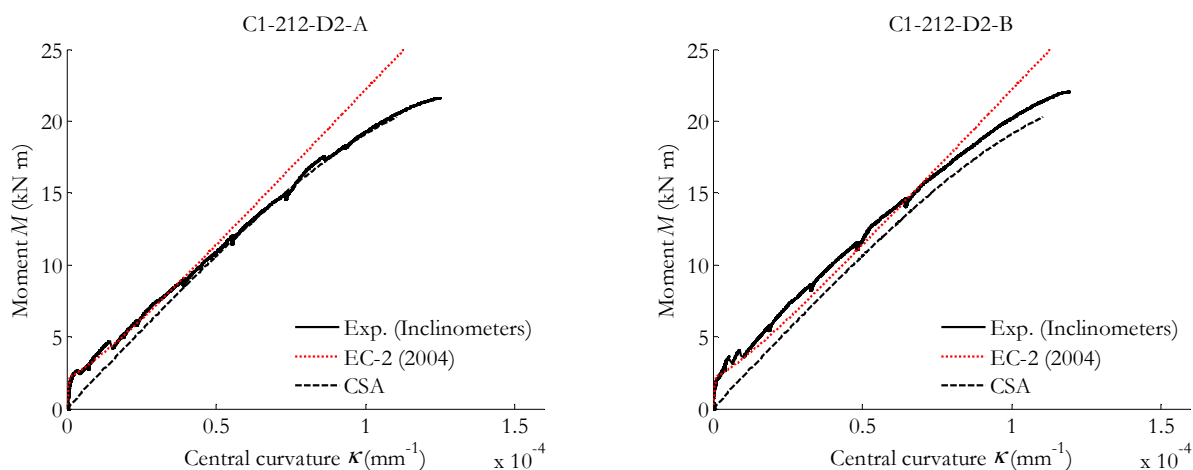
Figure B-22. Experimental moment-curvature from compared to Eurocode 2 (2004) and CSA predictions.

B.2.5. Results of the overall beam behaviour
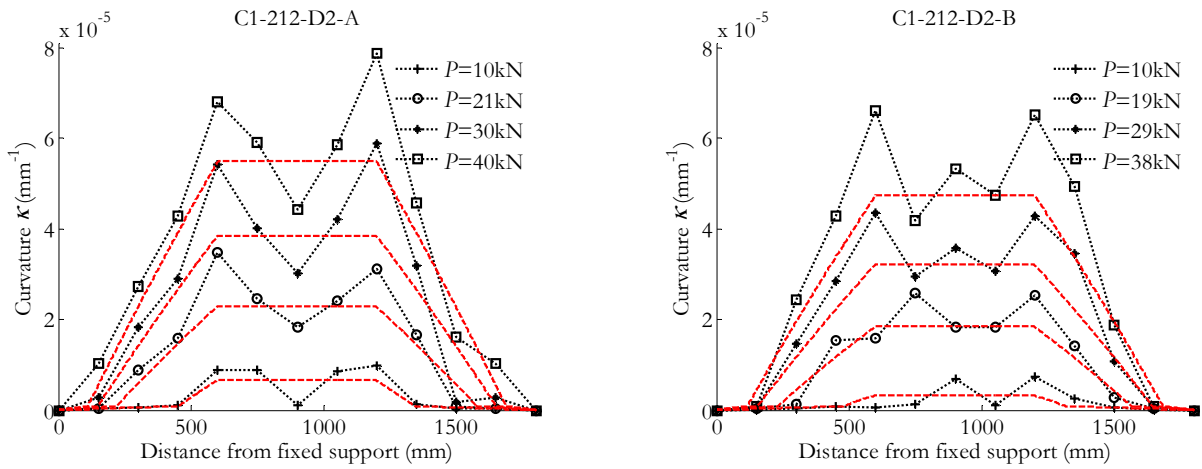
Figure B-23. Curvature along the length of the beam deduced form mechanical extensometer's data (dotted lines) compared to inclinometers' data (dashed lines).

B.2.6. Results on deflection
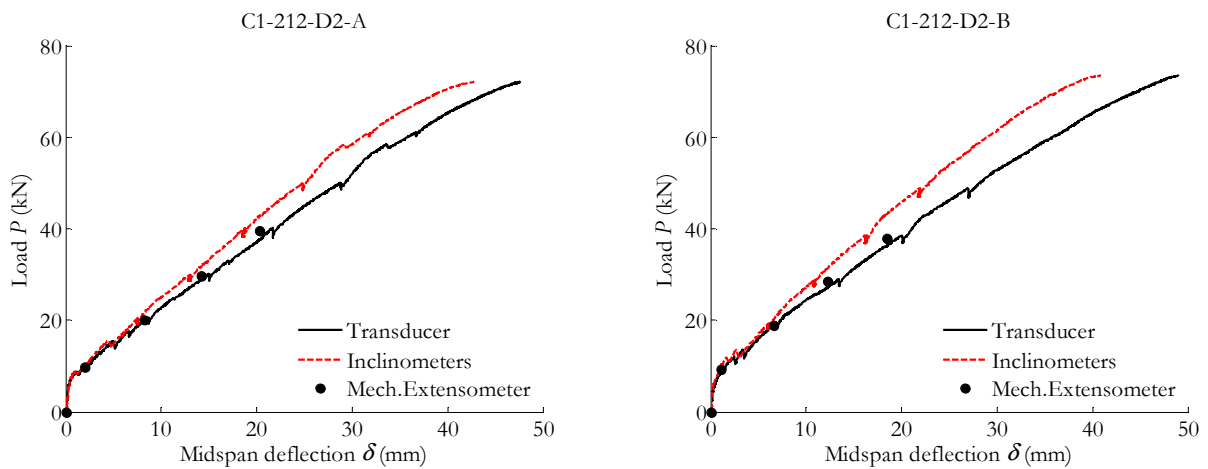
Figure B-24. Experimental midspan deflection.

C1-212-D2-A

C1-212-D2-B
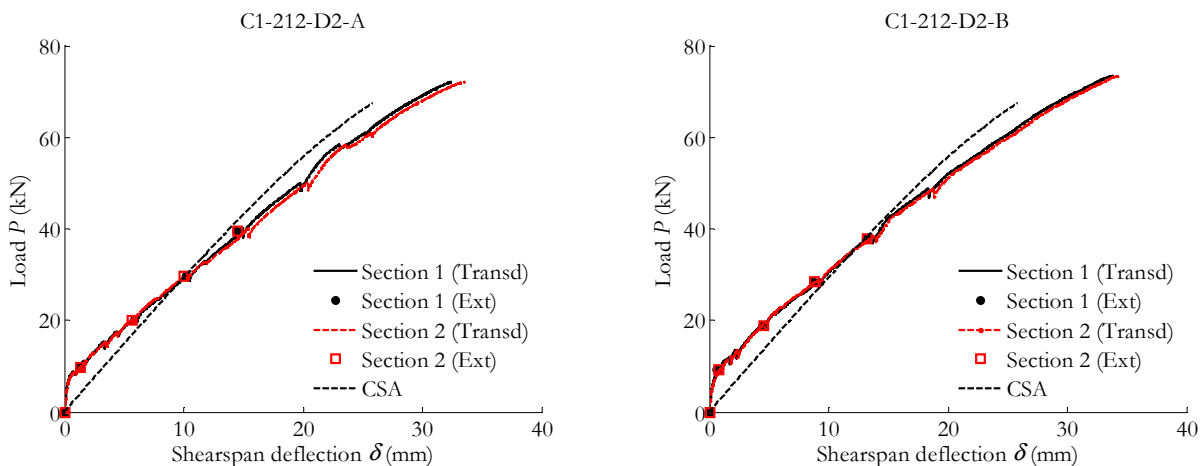
Figure B-25. Experimental shearspan deflection compared to cracked section analysis.

C1-212-D2

C1-212-D2
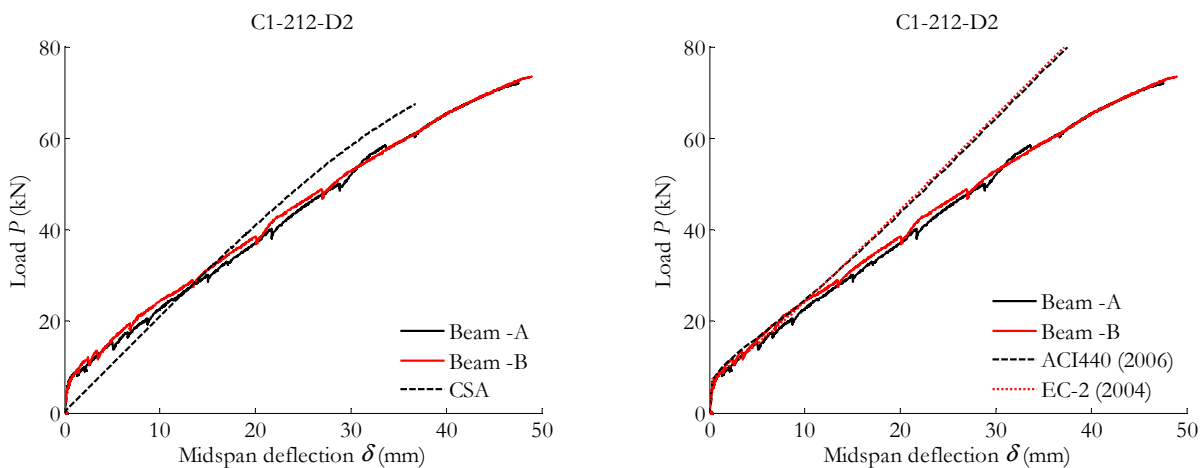
Figure B-26. Experimental midspan deflection (ultimate load) compared to cracked section analysis (left) / design codes (right).

C1-212-D2

C1-212-D2
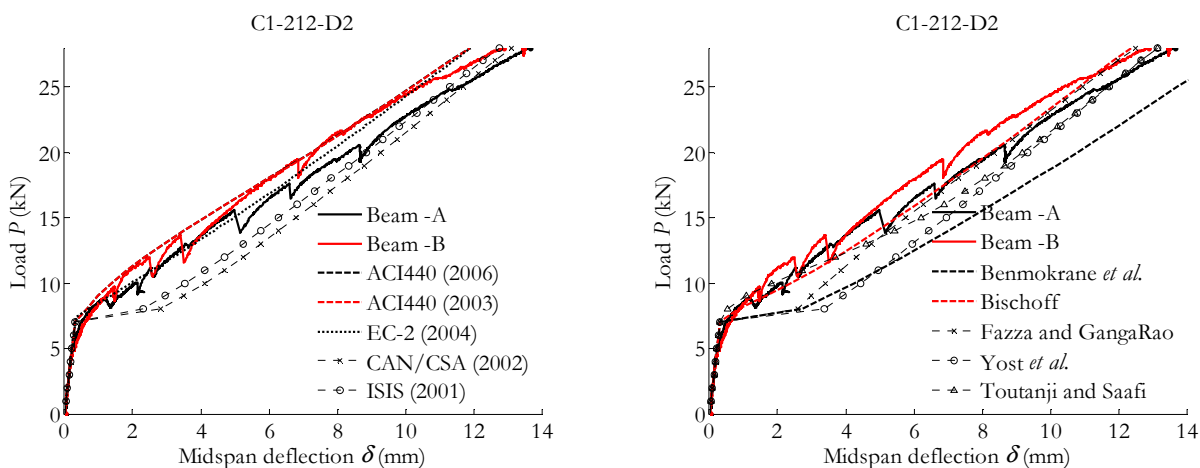
Figure B-27. Experimental vs theoretical midspan deflection (service load).

B.2.7. Results on cracking
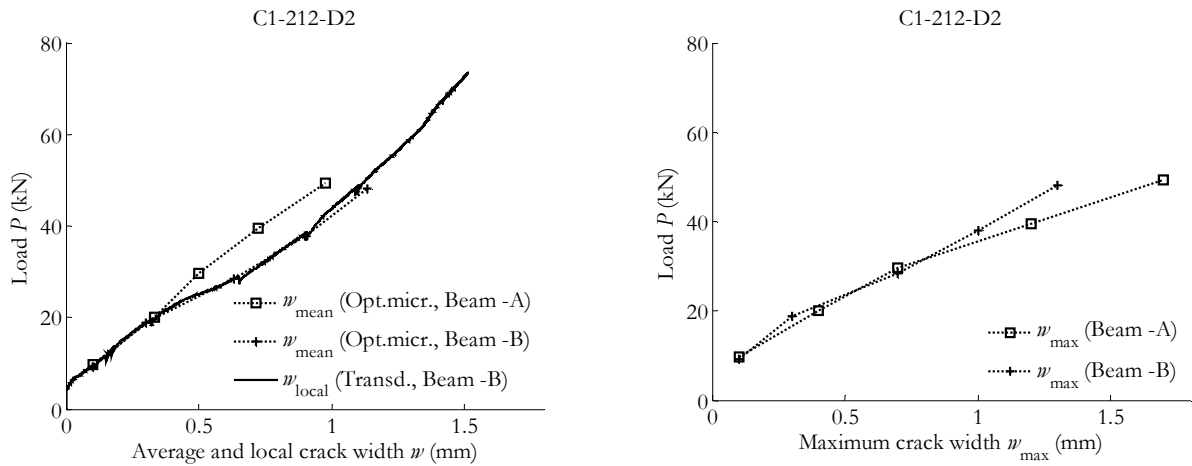
Figure B-28. Experimental crack width: average (left) and maximum (right).
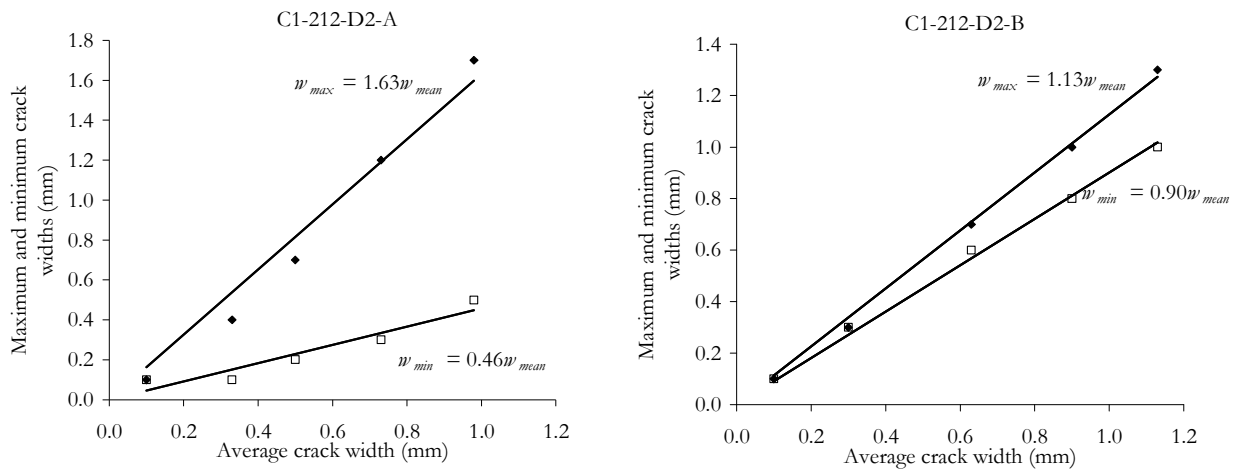
Figure B-29. Experimental crack width: maximum and minimum vs. average.
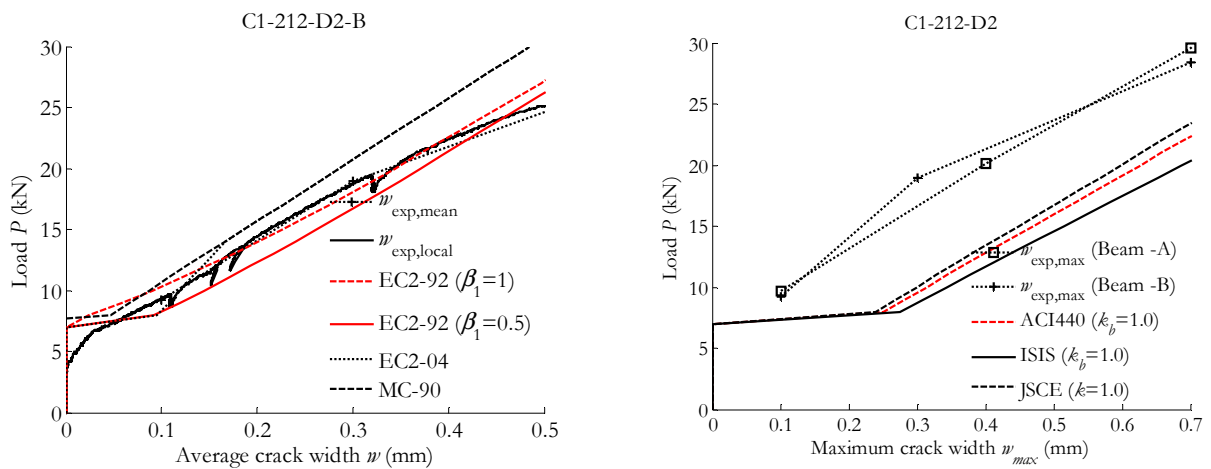
Figure B-30. Experimental vs theoretical crack width, (left) average (rigth) maximum.

Load = 9.7 kN
Av. Crack width = 0.10 mm

Load = 20.1 kN
Av. Crack width = 0.33 mm

Load = 29.6 kN
Av. Crack width = 0.50 mm

Load = 39.6 kN
Av. Crack width = 0.73 mm

Load = 49.4 kN
Av. Crack width = 0.98 mm

Failure
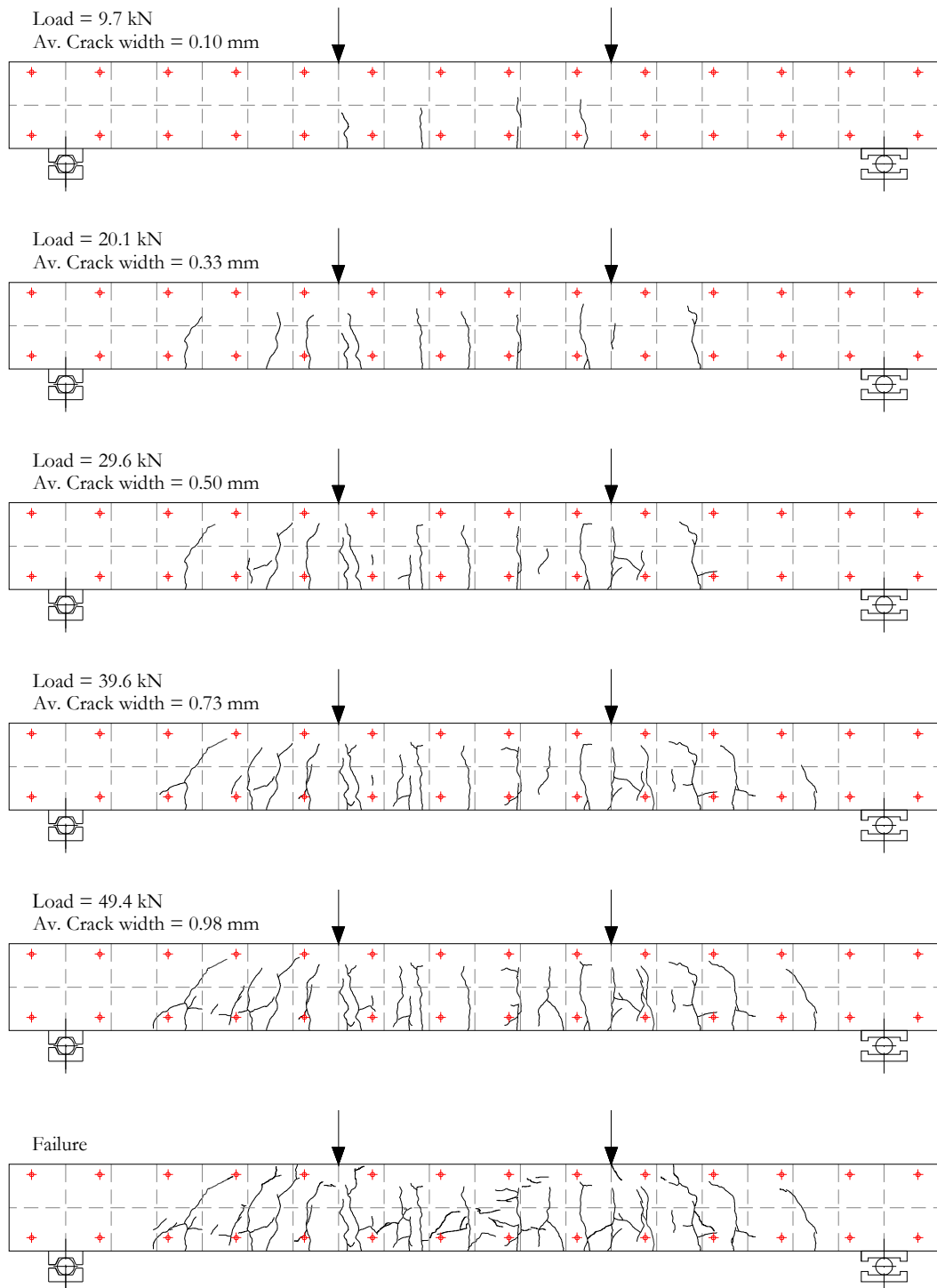
Figure B-31. Crack pattern (C1-212-D2-A).

Load = 9.2 kN
Av. Crack width = 0.10 mm

Load = 18.9 kN
Av. Crack width = 0.30 mm

Load = 28.4 kN
Av. Crack width = 0.63 mm

Load = 37.9 kN
Av. Crack width = 0.90 mm

Load = 48.1 kN
Av. Crack width = 1.13 mm

Failure
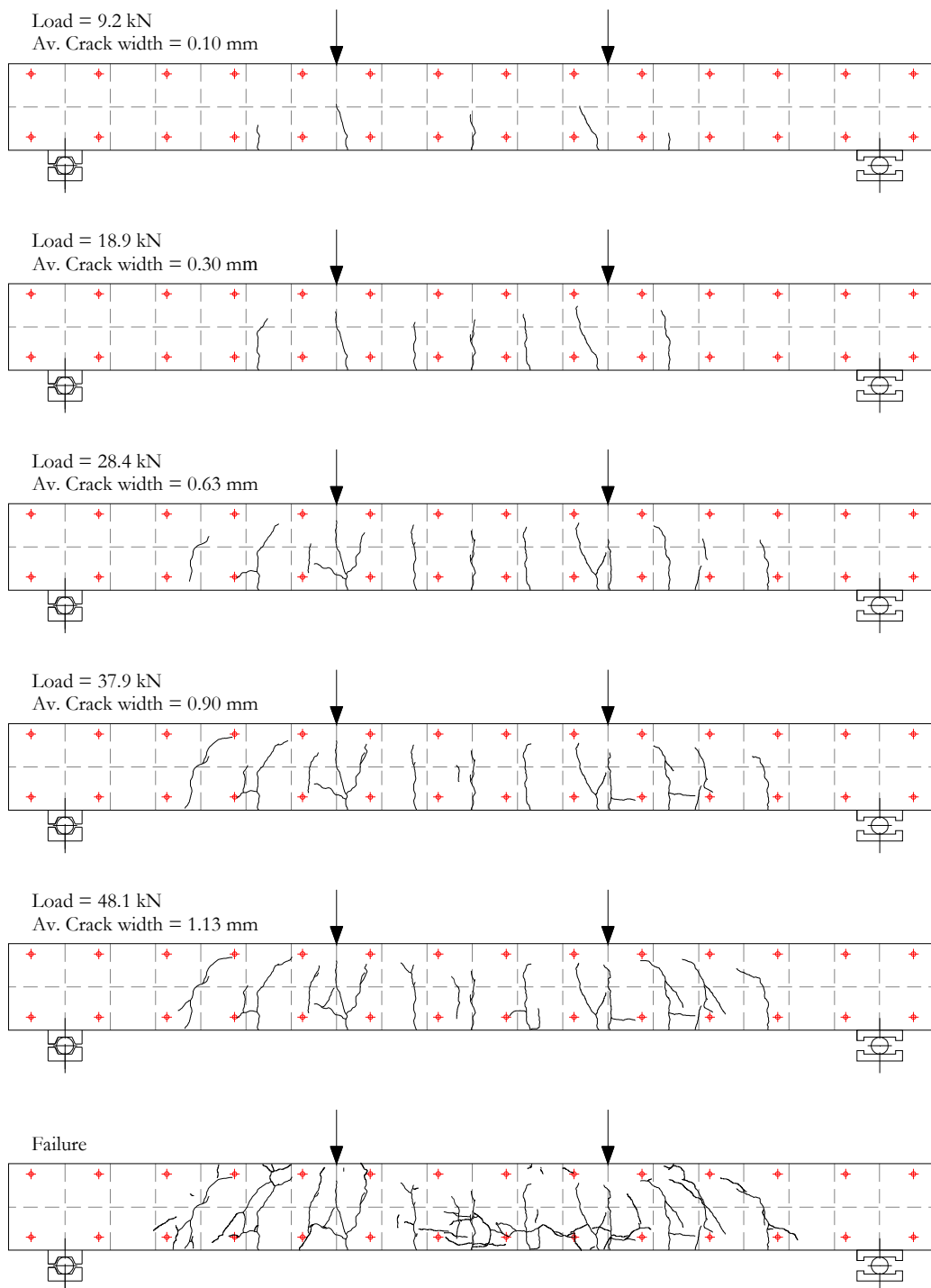
Figure B-32. Crack pattern (C1-212-D2-B).

B.3. Results for the C1-216-D1 series

B.3.1. General data

	C1-216-D1-A	C1-216-D1-B
Cracking load (kN)	7.2	7.5
Load at reaching stabilised cracking phase (kN)	29.5	19.6
Average crack spacing at stabilised cracking phase (mm)	61	80
Maximum crack spacing at stabilised cracking phase (mm)	95	90
Minimum crack spacing at stabilised cracking phase (mm)	33	75
Load at which $\sigma_c = 0.45\,f_c$ (kN)	--	18.8
Load at which w_{max}=0.5-0.7mm (kN)	69.1	69.3
Load at which $\delta=L/250$ (kN)	29.6	
Ultimate load (kN)	98.8	99.2
Ultimate midspan deflection (mm)	33.0	32.7
Ultimate concrete strain (x10^{-6})	--	4617

B.3.2. Failure mode
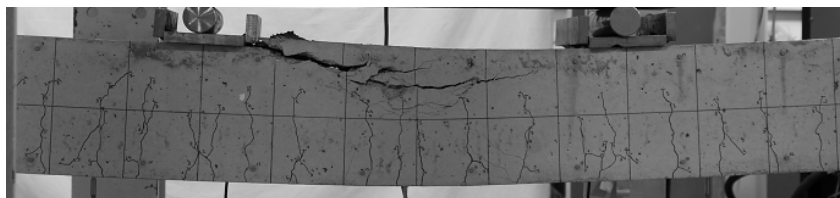
Figure B-33. Crushing of concrete for C1-216-D1-A.
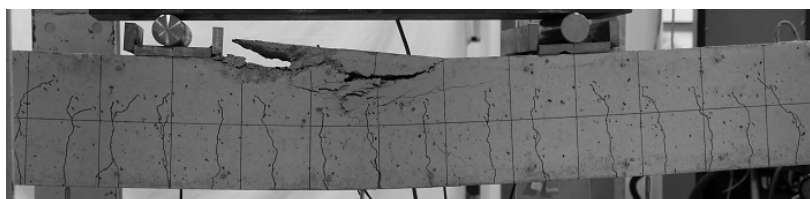
Figure B-34. Crushing of concrete for C1-216-D1-B.

B.3.3. Results at the midspan section
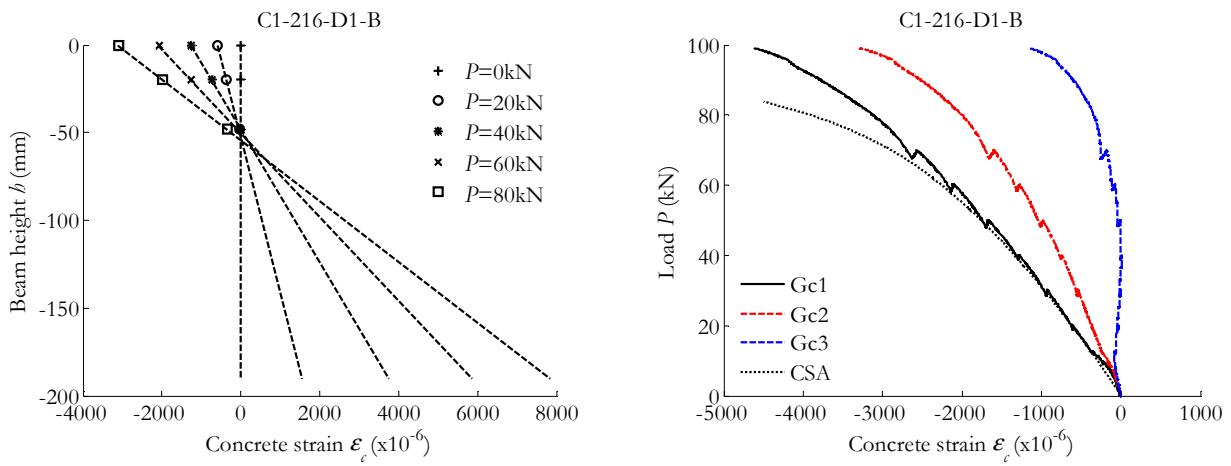
Figure B-35. Concrete strain in the midspan section: Along the height of the beam (left) / Versus the load applied and compared to CSA predictions (right).
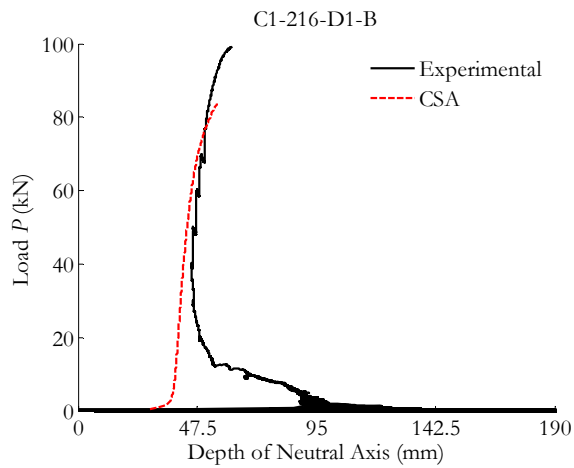
Figure B-36. Neutral axis depth compared to CSA predictions.

B.3.4. Results at the pure bending zone
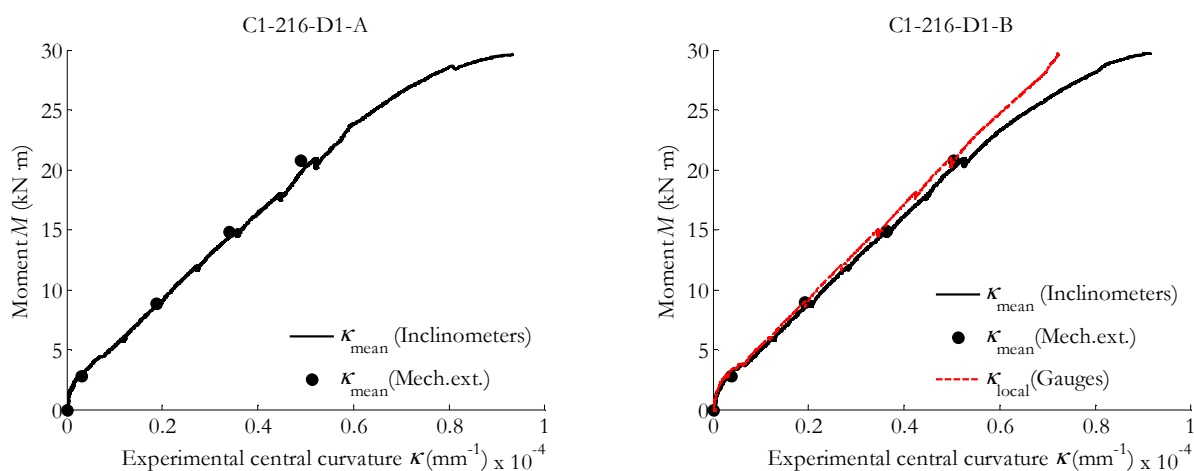
Figure B-37. Experimental moment-curvature from inclinometers, mechanical extensometer and strain gauges on concrete.
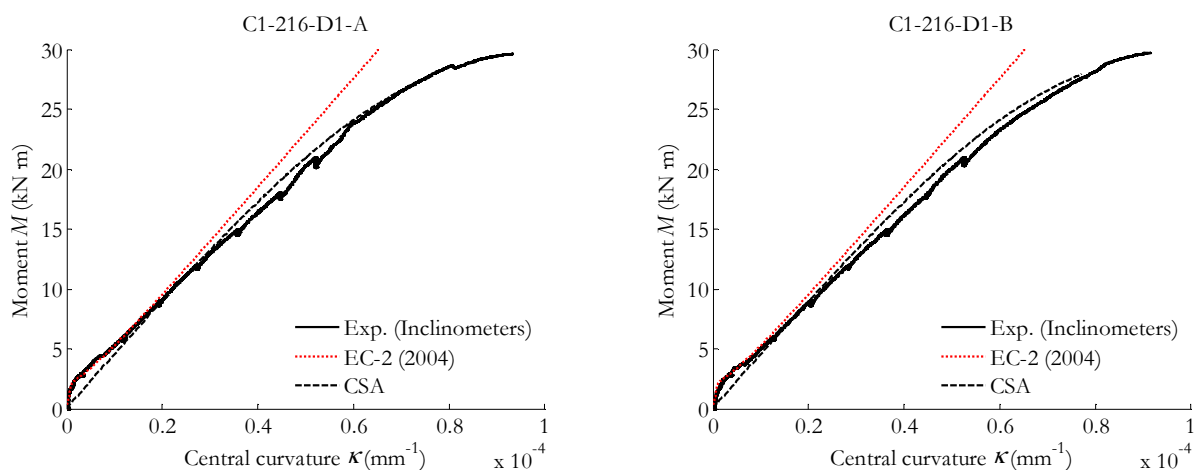
Figure B-38. Experimental moment-curvature from compared to Eurocode 2 (2004) and CSA predictions.

B.3.5. Results of the overall beam behaviour
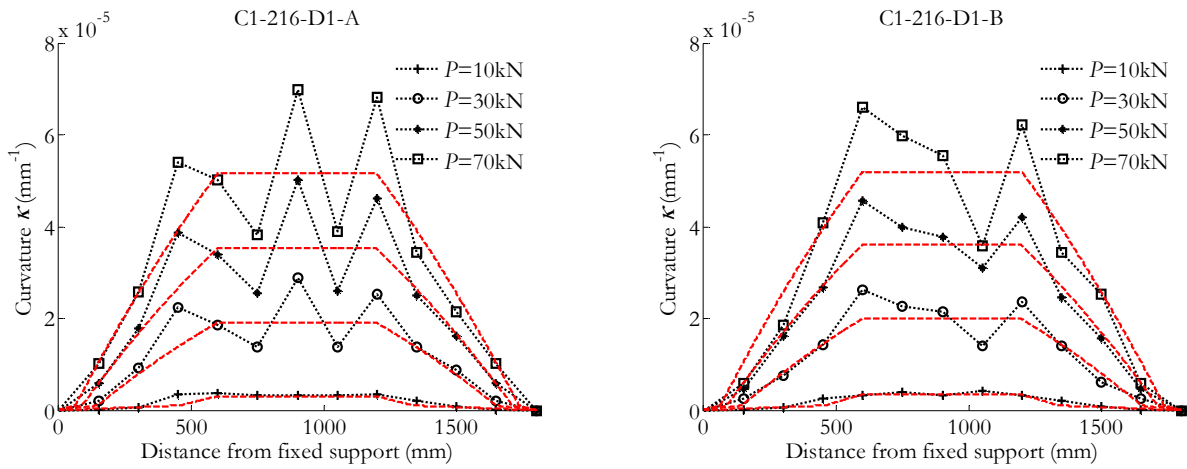
Figure B-39. Curvature along the length of the beam deduced form mechanical extensometer's data (dotted lines) compared to inclinometers' data (dashed lines).

B.3.6. Results on deflection
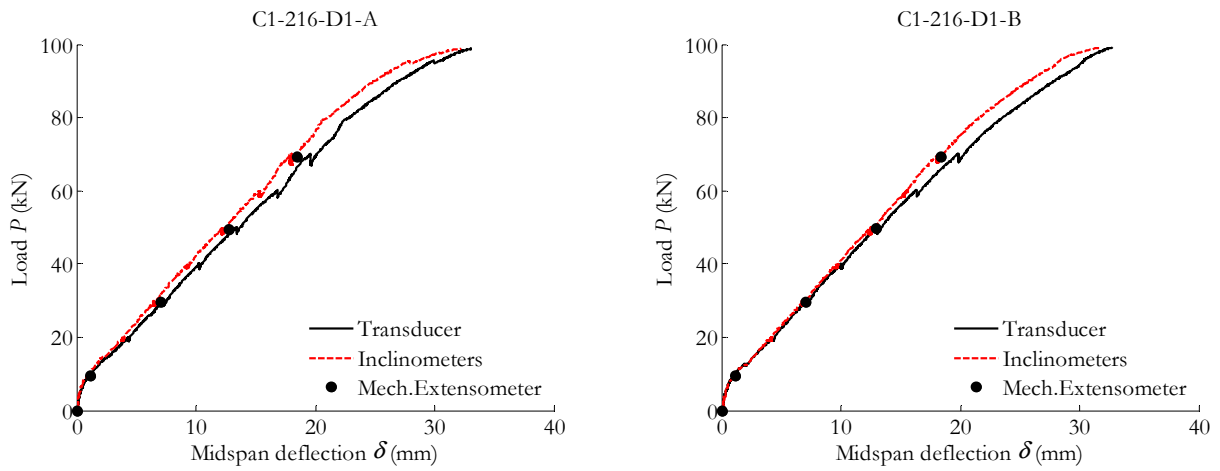
Figure B-40. Experimental midspan deflection.
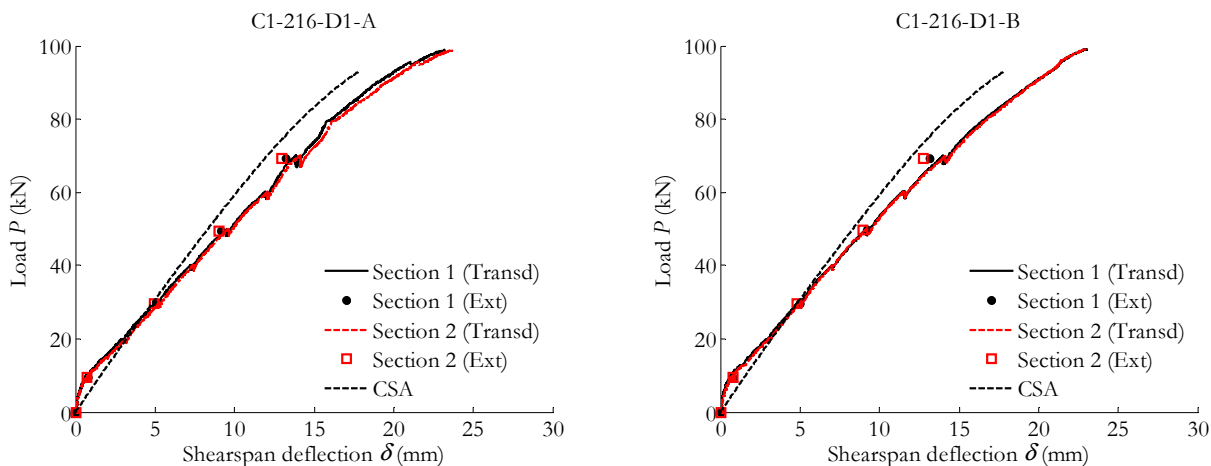
Figure B-41. Experimental shearspan deflection compared to cracked section analysis.
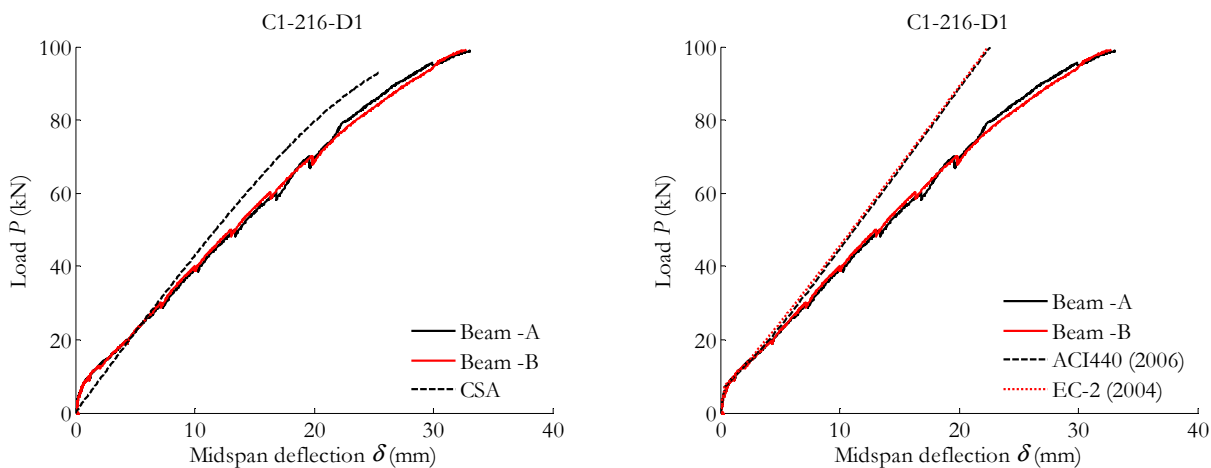
Figure B-42. Experimental midspan deflection (ultimate load) compared to cracked section analysis (left) / design codes (right).
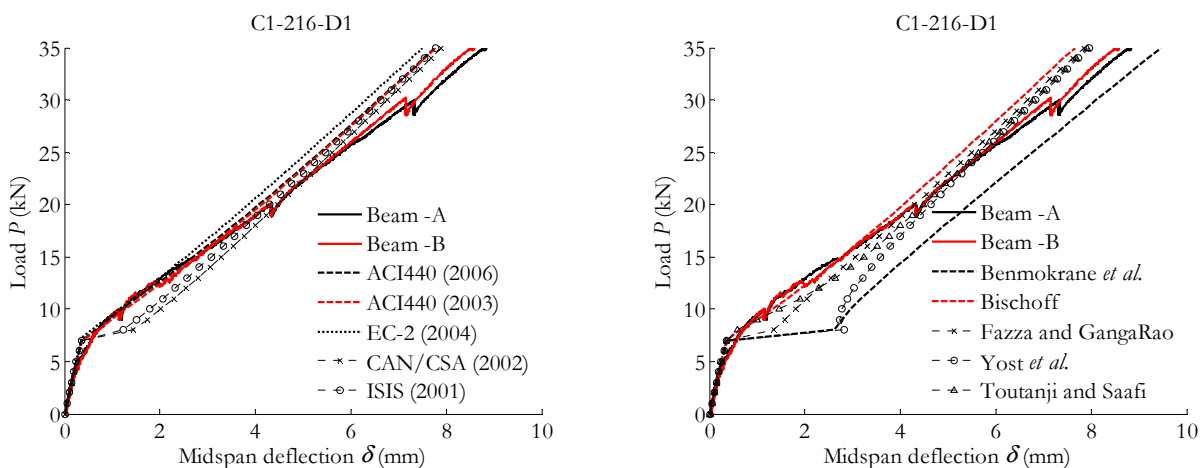
Figure B-43. Experimental vs theoretical midspan deflection (service load).

B.3.7. Results on cracking
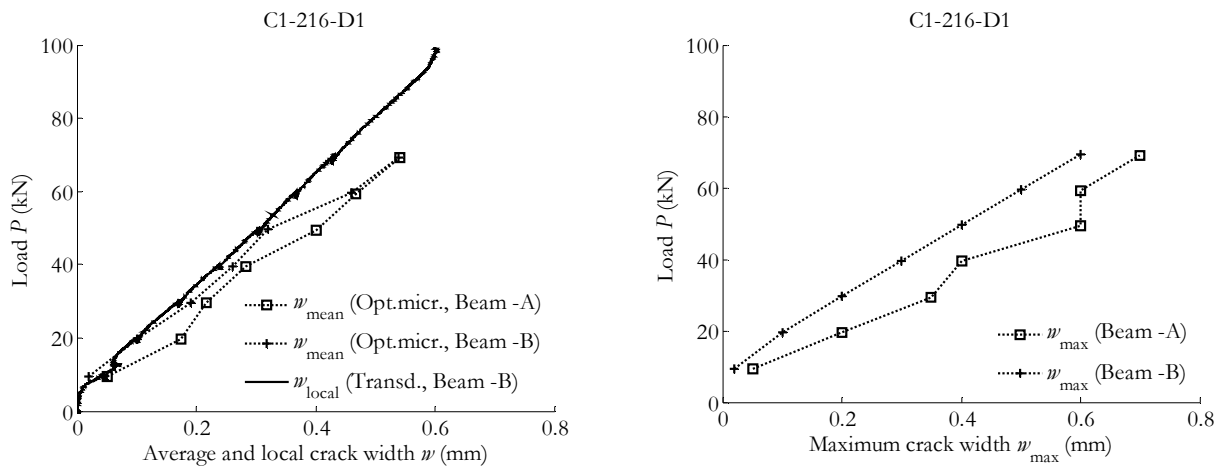
Figure B-44. Experimental crack width: average (left) and maximum (right).
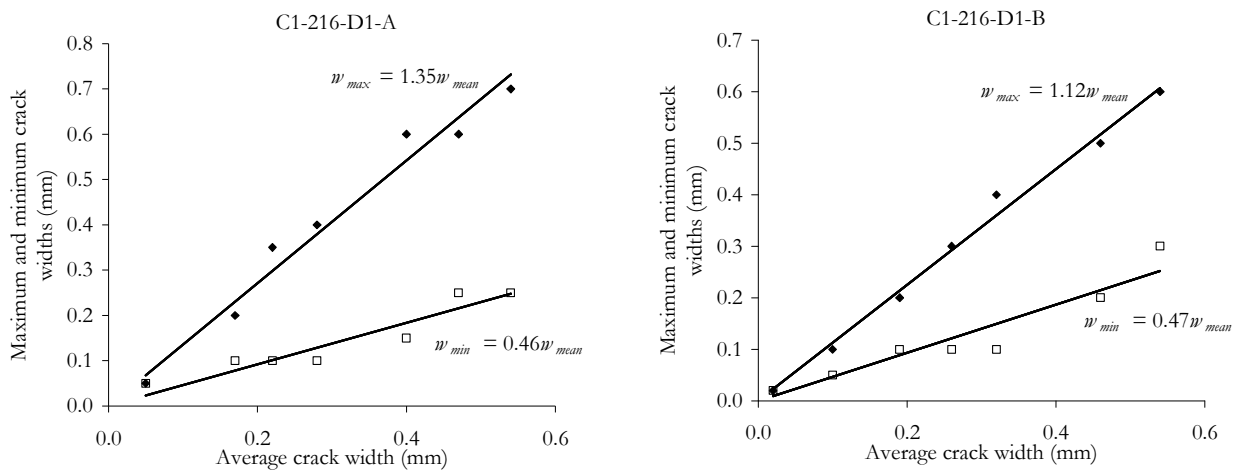
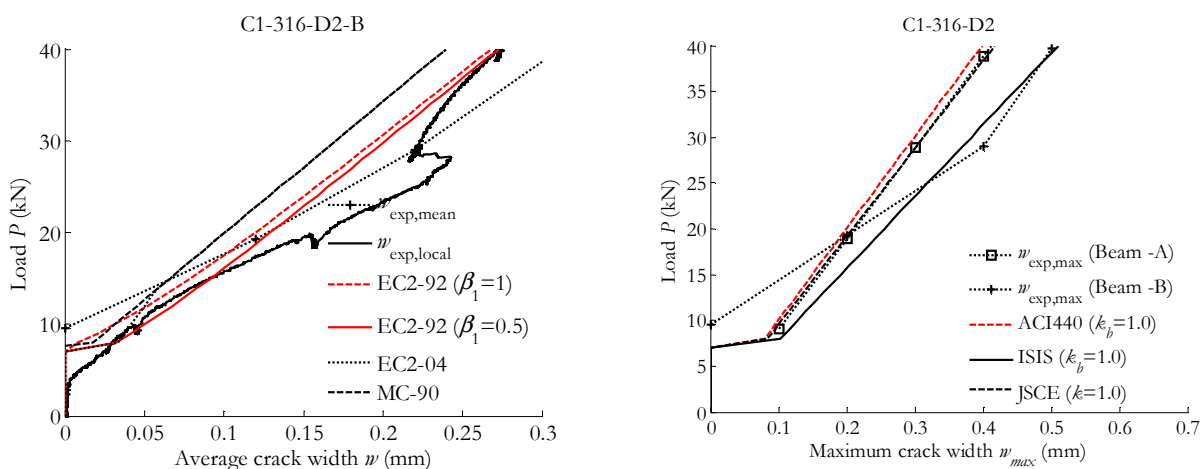Figure B-45. Experimental crack width: maximum and minimum vs. average.
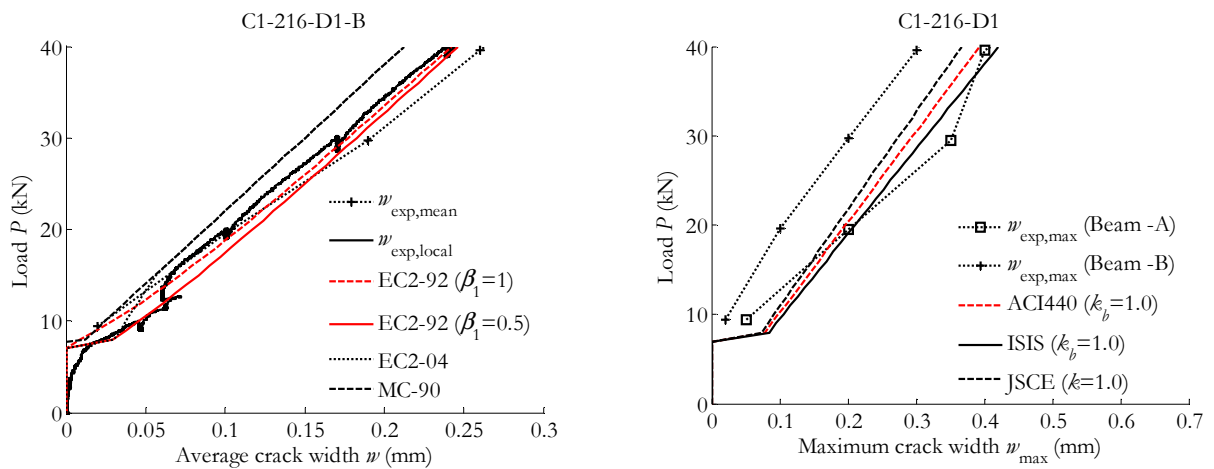
Figure B-46. Experimental vs theoretical crack width, (left) average (rigth) maximum.
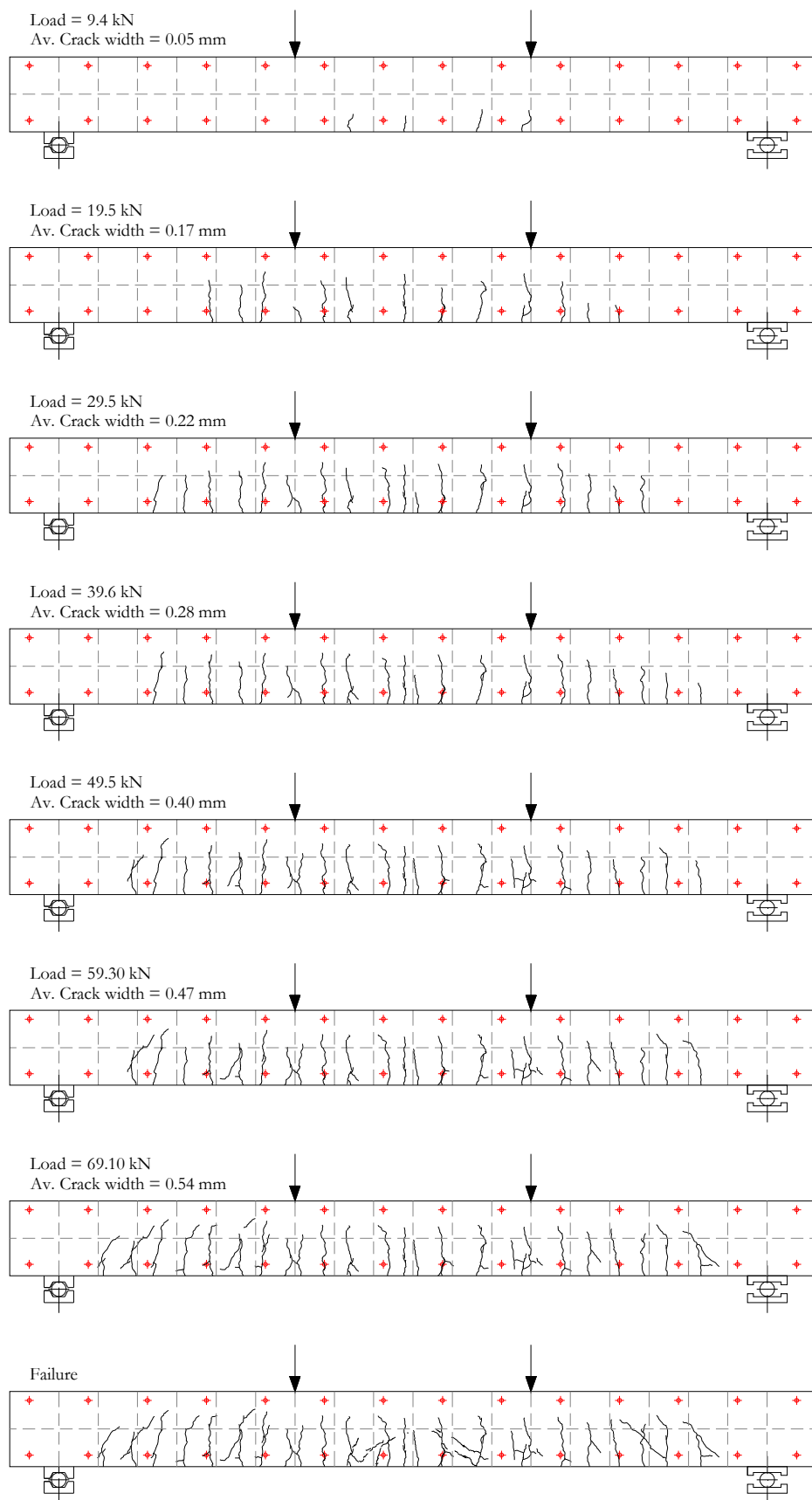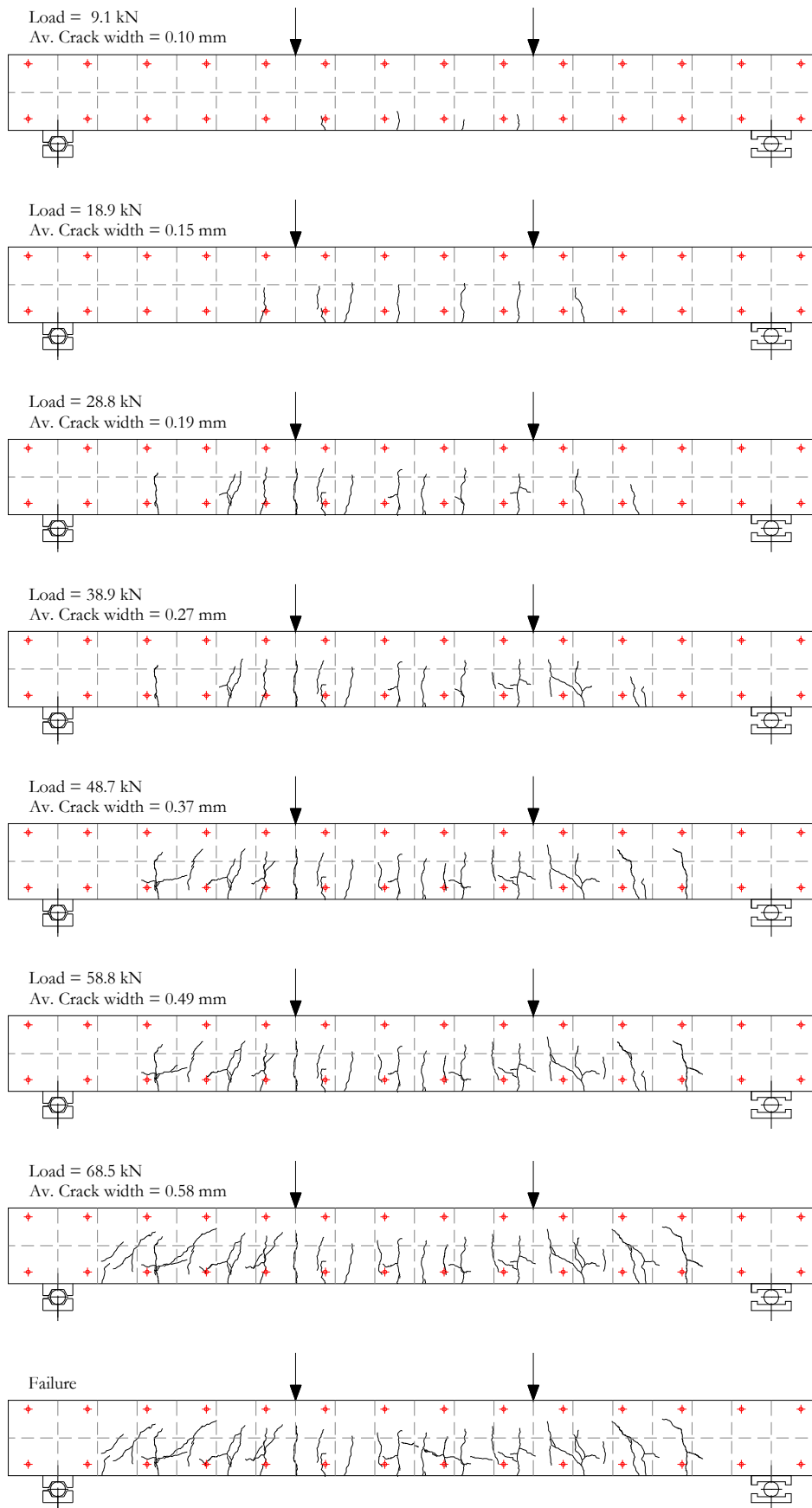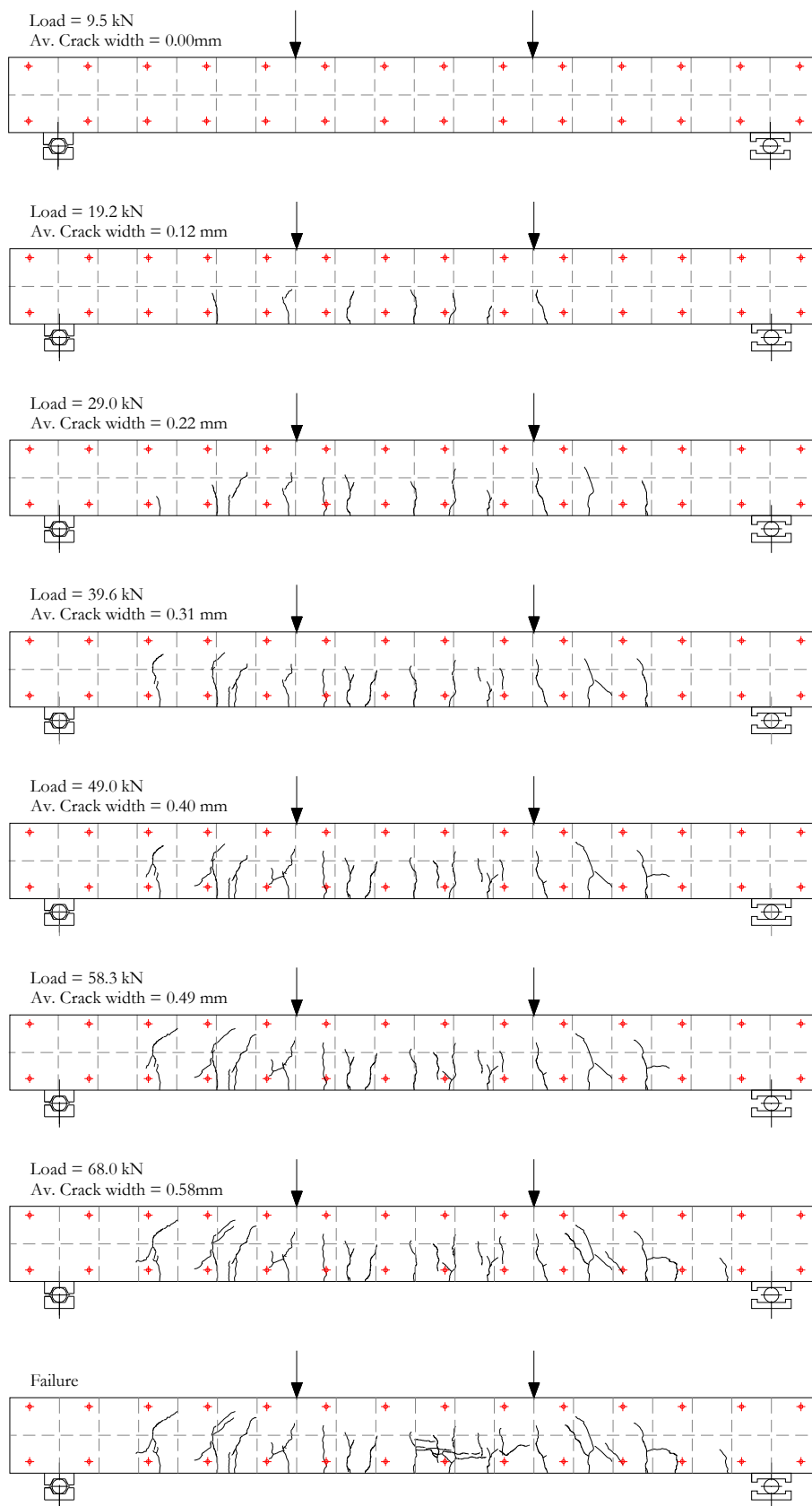
Figure B-47. Crack pattern (C1-216-D1-A).

Load = 9.4 kN
Av. Crack width = 0.02 mm

Load = 19.6 kN
Av. Crack width = 0.10 mm

Load = 29.7 kN
Av. Crack width = 0.19 mm

Load = 39.5 kN
Av. Crack width = 0.26 mm

Load = 49.6 kN
Av. Crack width = 0.32 mm

Load = 59.6 kN
Av. Crack width = 0.46 mm

Load = 69.3 kN
Av. Crack width = 0.54 mm

Failure
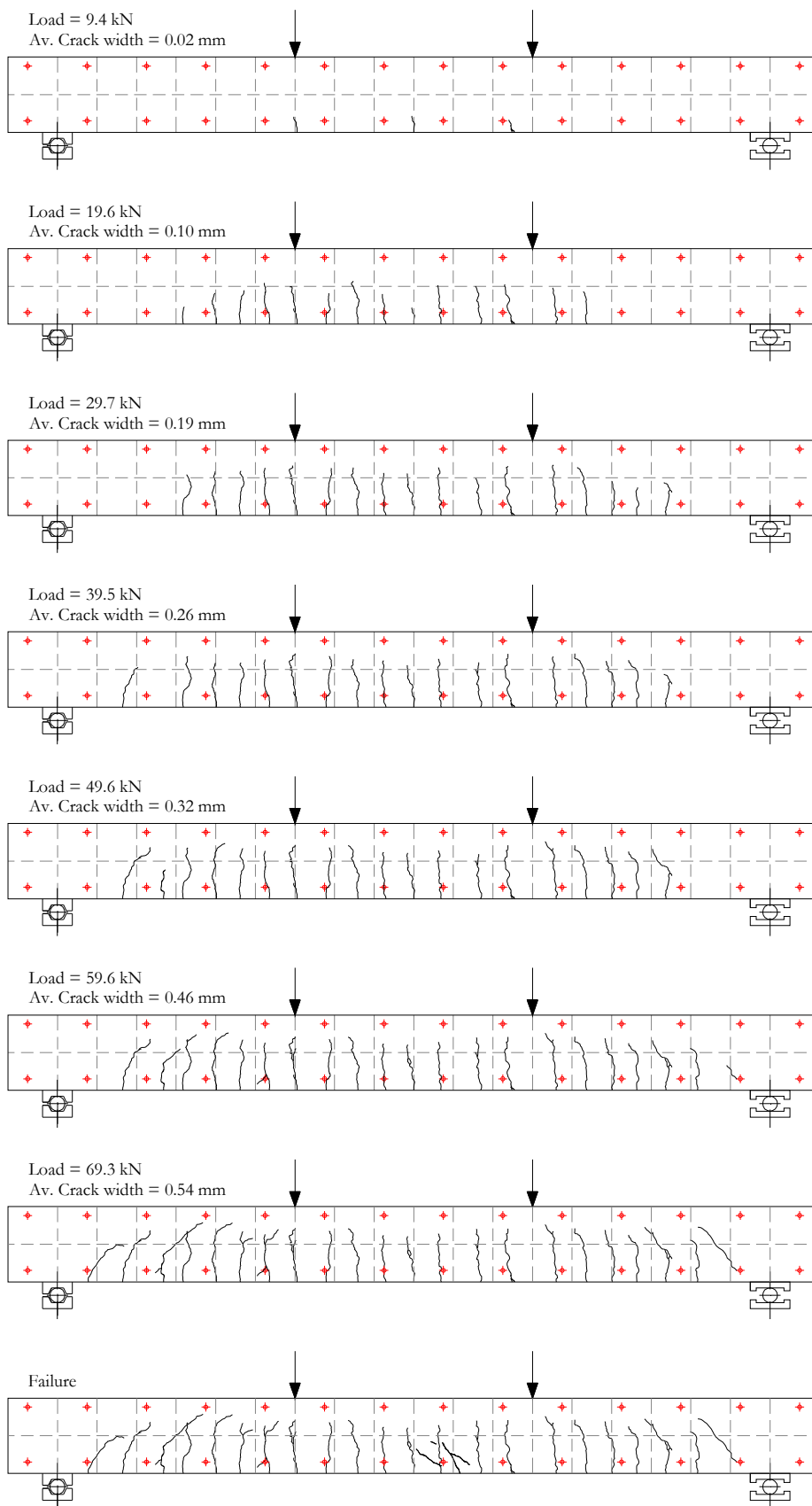
Figure B-48. Crack pattern (C1-216-D1-B).

B.4. Results for the C1-216-D2 series

B.4.1. General data

	C1-216-D2-A	C1-216-D2-B
Cracking load (kN)	6.1	6.3
Load at reaching stabilised cracking phase (kN)	17.9	9.6
Average crack spacing at stabilised cracking phase (mm)	127	150
Maximum crack spacing at stabilised cracking phase (mm)	181	152
Minimum crack spacing at stabilised cracking phase (mm)	71	148
Load at which $\sigma_c = 0.45 f_c$ (kN)	15.2	15.2
Load at which w_{max}=0.5-0.7mm (kN)	28.6	29.5
Load at which $\delta=L/250$ (kN)	23.7	25.5
Ultimate load (kN)	80.7	84.0
Ultimate midspan deflection (mm)	37.0	37.0
Ultimate concrete strain (x10^{-6})	3990	5059

B.4.2. Failure mode
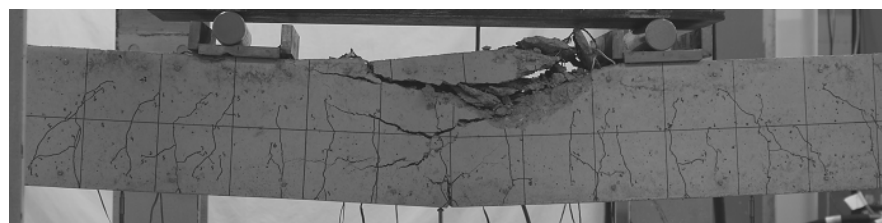
Figure B-49. Crushing of concrete for C1-216-D2-A.
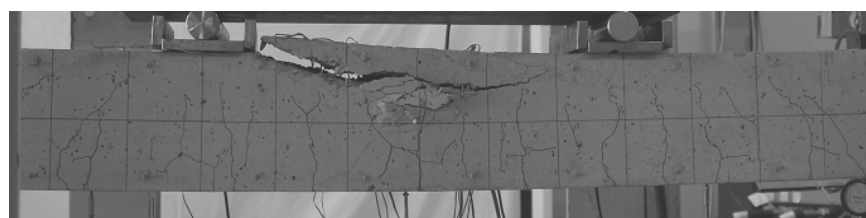
Figure B-50. Crushing of concrete for C1-216-D2-B.
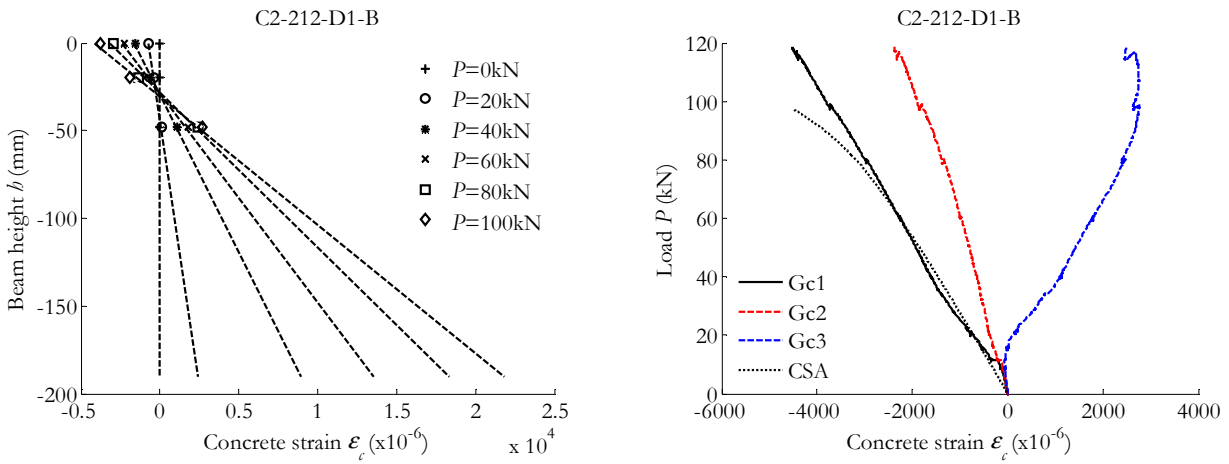
B.4.3. Results at the midspan section
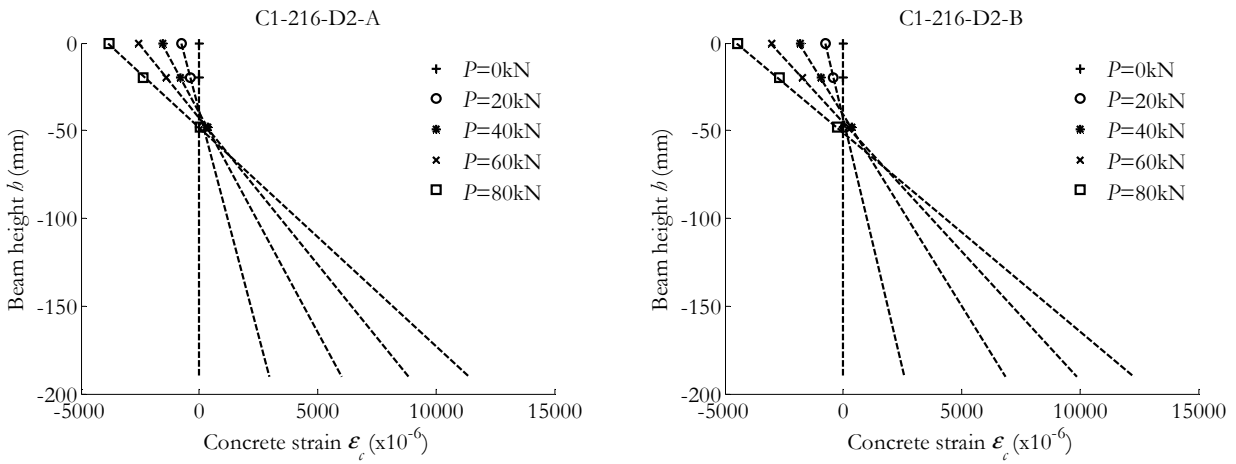
Figure B-51. Concrete strain along the height of the beam at the midspan section.
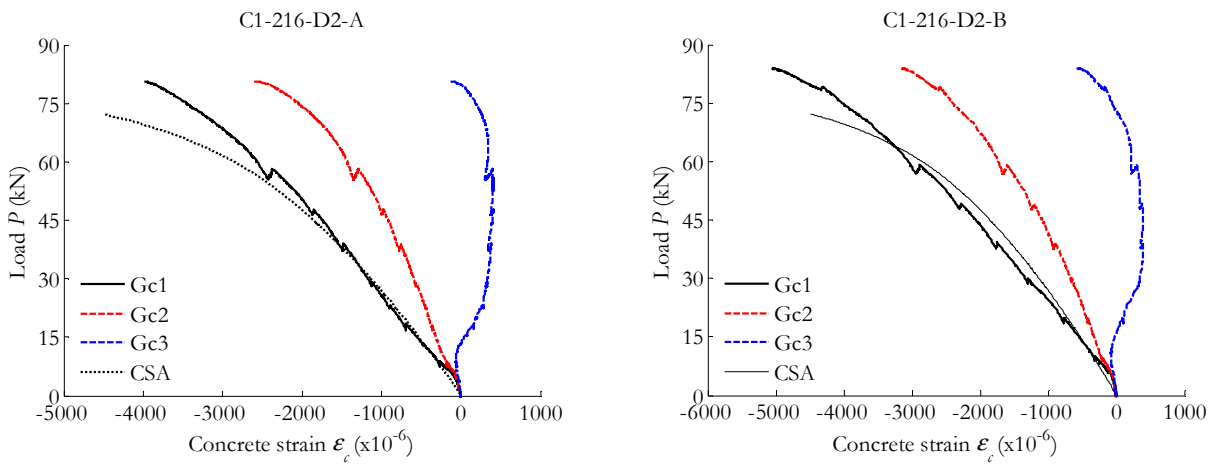
Figure B-52. Concrete strain vs. load at the midspan section compared to CSA predictions.
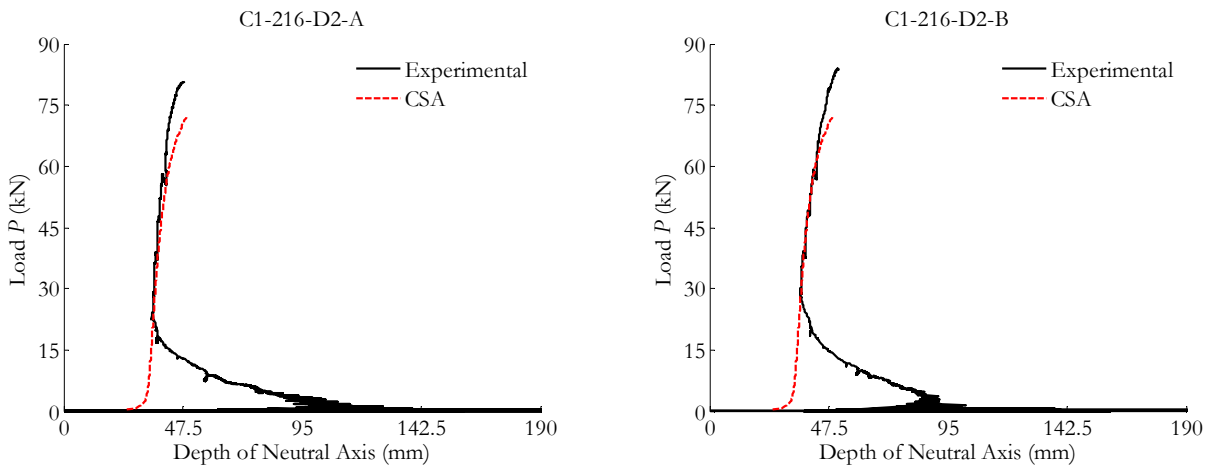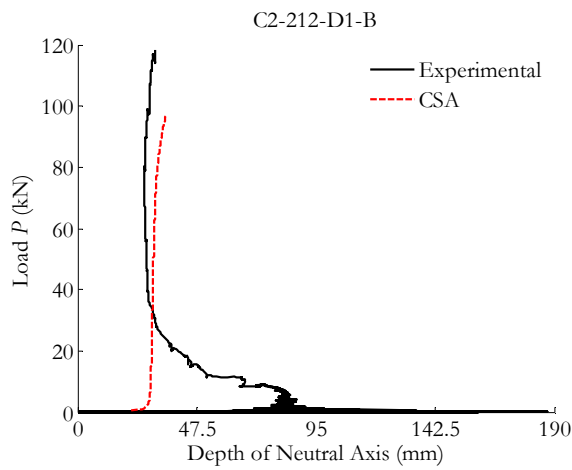

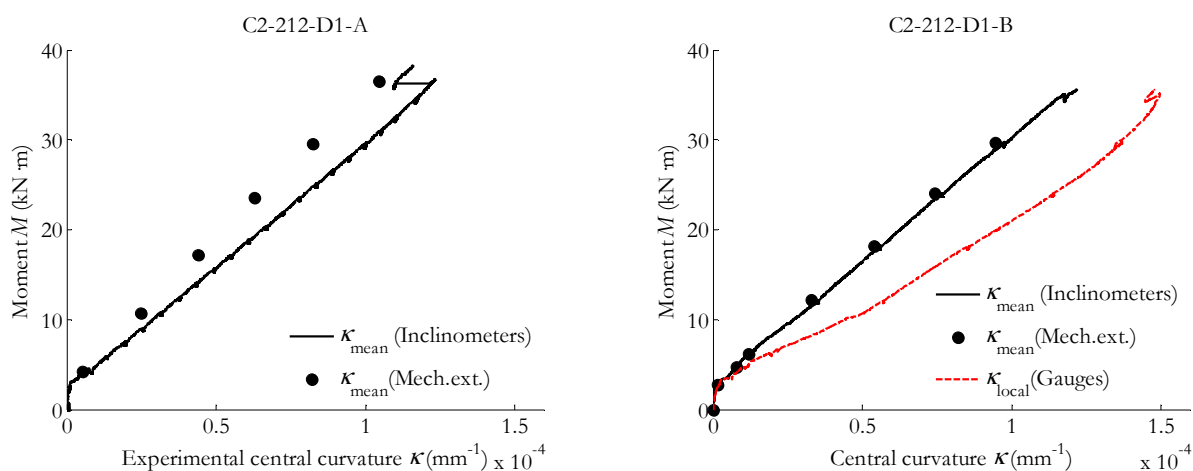Figure B-53. Neutral axis depth compared to CSA predictions.

B.4.4. Results at the pure bending zone
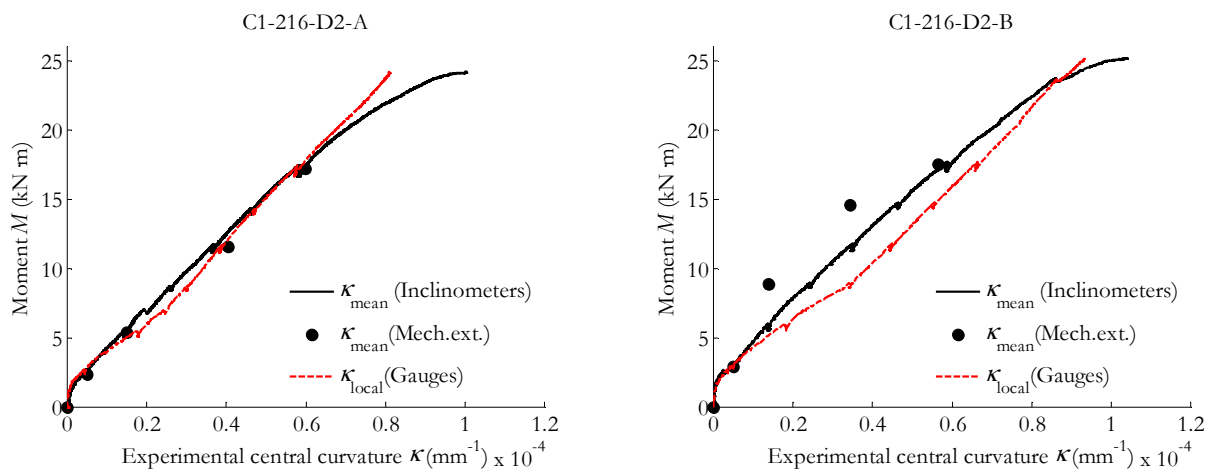
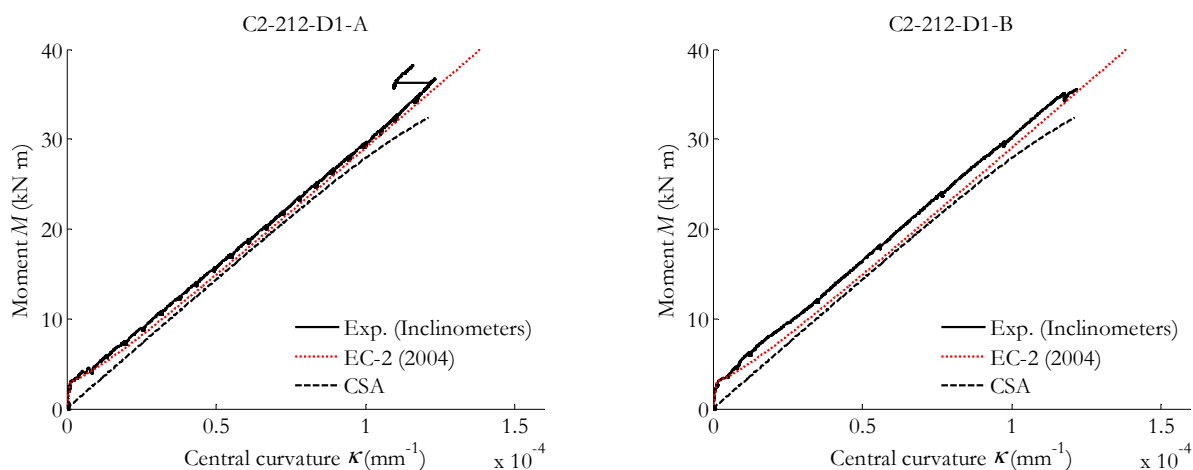Figure B-54. Experimental moment-curvature from inclinometers, mechanical extensometer and strain gauges on concrete.
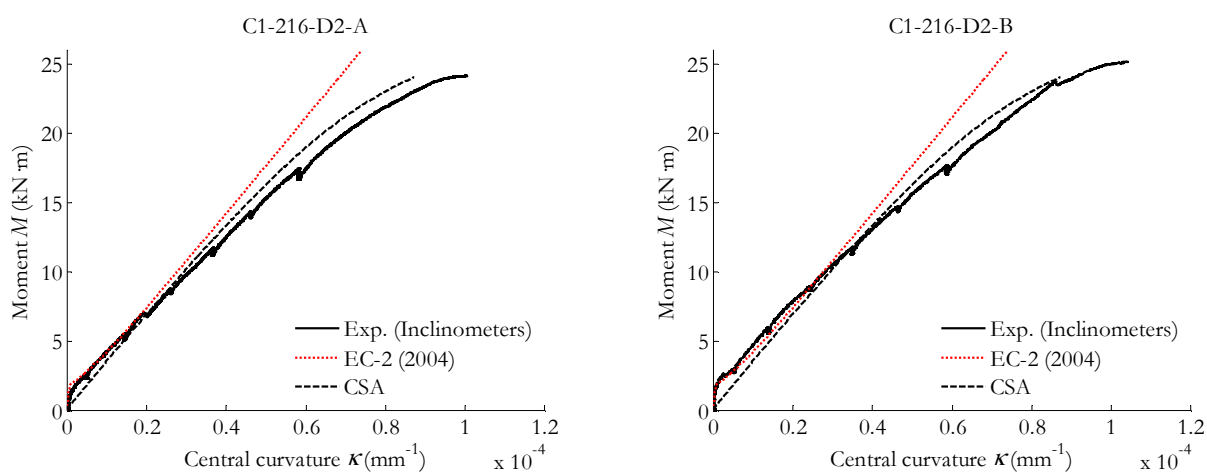
Figure B-55. Experimental moment-curvature compared to Eurocode 2 (2004) and CSA predictions.
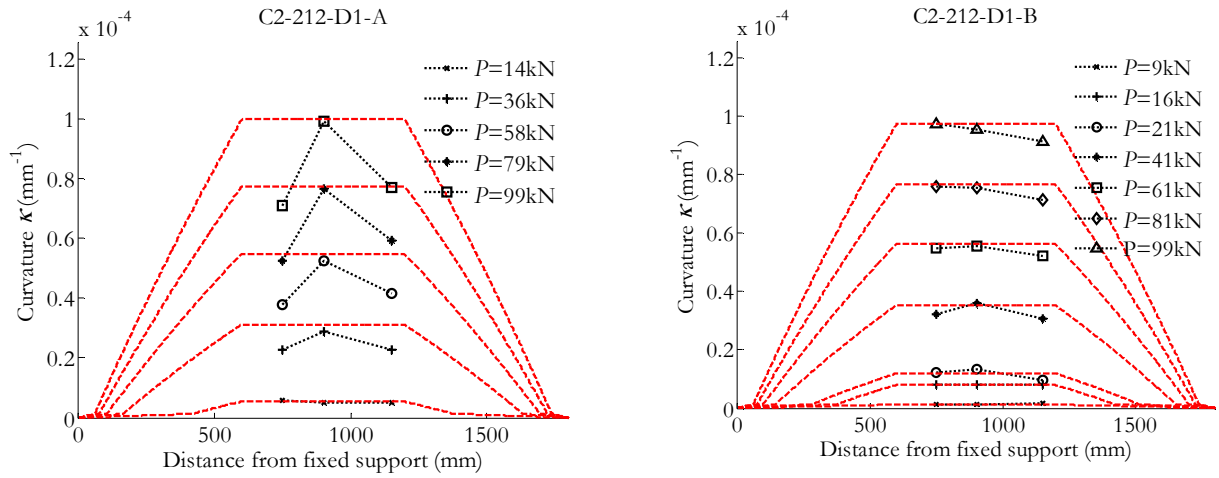
B.4.5. Results of the overall beam behaviour
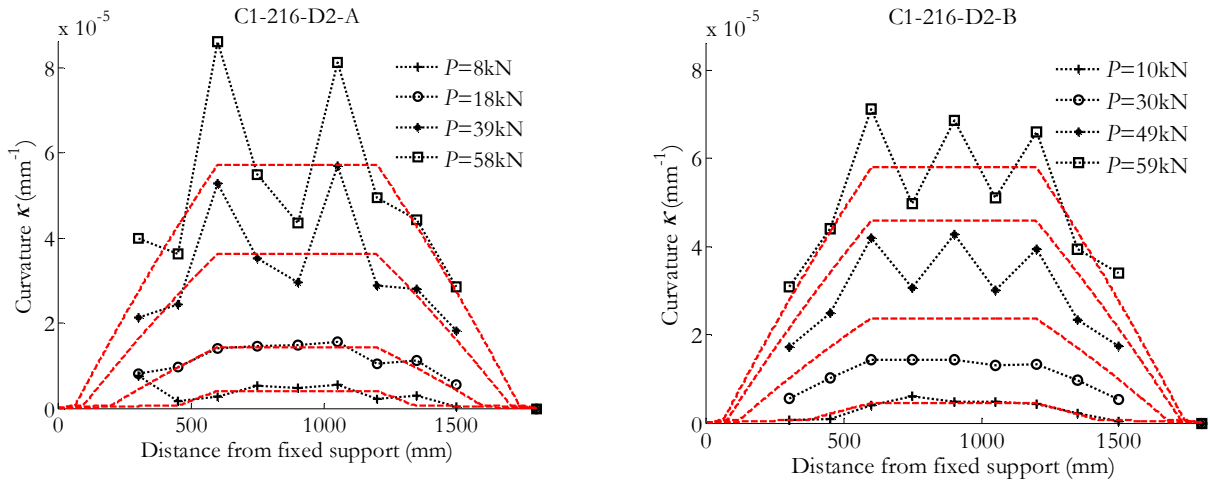
Figure B-56. Curvature along the length of the beam deduced form mechanical extensometer's data (dotted lines) compared to inclinometers' data (dashed lines).
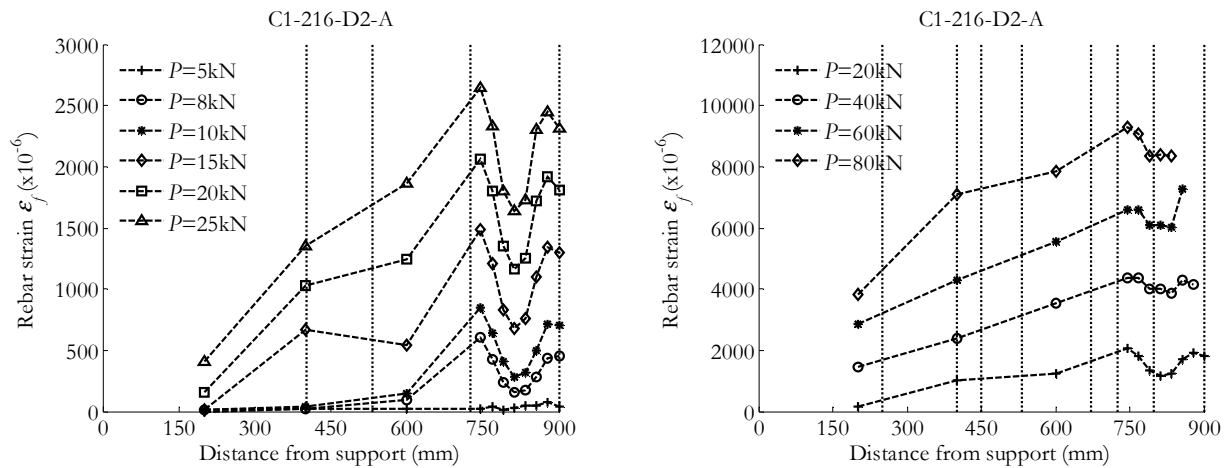
Figure B-57. Evolution of the rebar strain along the length of the beam (left) until service load (right) until failure (C1-216-D2-A).
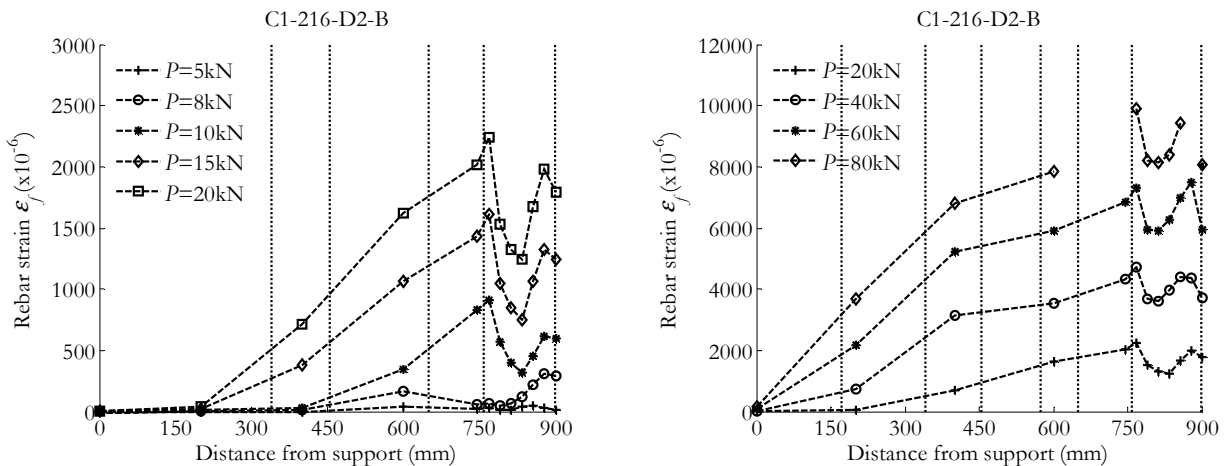
Figure B-58. Evolution of the rebar strain along the length of the beam (left) until service load (right) until failure (C1-216-D2-B).

B.4.6. Results on deflection
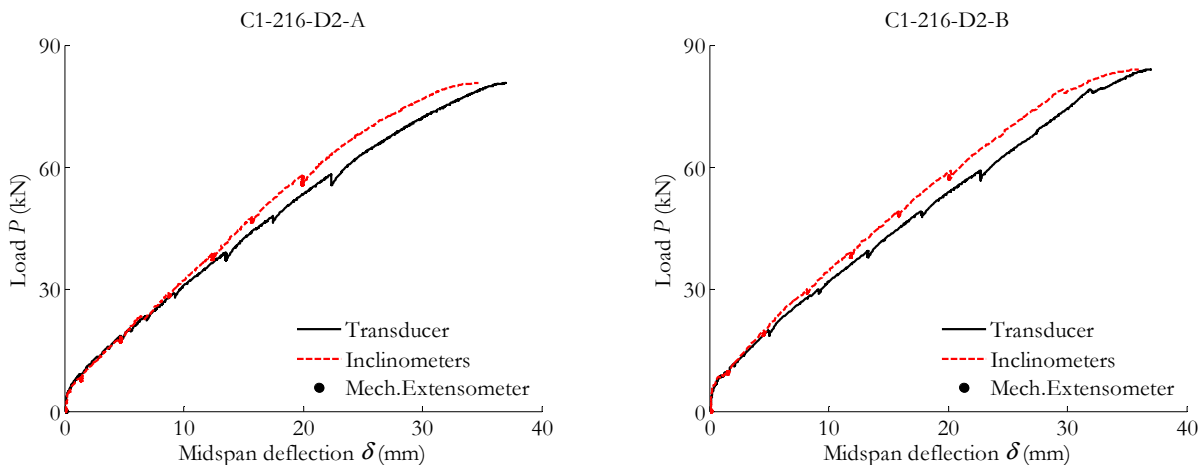
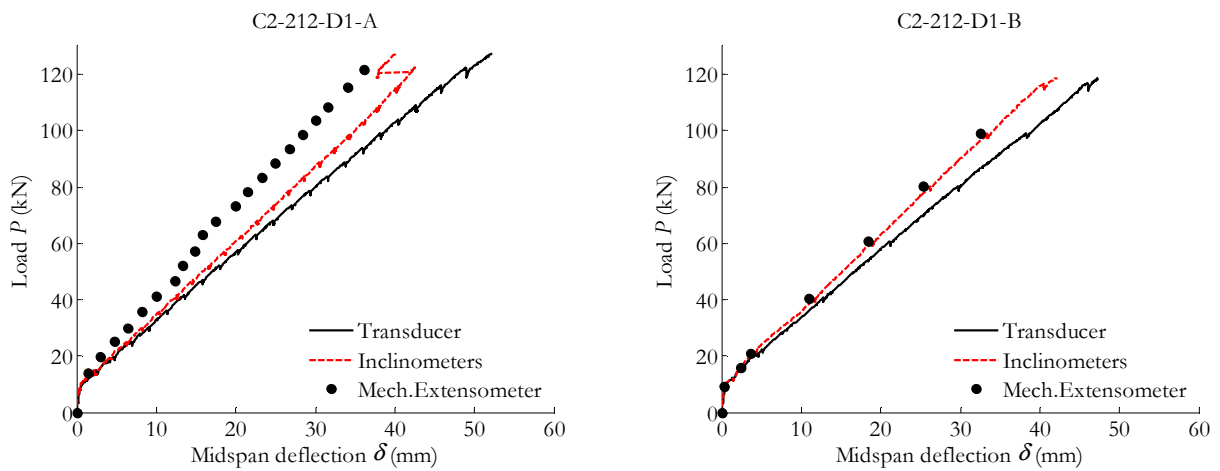Figure B-59. Experimental midspan deflection.
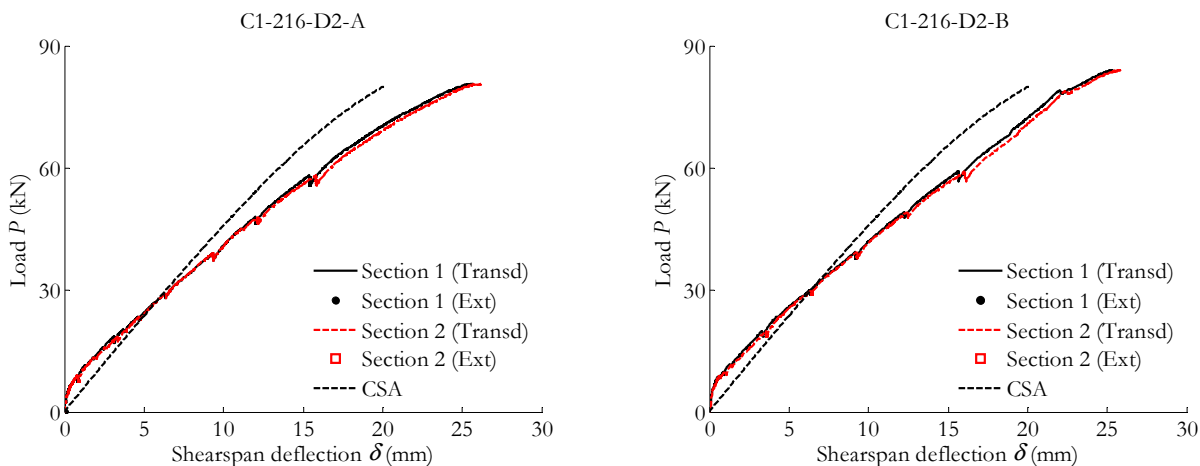
Figure B-60. Experimental shearspan deflection.
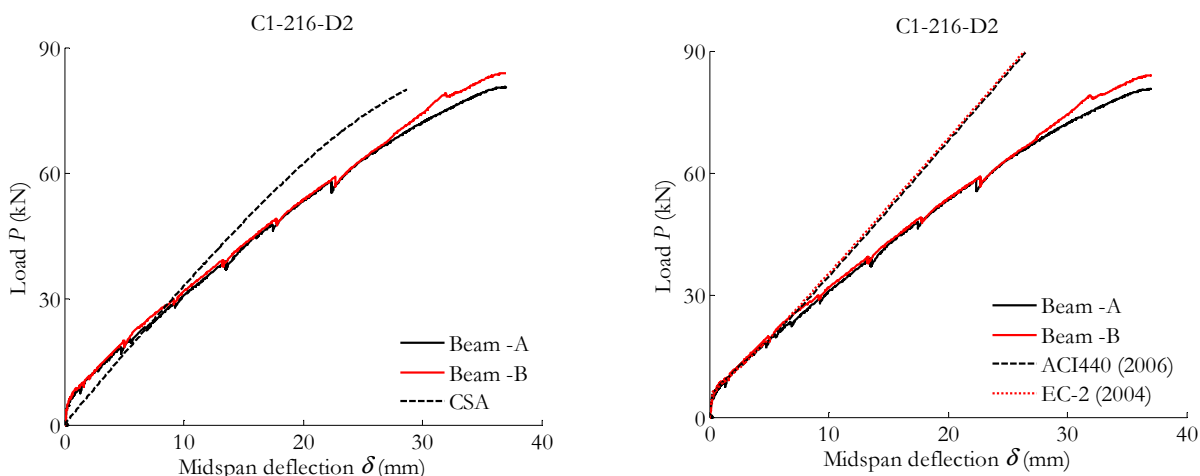
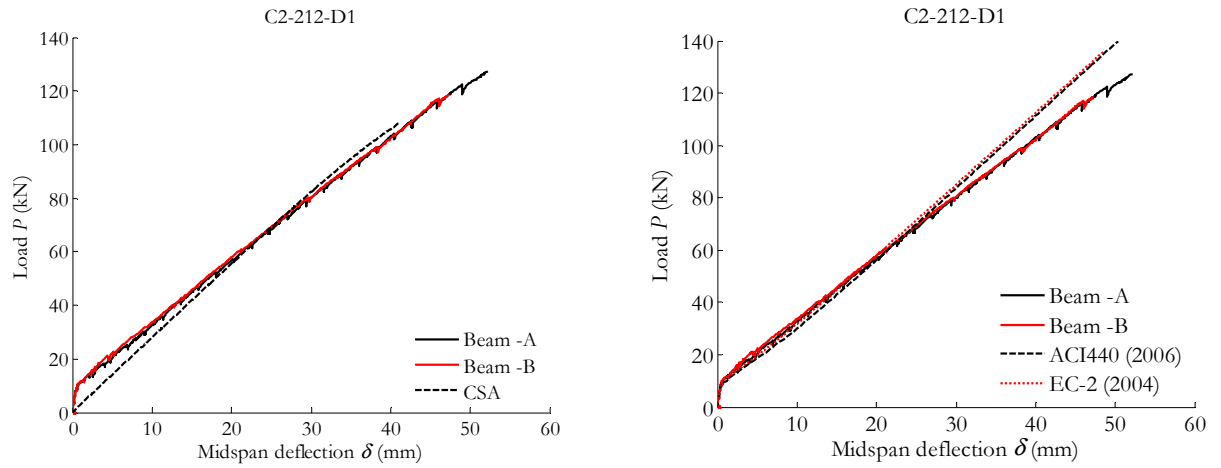

Figure B-61. Experimental midspan deflection (ultimate load) compared to cracked section analysis (left) / design codes (right).
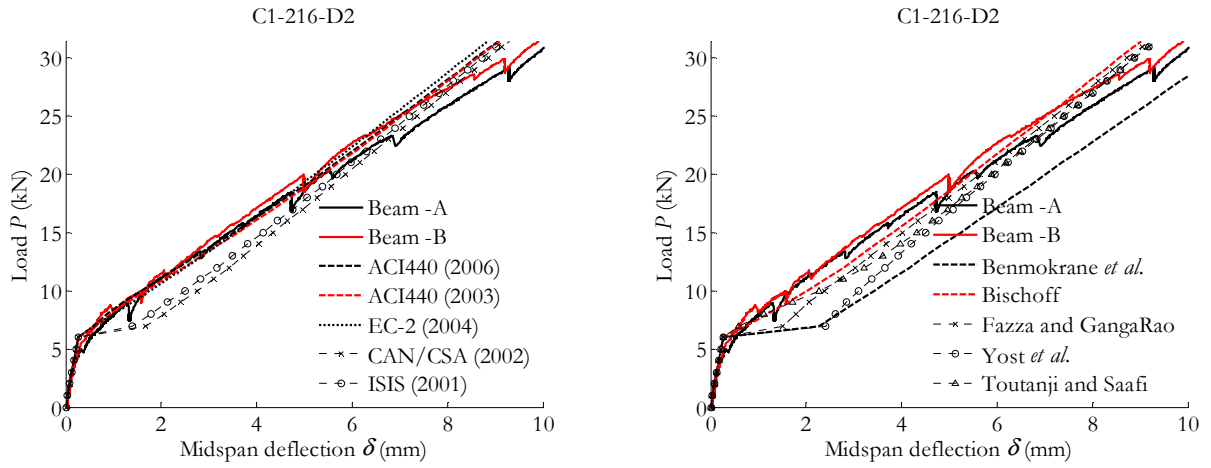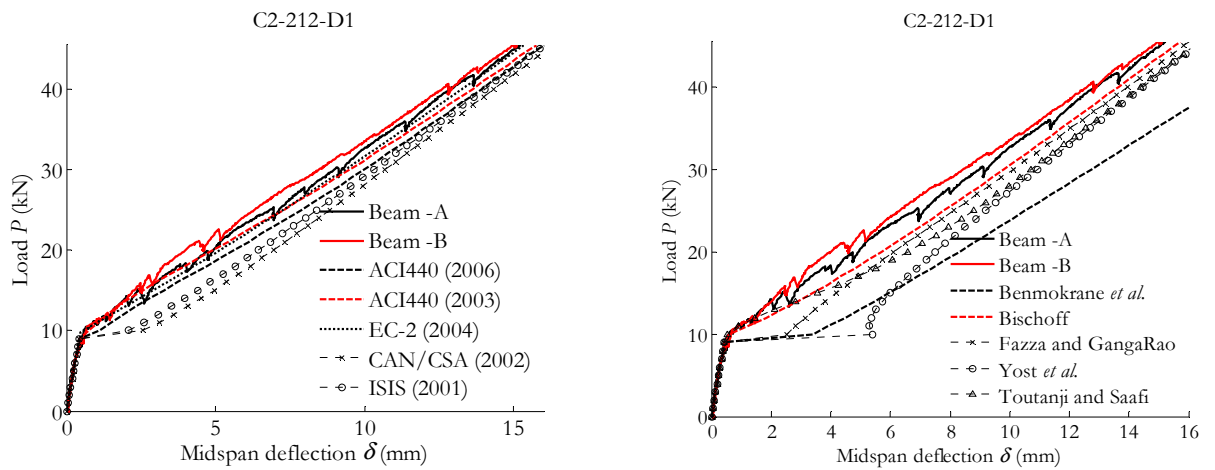
Figure B-62. Experimental vs theoretical midspan deflection (service load).

B.4.7. Results on cracking
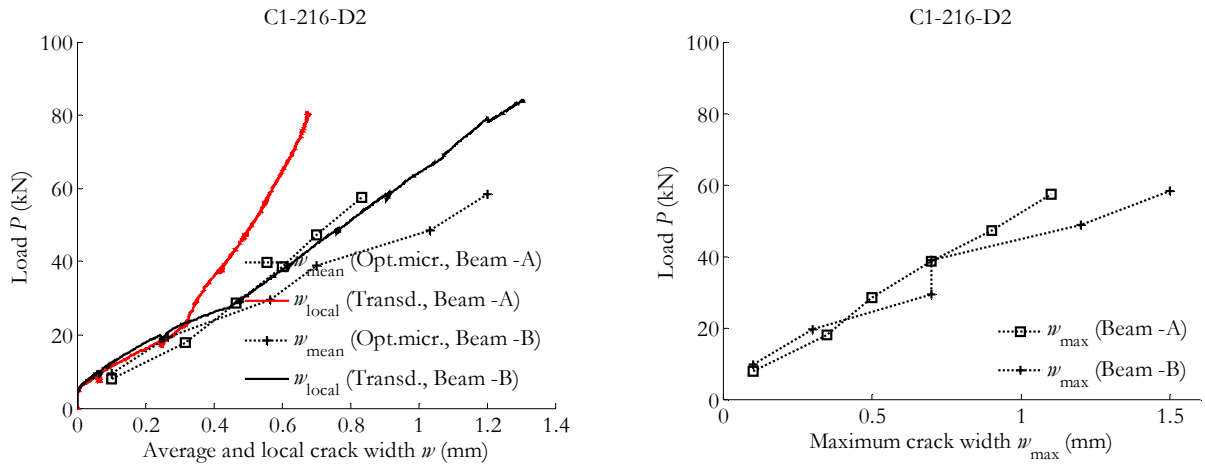
Figure B-63. Experimental crack width: average (left) and maximum (right).
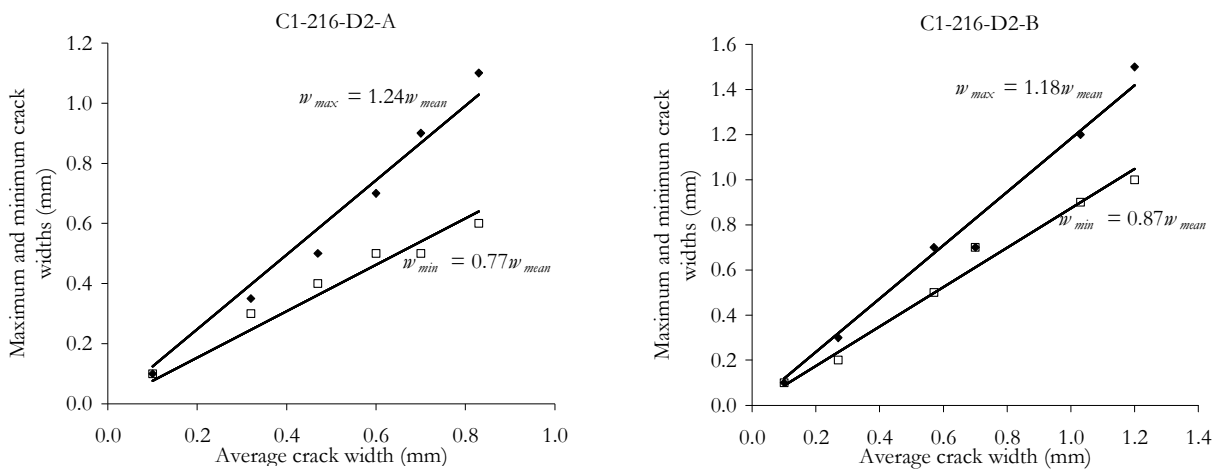
Figure B-64. Experimental crack width: maximum and minimum vs. average.
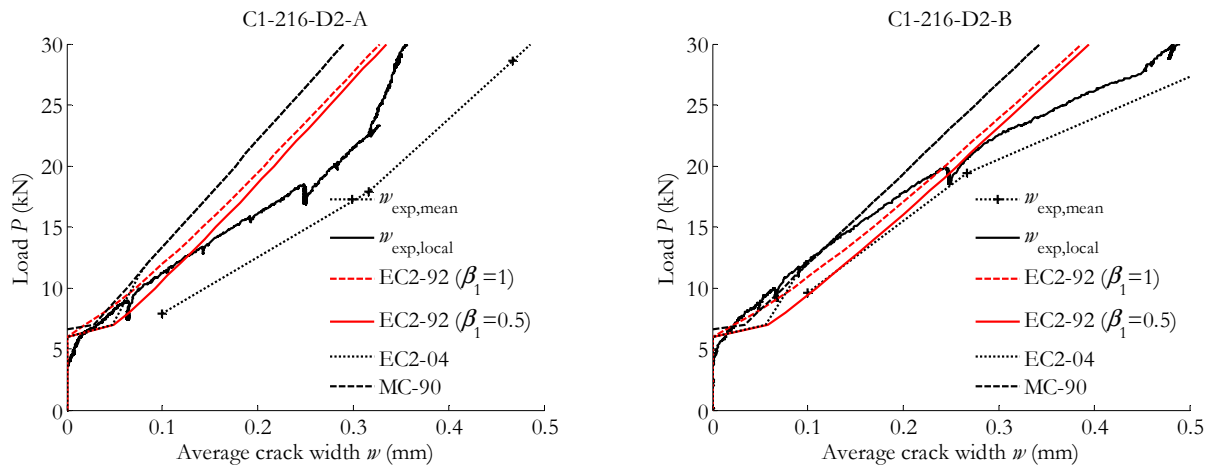
Figure B-65. Experimental vs theoretical average crack width, (left) Beam -A (rigth) Beam -B.
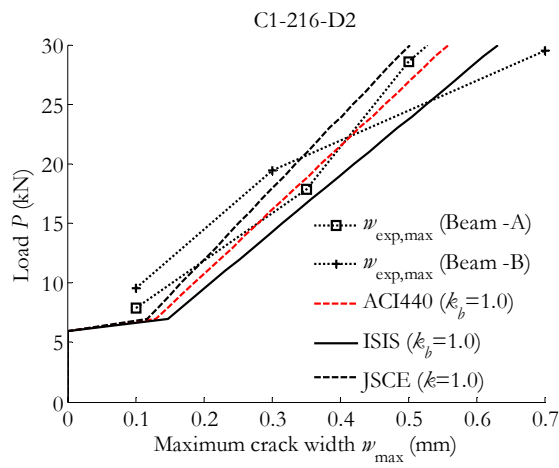
Figure B-66. Experimental vs theoretical maximum crack width.

Load = 7.9 kN
Av. Crack width = 0.10 mm

Load = 17.9 kN
Av. Crack width = 0.32 mm

Load = 28.6 kN
Av. Crack width = 0.47 mm

Load = 38.5 kN
Av. Crack width = 0.60 mm

Load = 47.2 kN
Av. Crack width = 0.70 mm

Load = 57.5 kN
Av. Crack width = 0.83 mm

Failure
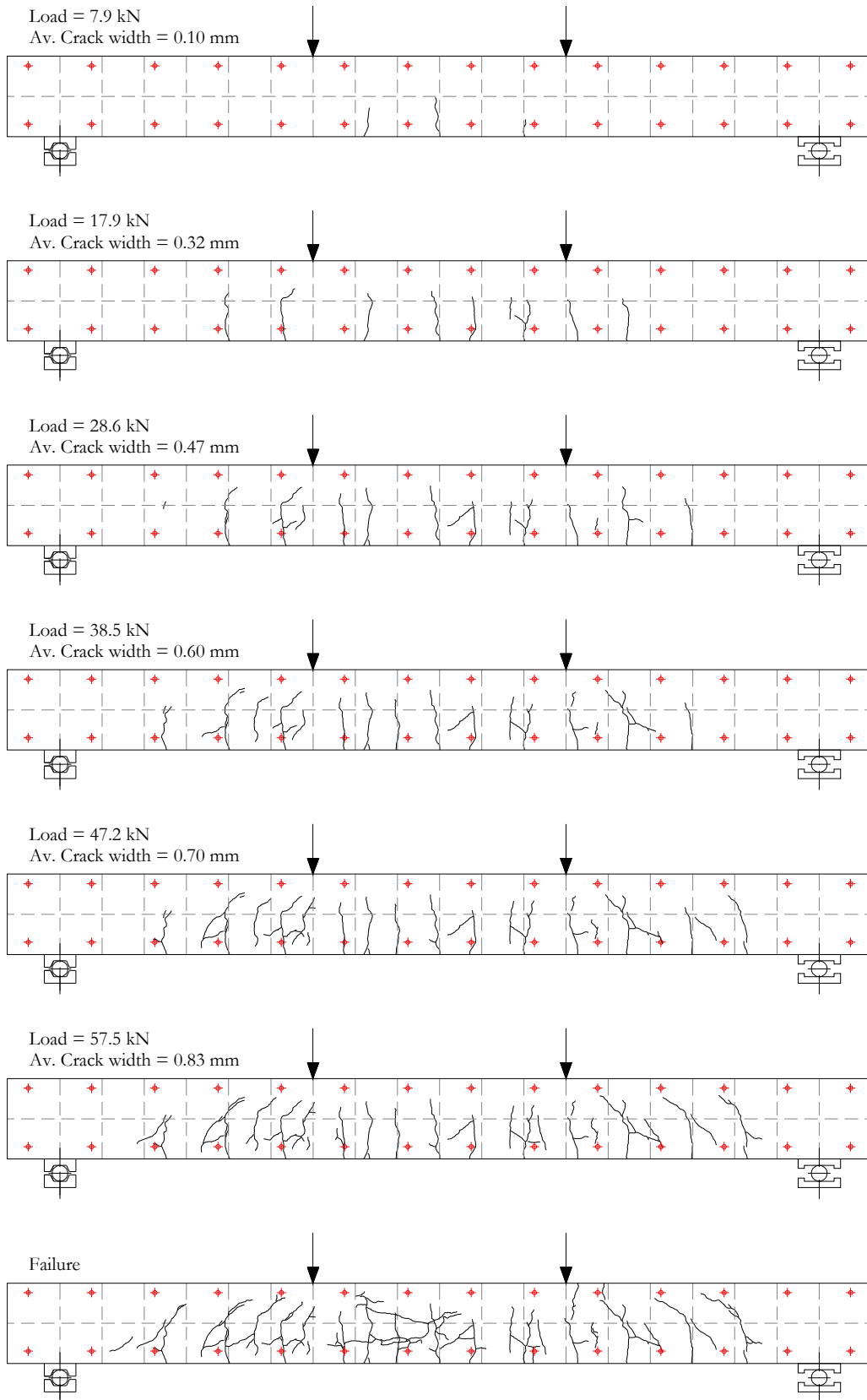
Figure B-67. Crack pattern (C1-216-D2-A).

Load = 9.6 kN
Av. Crack width = 0.10 mm

Load = 19.4 kN
Av. Crack width = 0.27 mm

Load = 29.5 kN
Av. Crack width = 0.57 mm

Load = 38.8 kN
Av. Crack width = 0.70 mm

Load = 48.6 kN
Av. Crack width = 1.03 mm

Load = 58.4 kN
Av. Crack width = 1.20 mm

Failure
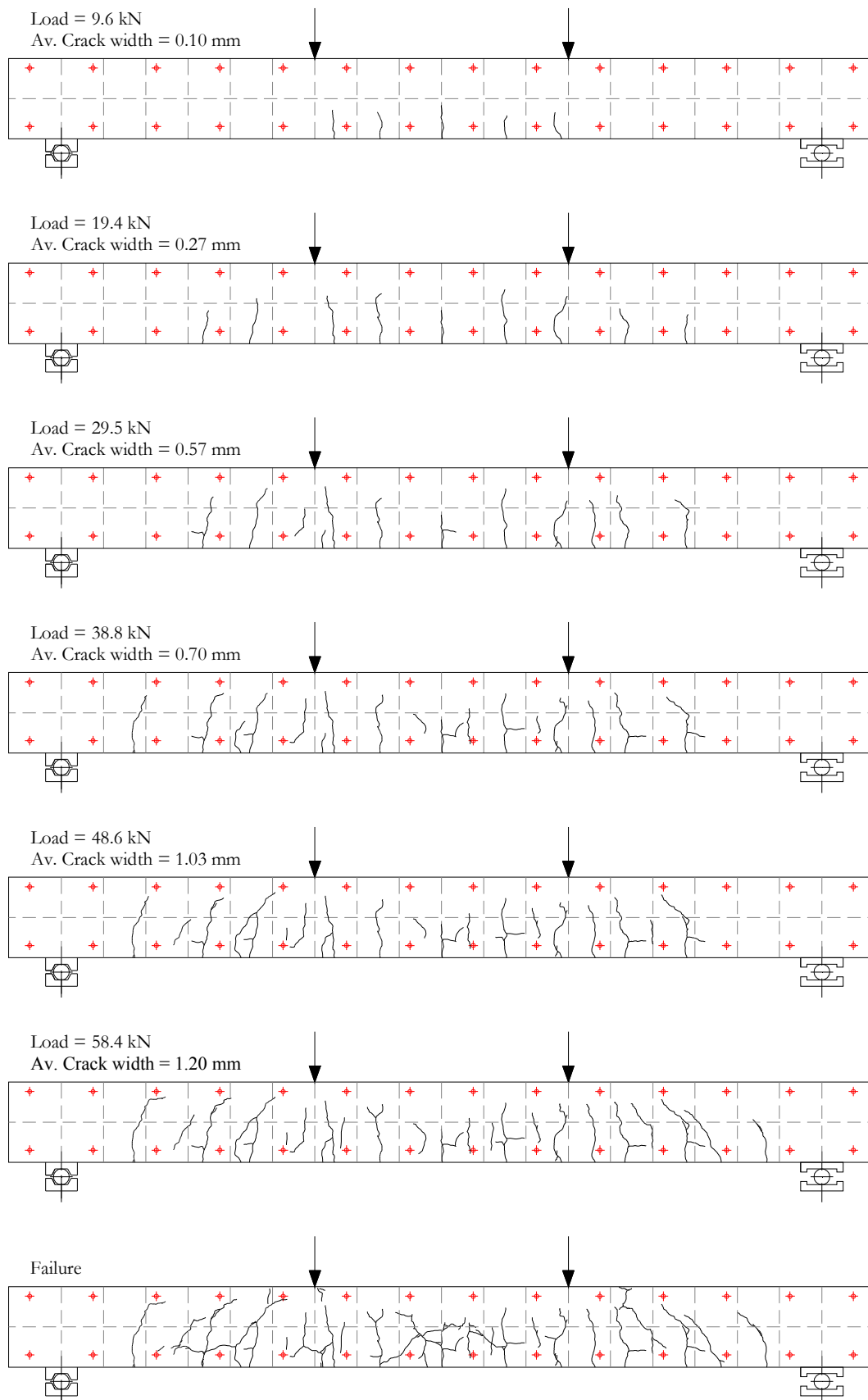
Figure B-68. Crack pattern (C1-216-D2-B).

B.5.   Results for the C1-316-D1 series

B.5.1.   General data

|	C1-316-D1-A	C1-316-D1-B
Cracking load (kN)	9.1	9.1
Load at reaching stabilised cracking phase (kN)	39.9	39.5
Average crack spacing at stabilised cracking phase (mm)	58	56
Maximum crack spacing at stabilised cracking phase (mm)	75	74
Minimum crack spacing at stabilised cracking phase (mm)	39	29
Load at which $\sigma_c = 0.45\, f_c$ (kN)	--	21.9
Load at which w_{max}=0.5-0.7mm (kN)	79.3	80.7
Load at which δ=L/250 (kN)	39.5	39.4
Ultimate load (kN)	104.8	109.9
Ultimate midspan deflection (mm)	26.4	28.9
Ultimate concrete strain (x10^{-6})	--	4746

B.5.2.   Failure mode
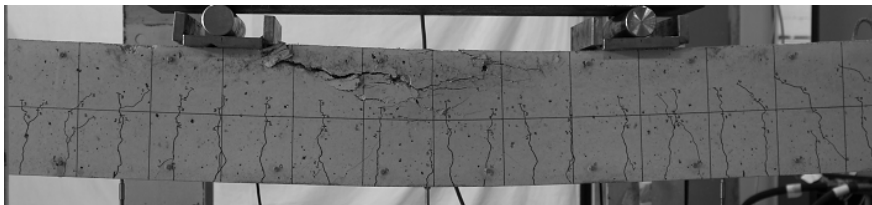
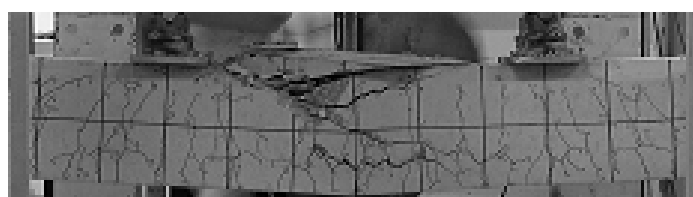

Figure B-69. Crushing of concrete for C1-316-D1-A.
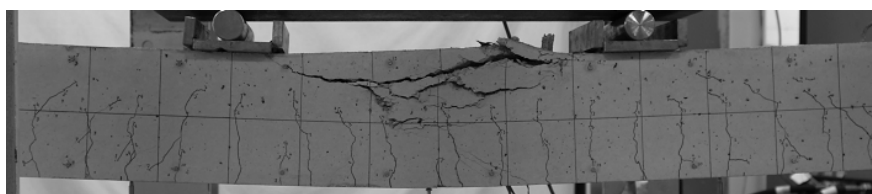
Figure B-70. Crushing of concrete for C1-316-D1-B.

B.5.3. Results at the midspan section
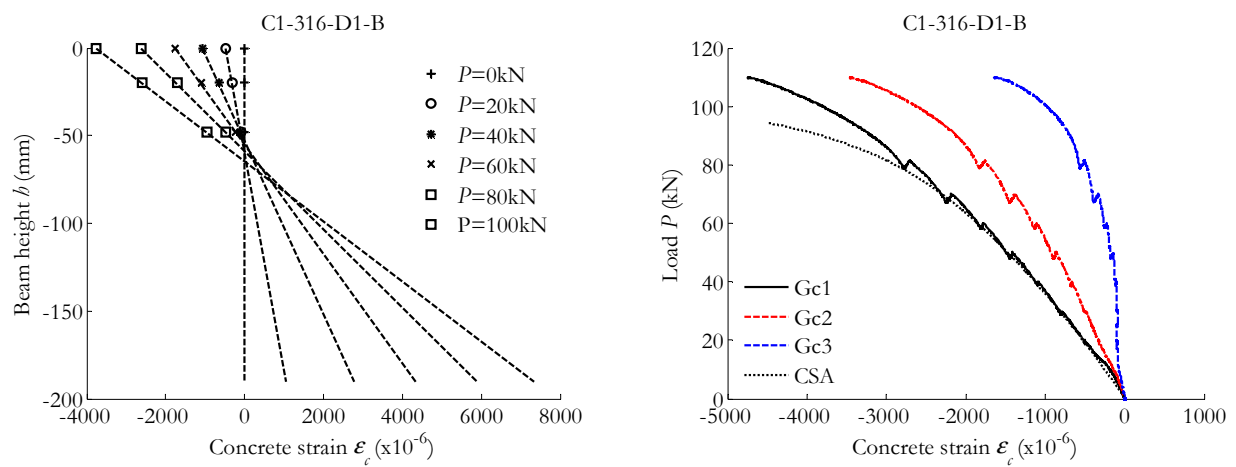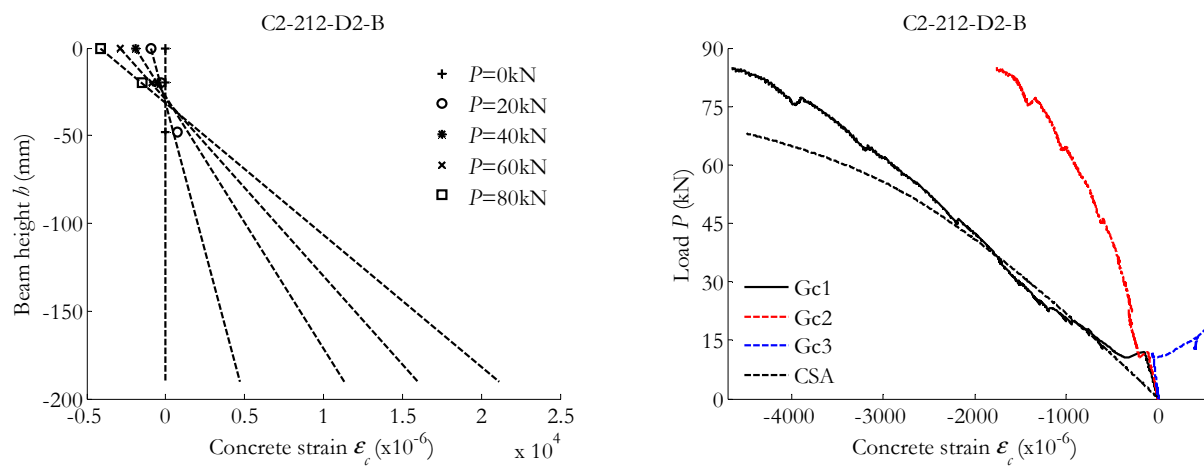

Figure B-71. Concrete strain in the midspan section: Along the height of the beam (left) / Versus the load applied and compared to CSA predictions (right).
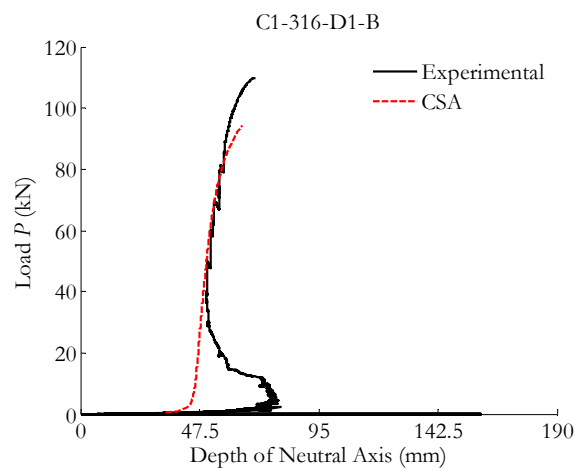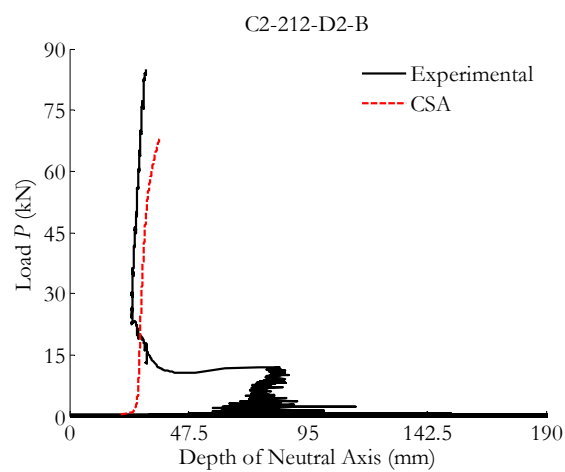

Figure B-72. Neutral axis depth compared to CSA predictions.
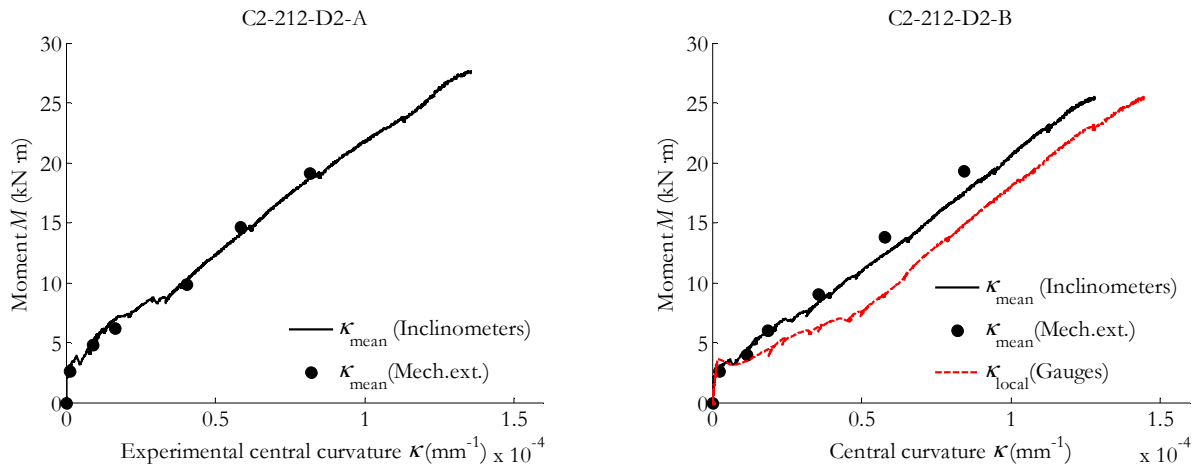
B.5.4. Results at the pure bending zone

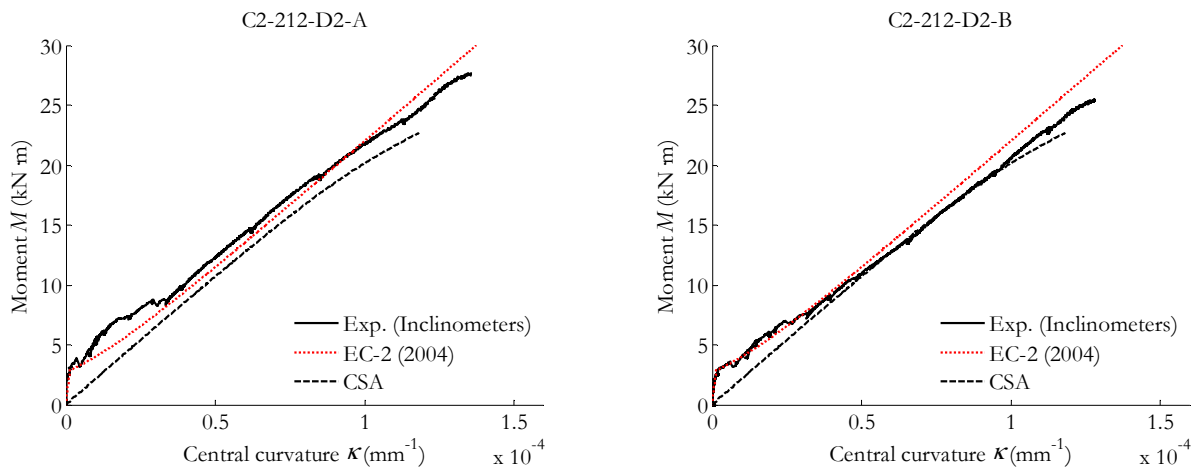Figure B-73. Experimental moment-curvature from inclinometers, mechanical extensometer and strain gauges on concrete.

Figure B-74. Experimental moment-curvature compared to Eurocode 2 (2004) and CSA predictions.
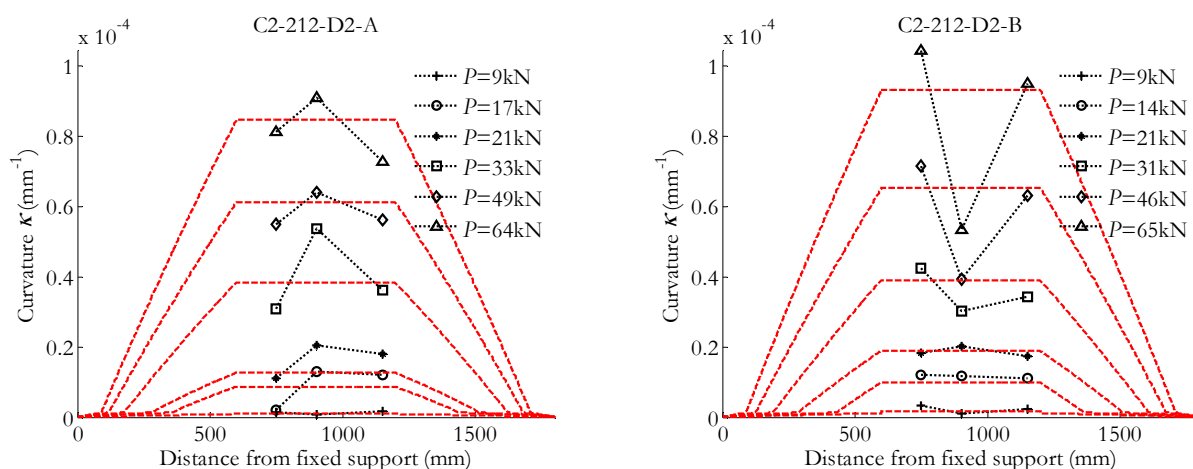
B.5.5. Results of the overall beam behaviour
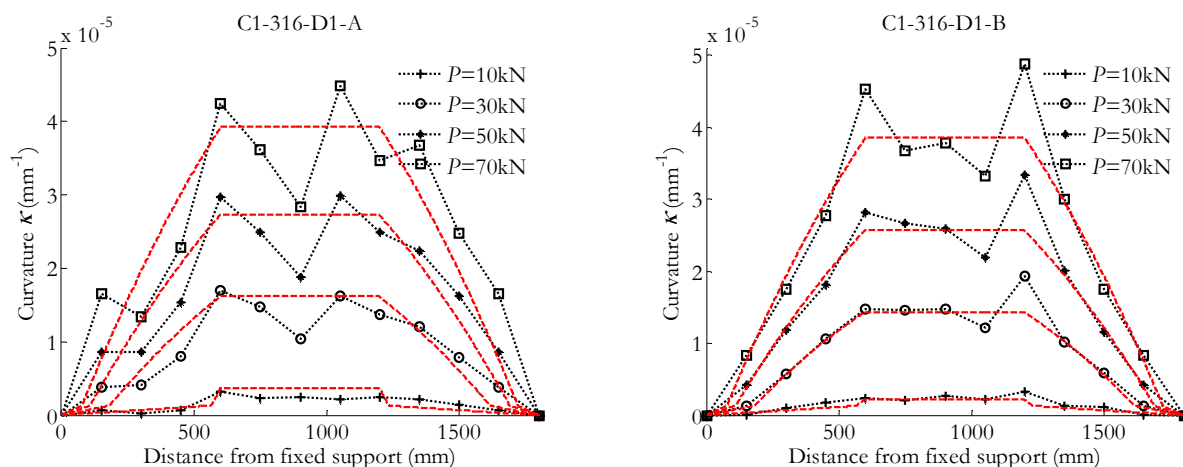
Figure B-75. Curvature along the length of the beam deduced form mechanical extensometer's data (dotted lines) compared to inclinometers' data (dashed lines).

B.5.6. Results on deflection
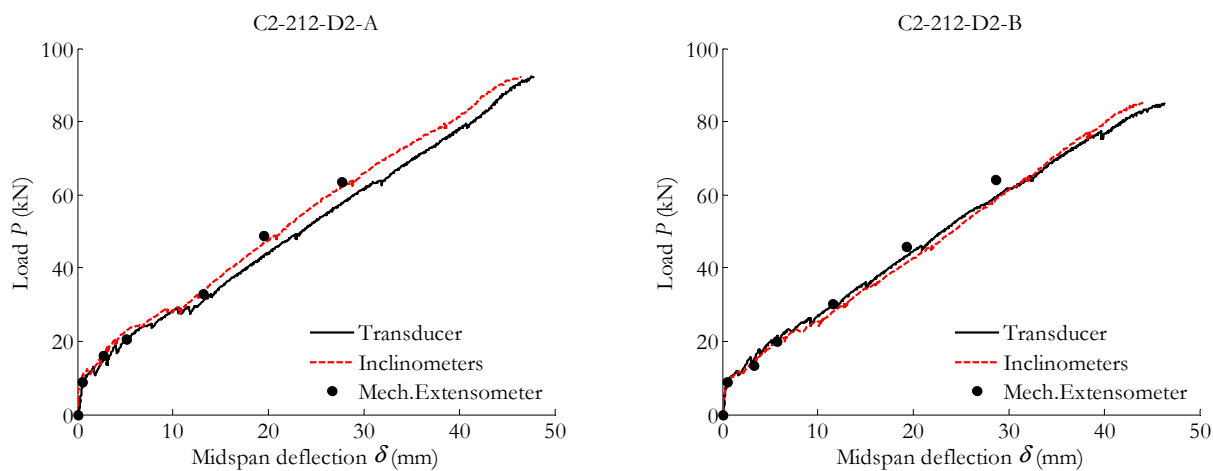

Figure B-76. Experimental midspan deflection

Figure B-77. Experimental shearspan deflection compared to cracked section analysis.

Figure B-78. Experimental midspan deflection (ultimate load) compared to cracked section analysis (left) / design codes (right).

Figure B-79. Experimental vs theoretical midspan deflection (service load).

B.5.7. Results on cracking

Figure B-80. Experimental crack width: average (left) and maximum (right).

Figure B-81. Experimental crack width: maximum and minimum vs. average.

Figure B-82. Experimental vs theoretical crack width, (left) average (rigth) maximum.

Figure B-83. Crack pattern (C1-316-D1-A).

Load = 9.5 kN
Av. Crack width = 0.05mm

Load = 19.4 kN
Av. Crack width = 0.07 mm

Load = 29.5 kN
Av. Crack width = 0.09 mm

Load = 39.5 kN
Av. Crack width = 0.12 mm

Load = 49.3 kN
Av. Crack width = 0.16 mm

Load = 59.3 kN
Av. Crack width = 0.21 mm

Load = 69.3 kN
Av. Crack width = 0.23mm

Load = 80.6 kN
Av. Crack width = 0.26 mm

Failure

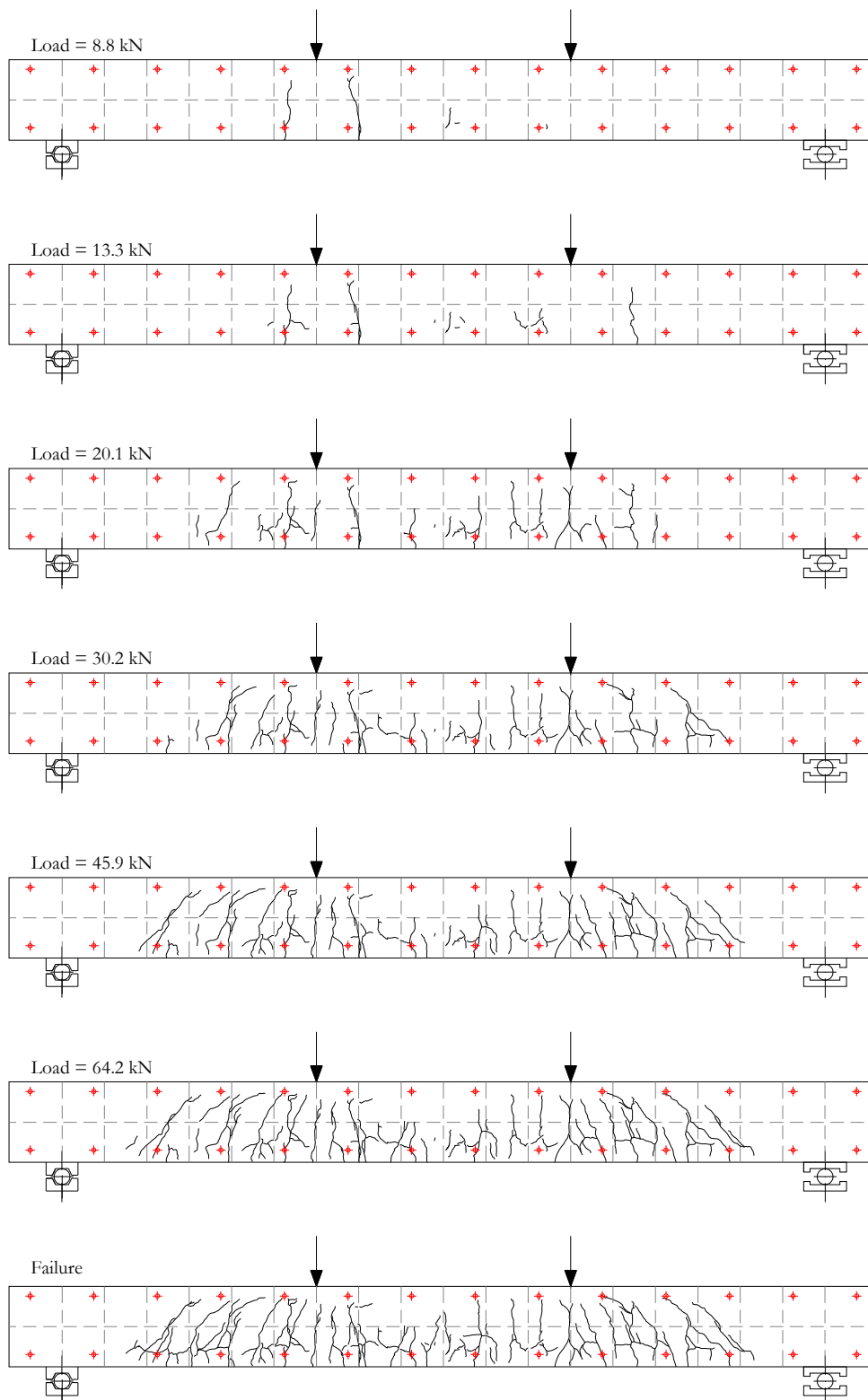Figure B-84. Crack pattern (C1-316-D1-B).

B.6. Results for the C1-316-D2 series

B.6.1. General data

|	C1-316-D2-A	C1-316-D2-B
Cracking load (kN)	7.3	7.4
Load at reaching stabilised cracking phase (kN)	28.9	19.2
Average crack spacing at stabilised cracking phase (mm)	102	114
Maximum crack spacing at stabilised cracking phase (mm)	137	156
Minimum crack spacing at stabilised cracking phase (mm)	65	88
Load at which $\sigma_c = 0.45\,f_c$ (kN)	--	18.9
Load at which w_{max}=0.5-0.7mm (kN)	48.7	39.7
Load at which δ=L/250 (kN)	30.0	31.8
Ultimate load (kN)	92.4	95.2
Ultimate midspan deflection (mm)	30.9	30.5
Ultimate concrete strain (x10^{-6})	--	4573

B.6.2. Failure mode

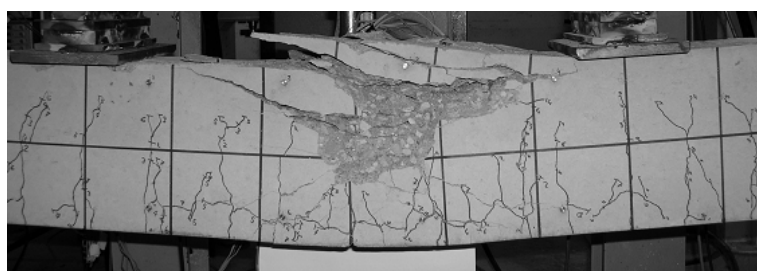Figure B-85. Crushing of concrete for C1-316-D2-A.

Figure B-86. Crushing of concrete for C1-316-D2-B.
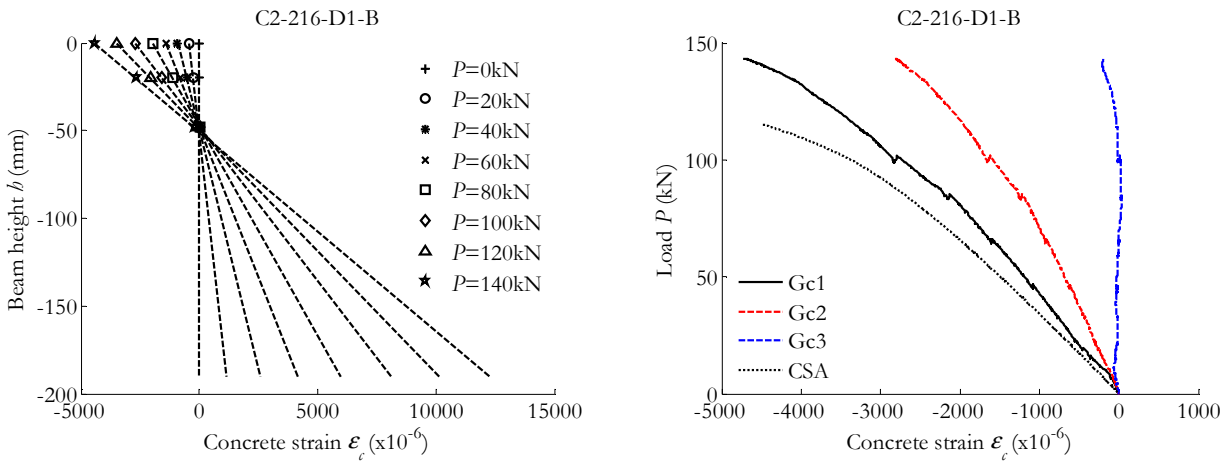
B.6.3. Results at the midspan section
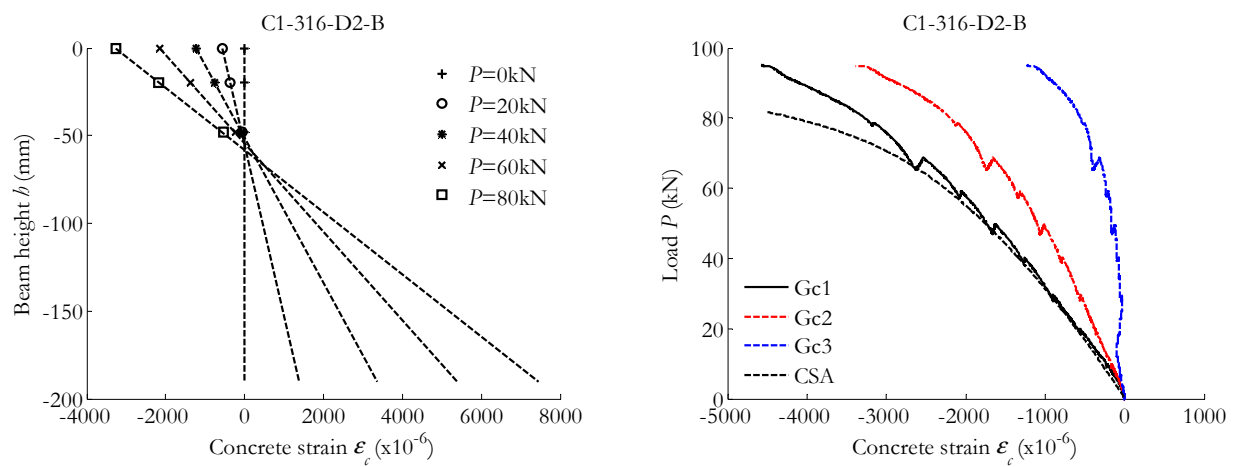
Figure B-87. Concrete strain in the midspan section: Along the height of the beam (left) / Versus the load applied and compared to CSA predictions (right).
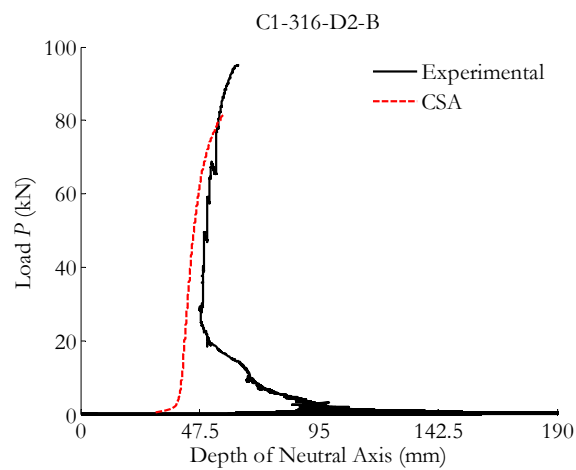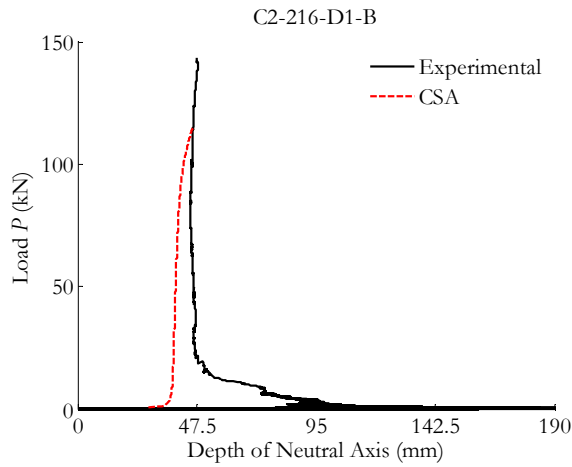

Figure B-88. Neutral axis depth compared to CSA predictions.
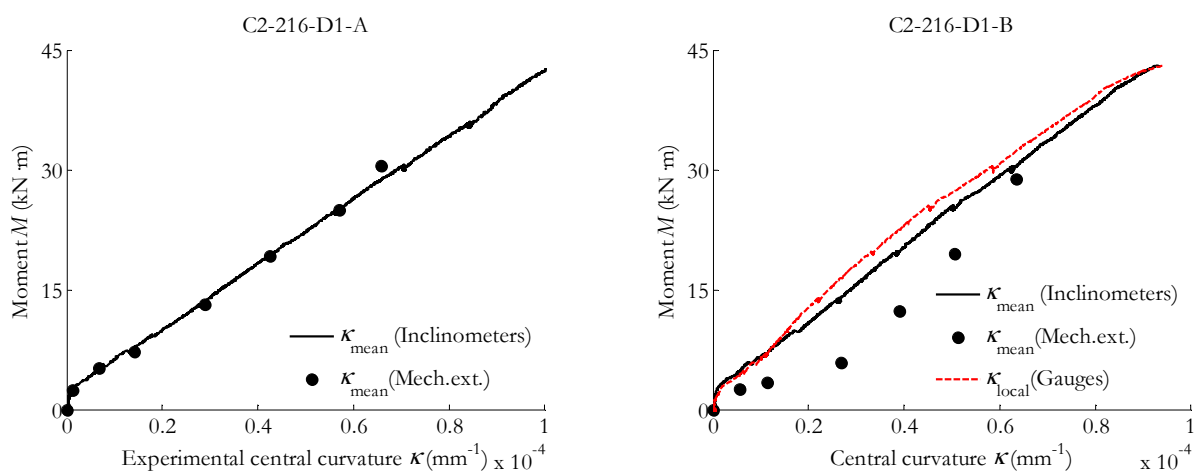
B.6.4. Results at the pure bending zone
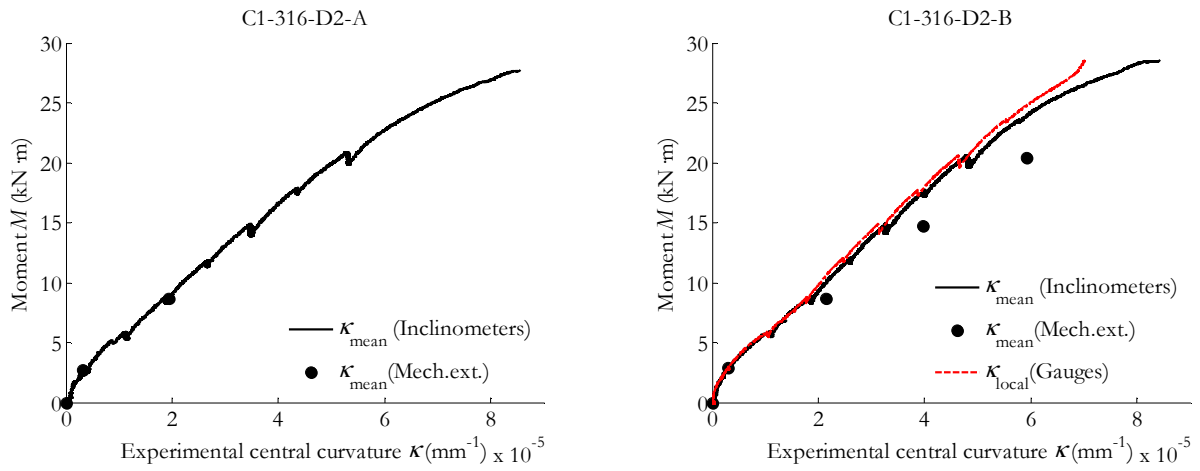
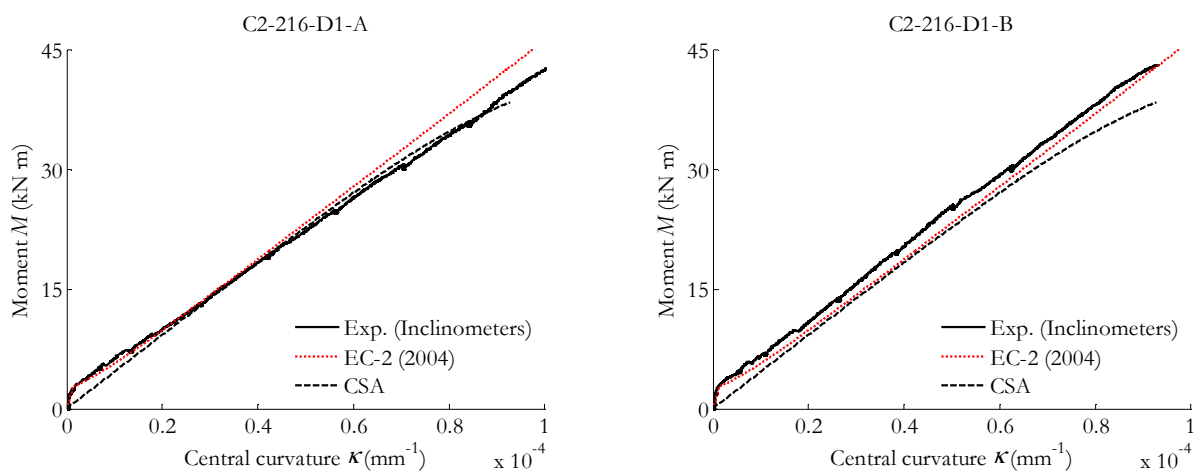Figure B-89. Experimental moment-curvature from inclinometers, mechanical extensometer and strain gauges on concrete.
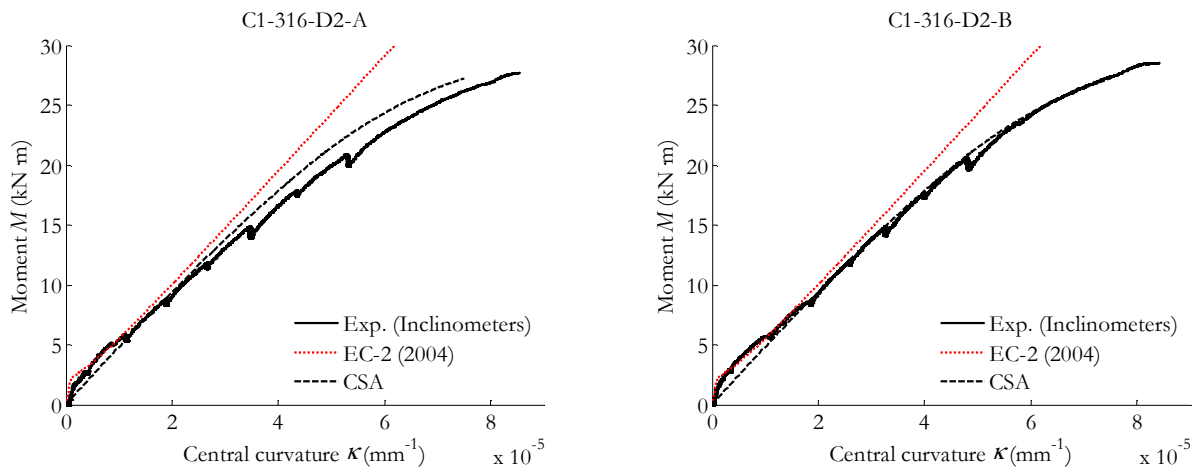
Figure B-90. Experimental moment-curvature compared to Eurocode 2 (2004) and CSA predictions.
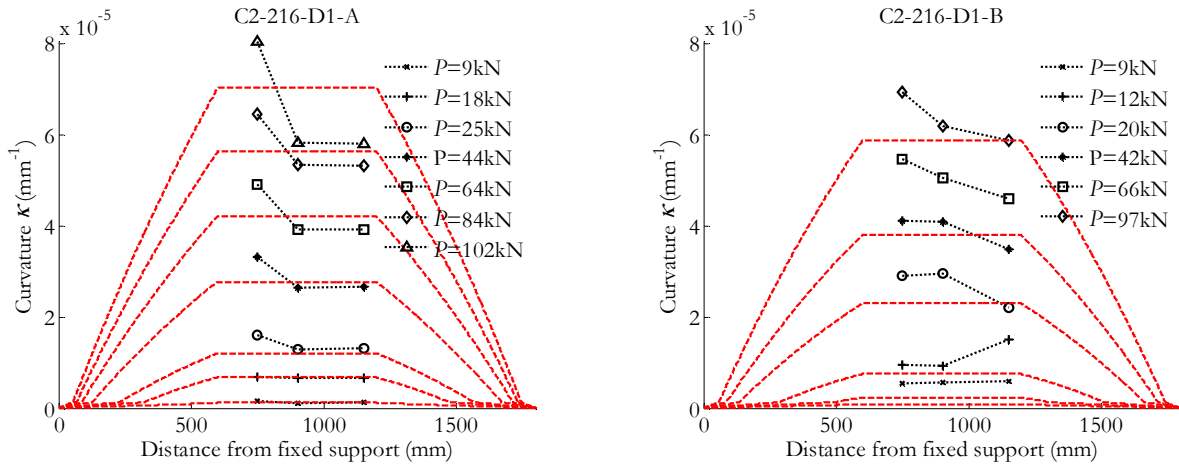
B.6.5. Results of the overall beam behaviour
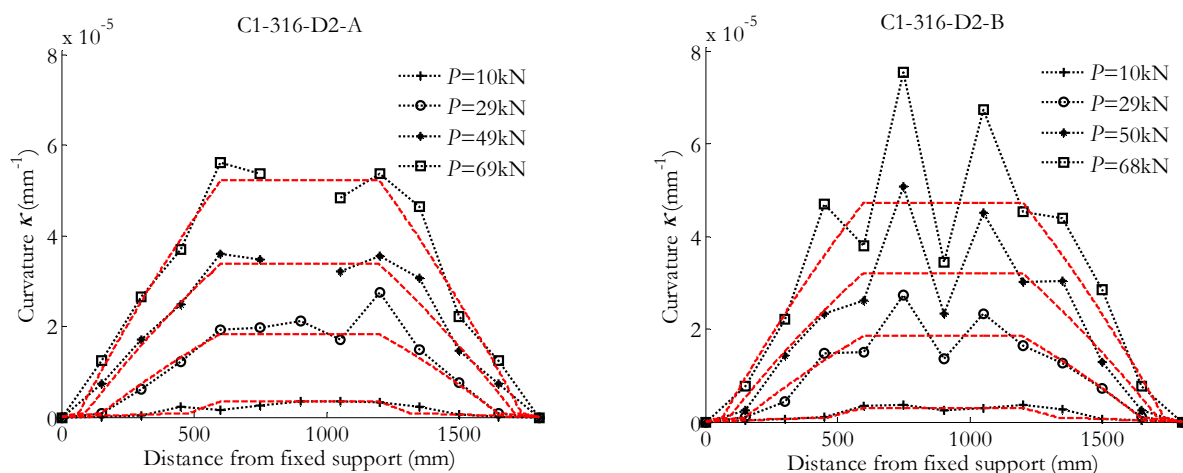
Figure B-91. Curvature along the length of the beam deduced form mechanical extensometer's data (dotted lines) compared to inclinometers' data (dashed lines).

B.6.6. Results on deflection
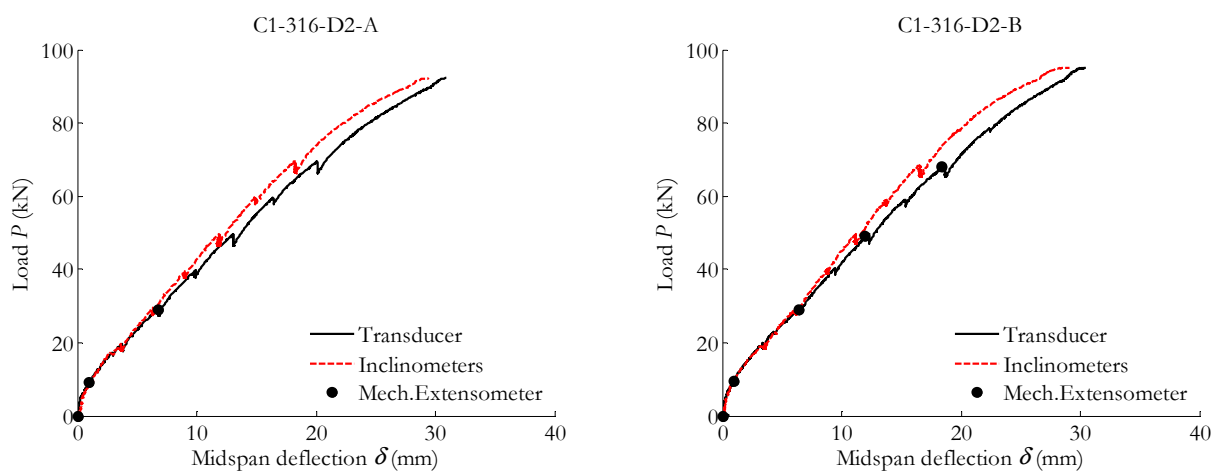
Figure B-92. Experimental midspan deflection.
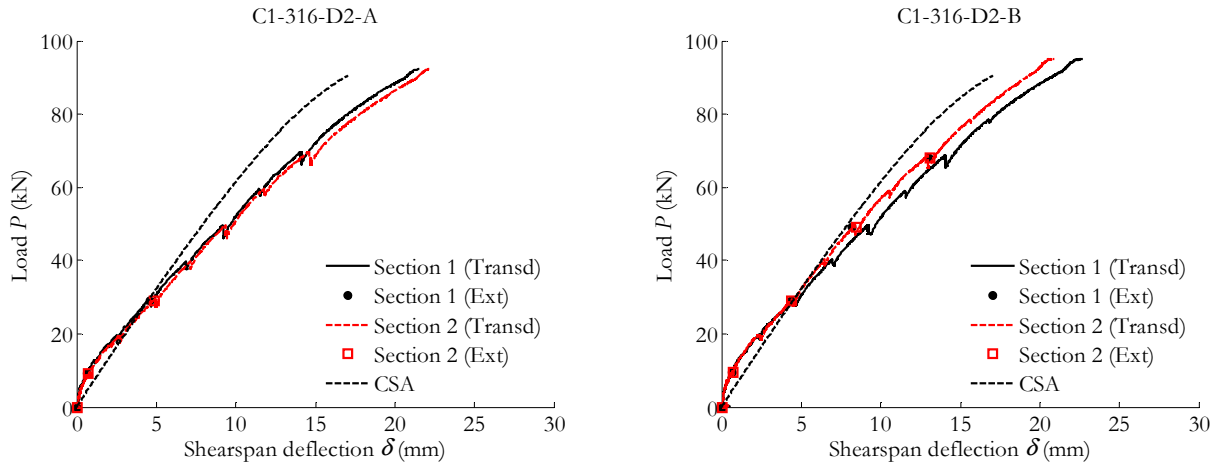
Figure B-93. Experimental shearspan deflection compared to cracked section analysis.
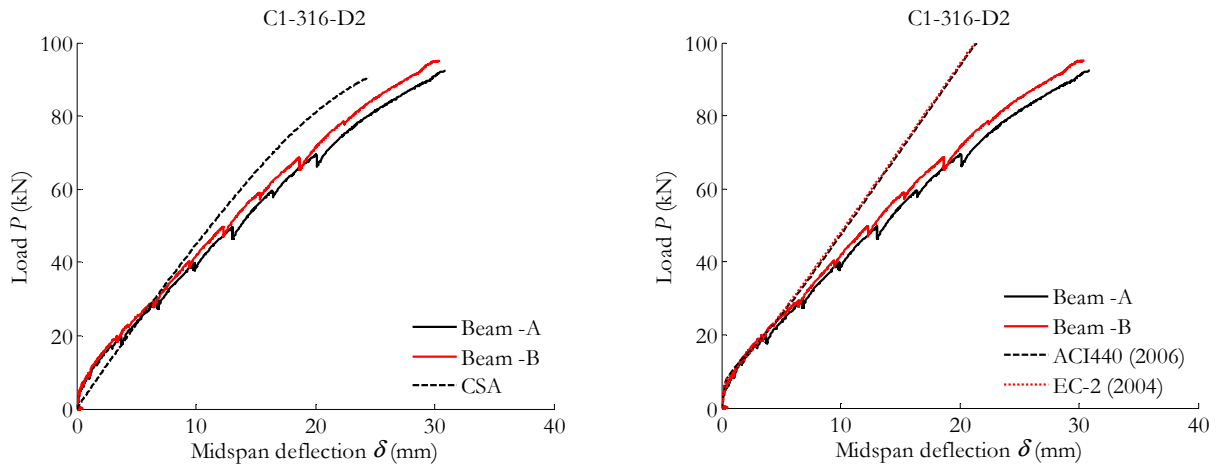
Figure B-94. Experimental midspan deflection (ultimate load) compared to cracked section analysis (left) / design codes (right).
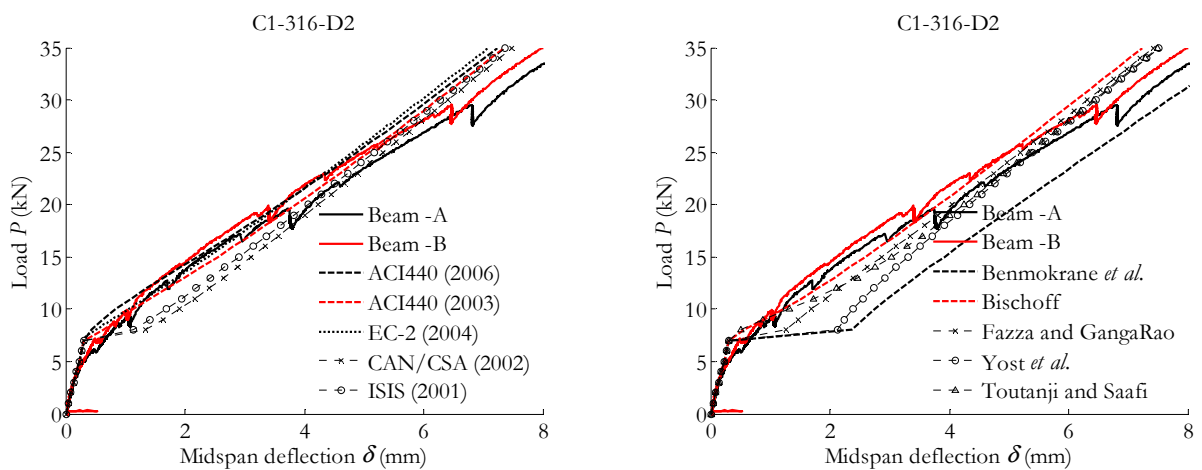
Figure B-95. Experimental vs theoretical midspan deflection (service load).

B.6.7. Results on cracking
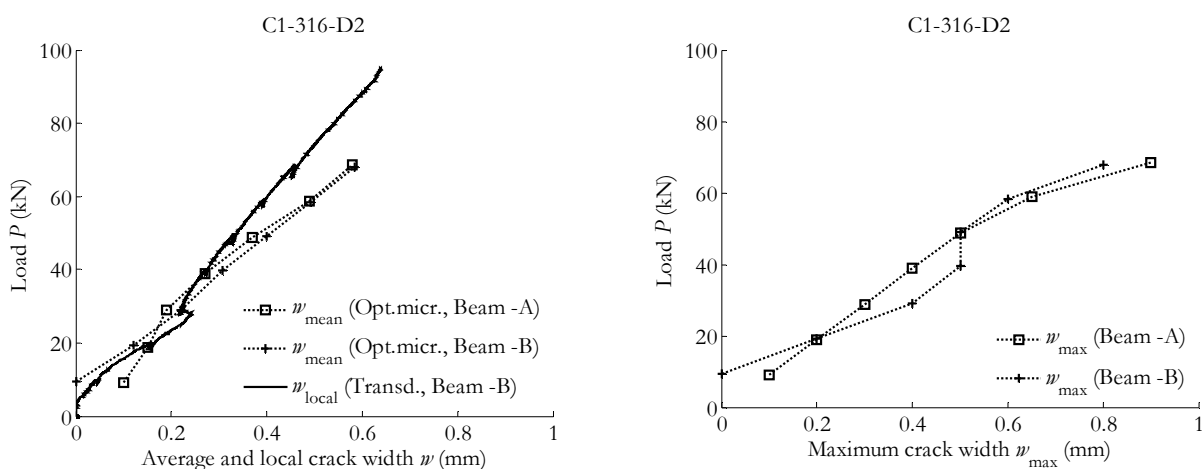
Figure B-96. Experimental crack width: average (left) and maximum (right).
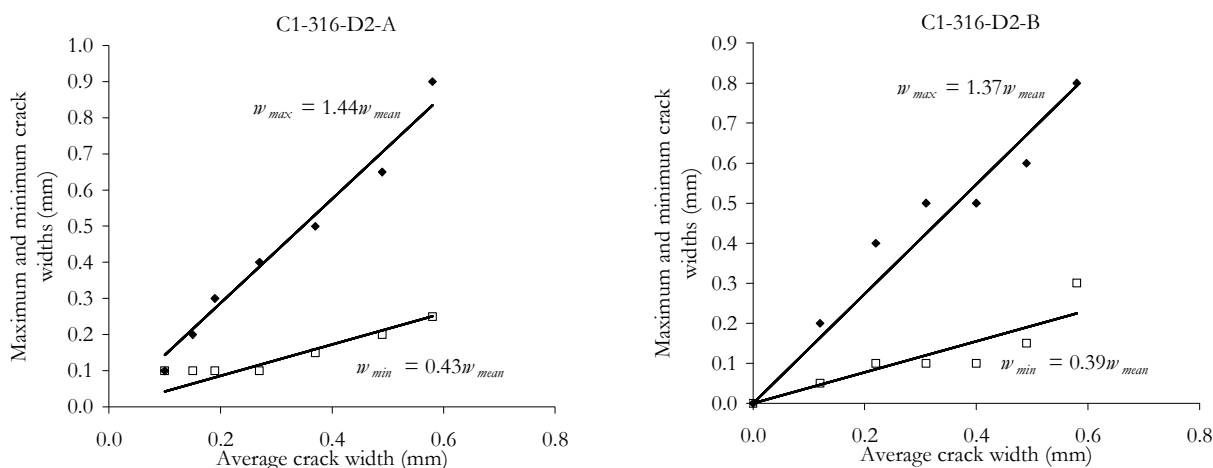
Figure B-97. Experimental crack width: maximum and minimum vs. average.

Figure B-98. Experimental vs theoretical crack width, (left) average (rigth) maximum.

Load = 9.1 kN
Av. Crack width = 0.10 mm

Load = 18.9 kN
Av. Crack width = 0.15 mm

Load = 28.8 kN
Av. Crack width = 0.19 mm

Load = 38.9 kN
Av. Crack width = 0.27 mm

Load = 48.7 kN
Av. Crack width = 0.37 mm

Load = 58.8 kN
Av. Crack width = 0.49 mm

Load = 68.5 kN
Av. Crack width = 0.58 mm

Failure

Figure B-99. Crack pattern (C1-316-D2-A).

Load = 9.5 kN
Av. Crack width = 0.00mm

Load = 19.2 kN
Av. Crack width = 0.12 mm

Load = 29.0 kN
Av. Crack width = 0.22 mm

Load = 39.6 kN
Av. Crack width = 0.31 mm

Load = 49.0 kN
Av. Crack width = 0.40 mm

Load = 58.3 kN
Av. Crack width = 0.49 mm

Load = 68.0 kN
Av. Crack width = 0.58mm

Failure

Figure B-100. Crack pattern (C1-316-D2-B).
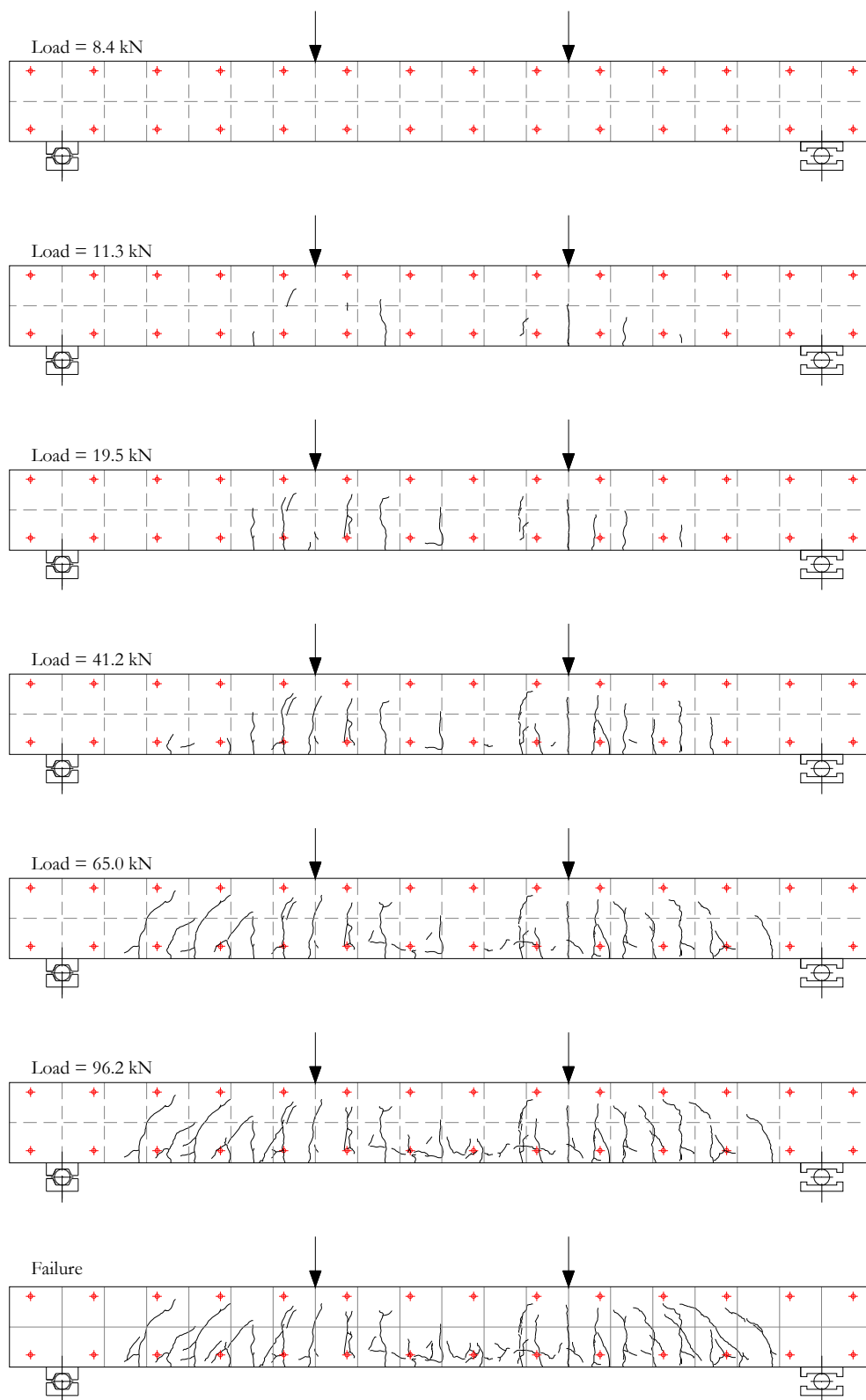
B.7. Results for the C2-212-D1 series

B.7.1. General data

	C2-212-D1-A	C2-212-D1-B
Cracking load (kN)	9.8	9.8
Load at reaching stabilised cracking phase (kN)	8.4	40.6
Average crack spacing at stabilised cracking phase (mm)	130	60
Maximum crack spacing at stabilised cracking phase (mm)	150	99
Minimum crack spacing at stabilised cracking phase (mm)	109	32
Load at which $\sigma_c = 0.45\,f_c$ (kN)	--	25.3
Load at which w_{max}=0.5-0.7mm (kN)	52.1	40.6
Load at which $\delta=L/250$ (kN)	25.4	27.3
Ultimate load (kN)	127.4	118.6
Ultimate midspan deflection (mm)	52.2	47.3
Ultimate concrete strain (x10^{-6})	--	4518

B.7.2. Failure mode

Figure B-101. Crushing of concrete for C2-212-D1-A.

Figure B-102. Crushing of concrete for C2-212-D1-B.

B.7.3. Results at the midspan section

Figure B-103. Concrete strain in the midspan section: Along the height of the beam (left) / Versus the load applied and compared to CSA predictions (right).

Figure B-104. Neutral axis depth compared to CSA predictions.

B.7.4. Results at the pure bending zone

Figure B-105. Experimental moment-curvature from inclinometers, mechanical extensometer and strain gauges on concrete.

Figure B-106. Experimental moment-curvature compared to Eurocode 2 (2004) and CSA predictions.

B.7.5. Results of the overall beam behaviour

Figure B-107. Curvature along the length of the beam deduced form mechanical extensometer's data (dotted lines) compared to inclinometers' data (dashed lines).

B.7.6. Results on deflection

Figure B-108. Experimental midspan deflection.

Figure B-109. Experimental midspan deflection (ultimate load) compared to cracked section analysis (left) / design codes (right).

Figure B-110. Experimental vs theoretical midspan deflection (service load).

B.7.7. Results on cracking
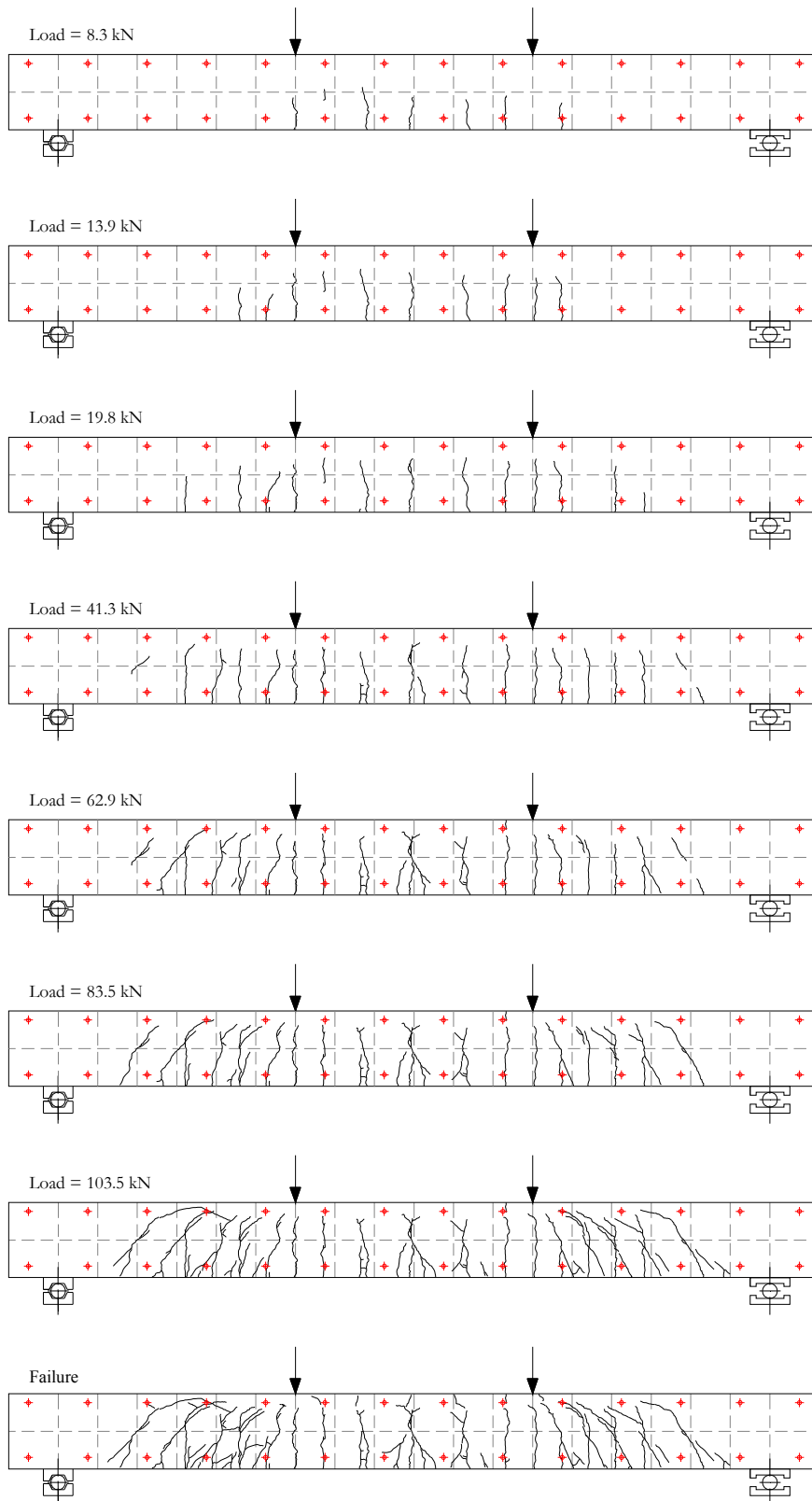
Figure B-111. Crack pattern (C2-212-D1-A).
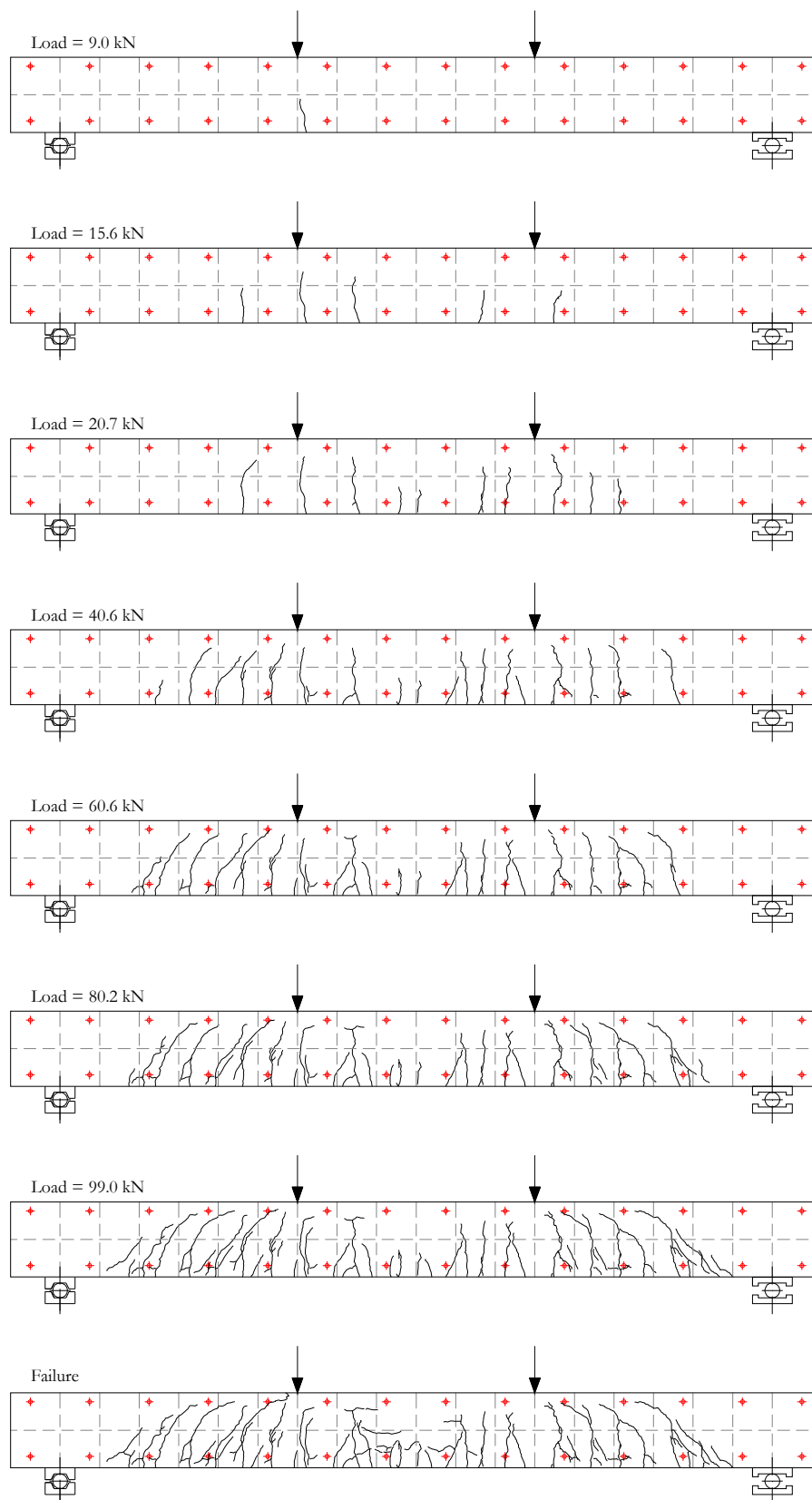
Figure B-112. Crack pattern (C2-212-D1-B).

B.8.   Results for the C2-212-D2 series

B.8.1.   General data

	C2-212-D2-A	C2-212-D2-B
Cracking load (kN)	9.9	9.3
Load at reaching stabilised cracking phase (kN)	32.8	30.2
Average crack spacing at stabilised cracking phase (mm)	81	71
Maximum crack spacing at stabilised cracking phase (mm)	127	134
Minimum crack spacing at stabilised cracking phase (mm)	64	27
Load at which $\sigma_c = 0.45\, f_c$ (kN)	--	17.2
Load at which $w_{max} = 0.5\text{-}0.7$mm (kN)	20.5	30.2
Load at which $\delta = L/250$ (kN)	24.1	23.4
Ultimate load (kN)	92.3	85.1
Ultimate midspan deflection (mm)	47.8	46.3
Ultimate concrete strain (x10^{-6})	--	4646

B.8.2.   Failure mode
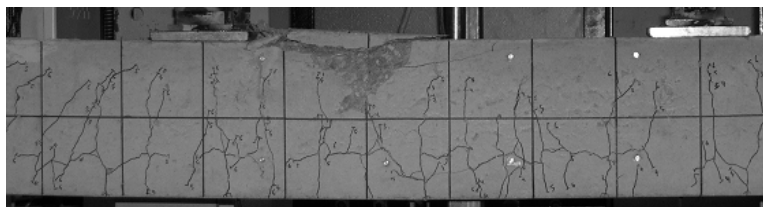
Figure B-113. Crushing of concrete for C2-212-D2-A.

Figure B-114. Crushing of concrete for C2-212-D2-B.

B.8.3. Results at the midspan section

Figure B-115. Concrete strain in the midspan section: Along the height of the beam (left) / Versus the load applied and compared to CSA predictions (right).

Figure B-116. Neutral axis depth compared to CSA predictions.
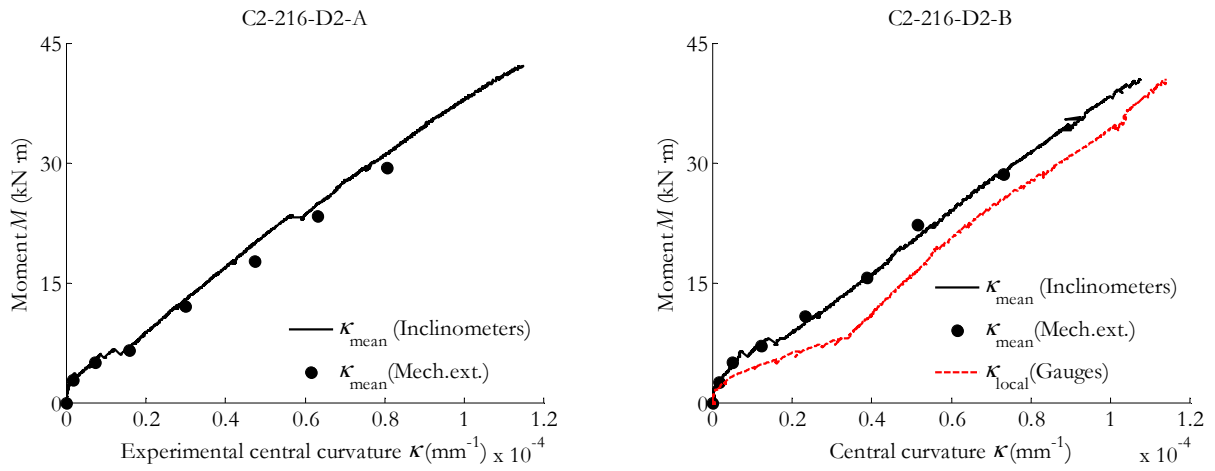
B.8.4. Results at the pure bending zone

Figure B-117. Experimental moment-curvature from inclinometers, mechanical extensometer and strain gauges on concrete.
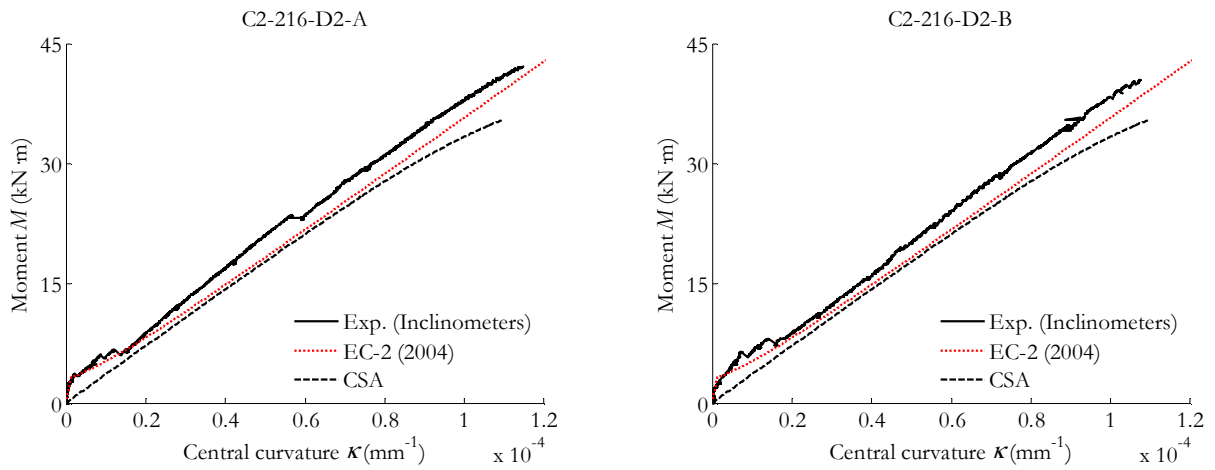

Figure B-118. Experimental moment-curvature compared to Eurocode 2 (2004) and CSA predictions.

B.8.5. Results of the overall beam behaviour

Figure B-119. Curvature along the length of the beam deduced form mechanical extensometer's data (dotted lines) compared to inclinometers' data (dashed lines).

B.8.6. Results on deflection

Figure B-120. Experimental midspan deflection.

C2-212-D2 　　　　　　　　　　　　　　　　　　　C2-212-D2
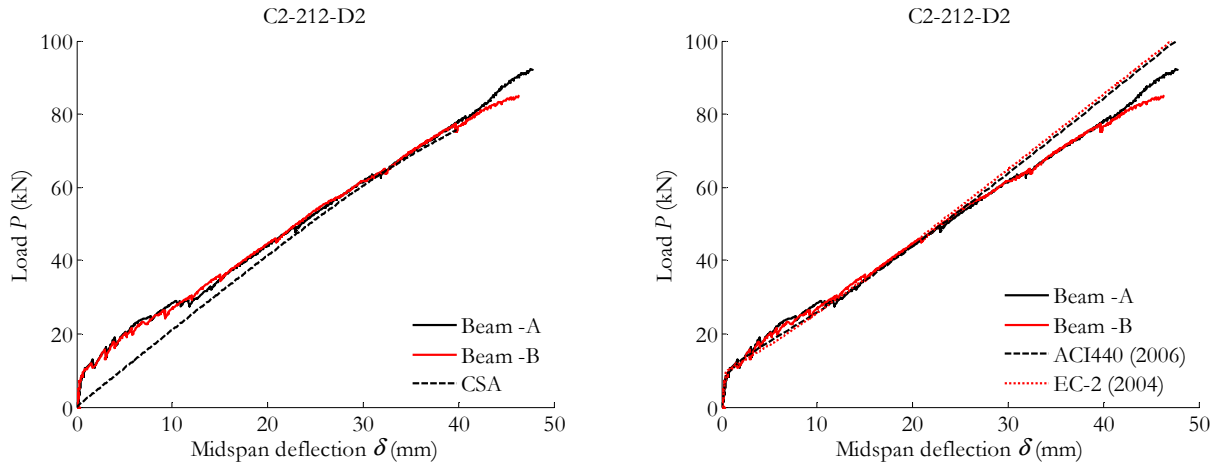
Figure B-121. Experimental midspan deflection (ultimate load) compared to cracked section analysis (left) / design codes (right).
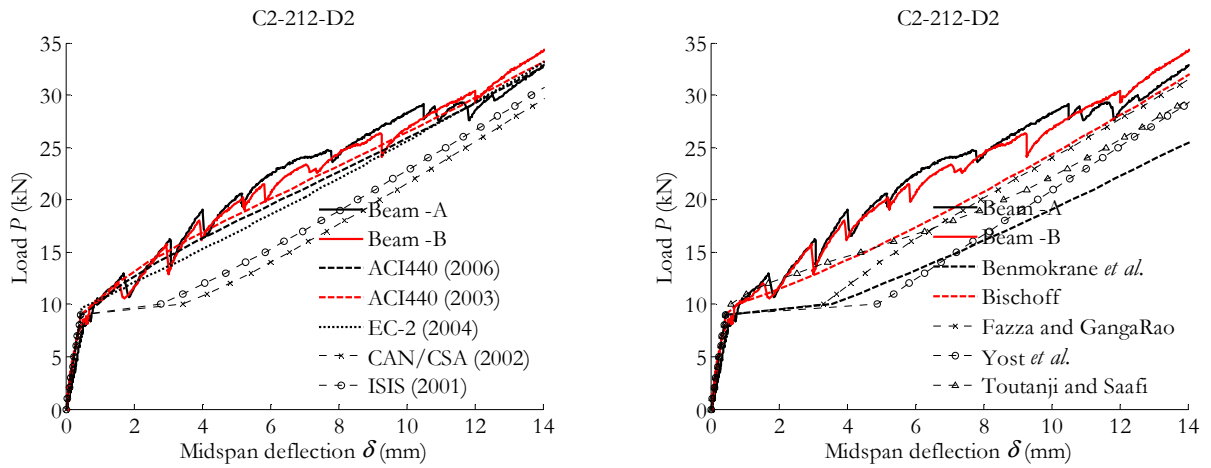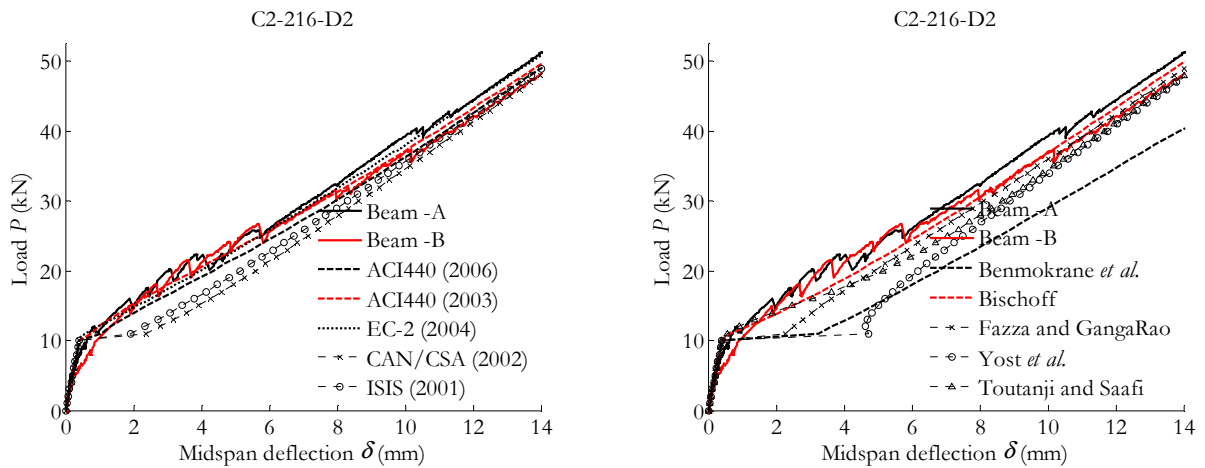
C2-212-D2 　　　　　　　　　　　　　　　　　　　C2-212-D2

Figure B-122. Experimental vs theoretical midspan deflection (service load).

B.8.7. Results on cracking
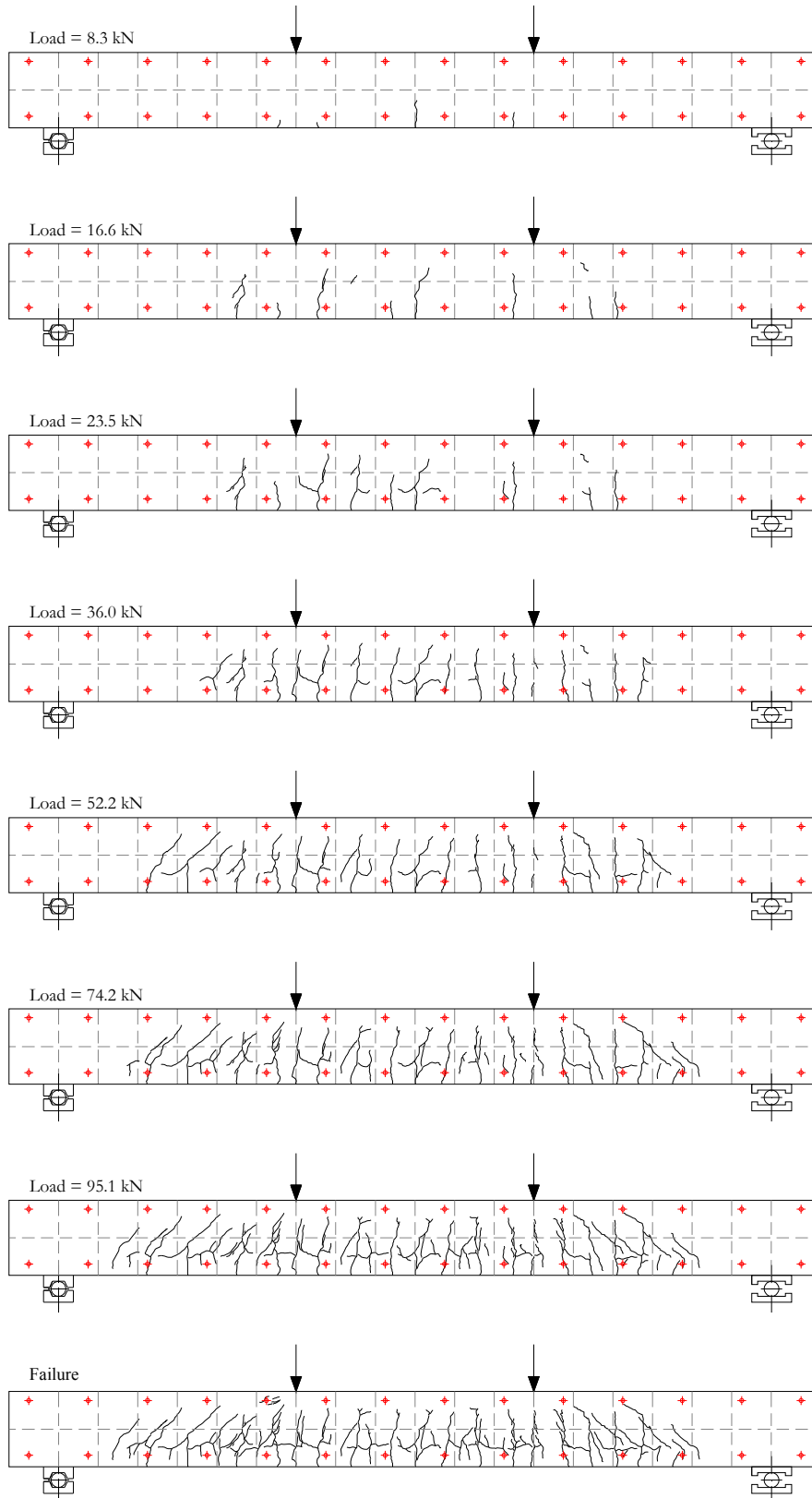

Figure B-123. Crack pattern (C2-212-D2-A).

Load = 8.8 kN

Load = 13.3 kN

Load = 20.1 kN

Load = 30.2 kN

Load = 45.9 kN

Load = 64.2 kN

Failure

Figure B-124. Crack pattern (C2-212-D2-B).

B.9. Results for the C2-216-D1 series

B.9.1. General data

	C2-216-D1-A	C2-216-D1-B
Cracking load (kN)	9.0	9.5
Load at reaching stabilised cracking phase (kN)	24.2	11.3
Average crack spacing at stabilised cracking phase (mm)	120	162
Maximum crack spacing at stabilised cracking phase (mm)	172	191
Minimum crack spacing at stabilised cracking phase (mm)	91	133
Load at which $\sigma_c = 0.45 f_c$ (kN)	--	41.0
Load at which w_{max}=0.5-0.7mm (kN)	83.1	65.1
Load at which $\delta=L/250$ (kN)	34.6	33.2
Ultimate load (kN)	150.2	143.4
Ultimate midspan deflection (mm)	40.5	40.3
Ultimate concrete strain (x10^{-6})	--	4725

B.9.2. Failure mode
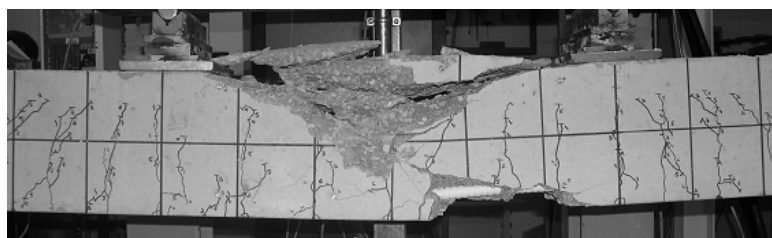
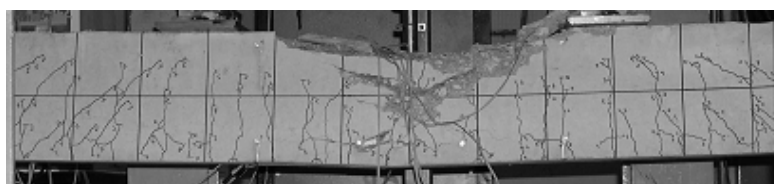Figure B-125. Crushing of concrete for C2-216-D1-A.

Figure B-126. Crushing of concrete for C2-216-D1-B.
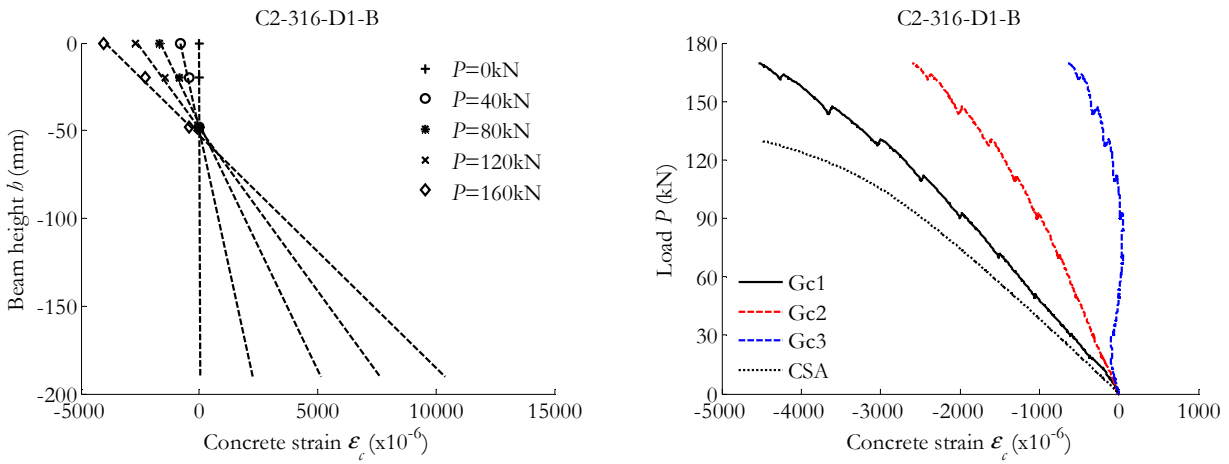
B.9.3. Results at the midspan section

Figure B-127. Concrete strain in the midspan section: Along the height of the beam (left) / Versus the load applied and compared to CSA predictions (right).
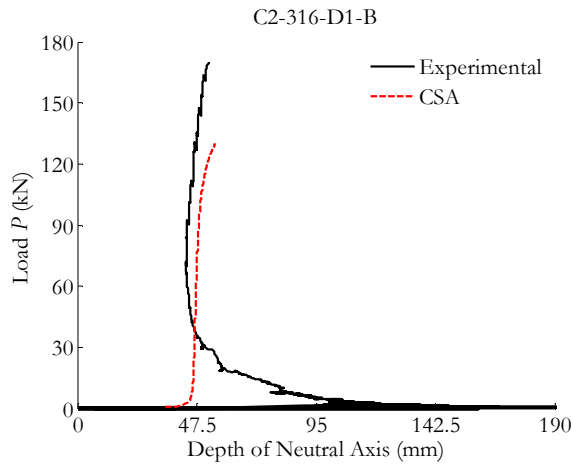

Figure B-128. Neutral axis depth compared to CSA predictions.
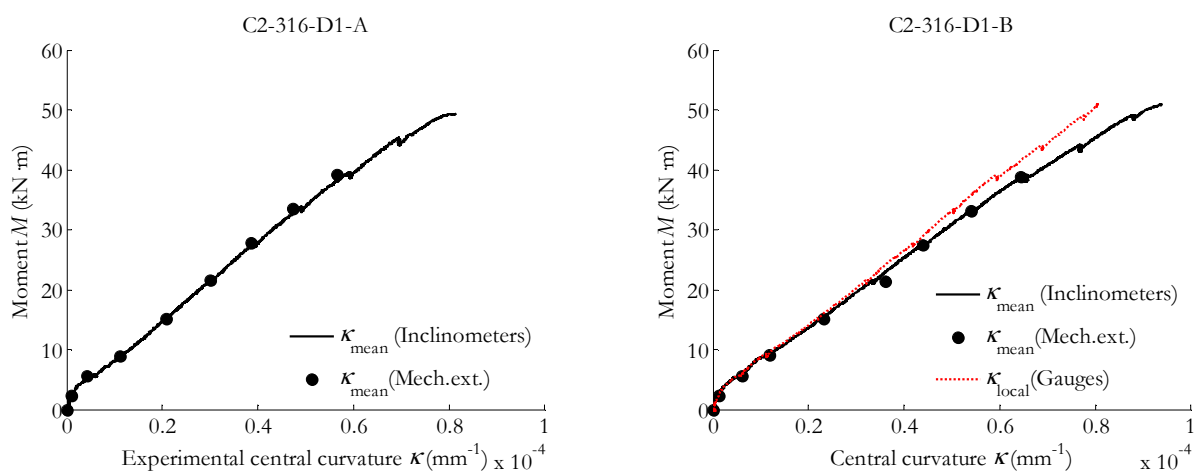
B.9.4. Results at the pure bending zone

Figure B-129. Experimental moment-curvature from inclinometers, mechanical extensometer and strain gauges on concrete.
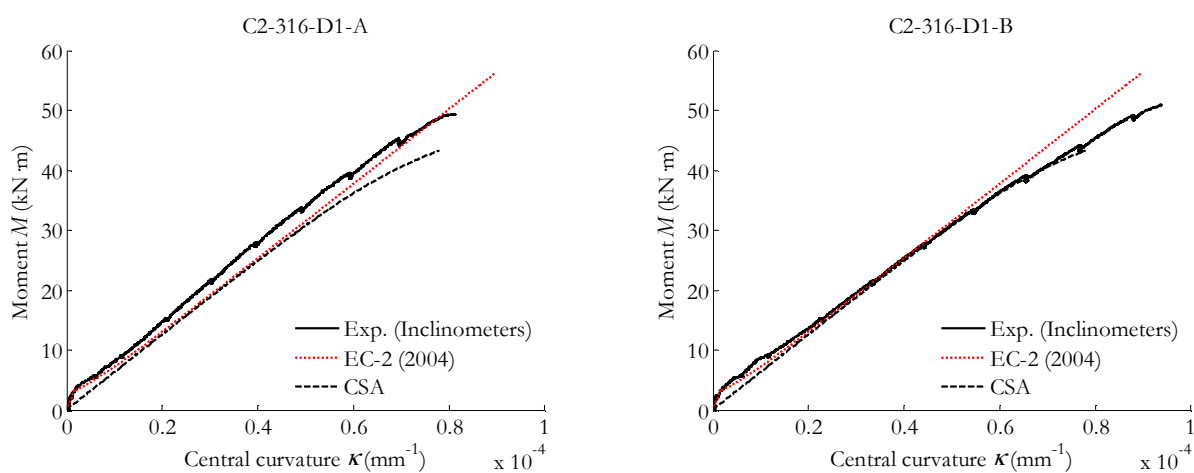

Figure B-130. Experimental moment-curvature compared to Eurocode 2 (2004) and CSA predictions.

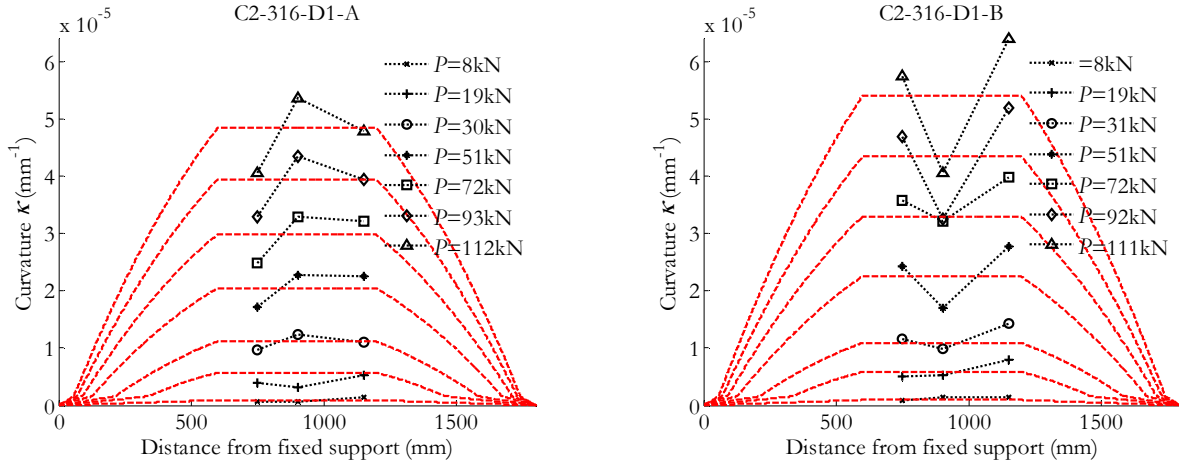## B.9.5. Results of the overall beam behaviour

Figure B-131. Curvature along the length of the beam deduced form mechanical
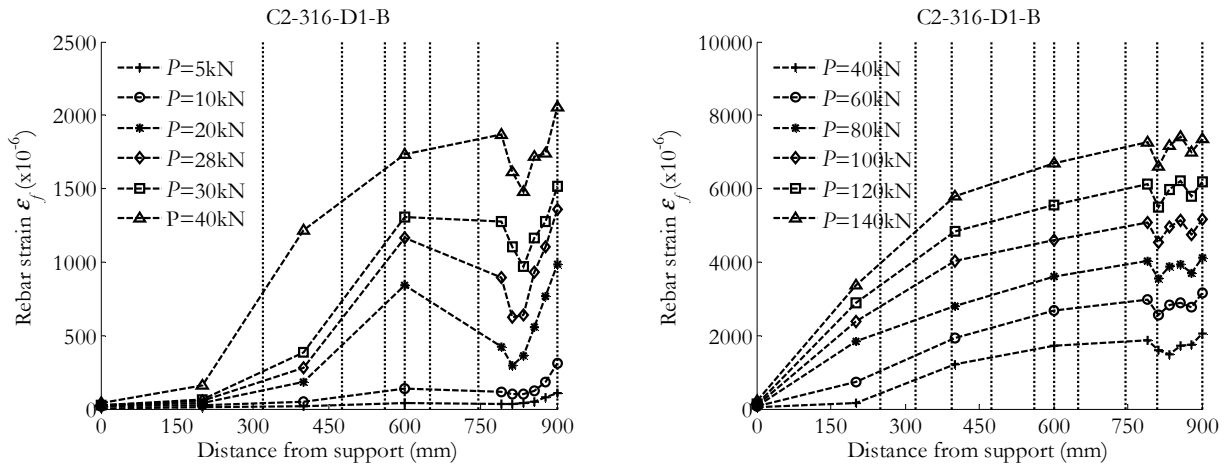extensometer's data (dotted lines) compared to inclinometers' data (dashed lines).
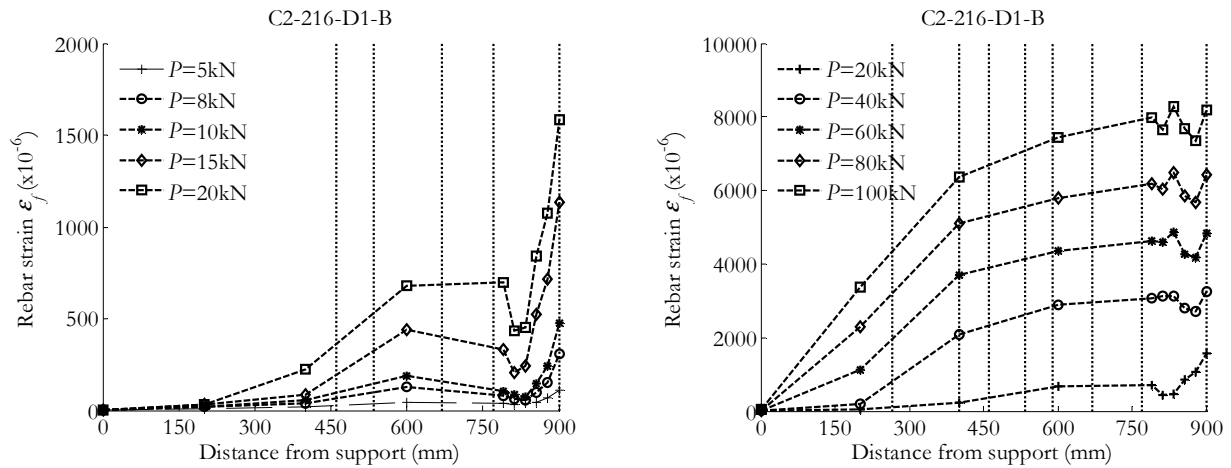
Figure B-132. Evolution of the rebar strain along the length of the beam (left) until service
load (right) until failure.

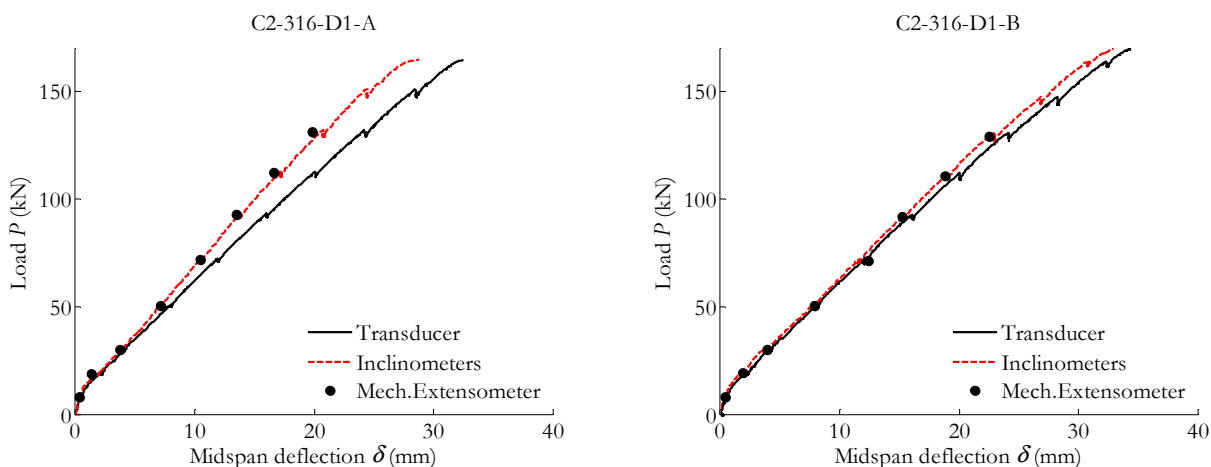### B.9.6. Results on deflection
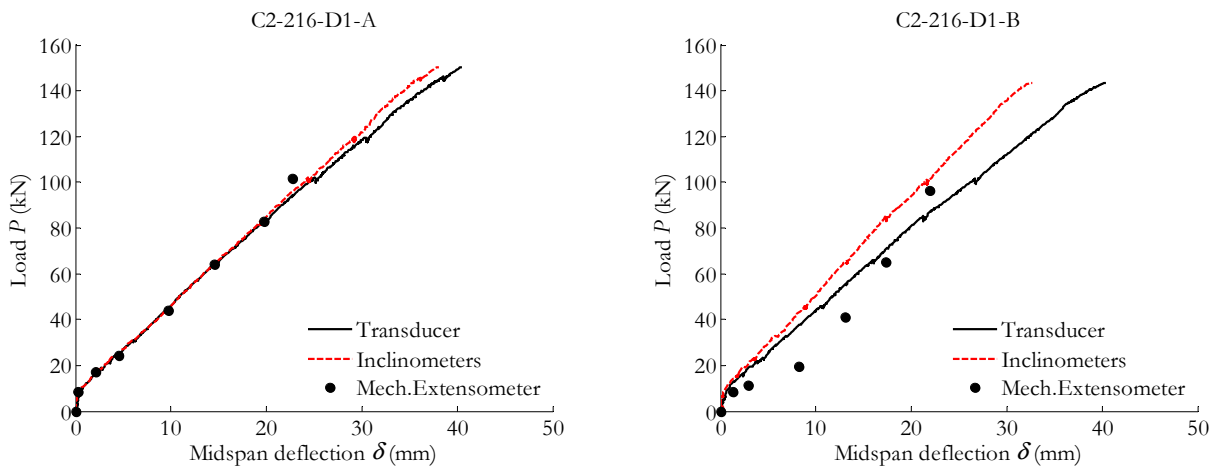
Figure B-133. Experimental midspan deflection.
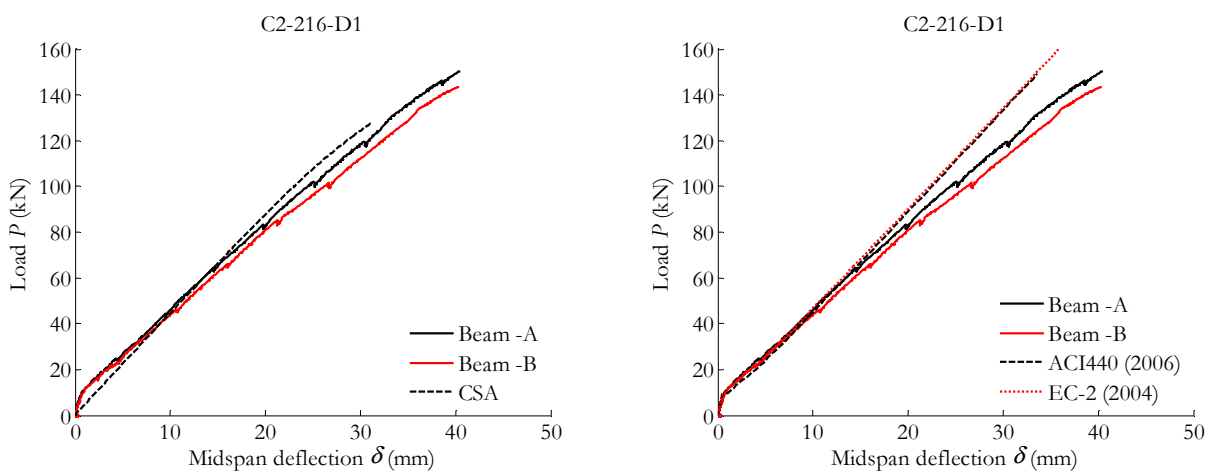
Figure B-134. Experimental midspan deflection (ultimate load) compared to cracked section analysis (left) / design codes (right).
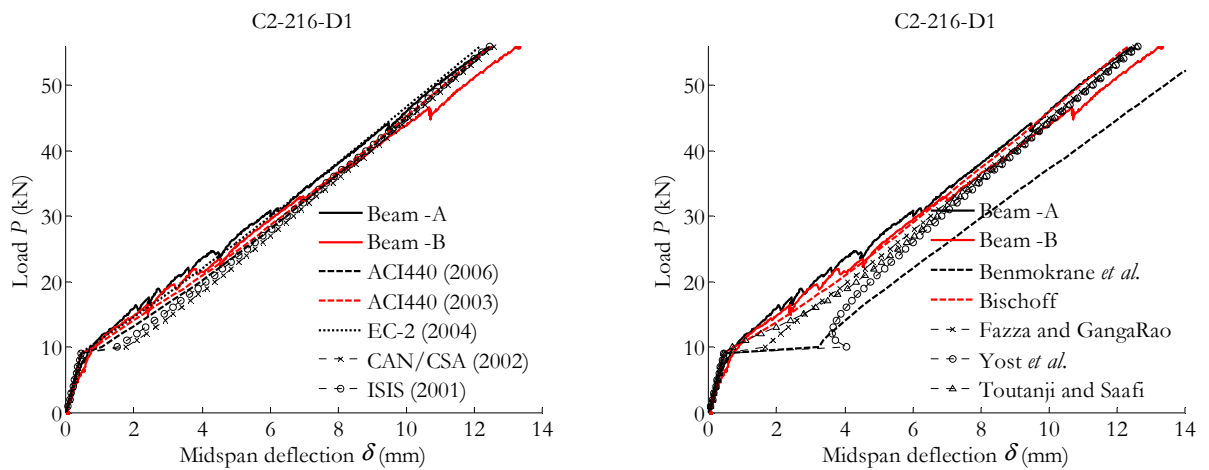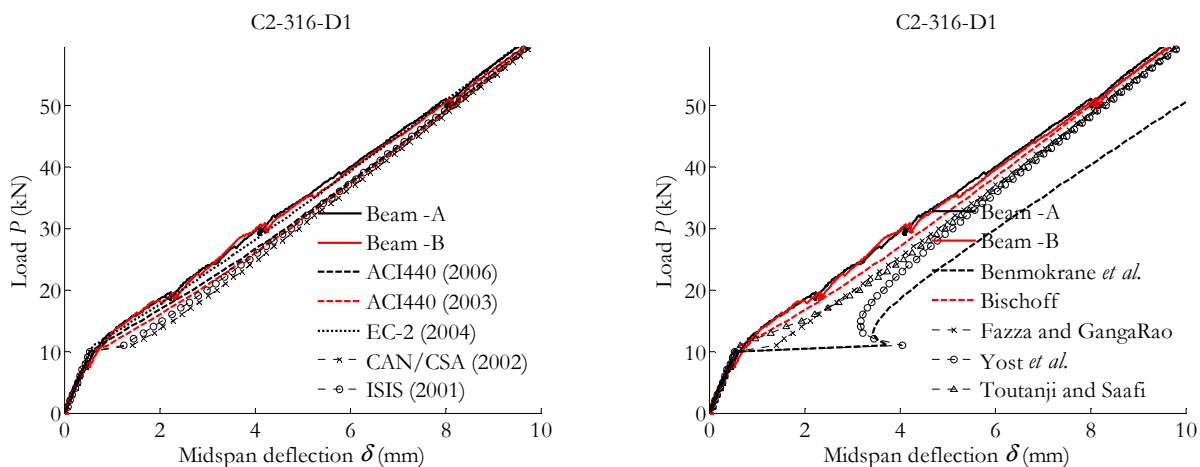

Figure B-135. Experimental vs theoretical midspan deflection (service load).

B.9.7. Results on cracking

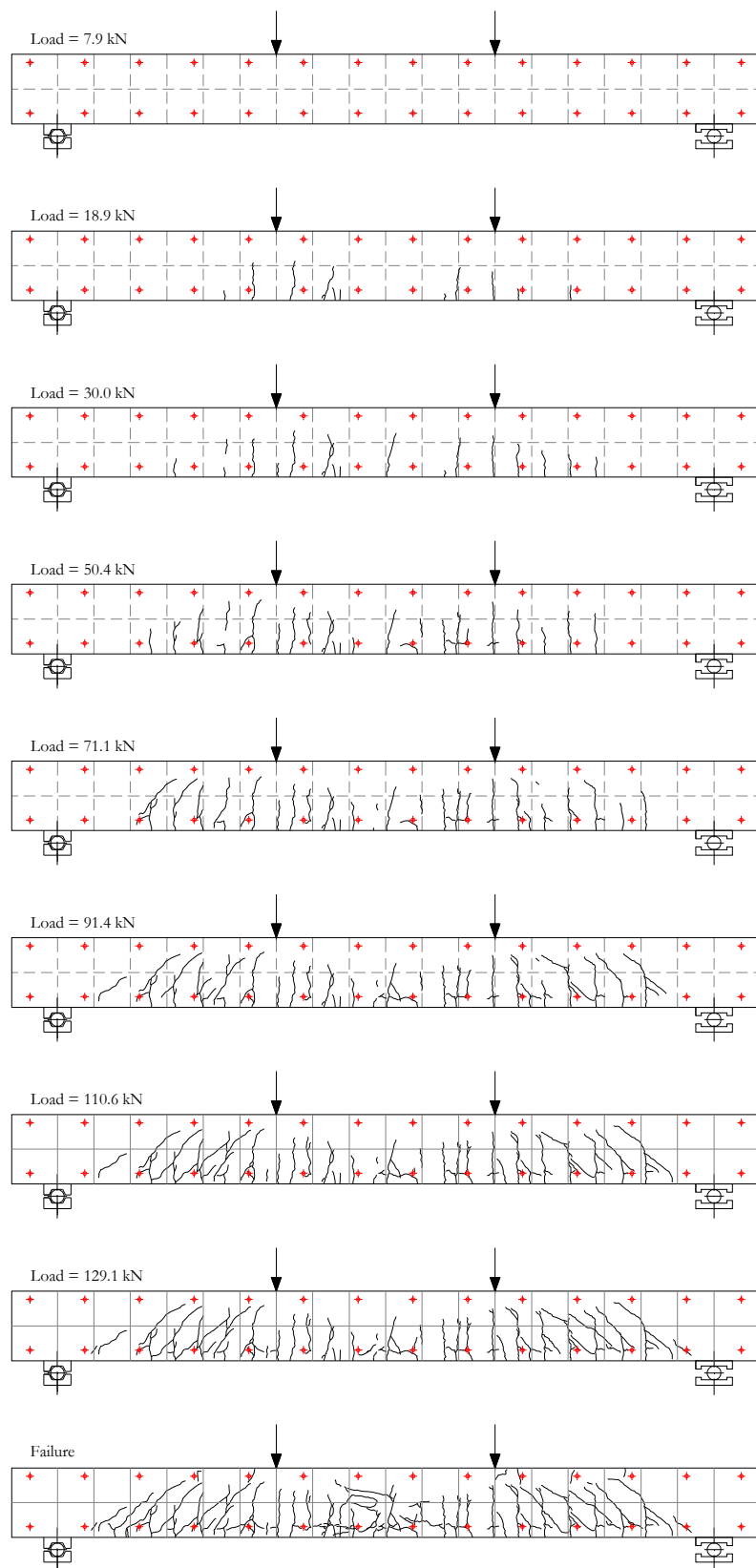Figure B-136. Crack pattern (C2-216-D1-A).

Load = 8.4 kN

Load = 11.3 kN

Load = 19.5 kN

Load = 41.2 kN

Load = 65.0 kN

Load = 96.2 kN

Failure

Figure B-137. Crack pattern (C2-216-D1-B).

B.10. Results for the C2-216-D2 series

B.10.1. General data

	C2-216-D2-A	C2-216-D2-B
Cracking load (kN)	10.6	10.6
Load at reaching stabilised cracking phase (kN)	40.0	36.0
Average crack spacing at stabilised cracking phase (mm)	88	81
Maximum crack spacing at stabilised cracking phase (mm)	148	105
Minimum crack spacing at stabilised cracking phase (mm)	47	59
Load at which $\sigma_c = 0.45\, f_c$ (kN)	--	32.4
Load at which w_{max}=0.5-0.7mm (kN)	40.0	36.0
Load at which $\delta=L/250$ (kN)	30.0	29.2
Ultimate load (kN)	140.5	134.9
Ultimate midspan deflection (mm)	45.4	42.3
Ultimate concrete strain (x10^{-6})	--	4288

B.10.2. Failure mode
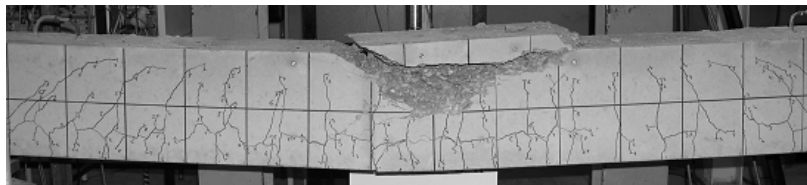
Figure B-138. Crushing of concrete for C2-216-D2-A.
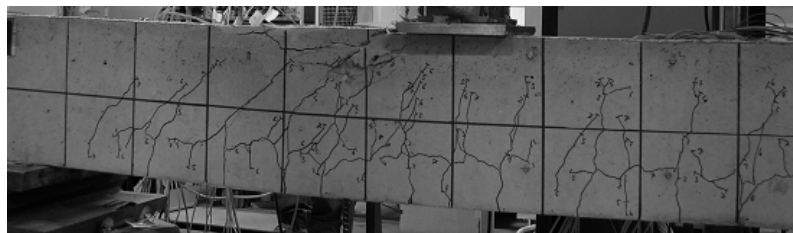
Figure B-139. Crushing of concrete for C2-216-D2-B.(*)

(*): The failure of concrete was attained at the shearspan close to the point load

B.10.3. Results at the midspan section
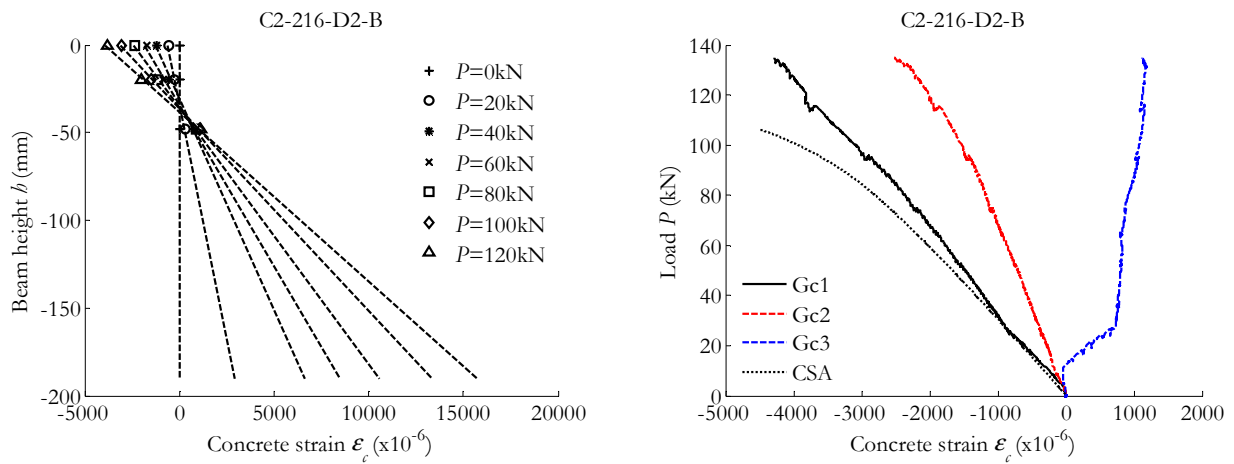
Figure B-140. Concrete strain in the midspan section: Along the height of the beam (left) / Versus the load applied and compared to CSA predictions (right).
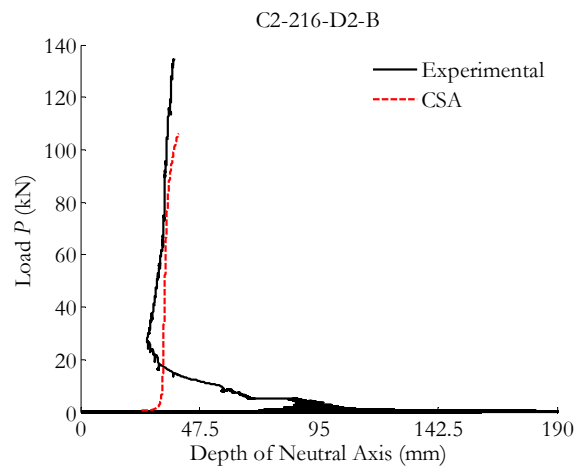
Figure B-141. Neutral axis depth compared to CSA predictions.

B.10.4. Results at the pure bending zone

Figure B-142. Experimental moment-curvature from inclinometers, mechanical extensometer and strain gauges on concrete.

Figure B-143. Experimental moment-curvature from inclinometers compared to Eurocode 2 (2004) and CSA prediction.

B.10.5. Results of the overall beam behaviour
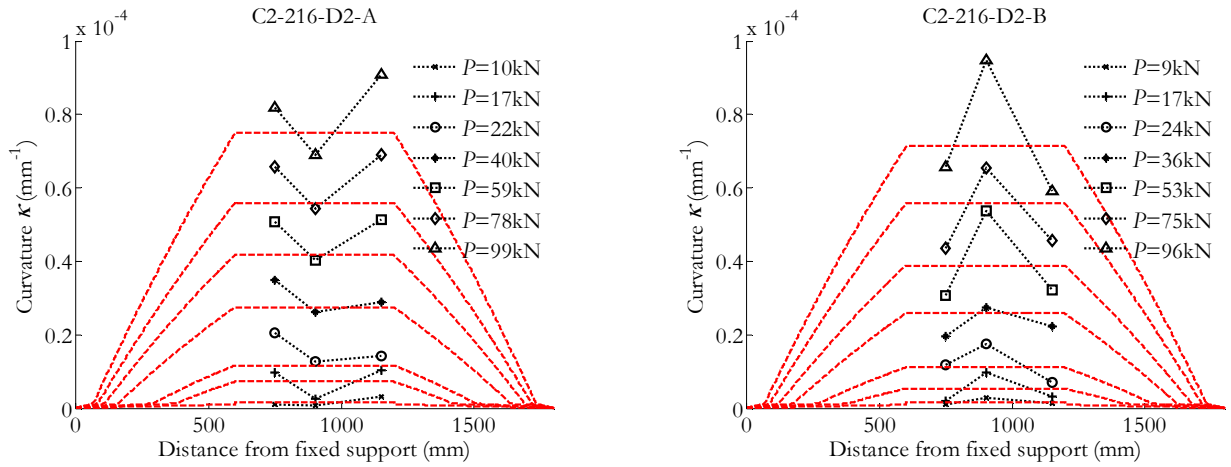
Figure B-144. Curvature along the length of the beam deduced form mechanical extensometer's data (dotted lines) compared to inclinometers' data (dashed lines).
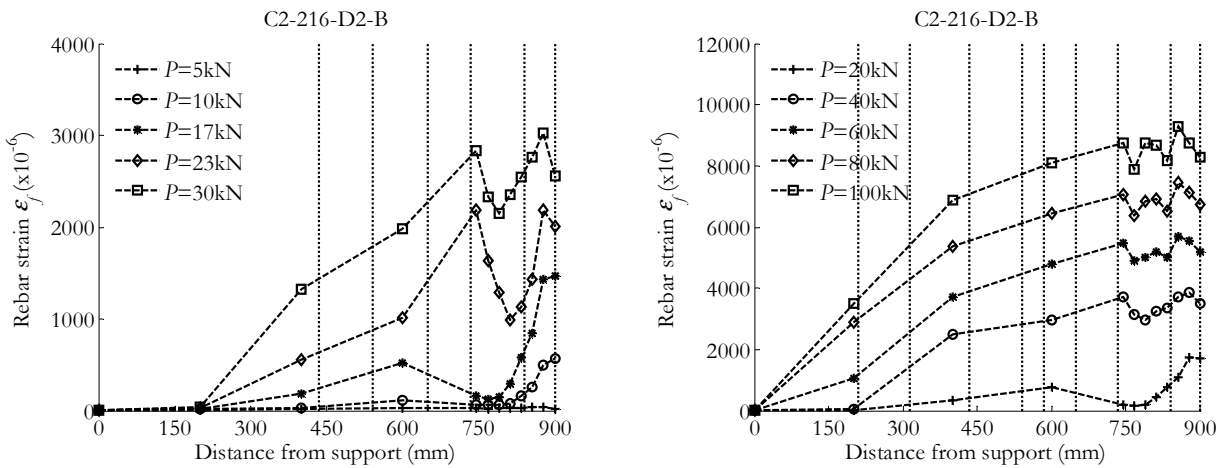
Figure B-145. Evolution of the rebar strain along the length of the beam (left) until service load (right) until failure.

B.10.6. Results on deflection
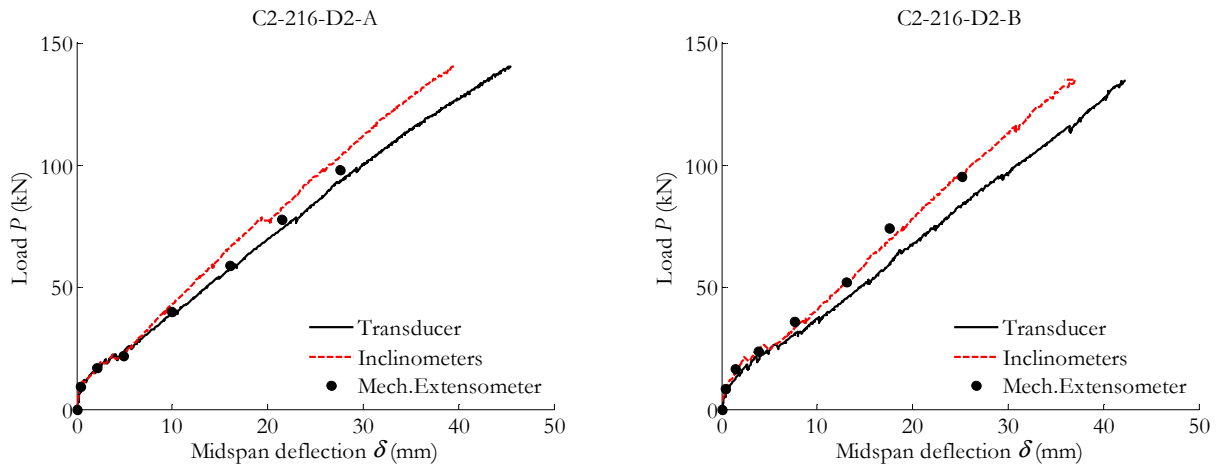
Figure B-146. Experimental midspan deflection.
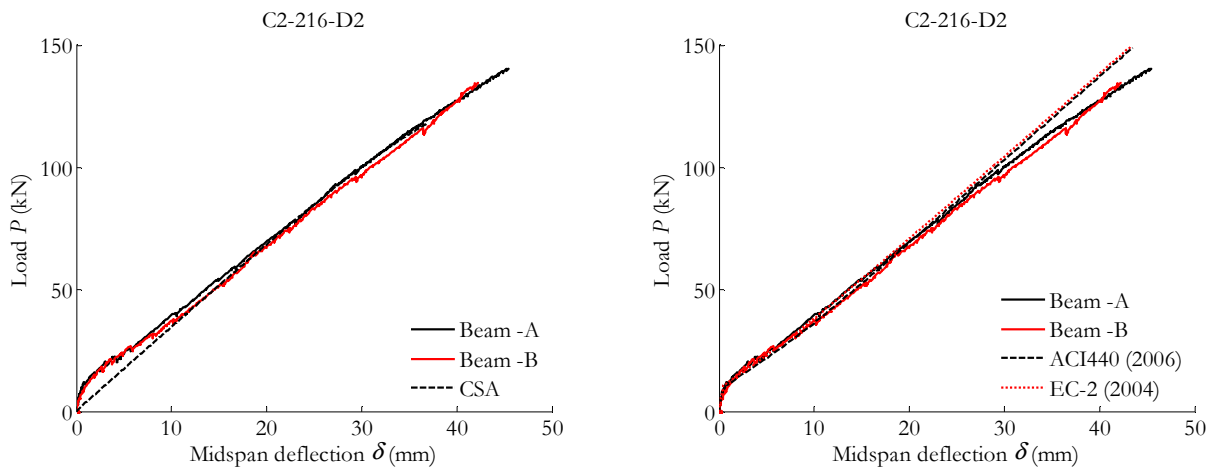
Figure B-147. Experimental midspan deflection (ultimate load) compared to cracked section analysis (left) / design codes (right).

Figure B-148. Experimental vs theoretical midspan deflection (service load).

B.10.7. Results on cracking
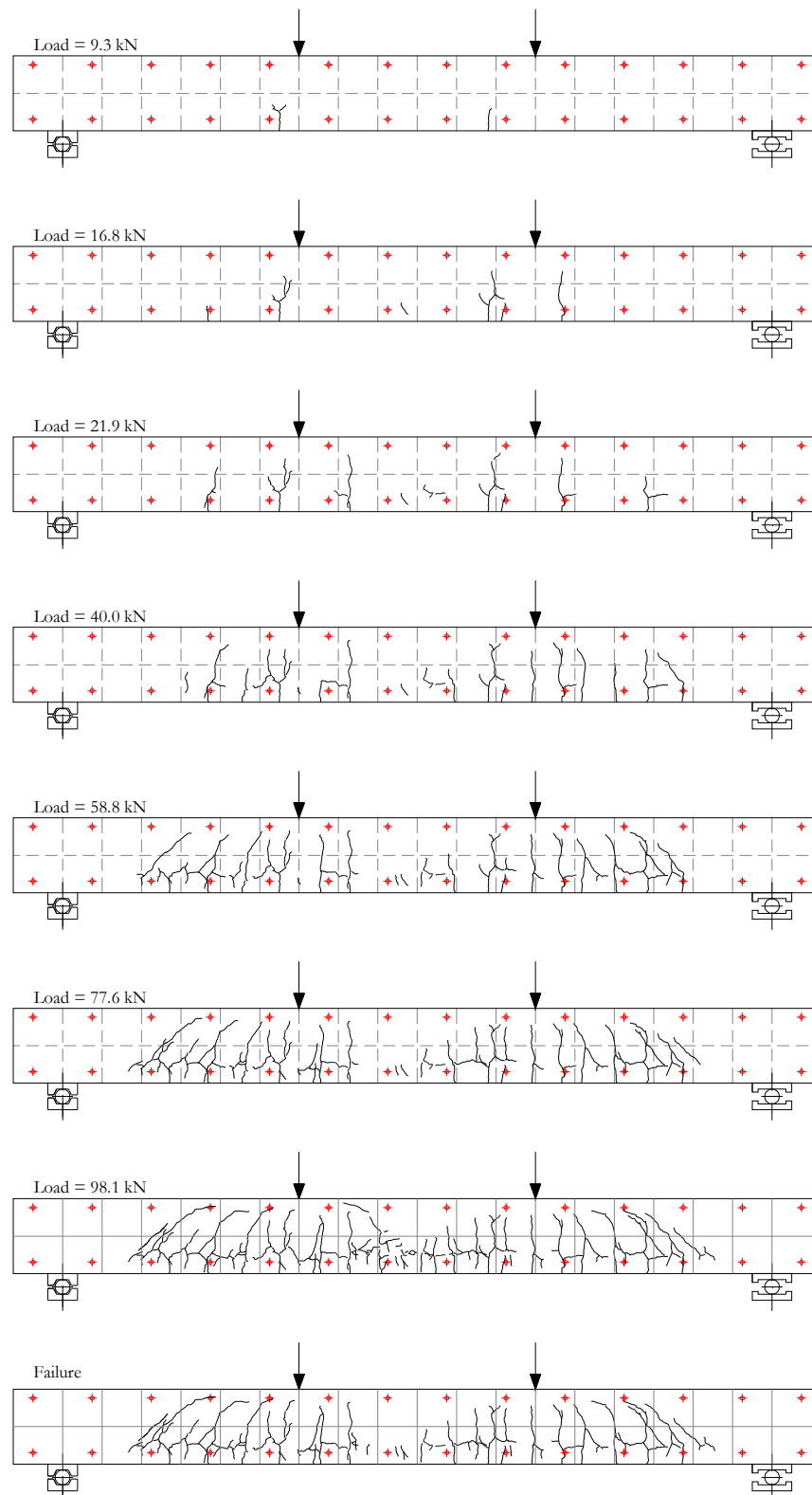
Figure B-149. Crack pattern (C2-216-D2-A).

Figure B-150. Crack pattern (C2-216-D2-B).

B.11. Results for the C2-316-D1 series

B.11.1. General data

	C2-316-D1-A	C2-316-D1-B
Cracking load (kN)	10.9	10.6
Load at reaching stabilised cracking phase (kN)	50.5	50.4
Average crack spacing at stabilised cracking phase (mm)	74	85
Maximum crack spacing at stabilised cracking phase (mm)	102	125
Minimum crack spacing at stabilised cracking phase (mm)	46	45
Load at which $\sigma_c = 0.45\,f_c$ (kN)	--	47.9
Load at which w_{max}=0.5-0.7mm (kN)	111.9	110.7
Load at which δ=L/250 (kN)	46.6	45.8
Ultimate load (kN)	164.6	169.8
Ultimate midspan deflection (mm)	34.4	32.5
Ultimate concrete strain (x10^{-6})	--	4534

B.11.2. Failure mode

Figure B-151. Crushing of concrete for C2-316-D1-A.

Figure B-152. Crushing of concrete for C2-316-D1-B.

B.11.3. Results at the midspan section

Figure B-153. Concrete strain in the midspan section: Along the height of the beam (left) / Versus the load applied and compared to CSA predictions (right).

Figure B-154. Neutral axis depth compared to CSA predictions.

B.11.4. Results at the pure bending zone

Figure B-155. Experimental moment-curvature from inclinometers, mechanical extensometer and strain gauges on concrete.
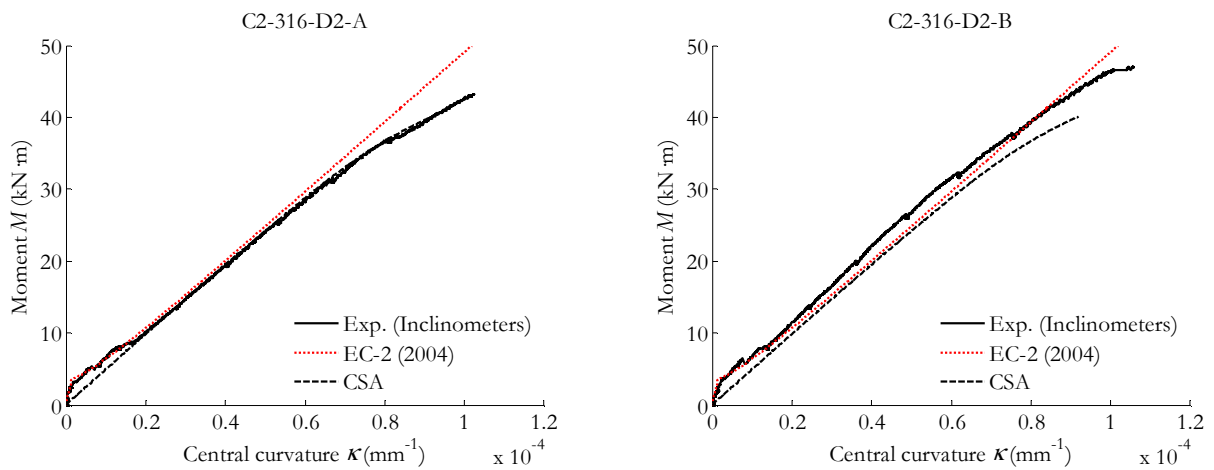

Figure B-156. Experimental moment-curvature compared to Eurocode 2 (2004) and CSA predictions.

B.11.5. Results of the overall beam behaviour

Figure B-157. Curvature along the length of the beam deduced form mechanical extensometer's data (dotted lines) compared to inclinometers' data (dashed lines).

Figure B-158. Evolution of the rebar strain along the length of the beam (left) until service load (right) until failure.

B.11.6. Results on deflection

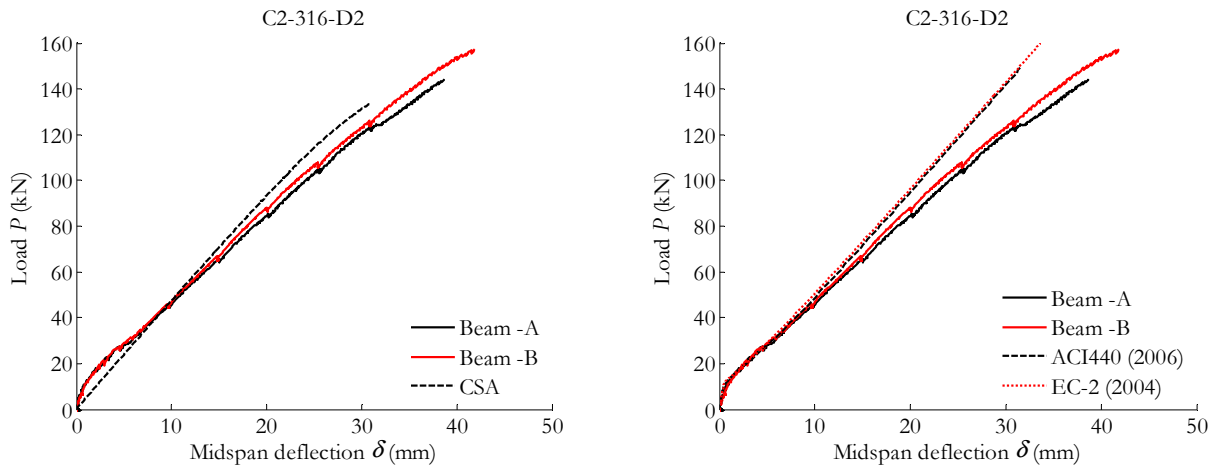Figure B-159. Experimental midspan deflection.
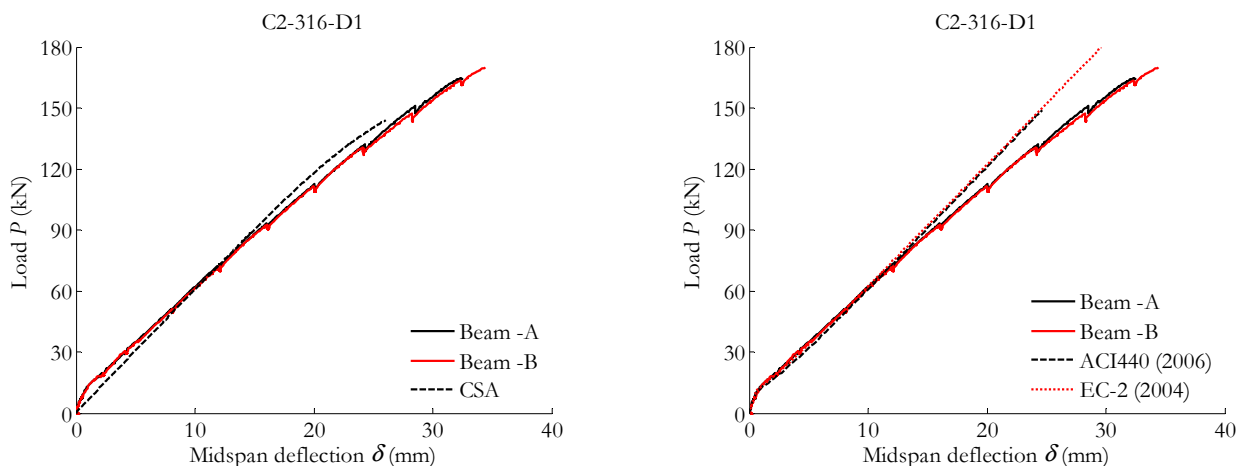
Figure B-160. Experimental midspan deflection (ultimate load) compared to cracked section analysis (left) / design codes (right).
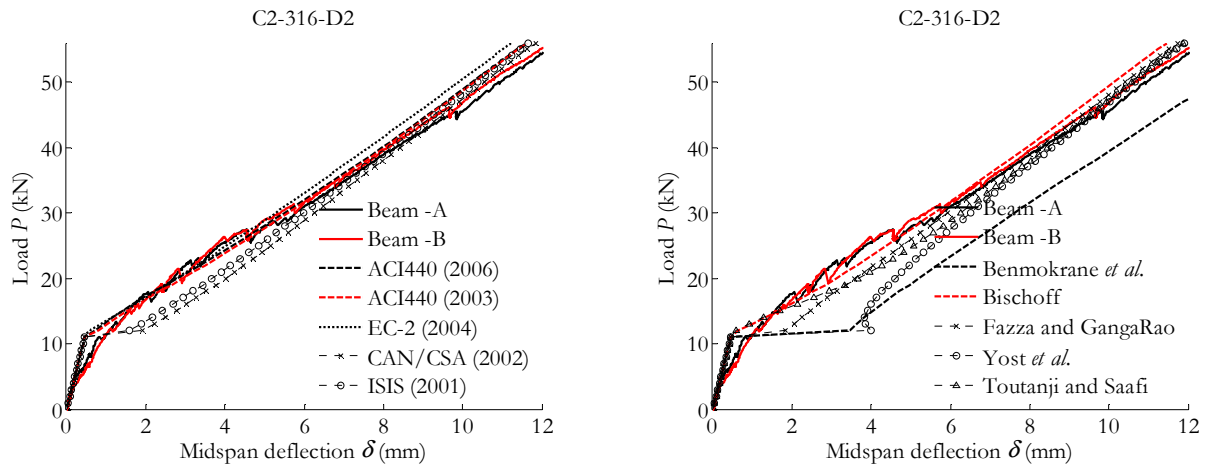

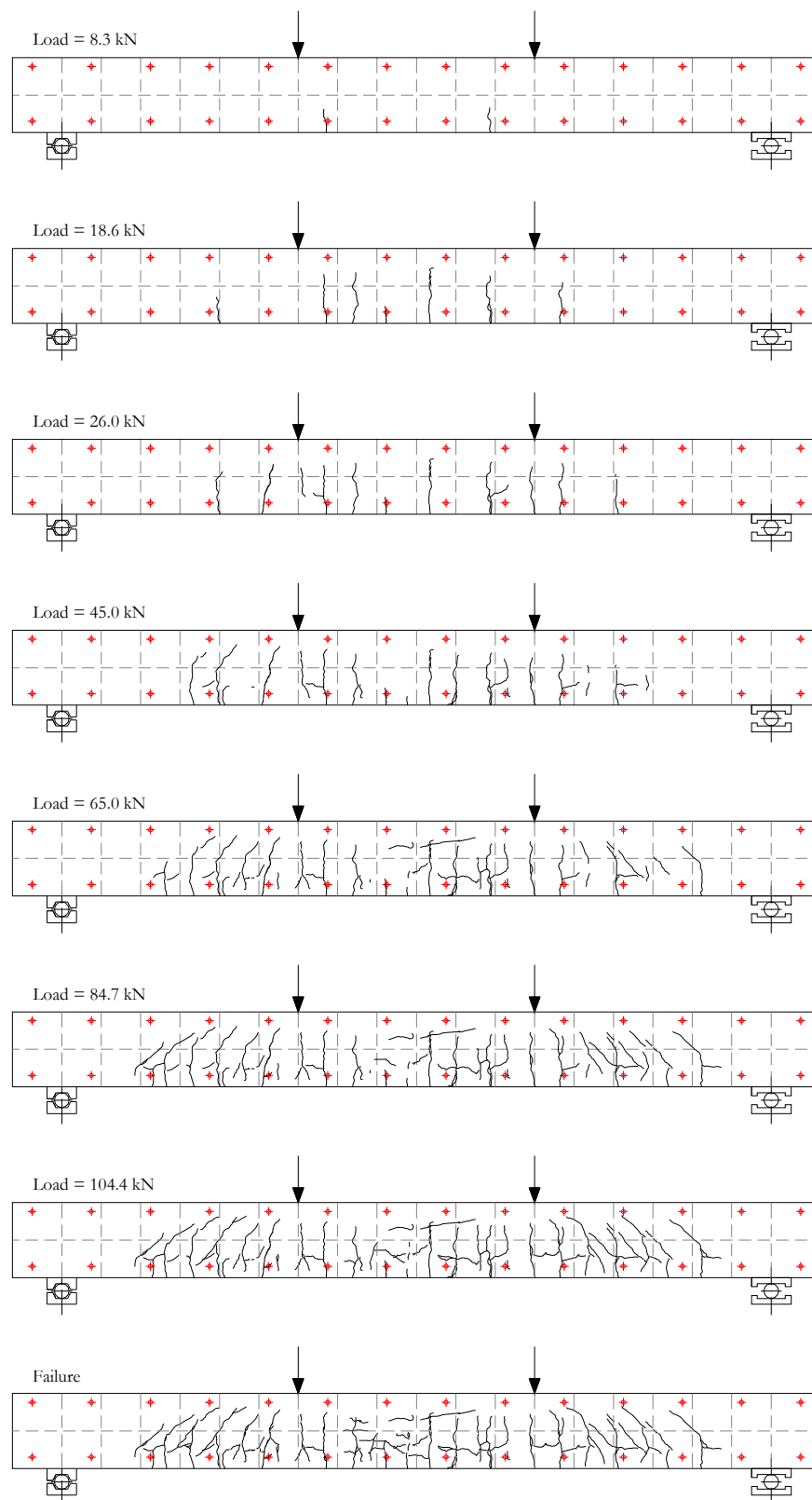Figure B-161. Experimental vs theoretical midspan deflection (service load).

B.11.7. Results on cracking
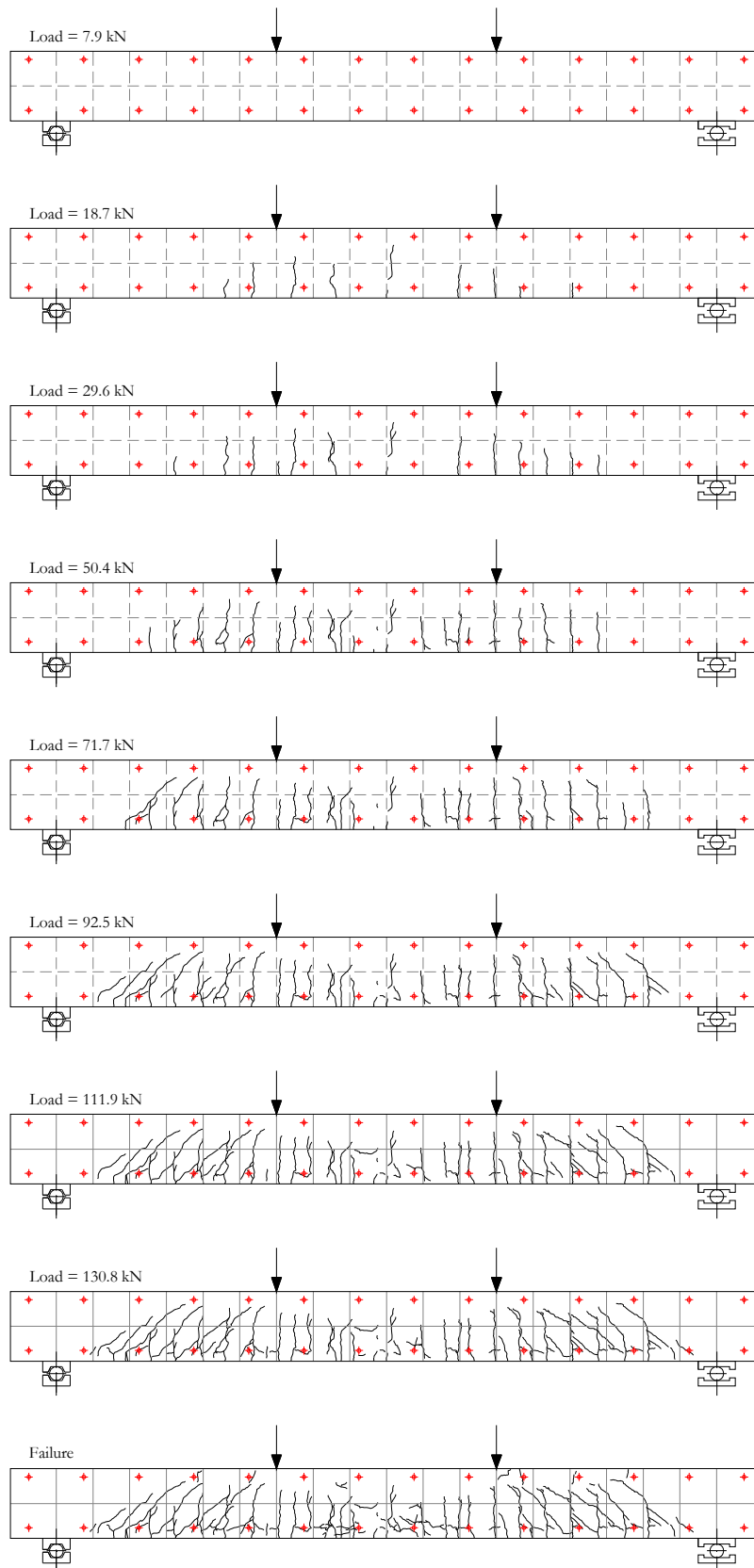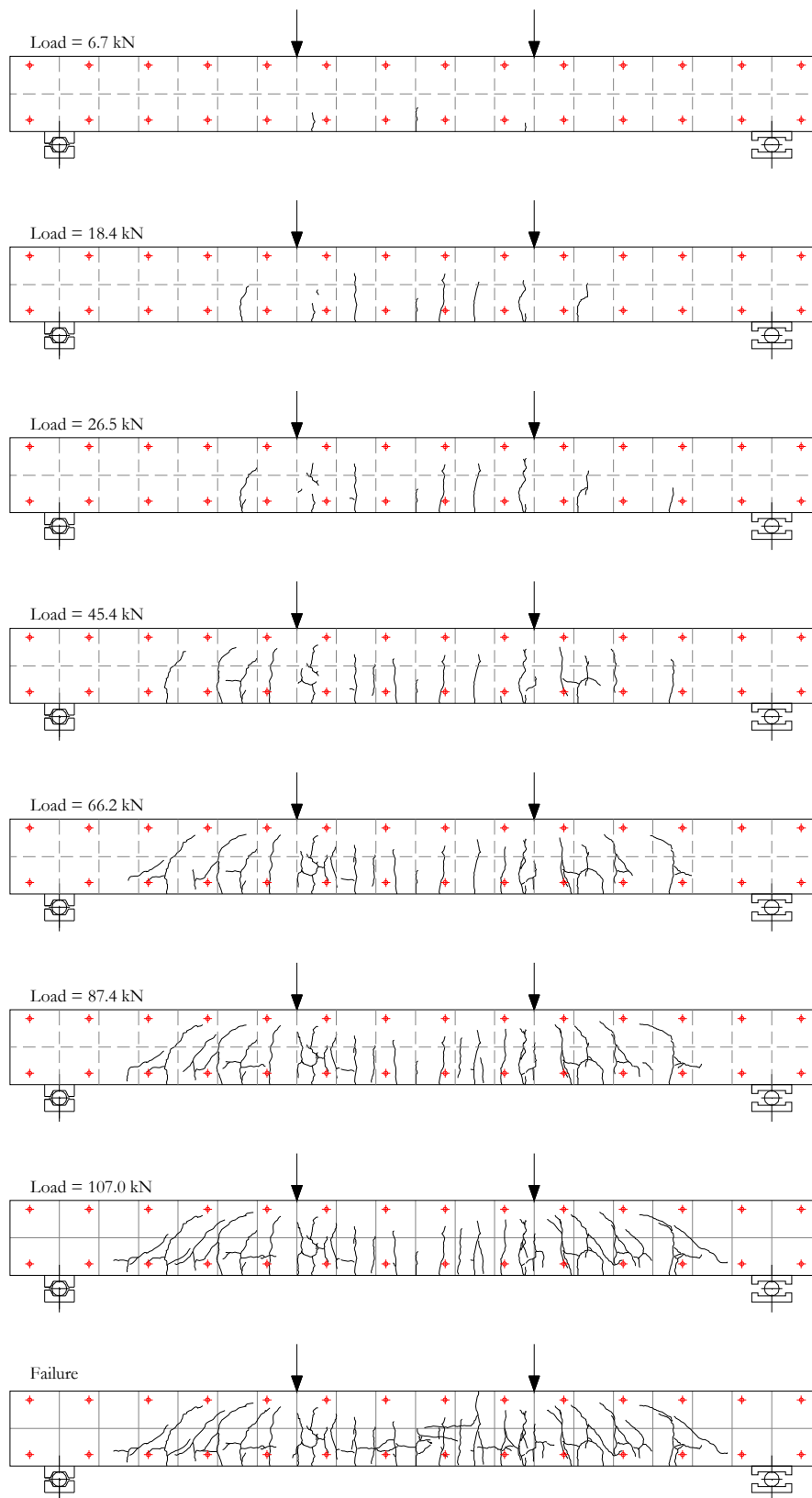

Figure B-162. Crack pattern (C2-316-D1-A).

Figure B-163. Crack pattern (C2-316-D1-B).

B.12. Results for the C2-316-D2 series

B.12.1. General data

|	C2-316-D2-A	C2-316-D2-B
Cracking load (kN)	11.1	11.7
Load at reaching stabilised cracking phase (kN)	45.0	45.5
Average crack spacing at stabilised cracking phase (mm)	70	75
Maximum crack spacing at stabilised cracking phase (mm)	95	102
Minimum crack spacing at stabilised cracking phase (mm)	57	48
Load at which $\sigma_c = 0.45\, f_c$ (kN)	--	38.5
Load at which w_{max}=0.5-0.7mm (kN)	45.0	66.2
Load at which δ=L/250 (kN)	35.6	36.1
Ultimate load (kN)	144.0	157.2
Ultimate midspan deflection (mm)	38.6	41.8
Ultimate concrete strain (x10^{-6})	--	5564

### B.12.2. Failure mode
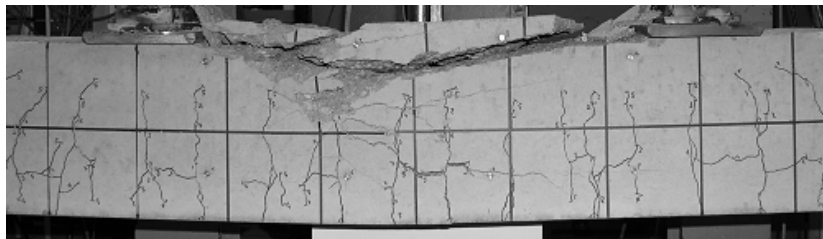
Figure B-164. Crushing of concrete for C2-316-D2-A.
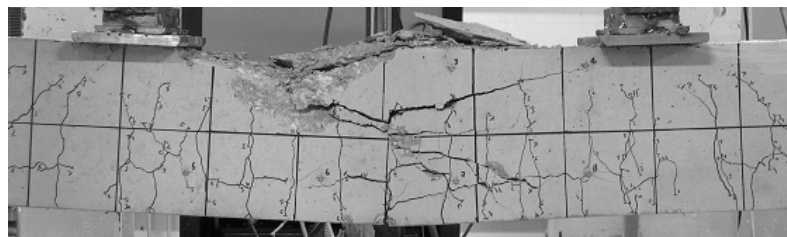
Figure B-165. Crushing of concrete for C2-316-D2-B.

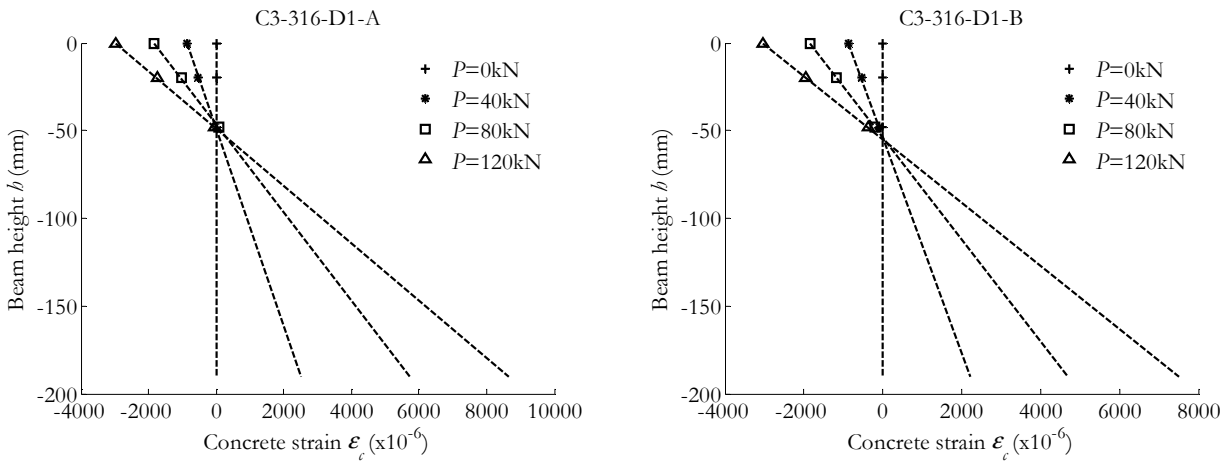## B.12.3. Results at the midspan section
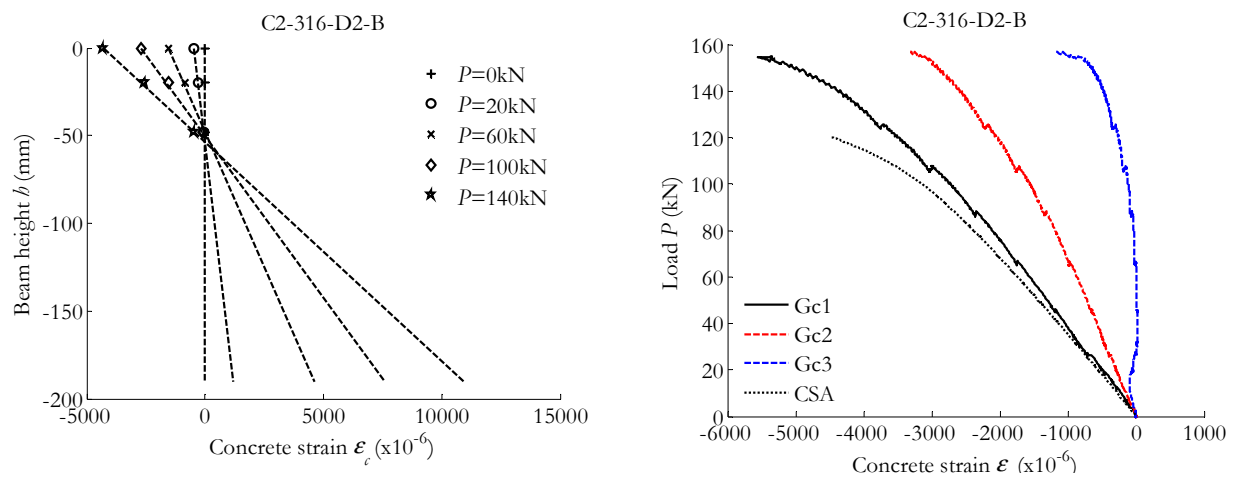
Figure B-166. Concrete strain in the midspan section: Along the height of the beam (left) / Versus the load applied and compared to CSA predictions (right).
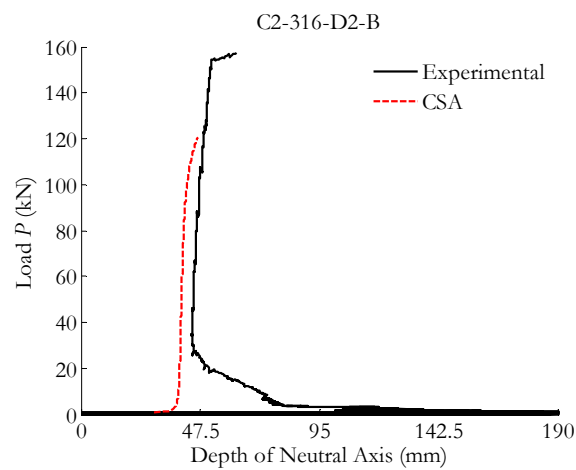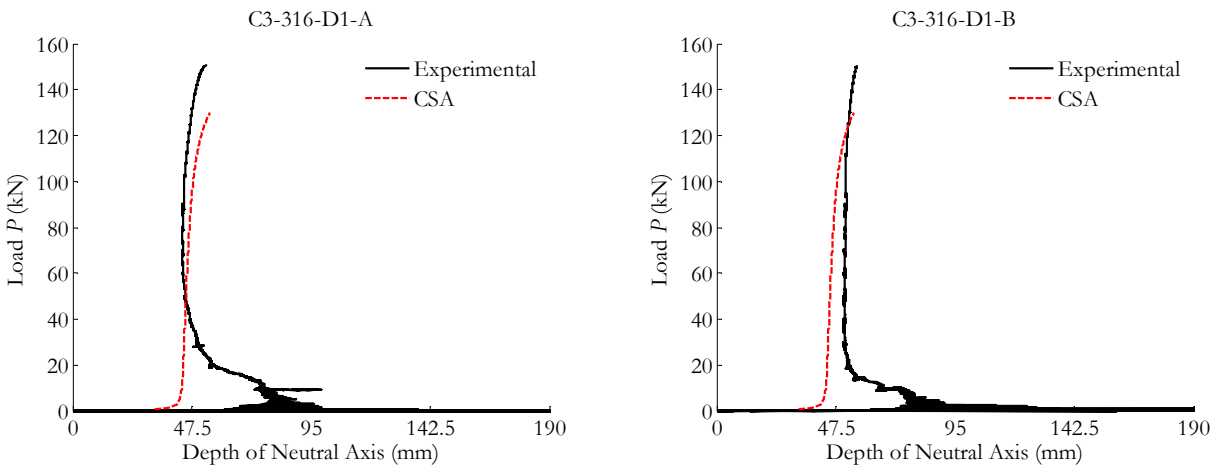

Figure B-167. Neutral axis depth compared to CSA predictions.
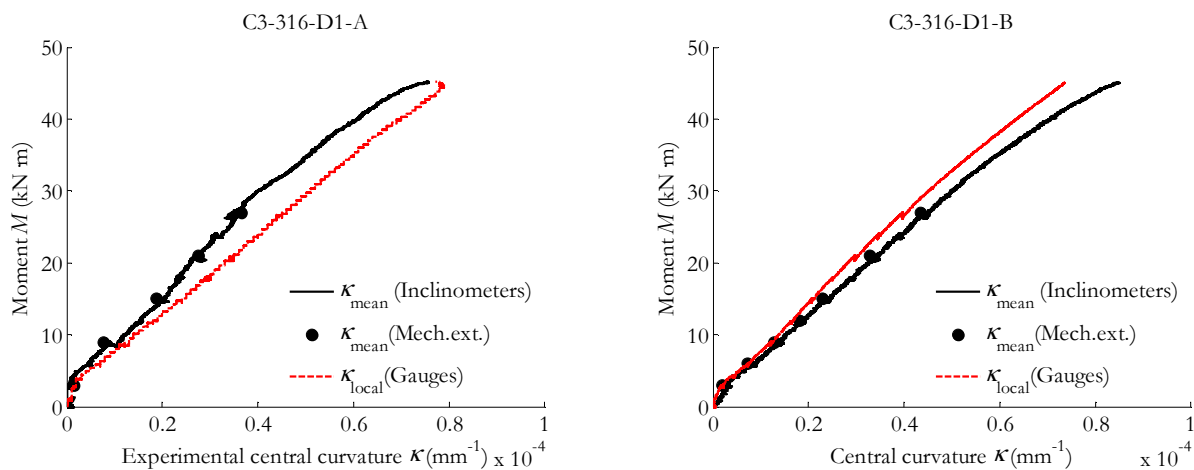
B.12.4. Results at the pure bending zone
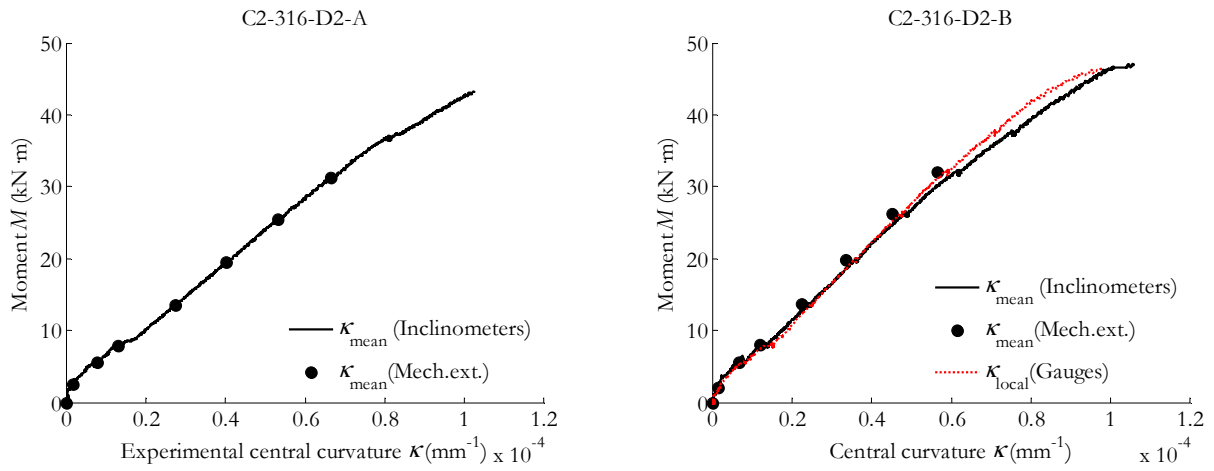
Figure B-168. Experimental moment-curvature from inclinometers, mechanical extensometer and strain gauges on concrete.
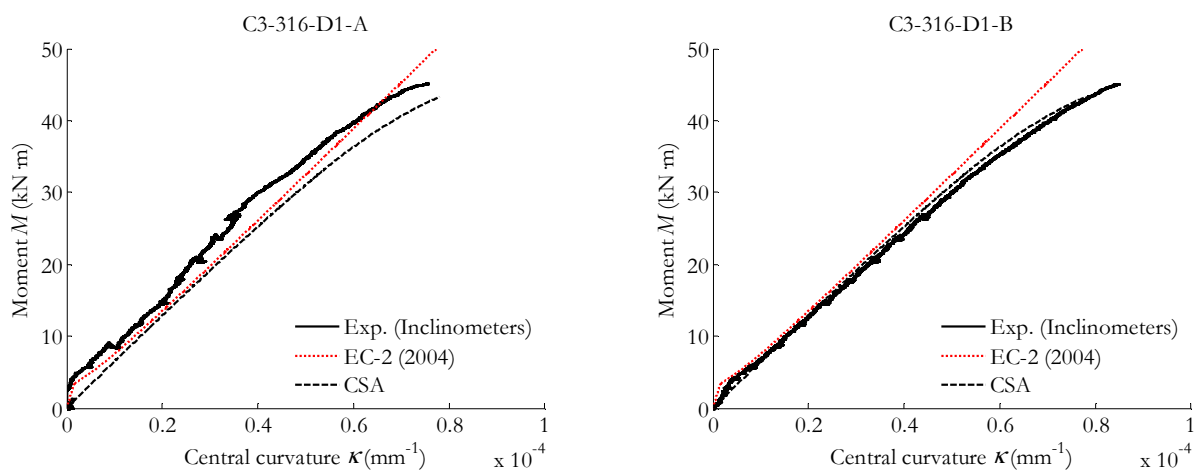

Figure B-169. Experimental moment-curvature compared to Eurocode 2 (2004) and CSA predictions.

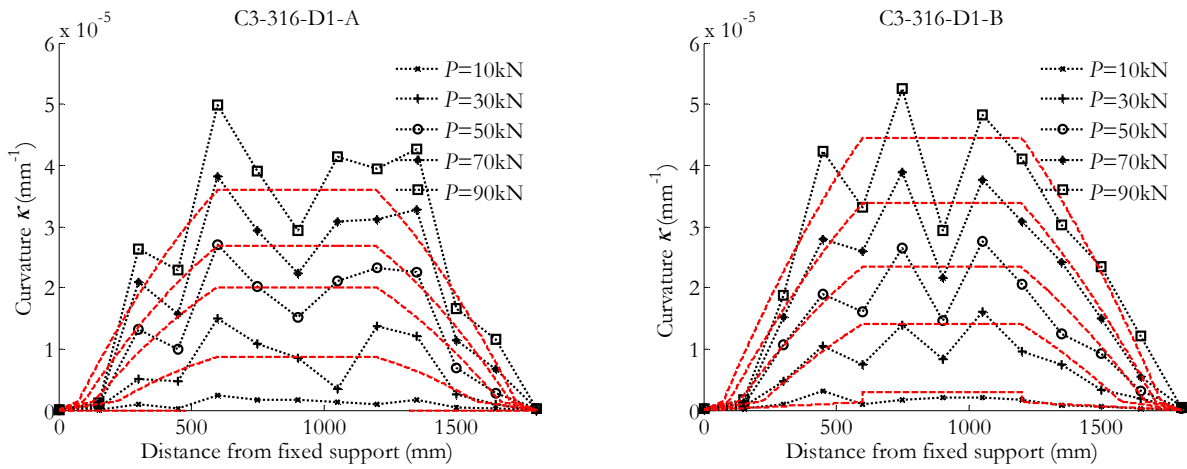## B.12.5. Results of the overall beam behaviour
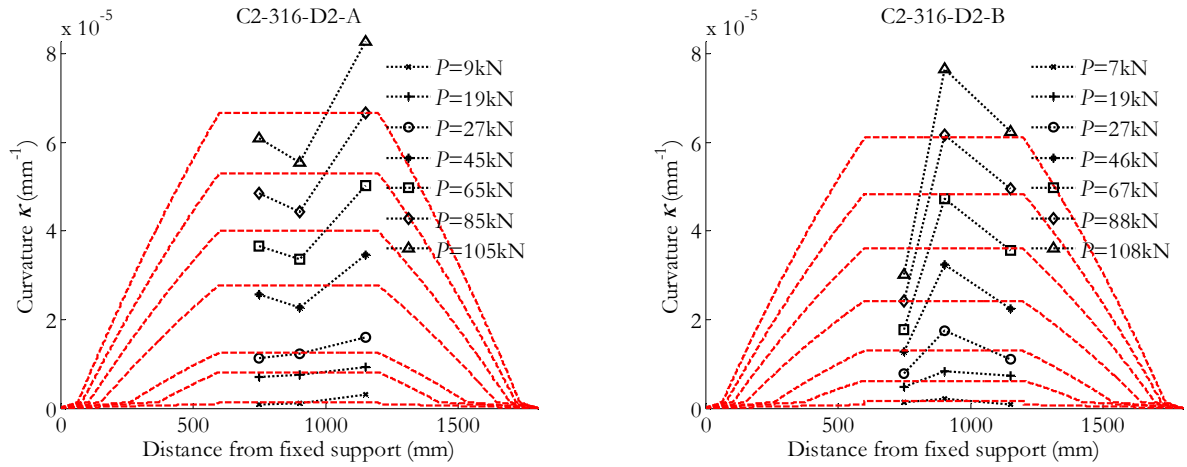
Figure B-170. Curvature along the length of the beam deduced form mechanical extensometer's data (dotted lines) compared to inclinometers' data (dashed lines).
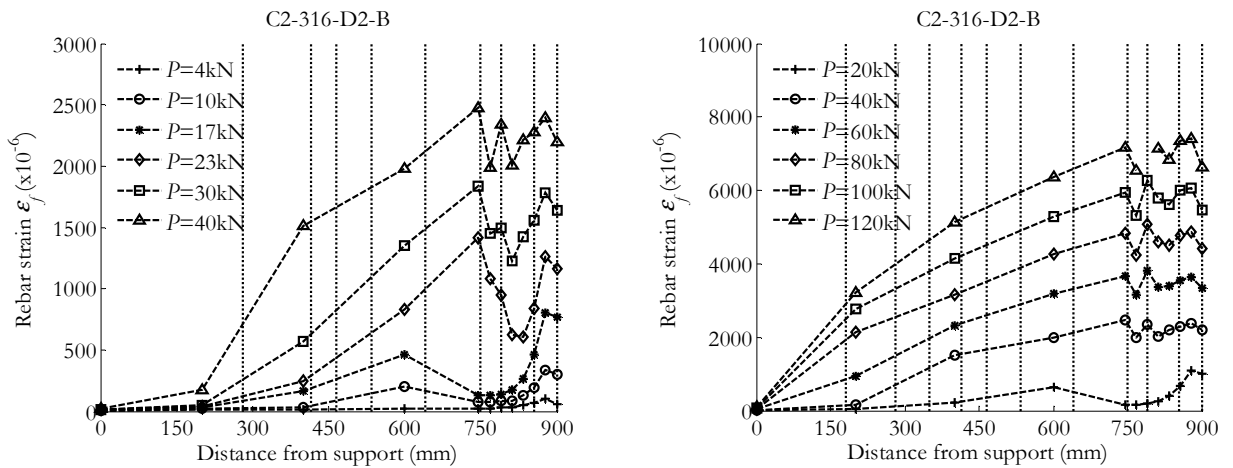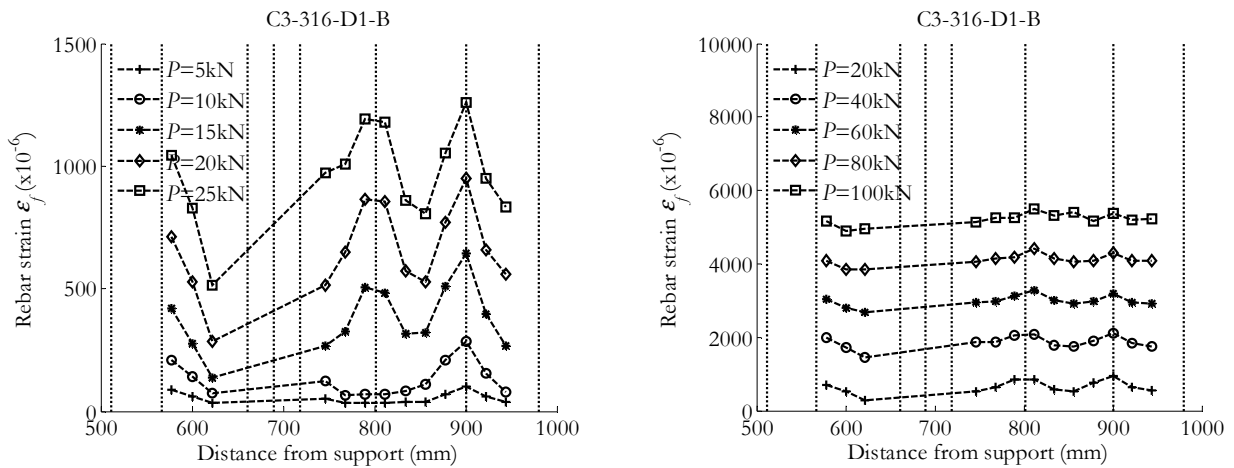

Figure B-171. Evolution of the rebar strain along the length of the beam (left) until service load (right) until failure.

B.12.6. Results on deflection
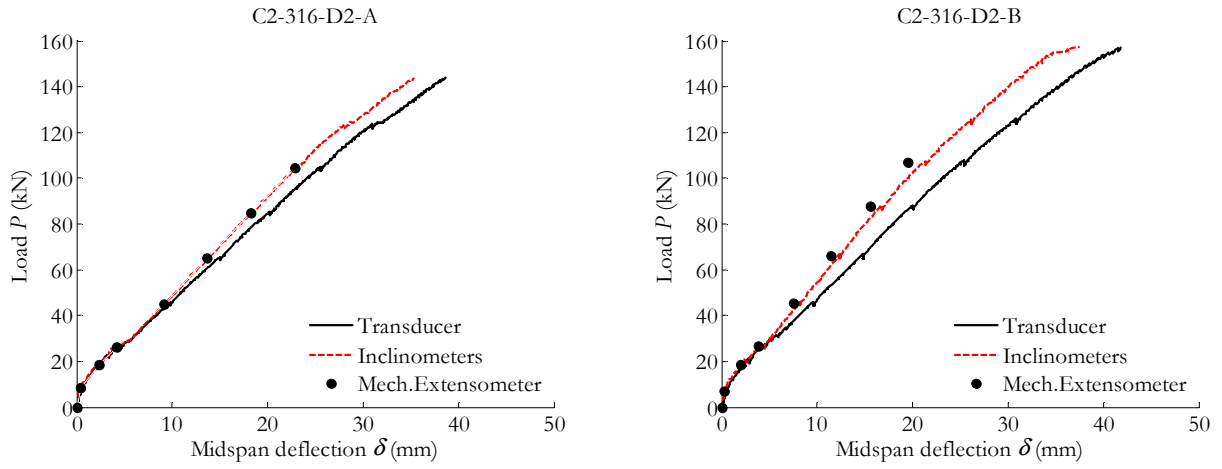
Figure B-172. Experimental midspan deflection.

Figure B-173. Experimental midspan deflection (ultimate load) compared to cracked section
analysis (left) / design codes (right).

Figure B-174. Experimental vs theoretical midspan deflection (service load).

B.12.7. Results on cracking

Figure B-175. Crack pattern (C2-316-D2-A).

Load = 6.7 kN

Load = 18.4 kN

Load = 26.5 kN

Load = 45.4 kN

Load = 66.2 kN

Load = 87.4 kN

Load = 107.0 kN

Failure

Figure B-176. Crack pattern (C2-316-D2-B).

B.13. Results for the C3-316-D1 series

B.13.1. General data

|	C3-316-D1-A	C3-316-D1-B
Cracking load (kN)	11.2	11.5
Load at reaching stabilised cracking phase (kN)	20.0	20.0
Average crack spacing at stabilised cracking phase (mm)	86	89.5
Maximum crack spacing at stabilised cracking phase (mm)	136	102
Minimum crack spacing at stabilised cracking phase (mm)	39	78
Load at which $\sigma_c = 0.45 f_c$ (kN)	38.4	38.9
Load at which w_{max}=0.5-0.7mm (kN)	90.0	90.0
Load at which $\delta = L/250$ (kN)	48.3	46.5
Ultimate load (kN)	150.6	150.3
Ultimate midspan deflection (mm)	28.4	30.8
Ultimate concrete strain ($\times 10^{-6}$)	4342	4309

B.13.2. Failure mode
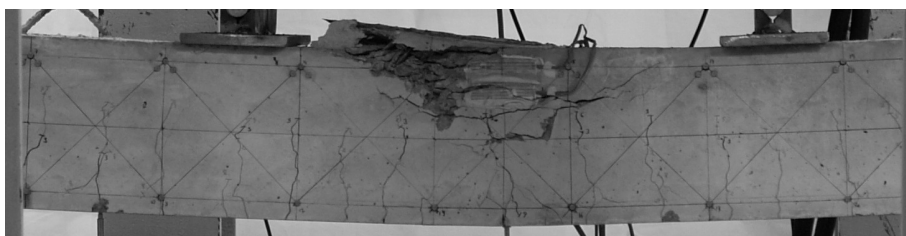
Figure B-177. Crushing of concrete for C3-316-D1-A.
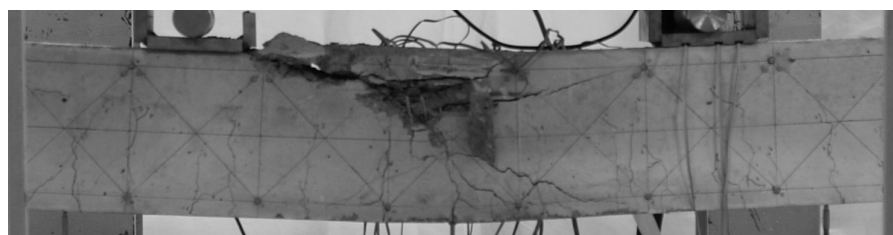
Figure B-178. Crushing of concrete for C3-316-D1-B.

B.13.3. Results at the midspan section

Figure B-179. Concrete strain along the height of the beam at the midspan section.
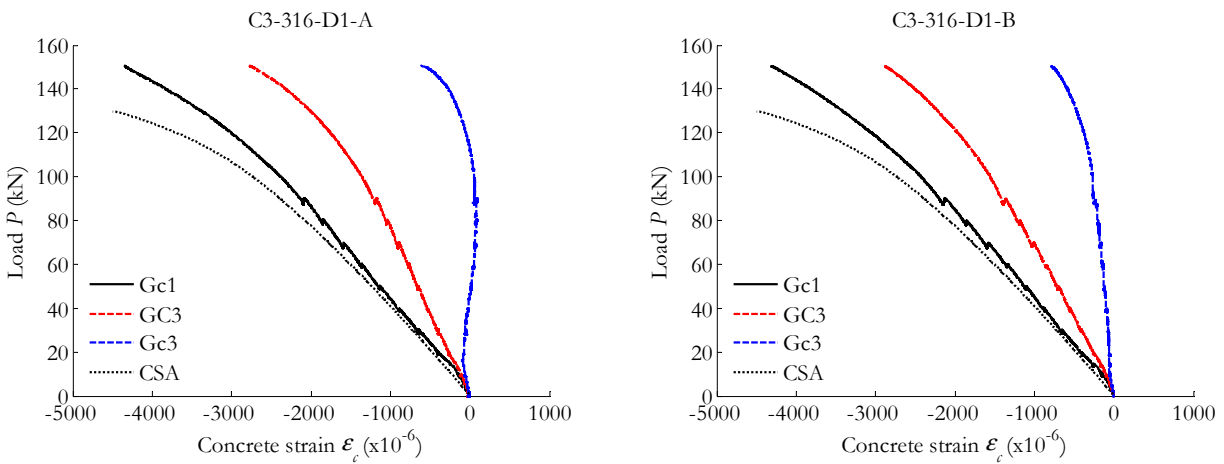
Figure B-180. Concrete strain vs. load at the midspan section.

Figure B-181. Neutral axis depth compared to CSA predictions.

B.13.4. Results at the pure bending zone

Figure B-182. Experimental moment-curvature from inclinometers, mechanical extensometer and strain gauges on concrete.

Figure B-183. Experimental moment-curvature compared to Eurocode 2 (2004) and CSA predictions.

B.13.5. Results of the overall beam behaviour

Figure B-184. Curvature along the length of the beam deduced form mechanical
extensometer's data (dotted lines) compared to inclinometers' data (dashed lines).

Figure B-185. Evolution of the rebar strain along part of the length of the beam (left) until
service load (right) until failure.

B.13.6. Results on deflection
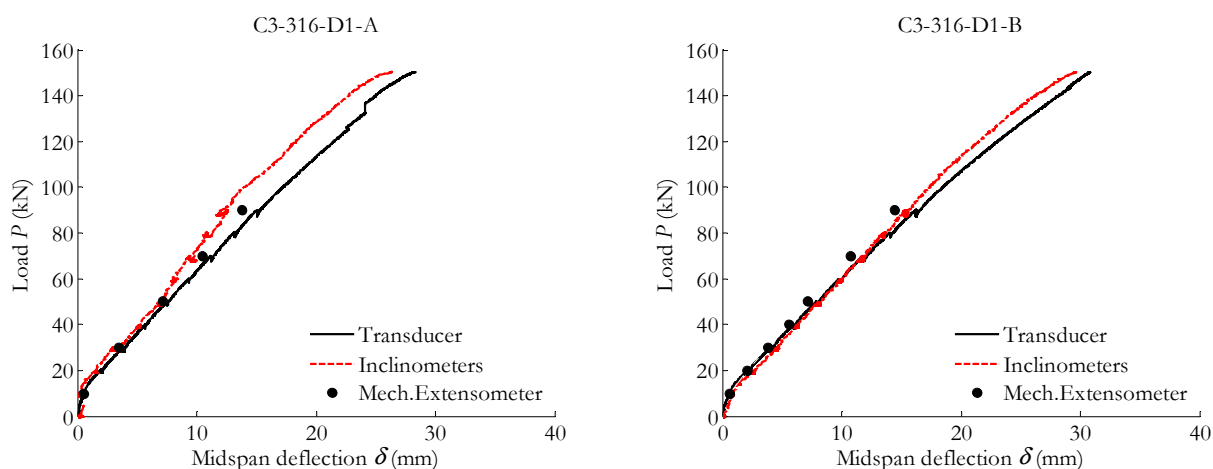
Figure B-186. Experimental midspan deflection.
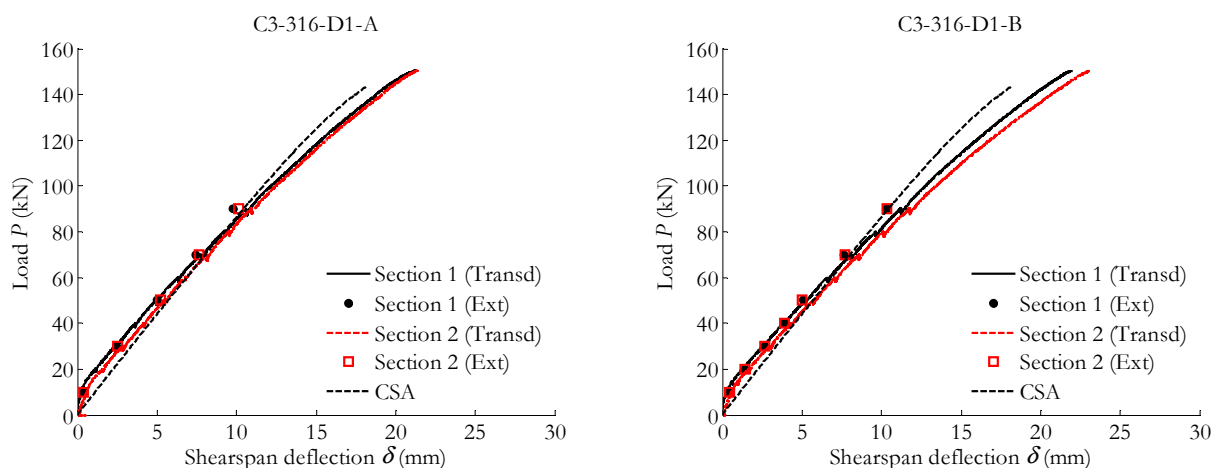
Figure B-187. Experimental shearspan deflection compared to cracked section analysis.
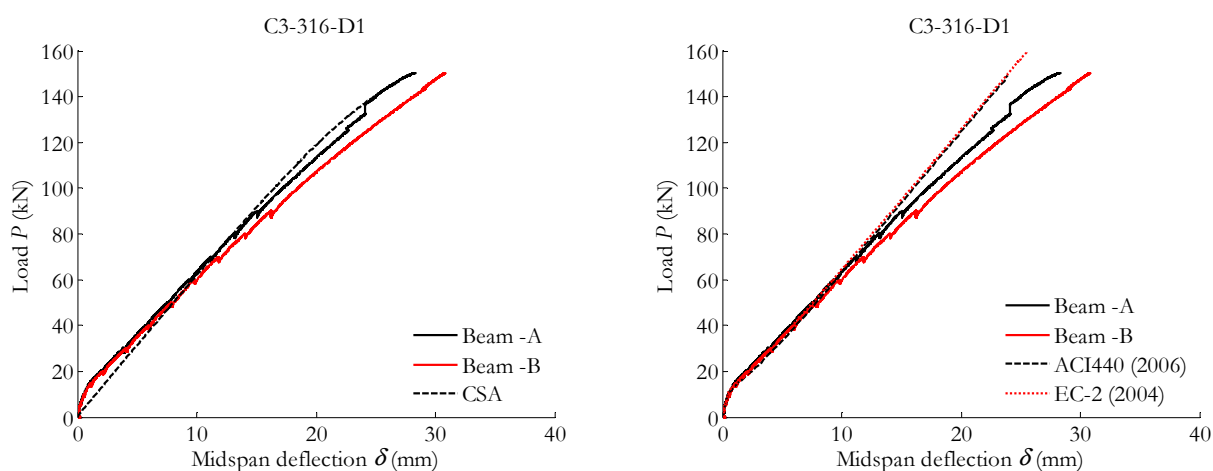
Figure B-188. Experimental midspan deflection (ultimate load) compared to cracked section analysis (left) / design codes (right).
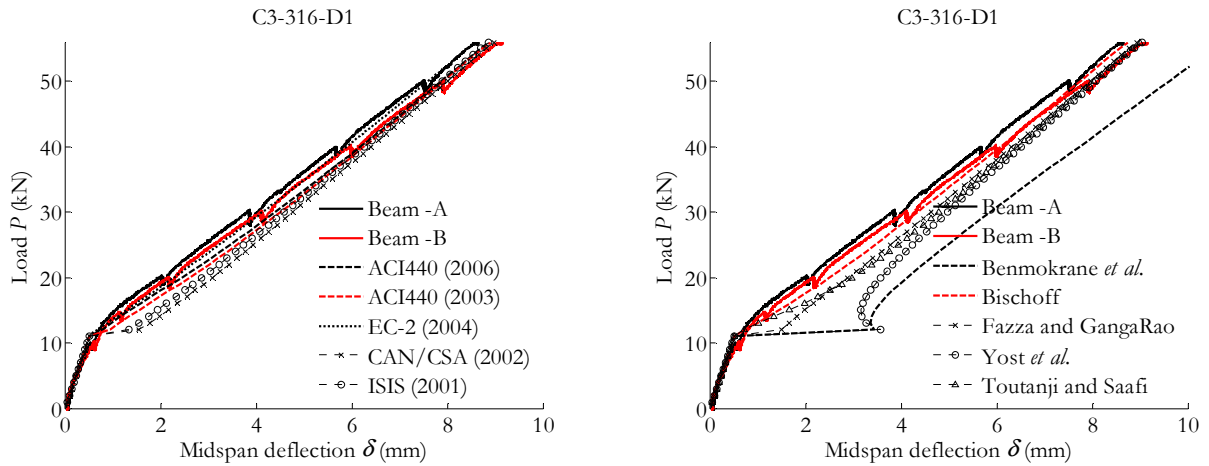
Figure B-189. Experimental vs theoretical midspan deflection (service load).

B.13.7. Results on cracking
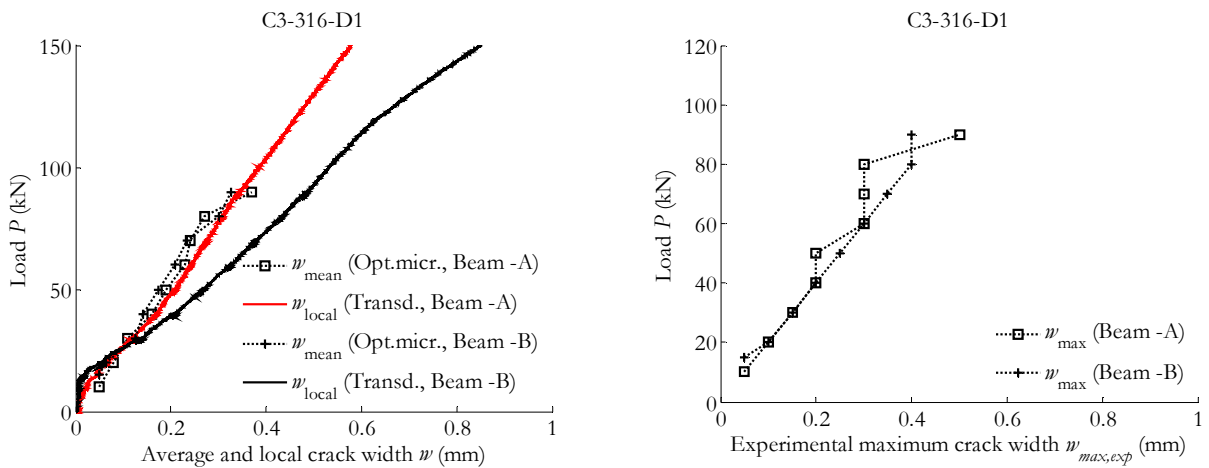
Figure B-190. Experimental crack width: average (left) and maximum (right).
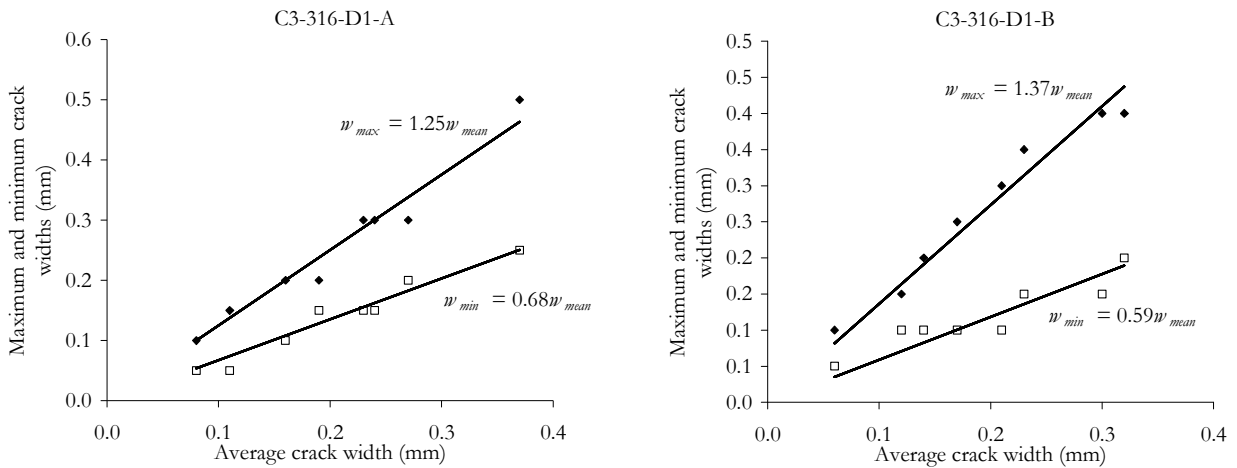
Figure B-191. Experimental crack width: maximum and minimum vs. average.
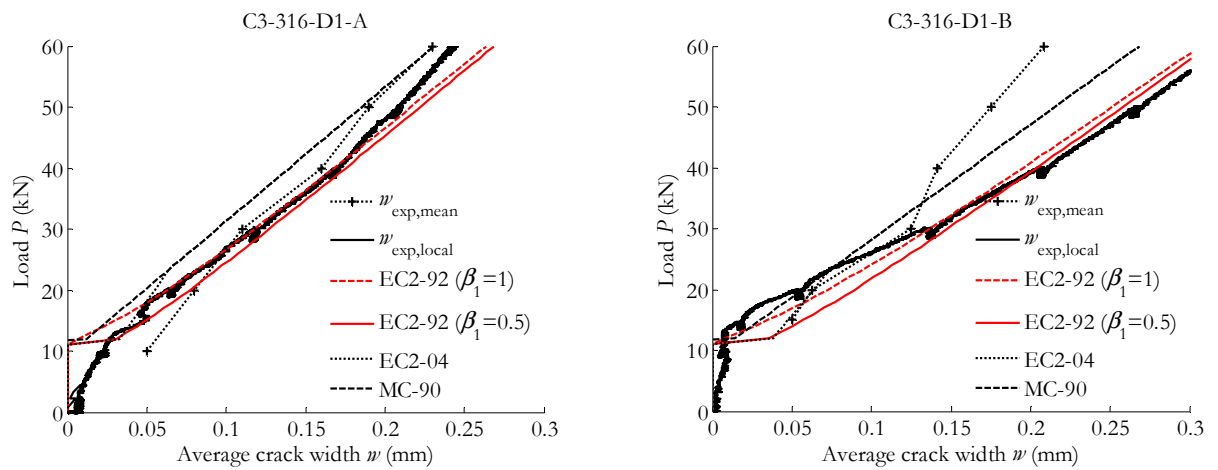
Figure B-192. Experimental vs theoretical average crack width, (left) Beam -A (rigth) Beam – B.
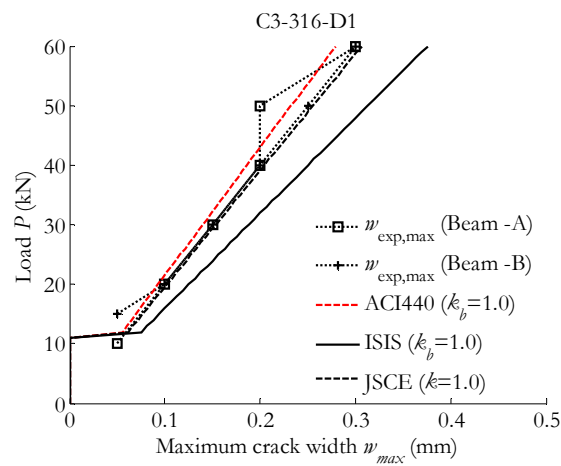
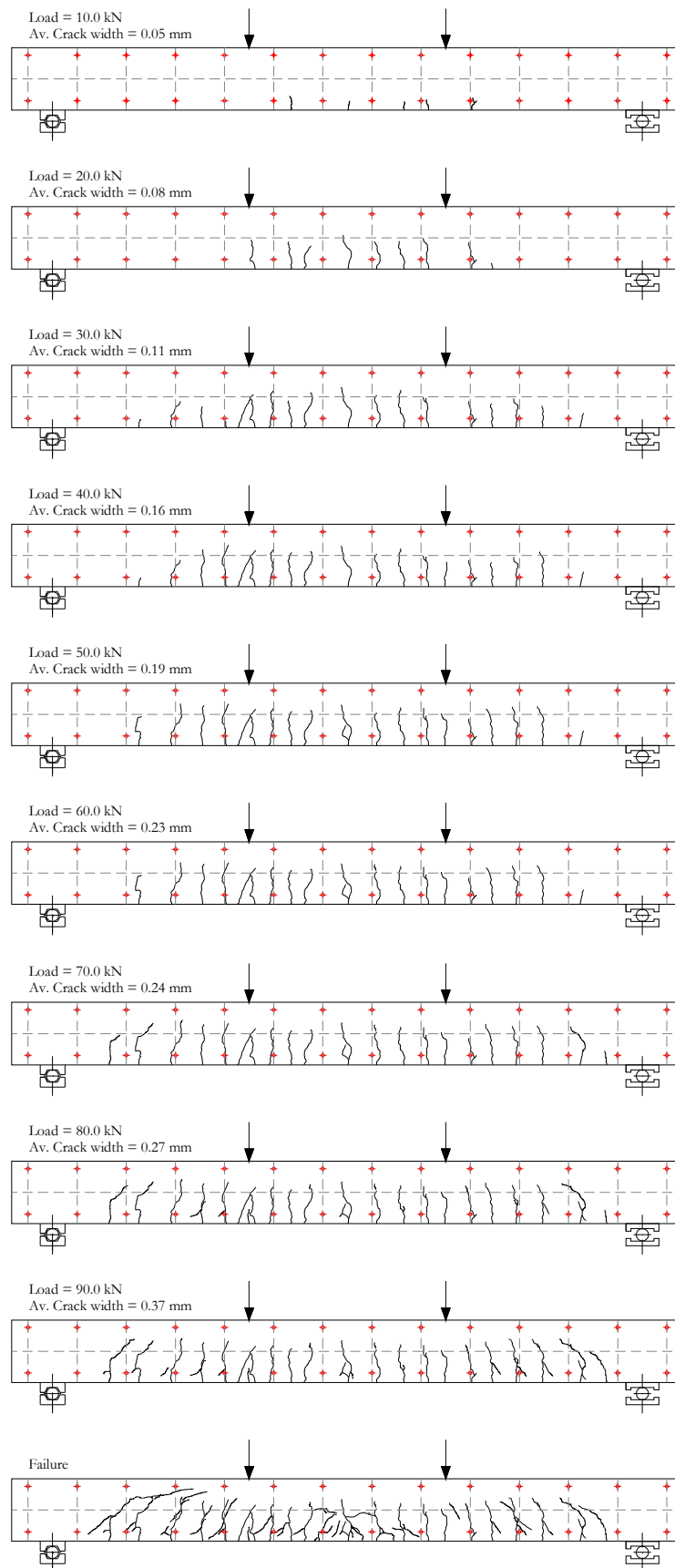Figure B-193. Experimental vs theoretical maximum crack width.
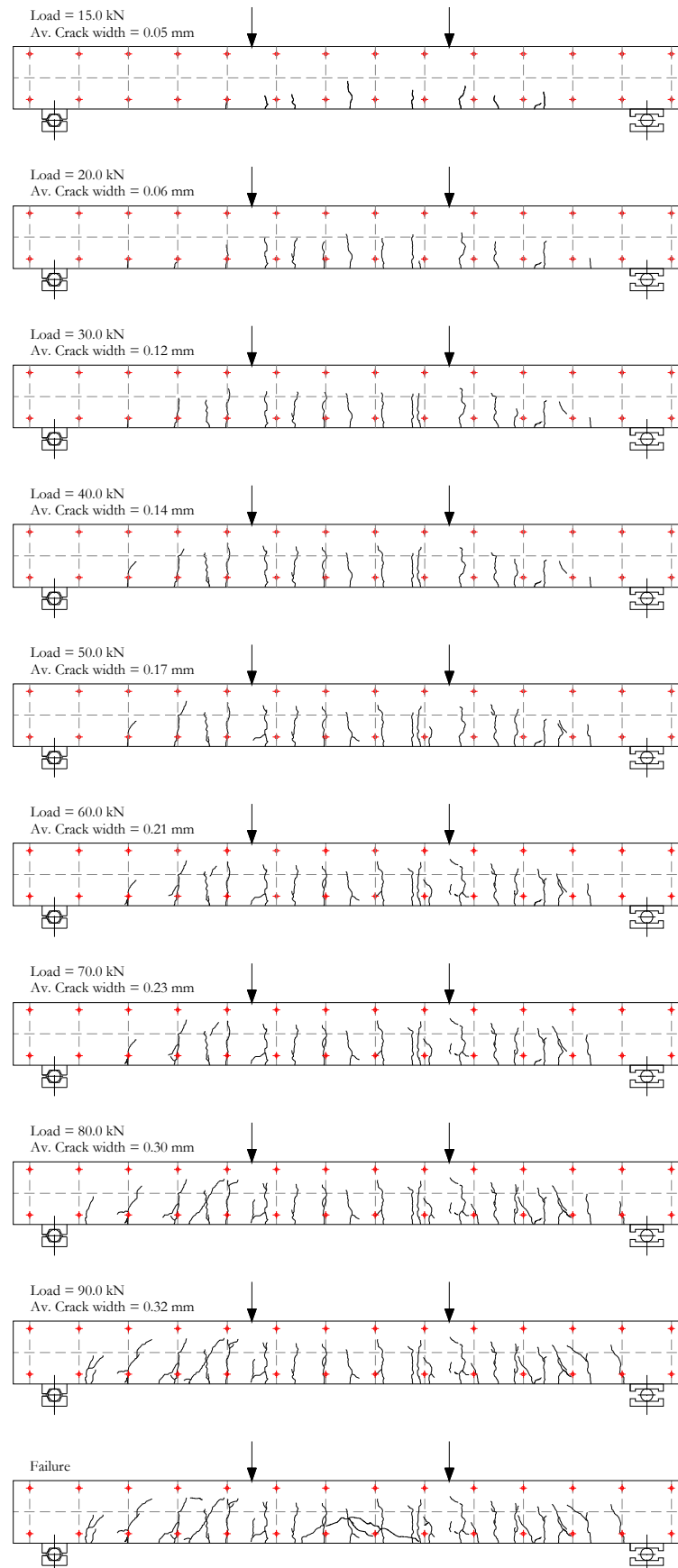
Figure B-194. Crack pattern (C3-316-D1-A).

Load = 15.0 kN
Av. Crack width = 0.05 mm

Load = 20.0 kN
Av. Crack width = 0.06 mm

Load = 30.0 kN
Av. Crack width = 0.12 mm

Load = 40.0 kN
Av. Crack width = 0.14 mm

Load = 50.0 kN
Av. Crack width = 0.17 mm

Load = 60.0 kN
Av. Crack width = 0.21 mm

Load = 70.0 kN
Av. Crack width = 0.23 mm

Load = 80.0 kN
Av. Crack width = 0.30 mm

Load = 90.0 kN
Av. Crack width = 0.32 mm

Failure

Figure B-195. Crack pattern (C3-316-D1-B).

B.14. Results for the C3-212-D1 series (steel RC beam)

B.14.1. General data

	C3-212-D1-S
Cracking load (kN)	12.5
Load at reaching stabilised cracking phase (kN)	30.0
Average crack spacing at stabilised cracking phase (mm)	102
Maximum crack spacing at stabilised cracking phase (mm)	122
Minimum crack spacing at stabilised cracking phase (mm)	93
Load at which $\sigma_c = 0.45\,f_c$ (kN)	41.0
Load at which w_{max}=0.5-0.7mm (kN)	50.0
Load at which $\delta=L/250$ (kN)	42.5
Ultimate load (kN)	62.9
Ultimate midspan deflection (mm)	
Ultimate concrete strain (x10^{-6})	--

B.14.2. Failure mode
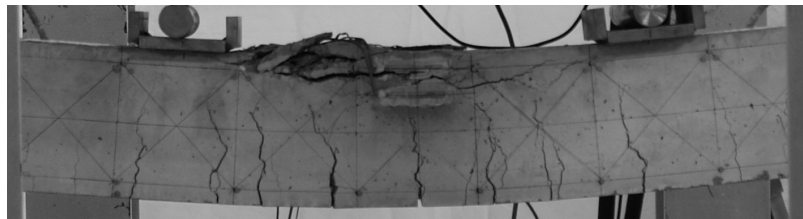
Figure B-196. Crushing of concrete for C3-212-D1-S.

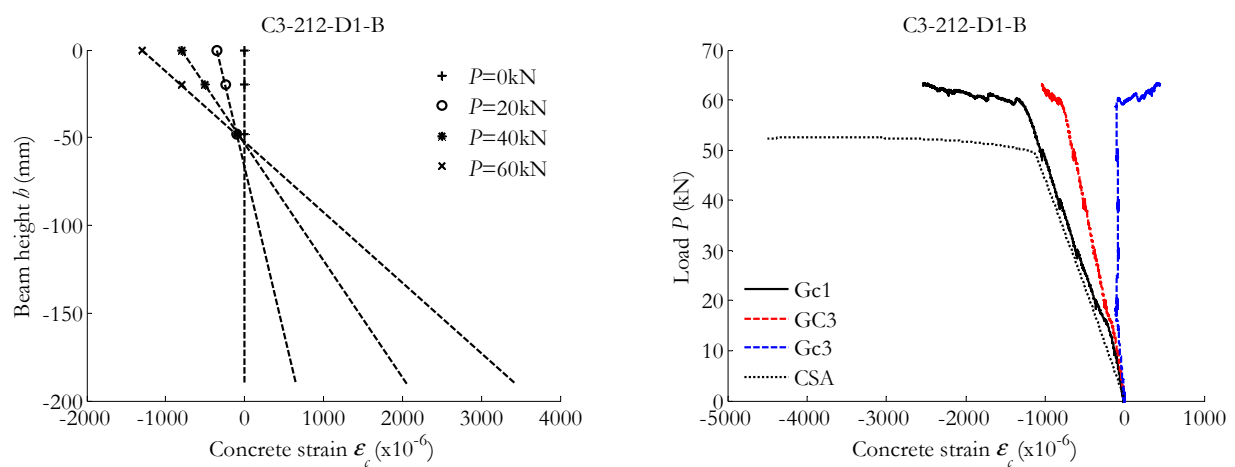### B.14.3. Results at the midspan section

Figure B-197. Concrete strain in the midspan section: Along the height of the beam (left) / Versus the load applied and compared to CSA predictions (right).
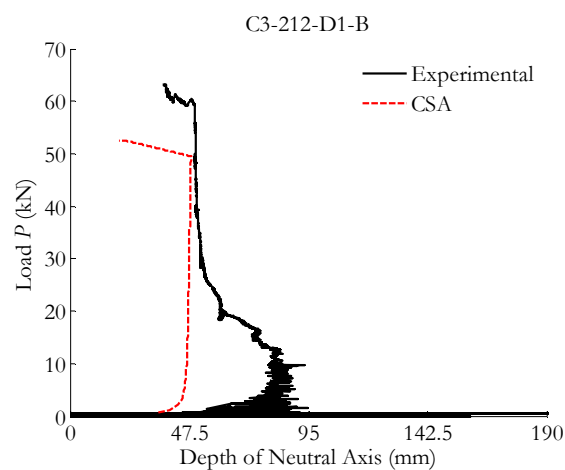

Figure B-198. Neutral axis depth compared to CSA predictions.
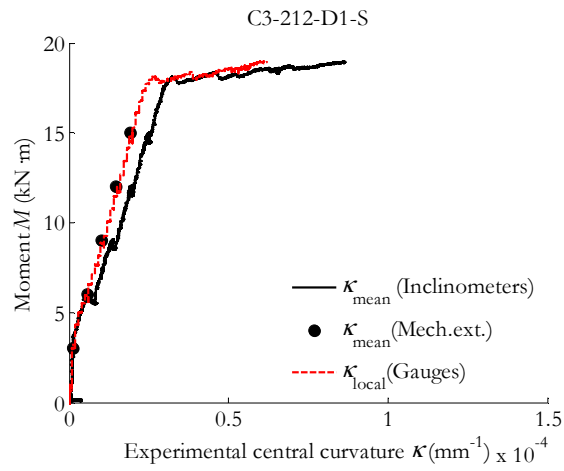
B.14.4. Results at the pure bending zone

Figure B-199. Experimental moment-curvature from inclinometers, mechanical extensometer and strain gauges on concrete.
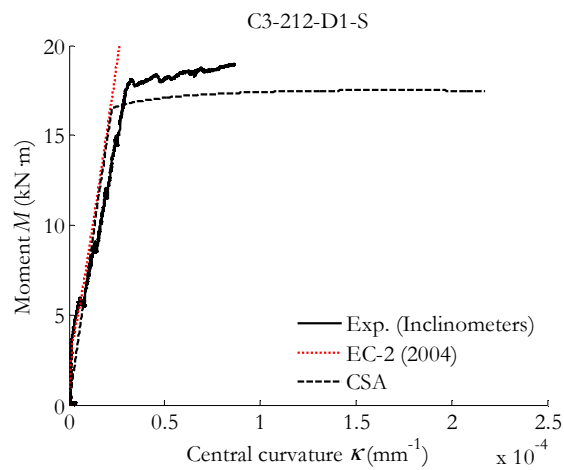

Figure B-200. Experimental moment-curvature from inclinometers compared to Eurocode 2 (2004) and CSA predictions.

B.14.5. Results of the overall beam behaviour
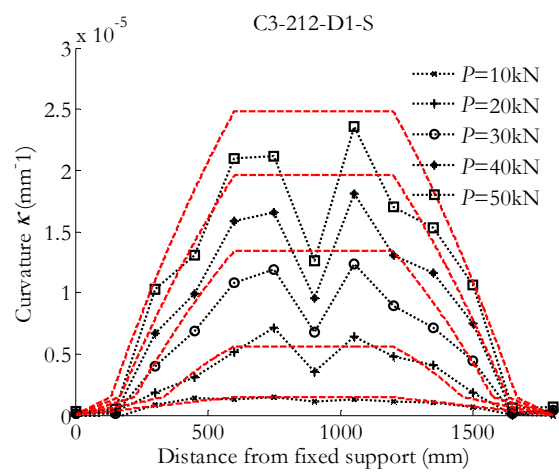
Figure B-201. Curvature along the length of the beam deduced form mechanical extensometer's data (dotted lines) compared to inclinometers' data (dashed lines).

B.14.6. Results on deflection
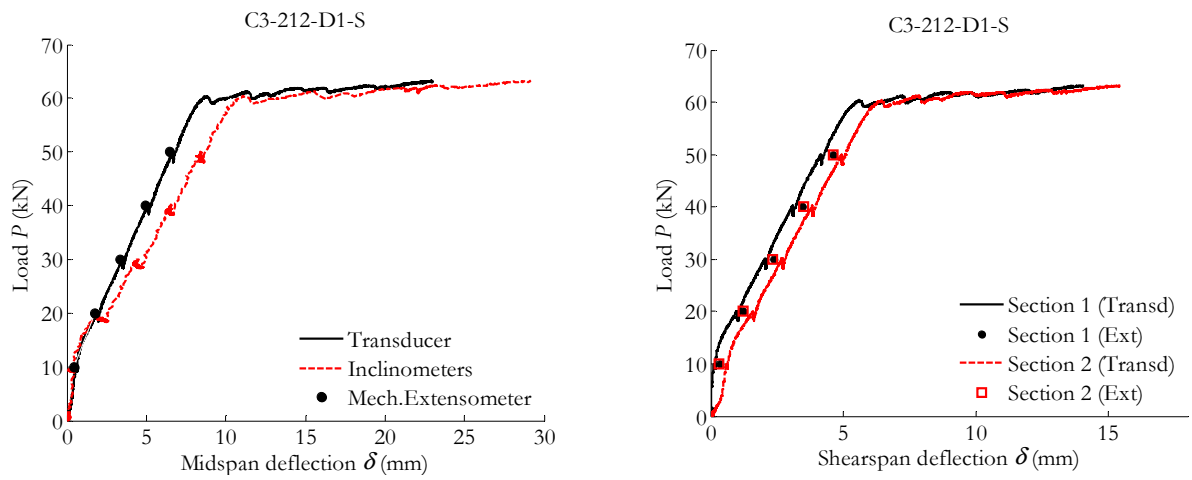
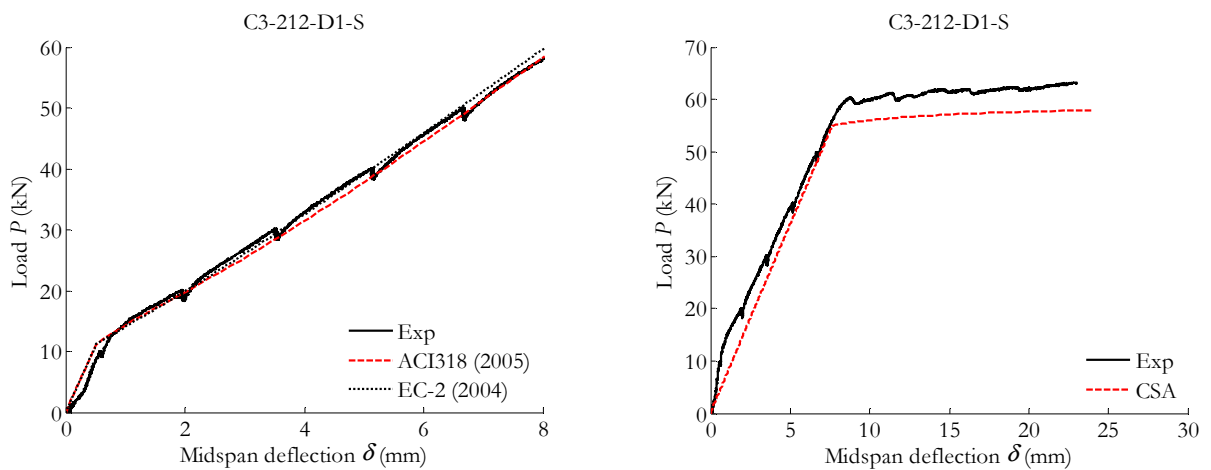Figure B-202. Experimental (left) midspan deflection (right) shearspan deflection,

Figure B-203. Experimental midspan deflection compared to (a) ACI 318 and Eurocode 2
proposals until service load, (b) cracked section analysis until rupture.
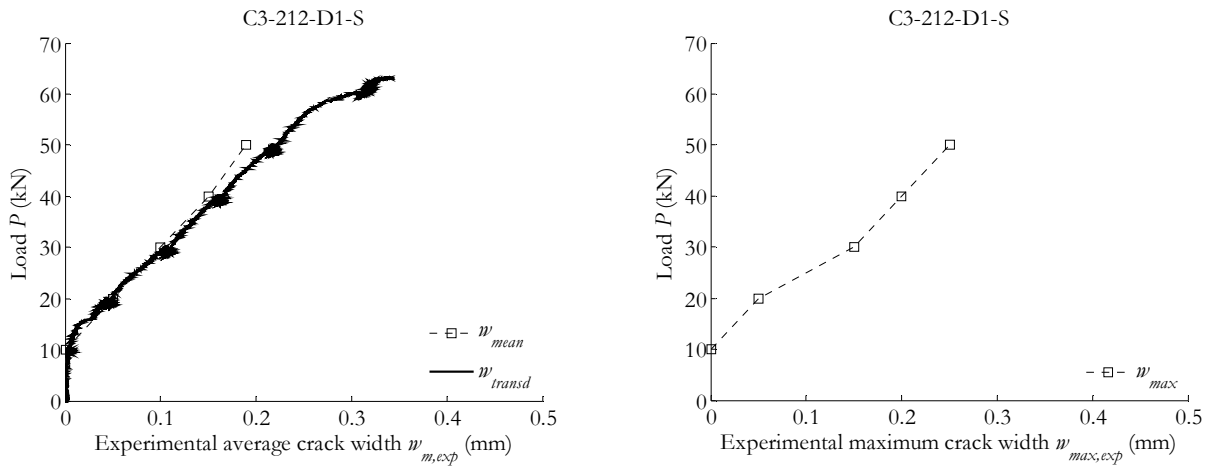
B.14.7. Results on cracking

Figure B-204. Experimental crack width: maximum, average and local at the midspan section.
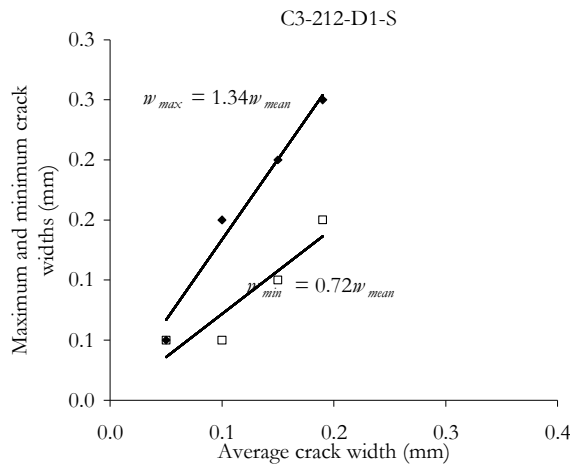

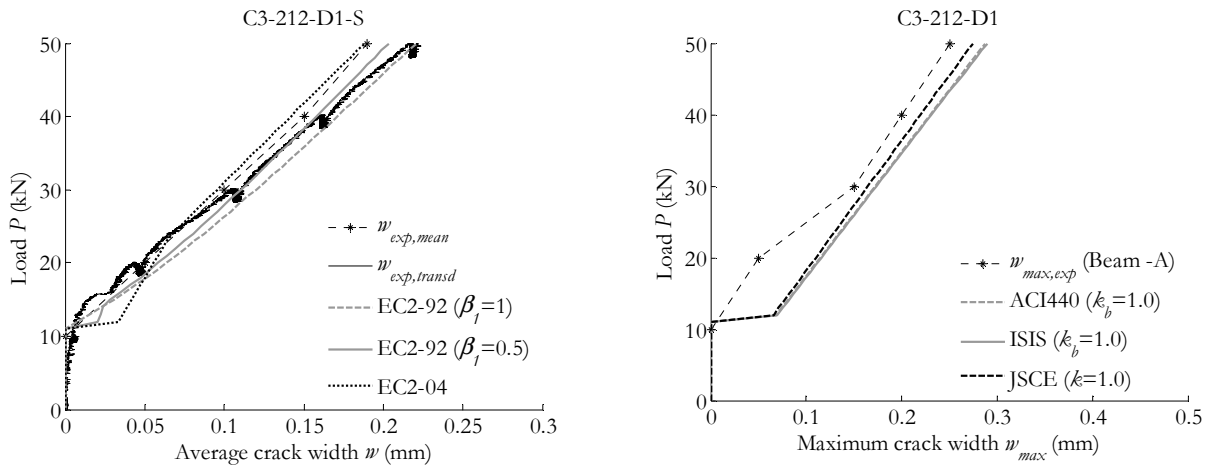Figure B-205. Experimental crack width: maximum and minimum vs. average.

Figure B-206. Experimental vs theoretical crack width, (left) average (right) maximum.

Load = 10.0 kN
Av. Crack width = 0.00 mm

Load = 20.0 kN
Av. Crack width = 0.05 mm

Load = 30.0 kN
Av. Crack width = 0.10 mm

Load = 40.0 kN
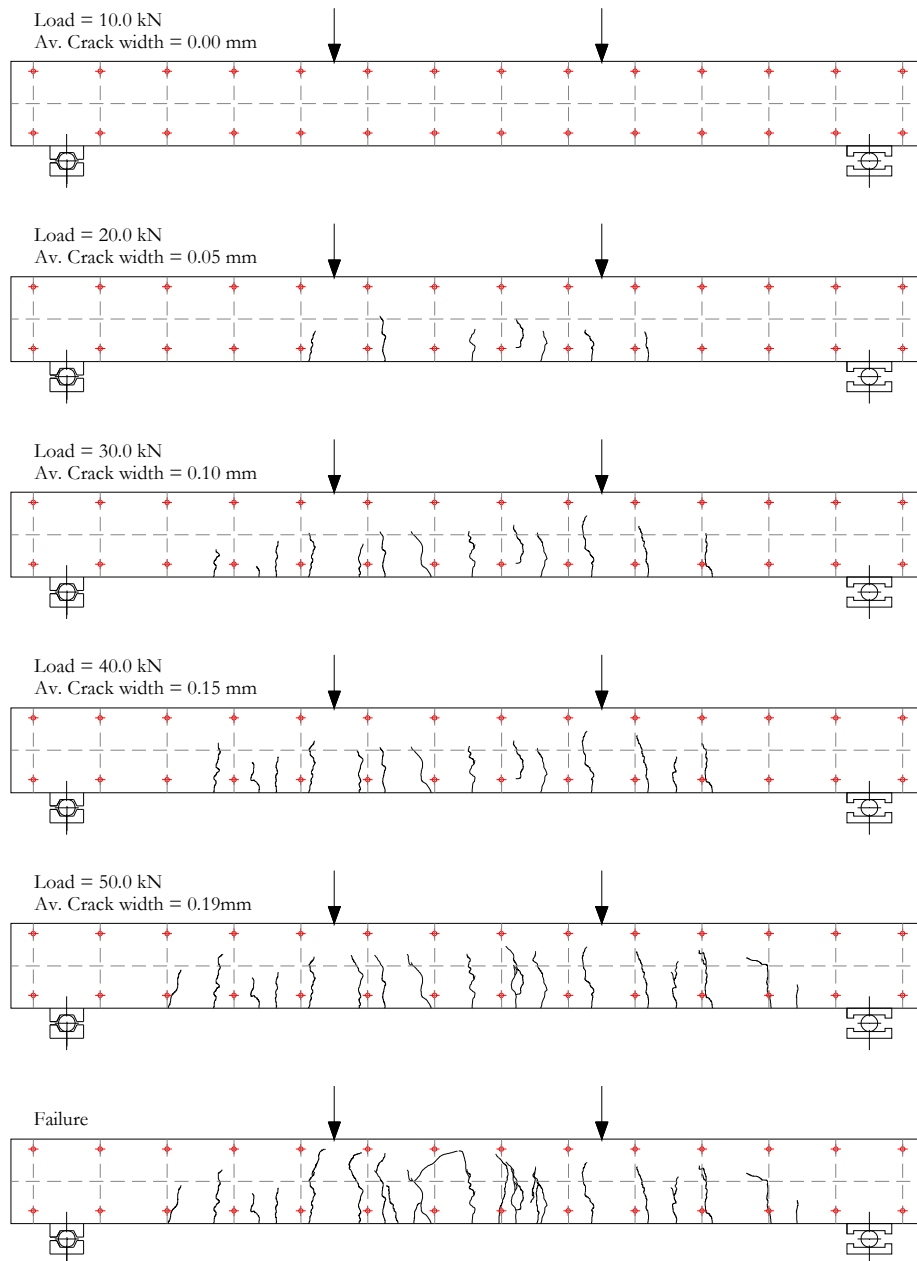Av. Crack width = 0.15 mm

Load = 50.0 kN
Av. Crack width = 0.19mm

Failure

Figure B-207. Crack pattern (C3-212-D1-S).